U.S. DEPARTMENT OF ENERGY

PNNL-21812, Rev. 1

Prepared for the U.S. Department of Energy
under Contract DE-AC05-76RL01830

# Integrated Disposal Facility FY 2012 Glass Testing Summary Report

EM Pierce
SN Kerisit
EJ Krogstad
SD Burton
BN Bjornstad
VL Freedman
KJ Cantrell
MM Valenta
JV Crum
JH Westsik, Jr.

March 2013

Pacific Northwest
NATIONAL LABORATORY

*Proudly Operated by* Battelle *Since 1965*

# MEMORANDUM

Pacific Northwest NATIONAL LABORATORY

| | | | |
|---|---|---|---|
| Date: | **August 23, 2022** | Memo No.: | **LTR-IGTP-017** |
| To: | **Whom It May Concern** | Project No.: | **79185** |
| From: | **Asmussen, Matthew** | Internal Distribution: | **File/LB** |
| Subject: | **PNNL-21812 Rev. 1. Erratum 2** | | |

**Ref.**: Erratum to PNNL-21812 Rev.1.0. Pierce et al. *Integrated Disposal Facility FY 2012 Glass Testing Summary Report* March 2013

To Whom It May Concern:

Report PNNL-21812 contains simulations of glass corrosion in which a value for the specific surface area of hydrated glass (LAW-H or LAWA44-H) was incorrectly transcribed from prior reports.

The following errors are found in these sections, tables, figures:

1. Page 7.14 describes the portion of the model where the transcription error was made for the specific surface area of LAWA44-H.
2. Sections 7.4 and 7.5 contain simulation results from STOMP that contain the incorrect specific surface area value. This includes:
    a. Figure 7.2, 7.3, 7.4, 7.5, 7.6, 7.7, 7.8, 7.9, 7.10, and 7.11.

Based on the simulations performed to evaluate the impact of the transcription error, the impact was minor (<0.2% overall release at 10,000 years) and it was deemed that there is no need to correct previous modeling data where the transcription error was present. A summary of the transcription error and the limited impact on simulation results can be found in a separate report (below).

R.M. Asmussen, Song, X. 2022. The Impact of Specific Surface Area on Reactive Transport Glass Modeling. PNNL-32974. Pacific Northwest National Laboratory, Richland, WA.

RMA

MEMORANDUM

Pacific Northwest NATIONAL LABORATORY

Proudly Operated by Battelle Since 1965

| | | | |
|---|---|---|---|
| Date: | **September 2, 2016** | Project No.: | |
| To: | **PNNL-21812, Rev 1.0** | Internal Distribution: | **File/LB** |
| From: | **Gary L. Smith** | | |
| Subject: | **Erratum** | | |

# Erratum

This report refers to or contains $K_g$ values for glasses LAWA44, LAWB45 and LAWC22 affected by calculations errors as identified by Papathanassiu et al. (2011)[1]

The corrected $K_g$ values are reported in an erratum included in the revised version of the original report. The revised report can be referenced as follows:

*Pierce E. M. et al. (2004) Waste Form Release Data Package for the 2005 Integrated Disposal Facility Performance Assessment.* ***PNNL-14805 Rev. 0 Erratum****. Pacific Northwest National Laboratory, Richland, WA, USA.*

[1] Papathanassiu A. et al. (2011) ILAW Glass Testing for Disposal at IDF: Phase 1 Testing. **VSL-11R2270-1**. Vitreous State Laboratory, Catholic University of America, Washington, DC, USA.

## DISCLAIMER



PACIFIC NORTHWEST NATIONAL LABORATORY
*operated by*
BATTELLE
*for the*
UNITED STATES DEPARTMENT OF ENERGY
*under Contract DE-AC05-76RL01830*

**Printed in the United States of America**

**Available to DOE and DOE contractors from the**
**Office of Scientific and Technical Information,**
**P.O. Box 62, Oak Ridge, TN 37831-0062;**
**ph: (865) 576-8401**
**fax: (865) 576-5728**
**email: reports@adonis.osti.gov**

**Available to the public from the National Technical Information Service**
**5301 Shawnee Rd., Alexandria, VA 22312**
**ph: (800) 553-NTIS (6847)**
**email: orders@ntis.gov <http://www.ntis.gov/about/form.aspx>**
**Online ordering: http://www.ntis.gov**

This document was printed on recycled paper.
(8/2010)

# Integrated Disposal Facility Glass Testing FY 2012 Summary Report

EM Pierce[1]
SN Kerisit
EJ Krogstad
SD Burton
BN Bjornstad
VL Freedman
KJ Cantrell
MM Valenta
JV Crum
JH Westsik, Jr.

March 2013

Prepared for
the U.S. Department of Energy
under Contract DE-AC05-76RL01830

Pacific Northwest National Laboratory
Richland, Washington 99352

[1]Oak Ridge National Laboratory, Oak Ridge, Tennessee.

# Executive Summary

Pacific Northwest National Laboratory (PNNL) was contracted by Washington River Protection Solutions, LLC, to provide the technical basis for estimating radionuclide release from the engineered portion of the disposal facility for Hanford immobilized low-activity waste (ILAW) (e.g., source term). Vitrifying the low-activity waste (LAW) at Hanford is expected to generate over $1.6 \times 10^5$ $m^3$ of glass (Certa and Wells 2010). The volume of ILAW at Hanford is the largest in the U.S. Department of Energy (DOE) complex and is one of the largest inventories of long-lived radionuclides (approximately $8.9 \times 10^{14}$ Bq total activity), principally $^{99}Tc$ ($t_{1/2} = 2.1 \times 10^5$ years), planned for disposal in a low-level waste facility. Before the ILAW can be disposed, DOE must conduct a performance assessment (PA) for the Integrated Disposal Facility (IDF) that describes the long-term impacts of the disposal facility on public health and environmental resources. As part of the ILAW glass testing program, PNNL is implementing a strategy, consisting of experimentation and modeling, to provide the technical basis for estimating radionuclide release from the glass waste form in support of future IDF PAs. The purpose of this report is to summarize the progress made in fiscal year (FY) 2012 toward implementing the strategy with the goal of developing an understanding of the long-term corrosion behavior of LAW glasses.

IDF PAs use a reactive transport simulator to perform the near-field calculations of radionuclide releases from the corroding glass. The STOMP (Subsurface Transport Over Multiple Phases) and eSTOMP simulators are being developed to support future PAs. Because the eSTOMP simulator is highly scalable, it is ideally suited for running waste-form calculations since long run times can result when they are executed with a serial code. During FY 2012, code development for eSTOMP, the parallel version of the STOMP computer code, included updating eSTOMP input structure and output capabilities to match those in (serial) STOMP. Key code capabilities that were incorporated into the code include: 1) the ability to hold a constant value for species concentrations; 2) the addition of diffusion models for aqueous species transport; 3) the addition of user-defined initial volume fractions for solid phases; and 4) the ability to scale reactive surface area linearly with water saturation. Other updates included the ability to output the kinetic rates and solid-phase surface areas already calculated internally in eSTOMP and the ability to calculate porosity and permeability changes as a result of precipitation and dissolution reactions. Testing for the reactive geochemical transport updates is also nearly complete. Small-scale differences between STOMP and eSTOMP still need to be resolved when using fixed species concentrations. Preparations for the benchmark simulations were also made.

The IDF PA modeling work must account for the long-term corrosion rate of the ILAW glasses. In FY 2012, the pressurized unsaturated flow (PUF) tests being conducted on three prototypic ILAW glasses: ORPLG9, ORPLB2, and ORPLF7 were terminated. The reacted glass from each experiment was collected and analyzed with scanning electron microscopy (SEM) with energy dispersive spectroscopy (EDS) and powder X-ray diffraction (XRD). Results show that a 10-µm-thick alteration layer developed on the surface of the reacted ORPLG9 glass. The EDS elemental profiles for the analyzed ORPLG9 glass grains, beginning at the pristine glass, show that Si decreases slightly in the first alteration layer; then it increases in the second alteration layer and further increases in the outer clay-like layer. Aluminum gradually increases from the glass to the outer layer. Calcium remains similar in all the layers except the second alteration layer where it is higher. Zirconium steps up in concentration in each alteration layer then significantly drops in the outer clay-like layer. Magnesium and zinc both remain constant, then increase in the clay-like layer. Alkali elements, Na and K, and B decrease significantly at the glass-to-alteration layer interface and continue to decrease in concentration from the second alteration

to the outer layer. The XRD results illustrated that the reacted glass was mainly amorphous and only contained a minor amount of crystalline phases. Both the SEM-EDS and XRD results are consistent with LAW glass samples previous reacted in PUF experiments. Solution concentration results are provided for the three glasses over the duration of the test. Although these glasses performed similarly to other ILAW glasses, the reason for elevated K release (a minor element) from ORPLB2 and ORPLF7 is unclear. Additional data interpretation from the solid-phase analysis of the reacted glass grains from ORPLB2 and ORPLF7 should provide additional insights into why this is occurring and these results will be discussed in future reports.

In addition to PUF results, the STOMP and eSTOMP codes also use as input the results from product consistency experiments to develop a series of reaction networks that predict which secondary phases may be forming during the weathering of the ILAW glasses. Geochemical modeling using Geochemist's Workbench®[1] was conducted to determine the reaction network. Product consistency test (PCT) data for 128 glasses from FY 2011 and another 10 in FY 2012 were used in the geochemical modeling effort. For a majority of these glasses, a secondary-phase reaction network previously developed for ILAW glass sample LAWA44 produced good model fits. Notable exceptions were predictions for K and Li solution concentrations in equilibrium with weathered glass. Developing a consistent reaction network of secondary phases for glass samples that had relatively high concentrations of Ca and Li and relatively low concentrations of Na was not feasible, probably due to the inability to identify and model the phase(s) that control Li concentrations and the lack of actual thermodynamic data for K-chabazite. Lastly, additional modeling work was conducted to evaluate whether or not sepiolite [$Mg_4Si_6O_{15}(OH)_2 \bullet H_2O$] or clinochlore [$Mg_5Al_2Si_3O_{10}(OH)_8$] controlled $Mg^{2+}$ concentrations in solution. The results proved to be inconclusive, suggesting that either phase could potentially control Mg concentrations. The inability to adequately model glass corrosion under these circumstances is not expected to be particularly problematic. This is because most ILAW glasses contain high concentrations of Na relative to Ca and Li, and Mg concentrations in ILAW glass are relatively low. Because Mg concentrations in ILAW glass are low, the formation of either sepiolite or clinochlore will not significantly impact the formation of the other major secondary phases.

Field-testing allows the IDF-PA program to obtain independent and site relevant data on glass corrosion at a length-scale more relevant to the actual disposal system. From 2002 through 2010, two ILAW glasses (LAWA44 and HAN28F) were buried at the Field Lysimeter Test Facility at the 200 Area on the Hanford Site. Over the 8 years of the test, the lysimeters were wetted with untreated Columbia River water through an overhead irrigation system in addition to natural precipitation. In the summer of 2010, the three lysimeters were excavated and the buried glass samples and cores of the surrounding soils were obtained for characterization. In 2012, selected glasses were examined by scanning electron microscopy at the glass/soil interface. Soil samples from the cores surrounding the glass were subjected to 1:1 water extracts and the extracts were chemically analyzed. Soil samples immediately adjacent to the glass were also characterized by X-ray diffraction. Analysis of soil and glass samples taken after dismantling the field lysimeter test illustrated a pronounced enrichment of rhenium and molybdenum in samples from all three lysimeters. The enrichment probably originated from the glass logs. XRD and SEM analysis revealed that iron-rich alloy globules were present at the glass-sediment interface, suggesting that a Fe-rich solid formed during the glass fabrication process and then was buried with the glass samples. These Fe-rich globules were also enriched in Re and Mo, suggesting these two elements partitioned to this phase that formed during glass manufacturing processes. These results suggest that the

[1] The Geochemist's Workbench is a registered trademark of the Board of Trustees of the University of Illinois.

pronounced Re and Mo enrichment in the pore-water is almost certainly due to the oxidative dissolution of the Fe-rich globules rather than the glass. Additionally, the boron concentration was enriched in the pore-water of the deeper soil samples and in cores collected immediately adjacent to the glass. The elevated boron levels may be due to other effects, including normal downward leaching and reprecipitation of elements in the unsaturated zone. Perhaps the origin of the elevated B levels could be identified by measurement of B-isotopic compositions in water extracts and comparison with B-isotopic compositions in the glasses. The weathered glass and the surrounding sediment and its water extract information will be used in the future for validating models used to forecast the long-term behavior of the glass waste form and the resulting environmental impacts of glass burial in the soil.

A Monte Carlo (MC) simulation tool is being developed to predict the composition, extent, and morphology of the weathered glass hydration layer as a function of glass composition. The developed simulation tool will then be used to provide input data for geochemical modeling of secondary phase formation to be used in PA analyses. The work carried out this fiscal year (FY 2012) was divided into two activities. The first activity was aimed at providing a quantitative comparison between calculated and experimental dissolution properties of borosilicate and aluminoborosilicate glasses using a single set of model parameters. The second activity consisted in extending the MC code to include high-field-strength cations, which adopt an octahedral coordination in borosilicate glasses. The results discussed in this report provided key insights into the role of aluminum and high-field-strength cations (such as Zr and Hf) on the hydrolysis and condensation reactions that occur during the dissolution of borosilicate glasses.

The MC simulations use as input glass compositions, glass structure, and the reactivity of the glass components. In FY 2012, a variety of chemically simple and complex glasses were characterized using $^{27}Al$, $^{11}B$, and $^{29}Si$ magic-angle spinning nuclear magnetic resonance spectroscopy. In previous fiscal years, a combination of Raman spectroscopy and X-ray photoelectron spectroscopy (XPS) was also used to characterize unreacted and reacted glasses. Here we briefly discuss recent results collected on hafnium-bearing aluminoborosilicate glasses. The hafnium-bearing glasses are used to provide insight into the effect of high-field-strength cations, such as Zr and Hf, on the glass structure and rate of glass corrosion.

# Acronyms and Abbreviations

| | |
|---|---|
| 2D | two-dimensional |
| $^{[3]}$B | boron in trigonal coordination |
| $^{[4]}$B | boron in tetragonal coordination |
| AREST-CT | Analyzer for RadionuclidE Source-Term with Chemical Transport |
| BSE | backscattered electron |
| CMP | configuration management plan |
| DIW | deionized water |
| DOE | U.S. Department of Energy |
| ECKEChem | Equilibrium-Conservation-Kinetic Equation Chemistry |
| EDS | energy dispersive spectroscopy |
| EQL | experimental quantification limits |
| eSTOMP | Subsurface Transport Over Multiple Phases (parallel version of computer model) |
| FY | fiscal year |
| HLW | high-level waste |
| ICP-MS | inductively coupled plasma-mass spectrometry |
| ICP-OES | inductively coupled plasma–optical emission spectroscopy |
| IDF | Integrated Disposal Facility |
| ILAW | immobilized low-activity waste |
| LAW | low-activity waste |
| MAS-NMR | magic-angle spinning nuclear magnetic resonance |
| MC | Monte Carlo |
| NQA-1 | ASME nuclear quality assurance standard for Safety Software |
| ORP | Office of River Protection |
| PA | performance assessment |
| PCT | product consistency test |
| PNNL | Pacific Northwest National Laboratory |
| PUF | pressurized unsaturated flow (test) |
| SEI | secondary electron imaging |
| SEM | scanning electron microscopy |
| $SiO_4$ | structural representation of the silicate tetrahedral in the glass |
| STOMP | Subsurface Transport Over Multiple Phases (serial version of computer model) |
| STORM | Subsurface Transport Over Reactive Multiphases (computer code) |
| TST | transition state theory |
| VHT | vapor hydration test |
| VSL/CUA | Vitreous State Laboratory at The Catholic University of America |
| WTP | Hanford Tank Waste Treatment and Immobilization Plant |

| | |
|---|---|
| XPS | X-ray photoelectron spectroscopy |
| XRD | X-ray diffraction |

## Units of Measure

| | |
|---|---|
| °C | temperature in degrees Celsius [T(°C) = T(K) – 273.15] |
| cm | centimeter |
| d | day |
| g | gram |
| K | Kelvin or concentration |
| kJ | kilojoules |
| L | liter |
| m | meter |
| M | molarity, mole/Liter |
| mL | milliliter |
| Mass% | mass percent |
| mm | millimeter |
| mol | mole |
| 1/Myr | per million years, equivalent to ppm/yr |
| nm | nanometer |
| ppm | parts per million |
| s | second |
| S | siemens |
| wt.% | weight percent |
| yr | year |
| µ | micro (prefix, $10^{-6}$) |

# Contents

# Figures

# Tables

# 1.0 Introduction

The federal facilities located on the Hanford Site in southeastern Washington State have been used extensively by the U.S. government to produce nuclear materials for the U.S. strategic defense arsenal. Currently, the Hanford Site is under the stewardship of the U.S. Department of Energy (DOE) Office of Environmental Management (EM). A large inventory of radioactive and mixed waste resulting from the production of nuclear materials has accumulated, mainly in 177 underground single- and double-shell tanks located in the central plateau of the Hanford Site (Mann et al. 2001). The DOE-EM Office of River Protection (ORP) is proceeding with plans to immobilize and permanently dispose of the low-activity waste (LAW) fraction onsite in a shallow subsurface disposal facility (the Integrated Disposal Facility [IDF]). Pacific Northwest National Laboratory (PNNL) was contracted to provide the technical basis for estimating radionuclide release from the engineered portion of the IDF (the source term) as part of an immobilized low-activity waste (ILAW) glass testing program to support future IDF performance assessments (PAs).

## 1.1 Overview—ILAW Glass Disposal at Hanford

Currently, DOE plans to dispose of the glasses made from nuclear waste stored in underground tanks at Hanford at two U.S. locations: 1) the ILAW glass will be stored onsite at the IDF and 2) the high-level waste (HLW) glass will be disposed of at a geologic repository (previously Yucca Mountain, Nevada). The solid and liquid waste recovered from the tanks will be pretreated to separate the low-activity fraction from the high-level and transuranic waste fractions. The LAW and HLW fractions will be immobilized into a vitrified matrix (i.e., glass). Vitrifying the LAW is expected to generate over $1.6 \times 10^5$ $m^3$ of glass (Certa and Wells 2010). Once vitrified, the volume of ILAW at Hanford will be one of the largest in the DOE complex and is one of the largest inventories (approximately $8.9 \times 10^{14}$ Bq total activity) of long-lived radionuclides, principally $^{99}Tc$ ($t_{1/2} = 2.1 \times 10^5$ years), planned for disposal in a low-level waste (LLW) facility.

Before the ILAW can be disposed of, DOE must conduct a PA for the IDF that describes the long-term impacts of the disposal facility on public health and environmental resources. One of the inputs to the PA is estimates of radionuclide release rates from the engineered portion of the disposal facility (source term). These estimates are expected to be based on chemical reactions that occur in the near field and are controlled by the dissolution of the vitrified matrix. Therefore, to provide credible estimates, a mechanistic understanding of the basic physical and geochemical processes that control glass dissolution and hence, radionuclide release, must be understood and incorporated into models to effectively simulate the glass-water reaction over the period of regulatory concern (approximately 10,000 years). Apart from glass composition, the dissolution rate is a function of temperature, pH, and solution composition of the liquid contacting the glass. The temperature of the IDF is a known constant, 15°C. However, both the pH and the composition of the liquid contacting the glass are variables that are affected by flow rate, reactions with other engineered materials, gas-water equilibria, secondary-phase precipitation, alkali-ion exchange, and dissolution of the glass itself. Consequently, glass dissolution rates vary both in time and as a function of position in the disposal system. There is no physical constant such as a “leach rate” or radionuclide release rate parameter that can be assigned to the glass waste form in such a dynamic system.

A model based on empirical release behavior of the glass cannot provide feedback regarding the effects of design options on the disposal-system performance. Therefore, the source-term analysis

requires the use of a reactive-chemical transport-modeling framework that takes into account the coupled effects of fluid flow and glass-water reactions on the chemistry of liquids percolating through the disposal facility. The fluid chemistry is coupled with kinetic rate equations that describe the response of the glass corrosion rate to changes in liquid composition in the disposal facility or repository, all computed as functions of time and space. These kinetic rate equations assume that 1) the dependence of dissolution and precipitation rates on departure from equilibrium are based on arguments and assumptions of Transition State Theory (TST) and 2) the driving force for the transformation of unstable to stable silicate materials is governed principally by the magnitude of displacement from thermodynamic equilibrium. This technical strategy (McGrail et al. 1998, 2001b, 2003; Mann et al. 2001) requires the use of a reactive-chemical transport code (e.g., Subsurface Transport Over Reactive Multiphases [STORM]) that integrates the results obtained from bench-scale laboratory test methods and from long-term accelerated weathering tests to simulate and model glass weathering. For the IDF PA program, data collection has been focused on measuring and quantifying the effects of environmentally relevant and sensitive parameters (e.g., effect of pH, temperature, and solution composition) that are needed to simulate and model, with a high level of confidence, the long-term behavior of glass. This methodology is similar to the strategy being used to analyze the Drigg LLW site in the United Kingdom (Abraitis et al. 2000; Small et al. 2000).

## 1.2 Purpose and Report Contents and Organization

The purpose of this report is to summarize the progress made in fiscal year (FY) 2012 toward implementing the strategy with the goal of developing an understanding of the long-term corrosion behavior of LAW glasses. Work completed in FY 2010 and FY 2011 is documented in the 2010 and 2011 annual reports (Pierce et al. 2010b, 2011).

Section 2.0 of this report introduces the theoretical aspects of glass weathering, modeling the glass-water reaction. Section 3.0 discusses the glass characterization results using magic-angle spinning nuclear magnetic resonance spectroscopy (MAS-NMR), to determine the relationships between local molecular structure and glass dissolution kinetics and to characterize the weathered hydration layer on leached glasses. The experimental results collected to date for pressurized unsaturated flow (PUF) test experiments conducted on three ILAW glasses are discussed in Section 4.0. Section 5.0 discusses the results from geochemical modeling calculations performed with long-term product consistency test (PCT) data on ILAW glasses to define the reaction network as input to near-field modeling calculations for PA analyses. Further development of the Monte Carlo (MC) modeling code to predict the composition, and extent, and morphology of the glass hydration layer as a function of glass composition is described in Section 6.0. Section 7.0 discusses the progress that has been made in transitioning from the use of STORM to Subsurface Transport Over Multiple Phases (STOMP) for the near-field modeling calculations. Section 8.0 presents the results of characterization of soil and glass samples from a lysimeter test spanning eight years. Finally, a brief summary of the information contained in this report is provided in Section 9.0.

# 2.0 Theoretical Considerations for Glass

This section briefly discusses the stages of glass dissolution, the application of a kinetic rate equation to model the glass-water reaction, how rate-law parameters vary with glass and solution composition (Bacon and Pierce 2010), and the numerical computer code used to simulate the glass weathering process over geologic timescales. We also discuss the technical basis for several of the assumptions used to define the base-case simulations.

## 2.1 Stages of Glass Dissolution

A large amount of information on the glass-water reaction collected over the past 25 years has been summarized in the ‘‘glass compendium” (Cunnane et al. 1994a,b) and numerous reviews (Barkatt et al. 1986; Hench et al. 1986; Bunker et al. 1988; Casey and Bunker 1990; Werme et al. 1990; Bourcier 1991, 1994; Vernaz and Dussossoy 1992; McGrail et al. 1997; Strachan and Croak 2000; Vernaz et al. 2001; Icenhower et al. 2004; Van Iseghem et al. 2004). Based on these reviews, the glass dissolution reaction can be divided into five regimes or stages (Figure 2.1) that occur as the reaction proceeds (e.g., Stage I, II, III, IV, and V).

- Stage I—Initial diffusion or interdiffusion
- Stage II—Initial or forward rate, $r_0$
- Stage III—Decreasing rate, $r(t)$
- Stage IV—Residual rate, $r_r$
- Stage V—Alteration renewal.

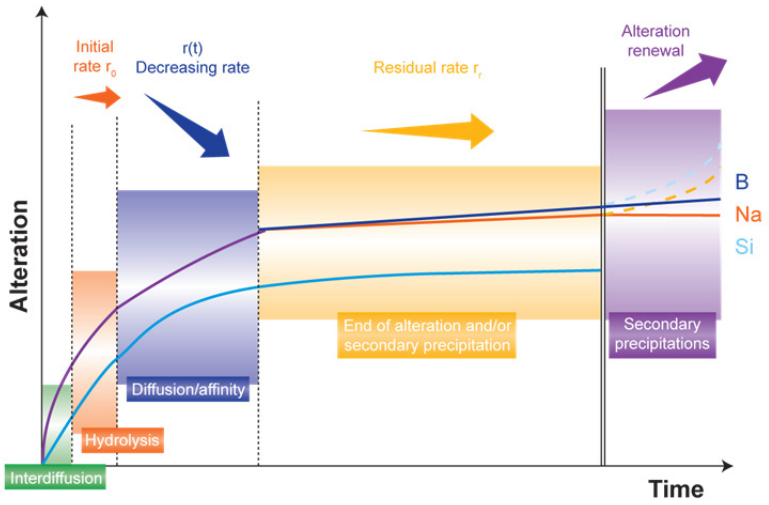


**Figure 2.1**. General Schematic of the Stages of Glass-Water Reaction

The initial stage (Stage I) of glass weathering begins when network-modifying cations and protons in solution are exchanged, a process referred to as interdiffusion. This mechanism has been identified experimentally during the leaching of numerous glasses, especially in acidic media (Doremus 1975). The

process of interdiffusion is followed by two simultaneous reactions: hydration and dissolution of the glass network, commonly referred to as the initial or forward rate (Stage II). In dilute solutions, the TST-based model successfully accounts for silicate dissolution in terms of temperature, pH, and reactive surface area. Stage III is reached as the concentration of dissolved components increases and the buildup of these components approaches the formation of a thermodynamically unstable phase (hydrated surface layer).

During Stage III, the matrix dissolution rate becomes dependent on the solution saturation state (concentration of elements in solution). Therefore, the process of ion exchange reaches a relatively constant rate in accordance with a diffusion-controlled process as a hydrated surface layer (e.g., gel layer) develops on the surface of the glass over time. The hydrated surface layer forms when relatively insoluble glass components (i.e., Al, Fe, and Si) accumulate in the bulk solution and condense at the glass-water interface. Unlike the rate of ion exchange, the dissolution rate of the glass network decreases because of the common-ion effect (i.e., as the solution becomes more concentrated in glass components). The difference in chemical potential between the glass and the aqueous phase decreases, which decreases the dissolution rate—corresponding to an incongruent release of B, Na, and Si. This decrease in the rate of matrix dissolution is partially caused by the effect silicic acid ($H_4SiO_4$(aq)) has on the dissolution rate and the formation of the hydrated surface layer (Abraitis et al. 2000; Pierce et al. 2004, 2008a,b). In other words, as the activity of $H_4SiO_4$(aq) increases in the aqueous solution, the rate of glass dissolution decreases. It is important to note that in the case of glass, the dissolution rate cannot become zero because silicate glasses are thermodynamically unstable in water.

During Stage IV, the solution becomes saturated, and secondary minerals begin to form. The alteration phases are often a clay mineral, such as a smectite or chlorite (Pierce et al. 2007). The precipitation kinetics associated with these phases can be complex, but in general, the rate of secondary-phase growth increases in response to the increase in magnitude of supersaturation (Nagy and Lasaga 1993; Nagy 1995). Depending on the type of alteration phase, the glass-water reaction can increase from the residual rate and return to a rate consistent with the saturation and pH conditions observed during Stage II (e.g., Stage V—alteration rate renewal). This type of behavior has been observed in accelerated weathering experiments and may be associated with the Al/Fe ratio of the glass formulation (Jantzen et al. 2008).

## 2.2 Kinetic Rate Equation

A mathematical model that describes glass reactivity is needed to predict the long-term fate of glass in the subsurface over the period of regulatory concern. Over the last few decades, a general rate equation has been developed to describe the dissolution of glass (and more ordered materials) into aqueous solution. As described below, the equation is based upon the TST of chemical kinetics, in which the overall reaction rate is governed by the slowest elementary reaction. Elementary reactions have simple stoichiometry and can be combined as an overall reaction. In many cases, the elementary reactions can only be inferred. As an example of an elementary reaction, consider the dissolution of $SiO_2$ polymorphs to form silicic acid:

$$SiO_2(s) + 2H_2O \leftrightarrow SiO_2 \cdot 2H_2O^{\ddagger} \rightarrow H_4SiO_4(aq) \tag{2.1}$$

in which $SiO_2 \bullet 2H_2O^{\ddagger}$ represents an activated complex. Note that a double-headed arrow, symbolizing a reversible reaction, links the reactants and the activated complex in Equation (2.1). Equation (2.1) also illustrates that the TST formulation assumes that the decay of the activated complex is an irreversible reaction.

Previous studies have established that the corrosion rate of silicate waste glasses is a complex process that depends strongly on temperature, pH, and the chemical composition of the aqueous solution contacting the glass (Cunnane et al. 1994a,b and the references contained therein). When the aqueous solution is dilute, the glass dissolves at a characteristic forward rate that depends only on glass composition, temperature, and solution pH (McGrail et al. 1997). In static systems, or where the rates of mass transport by fluid flow are slow, dissolution releases glass components into the aqueous solution, and the concentrations of these elements in the contacting fluid increase. The buildup of these dissolved components leads to slower glass corrosion rates as the contacting solution becomes more concentrated. As solution concentrations of dissolved elements continue to increase, solubility limits with respect to secondary phase(s) are reached, and these phases may begin to precipitate. Because silicate glasses are metastable solids, thermodynamics dictates that the glass will continue to dissolve or transform into more stable alteration phases. The key factor controlling long-term durability of waste glasses is the rate at which this process proceeds.

The rate law that appears to best describe this overall dissolution behavior, developed by Aagaard and Helgeson (1982) and applied to glass by Grambow (1985), is presented as follows:

$$r_i = \vec{k}_o v_i a_{H^+}^{\eta} \exp\left(\frac{E_a}{RT}\right)\left[1-\left(\frac{Q}{K_g}\right)^{\sigma}\right]\prod_j a_j \qquad (2.2)$$

where
$r_i$ = dissolution rate, g $m^{-2}$ $d^{-1}$
$\vec{k}_0$ = intrinsic rate constant, g $m^{-2}$ $d^{-1}$
$v_i$ = mass fraction of component *i*, unitless
$a_{H^+}$ = hydrogen ion activity (variable to be calculated by STOMP)
$E_a$ = activation energy, kJ/mol
$R$ = gas constant, kJ/(mol·K)
$T$ = temperature, K (assumed constant at 15°C or 288 K)
$Q$ = ion activity product for glass (variable to be calculated by STOMP)
$K_g$ = pseudo-equilibrium constant
$\eta$ = pH power law coefficient
$\sigma$ = Temkin coefficient ($\sigma$ = 1 assumed).

The chief virtue of Equation (2.2) is that it can be directly input into reaction-transport codes for simulating the dissolution behavior of glass under specific storage conditions. Another benefit of Equation (2.2) is that it is solidly based on the TST of chemical kinetics, in which a series of reaction rates are governed by the slowest elementary reaction. Therefore, it is simply necessary to ascertain the rate-limiting step in dissolution rather than attempt to fully understand all of the possible reactions and kinetic pathways that can occur during the reaction of glass with aqueous solution. Because this

rate-limiting step is an "elementary reaction," the stoichiometry of the reaction is typically simple and can be easily defined in a reactive transport model.

In addition, test results with ILAW and bulk-vitrification glasses show that these high-sodium containing glasses are susceptible to a secondary reaction mechanism, alkali-ion exchange. This reaction results in the selective extraction of Na via the reaction:

$$\text{LAWA44-Na} + H^+ \rightarrow \text{LAWA44-H} + Na^+ \qquad (2.3)$$

where LAWA44-Na represents the unreacted glass containing Na, and LAWA44-H represents a hydrated glass where the Na has been replaced with an equimolar amount of hydrogen. The rate of this ion-exchange reaction, referred to hereafter as $r_{IEX}$, has been determined from single-pass flow-through experiments (Pierce et al. 2004, 2005). In the STOMP code, the ion-exchange reaction is taken into account as the amount of hydrated glass is formed via Equation (2.3), and that hydrated glass is allowed to dissolve according to the same kinetic rate law, Equation (2.2), as the parent glass.

# 3.0 Glass Characterization

## 3.1 Overview

The objectives of the glass characterization task are to 1) determine relationships between local molecular structures in ILAW glasses and dissolution kinetics and 2) characterize the remnant of the gel layer on glasses that had undergone dissolution testing. To accomplish this task, a combination of MAS-NMR, Raman spectroscopy and X-ray photoelectron spectroscopy (XPS) were used during FY 2010 and FY 2011. During FY 2012, the MAS-NMR analyses focused on conducting experiments required to gain insight into the Al, B, and Si coordination in unreacted and reacted glass samples. An overview of the selected results is provided below for a glass that contained hafnium as an example of a high-field-strength cation. It is expected that a more detailed analysis of these data will be performed early in FY 2013. The results from these characterization measurements will provide key information for the development of the MC code discussed in Section 6.0.

## 3.2 MAS-NMR Spectroscopy

As part of ongoing effort to develop a link between structural variations in aluminoborosilicate glasses and the rate of glass dissolution in aqueous media, molecular structures present in chemically simple as well as chemically complex sodium aluminoborosilicate glasses are being evaluated with $^{27}$Al, $^{11}$B, and $^{29}$Si MAS-NMR. We have focused our attention on Al, B, and Si in these glasses because of their role in the network structure of aluminoborosilicate glasses. These measurements have been conducted on unreacted and reacted samples of glass to gain a better understanding of the processes that control elemental release under both dilute and near-saturated conditions. Here we focus our attention on how changes in the Hf/Si ratio impact element release rates for sodium aluminosilicate glasses (Table 3.1). In each case, the $^{27}$Al spectra for each sample change very little. In the case of B, the $^{11}$B spectra (shown in Figure 3.1) illustrate that the $^{[3]}$B fraction increases and $^{[4]}$B decreases with an increase in the Hf/Si ratio from 0.0 to 0.42. Lastly, the $^{29}$Si cross-polarized MAS-NMR analysis suggests a significant change in the silica environment with changes in the Hf/Si ratio. These results suggest an increased mixing between the Hf and Si (i.e., the proportion of Hf-O-Si bonds increase) as the Hf/Si ratio increases. High-field-strength elements (such as Hf and Zr) have been observed to play a significant role in the pore structure of the silica-rich hydrated layer and impact the rate of element release. This is probably the result of the low solubility for Hf and Zr under these experimental conditions, which results in the formation nanometer sized Hf- or Zr-oxide clusters within the pores of the silica-rich hydrated layer, but additional information is needed to fully understand the mechanisms associated with this interfacial reaction (Cailleteau et al. 2008).

**Table 3.1**. Composition of Hf Glass Series

| Oxides | Hf-1 | Hf-2 | Hf-3 | Hf-4 | Hf-5 |
|---|---|---|---|---|---|
| $Al_2O_3$ | 5.02 | 4.76 | 4.50 | 4.25 | 4.00 |
| $B_2O_3$ | 14.98 | 14.24 | 13.50 | 12.75 | 12.00 |
| $Na_2O$ | 20.03 | 18.99 | 18.00 | 17.00 | 16.00 |
| $SiO_2$ | 59.97 | 56.99 | 54.00 | 51.00 | 48.00 |
| $HfO_2$ | 0.00 | 5.02 | 10.00 | 15.00 | 20.00 |
| Hf/Si | 0.00 | 0.09 | 0.19 | 0.29 | 0.42 |

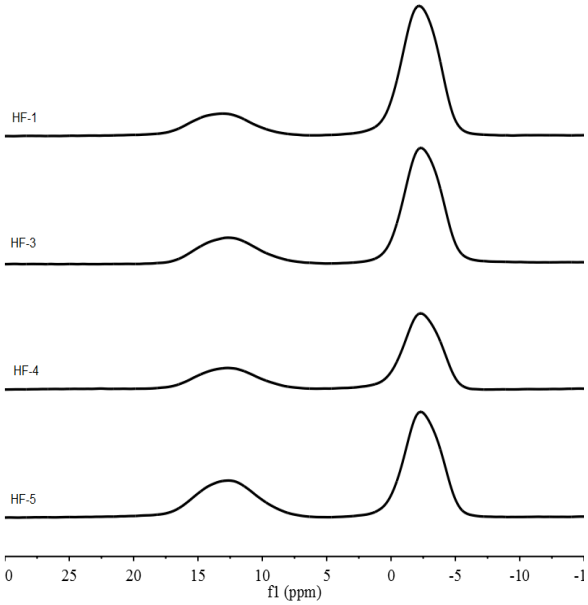


**Figure 3.1**. MAS-NMR Spectra for Hafnium Glasses. Results of trigonal ($^{III}B$) (10 to 15 ppm) and tetrahedral ($^{IV}B$) (0 to –5 ppm) peaks obtained from the integration of $^{11}B$ MAS-NMR spectra collected at 750 MHz. The peaks shown are for aluminoborosilicate glasses that vary in the Hf/Si ratio. The Hf/Si ratio increases from 0 mole% $HfO_2$ (Hf-1) to 20 mole% $HfO_2$ (Hf-5).

# 4.0 Pressurized Unsaturated Flow Experiments

IDF PA models must account for the long-term corrosion rate of a range of ILAW glass formulations. The corrosion rate, a key parameter in PA calculations, affects the overall performance of the ILAW source term and ultimately the IDF. As water migrates through the IDF and contacts the waste package, the solution in contact with the dissolving glass becomes more and more concentrated in glass components, until solubility limits for alteration phases begin to be exceeded. Once formed, these metastable, amorphous, and/or crystalline alteration phases begin to control the overall dissolution of the glass waste form. Therefore, to predict the long-term corrosion of these glasses in the disposal system environment, information on the glass transformation into a paragenetic assemblage of alteration products or minerals must be known. Although the suite of weathering products that will form as a consequence of the glass-water reactions cannot be determined a priori at this time, as discussed by McGrail et al. (2000b; 2003), PUF Tests can be used to simulate and accelerate the weathering process. PUF experiments were conducted on three prototypic ILAW glasses: ORPLG9, ORPLB2, and ORPLF7[1]. The compositions in weight percent for the ILAW glasses are shown below in Table 4.1. The PUF experiments conducted on the three ILAW glass were performed at 90°C and at a flow rate of 2-mL per day.

**Table 4.1**. Composition of PUF Glasses Tested

| Oxides | ORPLB2 | ORPLG9 | ORPLF7 |
|---|---|---|---|
| $Al_2O_3$ | 10.00 | 6.74 | 8.60 |
| $B_2O_3$ | 7.30 | 8.49 | 9.50 |
| CaO | 1.10 | 2.69 | 9.72 |
| $Fe_2O_3$ | 1.10 | 0.28 | 0.30 |
| $K_2O$ | 0.12 | 5.75 | 0.50 |
| $Li_2O$ | 0.00 | 0.00 | 4.35 |
| MgO | 1.10 | 0.95 | 0.98 |
| $Na_2O$ | 25.00 | 21.00 | 12.00 |
| $SiO_2$ | 39.98 | 40.75 | 42.14 |
| $SnO_2$ | 1.08 | 2.83 | 0.00 |
| $TiO_2$ | 0.00 | 0.00 | 0.00 |
| $V_2O_5$ | 2.00 | 0.00 | 2.50 |
| ZnO | 3.65 | 3.39 | 2.91 |
| $ZrO_2$ | 5.44 | 5.66 | 3.88 |
| Others | 2.13 | 1.48 | 2.62 |
| Sum | 100.0 | 100.0 | 100.0 |

[1] Muller IS, I Joseph, and IL Pegg. 2010. *Selection of Bounding Low Activity Waste Glasses for Leach Testing*. VSL-10L2000-1, Vitreous State Laboratory, The Catholic University of America, for Energy*Solutions* Federal EPC, Inc. and Washington River Protection *Solutions*, LLC, Washington D.C.

## 4.1 Description of the PUF Apparatus

The PUF apparatus (Figure 4.1) allows accelerated weathering experiments to be conducted under hydraulically unsaturated conditions, thereby mimicking the vadose zone environment while allowing the corroding glass to achieve a final reaction state (stage IV and occasionally stage V, as described in Section 2). The PUF apparatus provides the capability to vary the volumetric water content from saturation to 20% of saturation or less, minimize the flow rate to increase liquid residence time, and operate at a maximum temperature of 100°C. The PUF column operates under a hydraulically unsaturated condition by creating a steady-state vertical water flow, while maintaining uniform water content throughout the column, and by using gravity to assist in drainage.

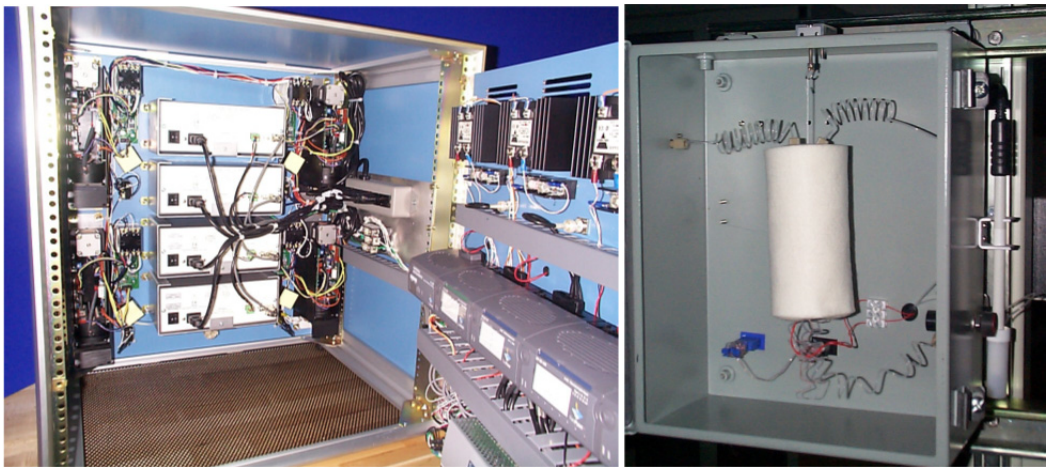

**Figure 4.1**. Pictures of PUF System Hardware (Patent #5974859)

The underlying principle for creating such conditions is Darcy's Law as modified by Richards (1931)

$$J_w = -K(\psi_m)\frac{\delta\Psi}{\delta z} \tag{4.1}$$

where $J_w$ = the volumetric flux density (m/s)
$\psi$ = the water potential; which is equal to the matrix potential ($\psi_m$) + gravitational potential ($\psi_g$) (m)
$K(\psi_m)$ = the conductivity as a function of matrix potential (m $s^{-1}$)
$z$ = the length of the column (m).

It can be easily shown that if uniform moisture content is established throughout the column, Equation (4.1) reduces to:

$$J_w = K\left(\psi_m\right) \tag{4.2}$$

Equation (4.2) simply states that under uniform water content conditions, the volumetric flux density of water is equal to the unsaturated hydraulic conductivity.

This system has been previously described in other publications (McGrail et al. 2000a, 2001c; Pierce et al. 2004), and an interested reader should consult these references, as well as the references contained therein, for more detail. Only a general description will be provided within this document. In general, the PUF system consists of a column (7.62-cm length and 1.91-cm diameter) fabricated from a chemically inert material, polyetheretherketone, so that dissolution reactions are not influenced by interaction with the column material. A porous titanium plate with nominal pore size of 0.2 μm is sealed in the bottom of the column to ensure an adequate pressure differential for the conductance of fluid while operating under unsaturated conditions (Wierenga et al. 1993). Titanium was chosen because it is highly resistant to corrosion and has excellent wetting properties. Once the porous titanium plate is water saturated, water but not air is allowed to flow through the 0.2-μm pores, as long as the applied pressure differential does not exceed the air-entry relief pressure or "bubble pressure" of the Ti plate. If the pressure differential is exceeded, air will escape through the plate and compromise the ability to maintain unsaturated flow conditions in the column. The computer control system runs LabVIEW™ (National Instruments Corporation) software for logging test data to disk from several thermocouples, pressure sensors, in-line sensors for effluent pH and conductivity, and column weight from an electronic strain gauge to accurately track water mass balance and saturation level. The column also includes a "PUF port," which is an electronically actuated valve that periodically vents the column gases. The purpose of column venting is to prevent reduction in the partial pressure of important gases, especially $O_2$ and $CO_2$, which may be consumed in a variety of chemical reactions.

## 4.2 Materials and Methods

### 4.2.1 Sample Preparation

The glass samples used for the PUF tests were crushed using a ball mill or mortar and pestle. The crushed glass was sieved to obtain the –40 to +60 mesh (420- to 250-μm diameter) size fraction. The sample was then washed in deionized water (DIW), sonicated, rinsed using ethanol, and then dried in an oven at 90°C.

### 4.2.2 Effluent Solution Analyses

All effluent solutions were monitored for pH and electrical conductivity with in-line sensors. Prior to starting the experiments, the in-line pH probe was calibrated with National Institute of Standards and Technology (NIST) buffers (pH = 7.00, 10.00, or 12.00 at 25°C). Precision of pH measurement was ±0.02 pH units. The in-line Pharmacia Biotech electrical conductivity sensor was calibrated with a freshly made solution of 1.0 M NaCl. The 1.0 M NaCl solution was prepared by adding 11.67 g of analytical grade NaCl powder to 200 mL of DIW. After passing by the in-line sensors and through the 0.2-μm Ti porous plate, aliquots of the effluent solutions were acidified with ultrahigh-purity concentrated $HNO_3$ and analyzed with inductively coupled plasma–mass spectrometry (ICP-MS) and with inductively coupled plasma-optical emission spectroscopy (ICP-OES) methods for Al, B, Cr, Mg, Na, Si, Ti, Zn, and Zr.

### 4.2.3 Post-Test Solid-Phase Analyses

Upon termination, the reacted solids were subsampled as found (loose and moist particles) and as a function of depth. The subsamples were placed in glass vials, dried at room temperature in a sealed container with $CaSO_4$ desiccant, and analyzed for secondary reaction products with X-ray diffraction (XRD) and scanning electron microscopy (SEM).

X-ray diffraction was performed on samples taken from three different locations (heights) in the PUF column. One sample was taken from the each of the top two subsamples in the column and one was taken from the bottom of the column. A subsample from each of these samples was combined with a measured amount of NIST 674b internal standard (concentrations given in Table 4.2) and ground to a fine well-mixed powder by hand using an agate mortar and pestle. These powders were then loaded into back-mount holders to minimize preferred orientation of the powders. The XRD patterns were collected on a Bruker D8 Advance system configured with Bragg-Brentano (focusing) optics and a Cu target. The goniometer was set at a radius of 250 mm, with 0.3° (0.6 mm) fixed divergent slit on the incident beam. Counts were collected on a Bruker LYNXEYE™ one-dimensional multi-strip detector with a 3° collection angle. An 8-mm iris was placed directly in front of the detector to minimize counts from air scatter. Scan parameters were as follows: 3 to 90° 2-theta scan range, 0.015° 2-theta step size, and a 2 s/step hold time. A nickel filter was used to remove the $K_\beta$ radiation from the diffracted beam. Analysis of the patterns was done using Bruker EVA (version 14) software. The background and $K_{\alpha 2}$ were fitted and removed to perform the search/match of the phases present in the patterns. Search/match was done using a chemistry filter to limit the phases to those chemistries possible for each reacted glass sample. In addition, matches were picked based on SEM observations, because of the very low signal-to-noise ratio in the patterns. The internal standards were added to each sample to verify that there was no significant error in peak locations.

**Table 4.2**. XRD Sample Preparation: Sample and NIST Standard Masses

| Sample ID | Sample, g | Standard ID | Standard, g | Standard, wt.% |
|---|---|---|---|---|
| IDF1G-Min1 | 1.1039 | 674b (ZnO) | 0.1027 | 8.51% |
| IDF1G-Min2 | 1.6774 | 674b (ZnO) | 0.1671 | 9.06% |
| IDF1G-Min5 | 1.8466 | 674b (ZnO) | 0.1847 | 9.09% |
| IDF1G-Min8 | 1.6593 | 674b (ZnO) | 0.1566 | 8.62% |
| IDF5R-Min1 | 1.3233 | 674b ($TiO_2$) | 0.1319 | 9.06% |
| IDF5R-Min2 | 1.2517 | 674b ($TiO_2$) | 0.1059 | 7.80% |
| IDF5R-Min5 | 1.3734 | 674b ($TiO_2$) | 0.178 | 11.47% |
| IDF5R-Min8 | 1.3914 | 674b ($TiO_2$) | 0.1578 | 10.19% |
| IDF4R-Min1 | 1.3132 | 674b ($TiO_2$) | 0.1224 | 8.53% |
| IDF4R-Min2 | 1.3487 | 674b ($TiO_2$) | 0.1159 | 7.91% |
| IDF4R-Min5 | 1.4295 | 674b ($TiO_2$) | 0.1096 | 7.12% |
| IDF4R-Min6 | 1.403 | 674b ($TiO_2$) | 0.1136 | 7.49% |

A select number of reacted glass samples collected from the PUF experiments were prepared by two different methods to examine both the surface features and the corrosion profile of individual glass grains. To examine the outer surface features, reacted glass grains were placed on carbon tape, which was

attached to an aluminum stub. To examine the corrosion profile, cross-sections of the reacted glass grains were made. The grains were vacuum impregnated with epoxy, then ground and polished to a 0.25-μm finish to expose the corrosion layers and unreacted glass center. Samples were then sputter coated with a very thin layer of Pd to provide a conductive coating. The mounted and coated SEM samples were placed into a JEOL 7001 field emission scanning electron microscope equipped with an EDAX, Inc. (Mahwah, New Jersey), silicon drift detector energy dispersive spectroscopy (EDS) detector with a 30-mm active area. Imaging was done using both a secondary electron imaging (SEI) and backscattered electron (BSE) imaging detectors. A series of magnifications were selected to document the morphology of the phases observed on the surfaces and in cross-section. The accelerating voltage of the microscope was set to 5 kV for imaging and/or 20 kV for imaging and elemental analysis. Elemental analysis was performed on all corrosion products or crystals observed on or in the glass grains by a combination of spot analysis, select area, line scans, and elemental dot mapping. Spot analysis and area analysis were used to measure the compositions of phases. Line scans and dot mapping were used to measure elemental variability from the glass-gel-corrosion products and interfaces between each.

## 4.3 Normalized Concentration Calculation

The results from chemical analyses on collected effluent samples will be used to calculate a normalized release rate for each major glass component according to Equation (4.3).

$$NC_i = \frac{(C_{iL} - \bar{C}_{ib})}{f_i} \tag{4.3}$$

where $NC_i$ = the normalized concentration of element $i$
$C_{iL}$ = the concentration of element $i$ contained in the effluent solution
$C_{ib}$ = the background concentration of element $i$
$f_i$ = is the mass fraction of element $i$ contained in the glass.

In the testing here, DIW was used and the background concentration was therefore assumed to be zero in Equation (4.3).

## 4.4 Experimental Results

The PUF results for each of the three glasses are presented below. A list of the concentrations of some elements is presented in Appendix A. Boron released in the glass is used as an indicator of matrix dissolution because boron serves as a network former in the glass structure and is not retained in the formation of alteration phases. Less-soluble elements such as aluminum and silica are often sequestered in alteration phases and can serve as network formers. Sodium, potassium, and lithium can be released by two separate mechanisms: matrix dissolution and alkali-ion exchange. Alkali-ion exchange is an important process because it can cause localized pH increases in the samples, which can then increase the glass dissolution rates.

### 4.4.1 ORPLG9 Glass Results

Results for the pH and conductivity from the computer-monitored test metrics for ORPLG9 (also referred to as IDF2G9) are presented in the left graphic in Figure 4.2. Results comparing the normalized release rates for the major components contained in ORPLG9 are shown in the right graphic in Figure 4.2. The experiment ran for approximately 140 days. Over the 140-day duration, the normalized concentration of the sodium in the effluent is 1 to 1.5 times higher than the release of the boron, and potassium in the effluent is 0.6 to 2.5 times higher than the release of boron, which indicates that Na and K are being released by a combination of matrix dissolution and alkali-ion exchange. This glass contains approximately 21 weight percent Na in the target composition, which is between the target Na compositions contained in the other two LAW glasses. Aluminum and Si are being released from the glass at a much lower rate than B, indicating that these elements are being sequestered by the formation of alteration phases.

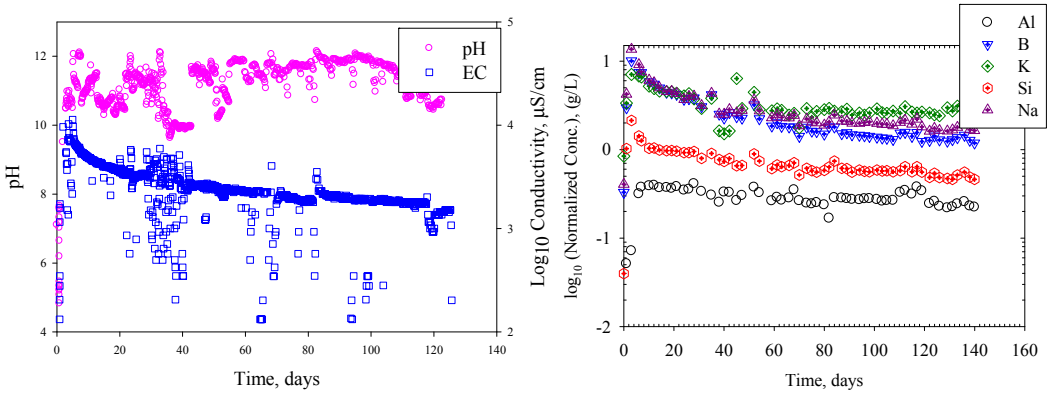


**Figure 4.2**. pH, Electrical Conductivity, and Normalized Concentrations for Glass ORPLG9 in the PUF Test. *Left*: Computer-monitored test metrics from PUF tests on ORPLG9 glass; *Right*: $Log_{10}$ normalized concentration as a function of time for the PUF experiment on ORPLG9 glass (also referred to as IDF2G9).

After termination of the PUF test with ORPLG9 glass, the solid material was subsampled from the column at intervals of 1 to 5 mm. The moisture content of these samples was measured by drying the samples in a vacuum desiccator. The dry solid material from the top, middle and bottom of the column was analyzed to identify secondary alteration phases using XRD and SEM.

Cross-sectional SEM images of PUF-reacted ORPLG9 glass are shown in Figure 4.3. Looking outward from the center of the glass grains, there appears to be an approximately 10-µm-thick alteration layer that has developed after 140 days of reaction in the PUF experiment at 90°C. At the top of the 10-µm-thick alteration layer is a thinner structured layer (possibly clay); however, the phase could not be confirmed by the XRD data (Figure 4.4). The elemental dot map shows the distribution of elements from the epoxy (carbon-rich region), two corrosion layers, and unreacted glass matrix. The approximately 10-µm-thick alteration layer appears at the top of the glass and migrates downward into the pristine glass matrix. This layer is enriched in Ca, Zr, and Sn relative to the bulk glass, while Si, Al, Mg, Zn, and S are at concentrations lower than the bulk glass, and Na and K are almost completely depleted from the corrosion layer. A chemically different thin layer appears at the outer surface of the grain (atop the thick corrosion layer). The thin layer is enriched in Al, Mg, and Zn and appears to have a plate-like

morphology. For each of the grains analyzed, beginning at the pristine glass, the Si decreases slightly in the first alteration layer, then it increases in the second alteration layer and further increases in the outer clay-like layer. Aluminum gradually increases from the glass to the outer layer. Calcium concentration remains similar in all the layers except the second alteration layer, where it is higher. Zirconium steps up in concentration in each alteration layer then significantly drops in the outer clay-like layer. Magnesium and zinc both remain constant, then increase in the clay-like layer. Alkali elements, Na and K (note: Li is not observed with the EDS), and B decrease significantly at the interface between the glass and the alteration layer and continue to decrease in concentration from the second alteration to the outer layer. These results are consistent with LAW glass samples previously reacted in PUF experiments.

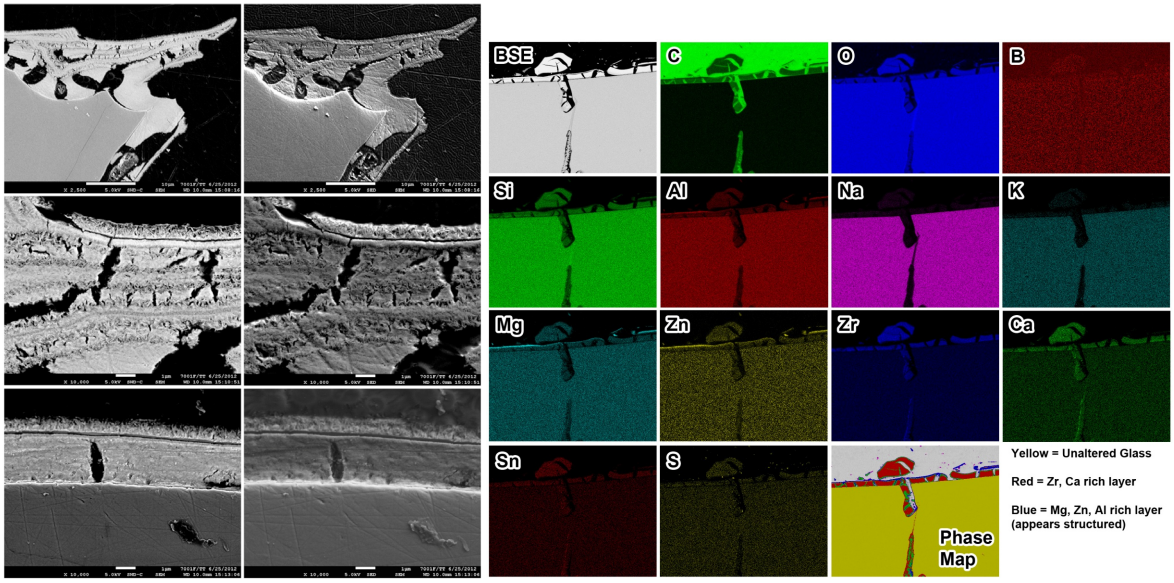


**Figure 4.3**. Cross-sectional SEM Images of PUF-Reacted ORPLG9 Glass from the Top of the PUF Column. *Left panel*: SEI (left column) and BSE (right column) images of ORPLG9 reacted glass grains prepared in cross-section at 2,500× magnification (top left images), 1,000× magnification (middle left images), and 10,000× magnification (bottom left images). *Right panel*: Elemental dot maps of ORPLG9 in cross-section, showing the elemental distribution of the different layers, from the altered glass layer (uppermost) to the remaining unreacted glass (innermost). Note: ORPLG9 is also referred to as IDF2G9.

The XRD patterns (Figure 4.4) collected on the PUF samples were nearly 100% amorphous, indicating that the fraction of crystalline phases was near or below the detection limits of the phases observed by SEM. The phases that are possible matches for the peaks in the XRD spectra include elpidite [$(Na_{1.31}Ca_{0.38}Zr(Si_6O_{15})(H_2O)_{2.73})$, ICDD# 01-083-2181], zinc aluminum silicate [$Zn_{0.75}Al_{1.5}Si_{1.5}O_6$, ICDD# 00-032-1455), and hemimorphite [$Zn_4Si_2O_7(OH)_2 \cdot H_2O$, ICDD# 00-005-0555]. The corrosion products given as possible matches in the XRD scans of ORPLG9 samples are best guesses based on the elements observed in the corrosion layer with SEM-EDS. It is also possible that the corrosion products are not very well structured or are amorphous. Based on the morphologies of the corrosion layers, it is likely that only the very top thin layer is structured (possibly clay) while the thicker corrosion layer is most likely altered glass or a gel.

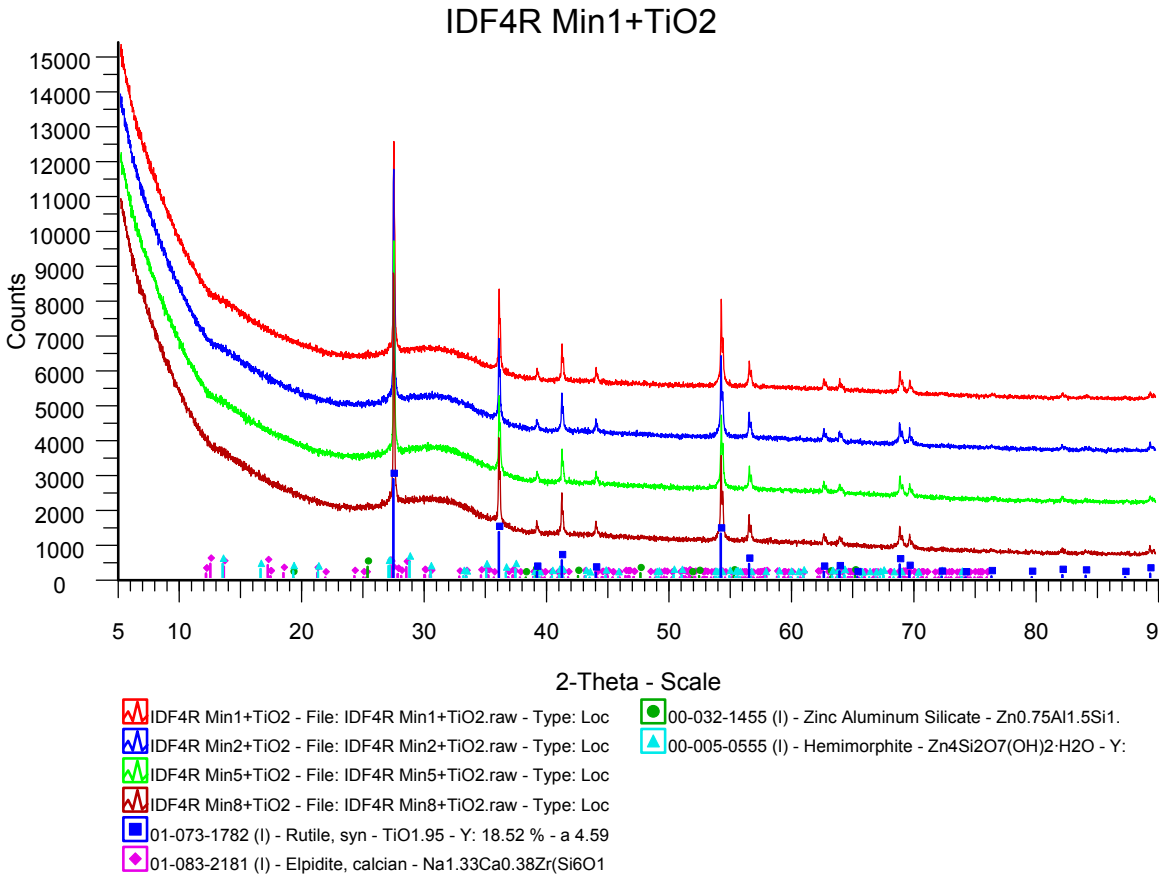


**Figure 4.4**. Raw XRD Pattern for ORPLG9 Glass Samples Removed from the Different Regions Within the PUF Column. Vertical top (sample #1-bright red and sample #2-blue), middle (#5-green), and bottom (#8-dark red)—with rutile ($TiO_2$) as the internal standard. Elpidite [$(Na_{1.31}Ca_{0.38}Zr(Si_6O_{15})(H_2O)_{2.73})$, ICDD# 01-083-2181], zinc aluminum silicate [$Zn_{0.75}Al_{1.5}Si_{1.5}O_6$, ICDD# 00-032-1455), and hemimorphite [$Zn_4Si_2O_7(OH)_2 \bullet H_2O$, ICDD# 00-005-0555] are all possible matches to the very weak diffraction peaks in the patterns.

### 4.4.2 PUF Results for ORPLB2 and ORPLF7 Glasses

Results for the pH and conductivity from the computer-monitored test metrics for ORPLB2 (also referred to as IDF1B2) are presented in the left panel of Figure 4.5. Results comparing the normalized release rates for the major components contained in ORPLB2 are shown in the right panel of Figure 4.5. The experiment ran for approximately 310 days. Over the 310-day duration at 90°C, the normalized concentration of the sodium in the effluent is 0.9 to 1.4 times higher than the release of the boron which indicates that Na is being released primarily by matrix dissolution with some alkali-ion exchange occurring. This glass contains approximately 25 weight % Na in the target composition, and is the glass with the highest Na composition. Unlike Li and Na, K is being released at an order of magnitude greater than any other element. Currently it is unclear why K, a relatively minor component in this glass, is being released faster than any of the other alkali elements. This will be evaluated more closely by analyzing the characterization results. Similar to the other two LAW glasses, Al and Si are being released from the glass at a lower rate than B indicating that these elements are being sequestered by the formation of alteration phases.

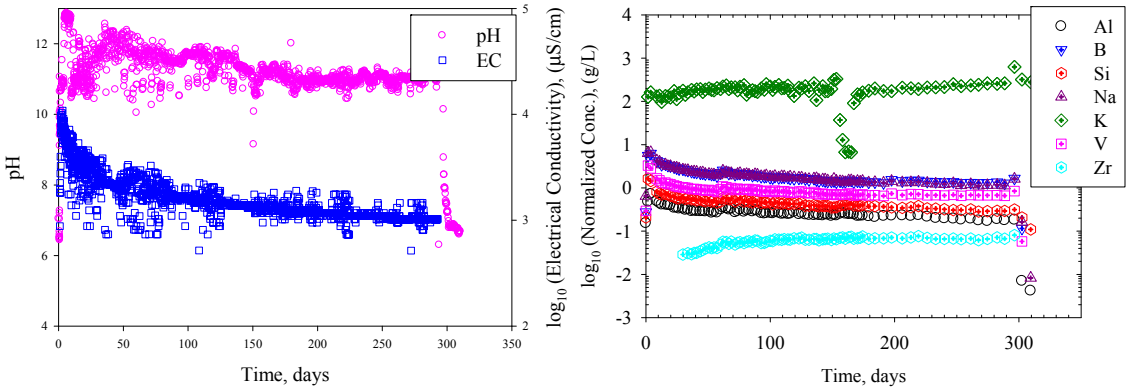


**Figure 4.5**. pH, Electrical Conductivity, and Normalized Concentrations for Glass ORPLB2 in the PUF Test. *Left*: Computer-monitored test metrics (pH and electrical conductivity) as a function of time for PUF Test on ORPLB2. *Right*: Normalized concentrations as a function of time for the PUF experiment on ORPLB2 glass (also referred to as IDF1B2).

Results for the pH and conductivity from the computer-monitored test metrics for ORPLF7 (also referred to as IDF3F7) are presented in the left panel of Figure 4.6. Results comparing the normalized release rates for the major components contained in ORPLF7 are shown in the right panel of Figure 4.6. The experiment ran for approximately 173 days. Over the 173-day duration, the normalized concentration of the sodium in the effluent is 0.5 to 2.1 times higher than the release of the boron, which indicates that Na is being released by a combination of matrix dissolution and alkali-ion exchange. This glass contains approximately 12 weight percent Na in the target composition, which is approximately 9–13 weight percent lower than the higher Na loaded glasses (which contain approximately 21–25% Na). Lithium is being released from the glass at approximately 0.3 to 2 times higher than the release of boron, which indicates that Li is being released from this glass by a combination of matrix dissolution and alkali-ion exchange. Similar to ORPLB2, the K release (not shown in Figure 4.6) is also higher than any other element for ORPLF7. Analysis of the characterization results should provide additional insight into the reason for abnormally high K release in comparison to the other alkali elements. Aluminum and Si normalized concentrations are 1 to 2 orders of magnitude lower than B indicating that these elements are being sequestered by the formation of alteration phases.

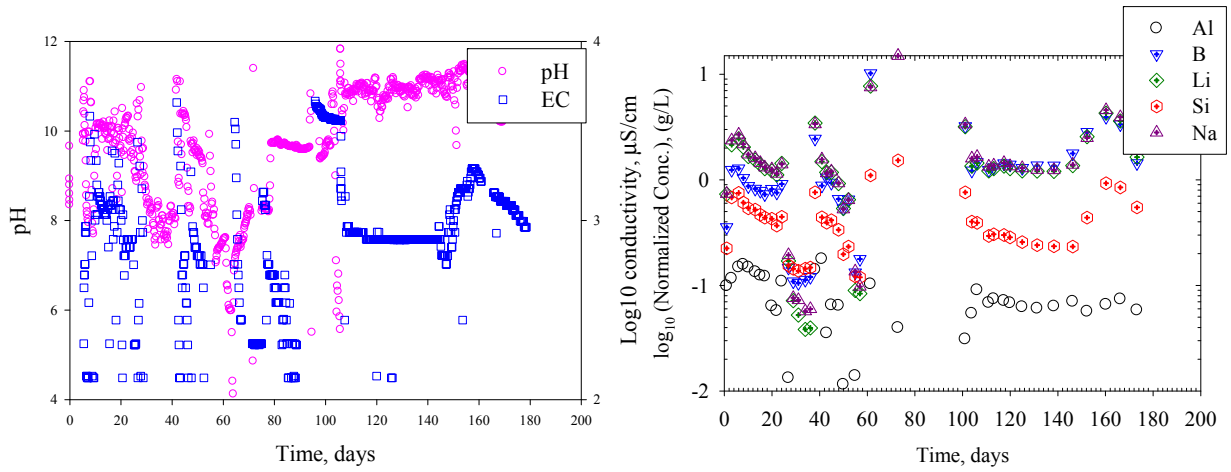


**Figure 4.6**. pH, Electrical Conductivity, and Normalized Concentrations for Glass ORPLF7 in the PUF Test. *Left:* Computer-monitored test (pH and Electrical Conductivity) metrics as a function of time for PUF Test on ORPLF7 Glass. Note: the pH and conductivity probes were not functioning properly up through approximately 100 days of data collection. *Right*: Normalized concentration as a function of time for the PUF experiment on ORPLF7 glass. Note: ORPLF7 is also referred to as IDF3F7.

The XRD and SEM data were also collected for ORPLB2 and ORPLF7. These results will be compiled, analyzed, and reported in a future summary report.

## 4.5 Summary of PUF Results

The IDF PA modeling work must account for the long-term corrosion rate of the ILAW glasses. In FY 2012, the PUF tests being conducted on three prototypic ILAW glasses (e.g., ORPLG9, ORPLB2, and ORPLF7) were terminated. The reacted glass from each experiment was collected and analyzed with SEM-EDS and powder XRD. Results collected on reacted ORPLG9 glass show that a 10-µm-thick alteration layer developed on the surface of the glass. The EDS elemental profiles for the analyzed ORPLG9 glass grains, beginning at the pristine glass, show that Si decreases slightly in the first alteration layer, then increases in the second alteration layer and further increases in the outer clay-like layer. Aluminum gradually increases from the glass to the outer layer. Calcium remains similar in all the layers except the second alteration layer, where it is higher. Zirconium steps up in concentration in each alteration layer then significantly drops in the outer clay-like layer. Magnesium and zinc both remain constant, then increase in the clay-like layer. Alkali elements, Na and K (note: Li is not observed with the EDS), and B decrease significantly at the interface between the glass and the alteration layer and continue to decrease in concentration from the second alteration to the outer layer. The XRD results illustrated that the reacted glass was mainly amorphous and only contained a minor amount of crystalline phases. Both the SEM-EDS and XRD results are consistent with LAW glass samples previously reacted in PUF experiments (McGrail et al. 2000a, 2001c; Pierce et al. 2004, 2007). Glass grains from ORPLB2 and ORPLF7 were also analyzed and will be discussed in future reports.

# 5.0 Geochemical Modeling

## 5.1 Overview

Low-activity waste PA models must account for the long-term corrosion rate of a range of ILAW glass formulations. The corrosion rate, a key parameter in PA calculations, affects the overall performance of the ILAW source term. As water migrates through the IDF and contacts the waste package, the solution in contact with the dissolving glass becomes more and more concentrated in glass components, until solubility limits for alteration phases begin to be exceeded. Once formed, these metastable, amorphous, and/or crystalline alteration phases begin to affect the overall dissolution of the glass waste form by incorporating key aqueous species, such as silicic acid. Therefore, to predict the long-term corrosion of these glasses in the disposal system environment, information on the paragenetic assemblage of alteration products or minerals resulting from the glass-water reaction must be known. Because the suite of weathering products that will form as a consequence of the glass-water reactions cannot be determined *a priori* at this time, as discussed by McGrail et al. (2000a, 2003), results from existing long-term PCTs conducted at 90°C (by the Vitreous State Laboratory at The Catholic University of America [VSL/CUA] and PNNL) were used to simulate and accelerate the weathering process. The chemical reaction network of secondary phases determined for ILAW glasses will be used as input for STOMP simulations of the IDF for ILAW. The STOMP code will be used to provide the near-field radionuclide-release source term for the future IDF PAs.

This section describes results of modeling performed at PNNL for Washington River Protection Solutions, LLC (WRPS) to develop a series of chemical reaction networks of secondary phases that form during the weathering of ILAW glasses for the next iteration of the IDF PA. Figure 5.1 illustrates schematically how geochemical modeling is used to develop a chemical reaction network of secondary phases based upon inputs that include initial glass composition, analytical results from PCT, PUF, and vapor hydration tests (VHT), and solid-phase characterization results of reaction products formed during the PCT, PUF, and VHT tests. This work is needed to accurately model corrosion (weathering) of new glass formulations anticipated to be produced by the Hanford Tank Waste Treatment and Immobilization Plant (WTP). The Phase I work scope focuses on acquiring this information for specific glass formulations to support the next iteration of the IDF PA. In Phase I, chemical reaction networks of secondary phases were developed using currently available data on newer glass formulations collected by PNNL since the 2001 PA (Bacon and McGrail 2001). The Phase II work scope supports the development of a technical basis that relates glass compositional ranges to a specific chemical reaction network of secondary phases. The intent is to reduce the amount of experimental and modeling work required when new glass formulations are developed. The work discussed below incorporates experimental data (VHT, PCT, etc.) on new and existing glass formulations collected by the VSL/CUA.

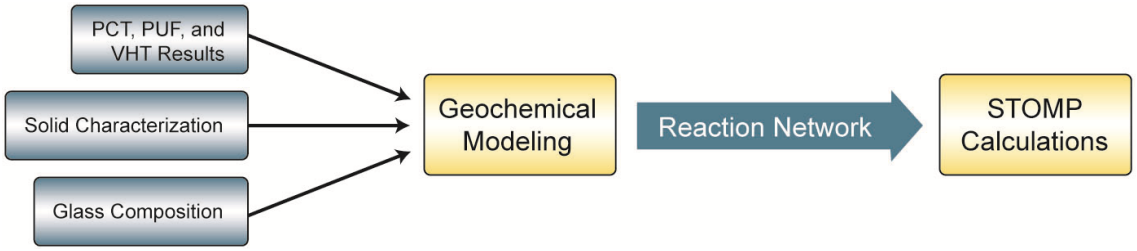


**Figure 5.1**. Schematic Representation of Data Inputs Needed for Geochemical Modeling to Develop the Chemical Reaction Network of Secondary Phases that Form During Glass Corrosion, which is Subsequently Used in STOMP Calculation to Model the Weathering of ILAW Glasses for the IDF PA

## 5.2 Geochemist's Workbench® for Modeling Secondary Phase Formation During Glass Corrosion

In the previous ILAW studies, the geochemical modeling program EQ3/EQ6 (Wolery and Daveler 1992) was used to model experimental ILAW glass weathering data for determining chemical reaction networks of secondary phases that form during glass weathering. Beginning this year, it is anticipated that the program Geochemist's Workbench (Bethke and Yeakel 2009) will also be used for reasons of convenience, which include convenient input and output interfaces and user-friendly graphical data presentation capabilities. The same thermodynamic database used previously for geochemical modeling of ILAW data with EQ3/EQ6 is also included in the suite of thermodynamic databases available in Geochemist's Workbench. To confirm that Geochemist's Workbench was computationally equivalent to EQ3/EQ6, a validation and verification exercise was completed using the same input data set (from LAWA44) and the same thermodynamic data file. The details of the approach and results of the validation and verification exercise were documented in a Validation and Verification Plan and Validation and Verification Report, which has been added to the project records. The conclusions of the report indicated that the Geochemist's Workbench and EQ3/EQ6 are computationally equivalent.

## 5.3 Description of Geochemical Modeling Approach for Determining Secondary Phase Formation During Glass Corrosion

To determine the suite of secondary phases that form during corrosion of a particular glass sample, the React Module of Geochemist's Workbench (Bethke and Yeakel 2009) is used to trace a reaction path that takes place as a particular sample of glass dissolves in water. To set up the model, the glass composition is placed in an input file in terms of its component metal oxide composition, e.g., $SiO_2$, $B_2O_3$, $Al_2O_3$, and $Na_2O$. In the case of the halides, these components are added as their elemental gases, e.g., $F_2$ and $Cl_2$. The quantity of material included in the input file is set to equal one mole of glass. This is done so that when one mole of glass dissolves, the reaction progress equals 100%. The input file is also set up so that the solution in which the glass dissolves is in equilibrium with air (the oxygen fugacity is set to 0.21 atmospheres, and the $CO_2$ fugacity is set to $10^{-3.5}$ atmospheres). As an increment of reactant (glass, in our case) is added to water, its components are initially completely dissolved in the water and are then allowed to come to equilibrium. The model accounts for all possible aqueous species that could potentially form, redox reactions that could occur, and mineral species that could precipitate at equilibrium (based upon the thermodynamic database that is used). If the saturation index (SI) of a

particular mineral phase exceeds 1.0, it will precipitate until the solution attains an equilibrium status (SI = 1.0 or less for all minerals considered). The program keeps track of how much glass has dissolved, which phases and quantities of minerals have precipitated, and the solution composition and speciation in equilibrium with the suite of minerals that have dissolved or precipitated.

To develop the correct mineral phases for the chemical reaction network, it is necessary to eliminate a large number of the phases from consideration for the following reasons: 1) the formation of some phases is kinetically inhibited at the disposal system temperature of 15°C, 2) the selection of some phases will violate the Gibbs phase rule, 3) simulations will be compared with experiments, and phases will be eliminated that generated solution compositions that were inconsistent with the experiments, or 4) phase stability will be considered over the range of chemical conditions expected for the ILAW disposal system. The bulk of the final set of phases appropriate for each glass type will be determined by simulating the solution chemistry observed in PCT experiments.

In addition to the computer simulations, characterization of alteration products is used to identify key secondary phases that are required to constrain the computer simulations. Alteration products formed at the surfaces of the glass in the PUF test and the VHT, and PCT experiments are characterized by XRD, SEM/EDS, and transmission electron microscopy.

## 5.4 Geochemical Modeling Results

Modeling of 128 glass samples was conducted in FY 2011 and an additional 10 samples were modeled in FY 2012. Initial modeling of the PCT results for the 138 glass samples was conducted using the secondary-phase reaction network listed in Table 5.1. This secondary-phase reaction network is the same as that developed for LAWA44 by Pierce et al. (2004). All PCTs were conducted at 90°C. In a number of cases, adjustments were made to the log K values from the original database to get the values shown in Table 5.1 in order to adequately reproduce the PCT solution concentration data. For analcime, 3.00 was added to the original log K value. For anatase, the original database contains a log K value only for 25°C; a value of 2.00 was added to the 25°C value for use at 90°C. For baddeleyite, 2.50 was added to the original log K value. For chalcedony, 0.30 was added to the original log K value. For $Fe(OH)_3(s)$, a value of 3.50 was added to the original log K value. For sepiolite, a value of 15.00 was added to the original log K value. For $Zn(OH)_2$-γ, a value of 3.50 was added to the original log K value. When necessary, the upward adjustments of the log K values were the consequence of the fact that amorphous phases rather than their crystalline analogs often form in laboratory experiments with waste glasses. Amorphous solids are typically much more soluble than their crystalline analogs. This is reflected in the larger log K values for the equilibrium constants.

Glass compositions used as input for the modeling are compiled in Papathanassiu et al. (2011). The measured compositions of the solutions contacting the glass in the PCT tests are also compiled in Papathanassiu et al. (2011). Results of the PCT modeling are presented in terms of the secondary phases calculated to form as a function of reaction progress (mol-glass/kg) and as comparisons with the measured solution concentrations (mg/L) for selected elements as a function of reaction progress. These results are presented graphically for each glass sample in Appendix B. The agreement between the experimental solution concentrations and the model results are in general quite good, particularly for the major glass components. Notable exceptions to this general condition include results for the components K, Li, Fe, Ti, and Zr. Calculated concentrations for K and Li determined by the model for these two

components are generally significantly higher than measured concentrations. This suggests that additional phases occur that are not included in the secondary-phase reaction network used for these calculations (Table 5.1). Alternative secondary-phase reaction networks that include possible phases that result in better model fits for these components are discussed in Section 5.6. Solid-phase characterization results (summarized in Section 5.5) were used to provide the basis for inclusion of additional phases not initially included in the secondary-phase reaction network (Table 5.1) to obtain better agreement between model results and experimental data. Predicted PCT modeling results for Fe, Ti, and Zr concentrations were typically much lower than measured concentrations. Under oxidizing conditions, these metals tend to form relatively insoluble hydroxide/oxide precipitates whose dissolved species are not effectively separated from colloidally dispersed forms by routine filtration techniques (Cho et al. 2005; Rajh et al. 1992; Fox 1988). This can result in measured concentrations that are significantly higher than the true dissolved concentrations. As a result, no attempt was made to obtain better fits for these three components.

**Table 5.1**. Secondary-Phase Reaction Network Used for Initial Modeling of PCT Results

| Phase | Reaction | Log K (90°C) |
|---|---|---|
| Analcime ($Na_{0.96}Al_{0.96}Si_{2.04}O_6 \bullet H_2O$) | analcime + $3.84H^+ \leftrightarrow 0.96Al^{3+} + 0.96Na^+ + 2.04SiO_2(aq) + 2.92H_2O$ | 3.40 |
| Anatase ($TiO_2$) | $TiO_2 + 2H_2O \leftrightarrow Ti(OH)_4(aq)$ | –6.56 |
| Baddeleyite ($ZrO_2$) | $ZrO_2 + 2H^+ \leftrightarrow Zr(OH)_2^{2+}$ | –5.20 |
| Calcite ($CaCO_3$) | $CaCO_3 + H^+ \leftrightarrow Ca^{2+} + HCO_3^-$ | 0.91 |
| Chalcedony ($SiO_2$) | $SiO_2 \leftrightarrow SiO_2(aq)$ | –2.65 |
| $Fe(OH)_3(s)$ | $Fe(OH)_3(am) + 3H^+ \leftrightarrow Fe^{3+} + 3H_2O$ | 3.04 |
| Gibbsite [$Al(OH)_3$] | $Al(OH)_3 + 3H^+ \leftrightarrow Al^{3+} + 3H_2O$ | 4.46 |
| Sepiolite [$Mg_4Si_6O_{15}(OH)_2 \bullet 6H_2O$] | sepiolite + $8H^+ \leftrightarrow 4Mg^{2+} + 6SiO_2(aq) + 11H_2O$ | 39.72 |
| $Zn(OH)_2$-γ | $Zn(OH)_2\text{-}\gamma + 2H^+ \leftrightarrow Zn^{2+} + 2H_2O$ | 11.88 |

## 5.5 Solid-Phase Characterization Results

To establish that the selected secondary-phase reaction network is correct, selected glass samples from the PCT tests were characterized with XRD and SEM/EDS. Phases identified by XRD analyses are shown in Table 5.2. Note that a crystalline phase must be present at greater than ~5–10 wt.% of the total sample mass (greater than 1 wt.% under optimum conditions) to be readily detected by XRD. The XRD spectra for each of these samples along with the SEM/EDS results are reported by Papathanassiu et al. (2011).

**Table 5.2**. Mineral Phases Identified in PCT Glass Samples by XRD

| Sample ID | Phases Identified |
|---|---|
| A1-AN105R2 | analcime – c – $Na(Si_2Al)O_6•H_2O$, gobbinsite – $Na_5(Si_{11}Al_5)O_{32}•11H_2O$ |
| A1C1-1 | analcime – c – $Na(Si_2Al)O_6•H_2O$, gobbinsite – $Na_5(Si_{11}Al_5)O_{32}•11H_2O$<br>hectorite-15a – $Na_{0.2}(Mg,Li)_3Si_4O_{10}(OH)_2·4H_2O$, stevensite – $(Ca,Na)_xMg_{3-x}Si_4O_{10}(OH)_2$ |
| A1C1-2 | analcime – c – $Na(Si_2Al)O_6•H_2O$, phillipsite-Na – $Na_4KAl_5Si_{11}O_{32}(H_2O)_{10}$,<br>stevensite – $(Ca,Na)_xMg_{3-x}Si_4O_{10}(OH)_2$ |
| A2-AP101 | chabazite – $Ca_2Al_4Si_8O_{24}•12H_2O$, herschelite – $NaAlSi_2O_6•3H_2O$ |
| A88AP101R1 | analcime – $Na(AlSi_2O_6)(H_2O)$ |
| A88Si-15 | None |
| C100GCC | analcime – $NaAl(Si_2O_6)H_2O$, stevensite – $(Ca,Na)_xMg_{3-x}Si_4O_{10}(OH)_2$ |
| LAWA44R10 | analcime – $Na(AlSi_2O_6)(H_2O)$ |
| LAWA53 | analcime – $NaAl(Si_2O_6)H_2O$ |
| LAWA88R1 | analcime – $NaAl(Si_2O_6)H_2O$ |
| LAWA126 | chabazite – $Ca_{1.96}Al_{3.9}Si_{8.1}O_{24}(H_2O)_{13}$, herschelite – $NaAlSi_2O_6•3H_2O$ |
| LAWB31 | None |
| LAWB32 | None |
| LAWB35 | None |
| LAWB60 | saponite-15Å – $Ca_{0.2}Mg_3(SiAl)_4O_{10}(OH)_2•4H_2O$, stevensite – $Ca_{0.2}Mg_{2.9}Si_4O_{10}(OH)_2•4H_2O$ |
| LAWB73 | stevensite – $(Ca,Na)_xMg_{3-x}Si_4O_{10}(OH)_2$, swinfordite-13Å - $Ca_{0.1}(Li,Al)_3Si_4O_{10}(OH)_2•2H_2O$ |
| LAWB81 | swinfordite-13a - $Ca_{0.1}(Li,Al)_3Si_4O_{10}(OH)_2•2H_2O$ |
| LAWB89 | None |
| LAWB90 | foshagite – $Ca_4(SiO_3)_3(OH)_2$ |
| LAWC23 | None |
| LAWC27 | None |
| LAWC31 | analcime – $NaAl(Si_2O_6)H_2O$, stevensite – $(Ca,Na)_xMg_{3-x}Si_4O_{10}(OH)_2$ |
| LAWC32 | analcime – $NaAl(Si_2O_6)H_2O$, stevensite – $(Ca,Na)_xMg_{3-x}Si_4O_{10}(OH)_2$,<br>swinfordite-13Å - $Ca_{0.1}(Li,Al)_3Si_4O_{10}(OH)_2•2H_2O$ |
| PNLA126CC | analcime – $NaAl(Si_2O_6)H_2O$, chabazite – $Ca_{1.96}Al_{3.9}Si_{8.1}O_{24}(H_2O)_{13}$ |

The most common phase identified in the samples was analcime [$Na(AlSi_2O_6)(H_2O)$]. This phase was frequently the second most abundant phase predicted to occur in the reaction progress modeling (after chalcedony). Using the initial secondary-phase reaction network, analcime was predicted by geochemical modeling to occur in the PCTs for all samples in Table 5.2. Gobbinsite [$Na_5(Si_{11}Al_5)O_{32}•11H_2O$], which is compositionally very similar to analcime, was identified in samples A1-AN105R2 and A1C1-1. Stevensite [$(Ca,Na)_xMg_{3-x}Si_4O_{10}(OH)_2$] was identified in 7 of the 24 samples analyzed. Hectorite-15a [$Na_{0.2}(Mg,Li)_3Si_4O_{10}(OH)_2•4H_2O$] was found only in sample A1C1-1. Phillipsite-Na [$Na_4KAl_5Si_{11}O_{32}(H_2O)_{10}$] was also identified in just one of the samples (A1C1-2). Chabazite [$Ca_2Al_4Si_8O_{24}•12H_2O$] was determined to occur in three of the samples (A2-AP101, LAWA126, and PNLA126CC). Herschelite [$NaAlSi_2O_6•3H_2O$] was identified in two samples (A2-AP101 and LAWA126). Saponite-15Å [$Ca_{0.2}Mg_3(SiAl)_4O_{10}(OH)_2•4H_2O$] was found in one sample (LAWB60). Swinfordite-13Å [$Ca_{0.1}(Li,Al)_3Si_4O_{10}(OH)_2•2H_2O$] was identified in three samples (LAWB73, LAWB81, LAWC32). Foshagite [$Ca_4(SiO_3)_3(OH)_2$] was identified in sample LAWB90. Of the phases in Table 5.2 identified by XRD, thermodynamic data are available only for analcime, saponite, and foshagite.

A summary of SEM/EDS analysis results in terms of likely phases present based upon elemental composition and morphology are compared with phases identified by XRD in Table 5.3. Elemental compositions determined by EDS and crystal morphology apparent from the SEM images provide compelling evidence for the presence of analcime in a majority of the samples (13 out of 24). Elemental compositions and crystal morphology provide credible evidence for the presence of chabazite in many of the samples (10 out of 24). Evidence supporting the possible presence of a number of phases (saponite, $Fe(OH)_3$, $Zn(OH)_2$, $Zr(OH)_4$, phillipsite, and stevensite) is less certain and is based primarily on analysis of locations that could be mixtures of some of the indicated phases. EDS analyses for LAWB60, LAWB73, LAWB90, and LAWC27 indicate the likely presence of a calcium silicate phase. EDS analyses for LAWB89, LAWB90, and LAWC27, indicate the likely presence of a calcium carbonate phase. This information will be used in Section 5.6 to rationalize the inclusion of additional phases to the secondary-phase reaction network to achieve better model fits of the PCT solution data.

**Table 5.3**. Mineral Phases Identified in PCT Glass Samples by SEM/EDS and XRD

| Sample ID | Possible Secondary Mineral Phase Compositions Based on SEM/EDS | Phases Identified by XRD |
|---|---|---|
| A1-AN105R2 | analcime, saponite, $Fe(OH)_3$, $Zn(OH)_2$, $Zr(OH)_4$, | analcime, gobbinsite |
| A1C1-1 | analcime, saponite, $Fe(OH)_3$, $Zn(OH)_2$, $Zr(OH)_4$ | analcime, gobbinsite, hectorite, stevensite |
| A1C1-2 | analcime, saponite, $Fe(OH)_3$, $Zn(OH)_2$ | analcime, phillipsite, stevensite |
| A2-AP101 | chabazite, phillipsite | chabazite, herschelite |
| A88AP101R1 | analcime, chabazite, phillipsite, $Fe(OH)_3$, $Zn(OH)_2$, $Zr(OH)_4$, | analcime |
| A88Si-15 | analcime, chabazite, saponite | None |
| C100GCC | analcime, chabazite, saponite, $Fe(OH)_3$, $Zn(OH)_2$, $Zr(OH)_4$ | analcime, stevensite |
| LAWA44R10 | analcime, saponite | analcime |
| LAWA53 | analcime, chabazite, saponite | analcime |
| LAWA88R1 | analcime, chabazite, saponite, $Fe(OH)_3$, $Zn(OH)_2$ | analcime |
| LAWA126 | analcime, chabazite, phillipsite, saponite | chabazite, herschelite |
| LAWB31 | None | None |
| LAWB32 | None | None |
| LAWB35 | saponite, $Zr(OH)_4$ | None |
| LAWB60 | chabazite, calcium silicate, stevensite, $Zr(OH)_4$ | saponite-15Å, stevensite |
| LAWB73 | calcium silicate, stevensite, $Zn(OH)_2$, $Zr(OH)_4$ | stevensite, swinfordite-13Å |
| LAWB81 | saponite, $Fe(OH)_3$, $Zn(OH)_2$, $Zr(OH)_4$ | swinfordite-13 Å |
| LAWB89 | calcium carbonate | None |
| LAWB90 | calcium carbonate, calcium silicate | foshagite |
| LAWC23 | chabazite, saponite, $Fe(OH)_3$, $Zn(OH)_2$ | None |
| LAWC27 | analcime, calcium carbonate, calcium silicate, saponite, stevensite | None |
| LAWC31 | stevensite, $Zn(OH)_2$, | analcime, stevensite |
| LAWC32 | analcime, saponite, stevensite, $Fe(OH)_3$, $Zn(OH)_2$, $Zr(OH)_4$ | analcime, stevensite, swinfordite-13Å |
| PNLA126CC | analcime, chabazite, saponite, $Fe(OH)_3$, $Zr(OH)_4$, | analcime, chabazite |

## 5.6 Alternative Secondary-Phase Reaction Networks

A certain fraction of the ILAW glass PCT results did not fit well with model predictions of concentrations. In these cases, the original secondary-phase reaction network (Table 5.1) was augmented with additional phases to achieve better agreement between the model results (predicted solution concentrations) and the experimental PCT data. Samples selected for further discussion in this section are confined to those for which XRD and SEM/EDS analyses were conducted. This was done because only these samples have solid-phase characterization data that can be used to support arguments for the occurrence of additional phases not included in the original secondary-phase reaction network. The most frequent discrepancies between measured and model results occurred with K and Li. Possible phases that could account for the lower K measured concentrations relative to model predictions of PCT data include an analcime phase in which Na is partially replaced with K (Savage et al. 2001) or a K-rich chabazite $(Ca_{0.5}, Na, K)_4[Al_4Si_8O_{24}]\bullet 12H_2O$. Analogous phases could potentially account for the lower Li concentrations as well. For example, Li chabazite is a stable phase that can be readily synthesized (e.g., Singh and Webley 2005). Accounting for these phases in the model is problematic because thermodynamic data for these phases is not currently available and the exact compositions of these phases in the PCT tests are unknown. For example, the distribution of exchangeable cations in chabazite is variable and will depend on their concentrations in the glass and the solution in contact with the glass. To determine whether K- and Li-rich forms of analcime or chabazite could potentially explain the discrepancies between the initial modeling results and the PCT data, further modeling was conducted in which the hypothetical phases K-analcime $[K(AlSi_2O_6)(H_2O)]$ and Li-analcime $[Li(AlSi_2O_6)(H_2O)]$ are assumed to control K and Li concentrations. These hypothetical phases were used for the modeling because analcime and chabazite have similar composition; with ratios of exchangeable cation charge to Al, Si, and O that are equal (only the degree of hydration is different).

An example of this approach is presented here for glass sample LAWA126. This sample was selected for illustration because it did not contain any Li and only one additional phase was required to improve the fit for K. The modeling was conducted iteratively, by manually adjusting the log K values for K-analcime until the best fit of the PCT data was obtained. Figure 5.2 shows K concentrations measured in the PCT solutions as a function of reaction progress determined for glass sample LAWA126, model results determined using the original secondary-phase reaction network listed in Table 5.1, and model results with the addition of K-analcime to the network. The results indicate that significantly better fits for K occur when K-analcime is included in the model. The best fit was obtained using log K = 5.304 for K-analcime. The log K used for Na-analcime in the model was 6.404 at 90°C, indicating that the hypothetical K-analcime has a lower solubility than that of Na-analcime. Results for the other elements are not shown because any change in the model results for these elements was nearly imperceptible. These model results do not prove that K-analcime did precipitate during the LAWA126 PCT; however, the results do indicate that precipitation of a phase with this composition is a reasonable explanation for the K concentrations determined for the PCTs. Based upon the XRD and SEM/EDS results from Papathanassiu et al. (2011), it is likely that rather than formation of a pure K-analcime phase, a chabazite phase in which K substitutes for other cations in the framework of the phase is what actually occurs. The solid-phase characterization results for LAWA126 support this assertion. The XRD results confirm the presence of chabazite, and the SEM/EDS results illustrate the occurrence of a crystalline phase consistent with the crystal morphology and composition of chabazite with an exchangeable cation composition dominated by Na but with a significant fraction of K.

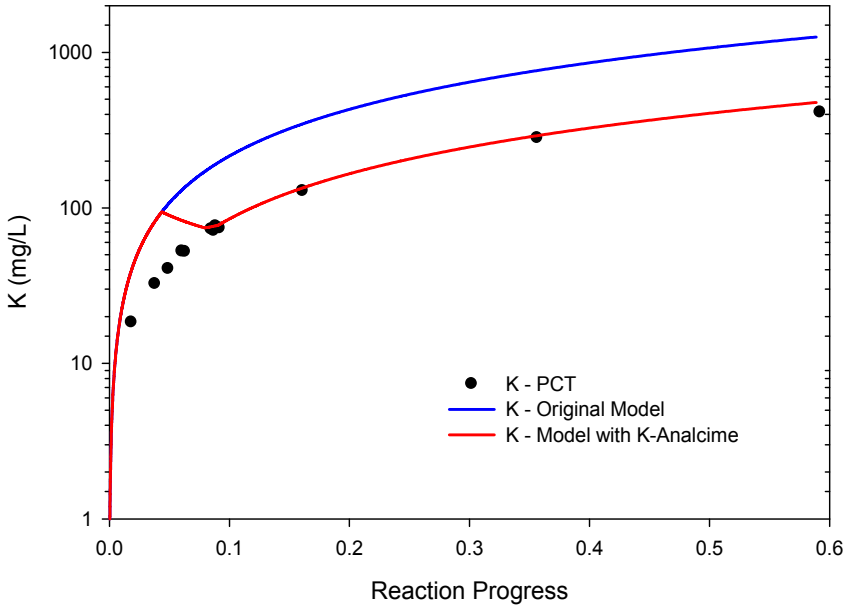


**Figure 5.2**. Measured Solution Concentrations in PCT for K (mg/L) and Model Results Using the Secondary Reaction Network Listed in Table 5.1 and Model Results with the Addition of K-Analcime to the Network as a Function of Reaction Progress (mol-glass/kg) Determined for Glass Sample LAWA126 (PCT conducted at 90°C)

For some glass samples containing Li, it was possible to get better model fits of the PCT data by including both the hypothetical K-analcime phase and a hypothetical Li-analcime phase. However, because XRD analysis indicates the presence of other Li-containing phases including hectorite-15a – $Na_{0.2}(Mg,Li)_3Si_4O_{10}(OH)_2 \cdot 4H_2O$ (sample A1C1-1) and swinfordite-13Å – $Ca_{0.1}(Li,Al)_3Si_4O_{10}(OH)_2 \cdot 2H_2O$ (samples LAWB73, LAWB81, and LAWC32), these results cannot be considered a reliable indication that a Li-analcime-type phase actually occurs. Because thermodynamic data for hectorite and swinfordite are not available, modeling cannot be used to test the applicability of these phases. Because of these factors, reliable and unambiguous modeling of glasses with significant Li content is problematic.

For glass samples that had relatively high concentrations of Ca and Li and relatively low concentrations of Na, modeling conducted with the reaction network in Table 5.1 resulted in particularly poor fits. For samples LAWB60 and LAWB73, the model fits for Ca were especially poor and the fits for Al and Si were poorer than typically observed. For samples LAWB89 and LAWB90, model fits for Ca, Al, and Si were all quite poor. For these samples, the measured calcium concentrations were significantly higher than model predictions when the solubility of calcite is assumed to control Ca concentrations (Table 5.1). Significant improvements to the model fits for Ca could be made by assuming the solubility of either monohydrocalcite ($CaCO_3 \cdot H_2O$) or gyrolite ($Ca_2Si_3O_7(OH)_2 \cdot 1.5H_2O$) controlled Ca concentrations. Using SEM/EDS a calcium carbonate phase was identified in samples LAWB89 and LAWB90 and a calcium silicate phase was identified in samples LAWB60, LAWB73, and LAWB90, suggesting that monohydrocalcite and gyrolite are plausible phases. Foshagite ($Ca_4Si_3O_9(OH)_2 \cdot 0.5H_2O$) was identified in LAWB90 by XRD. It is possible that gyrolite controlled Ca concentrations in solution for the LAWB90 PCT, but this phase subsequently transformed to foshagite as a result of sample dehydration prior to XRD analysis. Depending on the glass sample, model fits for Al, Si, and Na concentrations could be improved by 1) suppressing gibbsite and allowing boehmite, diaspore, or

kaolinite to control the aluminum concentrations and 2) reducing the chalcedony log K by 0.3 log units. No consistent approach was identified that would improve the model fits for glass samples that had relatively high concentrations of Ca and Li and relatively low concentrations of Na. It is suspected that the inability to identify and appropriately model the Li phase may have contributed to this problem. As a result, further efforts to improve the model fits for glass samples that were not adequately described by the secondary-phase reaction network in Table 5.1 and the hypothetical K-analcime phase was discontinued.

### 5.6.1 Clinochlore as an Alternative Secondary Phase in Place of Sepiolite

The modeling that was conducted in this work assumed that the solubility of sepiolite [$Mg_4Si_6O_{15}(OH)_2 \cdot H_2O$] controlled $Mg^{2+}$ concentrations in solution. This was consistent with previous modeling done in Pierce et al. (2004, 2005). In a more recently published work (Pierce and Bacon 2011), the solubility of clinochlore [$Mg_5Al_2Si_3O_{10}(OH)_8$] was assumed to control $Mg^{2+}$ concentrations in solution. The reason for this change was that clinochlore was identified in the reacted glass (PUF) sample by XRD.

To determine which of these two phases results in better modeling fits to the experimental PCT data, two of the previous PCT data sets were remodeled assuming that clinochlore was the secondary phase that controlled $Mg^{2+}$ concentrations in solution rather than sepiolite. The glasses modeled (A1-AN105R2 and A1C1-3) were glasses in which measureable Mg was found in the PCT test solutions. The modeling results indicated that the solubility of clinochlore is such that Mg concentrations are controlled to much lower concentrations than occurs when sepiolite is allowed to control the Mg solution concentration. At the onset of glass dissolution, the modeling with clinochlore predicts an initial spike in Mg concentrations. Subsequently, Mg concentrations were reduced to very low concentrations that were inconsistent with measured concentrations. The change in the modeling results for the other components was very minor to negligible. This is consistent with the fact that the quantity of clinochlore or sepiolite that was predicted to form was a minor fraction of the total secondary phases (1–2%).

Unfortunately, this analysis does not provide a conclusive indication of which phase is more appropriate to use. There are several reasons for this. For the samples in which Mg concentrations were above the detection limit, it would appear that sepiolite provides the better modeling fits to the data. However, for most of the PCT experiments, Mg concentrations were below the detection limit, suggesting that there is the potential that clinochlore would provide the better fit for these cases. In addition, the phase compositions that were assumed in the modeling may not be consistent with the phases that actually formed. For example, the phase identification for clinochlore [$(Mg, Fe, Al)_6(Si, Al)_4O)_{10}(OH)_8$] should be considered as qualitative in terms of the chemical composition of the clay mineral, whereas the modeling requires that a single specific composition be assumed with an associated thermodynamic solubility constant. Thermodynamic solubility constants for variable composition Mg-bearing aluminosilicate phases are not available.

## 5.7 Summary of Geochemical Modeling

It was determined that for the majority of the 138 glass samples that were modeled, a secondary-phase reaction network previously developed for ILAW glass sample LAWA44 produced good model fits for the major glass components. Notable exceptions were predictions for K and Li solution

concentrations in equilibrium with weathered glass. Model fits for glass samples that contained relatively high concentrations of Ca and Li and relatively low concentrations of Na also had relatively poor fits for Ca, Al, and Si concentrations in solution. For glass samples that did not contain Li, significantly better model fits for K were attained with the assumption that K concentrations were controlled by the solubility of a hypothetical K-analcime phase. Solid-phase characterization results indicated that rather than a pure K-analcime phase, a K-rich chabazite phase is more likely the phase that actually forms during glass weathering. XRD results confirmed the presence of chabazite and SEM/EDS results verified the presence of a crystalline phase consistent with the crystal morphology and composition of chabazite. EDS results indicated that the exchangeable cation composition for the chabazite was dominated by Na but with significant fractions of K. Because the hypothetical K-analcime phase and K-chabazite have an equivalent compositional stoichiometry for the structural elements (chabazite has more waters of hydration), the good model fits for K are consistent with chabazite being the phase that controls K concentrations during corrosion of ILAW glasses.

Modeling Li solution concentrations in equilibrium with weathered glass proved to be problematic due to an inability to identify the specific composition(s) of Li-containing secondary phase(s) and a lack of thermodynamic data for such phases. For glass samples that contained relatively high concentrations of Ca and Li and relatively low concentrations of Na, it was determined that monohydrocalcite ($CaCO_3 \bullet H_2O$) and/or gyrolite ($Ca_2Si_3O_7(OH)_2 \bullet 1.5H_2O$) could potentially control Ca concentrations rather than calcite, as was the case for more typical glass compositions. Better model fits of the experimental PCT solution concentrations for these types of glasses could be obtained by suppressing gibbsite precipitation and assuming that Al concentrations were controlled by boehmite, diaspore, or kaolinite (depending upon the specific glass sample). Developing a consistent reaction network of secondary phases for glass samples that had relatively high concentrations of Ca and Li and relatively low concentrations of Na was not feasible, probably due to the inability to identify and model the phase(s) that control Li concentrations and the lack of actual thermodynamic data for K-chabazite.

The modeling that was conducted in this work and previous work (Pierce et al. 2004, 2005), assumed that the solubility of sepiolite [$Mg_4Si_6O_{15}(OH)_2 \bullet H_2O$] controlled $Mg^{2+}$ concentrations in solution. More recent work (Pierce and Bacon 2011), suggested that the solubility of clinochlore [$Mg_5Al_2Si_3O_{10}(OH)_8$] controls $Mg^{2+}$ concentrations in solution. The reason for this change was that clinochlore was identified in the reacted ORPLG9 glass (PUF) sample by XRD. Additional modeling of PCT solution samples that had measureable Mg was conducted to determine whether clinochlore could provide better fits to the data relative to sepiolite. The results proved to be inconclusive, suggesting that either phase could potentially control Mg concentrations.

# 6.0 Monte Carlo Simulations

## 6.1 Overview

The primary objective of the MC simulations is to predict the composition, extent, and morphology of the hydration layer (also referred to as the alteration layer) as a function of glass composition and thus provide input data for geochemical modeling of secondary-phase formation.

In the MC model, the glass framework is mapped onto a cubic lattice wherein each lattice site represents a glass-former cation (e.g., Si, Al, or B) and its first oxygen coordination shell, and two connections are removed at each lattice site to represent the fourfold connectivity of the glass-former cations. Glass-modifier cations (e.g., Na) are placed in interstitial positions. When a site is dissolved, it is considered to be replaced by water. Connections between nearest-neighbor sites represent X-O-X linkages, where X is a glass-former cation and O is oxygen. The contacting (bulk) aqueous solution can either be considered infinite to mimic a single-pass flow-through test conducted under dilute conditions or have a fixed number of water sites calculated to obtain a particular surface-area-to-volume ratio (in $m^{-1}$). Each simulation step of the MC algorithm comprises five stages:

- a dissolution evaluation and execution stage, in which each surface site is evaluated for dissolution using dissolution probabilities determined using the approach described below;
- a glass connectivity evaluation stage, in which the new glass configuration is evaluated to determine whether clusters of lattice sites not connected to the main glass matrix are present and therefore should also be dissolved;
- a condensation stage, in which glass components can deposit back at surface sites;
- a liquid connectivity evaluation stage, in which, in a manner analogous to the glass connectivity evaluation stage, the connectivity of the water sites is evaluated to determine the water sites that are part of the bulk aqueous solution and those that belong to closed pores (we note that the current implementation of the MC algorithm only allows dissolution and condensation processes to occur at glass surface sites in contact with the bulk aqueous solution and not inside closed pores); and finally,
- a coordination evaluation stage, in which the coordination of each site in the final glass configuration is recalculated.

The different network formers have different dissolution and condensation probabilities. Boron atoms are considered to dissolve instantaneously once in contact with the bulk aqueous solution; therefore, their dissolution probability is set to 1 regardless of their coordination. In addition, they are considered fully soluble, and therefore cannot condense back on the glass surface. For silicon, dissolution probabilities $w_1$, $w_2$, and $w_3$ are used for sites with one, two, or three connections to silicon nearest neighbors. Silicon atoms can deposit back at surface sites with probability $w_r = w_{c\text{-}Si} c_{Si}$, where $w_{c\text{-}Si}$ is the silicon condensation probability and $c_{Si}$ is the silicon concentration in the aqueous solution (in atoms per aqueous site). The MC program also includes aluminum, and therefore Si and Al can find themselves in a number of possible bonding environments. To minimize the number of parameters used to describe all

possible bonding environments, we employed the formulation introduced by Ledieu et al. (2006), which defines the Si and Al dissolution probabilities as follows:

$$w_d(\mathrm{Si}, n, m) = \frac{w_n}{r_{Al}^m} \tag{6.1}$$

and

$$w_d(\mathrm{Al}, n, m) = \frac{w_n}{r_{Al}^{m+1}} \tag{6.2}$$

where $w_d$ = the dissolution probability for Si or Al
$n$ = the total number of connections
$m$ = the number of connections with Al
$r_{Al}$ = the relative strength between Si-O-Al and Si-O-Si linkages.

Aluminum atoms can deposit back on the surface in the same way as silicon atoms with condensation probability $w_{c\text{-}Al}$. To limit the number of parameters further, the ratios $w_1/w_2$ and $w_2/w_3$ were always set to be equal and this ratio was designated as $\delta$. Therefore, five parameters ($w_1$, $\delta$, $w_{c\text{-}Si}$, $w_{c\text{-}Al}$, and $r_{Al}$) are needed to model four-oxide glasses ($SiO_2$, $Al_2O_3$, $B_2O_3$, and $Na_2O$).

In FY 2010, initial developments of the MC code were implemented and the MC code was used to evaluate the effects of different structural features (presence of non-bridging oxygens, the formation and polymerization of boroxol rings, and the aluminum avoidance rule) on the rates and mechanisms of dissolution of borosilicate and aluminoborosilicate glasses. Moreover, the MC code was used to model the dissolution of the NeB (nepheline-based) glasses studied by Pierce et al. (2010a). This work resulted in the publication of a research article (Kerisit and Pierce 2011) in *Geochimica et Cosmochimica Acta*.

The work performed in FY 2010 focused on the dissolution of glasses in dilute conditions only. Therefore, the MC simulations were extended in FY 2011 to study the dissolution of glasses in near-equilibrium conditions, which are more representative of the conditions expected in the IDF. Condensation reactions were implemented in the MC code to allow for near-equilibrium simulations. These simulations required the MC code to keep track of the connectivity of the water sites and thus were much more demanding computationally than those performed previously under dilute conditions. Therefore, the MC code was transformed from a single-processor to a multiple-processor code to accelerate the simulations. This new implementation was used to simulate the dissolution of borosilicate glasses in contact with an aqueous solution of fixed volume in both static and flow-through conditions. This work led to the publication of a second research article (Kerisit and Pierce 2012) in the *Journal of Non-Crystalline Solids*.

The work carried out this fiscal year (FY 2012) was divided into two activities. The first activity was aimed at providing a quantitative comparison between calculated and experimental dissolution properties of borosilicate and aluminoborosilicate glasses using a single set of model parameters. The second activity consisted in extending the MC code to include high-field-strength cations, which adopt an octahedral coordination in borosilicate glasses. Progress achieved under these two activities is summarized in the following sections.

## 6.2 Monte Carlo Model Parameterization and Validation

The work carried out in FY 2010 and FY 2011 dealt for the most part with aqueous corrosion behavior as a function of glass structure and composition, and comparisons with experimental data were mostly limited to qualitative trends. Therefore, the first activity of this fiscal year focused on using experimental data to parameterize the MC model and thus enable direct quantitative comparison between experimental and calculated glass corrosion properties.

First, we note that, although the MC code can be used to model glasses containing boron in both trigonal and tetrahedral coordination environments, as well as silicon sites with or without non-bridging oxygens, all the simulations performed this fiscal year assume that all boron and aluminum ions are in tetrahedral coordination and are charge compensated by sodium ions, and that the simulated glasses do not contain non-bridging oxygens. Consequently, the $Na_2O$ mole fraction is always set to be equal to the sum of the $B_2O_3$ and $Al_2O_3$ mole fractions.

**Sodium borosilicate glasses**. Three parameters need to be determined ($w_1$, $\delta$, and $w_{c\text{-}Si}$) to model the dissolution of sodium borosilicate glasses. A series of MC simulations were performed to derive the parameters that yielded the best quantitative agreement with 1) the silicon leached thickness, 2) the silicon saturation concentration, and 3) the dissolution time constant obtained by Ledieu et al. (2004) as a function of boron content for glasses of composition (100–2$x$)% $SiO_2$ $x$% $B_2O_3$ $x$% $Na_2O$, where $10 < x < 25$% (Figure 6.1, Figure 6.2 and Figure 6.3). The experimental data of Ledieu and coworkers were obtained in static conditions (surface-to-volume ratio [S/V] = 100 and 2,000 $m^{-1}$), at 90°C, and at a pH of 8.5. The simulations were also carried out in static conditions but solely at a S/V ratio of 2,000 $m^{-1}$ to accelerate the corrosion process. The best-fit parameters thus obtained are $w_1$=0.01, $\delta$=10, and $w_{c\text{-}Si}$ = 10.

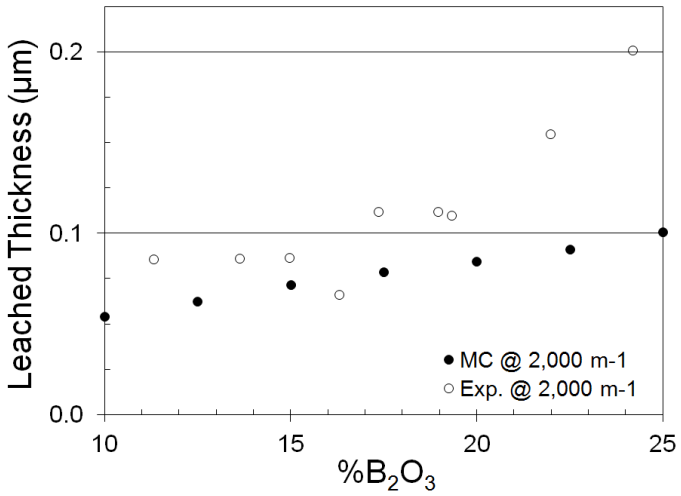


**Figure 6.1**. Calculated and Experimental Silicon Leached Thickness as a Function of Boron Content

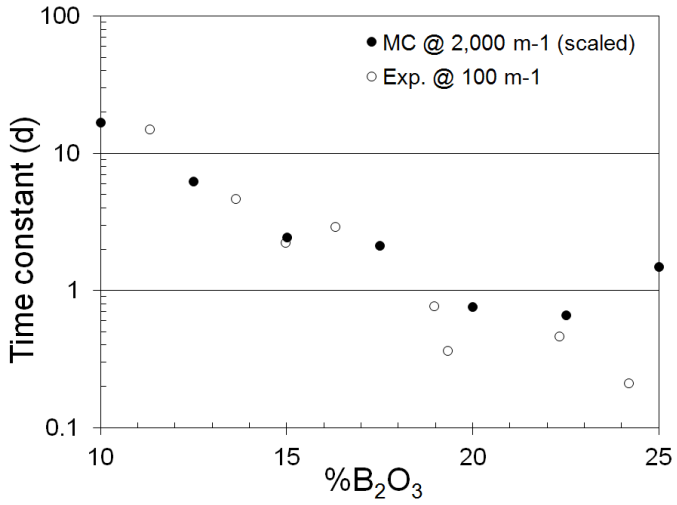


**Figure 6.2**. Calculated and Experimental Time Constants as a Function of Boron Content

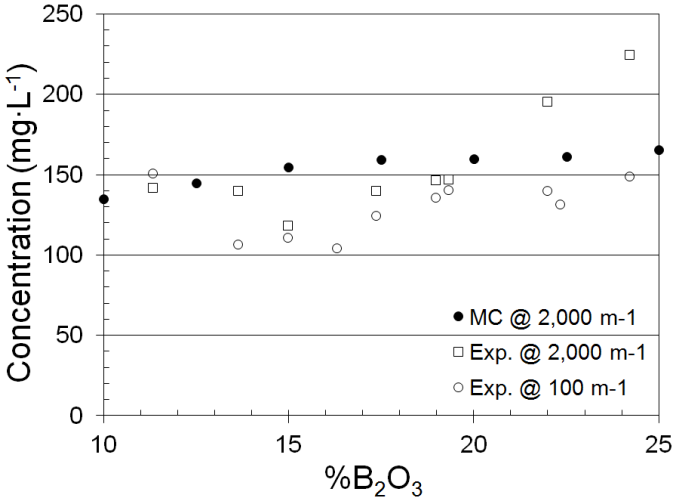


**Figure 6.3**. Calculated and Experimental Silicon Saturation Concentrations as a Function of Boron Content

Figure 6.1 indicates that the MC simulations show a good overall quantitative agreement with the experimental values of the Si leached thickness obtained by Ledieu et al. (2005) at 2,000 $m^{-1}$. The simulations appear to underestimate the Si leached thickness for the two data points above 20 mol% $B_2O_3$. This sudden increase at high boron content is consistent with the increase in Si solubility obtained from the same experiments and shown in Figure 6.3. However, the Si solubility values obtained at the same B contents but at 100 $m^{-1}$ do not show this sudden increase. Therefore, it is not clear whether the discrepancy at high B content and 2,000 $m^{-1}$ is real or not.

To construct Figure 6.2, the time evolution of the experimental and calculated B concentrations, $c_B(t)$, is fit to the following equation:

$$c_B(t) = c_B^{\infty}\left(1 - e^{-t/\tau}\right) \tag{6.3}$$

where $c_B^{\infty}$ is the final B concentration and $\tau$ is the time constant. Ledieu et al. (2005) only provided time constants for the series of experiments carried out at S/V = 100 $m^{-1}$. They noted that, given the frequency at which the leached solution was sampled, the kinetics of corrosion at S/V = 2000 $m^{-1}$ were too fast to obtain accurate time constant measurements and only reported that the same general trend was observed. Therefore, the calculated time constants were compared to the time constants obtained experimentally at S/V = 100 $m^{-1}$. Because the unit of time in the MC simulations is one computer step and because the simulations and experimental measurements were performed at different values of S/V, a scaling factor of 60 s per computer step was included to enable comparison between the two sets of data. Figure 6.2 shows that this scaling factor translates into a good agreement with the experimental data of Ledieu et al. (2005).

Finally, the calculated silicon saturation concentrations are also in good agreement with the experimental data obtained by Ledieu et al. (2005) at both 100 and 2,000 $m^{-1}$, as shown in Figure 6.3.

**Sodium aluminoborosilicate glasses**. Keeping the parameters determined for the borosilicate glasses constant, it remains to determine the parameters $w_{c\text{-}Al}$ and $r_{Al}$ to model the corrosion of sodium aluminoborosilicate glasses. The experimental data published by Ledieu et al. (2005) were used to determine the optimum values of the new parameters. The experimental data were obtained in static conditions (S/V = 100 $m^{-1}$), at 90°C, and at a pH of 8.5. The Al content was varied from 0 to 10 mol% by substituting Al for Si; therefore, the glass compositions were [(70–2$x$)% $SiO_2$ $x$% $Al_2O_3$ 15% $B_2O_3$ (15 + $x$)% $Na_2O$], where $0 < x < 10\%$. Four general observations were made by Ledieu et al. (2005) in their study:

- The Si solubility/leached fraction decreases with small Al addition and then remains approximately constant with further Al addition.
- The B leached fraction increases with increasing Al content.
- The time constants increase with increasing Al content.
- Al and Si leached fractions are approximately equal at all Al contents (except 0%).

The simulations were carried out with the same compositions but at S/V = 2,000 $m^{-1}$ to accelerate the corrosion process. The parameters that yielded the best overall agreement with the four observations listed above were $r_{Al}$=5 and $w_{c\text{-}Al}$=5.

Figure 6.4 shows the calculated leached thicknesses at S/V =2,000 $m^{-1}$ and the experimental leached fractions at 100 $m^{-1}$. Because the calculations were carried out for a much higher value of S/V than the experimental measurements, a direct quantitative comparison of the leached fractions/thicknesses is not possible; however, both quantities should follow the same trend with Al content. Indeed, the simulations show that the Si leached thickness decreases with increasing Al content as observed experimentally, although the MC simulations show an approximately linear decrease over the range of Al contents whereas an initial significant decrease at low Al content followed by little change at high Al content is seen experimentally. Although the Al and Si leached thicknesses are not approximately equal at all Al contents, the difference between the Si and Al leached thicknesses decreases with increasing Al content. It should also be noted that the experimental Al aqueous concentrations are low and that hence there are potentially large uncertainties in the experimental Al leached fractions that could account in part for this discrepancy.

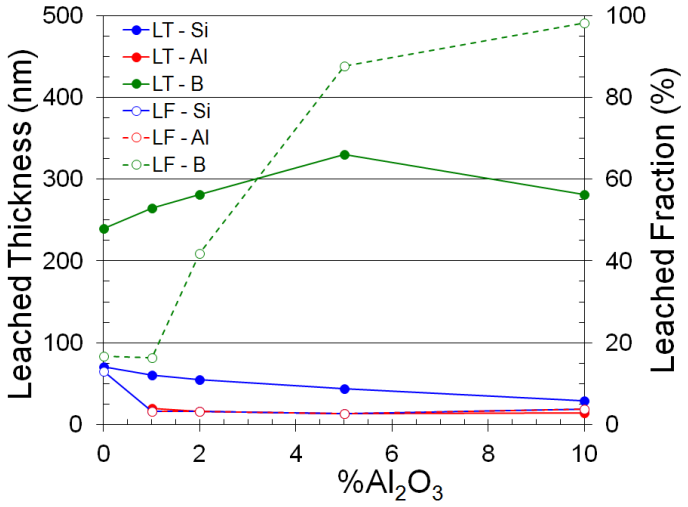


**Figure 6.4**. Calculated Si, Al, and B Leached Thicknesses (LT) Obtained at 2,000 $m^{-1}$ and Experimental Si, Al, B Leached Fractions (LF) Obtained at 100 $m^{-1}$ as a Function of Al Content

There is also good quantitative agreement between the time constants obtained in the MC simulations and those derived experimentally from the time evolution of the B aqueous concentration, as shown in Figure 6.5. It should be noted that the same scaling factor of 60 s per computer step used for the borosilicate glasses was also used here.

Importantly, the MC simulations reproduce the experimental observation that, although the presence of Al slows down the kinetics of corrosion, the extent of corrosion, as measured by the amount of B release, increases with increasing Al content (Figure 6.4). To understand this phenomenon, one needs to recall one of the conclusions from last fiscal year's work, namely, that the dynamics of hydrolysis/condensation reactions lead to the preferred removal of low-coordination sites and the formation of a denser Si network and that, because the upper part of the alteration layer has been exposed to the aqueous solution for a longer period of time than the lower part, the hydrolysis/condensation process is more advanced at the top of the alteration layer, leading to the growth of a dense Si layer that blocks water percolation and stops the corrosion process. Therefore, the decrease in the dissolution rate due to the presence of Al slows down the hydrolysis/condensation kinetics that drive the reorganization and eventual blockage of the altered layer. As a result, the time required for the corrosion to stop increases with Al content (Figure 6.5) and thus the final B leached fraction increases with Al content (Figure 6.4).

However, the simulations also predict a decrease in B leached thickness at the highest Al content. We suggest that this effect is due to the competition between two processes. The first process is that described in the previous paragraph, namely, Al slows down the overall hydrolysis/condensation kinetics. The second process is due to the fact that the presence of Al increases the lifetime of the upper part of the altered layer: the hardening effect of Al creates small clusters of network formers that are difficult to dissolve. At low Al content, these clusters are mostly isolated and the softer regions around those clusters can be dissolved first, leaving the clusters detached from the main glass matrix. At high Al content, these clusters are more likely to be linked and thus to form extended networks, thereby reducing their probability to be dissolved as a group. The formation of these extended networks provides a better support for the upmost part of the altered layer as water makes its way through the glass matrix, thus preventing it from being completely dissolved, as is the case for lower Al contents (Figure 6.6). This

results in an increased lifetime of the upper part of the altered layer, which is therefore able to reorganize over a longer period of time. This leads to 1) a more rapid formation of the blocking layer relative to that expected solely on the basis of the first process and 2) to the formation of the blocking layer at a position closer to the initial surface height the greater the Al content (Figure 6.6).

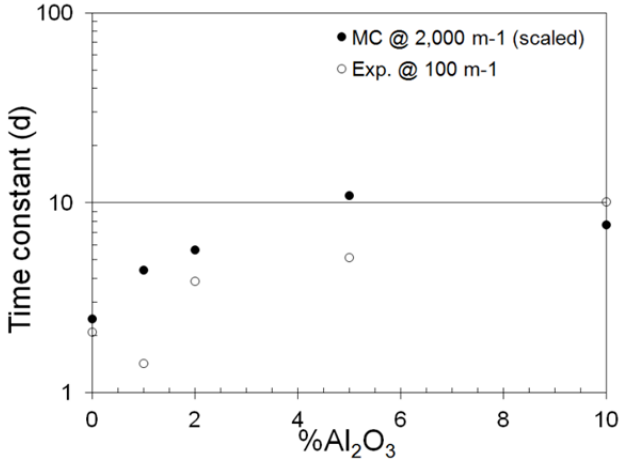


**Figure 6.5**. Calculated and Experimental Time Constants Based on B Release as a Function of Al Content

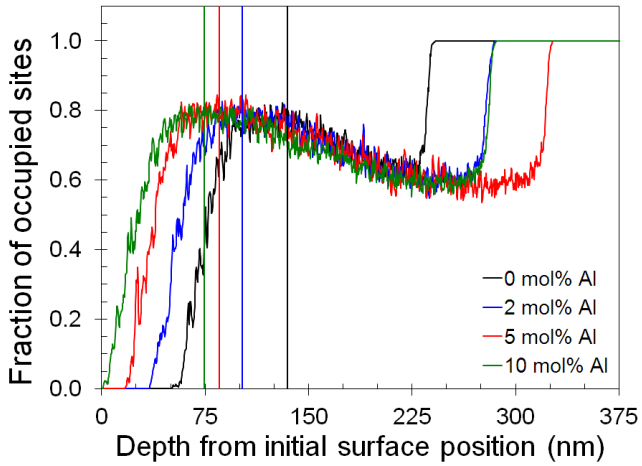


**Figure 6.6**. Glass Density (in fraction of occupied sites) as a Function of Depth (position of initial glass surface is 0) for a Range of Al Contents, Immediately Following Formation of the Blocking Layer. The solid vertical lines show the position of the deepest layer reached by the bulk aqueous solution once the blocking layer is formed (i.e., the position of the blocking layer).

Finally, the decrease in B leached thickness/fraction at the highest Al content is not seen experimentally. This could be due to the formation of secondary phases in the experiments. Indeed, the presence of Al is known to induce the formation of secondary phases containing Al, Si, and Na. The effect of such secondary phases is to remove dissolved glass components from the leaching solution. Removing Si and Al from the aqueous solution will diminish the extent of condensation at the altered glass surface, which, in turn, will increase the degree of corrosion (see above), particularly at the highest Al content where the likelihood for secondary-phase formation is the greatest. The MC model has now

been modified to allow for the formation of secondary phases. This feature is rather crude at this point but it does allow us to investigate the effect of the formation of secondary phases, that is, the removal of dissolved glass components from the aqueous solution following a given stoichiometry.

Three input parameters are needed to model the formation of a secondary phase: 1) its stoichiometry; 2) its solubility product; and 3) its precipitation rate. For the purposes of this activity, we assume its stoichiometry to be $SiAlNaO_4$. The $c_{Si} \times c_{Al} \times c_{Na}$ ionic product needs to be greater than the secondary-phase solubility product for the secondary-phase precipitation to be active. Three values of the solubility product were explored: $0.50 \times IP_{Al0}$, $1.25 \times IP_{Al0}$, and $2.50 \times IP_{Al0}$, where $IP_{Al0}$ is the steady-state $c_{Si} \times c_{Al} \times c_{Na}$ ionic product obtained in the absence of Al. The secondary phase precipitation was expressed as the probability of removing a $SiAlNaO_4$ unit, $P_{sp}$, at each computer step based on the lowest of the Si, Al, and Na aqueous concentrations:

$$P_{sp} = w_p \times \min(c_{Si}, c_{Al}, c_{Na}) \tag{6.4}$$

where $w_p$ was varied from 0.00001 to 0.001.

For the highest solubility product, little change was observed, as the secondary-phase formation process was only active for a short amount of time. Similarly, for the lowest value of $w_p$, the simulations did not differ significantly from the simulations without secondary phase formation, as the precipitation rate was too low to yield a sizeable amount of $SiAlNaO_4$. For the remaining cases, as expected, the effect of the formation of a secondary phase was to delay the formation of the blocking layer and thus to increase the extent of corrosion, particularly for the highest Al contents. Figure 6.7 and Figure 6.8 show the calculated Si, Al, and B leached thicknesses and the time constants, respectively, obtained for a solubility product of $1.25 \times IP_{Al0}$ and a value of $w_p$ of 0.0001. The main difference from the results shown in Figure 6.4 and Figure 6.5 is that the B leached fraction and the time constant for $Al_2O_3$ = 10 mol% do not decrease relative to the values calculated for $Al_2O_3$ = 5 mol% and are therefore now in accord with the experimental results of Ledieu et al. (2005).

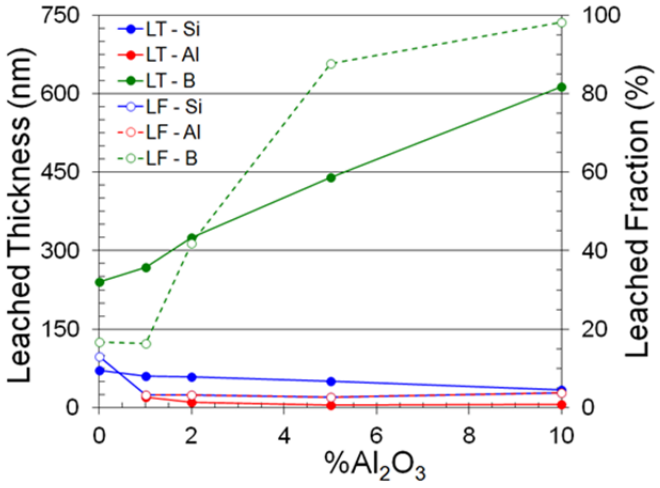


**Figure 6.7**. Calculated Si, Al, and B Leached Thickness (LT) Obtained at 2,000 $m^{-1}$ and Considering the Formation of a $SiAlNaO_4$ Secondary Phase (solubility product $1.25 \times IP_{A10}$ and $P_{sp} = 0.0001$) and Experimental Si, Al, B Leached Fractions Obtained (LF) at 100 $m^{-1}$ as a Function of Al Content

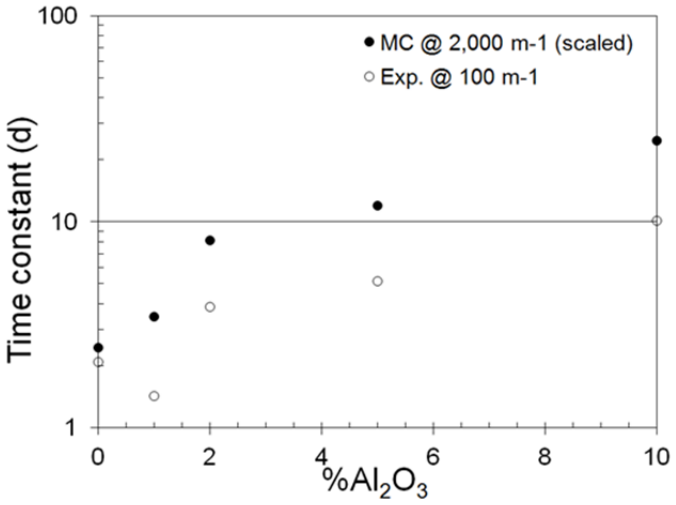


**Figure 6.8**. Calculated Time Constants, Based on B Release, Obtained at 2,000 $m^{-1}$ and Considering the Formation of $SiAlNaO_4$ Secondary Phase (solubility product = 1.25 × $IP_{Al0}$ and $P_{sp}$ = 0.0001) and Experimental Time Constants Obtained at 100 $m^{-1}$ as a Function of Al Content

## 6.3 Effect of High-Field-Strength Cations

The MC code was modified to include elements with octahedral coordination. This new feature allows for simulating the corrosion of glasses that contain high-field-strength cations such as Hf, Ce, or Zr. The implementation of octahedral cations follows that described by Arab et al. (2008). In this implementation, the octahedral cations are placed in the center of the common face of two adjacent unit cells in the *y* direction (Figure 6.9). In this configuration, the octahedral cation is linked to six network formers, and three linkages between network formers in the *z* direction are removed to maintain the coordination number of each glass component. The octahedral cation is charge compensated by two sodium ions. Zr will be used as an example of a high-field-strength octahedral cation hereafter. Zr is considered insoluble, which means that all the network formers in its coordination shell need to have dissolved for it to dissolve into solution. Zr-O-Si linkages are considered much stronger than Si-O-Si linkages; therefore, $r_{Zr}$ is set to 100. We also set $w_{c\text{-}Zr}$=$w_{c\text{-}Si}$=10.

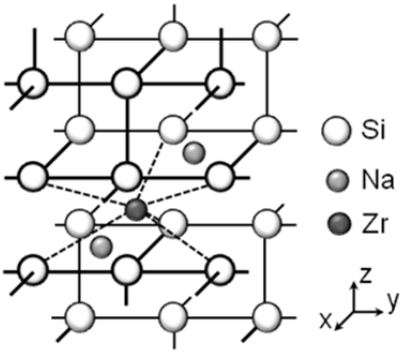


**Figure 6.9**. Structure of the Model Glass Showing How High-Field-Strength Cations (here Zr) are Positioned in Octahedral Site

A series of MC simulations were performed with four-component glasses (Si-B-Na-Zr) with a Zr content varying from 0 to 16% of the number of network former cations (i.e., of $SiO_2 + 2 \times B_2O_3$), which corresponds to 0 to 12 mol% $ZrO_2$. In these simulations, the Si/B ratio was kept constant at 1.79, B was considered to be in fourfold coordination exclusively, the Na content was set to exactly charge compensate $[BO_4]^-$ and $[ZrO_6]^{2-}$ groups (i.e., there were no non-bridging oxygens), and S/V was set to 2,000 $m^{-1}$. All the simulations were run for 100,000 computer steps.

The extent of corrosion as a function of time as represented by the B leached fraction is shown in Figure 6.10 for several values of the Zr content. The initial dissolution rate is seen to decrease with increasing Zr content due to the hardening effect of Zr. The decrease in initial dissolution rate is linearly dependent on the Zr content, as shown in Figure 6.11. As observed previously for Al, the diminished dissolution rate means that the hydrolysis/condensation kinetics are slowed down and thus the time required for the corrosion to stop increases with Zr content (Figure 6.12 – time constant), leading to a final B leached fraction that increases with Zr content. This result is in agreement with the experimental observation of Arab et al. (2008), who reported an increase of both the B time constant and the final B leached fraction with increasing Zr content. However, a direct quantitative comparison is not possible at this point as the experiments were carried out at a much lower S/V (15 $m^{-1}$) and for a slightly different composition range ($(61–x)SiO_2$-$17B_2O_3$-$18Na_2O$-$4CaO$-$xZrO_2$).

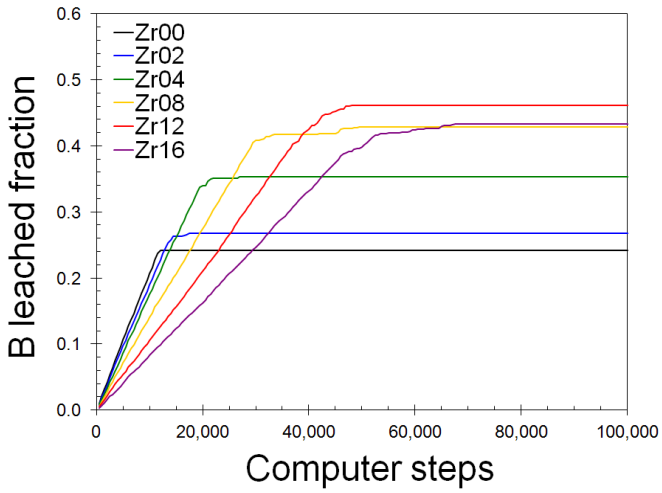


**Figure 6.10**. B Leached Fraction as a Function of Simulation Time for a Range of Octahedral Site Occupation Percentages

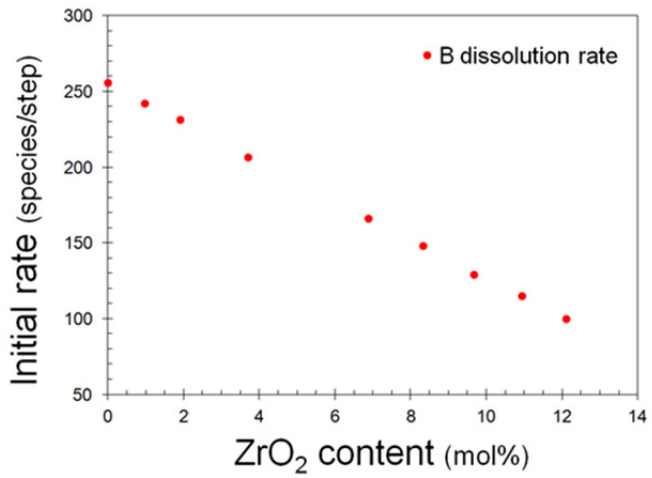


**Figure 6.11**. Initial Dissolution Rate, Based on B Release as a Function of $ZrO_2$ Content

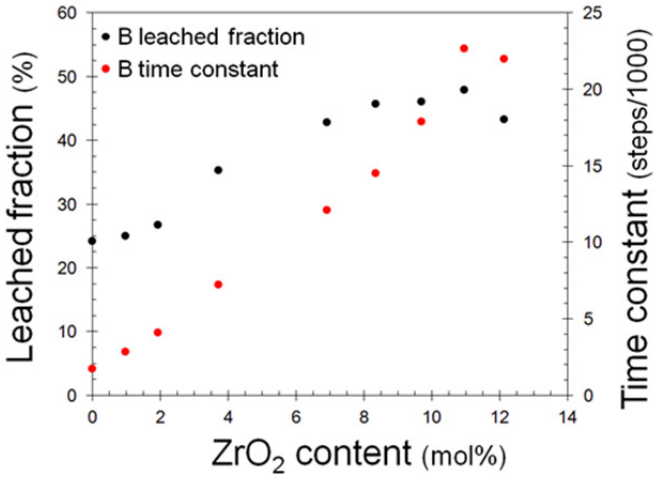


**Figure 6.12**. B Final Leached Fraction and Time Constant as a Function of $ZrO_2$ Content

The study of Arab et al. (2008) also reported the evolution of the specific surface area for different Zr contents. They observed an initial increase in surface area as the glass began to dissolve, in agreement with our MC simulations, but this was then followed by a decrease in surface area when the blocking layer began to form. This is not seen in our MC simulations, which predict instead that the surface area should plateau. This difference is likely due to the fact that, in the MC algorithm, hydrolysis and condensation processes can only occur at glass surface sites in contact with the bulk aqueous solution and not inside fully closed pores. Allowing hydrolysis and condensation processes to occur inside fully closed pores should translate into smoother pores with thicker walls, which in turn should lead to a decrease in surface area, as seen experimentally. Therefore, modifying the MC code to allow for hydrolysis and condensation processes inside closed pores should be a priority in future work.

## 6.4 Summary of Monte Carlo Modeling Results

Good quantitative agreement between the MC simulation results and experimental data on the extent and rate of aqueous corrosion was obtained, as a function of glass composition, for oxide glasses with up to four components (Si, B, Al, and Na), in particular for sodium borosilicate glasses.

The addition of Al to sodium borosilicate glasses was found to slow down the rate of corrosion but to also increase the final extent of corrosion. This is due to the fact that Al diminishes the kinetics of hydrolysis/condensation reactions that drive the reorganization of the altered layer and thus postpones the formation of the blocking layer. At high Al contents, the hardening effect of Al prevents the topmost region of the glass from dissolving completely, which facilitates the formation of a blocking layer close to the initial glass surface and thus directly opposes the effect of the Al-induced reduced hydrolysis/ condensation kinetics. As a result, the extent of corrosion decreases at the highest Al content. However, if we allow for the formation of a simple secondary phase, the formation of the blocking layer is delayed at high Al content and the extent of corrosion continues to increase with increasing Al content.

The MC code was also modified to allow for the addition of high-field-strength cations in octahedral sites. Similarly to what was observed for the addition of Al in borosilicate glasses, the addition of Zr in octahedral sites leads to a decrease in the rate of corrosion but leads to an increase in the final extent of corrosion, except at high Zr contents. Comparison with experimental data on the specific surface area of Zr-containing glasses highlighted the need to consider hydrolysis/condensation reactions inside closed pores in future work.

# 7.0 Near-Field Modeling

## 7.1 Previous PA Modeling

A critical component of the PA will be to provide quantitative estimates of radionuclide release rates from the engineered portion of the disposal facilities (source term). Computer models are essential for this purpose because effects on groundwater resources must be projected out 10,000 years and longer. Details on the recommended technical strategy for developing this source term have been published (McGrail et al. 2003) and have undergone review by an international panel of experts.

The 2001 ILAW PA (Mann et al. 2001) showed that a key variable was the waste-form release rate, calculated over thousands of years. In the 2001 PA, the waste-form release rate was evaluated by modeling the basic physical and chemical processes that are known to control the waste-form dissolution behavior instead of using empirical extrapolations from laboratory "leaching" experiments commonly used in other PAs. This methodology was adopted for the following reasons:

- The radionuclide release rate from dissolving silicate glass or grout cannot be determined independently of other system variables. For example, neglecting the waste-form composition, the glass dissolution rate is a function of three variables: temperature, pH, and composition of the fluid contacting the glass (McGrail et al. 2001b). The temperature of the IDF disposal system is assumed to be known and constant. However, both the pH and the composition of the fluid contacting the glass are variables affected by flow rate, reactions with other engineered materials, gas-water equilibria, secondary-phase precipitation, alkali-ion exchange, and the glass-dissolution classic-feedback mechanism. Consequently, glass dissolution rates vary both in time and as a function of position in the disposal system. A single-valued "leach rate" or radionuclide release rate parameter cannot be assigned to a waste form in such a dynamic system.
- One of the principal purposes of the IDF PA is to provide feedback to engineers regarding the effects of design options on disposal-system performance. A model based on empirical release rates for different waste forms is inadequate for this task. Unfortunately, the robust methodology we use comes with additional requirements. First, detailed information is needed on the reaction mechanisms controlling the dissolution behavior of the waste form; laboratory experiments are required to obtain the rate-law parameters needed for the models used for our simulations. Second, the model now being used (described in the next section) is markedly more complex than a model based on empirical release rates because of its capability to simulate reactive transport coupled with heterogeneous, unsaturated flow. Execution times with today's more sophisticated massively parallel computers can be two weeks for the two-dimensional simulations presented in this report. The benefits, however, particularly with regard to the technical defensibility of the methodology and results, far outweigh the penalties.

For the 2005 IDF PA, a variety of waste-form materials were simulated, including three WTP glasses (LAWA44, LAWB45, and LAWC22), grout, and two bulk-vitrification glasses (a six-tank composite and tank S-109) (Bacon and McGrail 2005).

## 7.2 Simulators

Historically, the IDF system PA used STORM (Bacon et al. 2000, 2004), a reactive transport simulator, to perform the near-field calculations of radionuclide releases from the corroding glass. STORM was developed by coupling STOMP, a non-isothermal multiphase flow simulator (White and Oostrom 2006), with AREST-CT (Analyzer for RadionuclidE Source-Term with Chemical Transport) Version 1.1, a reactive transport and porous medium alteration simulator (Chen et al. 1995, 1997). STORM represented subsurface flow and transport as a set of coupled, nonlinear, partial differential equations. The equations describe the rate of change of pore-water solute concentrations in variably water-unsaturated, nonisothermal porous media. STORM capabilities include kinetic dissolution of glass (or other waste forms), kinetically controlled precipitation and dissolution of secondary phases, speciation of equilibrium aqueous solutes, gas-aqueous equilibria, two-phase flow (water and air), and dynamic updates to porosity and permeability as changes in mineral volumes occur. Most importantly, STORM simulates the waste-form dissolution kinetic reaction in which equilibrium depends on only silica and aluminum. Reactive transport in STORM is coupled with unsaturated flow; the unsaturated flow field may be altered by mineral dissolution and precipitation reactions. STORM can also run efficiently in parallel on multi-core workstations and supercomputers, shortening execution times.

The STORM simulator, however, limits reactive transport to two dimensions and cannot simulate three-dimensional flow and transport resulting from heterogeneities in the subsurface. Moreover, STORM is no longer under active development, and has not received a Class C Safety and Hazard Analysis and Design Software classification. Therefore, under DOE Order 414.1C (DOE 2005) STORM cannot be used for future risk and PA analyses. More details on STORM can be found in Bacon et al. (2000, 2004), Bacon and McGrail (2001), McGrail et al. (2001a), and Mann et al. (2001).

Because STOMP (White and Oostrom 2000, 2006) can simulate flow and reactive transport in three dimensions, and adheres to rigorous quality assurance procedures that are compliant with DOE Order 414.1D (DOE 2011), STOMP was updated to perform the waste-form release calculations. This effort was carried out in FY 2011, and STOMP results were benchmarked against STORM (Pierce et al. 2011). STOMP is a general-purpose simulator that was developed at PNNL for modeling subsurface flow and transport under variably saturated conditions. The simulator uses a variable source-code configuration that allows the execution memory and speed to be tailored to the problem specifics. Quantitative predictions from the STOMP simulator are generated from the numerical solution of partial differential equations that describe subsurface environment transport phenomena. Governing equations for solute mass conservation are solved sequentially, following the solution of the coupled flow equations. The ECKEChem (Equilibrium-Conservation-Kinetic Equation Chemistry) module (White and McGrail 2005) is used to simulate reactive geochemistry. Using the variable source-code configuration of STOMP, simulations for the IDF PA use an executable designated as STOMP-W-R, which simulates the governing equations for flow, solute transport and reactive geochemistry.

STOMP development is managed under a Configuration Management Plan (CMP) (White and Freedman 2012) in conjunction with a Software Test Plan (Freedman and White 2012) that detail the procedures used to test, document and archive modifications to the source code. Formal procedures for software problem reporting and corrective actions for software errors and updates are maintained and rigorously implemented. Documentation of all verification and validation testing is publicly available.

eSTOMP is the highly scalable (parallel) version of STOMP that has been released for internal use within PNNL within the past year. The eSTOMP simulator was developed from STOMP using a component-based approach. The key features of this conversion were 1) the definition of a data model to describe a grid that is distributed over multiple processors, 2) the definition of a grid component interface based on this model, and 3) the implementation of the grid component and the conversion of the remaining portions of the code using the Global Arrays toolkit (GA) (Nieplocha et al. 2006). The GA toolkit supports a one-sided communication, shared-memory style programming model on both shared and distributed memory platforms. Because the eSTOMP simulator is highly scalable, it is ideally suited for running waste-form calculations since long run times can result when they are executed with a serial code. However, the eSTOMP simulator still requires additional documentation and testing to bring it into compliance with the ASME nuclear quality assurance standard NQA-1 for Safety Software (ASME 2001).

This year's efforts have been to incorporate the same waste-form calculations into eSTOMP that had already been incorporated into STOMP. These include the ability to fix species concentrations (e.g., fixed $pCO_2(g)$), the addition of the Power Law Model (Campbell 1985) for diffusion, the ability to scale reactive surface area linearly with water saturation, the addition of output variables for rates and surface areas, as well as updates to porosity and permeability as precipitation and dissolution occur. Because eSTOMP development focused on scalability, several derived quantities, such as additional output variables and surface flux calculations, were also needed to perform the benchmark simulations described in this report.

The benchmark simulations presented in the FY 2011 report (Pierce et al. 2011) are presented in Section 7.4.0. In that report, serial STOMP was benchmarked against STORM. In this report, the comparisons are performed between serial STOMP and scalable eSTOMP. A description of the required inputs is first presented in Section 7.3 and is taken from Bacon et al. (2004).

## 7.3 Benchmark Simulation

This report describes the development of a framework for near-field modeling of radionuclide release from WTP glass waste packages. The simulation of LAWA44 waste packages using STORM is used as a base case (Bacon and McGrail 2005). Section 7.3.1 describes, in detail, the model input required for any reactive transport simulator (e.g., STORM, STOMP, eSTOMP). eSTOMP results are compared to STOMP simulations, since they have already been benchmarked against STORM simulations as reported in Pierce et al. (2011). This process will validate the use of eSTOMP for future IDF PAs. Therefore, simulations for additional waste glasses for future IDF PAs can use either the STOMP or eSTOMP simulators.

### 7.3.1 Base-Case Model Setup and Parameterization

This section details the data required for the IDF reactive transport simulation (Bacon et al. 2004). Input data can be divided into two separate categories: 1) unsaturated flow and transport and 2) chemistry. Entries for unsaturated flow and transport include 1) lithographic units, 2) hydraulic properties, and 3) hydraulic initial and boundary conditions. Both STOMP and eSTOMP were used to compute the flow field in the near-field region based on hydraulic properties for the materials and specified initial and boundary conditions. Chemistry input to STOMP and eSTOMP consisted of entries

for aqueous, gas, and solid species; equilibrium reactions; kinetic reactions; and geochemical initial and boundary conditions. These are described below.

Four simulations were executed to verify eSTOMP against the STOMP code. The LAWA44 glass was used in each of the benchmarks, and is described here to document the data requirements. Data on this waste glass and near- and far-field materials were principally defined from facility design documents (Puigh 2004), the near-field hydraulic properties data package (Meyer et al. 2004), or the far-field hydraulic properties data package (Khaleel 2004). The properties of these materials are detailed below.

#### 7.3.1.1 Unsaturated Flow and Transport Input

### Lithographic Units

To establish a consistent framework for overlaying a computational grid on the spatial domain of interest, a set of material zones or lithographic units is defined for units with similar hydrogeological and geochemical properties. These zones are usually related to disposal design components, geologic formations, or geologic facies determined from borehole analyses. However, because there are practical limits to the resolution of the model grid, material zones may also include combinations of materials that are assigned uniform hydraulic and/or chemical properties. These materials were classified into appropriate zones as a part of the near-field hydraulics data package (Meyer et al. 2004).

The WTP glass simulations encompass a two-dimensional (2D) vertical stack of four waste packages near the center of a single trench (Figure 7.1). The WTP glass waste packages are 2.3 m tall, 1.22 m wide, and filled with glass to a height of 1.96 m. The layers in the IDF trench were assumed to be 1 m apart vertically, while waste packages were spaced 30 cm apart horizontally. It is not likely that the waste packages will be perfectly aligned horizontally, so to more realistically simulate flow, the waste packages are offset horizontally 10 cm relative to the waste package above or below.

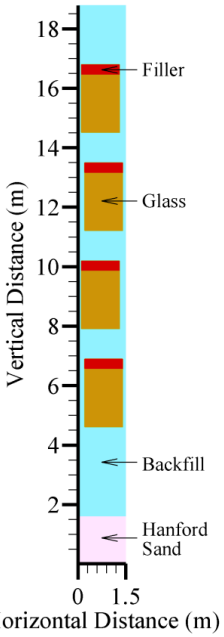


**Figure 7.1**. Lithographic Units for WTP Glass Waste Form Release Simulations

For each lithographic unit, a list of the solid species that make up the unit is required. For each solid, the relative volume and the specific surface area are needed. Initial values for these variables for each lithographic unit are listed in Table 7.1 and Table 7.2. For Hanford sands and backfill soil, petrologic and particle-size data were obtained from the near-field hydrology data package (Meyer et al. 2004). The specific surface area was inferred from the particle-size data. Assuming spherical grains, the specific surface area $A_m$ is related to the particle radius $R_m$ by

$$A_m = \frac{3V_r}{R_m(1-\theta_T)} \tag{7.1}$$

where $V_r$ is the relative volume, and $\theta_T$ is the total porosity.

The assumed specific surface area for Hanford sediments and backfill soil is consistent with petrologic and particle-size data obtained from laboratory-measured values (Serne et al. 1993). The specific surface area of the filler material in the WTP waste packages is assumed to be the same as the backfill.

**Table 7.1**. Relative Volumes of Solid Species in Material Zones

| | Glass | Quartz | Albite | K-Feldspar | Illite |
|---|---|---|---|---|---|
| Hanford Sand | 0 | 0.4 | 0.4 | 0.1 | 0.1 |
| Backfill | 0 | 0.4 | 0.4 | 0.1 | 0.1 |
| Glass | 1 | 0 | 0 | 0 | 0 |
| Filler | 0 | 0.4 | 0.4 | 0.1 | 0.1 |

**Table 7.2**. Specific Surface Area ($m^2/m^3$) of Solid Species in Material Zones

| | Glass | Quartz | Albite | K-Feldspar |
|---|---|---|---|---|
| Hanford Sand | 0 | 8,200 | 8,200 | 2,050 |
| Backfill | 0 | 8,200 | 8,200 | 2,050 |
| Glass | 50 | 0 | 0 | 0 |
| Filler | 0 | 8,200 | 8,200 | 2,050 |

The surface area assumed for the glass is consistent with the expected sparse degree of glass fracturing in the waste package based on previous experience with HLW glasses (Farnsworth et al. 1985; Peters and Slate 1981). Fracturing is expected to increase the glass surface area no more than 10 times its geometric surface area.

### Computational Grid

The computational grid was set at 2 cm in vertical resolution; this is smaller than the 5 cm grid spacing used in the 2001 ILAW PA. The smaller grid spacing was used to resolve the details in the backfill material between waste packages. The time step used in the calculations was calculated automatically by the code, given a convergence criterion of $1\times10^{-6}$. This verifies that predicted values of

aqueous species concentrations and mineral volumes are accurate between iterations for a given time step. If this cannot be achieved within a certain number of iterations, the time step is automatically reduced. Numerous simulations were conducted to verify that the grid spacing and convergence criteria chosen for the simulations were small enough for accuracy yet large enough to allow the simulations to finish in a reasonable amount of time. For comparison, the base-case, remote-handled trench simulation was run with a grid spacing of 1 cm and a convergence criterion of $5\times10^{-7}$. Results from these simulations were not significantly different from those with the grid spacing and convergence criterion used in the simulations reported in this document (Bacon and McGrail 2005).

## Material Hydraulic Properties

The hydraulic properties for each lithographic unit in the simulation (Table 7.3) were determined in the near-field hydraulics data package (Meyer et al. 2004) or the far-field hydraulic properties data package (Khaleel 2004). The pressure saturation relationship was described using the van Genuchten equation (1980).

**Table 7.3**. Material Hydraulic Properties Used in Simulations

| Material | Particle Density ($g/cm^3$) | Saturated Water Content (unitless) | Residual Water Content (unitless) | van Genuchten α ($cm^{-1}$) | van Genuchten n (unitless) | Saturated Hydraulic Conductivity (cm/s) |
|---|---|---|---|---|---|---|
| Hanford Sand | 2.63 | 0.394 | 0.049 | $6.31\times10^{-2}$ | 2.05 | $4.15\times10^{-3}$ |
| Backfill | 2.71 | 0.350 | $3.00\times10^{-2}$ | $6.50\times10^{-2}$ | 1.70 | $4.91\times10^{-3}$ |
| Glass | 2.68 | 0.020 | $4.60\times10^{-4}$ | $2.00\times10^{-1}$ | 3.00 | $1.00\times10^{-2}$ |
| Filler | 2.71 | 0.316 | $3.00\times10^{-2}$ | $6.50\times10^{-2}$ | 1.70 | $4.91\times10^{-3}$ |

## Hydraulic Initial Conditions

Initial hydraulic conditions for each lithographic unit include the following parameters:

- water content
- water flux
- dissolved gas content of aqueous phase
- gas pressure
- relative humidity of gas phase
- temperature.

The initial conditions were calculated by assuming a steady-state water flux at the upper boundary, which results in a steady-state water content distribution consistent with the hydraulic properties defined for each material. Water flux rates ranging from 0.1 to 4.2 mm/yr were used for different sensitivity cases. A constant subsurface temperature equal to the average ambient temperature of 15°C was

assumed. The dissolved gas content of the aqueous phase was assumed to be negligible with respect to flow. The relative humidity of the gas phase was assumed to be 100%.

### Hydraulic Boundary Conditions

The following data are needed as a function of time and space along each boundary:

- water flux
- dissolved gas content of aqueous phase
- gas pressure
- relative humidity of gas phase
- temperature.

The upper boundary is located just beneath the engineered barrier system and was assigned a specified flux. A range of water flux rates, from 0.1 mm/yr to 4.2 mm/yr, was used for different sensitivity cases. The lower bound of the recharge rates (0.1 mm/yr) was determined as a part of the recharge data package (Fayer and Szecsody 2004). The highest recharge rate (4.2 mm/yr) was implemented in the previous PA (Mann et al. 2001) and is provided here for comparison.

The location of the lower model boundary was selected so that horizontal gradients are small. The lower boundary is a free drainage boundary 4.5 m below the lowest layer of backfill. For hydraulic boundary conditions at this lower boundary, free drainage under gravity was assumed. Also, the side boundaries are placed at axes of symmetry so that no-flow boundaries can be assumed.

A constant subsurface temperature, equal to the average ambient temperature of 15°C, was assumed. The dissolved gas content of the aqueous phase was assumed to be negligible with respect to flow. The relative humidity of the gas phase was assumed to be 100%.

### Solute Transport Coefficients

The following data are needed for each gaseous and aqueous species:

- aqueous diffusion coefficient ($m^2/s$)
- gas diffusion coefficient ($m^2/s$) or an assumption that the gas partial pressure is fixed.

The aqueous molecular diffusion coefficient was calculated using a power law model (Campbell 1985), as recommended in the near-field hydrology data package (Meyer et al. 2004). This model has the form

$$D_i = aD_f\Theta^b \tag{7.2}$$

where $D_i$ = the diffusion coefficient in a porous medium
$D_f$ = the free-water diffusion coefficient,
$\Theta$ = the water content of the porous medium
$a$ and $b$ = empirical fitting parameters.

In this case, it was determined that $D_f = 1.84\times 10^{-5}$ cm$^2$/s, $a = 1.486$, and $b = 1.956$ by fitting to experimental data for Hanford sediments that used an ultracentrifuge to study diffusion.

The gas partial pressure for $CO_2$ was fixed at an atmospheric value of $3\times10^{-4}$ atm, so no gaseous diffusion coefficient needed to be specified.

#### 7.3.1.2 Chemistry Input

### Aqueous Species

Aqueous species are the cations, anions, or neutral complexes present in the aqueous phase. For each aqueous species, the following data are needed:

- molecular weight (g/mol)
- charge (unitless)
- hard-core diameter or "ion-size" in aqueous solution (unitless)
- number of elements in aqueous species (unitless)
- stoichiometric coefficient of each element (mol).

The aqueous species listed in Table 7.4 were identified by simulating the dissolution of waste glass in deionized water at 15°C with the EQ3/EQ6 code package (Wolery and Daveler 1992). All data were obtained from the EQ3/EQ6 data0.com.R8 database (Daveler and Wolery 1992). The EQ3/EQ6 software was used to extract a subset of aqueous (and solid) species from the large thermodynamic database that were relevant for the reactive transport simulations.

**Table 7.4**. Key Aqueous Species Produced by the Dissolution of Waste Glass

| Species | Mol. Wt. | Hard-Core Diameter |
|---|---|---|
| $AlO_2^-$ | 58.98 | 4.0 |
| $B(OH)_3(aq)$ | 61.83 | 3.0 |
| $BO_2^-$ | 42.81 | 3.0 |
| $Ca^{2+}$ | 40.08 | 6.0 |
| $CO_2(aq)$ | 44.01 | 3.0 |
| $CO_3^{2-}$ | 60.01 | 5.0 |
| $CrO_4^{2-}$ | 115.99 | 4.0 |
| $Fe(OH)_3(aq)$ | 106.87 | 3.0 |
| $H_2O$ | 18.01 | 3.0 |
| $H_2SiO_4^{2-}$ | 94.10 | 4.0 |
| $H^+$ | 1.01 | 9.0 |
| $HCO_3^-$ | 61.02 | 4.0 |
| $HCrO_4^-$ | 117.00 | 4.0 |
| $HSiO_3^-$ | 77.09 | 4.0 |
| $K^+$ | 39.10 | 3.0 |

**Table 7.4**. (contd)

| Species | Mol. Wt. | Hard-Core Diameter |
|---|---|---|
| KOH(aq) | 56.10 | 0.0 |
| $La^{3+}$ | 138.91 | 9.0 |
| $Mg^{2+}$ | 24.31 | 8.0 |
| $MgB(OH)_4^+$ | 103.15 | 4.0 |
| $MgCO_3$(aq) | 84.31 | 0.0 |
| $MgHCO_3^+$ | 85.32 | 4.0 |
| $Na^+$ | 22.99 | 4.0 |
| $NaB(OH)_4$(aq) | 101.83 | 3.0 |
| $NaCO_3^-$ | 83.00 | 4.0 |
| $NaHCO_3$(aq) | 84.01 | 3.0 |
| $NaHSiO_3$(aq) | 100.08 | 0.0 |
| NaOH(aq) | 40.00 | 3.0 |
| $Ni^{2+}$ | 58.69 | 4.5 |
| $OH^-$ | 17.01 | 3.0 |
| $SiO_2$(aq) | 60.08 | 3.0 |
| $TcO_4^-$ | 162.00 | 4.0 |
| $Ti(OH)_4$(aq) | 115.91 | 3.0 |
| $Zn(OH)_3^-$ | 116.41 | 4.0 |
| $Zn^{2+}$ | 65.39 | 6.0 |
| $ZnOH^+$ | 82.40 | 4.0 |
| $Zr(OH)_4$(aq) | 159.25 | 3.0 |

## Gas Species

Gas species such as $CO_2$(g) and $O_2$ (g) are components that make up the gas phase. For each gas species, the following data are needed:

- molecular weight (g/mol)
- charge (unitless)
- hard-core diameter (unitless)
- number of elements in aqueous species (unitless)
- stoichiometric coefficient of each element (mol).

No $O_2$ redox reactions were included in the current simulations. Only $CO_2$(g) was considered, and its properties are shown in Table 7.5.

**Table 7.5**. Gas Species

| Species | Mol. Wt. | Hard-Core Diameter |
|---|---|---|
| $CO_2$(g) | 44.01 | 3.0 |

### Solid Species

The mass density ($g/cm^3$) and the stoichiometric coefficient of each element are needed for each solid species, including any secondary minerals that precipitate from supersaturated conditions. The simulations will reference several WTP glasses; the composition of LAWA44 glass is given as an example (Table 7.6). The mole fraction of each of the elements in the waste glass is required as input to STOMP/STORM and is shown in Table 7.7.

**Table 7.6**. Composition (Mass%) and Particle Density for the Glass Specimen Used in Simulations

| Oxide | LAWA44 |
|---|---|
| $Al_2O_3$ | 6.20 |
| $B_2O_3$ | 8.90 |
| CaO | 1.99 |
| $Fe_2O_3$ | 6.98 |
| MgO | 1.99 |
| $Na_2O$ | 20.0 |
| $SiO_2$ | 44.55 |
| $TiO_2$ | 1.99 |
| ZnO | 2.96 |
| $ZrO_2$ | 2.99 |
| Others[(a)] | 1.42 |
| **Total** | **100.0** |
| Formula Weight, g/mol | 66.96 |
| Density, $g/m^3$ | $(2.698 \pm 0.008) \times 10^6$ |

(a) Others include minor amounts of Cl, F, $Cr_2O_3$, $K_2O$, $MoO_3$, $P_2O_5$, $Re_2O_7$, and $SO_3$.

**Table 7.7**. LAWA44 Composition in Mole Fraction Used in STORM Simulations

| Element | LAWA44 |
|---|---|
| Al | 8.15e-02 |
| B | 1.71e-01 |
| Ca | 2.38e-02 |
| Cl | 1.23e-02 |
| Cr | 1.76e-04 |
| F | 3.53e-04 |
| Fe | 5.86e-02 |
| K | 7.11e-03 |
| Mg | 3.31e-02 |
| Mo | 4.65e-05 |
| Na | 4.32e-01 |
| O | 1.83e+00 |
| P | 2.83e-04 |
| S | 8.37e-04 |
| Si | 4.97e-01 |
| Tc | 2.77e-04 |
| Ti | 1.67e-02 |
| Zn | 2.44e-02 |
| Zr | 1.63e-02 |

The compositions of materials that make up the backfill, filler, and Hanford sand are listed in Table 7.8 (Serne et al. 1993). The mass density is obtained by dividing the molecular weight by the molar volume of the compound.

Secondary phases are solids that precipitate from a supersaturated aqueous solution. A list of potential secondary phases that form from long-term weathering experiments with the various waste glass formulations and from modeling the solution chemistry observed in experiments with the EQ3/EQ6 code is provided in Pierce et al. (2004) and Pierce et al. (2005). A large number of phases were eliminated from consideration because 1) formation of the phase is kinetically prohibited at the disposal system temperature of 15°C, 2) selection of the phase would violate the Gibbs phase rule, 3) simulations show that allowing the phase to form is inconsistent with a large body of laboratory test data with borosilicate glasses, or 4) the phase is unstable over the range of chemical environments expected for the IDF system.

**Table 7.8**. Composition of Native and Surrounding Materials Used in Simulations

| Species | Formula | Mol. Wt. g/mole | Molar Volume, $cm^3$/mole |
|---|---|---|---|
| Albite | $NaAlSi_3O_8$ | 262.2 | 100.4 |
| Illite | $K_{0.6}Mg_{0.25}Al_{1.8}Al_{0.5}Si_{3.5}O_{10}(OH)_2$ | 383.9 | 500.0 |
| K-Feldspar | $KAlSi_3O_8$ | 278.3 | 108.8 |
| Quartz | $SiO_2$ | 60.1 | 22.6 |

The final phase assemblage used in STORM simulations (see Table 7.9) was further constrained because preliminary runs showed that certain phases never formed or formed in such small amounts that their effects on the chemical composition of the modeled system were insignificant. The composition of the secondary minerals used in the simulations is listed in Table 7.9. The mass density is obtained by dividing the molecular weight by the molar volume of the solid.

**Table 7.9**. Composition of Secondary Minerals Used in Simulations

| Species | Formula | Mol. Wt. (g/mole) | Molar Volume ($cm^3$/mole) |
|---|---|---|---|
| Analcime | $Na_{0.96}Al_{0.96}Si_{2.04}O_6$ | 201.2 | 96.8 |
| Anatase | $TiO_2$ | 79.8 | 20.5 |
| Baddeleyite | $ZrO_2$ | 123.2 | 21.9 |
| Calcite | $CaCO_3$ | 100.1 | 36.9 |
| Chalcedony | $SiO_2$ | 60.1 | 22.7 |
| Clinochlore-14A | $Mg_5Al_2Si_3O_{10}(OH)_8$ | 555.8 | 207.1 |
| $Fe(OH)_3$(am) | $Fe(OH)_3$ | 106.9 | 34.4 |
| Gibbsite | $Al(OH)_3$ | 78.0 | 31.9 |
| $Zn(OH)_2$(gamma) | $Zn(OH)_2$ | 99.4 | 30.0 |

## Equilibrium Reactions

For each equilibrium reaction, the stoichiometric coefficient of each aqueous species in each reaction and the equilibrium constant at a temperature of 15°C are needed. The equilibrium reactions in Table 7.10 were identified by simulating the dissolution of the waste glasses in deionized water at 15°C with the EQ3/EQ6 code package (Wolery and Daveler 1992) and the data0.com.R8 database (Daveler and Wolery 1992; Wolery and Daveler 1992). A significant number of secondary aqueous species were excluded from the simulations because their concentrations were extremely small over the range of chemical conditions anticipated for the ILAW disposal system.

**Table 7.10**. Equilibrium Reactions at 15°C

| Reaction | Log K |
|---|---|
| $BO_2^- + H_2O + H^+ \rightleftarrows B(OH)_3(aq)$ | 9.35 |
| $CO_2(aq) + H_2O \rightleftarrows H^+ + HCO_3^-$ | –6.42 |
| $CO_3^{2-} + H^+ \rightleftarrows HCO_3^-$ | 10.43 |
| $H_2SiO_4^{2-} + 2H^+ \rightleftarrows 2\ H_2O + SiO_2\ (aq)$ | 22.96 |
| $HCrO_4^- \rightleftarrows CrO_4^{2-} + H^+$ | –6.49 |
| $HSiO_3^- + H^+ \rightleftarrows SiO_2(aq) + H_2O$ | 10.10 |
| $KOH(aq) + H^+ \rightleftarrows H_2O + K^+$ | 14.46 |
| $MgB(OH)_4^+ + H^+ \rightleftarrows H_2O + B(OH)_3(aq) + Mg^{2+}$ | 7.35 |
| $MgCO_3(aq) + H^+ \rightleftarrows HCO_3^- + Mg^{2+}$ | 7.50 |
| $MgHCO_3^+ \rightleftarrows HCO_3^- + Mg^{2+}$ | –1.04 |
| $NaB(OH)_4(aq) + H^+ \rightleftarrows B(OH)_3(aq) + Na^+ + H_2O$ | 8.97 |
| $NaCO_3^- + H^+ \rightleftarrows HCO_3^- + Na^+$ | 9.82 |
| $NaHCO_3(aq) \rightleftarrows HCO_3^- + Na^+$ | –0.24 |
| $NaHSiO_3(aq) + H^+ \rightleftarrows Na^+ + SiO_2(aq) + H_2O$ | 8.36 |
| $NaOH(aq) + H^+ \rightleftarrows Na^+ + H_2O$ | 15.12 |
| $OH^- + H^+ \rightleftarrows H_2O$ | 14.34 |
| $Zn(OH)_2(aq) \rightleftarrows 2OH^- + Zn^{2+} + 2H_2O$ | –11.36 |
| $ZnOH^+ + H^+ \rightleftarrows Zn^{2+} + H_2O$ | –5.05 |

## Kinetic Reactions

For each kinetic reaction, the following data are needed:

- mass-action law type: 1. full, 2. reduced, or 3. glass (see definitions below)
- stoichiometric coefficient of aqueous species in each reaction
- equilibrium constant at a temperature of 15°C
- rate constant of reaction at a specified temperature.

A full mass-action law type was used for each solid phase except for the waste glass. A full mass-action law type allows a solid species to both dissolve and precipitate, and for equilibrium to depend on all aqueous species released by the kinetic reaction. In STOMP, this type of mass-action law is designated "TST."

A special mass-action law type was used for the glass because once dissolved, the glass does not reform and only secondary minerals precipitate. Hence, the glass only undergoes dissolution. In STOMP, when only dissolution (or precipitation) is permitted, the mass action law is termed a "reduced mass action law". Because experiments have shown that the equilibrium of the glass rate equation is only dependent upon aqueous silica, in STOMP, only dissolved silica is considered in the rate equation. This differs from the full mass-action law type, which considers all aqueous species in solution to determine its dissolution/precipitation rate. To invoke the reduced mass-action rate law for glass in STOMP, "TST toward reactants w/glass" keywords are used.

Compilations of kinetic rate constants equivalent to thermodynamic databases for important mineral phases are not available. Also, the available mineral dissolution/precipitation kinetics data are much more limited than thermodynamic data. Consequently, sufficiently large rate constants were used to approximate equilibrium conditions; that is, to make certain that the phase will precipitate rapidly if the local chemical environment at a grid node is saturated with respect to the particular phase.

For a dissolution reaction involving glass, parameters associated with the following kinetic rate law are needed:

$$r_g = \vec{k} a_{H^+}^{-\eta} e^{\frac{-E_a}{RT}} \left[ 1 - \left( \frac{Q}{K_g} \right)^{\sigma} \right] \tag{7.3}$$

where
$r_g$ = dissolution rate, g/(m$^2$ d)
$\vec{k}$ = intrinsic rate constant, g/(m$^2$ d)
$a_{H^+}$ = hydrogen ion activity (variable to be calculated by STORM)
$E_a$ = activation energy, kJ/mol
$R$ = gas constant, kJ/(mol·K)
$T$ = temperature, K (assumed constant at 15°C)
$Q$ = ion activity product for glass (variable to be calculated by STORM)
$K_g$ = pseudo-equilibrium constant
$\eta$ = pH power law coefficient
$\sigma$ = Temkin coefficient ($\sigma$ = 1 assumed).

Equation (7.3) is an approximation for glass because glass is metastable, and the reaction proceeds one way (i.e., glass dissolves). The unknown parameters in Equation (7.3) ($\vec{k}$, $E_a$, $K_g$, and $\eta$) have been determined for LAW glasses (Pierce et al. 2004) and bulk-vitrification glasses (Pierce et al. 2005); these values are given in Table 7.11.

Test results with LAW and bulk-vitrification glasses (excluding LAWB45) show that it is susceptible to a secondary reaction mechanism, alkali-ion exchange. This reaction results in the selective extraction of Na via the reaction:

$$\text{LAWA44-Na} + H^+ \rightarrow \text{LAWA44-H} + Na^+ \qquad (7.4)$$

where LAWA44-Na represents the unreacted glass containing Na, and LAWA44-H represents a hydrated glass where the Na has been replaced with an equimolar amount of hydrogen. The rate of this reaction has been determined from single-pass flow-through experiments (Pierce et al. 2004, 2005). STOMP keeps track of the amount of hydrated glass formed via reaction (7.4) and then allows it to dissolve according to the same kinetic rate law (reaction 7.3) as the parent glass.

**Table 7.11**. Summary of Kinetic Rate Parameters Used for Glass

| Parameter | Meaning | LAWA44 |
|---|---|---|
| $\vec{k}$ | Intrinsic rate constant, mol/($m^2$ s) | $2.2\times10^{-3}$ |
| $K_g$ | Apparent equilibrium constant for glass based on activity of $SiO_2$(aq) | $10^{-3.26}$ |
| $\eta$ | pH power law coefficient | 0.49 |
| $E_a$ | Activation energy of glass dissolution reaction, kJ/mol | 60 |
| $r_x$ | Na ion-exchange rate, mol/($m^2$ s) | $5.3\times10^{-11}$ |

Pierce et al. (2004, 2005) describe the methods used to develop a solubility product for the key secondary phases identified from laboratory testing and from simulations with the EQ3/EQ6 code. For convenience, the log *K* they derived for each secondary phase given in Table 7.9 is reproduced in Table 7.12. For the secondary phases, where a log *K* was not available or could not be estimated, the reaction was not included in the STOMP simulations.

**Table 7.12**. Secondary Phase Reaction Network

| Reaction | Log K (15°C) |
|---|---|
| $Analcime \rightleftarrows 0.96AlO_2^- + 0.96Na^+ + 2.04SiO_2(aq)$ | –16.47 |
| $Anatase + 2H_2O \rightleftarrows Ti(OH)_4(aq)$ | –6.56 |
| $Baddeleyite + 2H_2O \rightleftarrows Zr(OH)_4(aq)$ | –6.79 |
| $Calcite + H^+ \rightleftarrows Ca^{2+} + HCO_3^-$ | 2.00 |
| $Chalcedony \rightleftarrows SiO_2(aq)$ | –3.94 |
| $Clinochlore\text{-}14A + 8H^+ \rightleftarrows 3SiO_2(aq) + 5Mg^{2+} + 8H_2O + 2AlO_2^-$ | 22.93 |
| $Fe(OH)_3(am) + H_2O \rightleftarrows Fe(OH)_3(aq)$ | –11.09 |
| $Gibbsite \rightleftarrows AlO_2^- + H_2O$ | –13.10 |
| $Zn(OH)_2(gamma) + 2H^+ \rightleftarrows 2H_2O + Zn^{2+}$ | 11.88 |

### 7.3.1.3 Initial and Boundary Conditions

For each specified gas species concentration, the partial pressure of gaseous species is needed. The gas partial pressures for $CO_2$ and $O_2$ were fixed at atmospheric values of $3 \times 10^{-4}$ and $2.1 \times 10^{-1}$ atm, respectively.

For each specified aqueous species, the specified total concentration and the stoichiometric coefficient of each aqueous species are needed. Aqueous-species concentrations at the upper boundary, and for initial conditions, were specified as a part of the near-field geochemistry data package (Krupka et al. 2004) and are given in Table 7.13. Total aqueous species concentrations were specified at the upper boundary, and a no-diffusion condition was imposed across the lower boundary. The contaminant flux across the lower boundary was therefore limited to advection:

$$f = c\rho_w v \tag{7.5}$$

where $c$ is the concentration (mol/kg), $\rho_w$ is the density of water (kg/m$^3$), and $v$ is the specific discharge (m/s).

**Table 7.13**. Initial Aqueous Concentrations for the Primary Species Used in Simulations

| Species | Initial Concentration (mol/kg) |
|---|---|
| $AlO_2^-$ | $10^{-6}$ |
| $B(OH)_3(aq)$ | $10^{-10}$ |
| $Ca^{2+}$ | $10^{-7}$ |
| Cr (total) | $10^{-10}$ |
| $Fe(OH)_3(aq)$ | $10^{-10}$ |
| $H_2O$ | 1 |
| $H^+$ | $10^{-7}$ |
| $K^+$ | $10^{-6}$ |
| $Mg^{2+}$ | $10^{-10}$ |
| $Na^+$ | $10^{-6}$ |
| Si (total) | $10^{-5}$ |
| $TcO_4^-$ | $10^{-10}$ |
| $Ti(OH)_4(aq)$ | $10^{-10}$ |
| $Zn^{2+}$ | $10^{-10}$ |
| $Zr(OH)_4(aq)$ | $10^{-10}$ |

### 7.3.1.4 Model Output

The normalized flux to the vadose zone is calculated by summing the flux at each node across the bottom boundary of the model and normalizing the total flux according to the amount of each radionuclide in all the waste packages at the start of the simulation. This flux is reported in units of 1/Myr (pronounced “per million years”) and is equivalent to the “ppm/yr” units that were used in previous

PAs (Mann et al. 2001; Mann et al. 1998). The term ppm was used to express the fraction of radionuclide released from the waste packages per year in "per millionth," similar to the commonly used percent term. However, the unit ppm, when used in environmental science for expressing levels of pollutants in water, has the specific meaning of mg/liter (mg of contaminant per liter of water). Using ppm to mean "per millionth," while correct, may be confusing in this context so it has been replaced with units of 1/Myr.

The normalized flux across the lower boundary, $F$, in units of 1/Myr, was calculated using

$$F = \frac{\sum_{i=1}^{N} f_i \Delta x_i \Delta y_i}{I_j} \zeta \tag{7.6}$$

where $f_i$ = flux across the bottom of an individual grid block (mole/(m$^2$ s)

$\Delta x_i \Delta y_i$ = cross-sectional area of an individual grid block (m$^2$)

$\zeta = \frac{3.1558 \times 10^{13}\,\text{s}}{\text{Myr}}$

$I_j$ = inventory of $j^{\text{th}}$ radionuclide in the simulated waste packages (mol), where

$$I_j = V_{wp} \left(1 - \theta_T\right) \rho_G \gamma_j \tag{7.7}$$

where $V_{wp}$ = volume of the waste packages (m$^3$)

$\theta_T$ = total porosity of the material representing the waste packages (m$^3$/m$^3$)

$\rho_G$ = molar density of the material representing the waste packages (mol/m$^3$)

$\gamma_j$ = mole fraction of $j^{\text{th}}$ radionuclide in the material representing the waste packages (mol/mol).

The volume of the four simulated waste packages, $V_{wp}$, was 11.2 m$^3$ for the WTP glass simulations. The cross-sectional area of each grid block was 0.02 m$^2$.

The radionuclide concentrations, for instance Tc, are also normalized by the inventory,

$$\text{Tc}_{normalized} = \frac{\text{Tc}}{I_{\text{Tc}}} \tag{7.8}$$

## 7.4 Modifications to STOMP

Several modifications were made to the eSTOMP code so that model assumptions and results could be consistent with those used first in STORM, and later in STOMP (Pierce et al. 2011). Test cases were used to verify that STOMP and eSTOMP yielded similar results. Additional test cases were also run to make sure that modifications did not impact other reactive transport capabilities.

Fixed gas concentrations are a common option in many geochemical codes, including STORM. This feature was first implemented in STOMP by adding the character string "fix" to a given species name.

ECKEChem checks for this string in each species name, and if present, does not update that species concentration at each time step. This modification was tested by checking to make sure that the $CO_2(g)$ partial pressure remained fixed at $3.0\times10^{-4}$. However, careful review of the STOMP source code showed that the original implementation of the fixed gas concentration over-relaxed the convergence criterion. This was corrected in the STOMP code, and then implemented in eSTOMP. Faulty logic was also discovered in the chemistry updating when ECKEChem failed to converge. This was also corrected in both STOMP and eSTOMP. With these source code updates, small differences in concentrations were predicted from the STOMP and eSTOMP simulations in this report relative to the results reported in Pierce et al. (2011).

Dissolution and precipitation reactions can change the volume fractions of solids as a function of time, thus changing the porosity. Porosity changes as a function of mineral precipitation and dissolution. This option may be invoked by including the phrase "w/ porosity" in the second line of the solution control card. This modification was tested by running a simulation of a PUF test at 99°C, as described in another report (Bacon and Pierce 2010), which displayed measureable changes in porosity over a short amount of time. STOMP and eSTOMP show excellent agreement for an increase in porosity over 7 days (Figure 7.2).

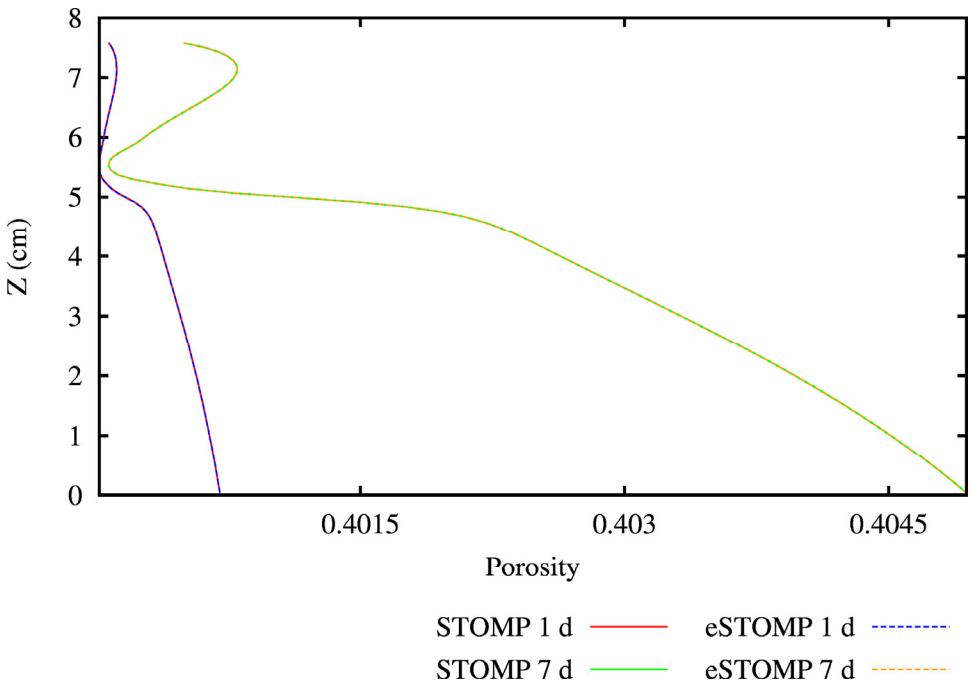


**Figure 7.2**. Comparison of Porosity Changes Predicted by STOMP and eSTOMP. Note that the STOMP and eSTOMP porosity curves lie on top of each other for each time period.

Intrinsic permeability, $k$, also varies as a function of porosity. The Kozeny-Carman equation describes the relationship between porosity ($\phi$) and permeability in both STOMP and eSTOMP. The

Kozeny-Carman relationship is obtained from a theoretical derivation of Darcy's law and includes numerical coefficients that must be determined empirically:

$$k = C_0 \frac{\phi_T^3}{(1-\phi_T)^2 M_S^2}, \tag{7.9}$$

where $M_S$ is the specific surface area of the porous matrix (defined per unit volume of solid), and $C_0$ is the coefficient for which Carman (1937) suggested the value of 1/5. This option may be invoked by adding the string "kozeny", followed by a comma, to the end of a Rock/Soil Hydraulic Properties Card input line for a particular material.

This modification was also tested by running a simulation of a PUF test at 99°C, as described in Bacon and Pierce (2010), which displayed measureable changes in permeability over a short amount of time. Excellent agreement results were obtained between STOMP and eSTOMP for an increase in permeability over 7 days as shown in Figure 7.3.

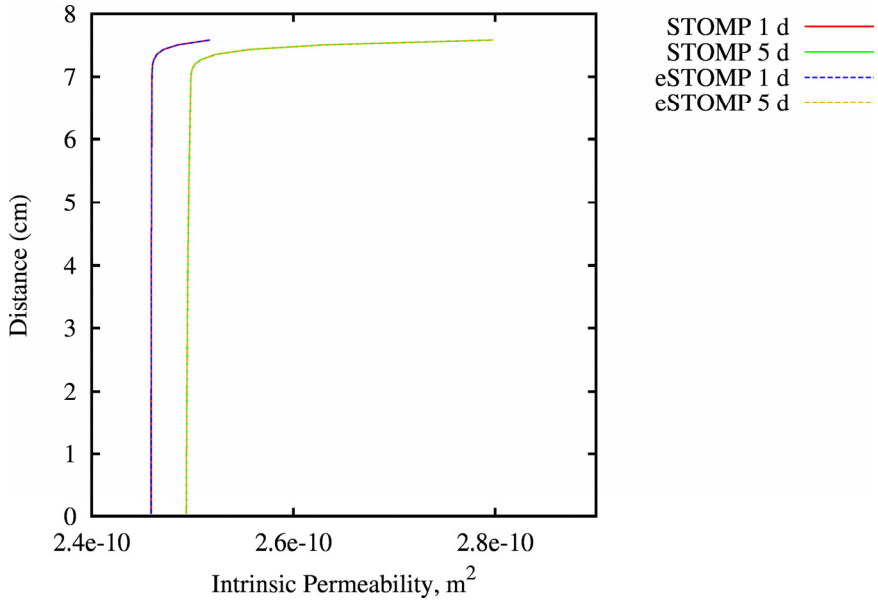


**Figure 7.3**. Comparison of Permeability Change Predicted by STOMP and eSTOMP. Note that the STOMP and eSTOMP permeability curves lie on top of each other for each time period.

Previously, the only diffusion model available for aqueous-species transport in STOMP was the conventional model. STORM utilized the complete set of molecular diffusion models available for solute transport for species transport as well. Therefore, the complete set of molecular diffusion models available for solutes was also implemented for aqueous species in STOMP, with the addition of the power law model (Campbell 1985). The conventional model for molecular diffusion in STOMP assumes that diffusion decreases linearly with a decrease in water content. In contrast, the power law model assumes that diffusion is proportional to the water content raised to a specified coefficient. In the case of the 2005 PA simulations (Bacon and McGrail 2005), this coefficient was close to 2, which means that the conventional diffusion model in STOMP would predict higher diffusion coefficients when using the conventional model to describe diffusion at low water contents. This would result in different rates of

transport and concentration distributions between the STORM and STOMP simulations. Hence, the power law model was incorporated into eSTOMP as well, so that diffusion-dominated transport rates would be equivalent between the two simulators.

Previously, STOMP assumed a default initial surface area for secondary minerals that was significantly higher than that calculated by STORM, resulting in faster secondary mineral precipitation. The capability to specify the initial surface area of secondary minerals was added to STOMP in 2011, and to eSTOMP in this year's effort. In the Lithology Card, if the surface area of a mineral is specified with an initial volume fraction of 0, the specified surface area will be used rather than the default value. If the secondary mineral is not listed in the Lithology Card, the default surface area will be used.

The new variables SP_RATE and SP_AREA were added to store mineral rate and surface area for output. The user may now list these output variables in the reference node and plot file sections of the Output Control Card, as shown here:

```
Species Mineral Rate,LAWA44-H,mol/s,
Species Mineral Area,Albite-high,m^2,
```

An option was added to scale reactive surface area linearly with water saturation, as in STORM. This option may be invoked by including the phrase "w/ area" in the second line of the solution control card.

Ultimately, these changes to STOMP were tested by running the benchmarking simulations described in the following section.

## 7.5 Benchmarking Results

Output from both STOMP and eSTOMP are compared for identical test cases, including aqueous species concentrations, glass dissolution rate, amounts of secondary minerals precipitated, and Tc flux across the model lower boundary. This comparison provides the technical basis for using eSTOMP in future IDF PAs since STOMP has already been validated against STORM.

### 7.5.1 1D Test Case

STOMP and eSTOMP were compared using a test case similar to the base case described in Section 7.3.1. Differences between the base case described in Section 7.3.1 and the test case used to compare eSTOMP and STOMP results are:

- 1D vs. 2D
- one waste package, rather than four,
- a shortened vertical domain, 7.8 m rather than 17.8 m,
- a coarser variable grid spacing of 20 cm rather than 2 cm, and
- shorter time steps of 1 day rather than 1 year.

There is excellent agreement between the two simulators for the Tc concentrations over time surrounding the waste packages (Figure 7.4), glass dissolution rate (Figure 7.5), and secondary mineral precipitation (Figure 7.6). Despite the fact that concentrations and mineral precipitation and dissolution

rates are nearly identical between STOMP and eSTOMP, there is still a small difference in the two Tc release rates that are calculated from the bottom of the repository (Figure 7.7). These flux calculations are a derived quantity in both codes, calculated based on the concentration and flow velocity. The small differences exhibited between the two codes are due to the difference in *when* the calculation takes place. In STOMP, the flux calculation is performed after the concentrations have been updated for the current time step. In eSTOMP, this calculation currently occurs prior to the concentration update. In a future release of eSTOMP, the surface flux calculation will be updated so that it is equivalent to the calculations made in STOMP.

a)

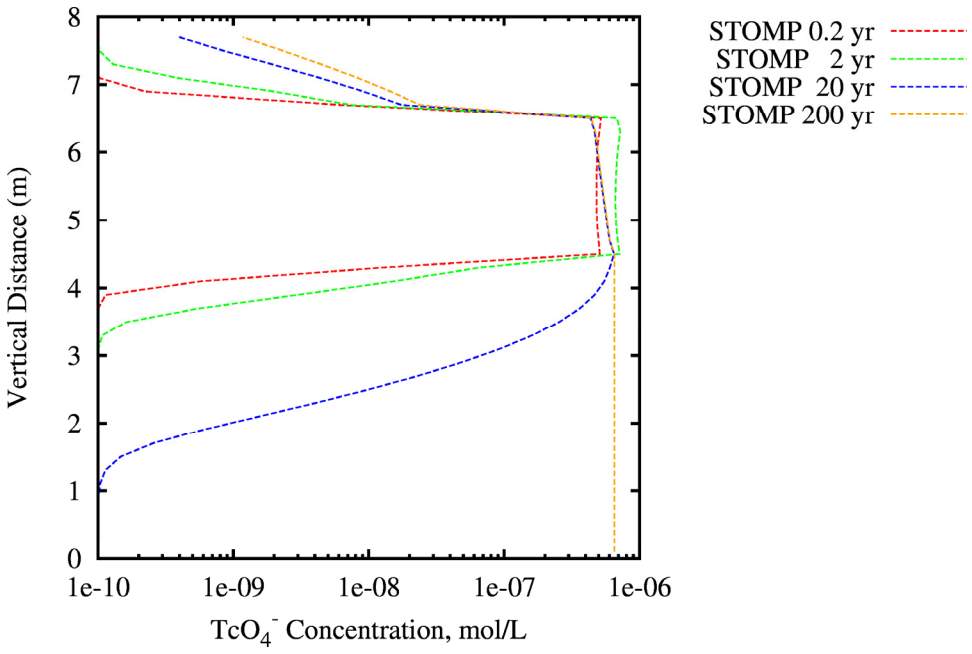


b)

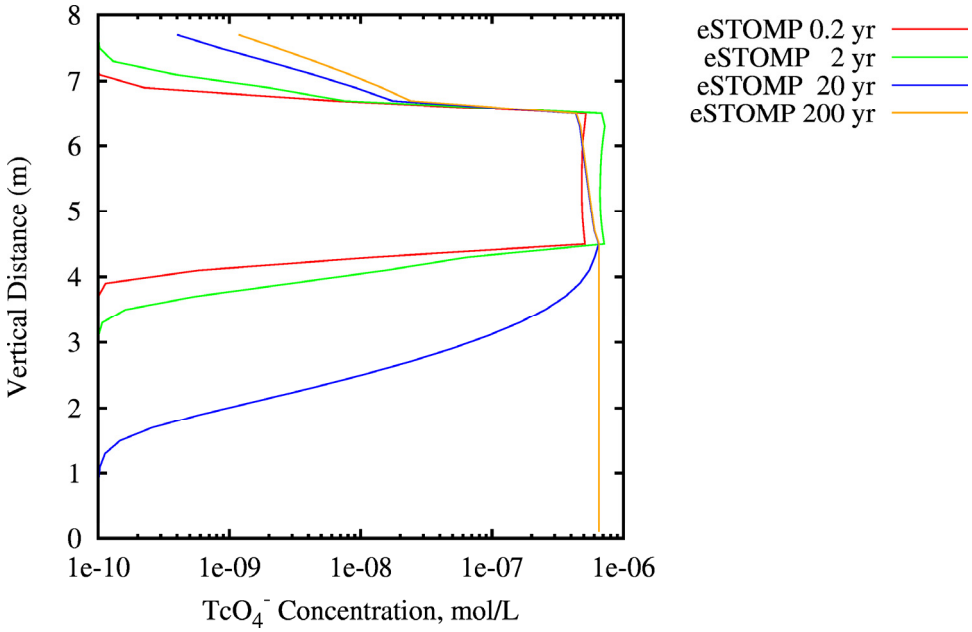


**Figure 7.4**. Comparison of Tc Concentrations vs. Depth and Time Predicted by a) STOMP and b) eSTOMP

a)

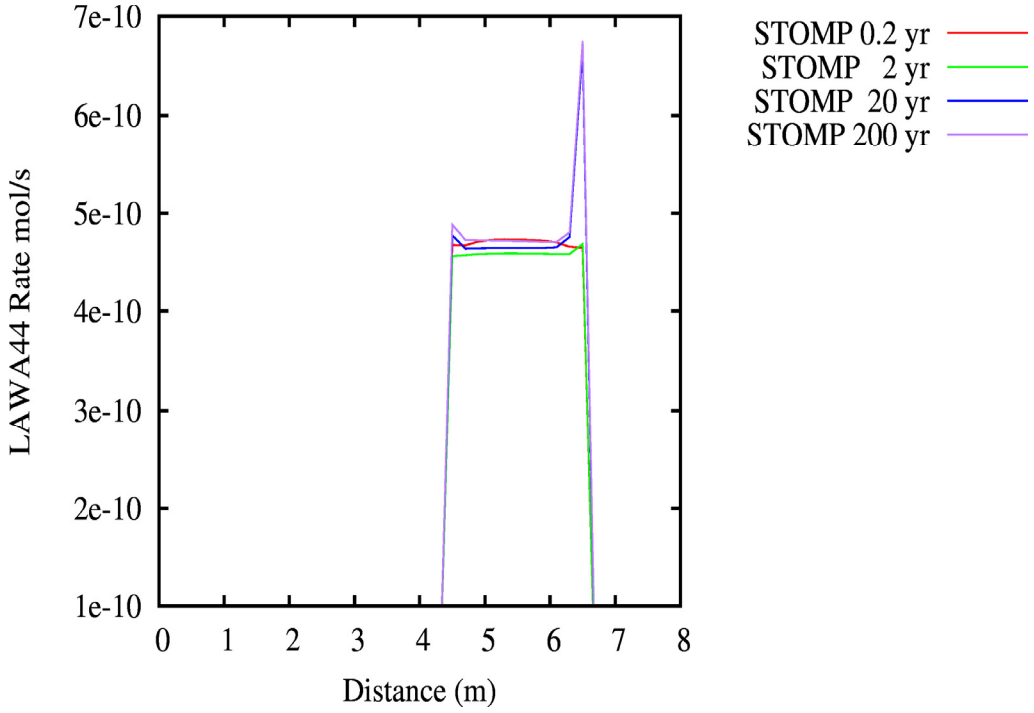


b)

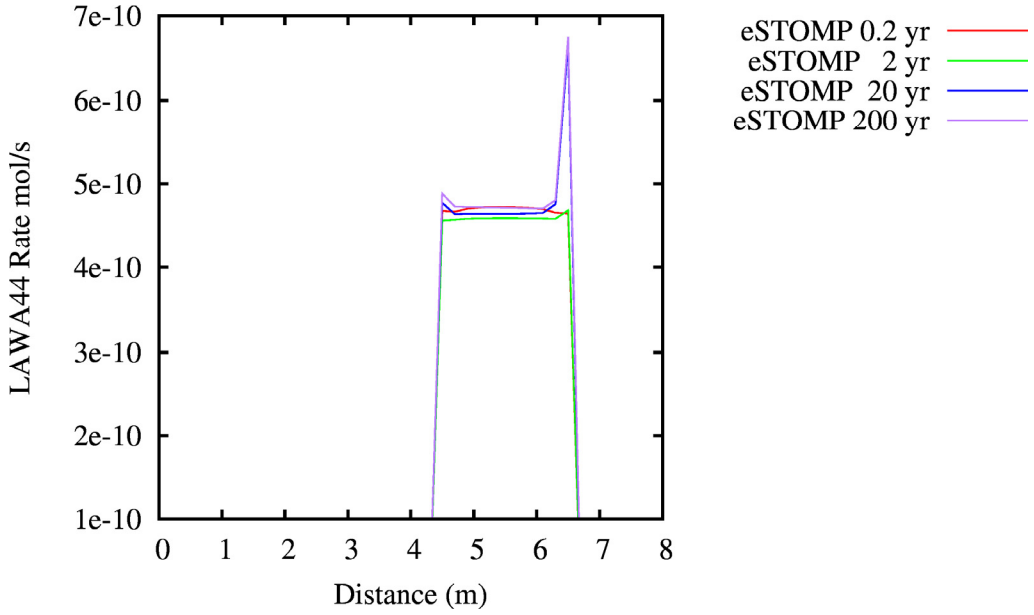


**Figure 7.5**. Comparison of LAWA44 Glass Dissolution Rate Predicted by a) STOMP and b) eSTOMP

a)

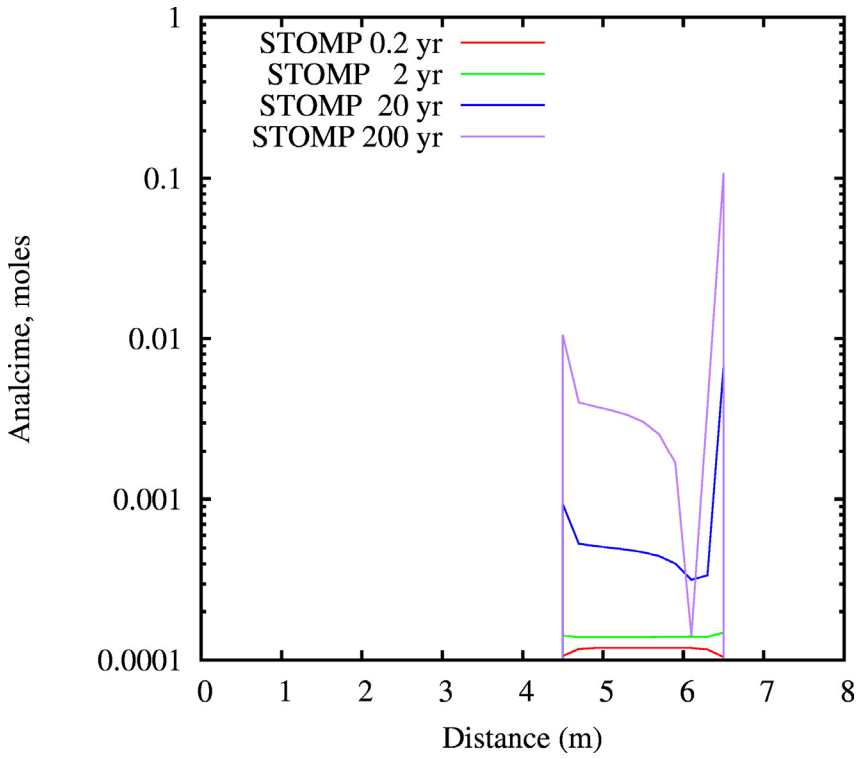


b)

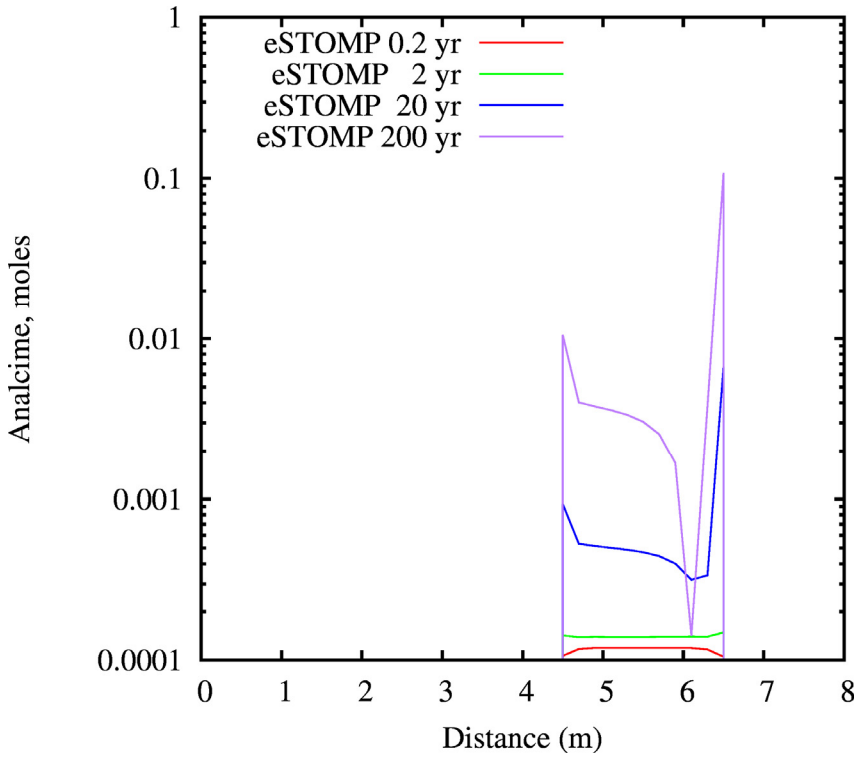


**Figure 7.6**. Comparison of Secondary Mineral Analcime Precipitation Predicted by a) STOMP and b) eSTOMP

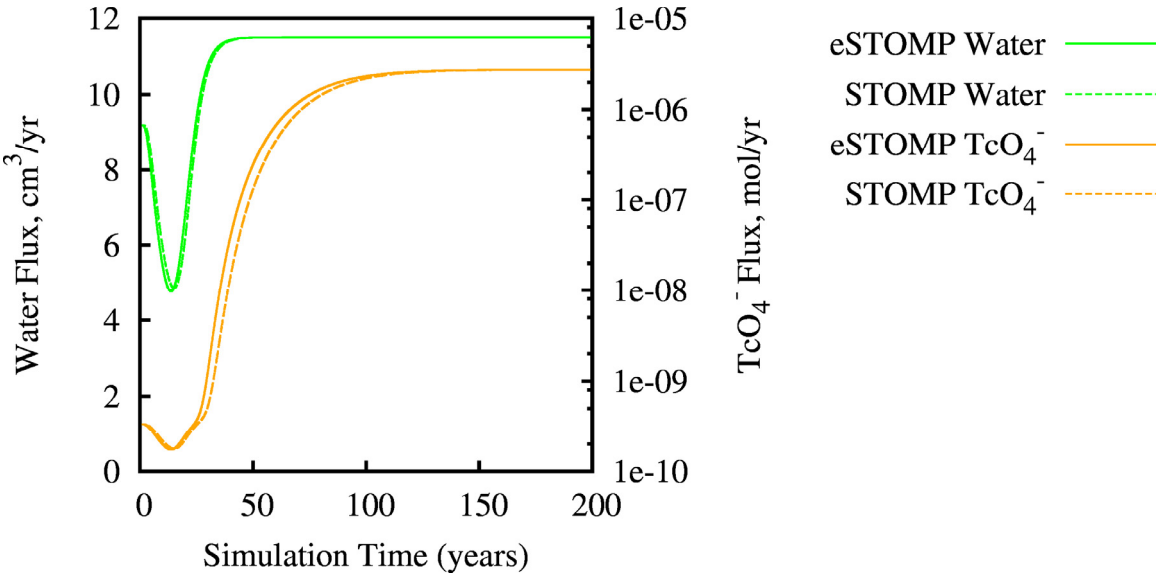


**Figure 7.7**. Comparison of Water and Tc Fluxes across Model Bottom Boundary Predicted by STOMP and eSTOMP

### 7.5.2 2D Test Case

A second two-dimensional test case was used to verify STOMP against STORM, and is also presented here for verifying eSTOMP against STOMP. Differences between the 2D benchmark problem presented in this section, and the full 2D simulation presented in Section 7.3.1 are

- one waste package, rather than four,
- a shortened vertical domain, 4.3 m rather than 17.8 m,
- a coarser variable grid spacing of 10 to 20 cm rather than 2 cm, and
- shorter time steps of 1.5 days rather than 1 year.

Tc release rates from the bottom of the repository differ by a small measure for a 300-year simulation (Figure 7.8). This is due to the differences in the way the surface fluxes are calculated between the codes, because the velocities and concentrations have nearly exact agreement between STOMP and eSTOMP. The surface flux calculation in eSTOMP will be updated so that it occurs after the concentration update as in serial STOMP. Agreement between Tc concentrations surrounding the waste packages (Figure 7.9), glass dissolution rate (Figure 7.10), and secondary mineral precipitation (Figure 7.11) is excellent. The contrast in hydraulic properties between the glass and backfill is much more significant in a 2D simulation than in the 1D simulation previously shown. Because the porosity of the glass is lower than that of the surrounding backfill, and because the pores drain easily, water flows mostly around the outside of each waste package, while a relatively small amount flows through the glass fractures. Peclet numbers are close to 10 in the glass, making this an advection-dominated problem. Both STOMP and eSTOMP use an operator-split transport scheme. The major advantage of the operator split approach is the lower memory requirement, and the greater speed with which a single time step can be completed. The most significant advantage of the time splitting approach is the ability to use algorithms for high Peclet number transport, which have less numerical dispersion than those in a global implicit scheme.

STORM uses the global implicit (or one-step method) to calculate subsurface solute transport. STOMP uses a total variation diminishing (TVD) method that results in less numerical dispersion than the global implicit upwind scheme in STORM. Consequently, STOMP takes smaller time steps than STORM to achieve convergence. STORM required 15 minutes to complete this simulation, whereas STOMP required 1 hour and 45 minutes due to the smaller time steps taken.

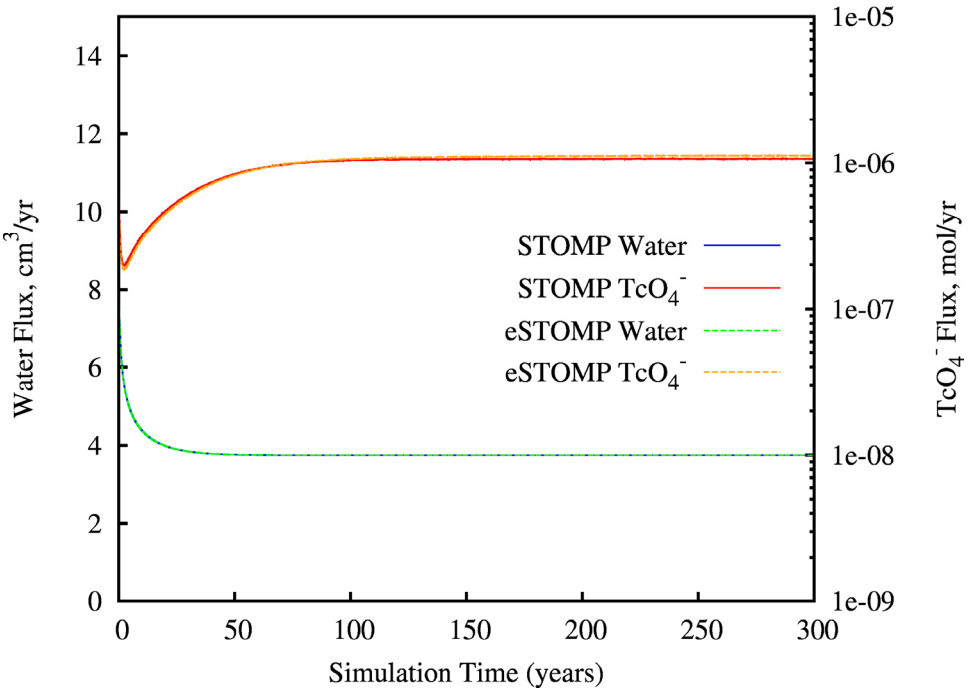


**Figure 7.8**. Comparison of Water and Tc Flux across Bottom Model Boundary for STOMP and eSTOMP 2D models

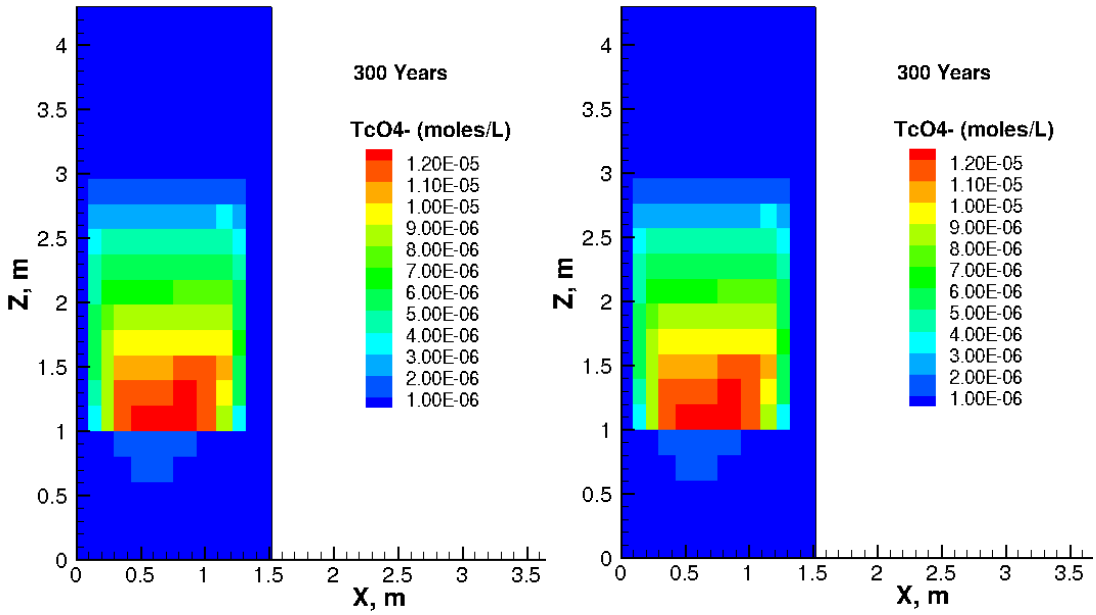


**Figure 7.9**. Comparison of Tc Concentrations at 300 Years Predicted by STOMP (left) and eSTOMP (right)

a)

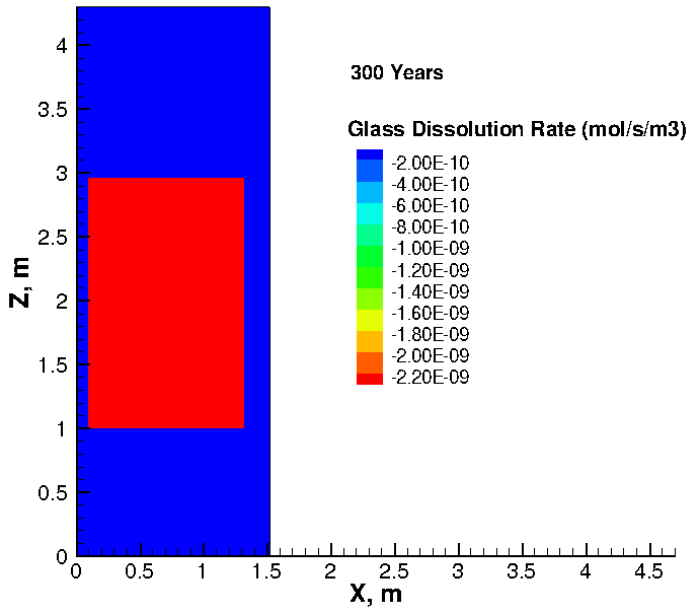


b)

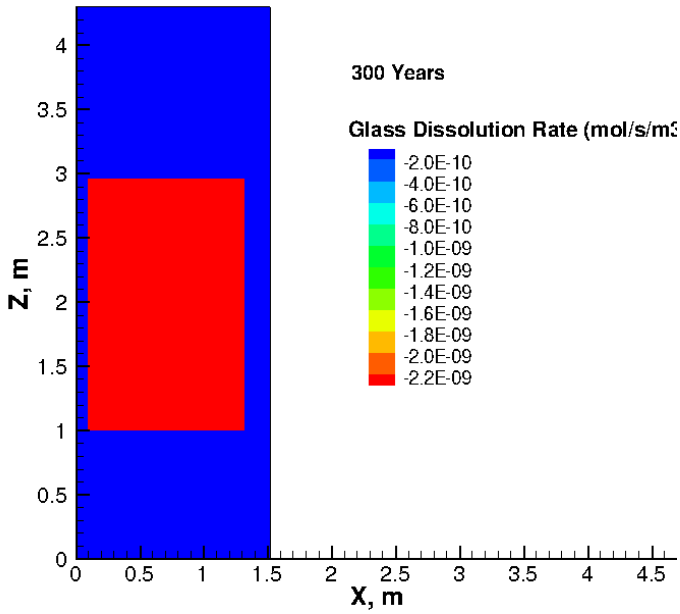


**Figure 7.10**. Comparison of LAWA44 Glass Dissolution Rate at 300 Years Predicted by a) STOMP and b) eSTOMP

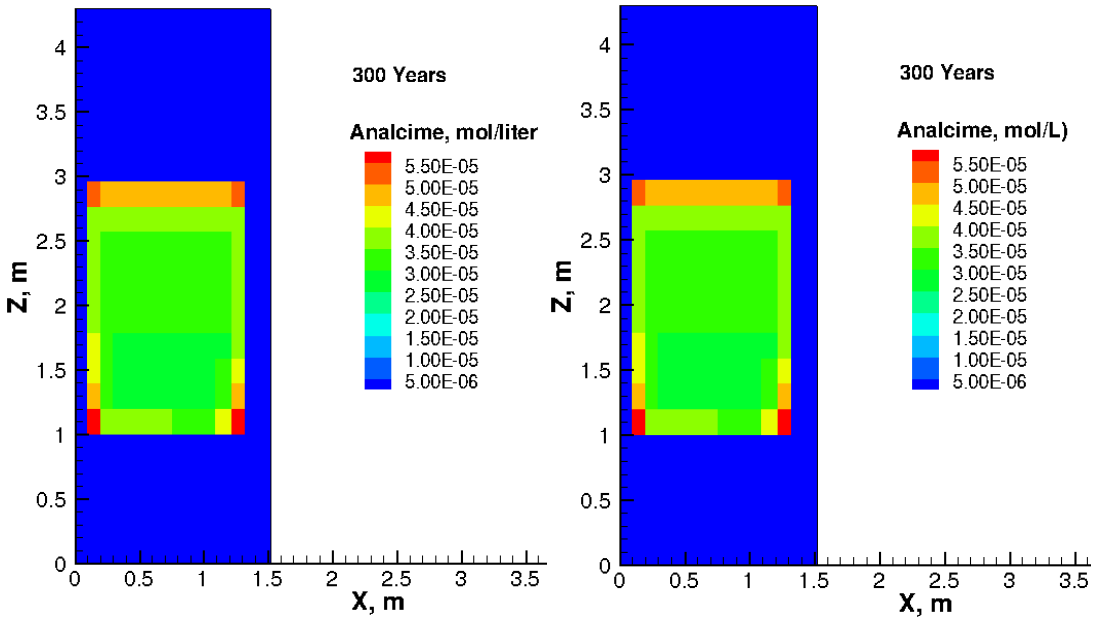


**Figure 7.11**. Comparison of Analcime Precipitated at 300 Years Predicted by STOMP (left) and eSTOMP (right)

## 7.6 eSTOMP Development

While a number of different capabilities critical for performing glass corrosion simulations were successfully incorporated into eSTOMP, its development is still incomplete. To meet performance expectations and to achieve the NQA-1 Safety Software Qualification, the following activities are recommended for further development:

1. Thorough testing of eSTOMP using the full suite of problems associated with the STOMP test suite. To date, only the benchmark problems presented in this report, as well as the ECKEChem (geochemistry) suite of test problems have been verified with eSTOMP. This subset of test problems (eight) was appropriate for the effort described in this report since the capability enhancements involved geochemistry.
    a. In this report, test simulations were formally benchmarked on a single processor core. Further testing is needed on multiple cores.
    b. Because the test problems are small, larger test problems need to be developed to assess performance on multiple cores.
2. The calculation of solute and aqueous-species surface fluxes needs to be performed after the concentrations have been updated. Currently, the calculation is done before the update and small differences in fluxes exist between serial STOMP and eSTOMP.
3. In its current implementation, every core reads the input file(s), which can cause performance issues when running on a large number of cores. The eSTOMP code needs to be updated so that the file read(s) occur on a single core, and the data are then broadcast to the other cores.
4. Only a subset of available outputs can be written to the output file. The eSTOMP code needs to be updated to include the same suite of output variables that are available in serial STOMP code.

5. Thorough error checking on eSTOMP inputs needs to be incorporated into eSTOMP. While the absence of error checking improves execution times, it is needed to identify potential user input errors.
6. For quality assurance documentation, users will need to capture an echo of all inputs to eSTOMP in the output file. Currently, only select outputs are echoed to the output file.
7. NQA-1 documentation on software requirements, design, management and testing is needed. While much of this documentation overlaps with STOMP documentation already in place, a focused effort on completing this documentation for eSTOMP is needed for compliance.
8. An eSTOMP User Guide is also needed for end-users. This documentation is currently envisioned as being wiki-based, and combined with an updated STOMP User Guide.

Once development, testing and documentation of eSTOMP have been completed, it will be reviewed by a Software Quality Engineer to receive a safety software qualification. At this point, the software will be ready for a broader user base (i.e., users external to PNNL), and will have the required NQA-1 qualification for performing glass corrosion simulations. In addition, none of the developments listed above will require additional documentation of the benchmark simulations presented in this report. However, all simulations will be re-executed and their results verified against serial STOMP.

Although not required for NQA-1 qualification, validation studies are necessary for determining that STOMP/eSTOMP is producing reasonable estimates of glass corrosion rates and COC releases. As part of the validation effort, simulations using the data from the lysimeter studies(Section 8) is planned for future work.

# 8.0 Lysimeter Sample Characterization

Performance assessment calculations for ILAW glass to be disposed at the Hanford site depend on simulations of long-term glass corrosion behavior and contaminant transport that are being performed via reactive chemical transport modeling (e.g., STOMP simulations). Confidence in the underlying physical and geochemical processes that are being simulated by such conceptual models and computer codes can be significantly enhanced through the use of carefully controlled field testing (Wicks 2001). Field-testing allows the IDF-PA program to obtain independent and site relevant data on glass corrosion at a length-scale more relevant to the actual disposal system. As a result, these data can be used to validate the models used to forecast the long-term behavior of the glass waste form and the resulting environmental impacts. For four decades, burial studies using glass waste forms were conducted in the United States—at the Waste Isolation Pilot Plant (e.g., salt geology) in Carlsbad, New Mexico—and internationally—at the SIA Radon Site in Russia (Bacon et al. 2003), at the Stripa Site in Sweden (e.g., granite geology), the Mol Site in Belgium (e.g., clay geology), and the Ballidon Site in the United Kingdom (e.g., limestone geology) (Wicks 2001). The geologic conditions used in the aforementioned studies spanned the range of geologic repositories that were under consideration by the international community. In addition to these field-scale burial studies, field tests with simulated Hanford low-activity waste glasses (e.g., HAN28F and LAWA44) were also started in the summer of 2002—approximately 11 years ago—at the Ballidon site in the United Kingdom (Ball 2003). Although the hydrology (water-saturated soil) and soil type (carboniferous limestone) do not directly relate to the conditions expected at Hanford (e.g., water under-saturated and dry-aerated sandy soils); commercial and simulated nuclear waste glasses have been buried at this site since 1970 and so burial studies at the Ballidon site provide a unique opportunity to compare findings from the long-term studies with more recent data on the glasses relevant to ILAW at Hanford. The discussion in this report focuses on field tests conducted for approximately 8 years with ILAW glass samples in a lysimeter facility on the Hanford Site (Meyer et al. 2001; McGrail et al. 2002).

## 8.1 Lysimeter Field Tests

At the Hanford Site, lysimeters are typically a corrugated steel pipe (e.g., a road culvert) buried flush with the ground surface. These systems range in size from ~4 cm in diameter and ~4 cm deep to large caissons that ~4 m wide and 10 m deep and can be installed in the ground with a wide variety of emplaced devices that can monitor temperature, water content and matric potential, and water sample collection for the purpose of obtaining leachates for chemical analysis.

Although lysimeters have several disadvantages, they are the logical choice for field-testing glass corrosion and contaminant transport for IDF PA model validation. The lysimeter system provides an approach to combine the LAW glass, Hanford soil, and other engineered materials in a well-controlled test at a length-scale that is not practical in the laboratory. The walls of the lysimeter: 1) form a physical boundary in the system being studied that defines a fixed volume for calculating water storage and tracer mass balance, and 2) restrict the geometry of flow within the lysimeter to essentially one dimension. Interpretation of complex temporal variations in tracer release and transport is much simpler in one spatial dimension. The field-scale affords the opportunity to monitor contaminant release and transport in time and space that is not possible in laboratory experiments.

## 8.2 Lysimeter Test Facility Description

The option selected for the lysimeter field studies was to conduct the experiments in existing lysimeters at the Field Lysimeter Test Facility (FLTF) at Hanford. The FLTF consists of 14 non-weighing lysimeters (2-m diameter by 3-m deep) and four weighing lysimeters installed within a subsurface concrete vault. Power and water are available at the site. Use of the existing FLTF infrastructure reduced the overall cost of the ILAW glass corrosion field experiments, while satisfying the scientific requirements of the study. Figure 8.1 shows the surface of the FLTF along with a schematic of how the glass cylinders were arranged in each lysimeter. Three FLTF lysimeters designated as D10, D11, and D14 were selected and modified for these experiments.

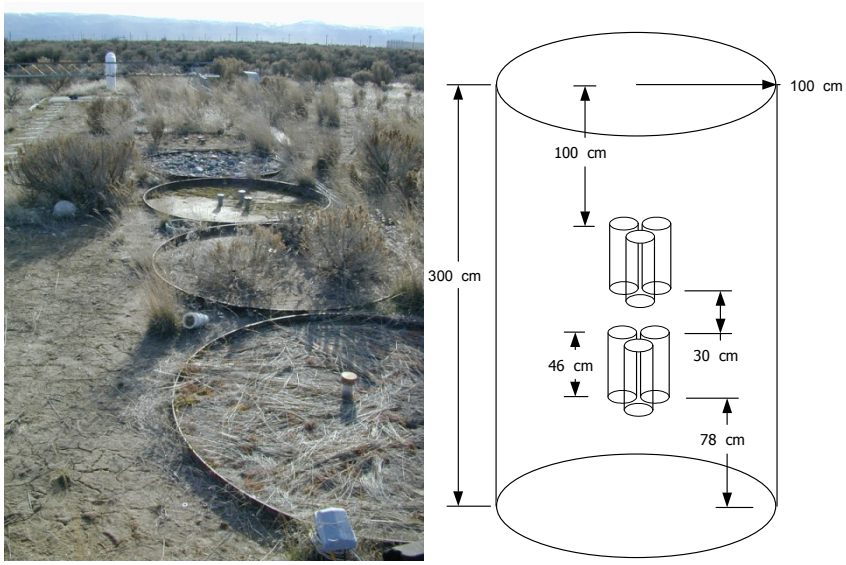


**Figure 8.1**. Surface of Field Lysimeter Test Facility (left) Showing Several Lysimeters and a Side View Diagram of ILAW Glass Test Lysimeters Showing that Each Consisted of Two Groups of Three Glass Cylinders at Upper and Lower Levels

The actual glass waste packages to be produced for the IDF disposal facility will be 213-cm high cylinders, 122-cm in diameter. However because of the cost to produce and handle full size glass cylinders, smaller samples—46 cm high and 20-cm in diameter—were used in the field experiments. These glass samples' dimensions represent a balance between the cost to produce the glass and the desire to represent the key aspects of the flow and transport characteristics of the full-scale facility. Innovatech Services, Inc. prepared twelve HAN28F glass cylinders and six LAWA44 (or equivalent) glass cylinders in 2002 and 2003, respectively (Meyer et al. 2001; McGrail et al. 2002). The glasses were prepared in graphite crucibles, but were transferred to the field in polyvinyl chloride (PVC) containers, which were removed as the glass was buried. The glasses did not include the steel canister of the planned ILAW waste form. Figure 8.2 was taken prior to glass burial and illustrates the degree of glass fracturing, which extended throughout the volume of the glass. The fracturing increased the glass surface area and made handling and burial more difficult. The nominal glass composition is shown in Table 8.1 and Table 8.2 for LAWA44 and HAN28F, respectively (Meyer et al. 2001).

**Figure 8.2**. Glass Cylinders Being Buried in a Lysimeter at the Hanford Site

**Table 8.1**. Composition of LAWA44 Glass (Meyer et al. 2001)

| | | XRF Analysis | |
|---|---|---|---|
| Oxide | Target Weight % | Average Sample Weight % | Average/ Target |
| $Al_2O_3$ | 6.20 | 5.71 | 0.92 |
| $B_2O_3$ | 8.90 | 10.45 | 1.17 |
| CaO | 1.99 | 1.77 | 0.89 |
| Cl | 0.65 | 0.43 | 0.67 |
| $Cr_2O_3$ | 0.02 | 0.02 | 1.05 |
| F | 0.01 | | 0.00 |
| $Fe_2O_3$ | 6.98 | 7.58 | 1.09 |
| $K_2O$ | 0.50 | 0.40 | 0.79 |
| MgO | 1.99 | 1.80 | 0.90 |
| $Na_2O$ | 20.00 | 21.79 | 1.09 |
| $P_2O_5$ | 0.03 | 0.14 | 4.58 |
| $SO_3$ | 0.10 | 0.17 | 1.66 |
| $SiO_2$ | 44.28 | 46.63 | 1.05 |
| $TiO_2$ | 1.99 | 1.75 | 0.88 |
| ZnO | 2.96 | 2.10 | 0.71 |
| $ZrO_2$ | 2.99 | 2.76 | 0.92 |
| $ReO_2$ | 0.10 | 0.06 | 0.55 |
| $MoO_3$ | 0.10 | 0.08 | 0.83 |
| I | 0.10 | | 0.00 |
| $SeO_2$ | 0.10 | 0.07 | 0.75 |

**Table 8.2**. Composition of HAN28F Glass (Meyer et al. 2001)

| Oxide | Target Weight % | ICP Analysis Sample Average Weight % | ICP Analysis Average/ Target | XRF Analysis Sample Average Weight % | XRF Analysis Average/ Target |
|---|---|---|---|---|---|
| Al2O3 | 10.15 | 10.34 | 1.01 | 9.64 | 0.94 |
| B2O3 | 2.00 | 2.07 | 1.03 | | |
| CaO | 2.59 | 2.62 | 1.01 | 2.09 | 0.81 |
| Cl | 0.13 | | | 0.09 | 0.68 |
| Cr2O3 | 0.08 | 0.10 | 1.21 | 0.15 | 1.88 |
| F | 0.31 | | | | |
| Fe2O3 | 2.53 | 2.67 | 1.05 | 2.06 | 0.78 |
| I2O5 | 0.10 | | | 0.08 | 0.83 |
| K2O | 1.96 | 2.20 | 1.12 | 3.61 | 1.84 |
| MgO | 1.18 | 1.18 | 1.00 | 0.91 | 0.78 |
| MoO3 | 0.10 | | | 0.08 | 0.85 |
| Na2O | 28.62 | 30.14 | 1.03 | 29.85 | 1.04 |
| P2O5 | 1.90 | 0.77 | 0.40 | 4.68 | 2.46 |
| ReO2 | 0.10 | 0.10 | 0.96 | 0.04 | 0.40 |
| SeO2 | 0.10 | 0.10 | 1.00 | 0.10 | 1.03 |
| SiO2 | 42.47 | 41.53 | 0.98 | 44.61 | 1.05 |
| SO3 | 0.30 | 0.55 | 1.85 | 0.34 | 1.14 |
| TiO2 | 0.38 | 0.44 | 1.15 | 0.36 | 0.96 |
| ZrO2 | 5.00 | 5.10 | 1.02 | 4.49 | 0.90 |

The lysimeter experiments were conducted on the irrigated side of the FLTF; therefore, the experiments received untreated Columbia River water in addition to natural precipitation. The track mounted overhead irrigation system was set to increase the applied water to three times the average natural precipitation for each month. Irrigation water was typically applied at a rate of 4-mm/hr in increments ranging from 3 to 344-mm per application (Fayer et al. 1999). The lysimeters were watered at 36 cm/year.

At the time this experiment was set up (FY 2002 and 2003), it was expected that the glass waste packages would be placed in the IDF disposal facility using a hexagonal packing arrangement. The hexagonal packing produces two distinct regions within a layer of the glass cylinders; a central region formed by three adjacent cylinders and the region along the edge of the layer (or row). Because of the differences in the hydraulic properties of the glass and backfill material, it is anticipated that more water will flow between the glass cylinders rather than through them. As a consequence, the water content in the region between the cylinders is expected to be higher than the water content outside the row(s) of waste packages. Results from Bacon and McGrail (2001) suggest that the chemistry and transport will also be different in these two regions. To represent both regions in the experimental facility, three glass cylinders were arranged as an equilateral triangle, as shown in Figure 8.1. The glass cylinders were buried in typical Hanford sandy loam or sandy gravel soils in sets of three per level, two levels in each lysimeter, at depths of 1.0 and 1.76 meters to the tops of the logs. Glass weathering and leachate transport simulation results also suggested that the multiple layers of waste packages will affect the chemistry and transport within the facility. To investigate these effects in this field experiment, two layers of three glass cylinders are included in the experimental design.

## 8.3 Lysimeter Test Characterization Objective

After approximately eight years of testing, all three of the lysimeters were excavated and soil and glass cylinders retrieved in FY 2010. The glass samples in one lysimeter (D-14 with LAWA44 glass) were largely intact when dismantled, as compared with the glass samples in lysimeters D-10 and D-11, which were only found in fragments.[1] Portions of the solids from all three lysimeters were archived for potential future solids and solution characterization. The soil and weathered glass samples were stored in refrigerated storage in the Research Technology Laboratory (RTL) Building at PNNL, and later moved to similar storage in the 331 Building.

The information derived from detailed characterization of the stored lysimeter samples (both sediments and glass waste forms) to support model validation efforts are described in this section of the annual report. These data include:

- Determining the elemental concentration profile for the lysimeter sediments to determine the flux of elements from the buried glass samples as a function of distance (depth) from the burial location. This information was achieved through the use of 1:1 water extracts of sediment samples collected from sediment cores taken from the three lysimeters. The concentration profile of key glass constituents was created using a select number of core samples removed from each lysimeter. In particular, large-diameter cores were taken approximately 30 cm from the glass cylinders and small-diameter cores (19 mm) were collected in the volume between the cylinders approximately 1 cm from the glass. These soil samples were collected both for the upper and lower glass cylinder arrays (see Figure 8.3, Figure 8.4, Figure 8.5, and Figure 8.6). Detailed schematics of the location, diameters and length of the soil cores obtained from the three lysimeters are found in Figure 8.7, Figure 8.8, and Figure 8.9 for lysimeters D10 with HAN28F glass, D11 with HAN28F glass, and D14 with LAWA44 glass, respectively. There were uncertainties in the sample labeling and locations within the lysimeters. These uncertainties may be somewhat mitigated by the experimental design and labeling conventions.
- Surface analyses of a select number of glass samples collected from the lysimeter facilities were performed on at least two of the weathered glass cylinders taken from each of the three lysimeters. Analyses included SEM-EDS and XRD.

[1] Sweeney M. 2010. *Integrated Disposal Facility Glass Testing Project Decommissioning Report: Lysimeter Decommissioning Report for the FLTF*. 58886-2010-02, Rev. 0, Pacific Northwest National Laboratory, Richland, Washington.

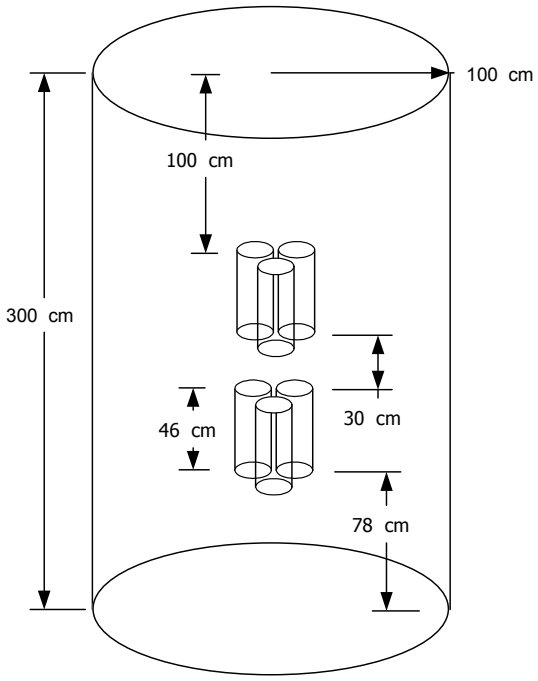


**Figure 8.3**. Side View Diagram of ILAW Glass Test Lysimeters Showing that Each Consisted of Two Groups of Three Glass Cylinders at Upper and Lower Levels

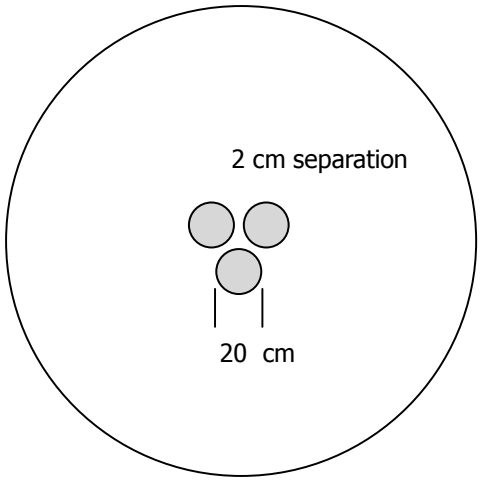


**Figure 8.4**. Planview of Glass Cylinder Arrays in Lysimeters. Sediment samples were collected in two types: large-diameter cores ca. 20–30 cm away from outside of the cylinder array and small-diameter cores between cylinders.

**Figure 8.5**. Field Photo of Lysimeter D-14 Showing Location of Large-Diameter Cores Outside Cylinder Array and the Channel (open hole) of a Small-Diameter Core between Cylinders

**Figure 8.6**. Photographs of Part of a Glass Cylinder (LAWA44) from Lysimeter D-14 Showing the Process of Collection of Glass with Attached Sediment

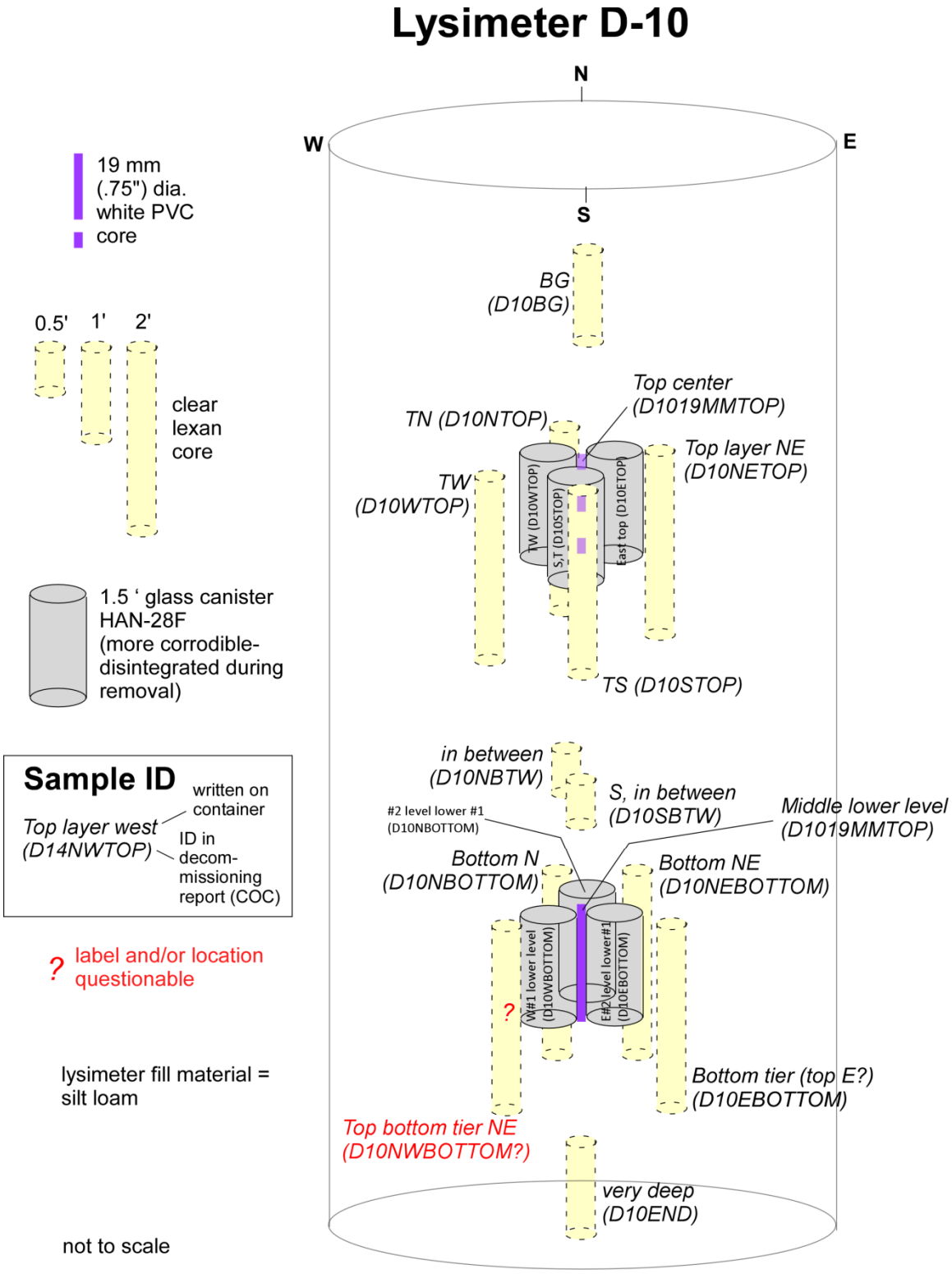


**Figure 8.7**. Lysimeter D-10 Glass and Sediment Core Locations

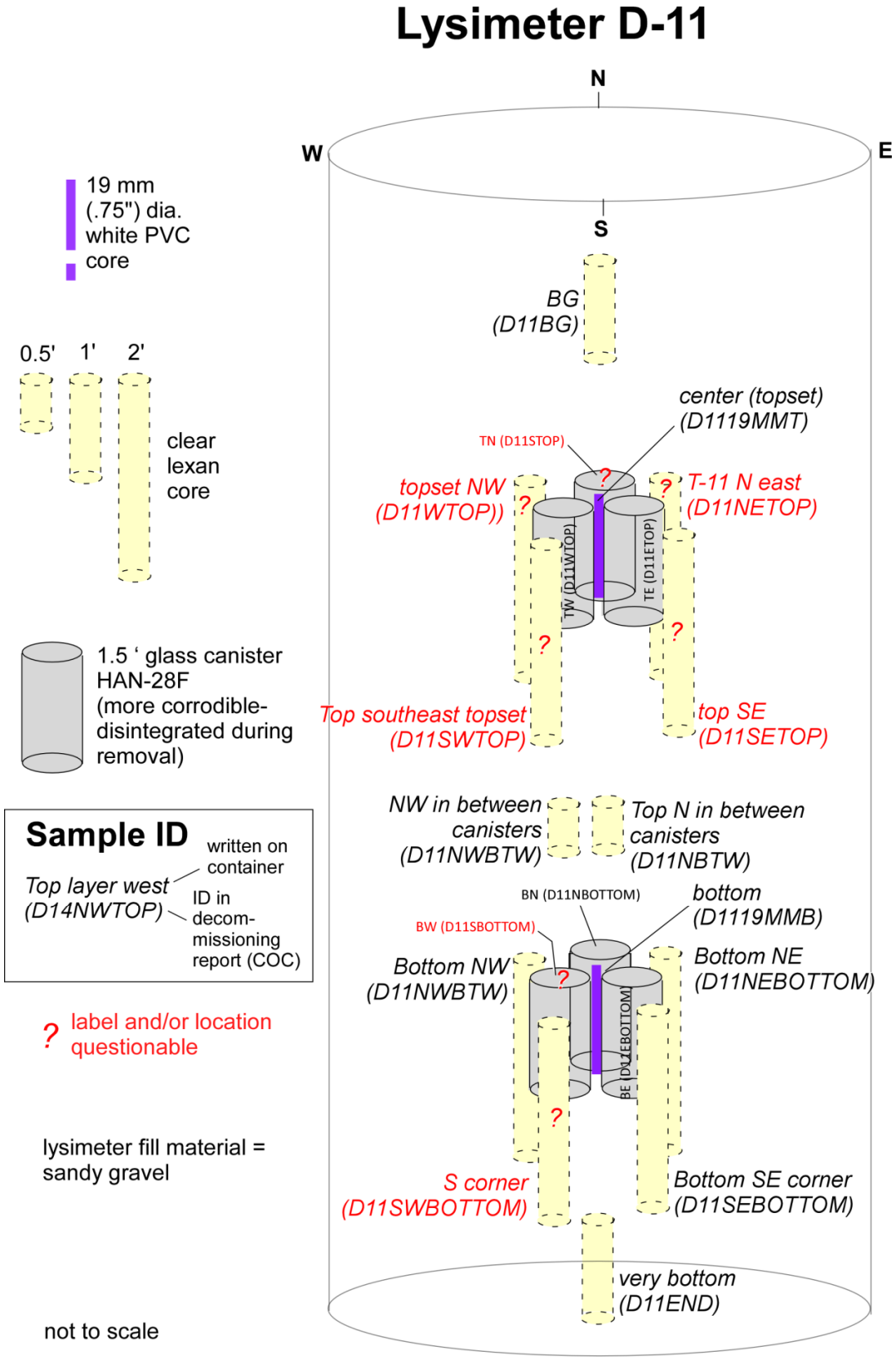


**Figure 8.8**. Lysimeter D-11 Glass and Sediment Core Locations

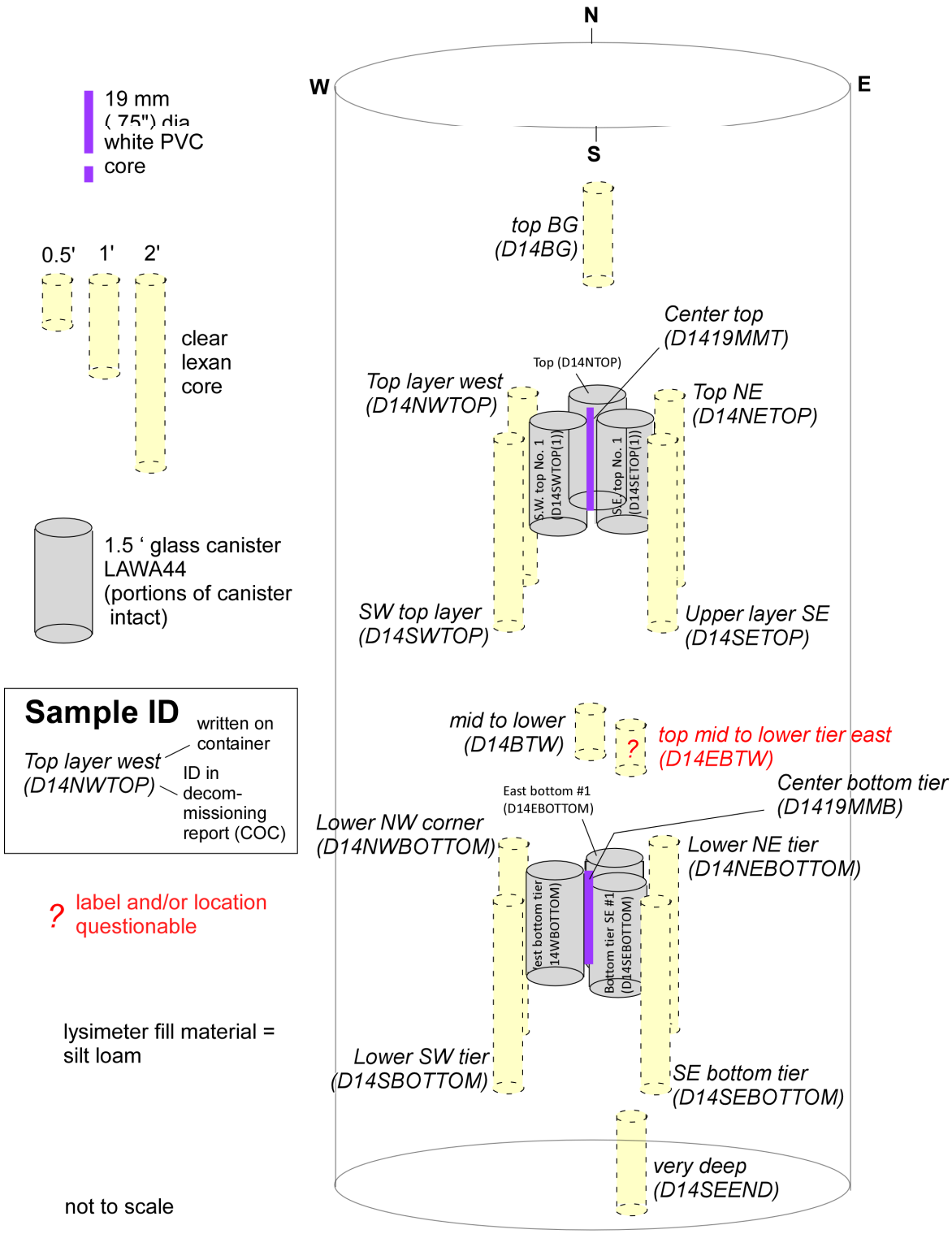


**Figure 8.9**. Lysimeter D-14 Glass and Sediment Core Locations

## 8.4 Laboratory Sampling and Preparation

Soil cores were opened, photographed and described in detail by a trained geologist. Aliquots of the soil were then sampled for 1:1 water extracts. A mass of sediment from each core, in most cases from the center of the core, midway between the core's top and bottom, was sampled.

Selected pieces of glass with sediment attached were transferred to the Applied Process Engineering Laboratory (APEL) lab of J. Crum, where these were impregnated with epoxy, cut by diamond saw, polished and mounted for SEM analysis. These weathered glass samples also had attached sediment scraped off, which was powdered and mounted on glass plates for XRD characterization of mineral phases present.

## 8.5 Analytical Methods

### 8.5.1 Water Extract Preparation, Data Collection and ICP-OES/ICP-MS Analysis

The 1:1 soil to deionized water extracts were performed as follows. The amount of deionized water needed was calculated based on the weight of the field-moisture already present in the samples (moisture contents are determined prior to conducting the water extractions). The pore water (determined from moisture content) is added to the weight of added deionized water to achieve a 1:1 weight ratio between oven dry sediment and the total water in the extraction vessel. That is, an appropriate amount of deionized water is added to the pre-weighed moist soil samples in a screw cap bottles to yield the 1:1 ratio. The bottles are sealed and placed on a mechanical orbital shaker for one hour. The samples are removed from the shaker and allowed to settle, typically overnight. The supernatant is carefully decanted and filtered through a 0.45 μm membrane. The filtered supernatant is then submitted for various chemical analyses after appropriate preservation when required.

Note that soil samples that were cored from near the surface of each lysimeter and labeled with BG for background (see Figure 8.7 through Figure 8.9) were used to represent soil that had not been influenced by glass corrosion. The BG soil water extracts were used to represent natural background conditions.

Acidified aliquots of the 1:1 extracts supernates were submitted for ICP (OES and MS) analysis at the Environmental Sciences Laboratory in the 331 building. Analyses were made using a standard analytical software program provided with the instruments by either Perkin Elmer (for the PE 3300 or 8300 ICP-OES), or Elan (for the DRC-II ICP-MS). Aliquots of the supernates were also characterized for pH, alkalinity, and anion concentrations.

### 8.5.2 pH Measurements

The pH of the extracts was measured using a solid-state pH electrode and a pH meter calibrated with standards traceable to the National Institute of Science and Technology (NIST).

### 8.5.3 Alkalinity

The alkalinity of water extracts was determined by standard titration with acid. This procedure is equivalent to the U.S. Geological Survey National Field Manual (USGS 2001) method.

### 8.5.4 Anions

The concentrations of major anions were determined by ion chromatography in the laboratory (164) in the 331 building. Anions to be determined were $F^-$, $Cl^-$, $NO_2^-$, $NO_3^-$, $Br^-$, $PO_4^{3-}$, and $SO_4^{2-}$. Analytical instrumentation was a Dionex ion chromatograph with a Dionex AS17 column using a gradient elution of 1 mM to 35 mM potassium hydroxide and measured with a conductivity detector.

## 8.6 Results

Data for measured analytes in the filtered water extracts are shown in Table 8.3, ordered by ICP-OES or -MS analyses first, followed by ion chromatography and other analyses. The data are grouped by lysimeter (D-10, D-11, and D-14). Several metals, e.g., Zr, Ti, Cr, and Al, either yielded no detectable concentrations above the experimental quantification limits (EQLs) or yielded only one or two such concentrations per lysimeter. Other metals concentrations, such as K, Ca, and Na were high enough in the water extracts from background samples for each lysimeter (D10BG, D11BG, D14BG; see Figure 8.7, Figure 8.8, and Figure 8.9) that their water extract concentrations do not appear to vary with depth in the soils obtained along side and below the glass cylinders.

An "enrichment factor" was calculated for elements in the water extracts that compared the concentration of an extract from a particular soil sample with that of the "background sample" for each lysimeter (i.e., enrichment factor = (concentration of water extract X)/(concentration of water extract BG). The background sample was the sample collected above the glass arrays (D10BG, D11BG, and D14BG), which was thought to be an indication of the compositions of water extracts in the absence of leached components from the glasses. In the event that the background sample had a concentration below the EQL, the EQL for that element was assigned as the value for the calculation. Therefore, the enrichment factor is the minimum value of concentration enrichment seen among samples.

The water extracts for some metals that are enriched in the glasses (see Table 8.1 and Table 8.4), notably Re and Mo, do vary considerably, with concentrations in water extracts increasing in sediments located below the glass cylinders and being highest in the sediments collected from the 19-mm PVC cores that were sited between, and within 2–3 centimeters of, the glass logs. The enrichment factors for Mo and Re are plotted versus sample number for each lysimeter in Figure 8.10. The degree of Re enrichment in some samples versus the background sample above the glass logs ranges up to 6 for D-11 samples, up to 69 for D-10 samples, and up to 34 for D-14 samples. The degree of Mo enrichment is higher than that for Re, with several Mo enrichment values of over $10^2$ and one reaching $10^3$.

**Table 8.3**. Water Extract Data

| **D-10** | | 1 | 2 | 3 | 4 | 5 | 6 |
|---|---|---|---|---|---|---|---|
| | | D10BG | D10NTOP | D10NETOP | D10STOP | D10WTOP | D1019MMTOP |
| Aluminum | µg/g dry | 2.44E-01 | <1.57E−01 | <1.56E−01 | 1.85E−01 | <1.57E−01 | 3.41E−01 |
| Barium | µg/g dry | 1.03E−02 | 9.98E−03 | 9.69E−03 | 9.93E−03 | 1.01E−02 | 1.02E−02 |
| Boron | µg/g dry | <2.45E+00 | <2.29E+00 | <2.28E+00 | <2.29E+00 | <2.29E+00 | <2.30E+00 |
| Calcium | µg/g dry | 1.16E+01 | 1.00E+01 | 9.58E+00 | 8.49E+00 | 9.03E+00 | 6.38E+00 |
| Chloride | µg/g dry | 3.07E−01 | 9.99E−01 | 1.88E+00 | 1.20E+00 | 1.43E+00 | 9.05E−01 |
| Chromium | µg/g dry | <7.41E−03 | <6.91E−03 | <6.89E−03 | <6.90E−03 | <6.91E−03 | <6.96E−03 |
| Fluoride | µg/g dry | 5.83E−01 | 7.01E−01 | 8.87E−01 | 8.93E−01 | 7.72E−01 | 6.49E−01 |
| Iron | µg/g dry | <1.88E−01 | <1.75E−01 | <1.75E−01 | 2.16E−01 | <1.75E−01 | 4.19E−01 |
| Magnesium | µg/g dry | 1.88E+00 | 1.87E+00 | 1.64E+00 | 1.35E+00 | 1.79E+00 | 4.50E−01 |
| Molybdenum | µg/g dry | <5.81E−03 | <5.43E−03 | <5.41E−03 | <5.42E−03 | <5.42E−03 | 1.01E−02 |
| Nitrate | µg/g dry | 8.04E−01 | 7.91E−01 | 8.18E−01 | 6.09E−01 | 7.23E−-01 | 8.41E−01 |
| Nitrite | µg/g dry | <5.38E−01 | <5.02E−01 | <5.00E−01 | <5.01E−01 | <5.01E−01 | <5.05E−01 |
| Phosphate | µg/g dry | <8.06E−01 | <7.53E−01 | <7.50E−01 | <7.51E−01 | <7.52E−01 | <7.57E−01 |
| Potassium | µg/g dry | 3.00E+00 | 3.15E+00 | 2.88E+00 | 2.71E+00 | 3.15E+00 | 2.53E+00 |
| Rhenium | µg/g dry | <4.55E−01 | <4.25E−01 | <4.23E−01 | <4.24E−01 | <4.24E−01 | <4.27E−01 |
| Selenium | µg/g dry | <1.70E−02 | <1.59E−02 | <1.58E−02 | <1.59E−02 | <1.59E−02 | <1.60E−02 |
| Silicon | µg/g dry | 1.21E+01 | 1.21E+01 | 1.39E+01 | 1.33E+01 | 1.29E+01 | 9.33E+00 |
| Sodium | µg/g dry | 1.26E+01 | 1.69E+01 | 2.06E+01 | 2.00E+01 | 2.06E+01 | 2.64E+01 |
| Sulfate | µg/g dry | 5.98E+00 | 8.48E+00 | 1.14E+01 | 8.84E+00 | 1.36E+01 | 5.34E+00 |
| Titanium | µg/g dry | <1.78E−01 | <1.66E−01 | <1.66E−01 | <1.66E−01 | <1.66E−01 | <1.67E−01 |
| Zinc | µg/g dry | 2.12E−01 | 1.85E−01 | <1.63E−01 | <1.63E−01 | <1.63E−01 | 2.33E−01 |
| Zirconium | µg/g dry | <2.30E−01 | <2.15E−01 | <2.14E−01 | <2.15E−01 | <2.15E−01 | <2.16E−01 |
| Alkalinity as $CaCO_3$ | µg/g dry | 7.17E+01 | 7.82E+01 | 7.23E+01 | 7.49E+01 | 7.58E+01 | 8.36E+01 |
| Moisture Content | % by Weight | 8.48E+00 | 8.73E+00 | 5.36E+00 | 6.06E+00 | 7.42E+00 | 7.31E+00 |
| pH | pH Units | 7.88E+00 | 7.80E+00 | 7.89E+00 | 8.01E+00 | 8.06E+00 | 8.18E+00 |

**Table 8.3**. (contd)

| **D-10** (contd) | | 7 | 8 | 9 | 10 | 11 |
|---|---|---|---|---|---|---|
| | | D10NBTW | D10NBOTTOM | D10EBOTTOM | D1019MMB (top sample) | D1019MMB (bottom sample) |
| Aluminum | µg/g dry | 4.19E−01 | <1.56E−01 | 5.26E−01 | 1.11E+00 | 1.81E−01 |
| Barium | µg/g dry | 9.37E−03 | 1.02E−02 | 1.41E−02 | 2.51E−02 | 1.51E−02 |
| Boron | µg/g dry | <2.28E+00 | <2.28E+00 | <2.44E+00 | 3.98E+00 | 1.23E+01 |
| Calcium | µg/g dry | 8.65E+00 | 9.81E+00 | 7.78E+00 | 1.20E+01 | 3.39E+00 |
| Chloride | µg/g dry | 1.49E+00 | 3.75E−01 | 7.27E−01 | 1.72E+00 | <2.50E−01 |
| Chromium | µg/g dry | <6.90E−03 | <6.89E−03 | <7.37E−03 | <6.89E−03 | <6.89E−03 |
| Fluoride | µg/g dry | 7.37E−01 | 6.85E−01 | 1.53E+00 | 4.09E+00 | 7.22E+00 |
| Iron | µg/g dry | <1.75E−01 | <1.75E−01 | 6.23E−01 | 1.25E+00 | <1.75E−01 |
| Magnesium | µg/g dry | 1.59E+00 | 1.70E+00 | 5.30E−01 | 7.24E−01 | 5.02E−01 |
| Molybdenum | µg/g dry | <5.41E−03 | 9.79E−03 | 2.48E−01 | 6.85E−01 | 9.61E−01 |
| Nitrate | µg/g dry | <5.01E−01 | 8.19E−01 | 9.63E−01 | 3.37E+00 | 2.45E+00 |
| Nitrite | µg/g dry | <5.01E−01 | <5.00E−01 | <5.35E−01 | <5.00E−01 | <5.00E−01 |
| Phosphate | µg/g dry | <7.51E−01 | <7.50E−01 | <8.02E−01 | 7.99E−01 | 1.23E+00 |
| Potassium | µg/g dry | 3.15E+00 | 3.28E+00 | 2.40E+00 | 2.72E+00 | 5.51E+00 |
| Rhenium | µg/g dry | <4.24E−01 | <4.23E−01 | 9.06E−01 | 2.40E+00 | 2.62E+00 |
| Selenium | µg/g dry | <1.59E−02 | <1.58E−02 | <1.69E−02 | 8.91E−02 | 1.13E−01 |
| Silicon | µg/g dry | 1.22E+01 | 1.25E+01 | 1.40E+01 | 2.00E+01 | 1.44E+01 |
| Sodium | µg/g dry | 1.95E+01 | 1.69E+01 | 4.53E+01 | 1.66E+02 | 4.21E+02 |
| Sulfate | µg/g dry | 1.00E+01 | 7.23E+00 | 9.24E+00 | 8.74E+00 | 9.54E+00 |
| Titanium | µg/g dry | <1.66E−01 | <1.66E−01 | <1.77E−01 | <1.66E−01 | <1.66E−01 |
| Zinc | µg/g dry | 1.89E−01 | 1.74E−01 | <1.74E−01 | 2.19E−01 | 1.70E−01 |
| Zirconium | µg/g dry | <2.14E−01 | <2.14E−01 | <2.29E−01 | <2.14E−01 | <2.14E−01 |
| Alkalinity as $CaCO_3$ | ug/g dry | 7.57E+01 | 7.58E+01 | 1.30E+02 | 4.75E+02 | 1.13E+03 |
| Moisture Content | % by wt. | 8.32E+00 | 8.07E+00 | 8.79E+00 | 8.31E+00 | 9.07E+00 |
| pH | pH Units | 8.05E+00 | 8.13E+00 | 8.85E+00 | 9.84E+00 | 9.97E+00 |

**Table 8.3**. (contd)

| **D-10** (contd) | | 12 | 13 | 14 |
|---|---|---|---|---|
| | | D10END | D10ETOP | D10NBOTTOM |
| Aluminum | µg/g dry | 2.33E-01 | 2.89E+00 | 8.26E+00 |
| Barium | µg/g dry | 1.23E-02 | 4.99E-02 | 1.53E-01 |
| Boron | µg/g dry | <2.29E+00 | 5.01E+00 | 3.08E+00 |
| Calcium | µg/g dry | 1.10E+01 | 1.52E+01 | 3.88E+01 |
| Chloride | µg/g dry | 7.72E-01 | <2.50E+00 | <3.05E+00 |
| Chromium | µg/g dry | <6.90E-03 | <6.88E-03 | <8.41E-03 |
| Fluoride | µg/g dry | 1.57E+00 | 4.55E+00 | 3.06E+00 |
| Iron | µg/g dry | 2.55E-01 | 1.00E+01 | 4.34E+01 |
| Magnesium | µg/g dry | 9.82E-01 | 1.39E+00 | 3.18E+00 |
| Molybdenum | µg/g dry | 3.21E-01 | 6.42E+00 | 1.53E+00 |
| Nitrate | µg/g dry | 9.17E-01 | <5.00E+00 | <6.10E+00 |
| Nitrite | µg/g dry | <5.01E-01 | <5.00E+00 | <6.10E+00 |
| Phosphate | µg/g dry | <7.51E-01 | 9.60E+00 | <9.15E+00 |
| Potassium | µg/g dry | 2.37E+00 | 3.44E+00 | 5.09E+00 |
| Rhenium | µg/g dry | 1.76E+00 | 3.16E+01 | 4.23E+00 |
| Selenium | µg/g dry | <1.59E-02 | 1.16E-01 | <1.93E-02 |
| Silicon | µg/g dry | 1.36E+01 | 2.04E+01 | 3.58E+01 |
| Sodium | µg/g dry | 3.32E+01 | 1.41E+02 | 1.41E+02 |
| Sulfate | µg/g dry | 9.63E+00 | 2.42E+01 | 6.01E+01 |
| Titanium | µg/g dry | <1.66E-01 | <1.66E-01 | 4.45E-01 |
| Zinc | µg/g dry | 1.83E-01 | 3.10E-01 | 5.77E-01 |
| Zirconium | µg/g dry | <2.15E-01 | <2.14E-01 | <2.61E-01 |
| Alkalinity as $CaCO_3$ | µg/g dry | 1.24E+02 | 3.26E+02 | 3.39E+02 |
| Moisture Content | % by wt. | 1.07E+01 | 1.35E+00 | 2.32E+00 |
| pH | pH Units | 7.89E+00 | 8.96E+00 | 8.64E+00 |

**Table 8.3**. (contd)

| **D-11** | | 1 | 2 | 3 | 4 | 5 |
|---|---|---|---|---|---|---|
| | | D11BG | D11WTOP | D11NETOP | D1119MMT (top sample) | D1119MMT (bottom sample) |
| Aluminum | µg/g dry | <1.56E−01 | 2.27E−01 | <1.57E−01 | 1.09E+00 | 9.50E−01 |
| Barium | µg/g dry | 1.23E−02 | 9.61E−03 | 9.54E−03 | 2.74E−02 | 2.11E−02 |
| Boron | µg/g dry | <2.28E+00 | <2.28E+00 | <2.30E+00 | <2.28E+00 | 2.57E+00 |
| Calcium | µg/g dry | 1.21E+01 | 7.13E+00 | 9.64E+00 | 1.46E+01 | 1.00E+01 |
| Chloride | µg/g dry | 1.28E+00 | 1.25E+00 | 1.04E+00 | 1.70E+00 | 1.73E+00 |
| Chromium | µg/g dry | <6.88E−03 | <6.89E−03 | <6.94E−03 | <6.88E−03 | <6.88E−03 |
| Fluoride | µg/g dry | 6.42E−01 | 1.38E+00 | 7.70E−01 | 1.56E+00 | 3.05E+00 |
| Iron | µg/g dry | <1.74E−01 | 2.66E−01 | <1.76E−01 | 1.34E+00 | 1.16E+00 |
| Magnesium | µg/g dry | 2.31E+00 | 5.71E−01 | 1.59E+00 | 6.09E−01 | 5.97E−01 |
| Molybdenum | µg/g dry | <5.40E−03 | 3.98E−02 | 1.73E−02 | 5.97E−02 | 1.78E−01 |
| Nitrate | µg/g dry | 3.97E+00 | 5.47E+00 | 5.68E+00 | 6.03E+00 | 5.81E+00 |
| Nitrite | µg/g dry | <4.99E−01 | <5.00E−01 | <5.04E−01 | <5.00E−01 | <4.99E−01 |
| Phosphate | µg/g dry | <7.49E−01 | <7.50E−01 | <7.56E−01 | <7.49E−01 | 9.05E−01 |
| Potassium | µg/g dry | 3.47E+00 | 2.66E+00 | 2.85E+00 | 2.16E+00 | 2.34E+00 |
| Rhenium | µg/g dry | <4.23E−01 | 5.61E−01 | 4.67E−01 | 7.99E−01 | 2.13E+00 |
| Selenium | µg/g dry | <1.58E−02 | <1.58E−02 | <1.60E−02 | 2.66E−02 | 5.95E−02 |
| Silicon | µg/g dry | 1.28E+01 | 1.29E+01 | 1.38E+01 | 1.95E+01 | 1.88E+01 |
| Sodium | µg/g dry | 1.36E+01 | 3.81E+01 | 1.98E+01 | 9.77E+01 | 1.26E+02 |
| Sulfate | µg/g dry | 1.47E+01 | 7.45E+00 | 7.72E+00 | 8.55E+00 | 6.41E+00 |
| Titanium | µg/g dry | <1.66E−01 | <1.66E−01 | <1.67E−01 | <1.66E−01 | <1.66E−01 |
| Zinc | µg/g dry | 1.87E−01 | <1.63E−01 | <1.64E−01 | <1.63E−01 | <1.63E−01 |
| Zirconium | µg/g dry | <2.14E−01 | <2.14E−01 | <2.16E−01 | <2.14E−01 | <2.14E−01 |
| Alkalinity as $CaCO_3$ | µg/g dry | 7.39E+01 | 1.24E+02 | 8.88E+01 | 3.21E+02 | 3.57E+02 |
| pH | pH Units | 8.04 | 8.40 | 8.03 | 9.01 | 9.38 |
| Moisture Content | % by wt. | 1.03E+01 | 1.30E+01 | 1.38E+01 | 1.20E+01 | 9.01E+00 |

**Table 8.3**. (contd)

| **D-11** (contd) | | 6 | 7 | 8 | 9 | 10 |
|---|---|---|---|---|---|---|
| | | D11NBTW | D11NEBOTTOM | D11NWBOTTOM | D11SEBOTTOM | D11SWBOTTOM |
| Aluminum | µg/g dry | <1.56E−01 | <1.56E−01 | <1.56E−01 | <1.57E−01 | <1.56E−01 |
| Barium | µg/g dry | 9.45E−03 | 1.07E−02 | 1.08E−02 | 1.07E−02 | 1.09E−02 |
| Boron | µg/g dry | <2.28E+00 | <2.28E+00 | <2.28E+00 | <2.29E+00 | <2.28E+00 |
| Calcium | µg/g dry | 9.80E+00 | 1.05E+01 | 1.06E+01 | 1.06E+01 | 1.00E+01 |
| Chloride | µg/g dry | <2.50E+00 | 7.64E−01 | 9.39E−01 | 9.76E−01 | 1.01E+00 |
| Chromium | µg/g dry | <6.89E−03 | <6.88E−03 | <6.89E−03 | <6.91E−03 | <6.89E−03 |
| Fluoride | µg/g dry | <1.00E+00 | 7.11E−01 | 6.56E−01 | 6.26E−01 | 5.84E−01 |
| Iron | µg/g dry | <1.75E−01 | <1.75E−01 | <1.75E−01 | <1.75E−01 | <1.75E−01 |
| Magnesium | µg/g dry | 1.74E+00 | 1.98E+00 | 2.14E+00 | 1.99E+00 | 2.13E+00 |
| Molybdenum | µg/g dry | 1.01E−02 | 1.31E−02 | 5.42E−02 | 4.93E−02 | 1.24E−01 |
| Nitrate | µg/g dry | <5.00E+00 | 7.91E+00 | 9.65E+00 | 1.06E+01 | 1.03E+01 |
| Nitrite | µg/g dry | <5.00E+00 | <5.00E−01 | <5.00E−01 | <5.02E−01 | <5.00E−01 |
| Phosphate | µg/g dry | <7.50E+00 | <7.49E−01 | <7.50E−01 | <7.53E−01 | <7.50E−01 |
| Potassium | µg/g dry | 2.79E+00 | 3.13E+00 | 3.06E+00 | 3.37E+00 | 3.22E+00 |
| Rhenium | µg/g dry | <4.23E−01 | <4.23E−01 | 1.01E+00 | 9.47E−01 | 6.16E−01 |
| Selenium | µg/g dry | <1.58E−02 | <1.58E−02 | <1.58E−02 | <1.59E−02 | <1.58E−02 |
| Silicon | µg/g dry | 1.34E+01 | 1.35E+01 | 1.29E+01 | 1.21E+01 | 1.11E+01 |
| Sodium | µg/g dry | 1.88E+01 | 1.81E+01 | 1.93E+01 | 1.99E+01 | 1.87E+01 |
| Sulfate | µg/g dry | <7.50E+00 | 7.27E+00 | 8.22E+00 | 9.58E+00 | 9.95E+00 |
| Titanium | µg/g dry | <1.66E−01 | <1.66E−01 | <1.66E−01 | <1.66E−01 | <1.66E−01 |
| Zinc | µg/g dry | 1.87E−01 | <1.63E−01 | 1.66E−01 | <1.63E−01 | <1.63E−01 |
| Zirconium | µg/g dry | <2.14E−01 | <2.14E−01 | <2.14E−01 | <2.15E−01 | <2.14E−01 |
| Alkalinity as $CaCO_3$ | µg/g dry | 8.87E+01 | 8.78E+01 | 9.33E+01 | 9.09E+01 | 8.91E+01 |
| pH | pH Units | 8.20 | 7.66 | 7.79 | 7.82 | 7.85 |
| Moisture Content | % by wt. | 1.51E+01 | 1.59E+01 | 1.87E+01 | 1.79E+01 | 1.60E+01 |

**Table 8.3**. (contd)

| **D-11** (contd) | | 11 | 12 | 13 |
|---|---|---|---|---|
| | | D1119MMB (top sampling) | D1119MMB (bottom sampling) | D11NEND |
| Aluminum | µg/g dry | 1.09E+00 | 1.14E+00 | <1.56E−01 |
| Barium | µg/g dry | 2.55E−02 | 2.66E−02 | 1.31E−02 |
| Boron | µg/g dry | <2.29E+00 | <2.28E+00 | <2.28E+00 |
| Calcium | µg/g dry | 1.10E+01 | 1.13E+01 | 1.04E+01 |
| Chloride | µg/g dry | <2.51E+00 | 8.97E−01 | 9.35E−01 |
| Chromium | µg/g dry | <6.91E−03 | <6.89E−03 | <6.88E−03 |
| Fluoride | µg/g dry | <1.00E+00 | 7.92E−01 | 7.97E−01 |
| Iron | µg/g dry | 1.39E+00 | 1.45E+00 | <1.75E−01 |
| Magnesium | µg/g dry | 7.88E−01 | 7.95E−01 | 2.46E+00 |
| Molybdenum | µg/g dry | 2.72E−02 | 7.14E−02 | 1.14E−01 |
| Nitrate | µg/g dry | <5.02E+00 | 3.95E+00 | 1.02E+01 |
| Nitrite | µg/g dry | <5.02E+00 | <5.00E−01 | <4.99E−01 |
| Phosphate | µg/g dry | <7.52E+00 | <7.50E−01 | <7.49E−01 |
| Potassium | µg/g dry | 2.92E+00 | 2.75E+00 | 3.37E+00 |
| Rhenium | µg/g dry | 4.54E−01 | 1.50E+00 | 2.48E+00 |
| Selenium | µg/g dry | <1.59E−02 | <1.58E−02 | <1.58E−02 |
| Silicon | µg/g dry | 1.80E+01 | 1.86E+01 | 1.51E+01 |
| Sodium | µg/g dry | 4.04E+01 | 4.23E+01 | 2.27E+01 |
| Sulfate | µg/g dry | <7.52E+00 | 5.15E+00 | 1.14E+01 |
| Titanium | µg/g dry | <1.66E−01 | <1.66E−01 | <1.66E−01 |
| Zinc | µg/g dry | 1.76E−01 | 1.99E−01 | <1.63E−01 |
| Zirconium | µg/g dry | <2.15E−01 | <2.14E−01 | <2.14E−01 |
| Alkalinity as $CaCO_3$ | µg/g dry | 1.34E+02 | 1.28E+02 | 1.01E+02 |
| pH | pH Units | 8.33 | 8.42 | 8.14 |
| Moisture Content | % by wt. | 3.48E+00 | 1.83E+00 | 1.92E+01 |

**Table 8.3**. (contd)

| **D-14** | | 1 | 2 | 3 | 4 | 5 |
|---|---|---|---|---|---|---|
| | | D14BG | D14SWTOP | D14NWTOP | D14NETOP | D14SETOP |
| Aluminum | µg/g dry | <1.49E−01 | <1.67E−01 | <1.57E−01 | <1.56E−01 | <1.56E−01 |
| Barium | µg/g dry | 1.45E−02 | 1.23E−02 | 1.20E−02 | 1.28E−02 | 1.53E−02 |
| Boron | µg/g dry | <2.18E+00 | <2.44E+00 | <2.29E+00 | <2.28E+00 | <2.28E+00 |
| Calcium | µg/g dry | 1.18E+01 | 1.24E+01 | 1.10E+01 | 1.13E+01 | 1.10E+01 |
| Chloride | µg/g dry | 3.13E+00 | 1.08E+00 | 1.46E+00 | 1.31E+00 | 2.02E+00 |
| Chromium | µg/g dry | <6.58E−03 | <7.38E−03 | <6.90E−03 | <6.87E−03 | <6.89E−03 |
| Fluoride | µg/g dry | 6.55E−01 | 8.83E−01 | 9.18E−01 | 8.17E−01 | 7.96E−01 |
| Iron | µg/g dry | <1.67E−01 | <1.87E−01 | <1.75E−01 | <1.74E−01 | <1.75E−01 |
| Magnesium | µg/g dry | 2.83E+00 | 2.35E+00 | 2.41E+00 | 2.45E+00 | 2.71E+00 |
| Molybdenum | µg/g dry | <5.17E−03 | <5.79E−03 | <5.42E−03 | <5.40E−03 | <5.41E−03 |
| Nitrate | µg/g dry | 7.98E+00 | 1.17E+00 | 4.49E+00 | 7.68E+00 | 1.05E+01 |
| Nitrite | µg/g dry | <4.78E−01 | <5.36E−01 | <5.01E−01 | <4.99E−01 | <5.00E−01 |
| Phosphate | µg/g dry | <7.17E−01 | <8.03E−01 | <7.51E−01 | <7.48E−01 | <7.50E−01 |
| Potassium | µg/g dry | 2.65E+00 | <2.31E+00 | <2.16E+00 | <2.15E+00 | <2.15E+00 |
| Rhenium | µg/g dry | <4.04E−01 | <4.53E−01 | <4.24E−01 | <4.22E−01 | <4.23E−01 |
| Selenium | µg/g dry | <1.51E−02 | <1.70E−02 | <1.59E−02 | <1.58E−02 | <1.58E−02 |
| Silicon | µg/g dry | 1.49E+01 | 1.80E+01 | 1.71E+01 | 1.69E+01 | 1.69E+01 |
| Sodium | µg/g dry | 1.97E+01 | 2.05E+01 | 2.04E+01 | 2.06E+01 | 2.13E+01 |
| Sulfate | µg/g dry | 2.14E+01 | 1.07E+01 | 1.26E+01 | 1.50E+01 | 1.44E+01 |
| Titanium | µg/g dry | <1.58E−01 | <1.78E−01 | <1.66E−01 | <1.65E−01 | <1.66E−01 |
| Zinc | µg/g dry | <1.56E−01 | 1.80E−01 | <1.63E−01 | <1.63E−01 | 1.77E−01 |
| Zirconium | µg/g dry | <2.05E−01 | <2.29E−01 | <2.15E−01 | <2.14E−01 | <2.14E−01 |
| Alkalinity as $CaCO_3$ | µg/g dry | 8.40E+01 | 8.52E+01 | 8.23E+01 | 8.50E+01 | 8.25E+01 |
| Moisture Content | % by wt. | 1.36E+01 | 8.90E+00 | 9.47E+00 | 1.13E+01 | 1.01E+01 |
| pH | pH Units | 8.02E+00 | 8.09E+00 | 8.08E+00 | 8.07E+00 | 8.11E+00 |

**Table 8.3**. (contd)

| **D-14** (contd) | | 6 | 7 | 8 | 9 | 10 |
|---|---|---|---|---|---|---|
| | | D1419MMT (top sampling) | D1419MMT (bottom sampling) | D14NEBOTTOM | D14NWBOTTOM | D14SEBOTTOM |
| Aluminum | µg/g dry | <1.57E−01 | 2.80E−01 | <1.56E−01 | <1.56E−01 | <1.56E−01 |
| Barium | µg/g dry | 2.17E−02 | 1.52E−02 | 1.70E−02 | 1.62E−02 | 1.59E−02 |
| Boron | µg/g dry | <2.29E+00 | <2.28E+00 | <2.28E+00 | <2.28E+00 | <2.28E+00 |
| Calcium | µg/g dry | 2.03E+01 | 1.38E+01 | 1.31E+01 | 1.33E+01 | 1.32E+01 |
| Chloride | µg/g dry | 6.08E+00 | 1.93E+00 | 2.15E+00 | 1.94E+00 | 2.26E+00 |
| Chromium | µg/g dry | <6.90E−03 | <6.89E−03 | <6.88E−03 | <6.89E−03 | <6.89E−03 |
| Fluoride | µg/g dry | <1.00E+00 | 8.07E−01 | 7.73E−01 | 8.30E−01 | 8.38E−01 |
| Iron | µg/g dry | <1.75E−01 | 3.33E−01 | <1.75E−01 | <1.75E−01 | <1.75E−01 |
| Magnesium | µg/g dry | 5.10E+00 | 9.64E−01 | 3.29E+00 | 3.37E+00 | 3.48E+00 |
| Molybdenum | µg/g dry | 1.33E−02 | 1.85E−02 | 5.93E−03 | 7.35E−03 | 1.03E−02 |
| Nitrate | µg/g dry | 2.45E+01 | 8.53E+00 | 1.59E+01 | 1.43E+01 | 1.65E+01 |
| Nitrite | µg/g dry | <5.01E+00 | <5.00E−01 | <4.99E−01 | <5.00E−01 | <5.00E−01 |
| Phosphate | µg/g dry | <7.52E+00 | <7.50E−01 | <7.49E−01 | <7.50E−01 | <7.50E−01 |
| Potassium | µg/g dry | 2.68E+00 | <2.15E+00 | 2.32E+00 | 2.43E+00 | 2.62E+00 |
| Rhenium | µg/g dry | 1.62E+00 | 8.23E−01 | 9.89E−01 | 7.95E−01 | 1.04E+00 |
| Selenium | µg/g dry | <1.59E−02 | <1.58E−02 | <1.58E−02 | <1.58E−02 | <1.58E−02 |
| Silicon | µg/g dry | 1.44E+01 | 1.74E+01 | 1.76E+01 | 1.80E+01 | 1.75E+01 |
| Sodium | µg/g dry | 2.31E+01 | 4.15E+01 | 2.46E+01 | 2.50E+01 | 2.52E+01 |
| Sulfate | µg/g dry | 3.50E+01 | 7.42E+00 | 2.05E+01 | 2.05E+01 | 2.00E+01 |
| Titanium | µg/g dry | <1.66E−01 | <1.66E−01 | <1.66E−01 | <1.66E−01 | <1.66E−01 |
| Zinc | µg/g dry | 1.69E−01 | <1.63E−01 | <1.63E−01 | <1.63E−01 | 2.07E−01 |
| Zirconium | µg/g dry | <2.15E−01 | <2.14E−01 | <2.14E−01 | <2.14E−01 | <2.14E−01 |
| Alkalinity as $CaCO_3$ | µg/g dry | 8.39E+01 | 1.56E+02 | 9.66E+01 | 1.07E+02 | 1.03E+02 |
| Moisture Content | % by wt. | 1.41E+01 | 1.31E+01 | 1.75E+01 | 1.90E+01 | 1.88E+01 |
| pH | pH Units | 7.83E+00 | 8.33E+00 | 8.06E+00 | 8.01E+00 | 7.98E+00 |

**Table 8.3**. (contd)

| **D-14** (contd) | | 11 | 12 | 13 | 14 | 15 | 16 |
|---|---|---|---|---|---|---|---|
| | | D14SBOTTOM | D1419MMB (top sample) | D1419MMB (bottom sample) | D14SEEND | D14NTOP | D14SEBOTTOM |
| Aluminum | µg/g dry | <1.77E−01 | <1.68E−01 | <1.56E−01 | 2.61E−01 | 4.59E−01 | <1.56E−01 |
| Barium | µg/g dry | 1.75E−02 | 1.86E−02 | 1.51E−02 | 1.45E−02 | 4.28E−02 | 2.49E−02 |
| Boron | µg/g dry | <2.58E+00 | <2.46E+00 | <2.29E+00 | <2.28E+00 | 4.03E+00 | 7.25E+00 |
| Calcium | µg/g dry | 1.38E+01 | 1.70E+01 | 1.55E+01 | 1.12E+01 | 3.84E+01 | 2.60E+01 |
| Chloride | µg/g dry | 2.00E+00 | 4.55E+00 | 3.94E+00 | <2.50E+00 | 7.19E+00 | 1.76E+01 |
| Chromium | µg/g dry | <7.80E−03 | <7.43E−03 | <6.90E−03 | <6.88E−03 | <9.81E−03 | <6.89E−03 |
| Fluoride | µg/g dry | 8.37E−01 | <1.08E+00 | <1.00E+00 | <9.99E−01 | <1.42E+00 | 1.39E+00 |
| Iron | µg/g dry | <1.98E−01 | <1.88E−01 | <1.75E−01 | 2.91E−01 | 4.64E+00 | 7.43E−01 |
| Magnesium | µg/g dry | 3.57E+00 | 3.45E+00 | 3.41E+00 | 1.69E+00 | 5.20E+00 | 5.94E+00 |
| Molybdenum | µg/g dry | 1.16E−02 | 7.48E−02 | 4.91E−02 | 2.85E−01 | 1.20E+00 | 1.10E−01 |
| Nitrate | µg/g dry | 1.52E+01 | 2.10E+01 | 2.65E+01 | <5.00E+00 | <7.12E+00 | 3.71E+01 |
| Nitrite | µg/g dry | <5.66E−01 | <5.39E+00 | <5.01E+00 | <5.00E+00 | <7.12E+00 | <5.00E+00 |
| Phosphate | µg/g dry | <8.49E−01 | <8.09E+00 | <7.51E+00 | <7.50E+00 | <1.07E+01 | <7.50E+00 |
| Potassium | µg/g dry | 2.67E+00 | 2.32E+00 | 2.31E+00 | 2.79E+00 | 4.01E+00 | 3.37E+00 |
| Rhenium | µg/g dry | 1.07E+00 | 8.85E+00 | 1.23E+01 | 2.13E+00 | 1.07E+01 | 1.38E+01 |
| Selenium | µg/g dry | <1.79E−02 | <1.71E−02 | <1.59E−02 | <1.58E−02 | <2.25E−02 | 3.88E−02 |
| Silicon | µg/g dry | 1.85E+01 | 1.63E+01 | 1.48E+01 | 1.61E+01 | 1.58E+01 | 9.11E+00 |
| Sodium | µg/g dry | 2.60E+01 | 2.19E+01 | 2.80E+01 | 2.35E+01 | 9.83E+01 | 1.10E+02 |
| Sulfate | µg/g dry | 2.08E+01 | 1.90E+01 | 1.91E+01 | 1.26E+01 | 7.33E+01 | 1.49E+02 |
| Titanium | µg/g dry | <1.88E−01 | <1.79E−01 | <1.66E−01 | <1.66E−01 | <2.36E−01 | <1.66E−01 |
| Zinc | µg/g dry | <1.84E−01 | <1.76E−01 | 1.69E−01 | <1.63E−01 | 2.52E−01 | <1.63E−01 |
| Zirconium | µg/g dry | <2.43E−01 | <2.31E−01 | <2.15E−01 | <2.14E−01 | <3.05E−01 | <2.14E−01 |
| Alkalinity as $CaCO_3$ | µg/g dry | 9.69E+01 | 8.38E+01 | 1.00E+02 | 9.36E+01 | 1.82E+02 | 1.58E+02 |
| Moisture Content | % by wt. | 1.92E+01 | 1.63E+01 | 1.75E+01 | 8.86E+00 | 1.36E+00 | 7.23E+00 |
| pH | pH Units | 8.06E+00 | 7.97E+00 | 8.02E+00 | 8.03E+00 | 8.14E+00 | 8.26E+00 |

Note: Values shown as less than ("<X.XX") had concentrations below the EQL, which for this method was equal to the values shown by "X.XX."

**Table 8.4**. Enrichment Factors Based on Water Extracts for Each Sample Compared to the "Background Sample" (BG) for Each Lysimeter

| **D-10** | 1 | 2 | 3 | 4 | 5 | 6 | 7 | 8 | 9 | 10 | 11 | 12 | 13 | | | |
|---|---|---|---|---|---|---|---|---|---|---|---|---|---|---|---|---|
| Ba | 1 | 0.78 | 0.78 | 2.23 | 1.72 | 0.77 | 0.87 | 0.88 | 0.87 | 0.89 | 2.07 | 2.16 | 1.07 | | | |
| Ca | 1 | 0.59 | 0.80 | 1.21 | 0.83 | 0.81 | 0.87 | 0.88 | 0.88 | 0.83 | 0.91 | 0.93 | 0.86 | | | |
| Chloride | 1 | 0.98 | 0.81 | 1.33 | 1.35 | #N/A | 0.60 | 0.73 | 0.76 | 0.79 | #N/A | 0.70 | 0.73 | | | |
| Mo | 1 | 7.4 | 3.2 | 11.1 | 33.0 | 1.9 | 2.4 | 10.0 | 9.1 | 23.0 | 5.0 | 13.2 | 21.1 | | | |
| Re | 1 | 1.3 | 1.1 | 1.9 | 5.0 | #N/A | #N/A | 2.4 | 2.2 | 1.5 | 1.1 | 3.5 | 5.9 | | | |
| **D-11** | 1 | 2 | 3 | 4 | 5 | 6 | 7 | 8 | 9 | 10 | 11 | 12 | 13 | | | |
| Ba | 1 | 0.78 | 0.78 | 2.23 | 1.72 | 0.77 | 0.87 | 0.88 | 0.87 | 0.89 | 2.07 | 2.16 | 1.07 | | | |
| Ca | 1 | 0.59 | 0.80 | 1.21 | 0.83 | 0.81 | 0.87 | 0.88 | 0.88 | 0.83 | 0.91 | 0.93 | 0.86 | | | |
| Chloride | 1 | 0.98 | 0.81 | 1.33 | 1.35 | #N/A | 0.60 | 0.73 | 0.76 | 0.79 | #N/A | 0.70 | 0.73 | | | |
| Mo | 1 | 7.37 | 3.20 | 11.06 | 32.96 | 1.87 | 2.43 | 10.04 | 9.13 | 22.96 | 5.04 | 13.22 | 21.1 | | | |
| Re | 1 | 1.33 | 1.10 | 1.89 | 5.04 | #N/A | #N/A | 2.39 | 2.24 | 1.46 | 1.07 | 3.55 | 5.86 | | | |
| **D-14** | 1 | 2 | 3 | 4 | 5 | 6 | 7 | 8 | 9 | 10 | 11 | 12 | 13 | 14 | 15 | 16 |
| Ba | 1 | 0.85 | 0.83 | 0.88 | 1.06 | 1.50 | 1.05 | 1.17 | 1.12 | 1.10 | 1.21 | 1.28 | 1.04 | 1.00 | 2.95 | 1.72 |
| Ca | 1 | 1.05 | 0.93 | 0.96 | 0.93 | 1.72 | 1.17 | 1.11 | 1.13 | 1.12 | 1.17 | 1.44 | 1.31 | 0.95 | 3.25 | 2.20 |
| Chloride | 1 | 0.35 | 0.47 | 0.42 | 0.65 | 1.94 | 0.62 | 0.69 | 0.62 | 0.72 | 0.64 | 1.45 | 1.3 | #N/A | 2.3 | 5.6 |
| Mo | 1 | 1.00 | 1.00 | 1.00 | 1.00 | 2.57 | 3.58 | 1.15 | 1.42 | 1.99 | 2.24 | 14.47 | 9.5 | 55.1 | 232 | 21.3 |
| Re | 1 | 1.00 | 1.00 | 1.00 | 1.00 | 4.01 | 2.04 | 2.45 | 1.97 | 2.57 | 2.65 | 21.91 | 30.4 | 5.3 | 26.5 | 34.2 |

Note: Enrichment factors calculated by dividing the concentration of each element for each sample by the concentration for that element in the background sample. In the event that the background sample had elemental concentrations below the EQL for that element, the EQL was used as the concentration; this means that the enrichment factors are minimum values.

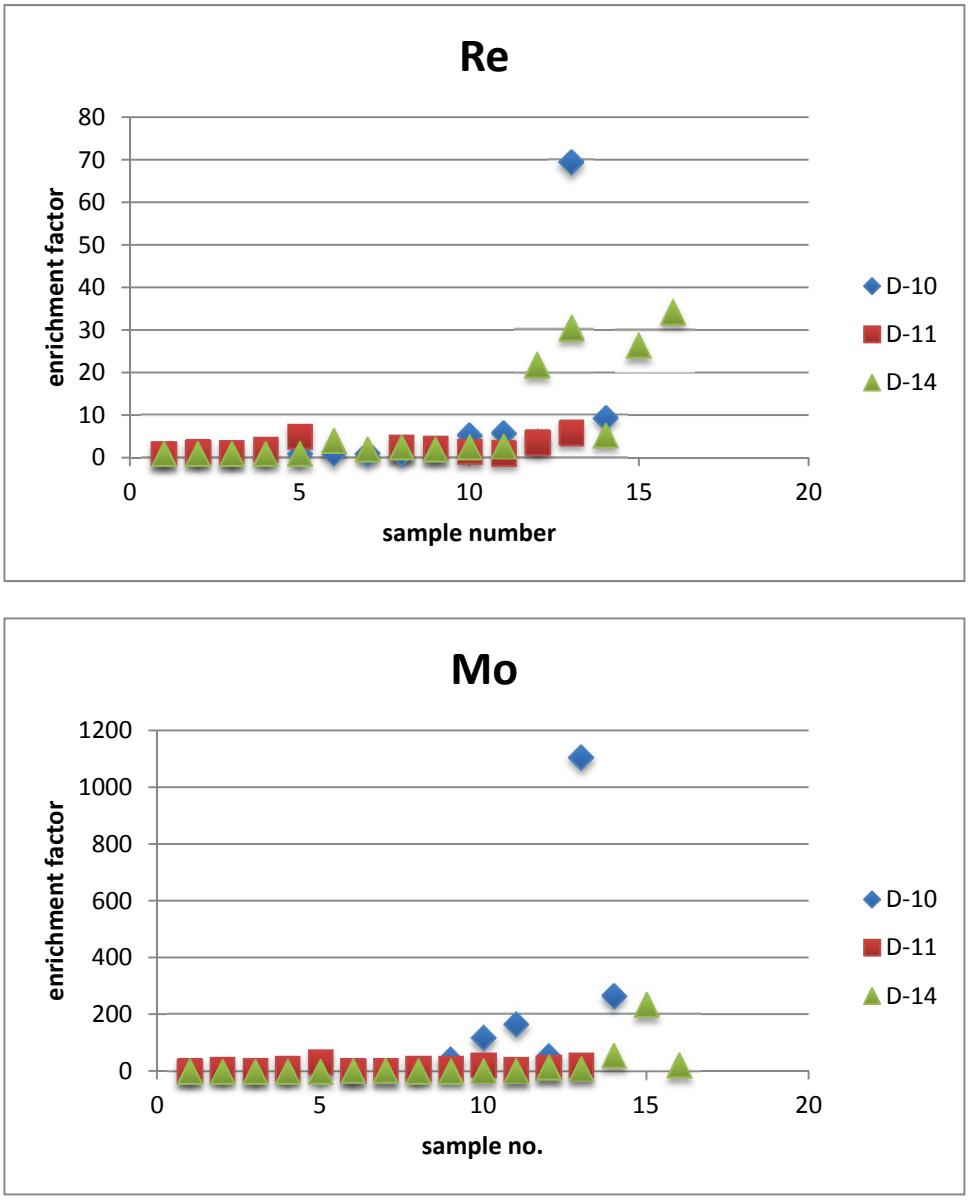


**Figure 8.10**. Enrichment Factor (see text and Table 8.4) for Re and Mo Plotted versus Sample Number for the Three Lysimeter Arrays. Rhenium and molybdenum enrichment are found in soils associated with LAWA44 (D-14) and HAN-28F (D-10 and D-11) glass samples. Low sample numbers are shallow depths, so depth increases to the right in each figure. Samples with the highest enrichments of Re and Mo (D-10 samples 9-14, D-11 samples 8-13, and D-14 samples 12-16) were collected from (1) positions at the bottom of the lysimeters below the bottom glass samples (e.g., D10END, D11NEND, D14SEEND), or (2) positions within 2-3 centimeters of glass-soil interfaces (all others, such as D1019MMB, Figure 8.7).

Boron also has increased concentrations (above EQL) in several samples, four from D-10, one from D-11 (both HAN28F glass), and two from D-14 (LAWA44 glass). These enrichments, however, are not as pronounced (one sample from D-10 has a boron enrichment of 5 over the EQL, the other six have boron levels above the EQL that are only enriched by factors of 1–3).

## 8.7 Results from SEM Studies

Samples were prepared by first encapsulating them in epoxy to preserve the glass-to-soil interface. Samples were then cross-sectioned with a diamond impregnated wafer blade that was water lubricated. Finally, the cross-sectioned samples were ground and polished using a series of grits to a final polish of 1 μm diamond.

Samples were sputter coated with Au to provide a conductive surface for the electron beam. Samples were put into a JEOL 7001 field emission SEM equipped with an EDAX silicon drift energy dispersive spectrometer. The microscope was operated at a 20-kV accelerating voltage with a spot size that provided ~50–100 kcps for elemental dot map collection. Dot maps were collected at various resolutions from 512 × 400 to 1024 × 800 pixels with a drift correction algorithm built into the software. In all of the SEM images and dot maps, soil is in the upper portion of the images and glass is in the lower portion, with red dashed lines indicating the interface between them.

Figure 8.11 through Figure 8.15 show the elemental dot maps, which were collected at the glass-to-soil interfaces for samples of both types of glass, HAN-28F and LAWA44 In these images, brightness of color is proportional to the concentration of the element. Iron-rich metal globules occur at the outer surfaces of the glass. Rhenium is clearly co-located with the Fe-rich phase. The metal appears to have oxidized considerably whereas the glass phase showed no significant signs of an altered glass layer. The source of the metal particles is identified below. Reddish colored stains are very apparent visually in the soil next to the glass, which indicates hematite. The elemental dot maps all appear to confirm that soil grains are surrounded by a phase concentrated in Fe and O. The Fe-rich alteration phase was also observed in the cracks within the glass. In a few locations, a calcium-rich phase was also observed in the dot maps (Figure 8.15). In other locations some enrichment of Zr, P, and S were also observed to encapsulate the soil grains. Figure 8.16 through Figure 8.19 show backscatter images of the glass-soil interface. Figure 8.20 and Figure 8.21 show the secondary electron image for a glass-soil interface from the D14 and D11 lysimeters, respectively.

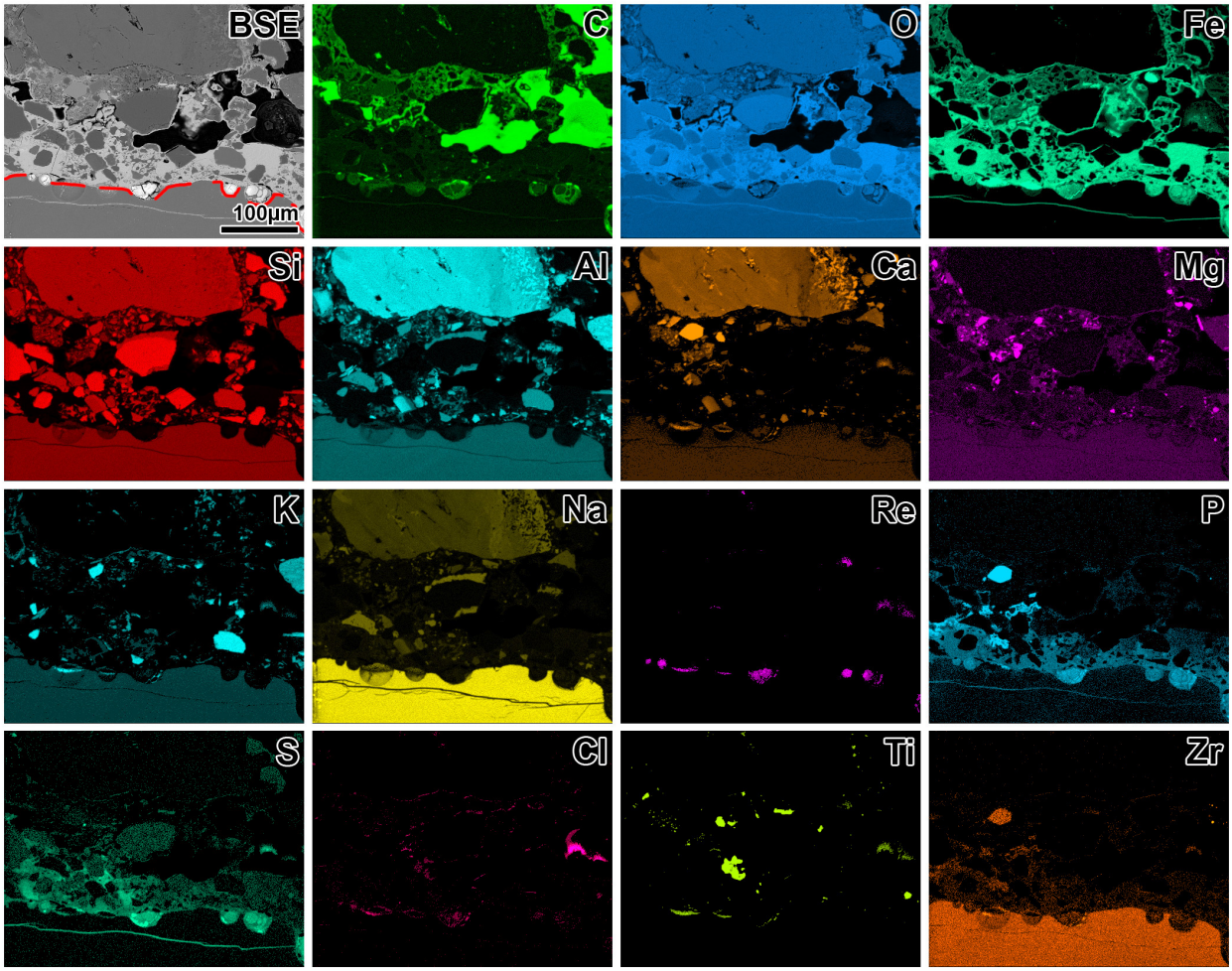


**Figure 8.11**. Elemental Dot Map of D10-Bottom Sample at the Glass-to-Soil (top) Interface (HAN-28F glass). Iron alloy particles at the glass surface appear to corrode and form Fe-oxide. Phosphorous, S, O, and Fe are elevated in the soil boundaries and glass crack. (BSE = backscattered electron image.)

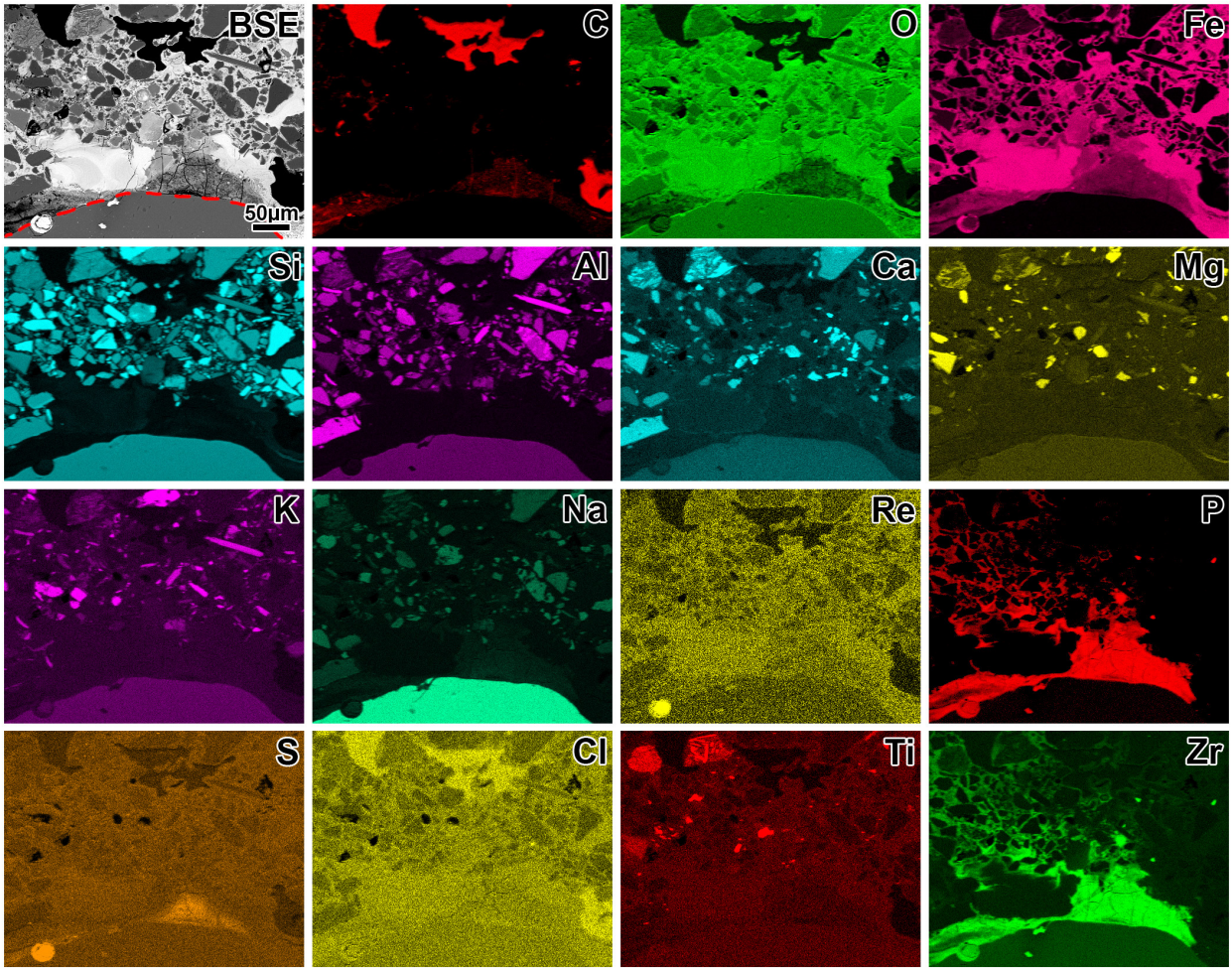


**Figure 8.12**. Elemental Dot Map of D11-North Top Sample at the Glass (bottom)-to-Soil (top) Interface (HAN-28F glass). Iron alloy particles at glass surface appear to corrode and form oxides of Fe and Re. Other elements also contain elevated concentrations in the soil boundaries: P, Zr, S, and Cl.

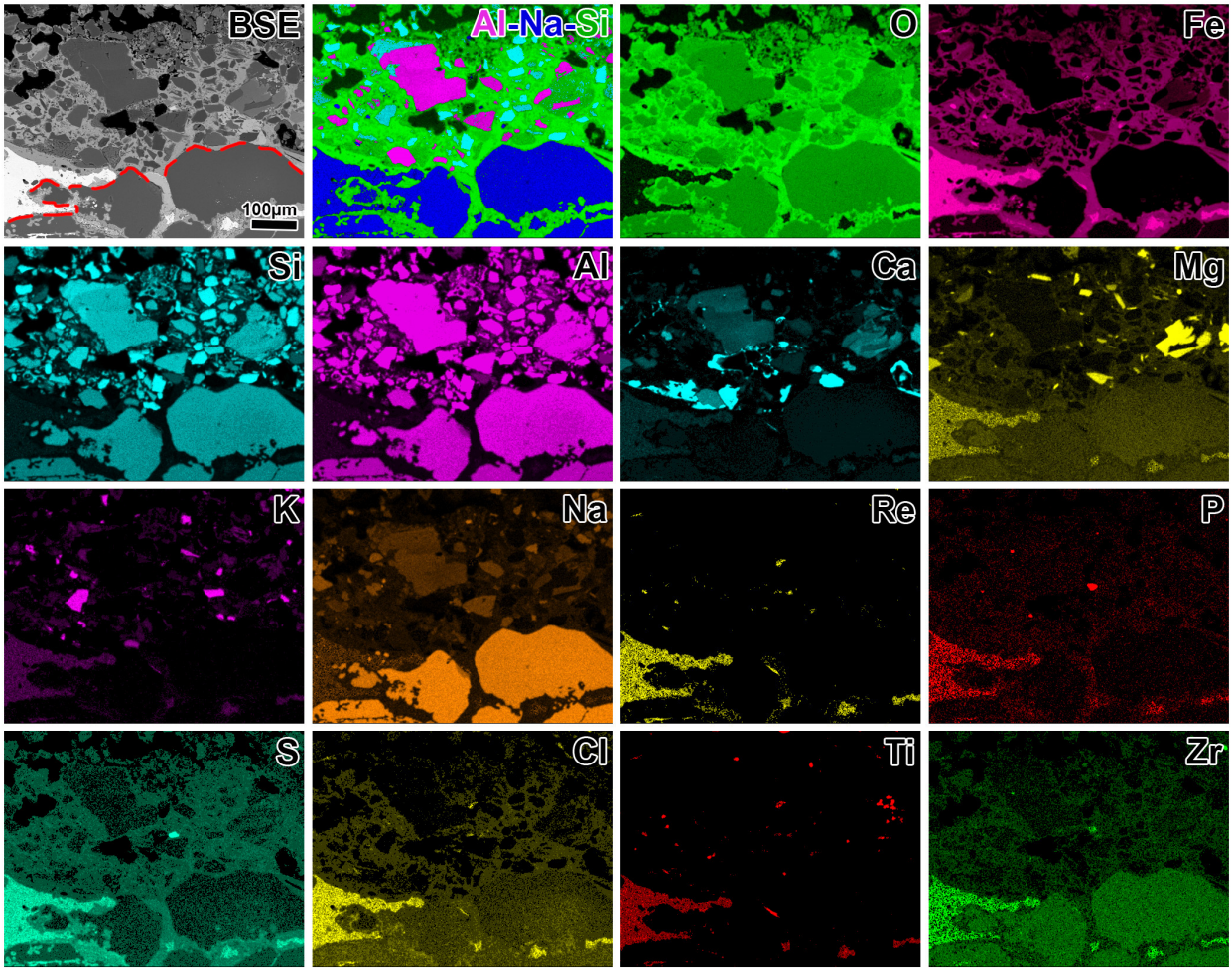


**Figure 8.13**. Elemental Dot Map of D14-North Bottom Sample (LAWA44 glass) at the Glass (bottom)-to-Soil (top) Interface. Iron alloy particles at the glass surface appear to corrode and form Fe-oxide that surrounds all the glass and soil particles. Magnesium, P, S, Cl, and Zr are also concentrated between the glass and soil particles. Calcium is very concentrated in some locations along the glass-soil boundary.

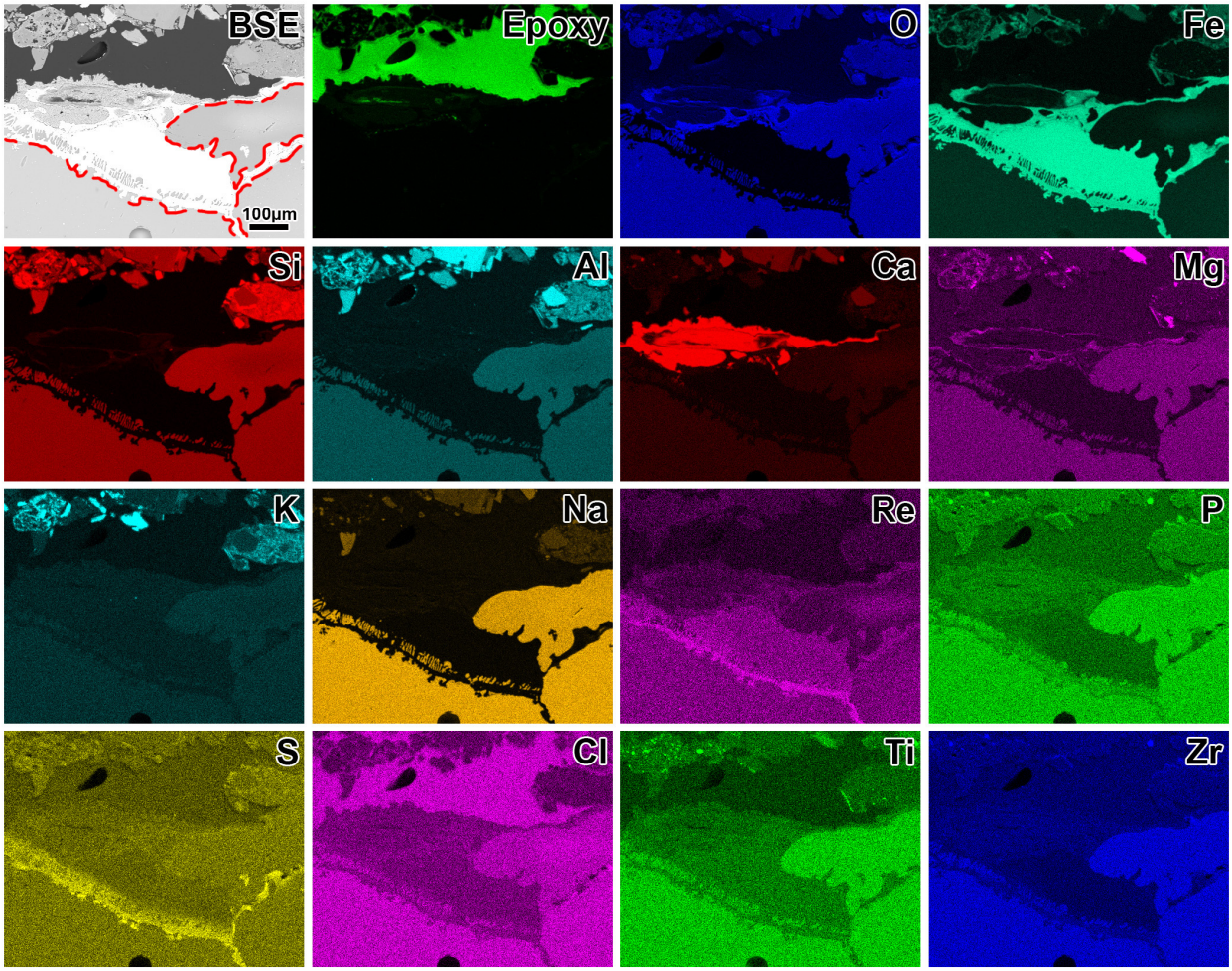


**Figure 8.14**. Elemental Dot Map of D14-North Top Sample at the Glass (bottom), Metal (center), and Soil (top) Interfaces (LAWA44 glass). Iron alloy particles at the glass surface appear less corroded than the D10 and D11 samples, but forms Fe-oxide between all the boundaries. Calcium is concentrated above the metal phase. Rhenium and S are somewhat concentrated just below the metal phase.

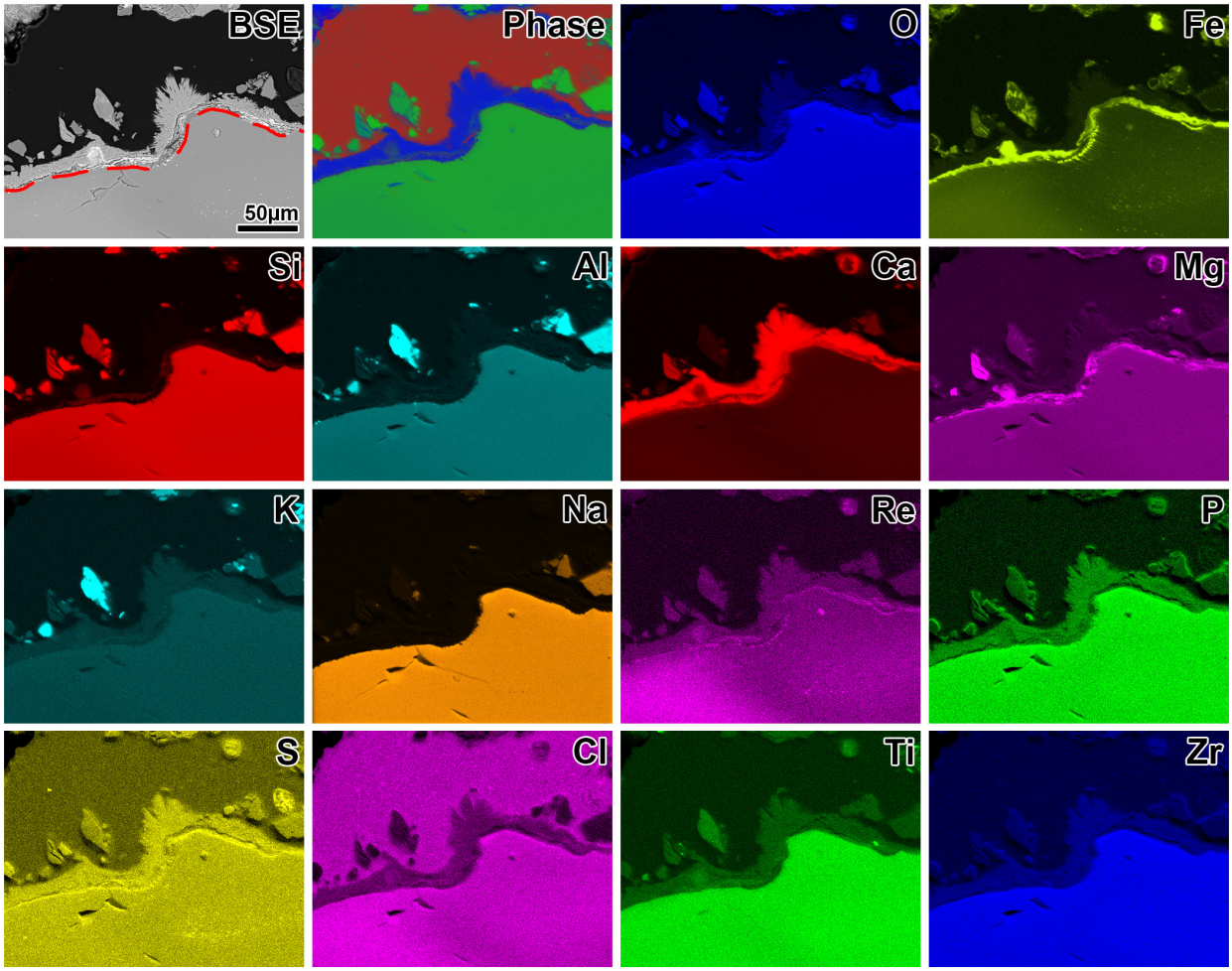


**Figure 8.15**. Elemental Dot Map of D14-North Top Sample at the Glass (bottom) and Soil (top) Interface (LAWA44 glass). There are only a few small Fe-alloy particles at the glass surface. In the colored phase map, calcium is concentrated as the blue phase and glass (bottom) and minerals (top) are green; red is the epoxy used to encapsulate the sample.

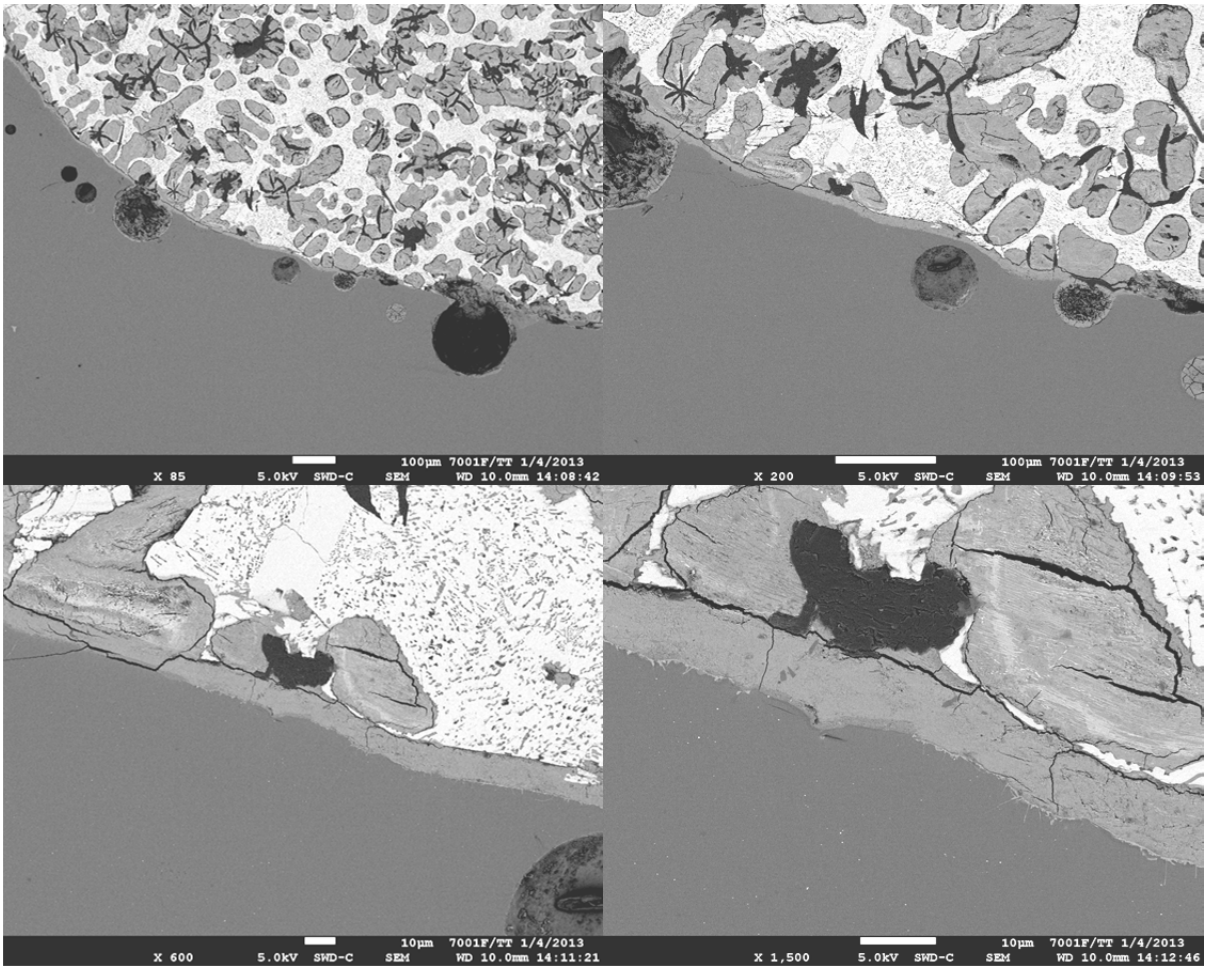


**Figure 8.16**. Backscattered Electron Images of Glass-to-Metal Interface in Sample D10 North Bottom (HAN-28F glass) at Magnifications of 85, 200, 400, and 1,500×

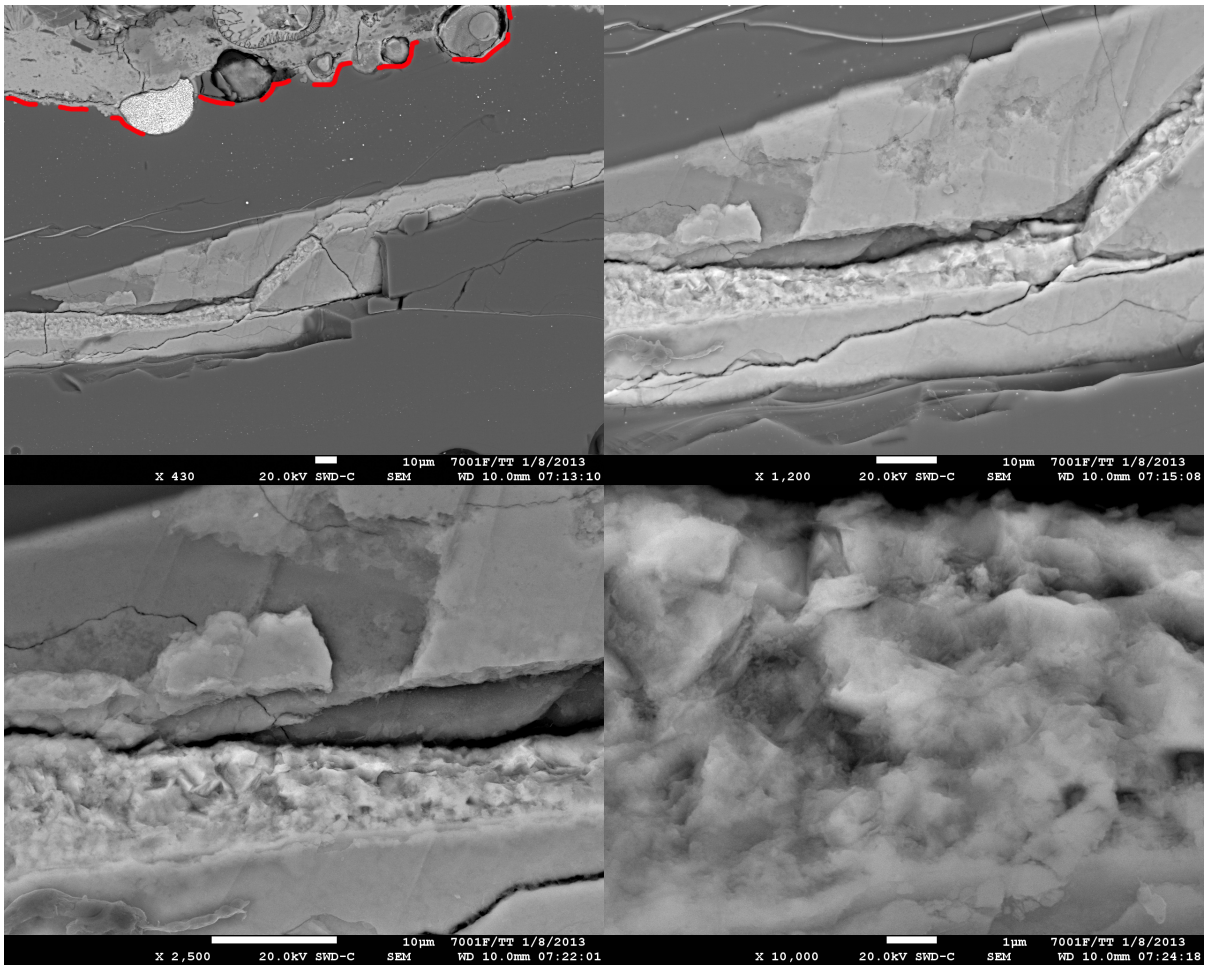


**Figure 8.17**. Backscattered Electron Images of Crack in Glass (HAN-28F glass) in Sample D10 North Bottom at Magnifications of 430, 1,200, 2,500, and 10,000×

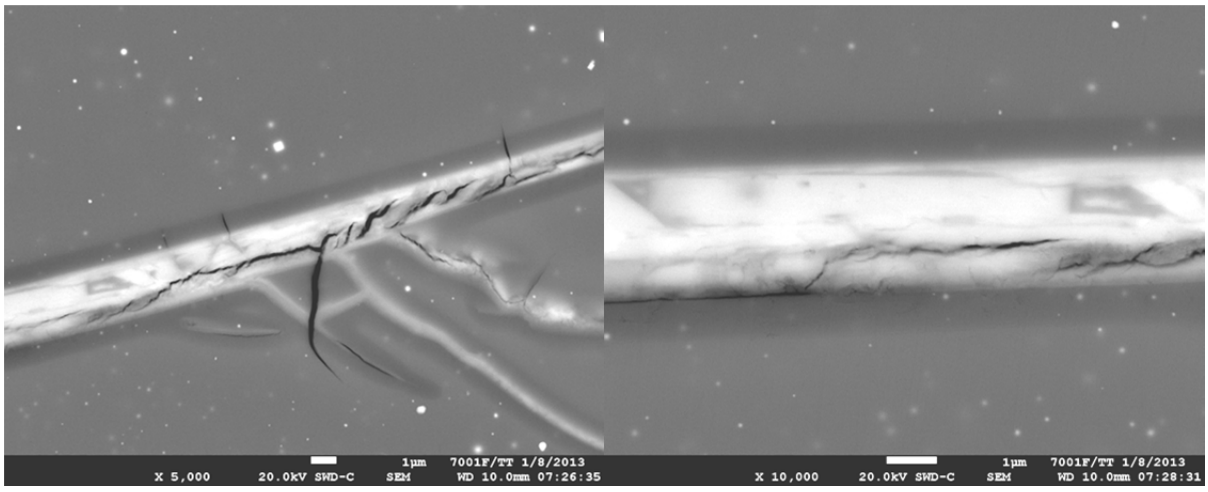


**Figure 8.18**. Backscattered Electron Images of Crack in Glass (HAN-28F glass) in Sample D10 North Bottom at Magnifications of 5,000, and 10,000×

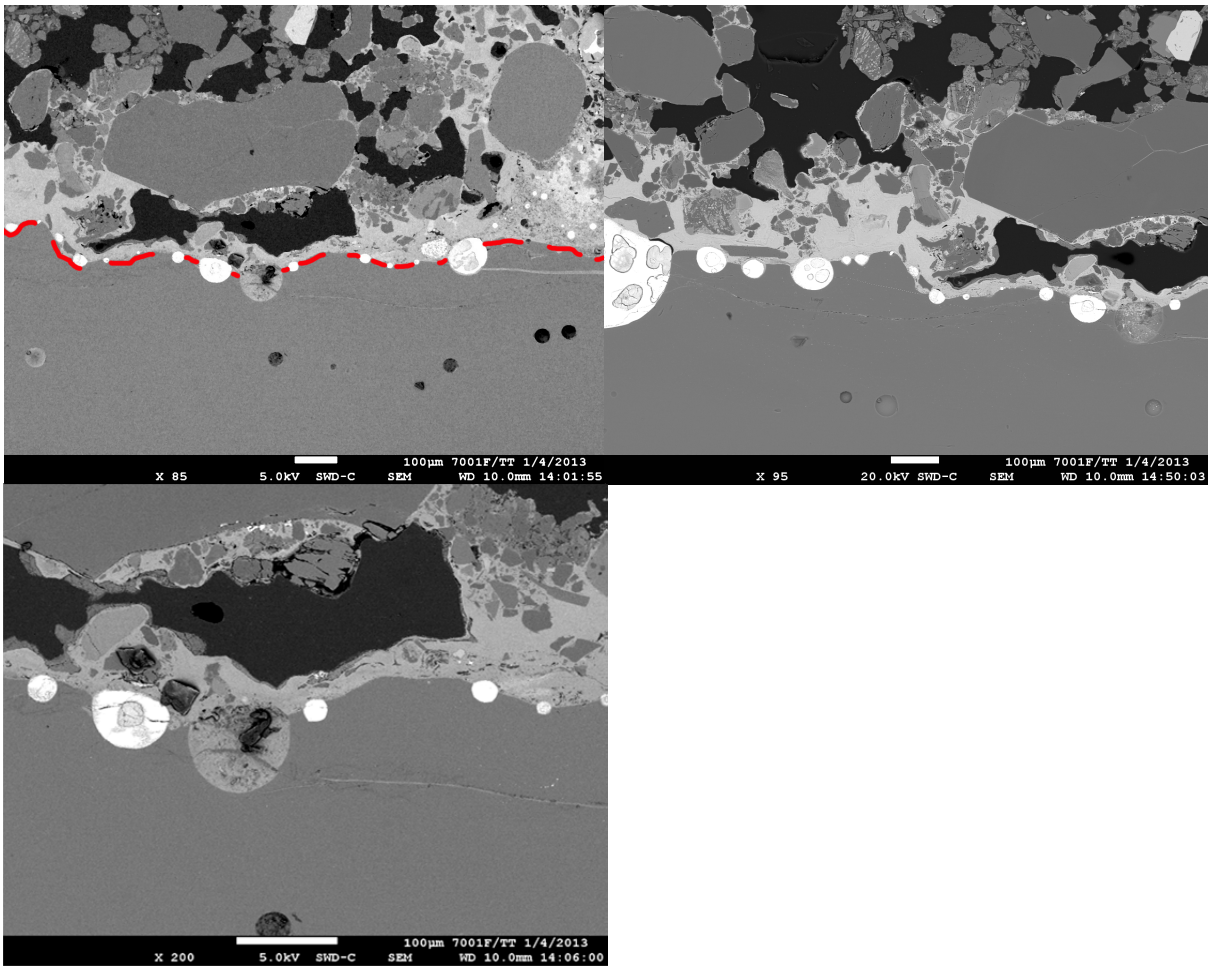


**Figure 8.19**. Backscattered Electron Images of Glass-Metal-Soil Interface in Sample D10-North Bottom at Magnifications of 85, 95 and 200×

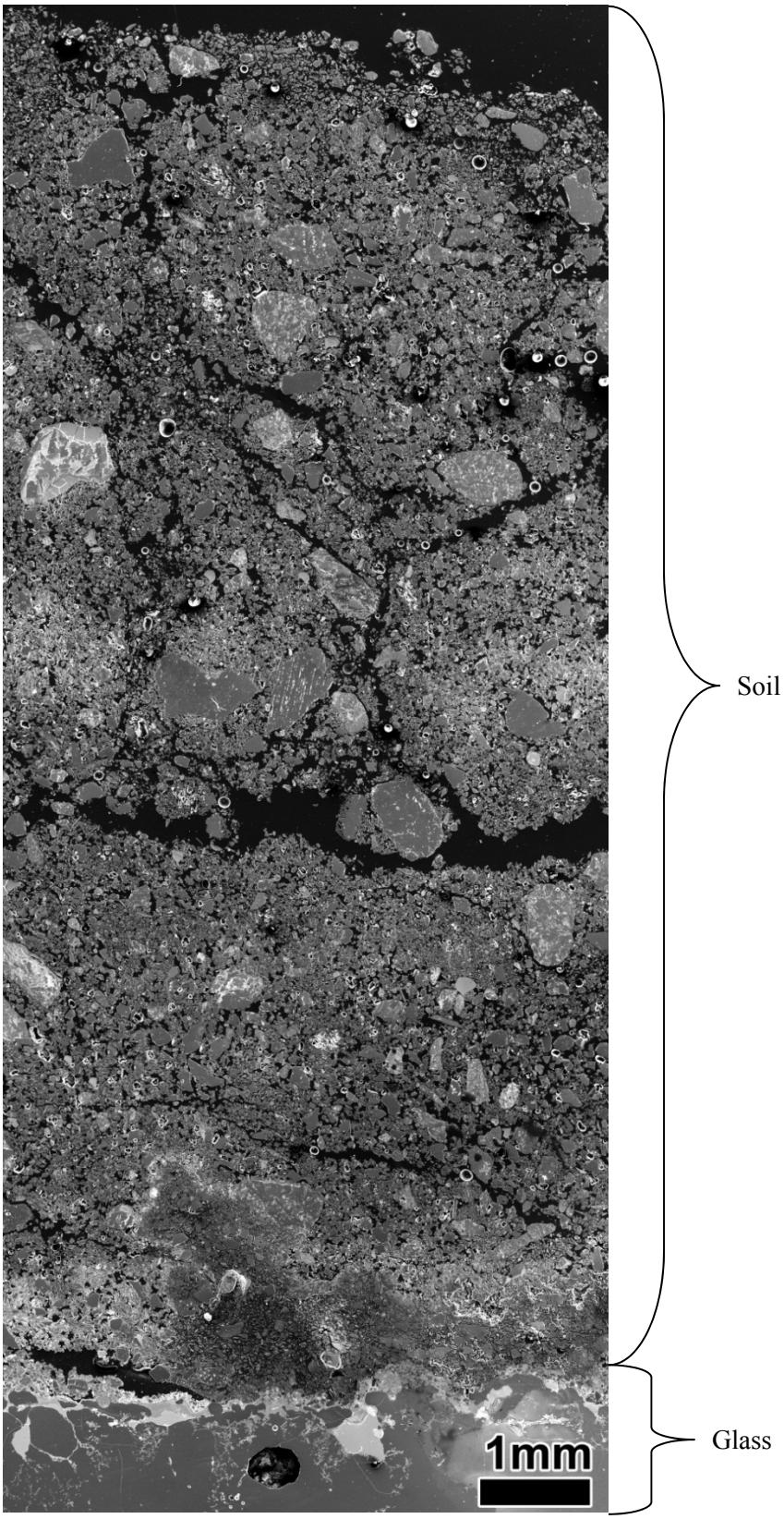


**Figure 8.20**. Secondary Electron Image of D14-North Bottom Showing the LAWA44 Glass and Attached Layer of Soil

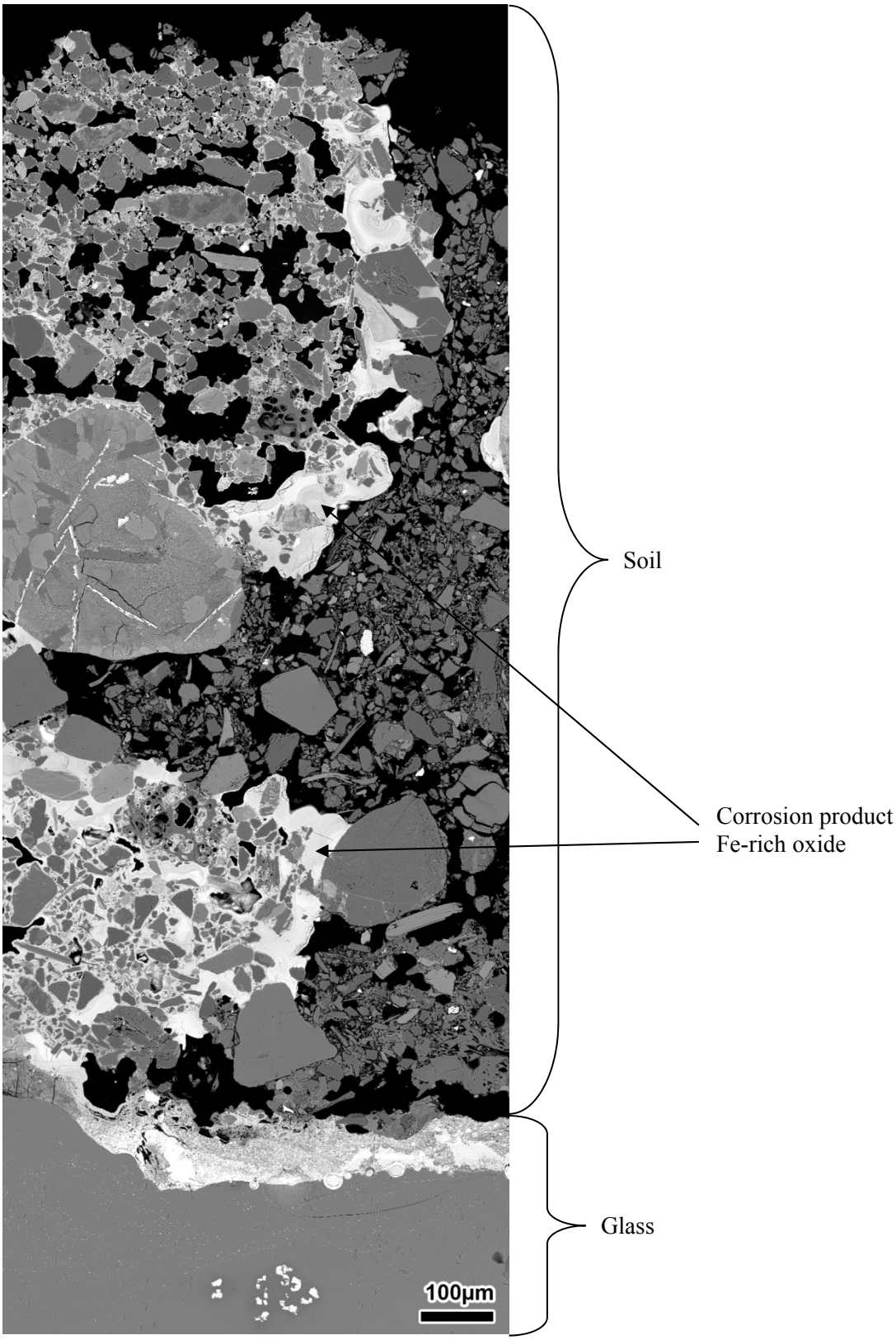


**Figure 8.21**. Secondary Electron Image of D11-East Top Showing the HAN28F Glass, Attached Layer of Soil, and Corrosion Product

## 8.8 Results from XRD Analyses

XRD analysis was performed on samples taken at the glass-to-soil interfaces (Figure 8.14, Figure 8.17 to Figure 8.19) from locations similar to those examined by SEM. Samples were spiked with a known amount of NIST 674b (rutile) standard and ground to a fine powder in a tungsten carbide shaker mill for 2 minutes. Samples were mounted in a back-loading powder mount and scanned from 3–70° 2-theta, at a step size of 0.02° 2-theta, and a hold time of 0.5 sec/step on a D-8 Advance Bruker X-ray diffractometer, using a copper target.

The XRD patterns were analyzed using Bruker EVA 14.0 software loaded with powder diffraction database (PDF-2) release 2008. The software was used to fit and remove both the background curve and $K\alpha_2$ peaks. Then the software was used to perform search match using the known chemistry of the glasses to identify possible phases.

The XRD patterns of the background soil and the glass/soil interface are shown in Figure 8.22 through Figure 8.39. The XRD patterns of the background soil identified quartz, albite, anorthite, microcline, diopside, muscovite-2M1, amphibole, clinochlore and possibly talc. The background soil samples all have similar patterns with the same identified phases. The XRD patterns of the glass-soil interfaces were all similar to each other as well. However, these soil-glass interface samples have an amorphous hump from the glass and iron metal. Muscovite, amphibole, clinochlore and talc were very difficult to confirm by XRD in the glass-soil interface samples. Each of the scans below are given twice, once at full scale, and once with the Y-axis zoomed in to show the locations of low-intensity peaks/phases.

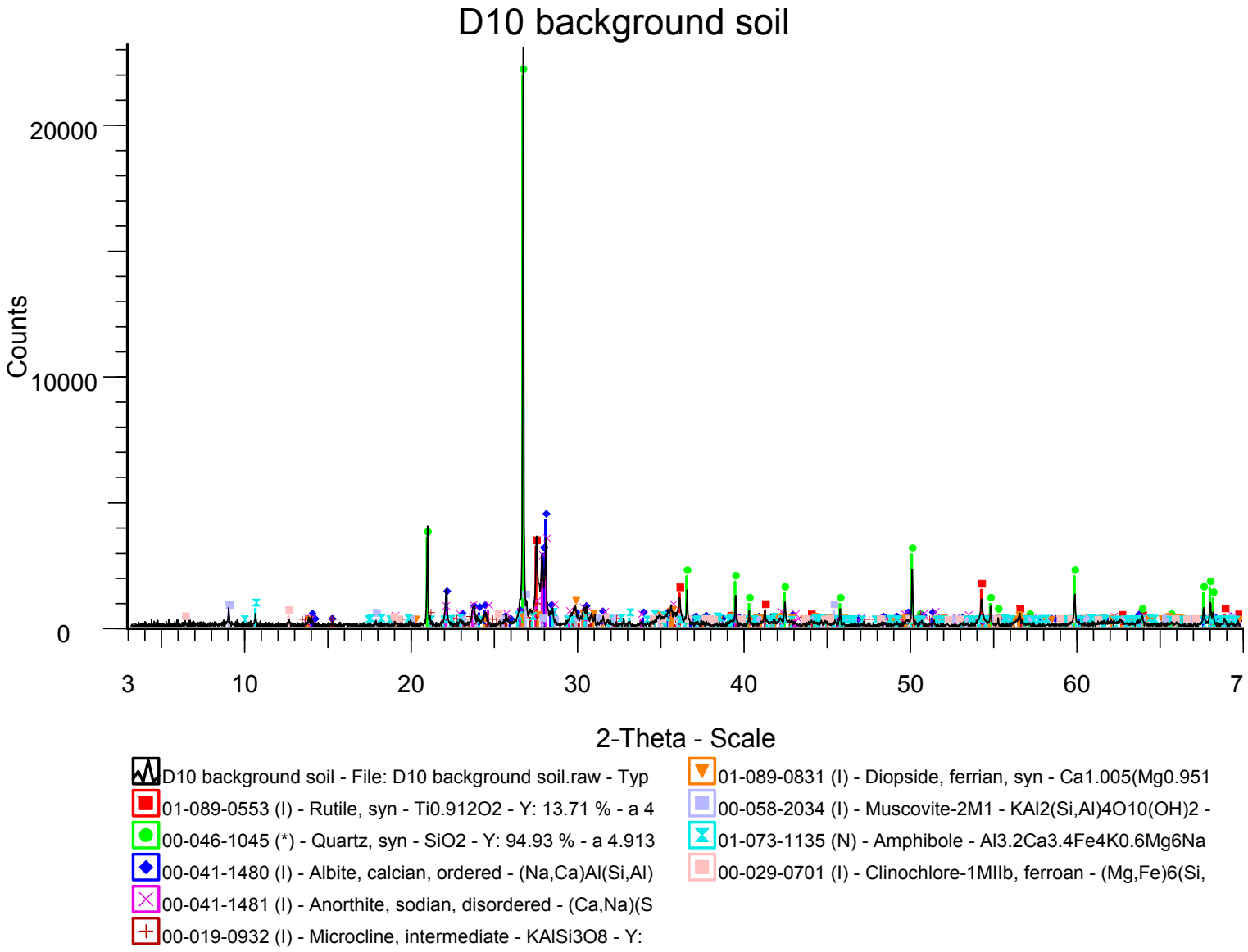


**Figure 8.22**. Full-Scale XRD Pattern for D-10 Background Soil

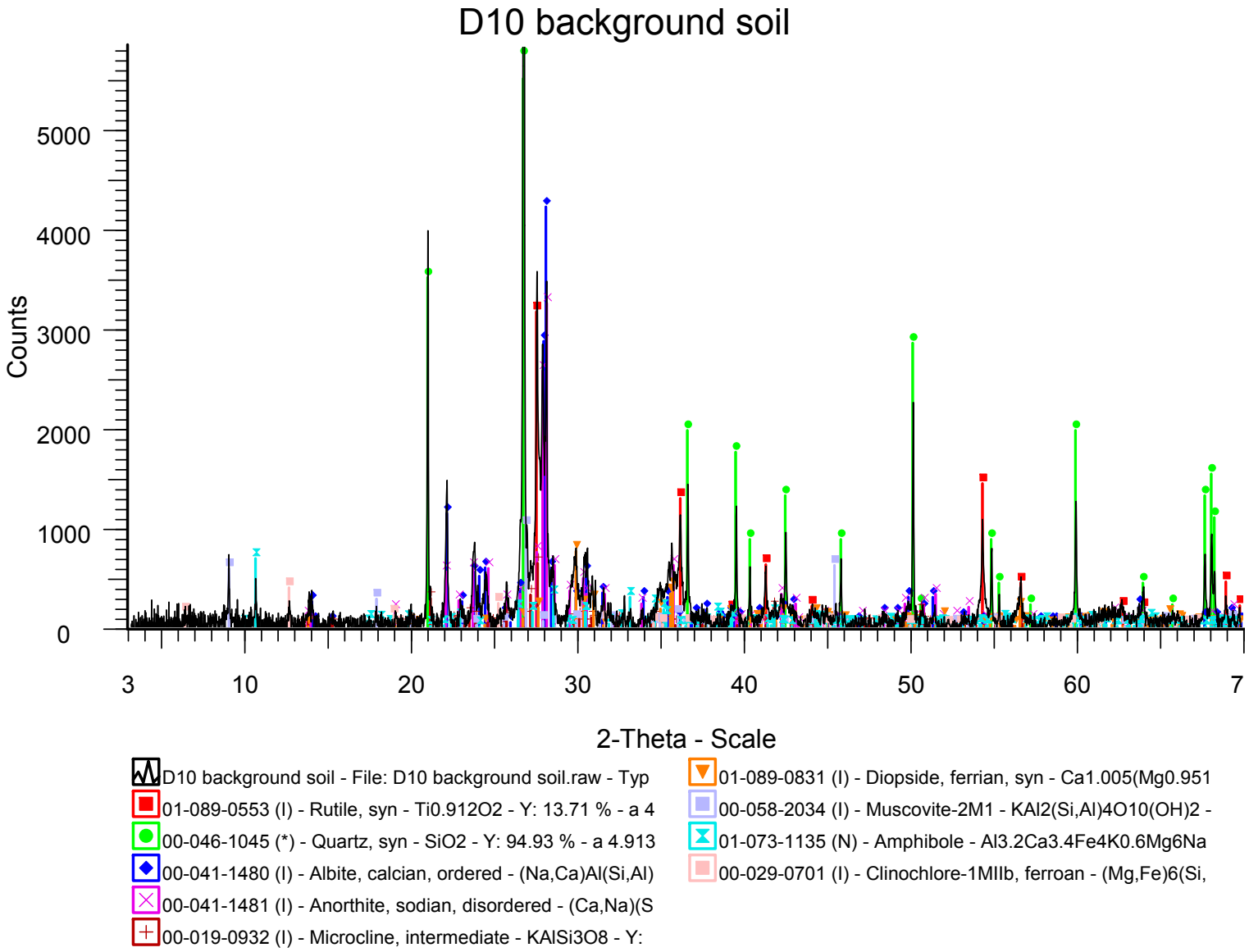


**Figure 8.23**. Zoomed-in XRD Pattern for D-10 Background Soil

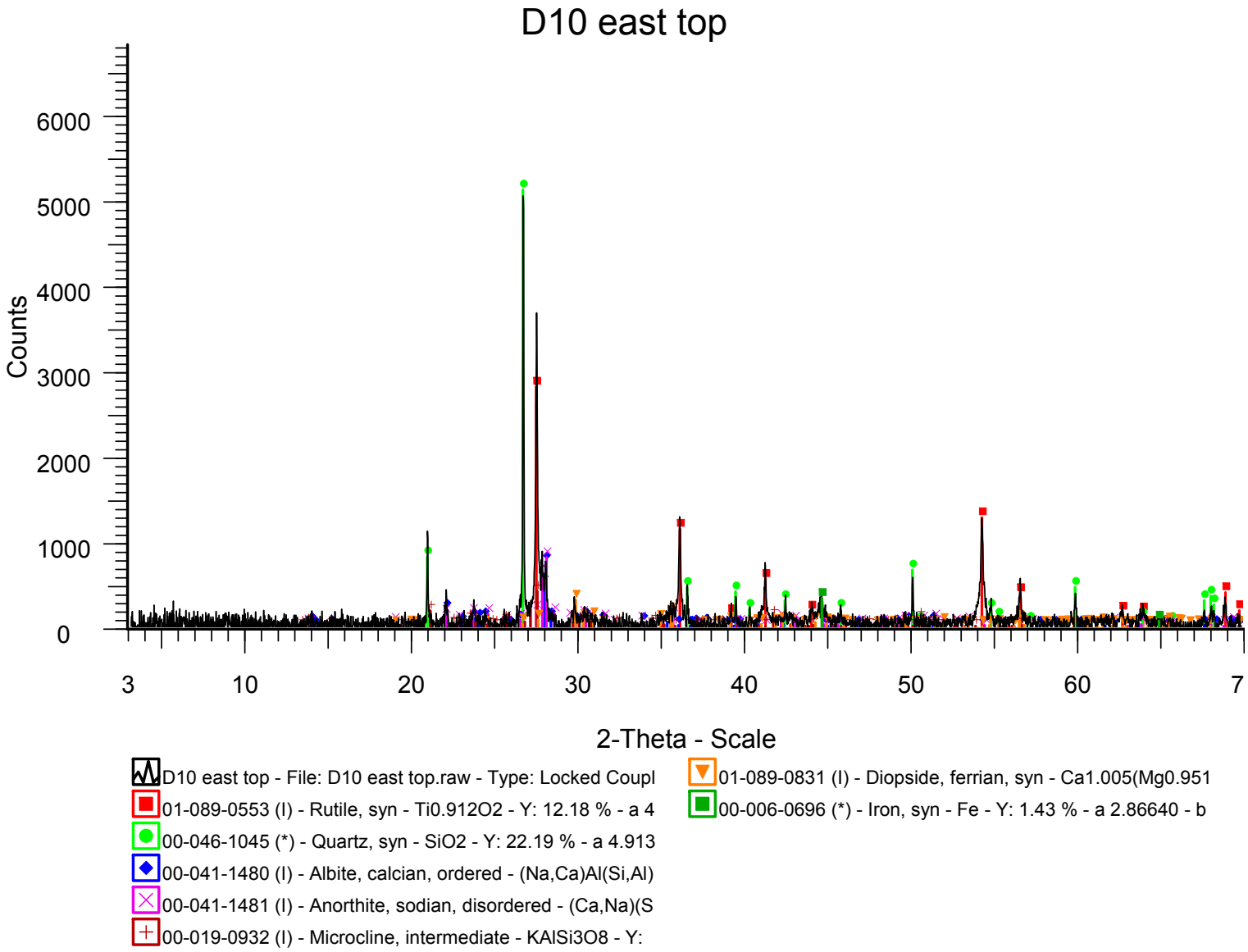


**Figure 8.24**. Full-Scale XRD Pattern for Glass-Soil Interface Solids in D-10 East Top

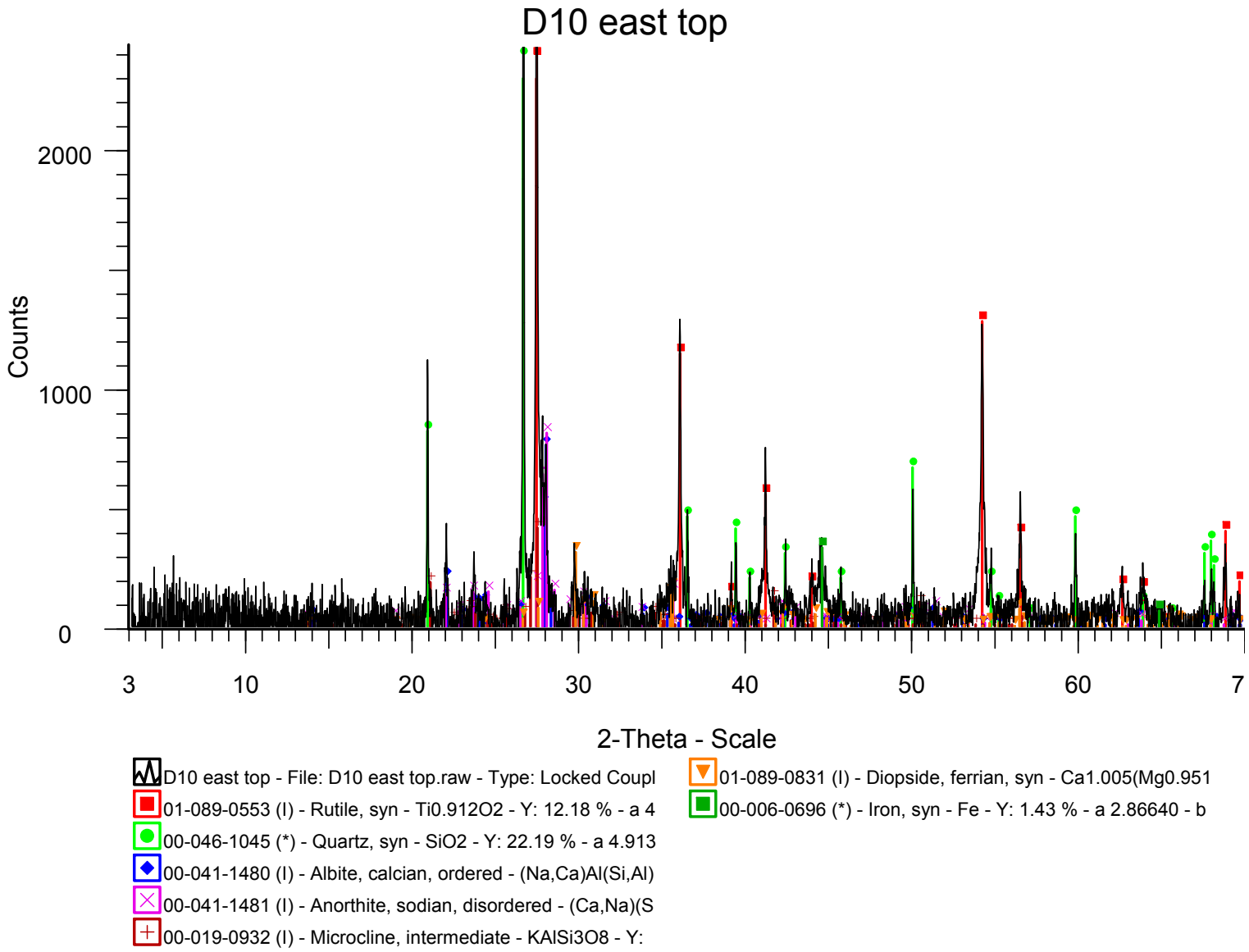


**Figure 8.25**. Zoomed-In XRD Pattern for Glass-Soil Interface Solids in D-10 East Top

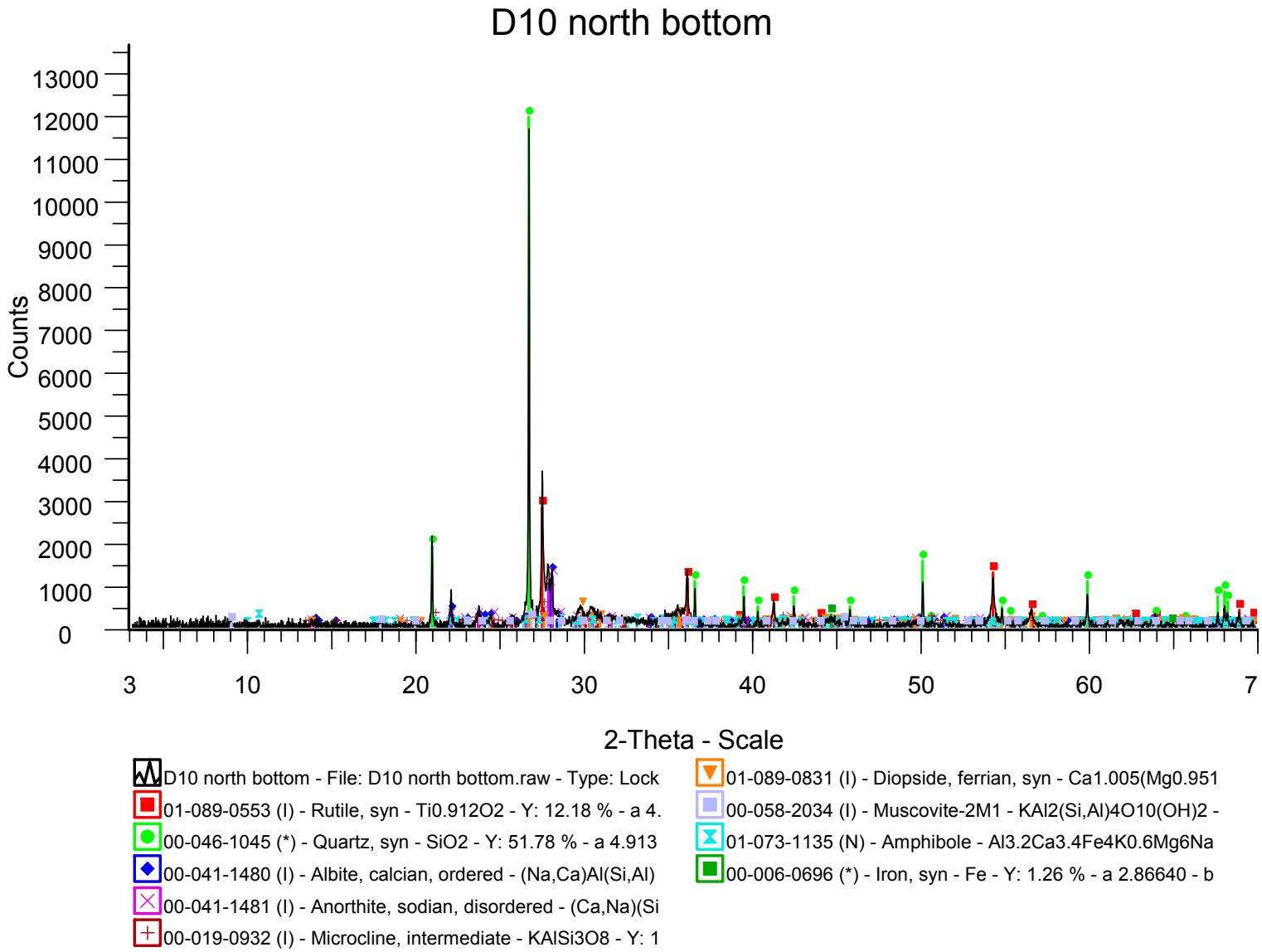


**Figure 8.26**. Full-Scale XRD Pattern for Glass-Soil Interface Solids in D-10 North Bottom

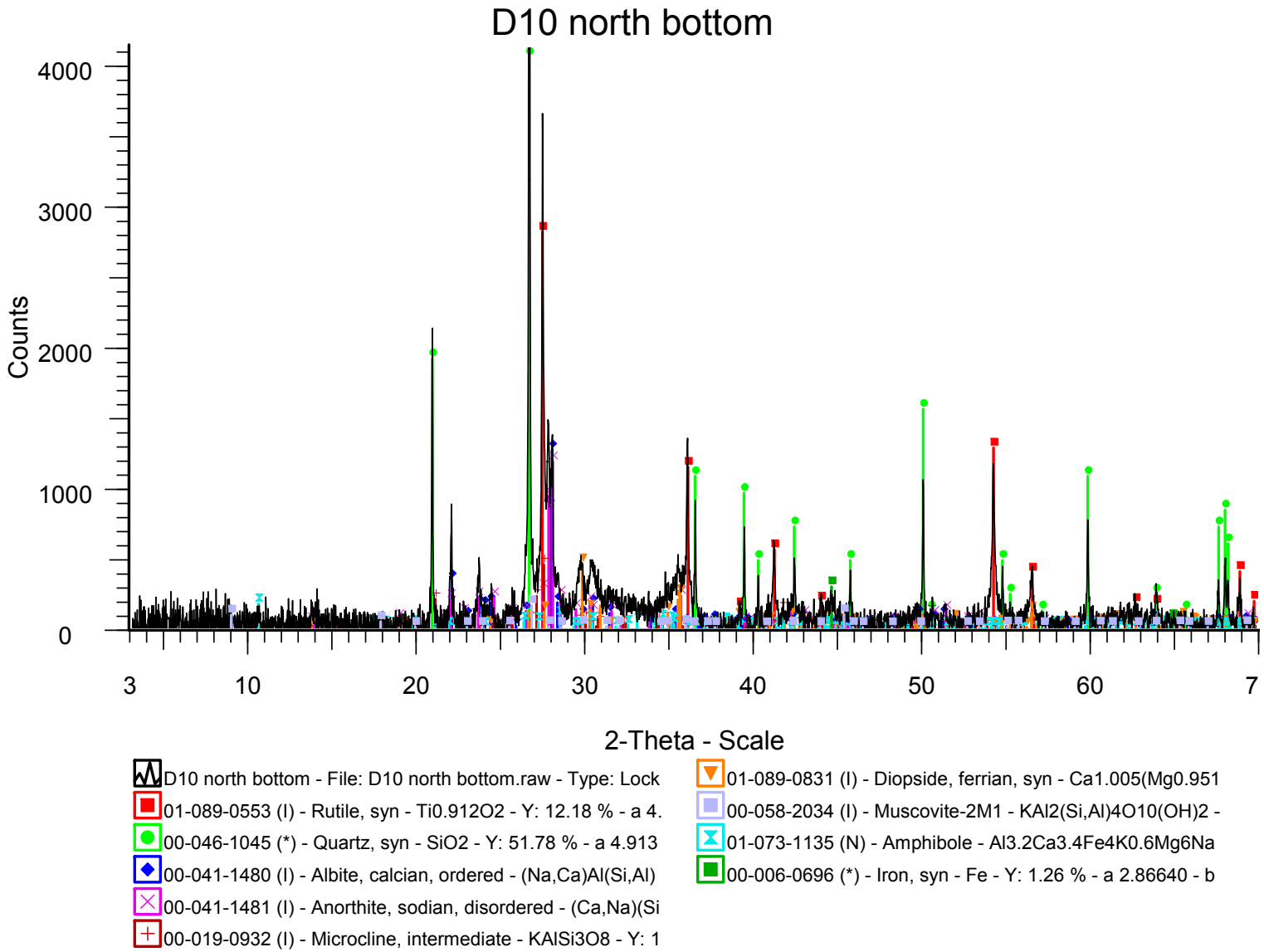


**Figure 8.27**. Zoomed-In XRD Pattern for Glass-Soil Interface Solids in D-10 North Bottom

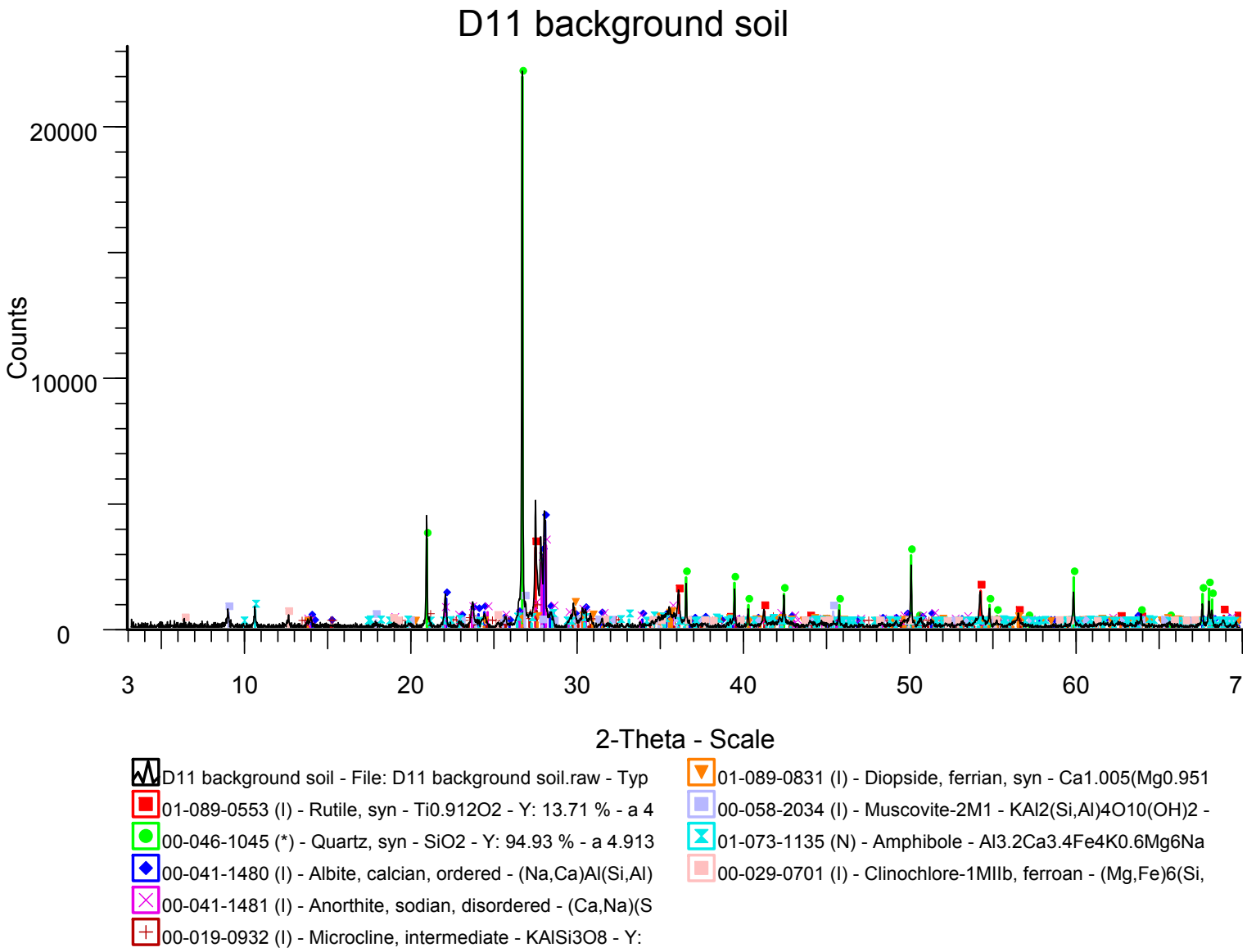


**Figure 8.28**. Full-Scale XRD Pattern for D-11 Background Soil

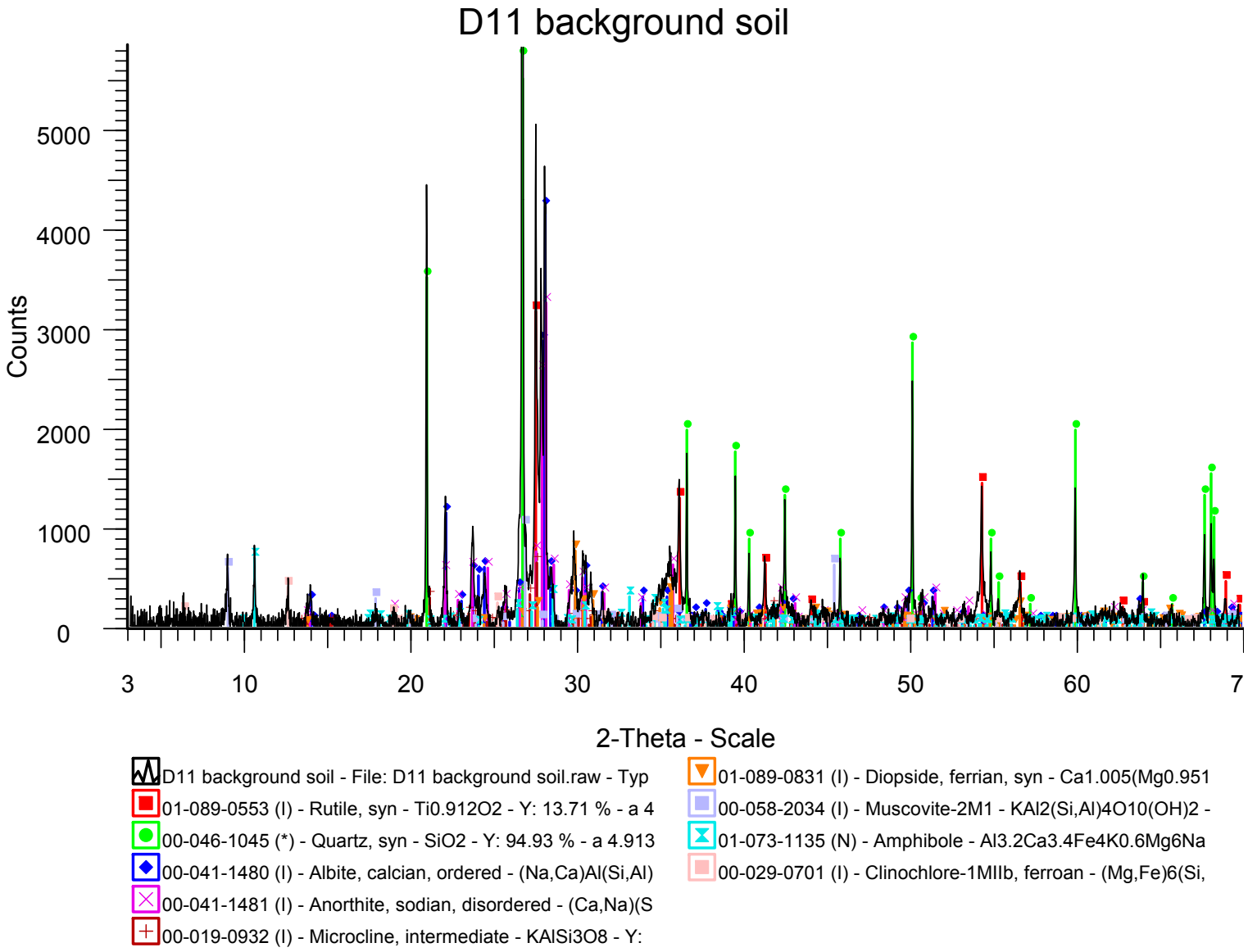


**Figure 8.29**. Zoomed-In XRD Pattern for D-11 Background Soil

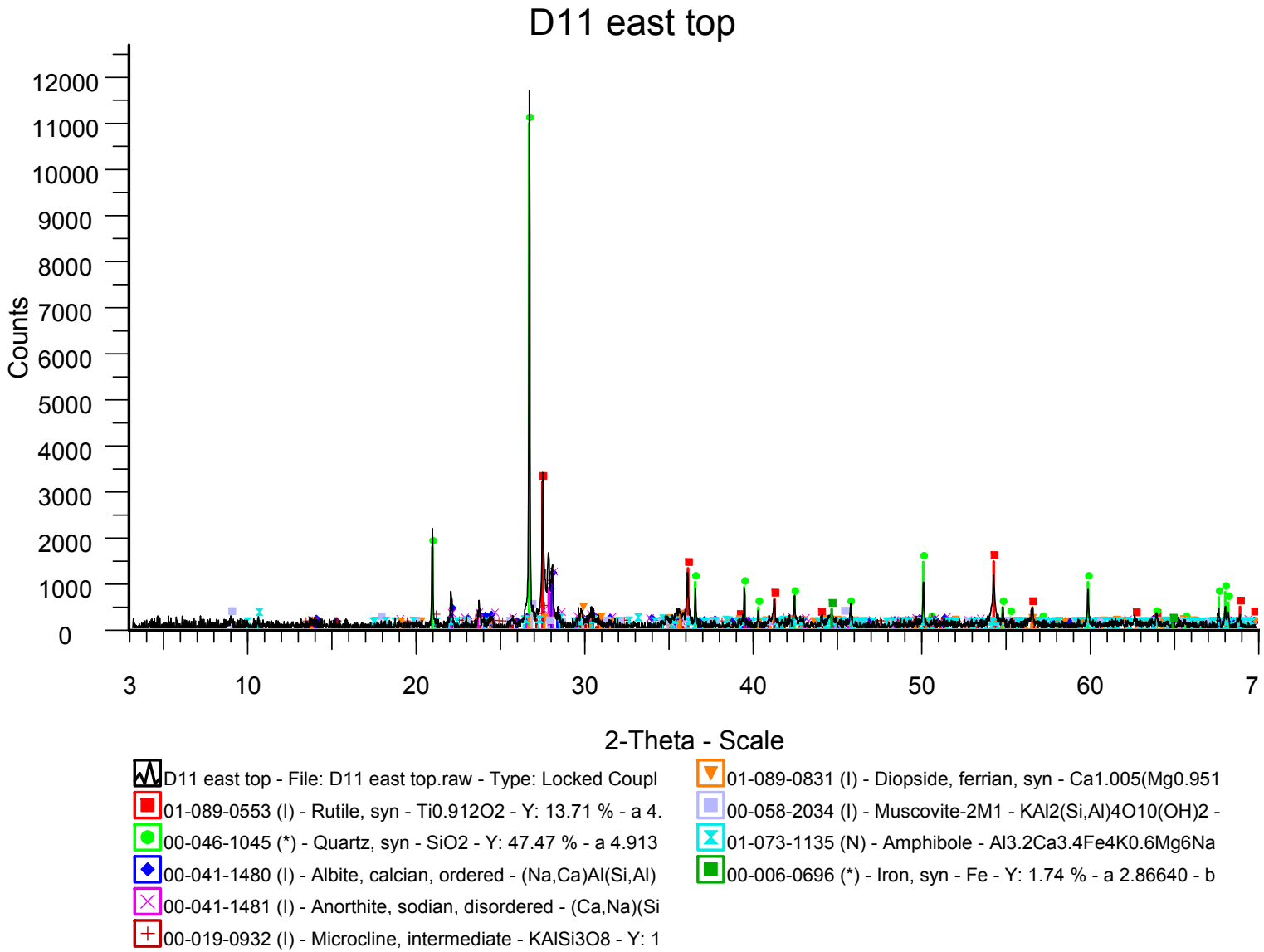


**Figure 8.30**. Full-Scale XRD Pattern for Glass-Soil Interface Solids in D-11 East Top

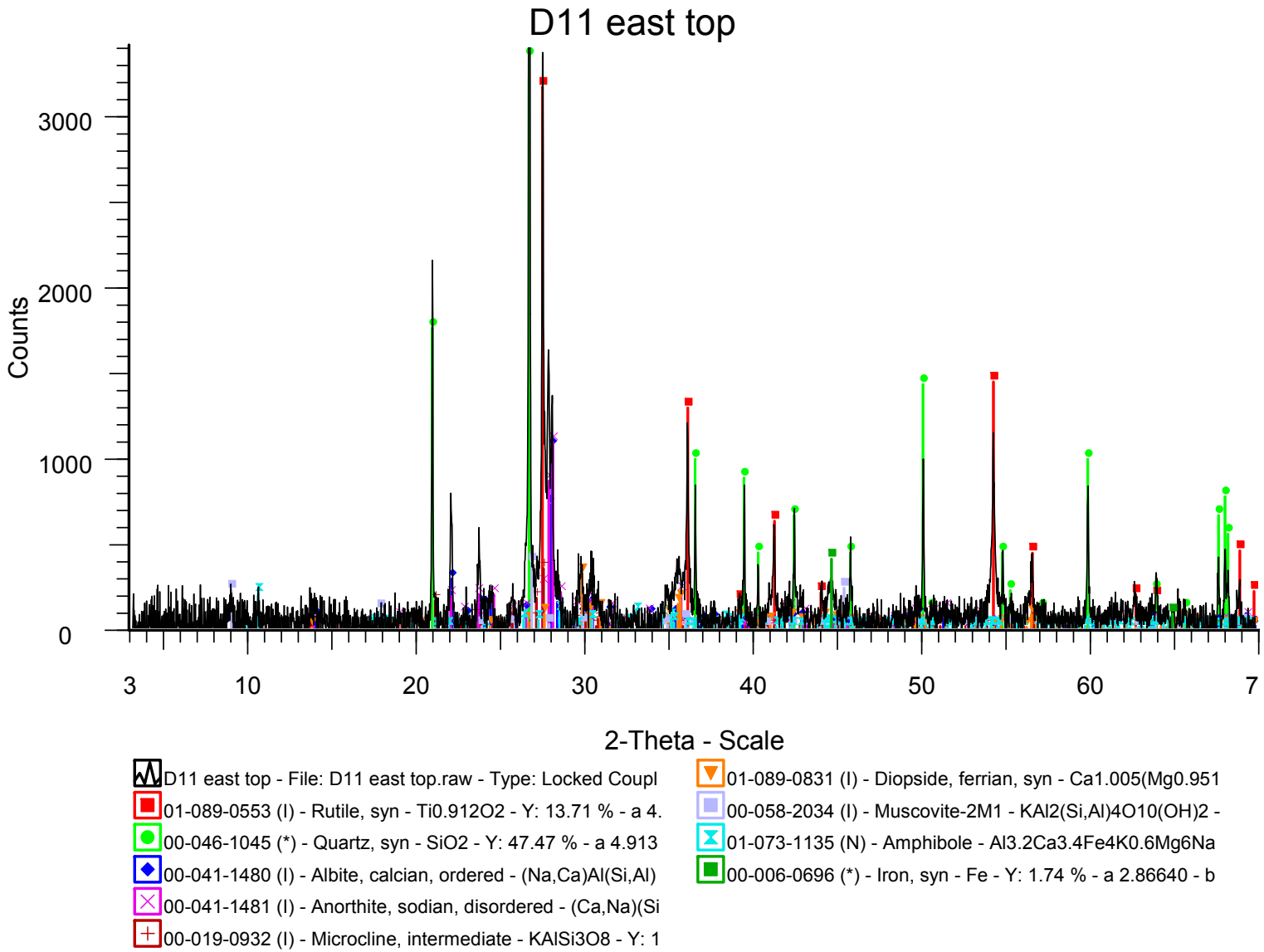


**Figure 8.31**. Zoomed-In XRD Pattern for Glass-Soil Interface Solids in D-11 East Top

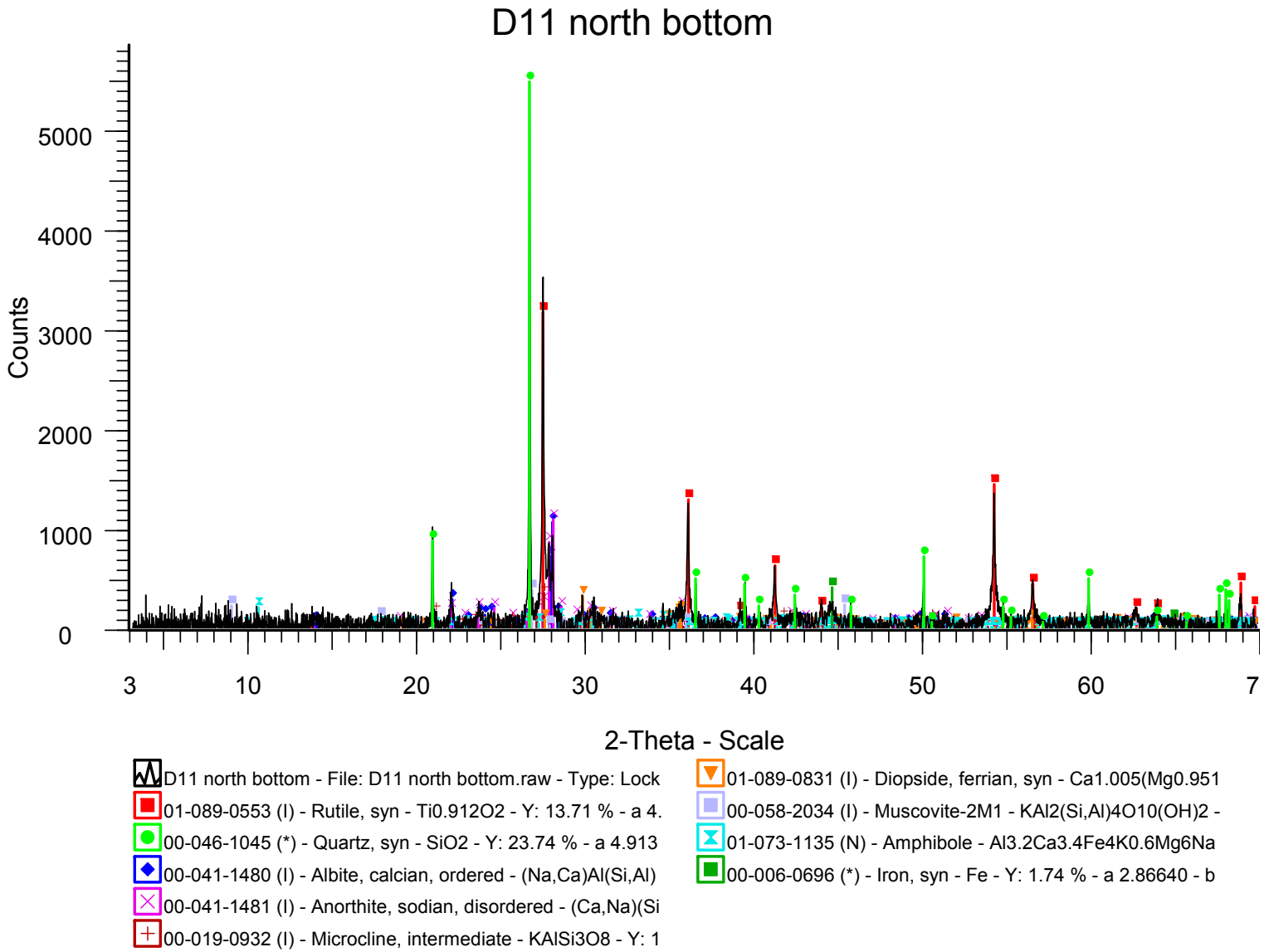


**Figure 8.32**. Full-Scale XRD Pattern for Glass-Soil Interface Solids in D-11 North Bottom

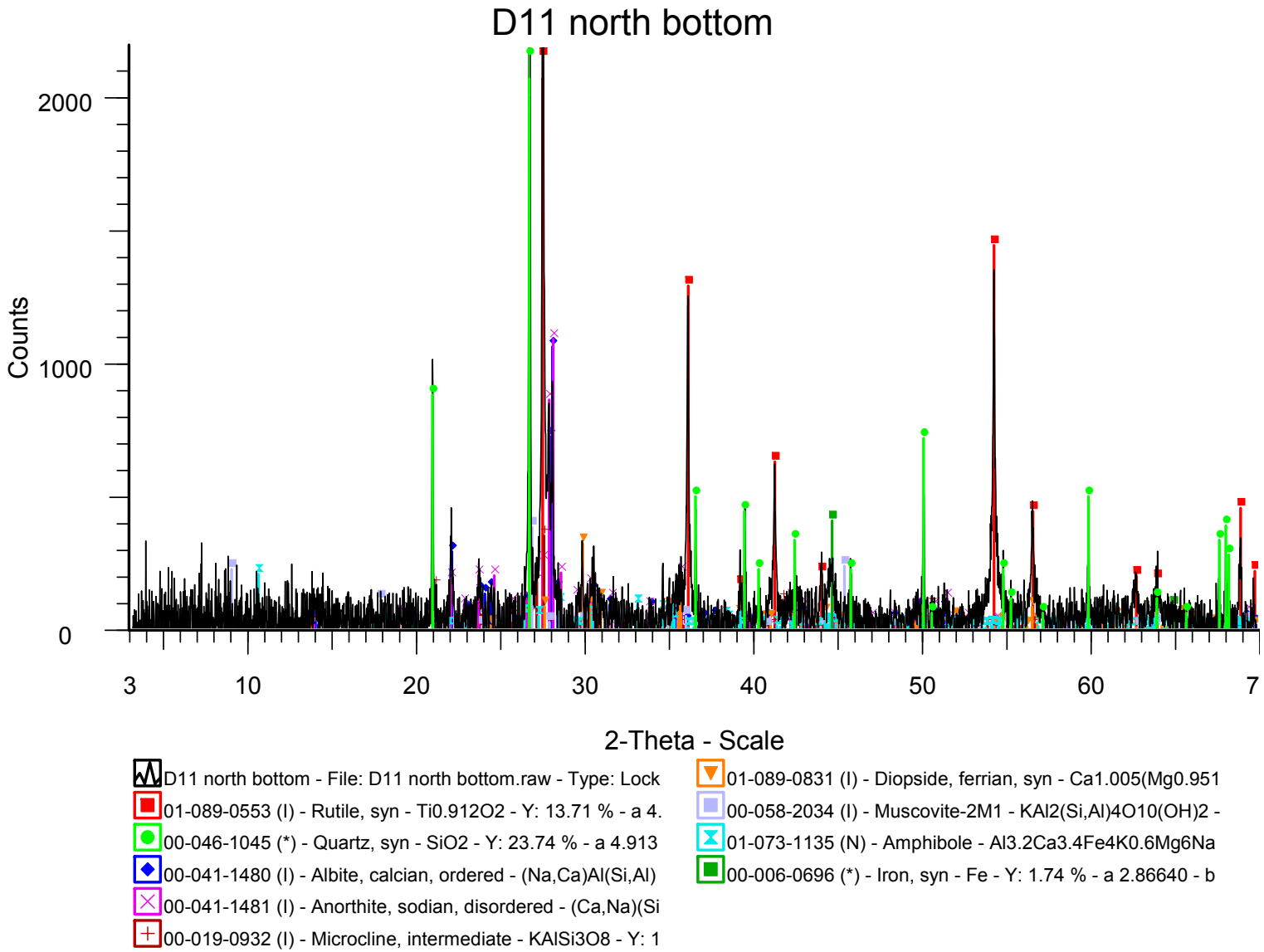


**Figure 8.33**. Zoomed-In XRD Pattern for Glass-Soil Interface Solids in D-11 North Bottom

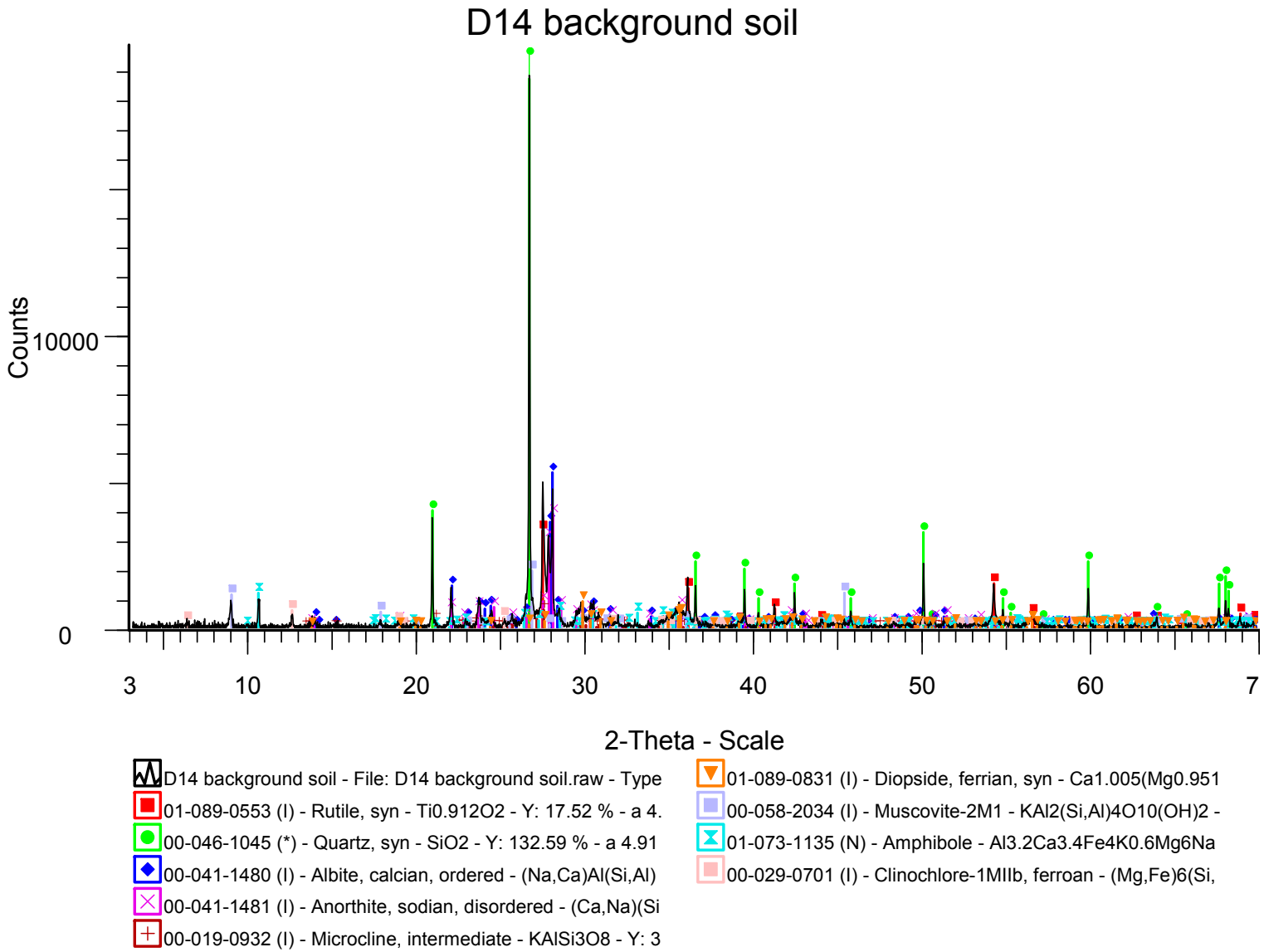


**Figure 8.34**. Full-Scale XRD Pattern for D-14 Background Soil

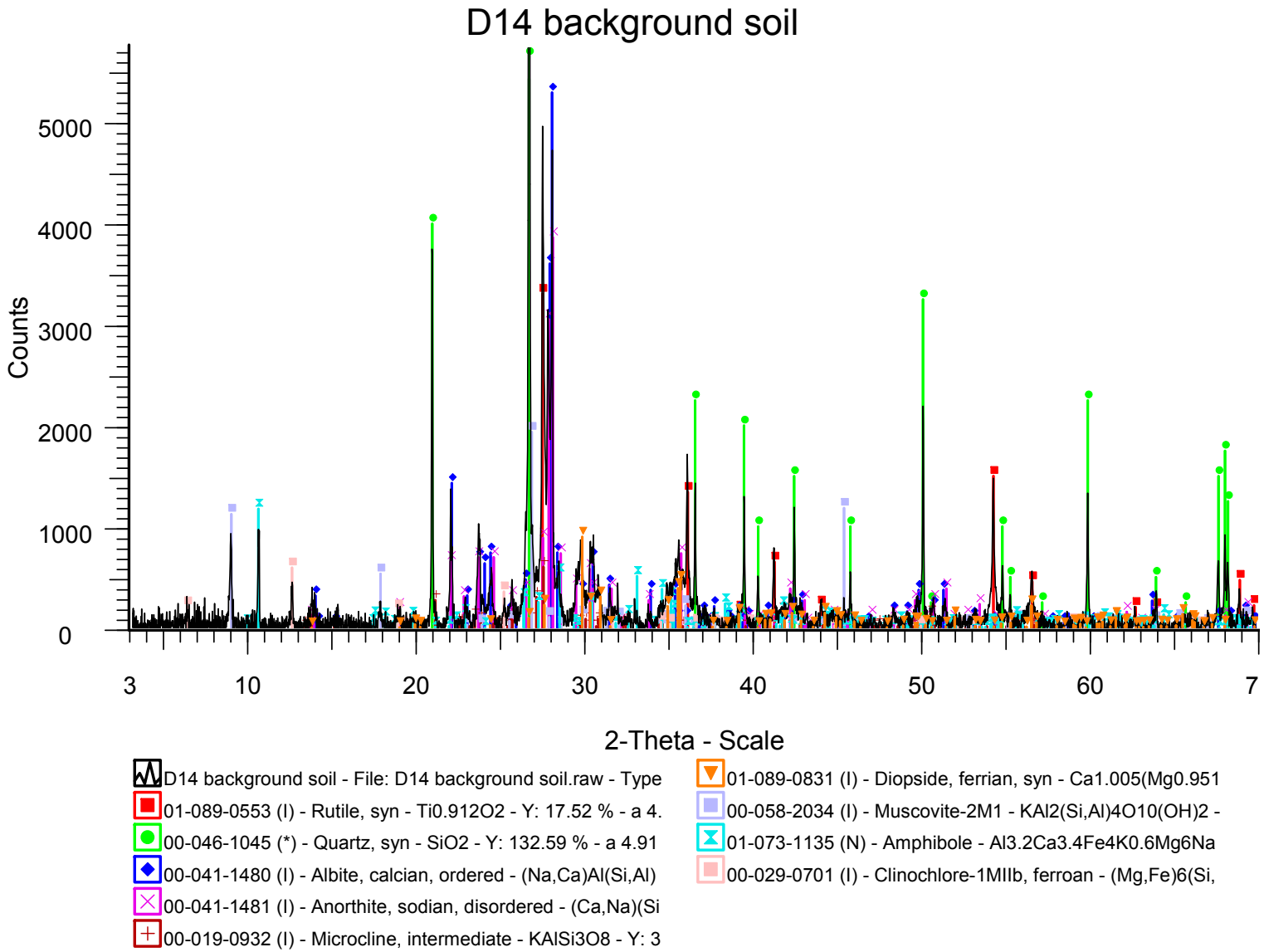


**Figure 8.35**. Zoomed-In XRD Pattern for D-14 Background Soil

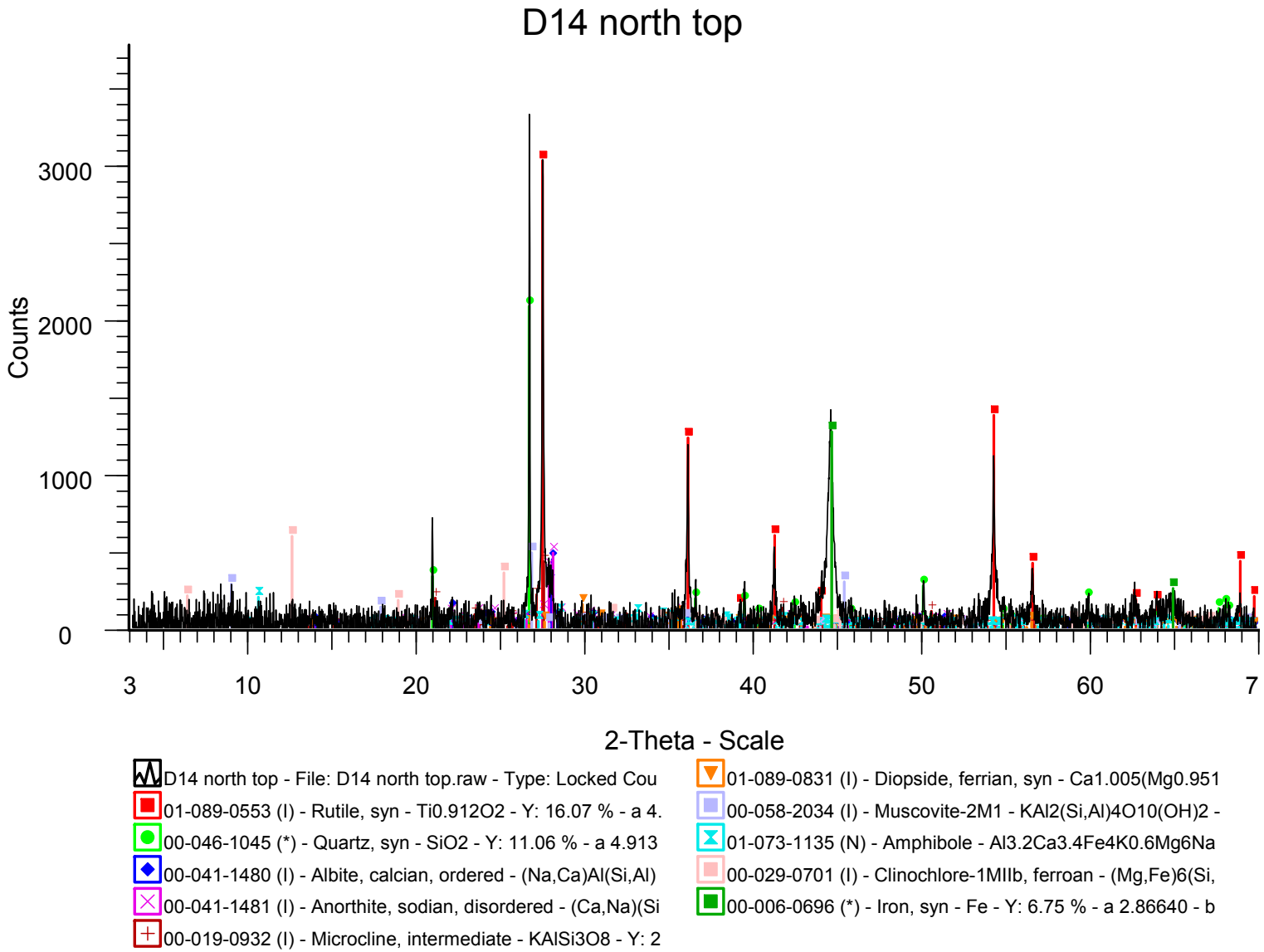


**Figure 8.36**. Full-Scale XRD Pattern for Glass-Soil Interface Solids in D-14 North Top

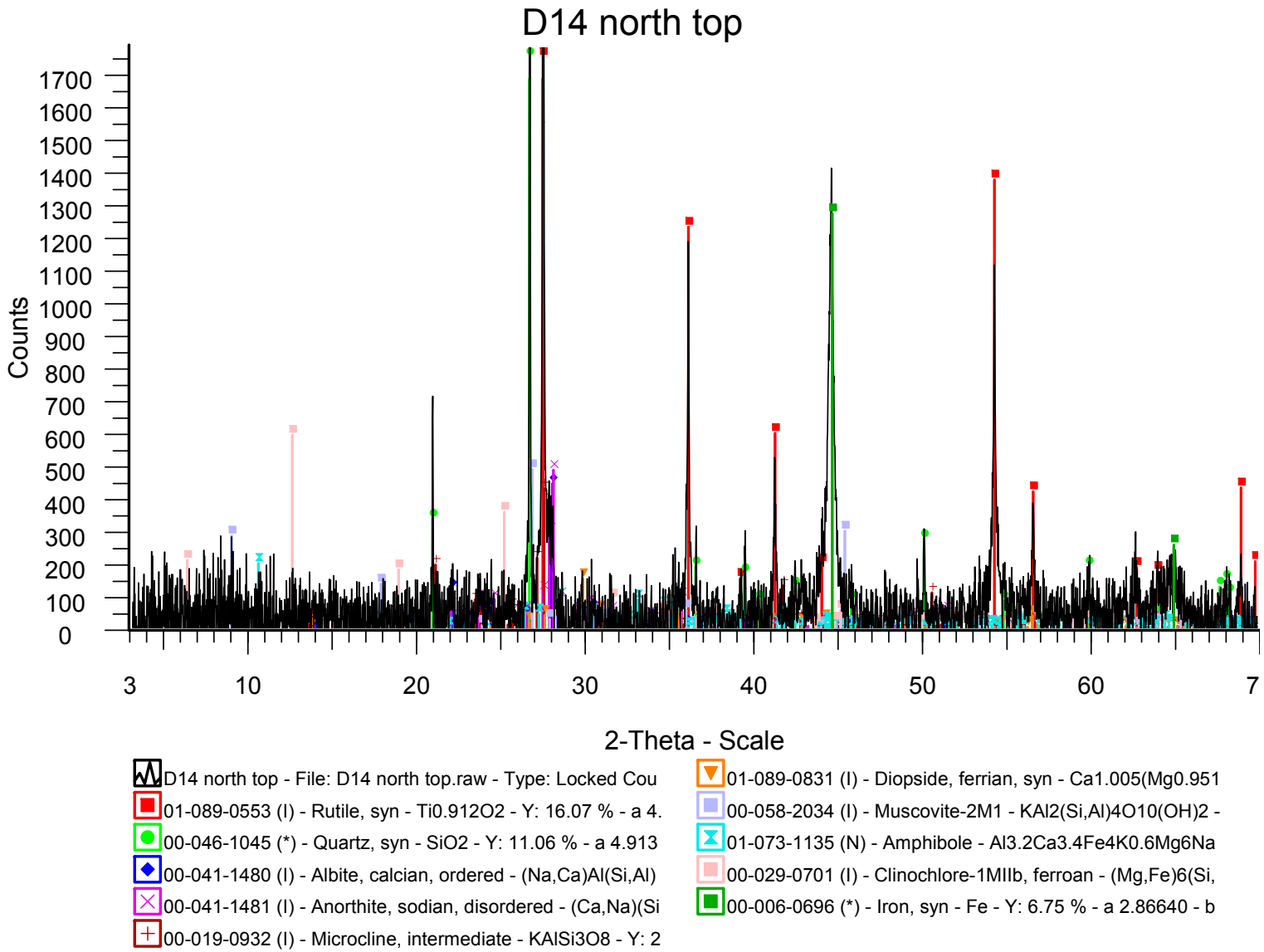


**Figure 8.37**. Zoomed-In XRD Pattern for Glass-Soil Interface Solids in D-14 North Top

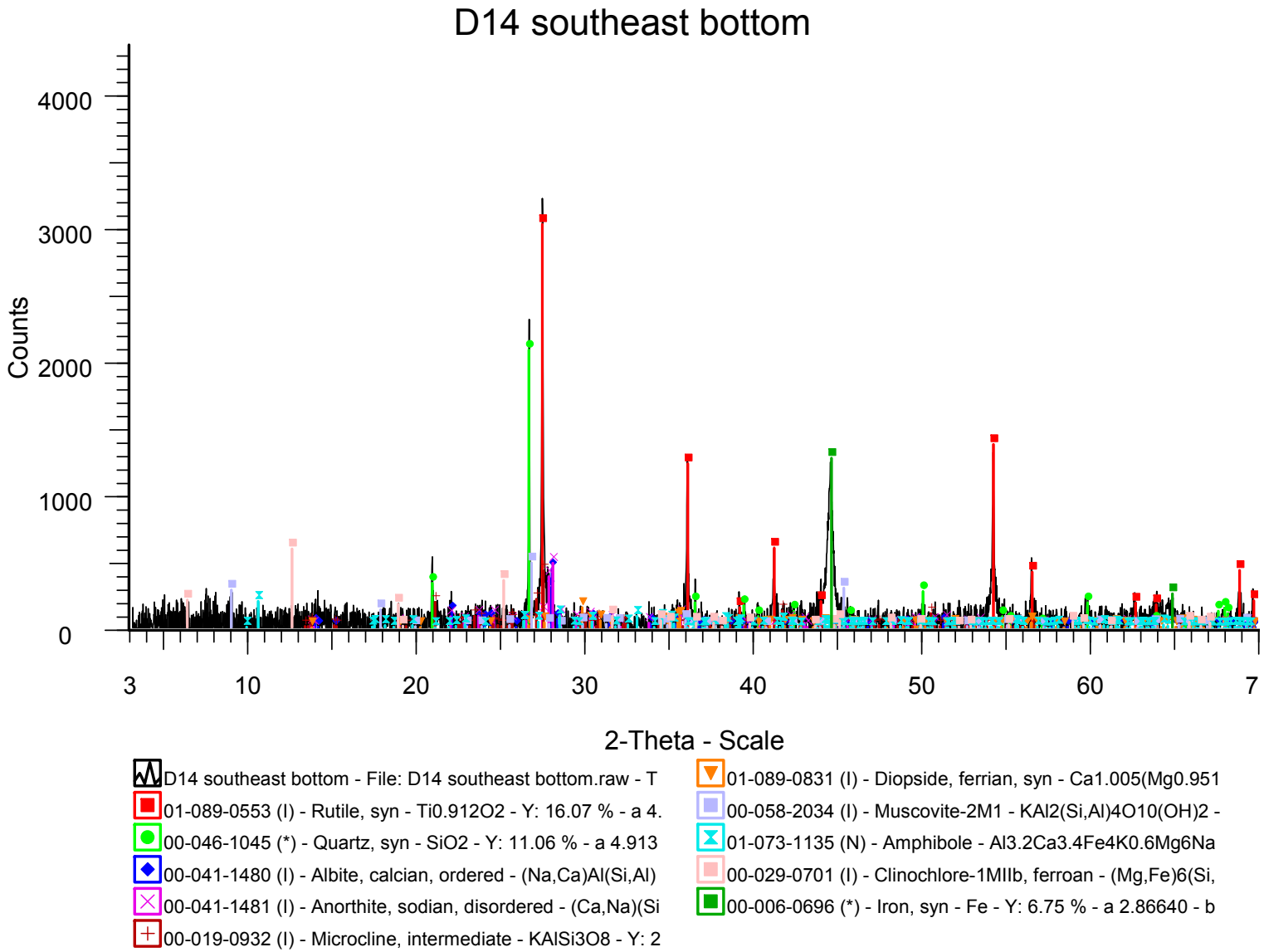


**Figure 8.38**. Full-Scale XRD Pattern for Glass-Soil Interface Solids in D-14 Southeast Bottom

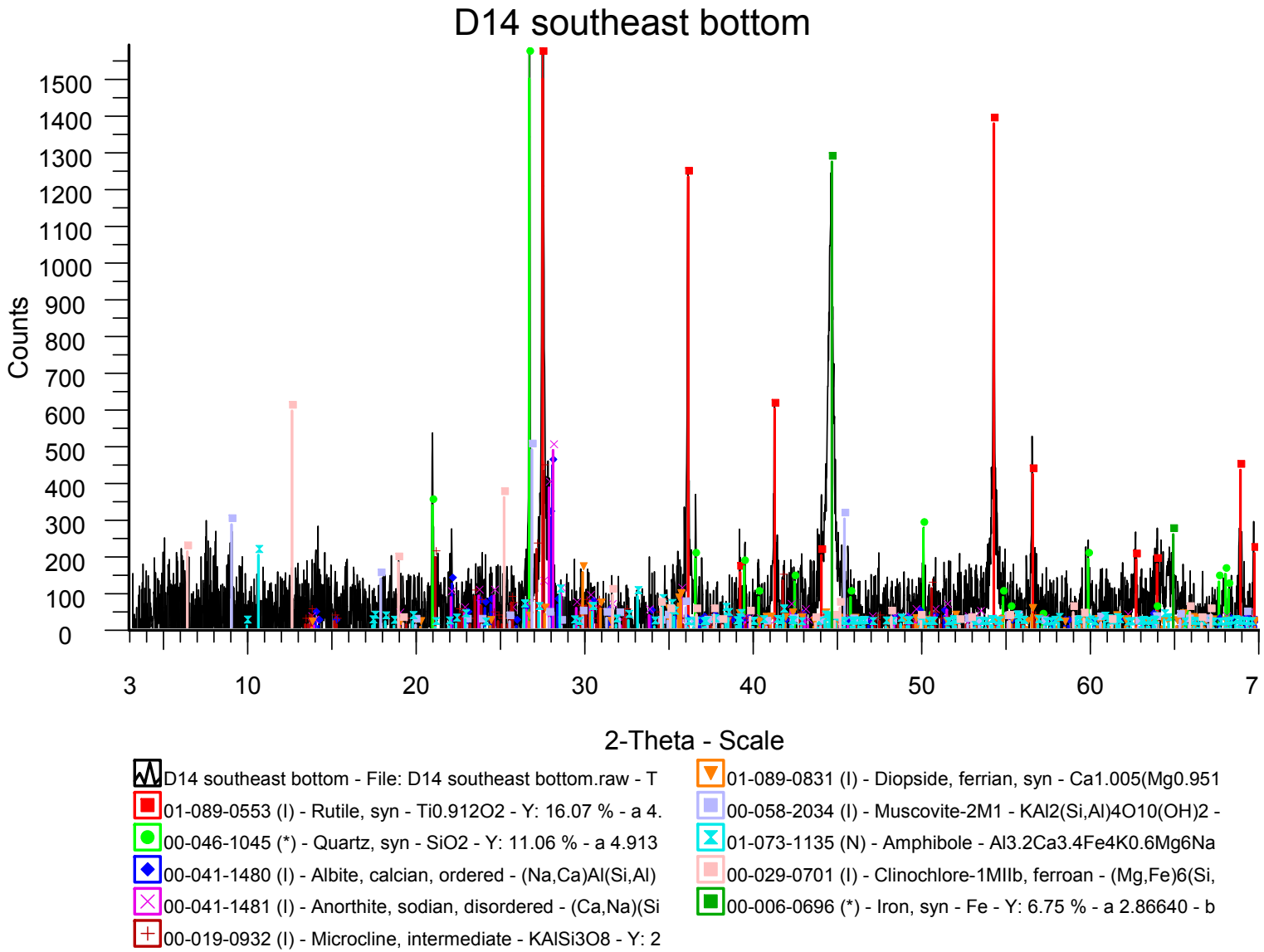


**Figure 8.39**. Zoomed-In XRD Pattern for Glass-Soil Interface Solids in D-14 Southeast Bottom

## 8.9 Source of Elemental Enrichment: Re and Mo

The pronounced enrichment of rhenium and molybdenum in the soil samples adjacent to the glass cylinders from all three lysimeters probably originated from the glass logs. In Figure 8.11 through Figure 8.15, iron-rich alloy globules are seen to occur along the glass-sediment interface, suggesting that exsolved Fe-rich melts were present upon quenching of the glasses and were buried still attached to the glass. The metals have reacted, forming various Fe-rich mineral phases. The co-occurrence of Re and Mo is easily seen in the SEM-EDS elemental dot maps. Rhenium and Mo are highly siderophilic elements that partition into the metallic-melt phase in cases of binary immiscibility between silicate and Fe-rich melts (Goldschmidt 1937). Such partitioning is likely to have exposed large amounts of Re and Mo to mobility due to the subsequent oxidative weathering of the Fe-alloy globules.

## 8.10 Source of Boron Enrichment

Some alteration of glass may have led to the enrichment of B in deeper soil samples, and in soil cores collected immediately adjacent to the glass logs, although the degree of glass alterations is minimal (see Figure 8.15 and Figure 8.16). The elevated boron levels may be due to other effects, including normal downward leaching and reprecipitation of elements in the unsaturated soil zone. Perhaps the origin of the elevated B levels could be tested by measurement of B-isotopic compositions in water extracts and comparison with B-isotopic compositions in the glasses.

# 9.0 Summary

A combined experimental and computational approach is being used to predict the long-term performance of ILAW glass in a near-surface disposal facility. This report highlights the activities that were performed at PNNL during FY 2012. In summary, code development for eSTOMP included updating eSTOMP input structure and output capabilities to match those in (serial) STOMP. Key code capabilities that were incorporated into the eSTOMP code include: 1) the ability to hold a constant value for species concentrations; 2) the addition of diffusion algorithms/models for aqueous transport; 3) the addition of user-defined initial volume fractions for solid phases; and 4) the ability to scale reactive surface area linearly with water saturation. Other updates included the ability to output the kinetic rates and solid-phase surface areas already calculated internally in eSTOMP, and the ability to calculate porosity and permeability changes as a result of precipitation and dissolution reactions. Also, testing for the reactive geochemical transport updates is nearly complete. Small-scale differences between STOMP and eSTOMP still need to be resolved when using fixed species concentrations. Preparations for the benchmark simulations between eSTOMP and the serial version of STOMP were also made.

In addition to improving the continuum-scale simulations of glass weathering, geochemical modeling was performed on the remaining 10 ILAW glass compositions that have been undergoing long-term weathering experiments using the PCT method. These geochemical modeling results suggest that of the 128 glasses from FY 2011 and 10 glasses from FY 2012 that were modeled, a secondary-phase reaction network previously developed for ILAW glass sample LAWA44 produced good model fits for the major glass components. Notable exceptions were predicting the solution concentrations of K and Li in contact with glass as it weathers with time. This is probably because of the lack of thermodynamic data for solid phases that are enriched in K or Li and that control their resultant solution concentrations.

In addition to PCT results, the suite of STOMP codes also uses the results from PUF experiments to support the development of a reaction network of secondary phases that form during the weathering of the ILAW glasses. In FY 2012, the PUF tests being conducted on three prototypic ILAW glasses (ORPLG9, ORPLB2, and ORPLF7) were terminated. The reacted glass from each experiment was collected and analyzed using SEM with EDS and XRD. Results for the ORPLG9 glass show that a 10-μm-thick alteration layer, composed of three distinct sub-layers, developed on the surface of the reacted glass. The EDS elemental profiles for the analyzed ORPLG9 glass grains, beginning at the pristine glass, show that Si decreases slightly in the first alteration layer, then increases in the second alteration layer and further increases in the outer clay-like layer. Aluminum in the reacted solid gradually increases from the unreacted glass core to the outer sub-layer. Calcium concentrations remain similar in all the layers except the second alteration layer, where it is higher. Zirconium steps up in concentration in each alteration layer then drops significantly in the outer clay-like layer. Magnesium and zinc concentrations both remain constant in the inner two sub-layers, then increase in the clay-like outer layer. Alkali elements, Na and K, and B concentrations decrease significantly at the glass-to-alteration-layer interface and continue to decrease in concentration from the second alteration to the outer layer. The XRD results illustrated that the reacted glass was mainly amorphous and only contained a minor amount of crystalline phases. Both the SEM-EDS and XRD results are consistent with LAW glass samples previously reacted in PUF experiments. Although these glasses performed similarly to other ILAW glasses, the reason for the abnormally high K release (a minor element) from ORPLB2 and ORPLF7 is unclear. Additional data interpretation from the solid-phase analysis of the reacted glass grains from ORPLB2 and ORPLF7

should provide additional insights into why the high K release is occurring and the results of the additional data analyses will be discussed in future reports.

Lysimeter field-testing allows the IDF-PA program to obtain independent and site relevant data on glass corrosion at a length-scale more relevant to the actual disposal system. Some of the results collected, specifically the characterization of weathered glass, sediment, and pore-water; from an eight-year long field lysimeter experiment are discussed in this report. Analysis of soil and glass samples taken after dismantling the field lysimeter test illustrated a pronounced enrichment of rhenium and molybdenum in soil samples in contact and immediately surrounding the buried glass logs from all three lysimeters. The elevated rhenium and molybdenum in the soil probably originated from the glass logs. XRD and SEM analysis revealed that iron-rich alloy globules were present at the glass-sediment interface, suggesting that the Fe-rich solid formed during the glass fabrication process and then was buried with the glass samples. These Fe-rich globules were also enriched in Re and Mo, suggesting these two elements partitioned to this phase. These results suggest that the pronounced Re and Mo enrichment in the pore-water is almost certainly due to the oxidative dissolution of the Fe-rich globules rather than the bulk ILAW glass. Additionally, the boron concentration was enriched in the pore-water of the deeper soil samples and in sediments collected immediately adjacent to the buried glass logs. The elevated boron levels may be due to other effects, including normal downward leaching and reprecipitation of boron naturally present in the unsaturated zone sediments. The origin of the elevated B levels in the sediments could be tested by measurement of B-isotopic compositions in water extracts and comparison with B-isotopic compositions in the glasses.

An MC simulation tool is being developed to predict the composition, extent, and morphology of the weathered glass hydration layer as a function of glass composition. The developed simulation tool will then be used to provide input data for geochemical modeling of secondary-phase formation to be used in future PA analyses. The work carried out this fiscal year (FY 2012) was divided into two activities. The first activity was aimed at providing a quantitative comparison between calculated and experimental dissolution properties of borosilicate and aluminoborosilicate glasses using a single set of model parameters. The second activity consisted in extending the MC code to include high-field-strength cations, which adopt an octahedral coordination in borosilicate glasses. The MC simulation results show good quantitative agreement with experimental data on the extent, as described by weathered layer thickness, and rate of aqueous corrosion as a function of glass composition, for oxide glasses with up to four components (Si, B, Al, and Na), in particular for sodium borosilicate glasses. Results also provided key insight into the role of Al and high-field-strength cations (such as Zr and Hf) on the hydrolysis/ condensation reactions that occur during the dissolution of borosilicate glasses.

Lastly, the MC simulations use as input glass compositions, glass structure, and the reactivity of the glass components. In FY 2012, a variety of chemically simple and complex glasses were characterized using $^{27}$Al, $^{11}$B, and $^{29}$Si MAS-NMR. In previous fiscal years, a combination of Raman spectroscopy and XPS was also used to characterize unreacted and reacted glasses. A summary of these results will be discussed in a future project summary report. Here we briefly discuss recent results collected on hafnium-bearing aluminoborosilicate glasses. The hafnium-bearing glasses are used to provide insight into the effect of high-field-strength cations, such as Zr and Hf, on the glass structure and rate of glass corrosion. These results illustrate that the ratio of Hf/Si has a significant impact on the percentage of trigonal ($^{III}$B) and tetrahedral ($^{IV}$B) boron. Furthermore, these results also suggest an increase in mixing between the Hf and Si (i.e., the proportion of Hf-O-Si bonds increase) as the Hf/Si ratio increases.

# 10.0 References


Aagaard P and HC Helgeson. 1982. "Thermodynamic and Kinetic Constraints on Reaction Rates among Minerals and Aqueous Solutions. I. Theoretical Considerations." *American Journal of Science* 282:237–285.

Abraitis PK, FR Livens, JE Monteith, JS Small, DP Trivedi, DJ Vaughan, and RA Wogelius. 2000. "The Kinetics and Mechanisms of Simulated British Magnox Waste Glass Dissolution as a Function of pH, Silicic Acid Activity, and Time in Low-Temperature Aqueous Systems." *Applied Geochemistry* 15:1399–1416.

Arab M, C Cailleteau, F Angeli, F Devreux, L Girard, and O Spalla. 2008. "Aqueous Alteration of Five-Oxide Silicate Glasses: Experimental Approach and Monte Carlo Modeling." *Journal of Non-Crystalline Solids* 354:155–161.

ASME NQA-1-2000. 2001. *Quality Assurance Requirements for Nuclear Facility Applications*. The American Society of Mechanical Engineers, New York, New York.

Bacon DH, MD White, and BP McGrail. 2000. *Subsurface Transport Over Reactive Multiphases (STORM): A General, Coupled, Nonisothermal Multiphase Flow, Reactive Transport, and Porous Medium Alteration Simulator, Version 2, User's Guide*. PNNL-13108, Pacific Northwest National Laboratory, Richland, Washington.

Bacon DH and BP McGrail. 2001. *Waste Form Release Calculations for the 2001 Immobilized Low-Activity Waste Performance Assessment*. PNNL-13369, Pacific Northwest National Laboratory, Richland, Washington.

Bacon DH and BP McGrail. 2005. *Waste Form Release Calculations for the 2005 Integrated Disposal Facility Performance Assessment*. PNNL-15198, Pacific Northwest National Laboratory, Richland, Washington.

Bacon DH, MD White, and BP McGrail. 2004. *Subsurface Transport Over Reactive Multiphases (STORM): A Parallel, Coupled, Nonisothermal Multiphase Flow, Reactive Transport, and Porous Medium Alteration Simulator, Version 3.0, User's Guide*. PNNL-14783, Pacific Northwest National Laboratory, Richland, Washington.

Bacon DH, MI Ojovan, BP McGrail, NV Ojovan, and IV Startsceva. 2003. "Vitrified Waste Corrosion Rates from Field Experiment and Reactive Transport Modeling." *9th International Conference on Radioactive Waste Management and Environmental Remediation*, Proceedings of ICEM '03, Oxford, England.

Bacon DH and EM Pierce. 2010. *Sensitivity Analysis of Kinetic Rate-Law Parameters Used to Simulate Long-Term Weathering of ILAW Glass*. PNNL-19472, Pacific Northwest National Laboratory, Richland, Washington.

Ball P. 2003. "To the heart of glass." *Nature* 421:783–784.

Barkatt A, BC Gibson, PB Macedo, CJ Montrose, W Sousanpour, A Barkatt, MA Boroomand, V Rogers, and M Penafiel. 1986. "Mechanisms of Defense Waste Glass Dissolution." *Nuclear Technology* 73:140–164.

Bethke CM and S Yeakel. 2009. *The Geochemist's Workbench®, Release 8.0, Reference Manual*. Hydrogeology Program, University of Illinois, Urbana, Illinois.

Bourcier WL. 1991. "Overview of Chemical Modeling of Nuclear Waste Glass Dissolution." *Material Research Symposium Proceedings* 212:3–17.

Bourcier WL. 1994. "Waste Glass Corrosion Modeling: Comparison with Experimental Results." *Materials Research Symposium Proceedings* 333:69–81.

Bunker BC, DR Tallant, TJ Headley, GL Turner, and RJ Kirkpatrick. 1988. "The Structure of Leached Sodium Borosilicate Glass." *Physics and Chemistry of Glasses* 29(3):106–120.

Bruker. 2005a. *D8 Advance D8 Discover User's Manual, vol. 1*. DOC-M88-EXX036 V.5, Bruker ASX GmbH, Karlsruhe, Germany.

Bruker. 2005b. *D8 Advance User's Manual, vol. 2*. DOC-M88-E02054, Bruker ASX GmbH, Karlsruhe, Germany.

Bruker. 2008. *Instrument Performance Verification Booklet*. DOC-M88-ZXX041 V.11, Bruker ASX GmbH, Karlsruhe, Germany.

Cailleteau CF Angeli, F Devreux, S Gin, J Jestin, P Jollivet, and O Spalla. 2008. "Insight into silicate-glass corrosion mechanisms." *Nature Materials* 7:978–983.

Campbell GS. 1985. *Soil Physics with BASIC: Transport Models for Soil-Plant Systems*. Elsevier, New York.

Carman PC. 1937. "Fluid flow through a granular bed." *Transactions of the Institution of Chemical Engineers (London)* 15:150–156.

Casey WH and BC Bunker. 1990. "Leaching of Mineral and Glass Surfaces During Dissolution." *Reviews in Mineralogy* 23:397–426. MF Hochella, Jr. and AF White (eds.), Mineralogical Society of America.

Certa PJ and MN Wells. 2010. *River Protection Project System Plan*. ORP-11242, Rev. 5, U.S. Department of Energy, Office of River Protection, Richland, Washington.

Chen Y, DW Engel, BP McGrail, and KS Lessor. 1995. *AREST-CT V1.0 Software Verification*. PNL-10692, Pacific Northwest Laboratory, Richland, Washington.

Chen Y, BP McGrail, and DW Engel. 1997. "Source-Term Analysis for Hanford Low-Activity Tank Waste using the Reaction-Transport Code AREST-CT." In *Scientific Basis for Nuclear Waste Management XX*, Pittsburgh, Pennsylvania.

Cho HR, C Walther, J Rothe, V Neck, MA Denecke, K Dardenne, and T Fanghanel. 2005. "Combined LIBD and XAFS Investigation of the Formation and Structure of Zr(IV) Colloids." *Analytical and Bioanalytical Chemistry* 383:28–40.

Crum JV. 2011. *Operation of Bruker D-8 Advanced X-ray Diffractometer*. SOP, APEL-D-8-ADV Rev. 0, Pacific Northwest National Laboratory, Richland, Washington.

Cunnane JC, JK Bates, and CR Bradley. 1994a. *High-Level Waste Borosilicate Glass: A Compendium of Corrosion Characteristics*, Vol. 1. DOE-EM-0177, U.S. Department of Energy, Office of Waste Management, Springfield, Virginia.

Cunnane JC, JK Batesand CR Bradley. 1994b. *High-Level Waste Borosilicate Glass: A Compendium of Corrosion Characteristics*, Vol. 2. DOE-EM-0177, U.S. Department of Energy, Office of Waste Management, Springfield, Virginia.

Daveler SA and TJ Wolery. 1992. *EQPT, A Data File Preprocessor for the EQ3/6 Software Package: User's Guide and Related Documentation (Version 7.0)*. UCRL-MA-110662 PT II, Lawrence Livermore National Laboratory, Livermore, California.

Doremus RH. 1975. "Interdiffusion of Hydrogen and Alkali Ions in a Glass Surface." *Journal of Non-Crystalline Solids* 19:137–144.

DOE – U.S. Department of Energy. 2005. *Quality Assurance*. DOE Order 414.1C. U.S. Department of Energy, Washington, D.C. Available on line at http://www.directives.doe.gov.

DOE – U.S. Department of Energy. 2011. *Quality Assurance*. DOE Order 414.1D. U.S. Department of Energy, Washington, D.C. Available on line at http://www.directives.doe.gov.

EPA – U.S. Environmental Protection Agency. 2008. *Methods for Evaluating Solid Waste, Physical/ Chemical Methods*. Method 6020A, "Inductively Coupled Plasma-Mass Spectrometry." SW-846, U.S. Environmental Protection Agency, Washington, D.C. Available at http://www.epa.gov/epawaste/hazard/testmethods/sw846/pdfs/6020a.pdf.

Farnsworth RK, MKW Chan, and SC Slate. 1985. "The Effect of Radial Temperature Gradients on Glass Fracture in Simulated High-Level Waste Canisters." *Materials Research Society Symposium Proceedings* 44:831–838.

Fayer MJ, EM Murphy, JL Downs, FO Khan, CW Lindenmeier, and BN Bjornstad. 1999. *Recharge Data Package for the Immobilized Low-Activity Waste 2001 Performance Assessment*. PNNL-13033, Pacific Northwest National Laboratory, Richland, Washington.

Fayer MJ and JE Szecsody. 2004. *Recharge Data Package for the 2005 Integrated Disposal Facility Performance Assessment*. PNNL-14744, Pacific Northwest National Laboratory, Richland, Washington.

Fox LE. 1988. "The Solubility of Colloidal Ferric Hydroxide and its Relevance to Iron Concentrations in River Water." *Geochimica et Cosmochimica Acta* 53(3):771–777.

Freedman VL and MD White. 2007. *STOMP Software Test Plan*. PNNL-SA-54022, Pacific Northwest National Laboratory, Richland, Washington.

Goldschmidt VM. 1937. "The principles of distribution of chemical elements in minerals and rocks." *Journal of the Chemical Society* 655–673, DOI: 10.1039/JR9370000655.

Grambow B. 1985. "A General Rate Equation for Nuclear Waste Glass Corrosion." In *Materials Research Society Symposium Proceedings* 44:15–27.

Hench LL, DE Clark, and AB Harker. 1986. "Nuclear Waste Solids." *Journal of Materials Science* 21:1457–1478.

Icenhower JP, S Samson, A Luttge, and BP McGrail. 2004. "Towards a Consistent Rate Law: Glass Corrosion Kinetics Near Saturation." In *Energy, Waste, and the Environment: A Geochemical Perspective*, R Giere and P Stille (eds.), *Geological Society of London* 236:579–594.

Jantzen CM, DI Kaplan, NE Bibler, DK Peeler, and MJ Plodinec. 2008. "Performance of a Buried Radioactive High-Level Waste (HLW) Glass after 24 Years." *Journal of Nuclear Materials* 378:244–256.

Kerisit S and EM Pierce. 2011. "Monte Carlo Simulations of the Dissolution of Borosilicate and Aluminoborosilicate Glasses in Dilute Conditions." *Geochimica et Cosmochimica Acta* 75:5296–5309.

Kerisit S and EM Pierce. 2012. "Monte Carlo simulations of the dissolution of borosilicate glasses in near-equilibrium conditions." *Journal of Non-Crystalline Solids* 358:1324–1332.

Khaleel R. 2004. *Far-Field Hydrology Data Package for the Integrated Disposal Facility Performance Assessment*. RPP-20621, Rev. 0, CH2M Hill Hanford Group, Richland, Washington

Krupka KM, RJ Serne, and DI Kaplan. 2004. *Geochemical Data Package for the 2005 Hanford Integrated Disposal Facility Performance Assessment*. PNNL-13037, Rev. 2, Pacific Northwest National Laboratory, Richland, Washington.

Ledieu A, F Devreux, P Barboux, L Sicard, and O Spalla. 2004. "Leaching of borosilicate glasses. I. Experiments." *Journal of Non-Crystalline Solids* 343:3–12.

Ledieu A, F Devreux, and P Barboux. 2005. "The role of aluminium in the durability of alumino-borosilicate glasses." *Physics and Chemistry of Glasses* 46:12–20.

Ledieu A, F Devreux, P Barboux, and Y Minet. 2006. "Contribution of Monte Carlo Modeling to Understanding the Alteration of Nuclear Glasses by Water." *Nuclear Science Engineering* 153:285–300.

Mann FM, KC Burgard, WR Root, RJ Puigh, SH Finfrock, R Khaleel, DH Bacon, EJ Freeman, BP McGrail, SK Wurstner, and PE LaMont. 2001. *Hanford Immobilized Low-Activity Waste Performance Assessment: 2001 Version*. DOE/ORP-2000-24, Rev. 0, U.S. Department of Energy, Office of River Protection, Richland, Washington.

Mann FM., BP McGrail, DH Bacon, RJ Serne, KM Krupka, RJ Puigh, R Khaleel, and S Finfrock. 2003. *Risk Assessment Supporting the Decision on the Initial Selection of Supplemental ILAW Technologies*. RPP-17675, Rev. 0, CH2MHILL Hanford Group Inc., Richland, Washington.

Mann FM, RJ Puigh, II, CR Eiholzer, Y Chen, NW Kline, AH Lu, BP McGrail, PD Rittmann, GF Williamson, NR Brown, and PE LaMont. 1998. *Hanford Immobilized Low Activity Tank Waste Performance Assessment*. DOE/RL-97-69, Rev. B, Project Hanford Management Contractor, Richland, Washington.

McGrail, BP, DH Bacon, PD Meyer, MI Ojovan, DM Strachan, NV Ojovan, and IV Startceva. 2002. "New Developments in Field Studies of Low Activity Waste Glass Corrosion and Contaminant Transport." *MRS Proceedings: Scientific Basis for Nuclear Waste Management XXVI*, 757:1–14

McGrail BP, WL Ebert, AJ Bakel, and DK Peeler. 1997. "Measurement of Kinetic Rate Law Parameters on a Na-Ca-Al Borosilicate Glass for Low-Activity Waste." *Journal of Nuclear Materials* 249(2–3):175–189.

McGrail BP, DH Bacon, WL Ebert, and KP Saripalli. 1998. *A Strategy to Conduct an Analysis of the Long-Term Performance of Low-Activity Waste Glass in a Shallow Subsurface Disposal System at Hanford*. PNNL-11834, Pacific Northwest National Laboratory, Richland, Washington.

McGrail BP, DH Bacon, WL Ebert, and KP Saripalli. 2000a. *A Strategy to Conduct an Analysis of the Long-Term Performance of Low-Activity Waste Glass in a Shallow Subsurface Disposal System at Hanford*. PNNL-11834, Rev. 1, Pacific Northwest National Laboratory, Richland, Washington.

McGrail BP, JP Icenhower, PF Martin, DR Rector, HT Schaef, EA Rodriguez, and JL Steele. 2000b. Low-*Activity Waste Glass Studies: FY2000 Summary Report*. PNNL-13381, Pacific Northwest National Laboratory, Richland, Washington.

McGrail BP, DH Bacon, JP Icenhower, WL Ebert, PF Martin, HT Schaef, and EA Rodriguez. 2001a. *Waste Form Release Data Package for the 2001 Immobilized Low-Activity Waste Performance Assessment*. PNNL-13043, Rev. 2, Pacific Northwest National Laboratory, Richland, Washington.

McGrail BP, DH Bacon, JP Icenhower, FM Mann, RJ Puigh, HT Schaef, and SV Mattigod. 2001b. "Near-Field Performance Assessment for a Low-Activity Waste Glass Disposal System: Laboratory Testing to Modeling Results." *Journal of Nuclear Materials* 298:95–111.

McGrail BP, JP Icenhower, PF Martin, HT Schaef, MJ O'Hara, EA Rodriguez, and JL Steele. 2001c. *Waste Form Release Data Package for the 2001 Immobilized Low-Activity Waste Performance Assessment*. PNNL-13043, Rev. 2, Pacific Northwest National Laboratory, Richland, Washington.

McGrail BP, DH Bacon, RJ Serne, and EM Pierce. 2003. *A Strategy to Assess Performance of Selected Low-Activity Waste Forms in an Integrated Disposal Facility*. PNNL-14362, Pacific Northwest National Laboratory, Richland, Washington.

Meyer PD, BP McGrail, and DH Bacon. 2001. *Test Plan for Field Experiments to Support the Immobilized Low-Activity Waste Disposal Performance Assessment at the Hanford Site*. PNNL-13670, Pacific Northwest National Laboratory, Richland, Washington.

Meyer PD, KP Saripalli, and VL Freedman. 2004. *Near-Field Hydrology Data Package for the Integrated Disposal Facility 2005 Performance Assessment*. PNNL-14700, Pacific Northwest National Laboratory, Richland, Washington.

Nagy KL and AC Lasaga. 1993. "Letter: Simultaneous Precipitation Kinetics of Kaolinite and Gibbsite at 80°C and pH 3." *Geochimica et Cosmochimica Acta* 57:4329–4335.

Nagy KL. 1995. "Dissolution and Precipitation Kinetics of Sheet Silicates." Chapter 5 in *Chemical Weathering Rates of Silicate Minerals. Reviews in Mineralogy,* AF White and SL Brantley (eds.), 31:173–233. Mineralogical Society of America, Washington, D.C.

Nieplocha J, BJ Palmer, V Tipparaju, MK Krishnan, HE Trease, and E Apra. 2006. "Advances, Applications and Performance of the Global Arrays Shared Memory Programming Toolkit." *International Journal of High Performance Computing Applications* 20(2):203–231.

NIST – National Institute of Standards and Technology. 2008. *SRM 1976A: Instrument Response Standard for X-Ray Powder Diffraction.* National Institute of Standards and Technology, Department of Commerce, Gaithersburg, Maryland.

Papathanassiu A, IS Muller, M Brandys, K Gilbo, A Barkatt, I Joseph, and IL Pegg. 2011. *ILAW Glass Testing for Disposal at IDF: Phase 1 Testing*. VSL-11R2270-1, Vitreous State Laboratory, The Catholic University of America, Washington, D.C.

Peters RD and SC Slate. 1981. "Fracturing of Simulated High-Level Waste Canisters." *Nuclear Engineering and Design* 67:425–445.

Pierce EM, DH Bacon, SN Kerisit, CF Windisch, Jr, KJ Cantrell, MM Valenta, SD Burton, and JH Westsik, Jr. 2011. *Integrated Disposal Facility FY2011 Glass Testing Summary Report*. PNNL-20781, Pacific Northwest National Laboratory, Richland, Washington.

Pierce EM, BP McGrail, EA Rodriguez, HT Schaef, KP Saripalli, RJ Serne, KM Krupka, PF Martin, SR Baum, KN Geiszler, LR Reed, and WJ Shaw. 2004. *Waste Form Release Data Package for the 2005 Integrated Disposal Facility Performance Assessment*. PNNL-14805, Pacific Northwest National Laboratory, Richland, Washington.

Pierce EM, BP McGrail, EA Rodriguez, DM Wellman, LR Reed, DH Bacon, HT Schaef, and SR Baum. 2005. *Laboratory Testing of Bulk Vitrified Low-Activity Waste Form to Support the 2005 Integrated Disposal Facility Performance Assessment*. PNNL-15126, Pacific Northwest National Laboratory, Richland, Washington.

Pierce EM, BP McGrail, J Marra, PF Martin, BW Arey, and KN Geiszler. 2007. "Accelerated Weathering of a High-Level and Pu-bearing Lanthanide Borosilicate Waste Glass in a Can-in-Canister Configuration." *Applied Geochemistry* 22:1841–1859.

Pierce EM, EL Richards, AM Davis, LR Reed, and EA Rodriguez. 2008a. "Aluminoborosilicate Waste Glass Dissolution under Alkaline Conditions at 40°C: Implications for a Chemical Affinity-based Rate Equation." *Environmental Chemistry* 5:1–13.

Pierce EM, EA Rodriguez, LJ Calligan, WJ Shaw, and BP McGrail. 2008b. "An Experimental Study of the Dissolution Rates of Simulated Aluminoborosilicate Waste Glasses as a Function of pH and Temperature under Dilute Conditions." *Applied Geochemistry* 23:2559–2573.

Pierce EM, LR Reed, WJ Shaw, BP McGrail, JP Icenhower, CF Windisch, EA Cordova, and J Broady. 2010a. "Experimental Determination of the Effect of the Ratio of B/Al on Glass Dissolution Along the Nepheline ($NaAlSiO_4$) - Malinkoite ($NaBSiO_4$) Join." *Geochimica et Cosmochimica Acta* 74:2634–2654.

Pierce EM, DH Bacon, SN Kerisit, CF Windisch, KJ Cantrell, MM Valenta, SD Burton, RJ Serne, and SV Mattigod. 2010b. *Integrated Disposal Facility Glass Testing FY2010 Summary Report*. PNNL-19736, Pacific Northwest National Laboratory, Richland, Washington.

Pierce EM and DH Bacon. 2011. "Combined Experimental and Computational Approach to Predict the Glass-Water Reaction." *Nuclear Technology* 176(1):22–39.

Pierce EM, DH Bacon, SN Kerisit, CF Windisch, KJ Cantrell, MM Valenta, and SD Burton. 2011. *Integrated Disposal Facility Glass Testing FY2011 Summary Report*. PNNL-20781, Pacific Northwest National Laboratory, Richland, Washington.

Puigh RJ. 2004. *Facility Data for the Hanford Integrated Disposal Facility Performance Assessment*. RPP-20691, Rev. 0, Fluor Government Group, Richland, Washington.

Rajh T, ZV Saponjic, and OI Micic. 1992. "Reactions of Hydrous Titanium Oxide Colloids with Strong Oxidizing Agents." *Langmuir* 8:1265–1270.

Richards LA. 1931. "Capillary Conduction of Liquids through Porous Mediums." *Physics* 1:318–333.

Savage B, D Rochelle, Y Moore, A Milodowski, K Bateman, D Bailey, and M Mihara. 2001. "Analcime Reactions at 25-90ºC in Hyperalkaline Fluids." *Mineralogical Magazine* 65(5):571–587.

Serne RJ, JL Conca, VL LeGore, KJ Cantrell, CW Lindenmeier, JA Campbell, JE Amonette, and MI Wood. 1993. *Solid-Waste Leach Characteristics and Contaminant-Sediment Interactions. Volume 1: Batch Leach and Adsorption Tests and Sediment Characterization*. PNL-8889, Vol. 1, Pacific Northwest Laboratory, Richland, Washington.

Singh RK and P Webley. 2005. "Adsorption of $N_2$, $O_2$, and Sr in Potassium Chabazite." *Adsorption* 11:173–177.

Small JS, PN Humphrey, TL Johnstone, R Plant, MG Randall, and DP Trivedi. 2000. "Results of an Aqueous Source Term Model for a Radiological Risk Assessment of the Drigg LLW Site, UK." In *Scientific Basis for Nuclear Waste Management XXIII*, Materials Research Society, Boston, Massachusetts.

Strachan DM and TL Croak. 2000. "Compositional Effects on Long-term Dissolution of Borosilicate Glass." *Journal of Non-Crystalline Solids* 272:22–33.

Suryanarayana C and MG Norton. 1998. *X-Ray Diffraction A Practical Approach*. Plenum Press, New York.

USGS – United States Geological Survey. 2001. "Alkalinity and Acid Neutralizing Capacity." *National Field Mnaual for the Collectin of Water-Quality Data*, 2nd ed., SA Rounds and FD Wilde (eds.), March 23, 2004. Available at http://water.usgs.gov/owq/FieldManutal/Chapter6/section6.6/.

van Genuchten MTh. 1980. "A closed-form equation for predicting the hydraulic conductivity of unsaturated soils." *Soil Science Society of America Journal* 44(5):892–898.

Van Iseghem P, M Aetsens, K Lemmens, S Gin, D Deneele, B Grambow, BP McGrail, DM Strachan, G Wicks, and T McMenamin. 2004. "GLAMOR--A Critical Evaluation of the Dissolution Mechanisms of High-level Waste Glasses in Conditions of Relevance for Geological Disposal." In *Euradwaste '04: Radioactive Waste Management: Community Policy and Research Initiatives: Proceedings of the Sixth European Commission Conference on the Management and Disposal of Radioactive Waste*. C Davies (ed.), March 29–31, Luxembourg. Directorate-General for Research, European Commission, Luxembourg.

Vernaz EY and JL Dussossoy. 1992. "Current State of Knowledge of Nuclear Waste Glass Corrosion Mechanisms – The Case of R7T7 Glass." *Applied Geochemistry* 1:13–22.

Vernaz E, S Gin, C Jegou, and I Ribet. 2001. "Present Understanding of R7T7 Glass Alteration Kinetics and their Impact on Long-term Behavior Modeling." *Journal of Nuclear Materials* 298:27–36.

Werme LO, IK Bjorner, G Bart, HU Zwicky, B Grambow, W Lutze, RC Ewing, and C Magrabi. 1990. "Chemical Corrosion of Highly Radioactive Borosilicate Nuclear Waste Glass under Simulated Repository Conditions." *Journal of Materials Research* 5(5):1130–1146.

Wicks GG. 2001. "US field testing program and results." *Journal of Nuclear Materials* 298:78–85.

White MD and VL Freedman. 2007. *STOMP Software Configuration Management Plan*. PNNL-SA-54023, Pacific Northwest National Laboratory, Richland, Washington.

White MD and VL Freedman. 2012. *STOMP Software Configuration Management Plan,* PNNL-SA-92584, Pacific Northwest National Laboratory, Richland, Washington.

White MD and BP McGrail. 2005. *STOMP, Subsurface Transport Over Multiple Phases, Version 1.0, Addendum: ECKEChem, Equilibrium-Conservation-Kinetic Equation Chemistry and Reactive Transport*. PNNL-15482, Pacific Northwest National Laboratory, Richland, Washington.

White MD and M Oostrom. 2000. *STOMP: Subsurface Transport Over Multiple Phases Version 2.0 Theory Guide*. PNNL-12030, Pacific Northwest National Laboratory, Richland, Washington.

White MD and M Oostrom. 2006. *STOMP: Subsurface Transport Over Multiple Phases, Version 4.0, User's Guide*. PNNL-15782, Pacific Northwest National Laboratory, Richland, Washington.

Wierenga PJ, MH Young, GW Gee, RG Hills, CT Kincaid, TJ Nicholson, and RE Cady. 1993. *Soil Characterization Methods for Unsaturated Low-Level Waste Sites*. PNL-8480, Pacific Northwest Laboratory, Richland, Washington.

Wolery TJ and SA Daveler. 1992. *EQ6, A Computer Program for Reaction Path Modeling of Aqueous Geochemical Systems: Theoretical Manual, User's Guide and Related Documentation*. UCRL-MA-110662 PT IV, Lawrence Livermore National Laboratory, Livermore, California.

# Appendix A

# PUF Test Results

**Table A.1**. PUF Results for ORPLF7

| Vial # | Time | Al | B | Ca | Cr | Li | K | Si | Na | V | Zn | Zr | Cs | Re |
|---|---|---|---|---|---|---|---|---|---|---|---|---|---|---|
| | days | µg/L | µg/L | µg/L | µg/L | µg/L | µg/L | µg/L | µg/L | µg/L | µg/L | µg/L | µg/L | µg/L |
| **1** | 0.49 | 4.5E+03 | 1.1E+04 | ND | 3.2E+02 | 1.5E+04 | 1.6E+05 | 4.4E+04 | 6.6E+04 | 4.4E+03 | ND | ND | ND | 2.0E+02 |
| **2** | 2.55 | 5.3E+03 | 3.7E+04 | 1.4E+03 | 1.3E+03 | 4.3E+04 | 2.2E+05 | 1.3E+05 | 2.1E+05 | 1.5E+04 | ND | ND | 6.8E-01 | 7.8E+02 |
| **3** | 5.52 | 6.8E+03 | 3.8E+04 | 1.1E+03 | 1.5E+03 | 5.0E+04 | 1.3E+05 | 1.5E+05 | 2.4E+05 | 1.7E+04 | ND | ND | 8.7E-01 | 9.3E+02 |
| **4** | 7.47 | 7.2E+03 | 3.1E+04 | ND | 1.2E+03 | 4.1E+04 | 2.0E+05 | 1.2E+05 | 1.9E+05 | 1.4E+04 | ND | ND | 8.8E-01 | 7.8E+02 |
| **5** | 9.54 | 6.8E+03 | 2.6E+04 | ND | 1.1E+03 | 3.4E+04 | 1.4E+05 | 1.1E+05 | 1.6E+05 | 1.2E+04 | ND | ND | 9.7E-01 | 6.4E+02 |
| **6** | 12.50 | 6.1E+03 | 2.4E+04 | ND | 9.5E+02 | 3.1E+04 | 1.1E+05 | 1.0E+05 | 1.4E+05 | 1.2E+04 | ND | ND | 9.6E-01 | 5.9E+02 |
| **7** | 14.61 | 5.7E+03 | 2.3E+04 | ND | 8.6E+02 | 2.8E+04 | 1.3E+05 | 9.2E+04 | 1.3E+05 | 1.1E+04 | ND | ND | 8.7E-01 | 5.1E+02 |
| **8** | 16.51 | 5.5E+03 | 2.2E+04 | ND | 7.6E+02 | 2.6E+04 | 1.0E+05 | 8.6E+04 | 1.2E+05 | 1.1E+04 | ND | ND | 9.1E-01 | 4.7E+02 |
| **9** | 19.43 | 2.9E+03 | 2.4E+04 | ND | 8.2E+02 | 2.5E+04 | 1.1E+05 | 8.4E+04 | 1.1E+05 | 1.1E+04 | ND | ND | 7.2E-01 | 5.0E+02 |
| **10** | 21.53 | 2.6E+03 | 2.2E+04 | 5.5E+02 | 7.5E+02 | 2.3E+04 | 9.8E+04 | 7.3E+04 | 1.0E+05 | 1.1E+04 | ND | ND | 4.8E-01 | 4.7E+02 |
| **11** | 23.65 | 5.0E+03 | 2.7E+04 | 5.0E+02 | 9.1E+02 | 2.9E+04 | 9.5E+04 | 8.8E+04 | 1.3E+05 | 1.3E+04 | ND | ND | 7.2E-01 | 5.4E+02 |
| **12** | 26.45 | 6.1E+02 | 4.3E+03 | ND | ND | 3.5E+03 | 1.7E+05 | 3.1E+04 | 1.7E+04 | 7.4E+02 | ND | ND | 4.5E-01 | 3.5E+01 |
| **13** | 28.43 | 2.4E+02 | 3.2E+03 | ND | ND | 1.5E+03 | 9.7E+04 | 2.8E+04 | 6.8E+03 | ND | ND | ND | ND | 7.6E+00 |
| **14** | 30.60 | ND | 3.1E+03 | 8.4E+02 | ND | 1.1E+03 | 2.7E+05 | 2.7E+04 | 6.5E+03 | ND | ND | ND | 3.5E-01 | 6.2E+00 |
| **15** | 33.49 | ND | 3.3E+03 | 7.7E+02 | ND | 7.8E+02 | 2.8E+05 | 2.8E+04 | 5.1E+03 | ND | ND | ND | ND | 7.2E+00 |
| **16** | 35.65 | ND | 3.6E+03 | 7.3E+02 | ND | 8.0E+02 | 2.0E+05 | 2.9E+04 | 5.3E+03 | ND | ND | ND | ND | 9.4E+00 |
| **17** | 37.61 | 6.4E+03 | 7.2E+04 | 1.4E+03 | 2.9E+03 | 7.0E+04 | 1.2E+05 | 1.5E+05 | 3.0E+05 | 3.8E+04 | ND | ND | 7.4E-01 | 1.7E+03 |
| **18** | 40.45 | 8.1E+03 | 2.6E+04 | ND | 9.6E+02 | 3.0E+04 | 1.3E+05 | 8.7E+04 | 1.4E+05 | 1.2E+04 | ND | ND | 5.9E-01 | 6.2E+02 |
| **19** | 42.47 | 1.6E+03 | 3.1E+04 | ND | 9.8E+02 | 2.4E+04 | 1.7E+05 | 7.7E+04 | 1.0E+05 | 1.4E+04 | ND | ND | 3.8E-01 | 6.2E+02 |
| **20** | 44.46 | 3.0E+03 | 2.8E+04 | ND | 8.4E+02 | 2.4E+04 | 1.6E+05 | 8.2E+04 | 1.1E+05 | 1.2E+04 | ND | ND | 3.6E-01 | 5.4E+02 |
| **21** | 47.45 | 2.9E+03 | 1.9E+04 | ND | 5.9E+02 | 1.9E+04 | 1.6E+05 | 6.6E+04 | 8.3E+04 | 8.8E+03 | ND | ND | ND | 3.7E+02 |
| **22** | 49.46 | 5.3E+02 | 1.6E+04 | ND | 4.8E+02 | 1.1E+04 | 2.6E+05 | 3.9E+04 | 4.7E+04 | 6.8E+03 | ND | ND | 3.4E-01 | 2.8E+02 |
| **23** | 51.62 | 3.2E+02 | 1.9E+04 | ND | 5.7E+02 | 1.3E+04 | 2.6E+05 | 4.6E+04 | 5.7E+04 | 8.2E+03 | ND | ND | 3.1E-01 | 3.7E+02 |
| **24** | 54.44 | 6.4E+02 | 3.9E+03 | ND | ND | 1.8E+03 | 9.6E+03 | 2.4E+04 | 1.2E+04 | 2.3E+02 | ND | ND | ND | 1.5E+01 |
| **25** | 56.43 | 2.1E+02 | 5.3E+03 | ND | ND | 1.7E+03 | 5.2E+03 | 2.4E+04 | 8.7E+03 | ND | ND | ND | ND | 2.4E+01 |
| **26** | 61.38 | 4.7E+03 | 3.0E+05 | 2.3E+03 | 8.4E+03 | 1.6E+05 | 7.1E+04 | 2.2E+05 | 6.7E+05 | 1.4E+05 | ND | ND | NM | 5.3E+03 |

**Table A.1**. (contd)

| Vial # | Time | Al | B | Ca | Cr | Li | K | Si | Na | V | Zn | Zr | Cs | Re |
|---|---|---|---|---|---|---|---|---|---|---|---|---|---|---|
| | days | µg/L | µg/L | µg/L | µg/L | µg/L | µg/L | µg/L | µg/L | µg/L | µg/L | µg/L | µg/L | µg/L |
| **27** | 72.45 | 1.8E+03 | 7.6E+05 | 6.3E+03 | 2.2E+04 | 3.6E+05 | 1.6E+04 | 3.0E+05 | 1.3E+06 | 3.5E+05 | ND | ND | NM | 1.4E+04 |
| **28** | 100.63 | 1.4E+03 | 9.5E+04 | 9.8E+02 | 2.2E+03 | 6.4E+04 | 4.0E+05 | 1.5E+05 | 3.0E+05 | 3.9E+04 | ND | ND | NM | 1.6E+03 |
| **39** | 103.42 | 2.5E+03 | 3.6E+04 | 5.5E+02 | 9.8E+02 | 2.7E+04 | 2.6E+05 | 7.9E+04 | 1.4E+05 | 1.4E+04 | ND | ND | NM | 7.3E+02 |
| **30** | 105.61 | 4.1E+03 | 4.4E+04 | ND | 1.4E+03 | 2.9E+04 | 1.5E+05 | 7.7E+04 | 1.5E+05 | 1.8E+04 | ND | ND | NM | 9.2E+02 |
| **31** | 110.54 | 3.1E+03 | 3.7E+04 | ND | 1.1E+03 | 2.5E+04 | 1.4E+05 | 5.8E+04 | 1.2E+05 | 1.6E+04 | ND | ND | NM | 7.5E+02 |
| **32** | 112.61 | 3.4E+03 | 3.9E+04 | ND | 1.2E+03 | 2.6E+04 | 1.0E+05 | 6.0E+04 | 1.2E+05 | 1.7E+04 | ND | ND | NM | 8.1E+02 |
| **33** | 117.37 | 3.3E+03 | 4.2E+04 | 5.3E+02 | 1.3E+03 | 2.7E+04 | 1.6E+05 | 5.9E+04 | 1.3E+05 | 1.8E+04 | ND | ND | NM | 8.2E+02 |
| **34** | 119.44 | 3.1E+03 | 4.1E+04 | 6.3E+02 | 1.2E+03 | 2.6E+04 | 1.7E+05 | 5.6E+04 | 1.2E+05 | 1.8E+04 | ND | ND | NM | 8.3E+02 |
| **35** | 124.56 | 2.9E+03 | 3.8E+04 | 6.2E+02 | 1.1E+03 | 2.5E+04 | 1.4E+05 | 5.1E+04 | 1.2E+05 | 1.7E+04 | ND | ND | NM | 7.5E+02 |
| **36** | 131.33 | 2.8E+03 | 4.0E+04 | 7.3E+02 | 1.2E+03 | 2.4E+04 | 1.5E+05 | 4.7E+04 | 1.1E+05 | 1.7E+04 | ND | ND | NM | 7.7E+02 |
| **37** | 138.40 | 2.9E+03 | 4.0E+04 | 8.0E+02 | 1.2E+03 | 2.4E+04 | 1.4E+05 | 4.6E+04 | 1.1E+05 | 1.7E+04 | ND | ND | NM | 7.7E+02 |
| **38** | 146.27 | 3.2E+03 | 5.2E+04 | 1.7E+03 | 1.6E+03 | 2.8E+04 | 1.4E+05 | 4.6E+04 | 1.2E+05 | 2.3E+04 | ND | ND | NM | 1.0E+03 |
| **39** | 152.32 | 2.6E+03 | 8.4E+04 | 2.2E+03 | 2.3E+03 | 5.2E+04 | 2.1E+05 | 8.6E+04 | 2.2E+05 | 3.9E+04 | ND | ND | NM | 1.3E+03 |
| **40** | 160.26 | 3.0E+03 | 1.2E+05 | 2.9E+03 | 3.0E+03 | 8.6E+04 | 5.4E+05 | 1.8E+05 | 4.1E+05 | 5.0E+04 | ND | ND | NM | 1.9E+03 |
| **41** | 166.26 | 3.4E+03 | 9.9E+04 | 2.0E+03 | 2.9E+03 | 7.3E+04 | 7.2E+05 | 1.7E+05 | 3.5E+05 | 4.0E+04 | ND | ND | NM | 1.9E+03 |
| **42** | 173.25 | 2.7E+03 | 4.2E+04 | 6.0E+02 | 1.3E+03 | 3.3E+04 | 1.8E+05 | 1.1E+05 | 1.7E+05 | 1.7E+04 | ND | ND | NM | 8.8E+02 |

ND indicates “not detected” below quantification level.

**Table A.2**. PUF Results for ORPLG9

| Vial # | Time | Al | B | Ca | Cr | K | Si | Na | Sn | Zn | Zr | Cs | Re |
|---|---|---|---|---|---|---|---|---|---|---|---|---|---|
| | days | µg/L | µg/L | µg/L | µg/L | µg/L | µg/L | µg/L | µg/L | µg/L | µg/L | µg/L | µg/L |
| **1** | 0.00 | ND | 8.7E+03 | ND | ND | 4.0E+04 | 7.6E+03 | 6.3E+04 | ND | ND | ND | 3.7E-01 | 1.0E+02 |
| **2** | 1.09 | 1.8E+03 | 7.8E+04 | ND | 1.5E+03 | 1.6E+05 | 2.0E+05 | 6.6E+05 | ND | ND | ND | 4.0E+00 | 1.9E+03 |
| **3** | 3.05 | 2.6E+03 | 2.7E+05 | ND | 5.1E+03 | 3.4E+05 | 4.1E+05 | 2.1E+06 | 5.6E+03 | ND | ND | 6.6E+00 | 4.6E+03 |
| **4** | 6.03 | 1.1E+04 | 2.0E+05 | ND | 2.8E+03 | 3.2E+05 | 2.7E+05 | 1.4E+06 | 9.6E+03 | ND | ND | 3.5E+00 | 2.4E+03 |
| **5** | 7.01 | 1.3E+04 | 2.0E+05 | ND | 2.3E+03 | 3.2E+05 | 2.4E+05 | 1.2E+06 | 8.9E+03 | ND | ND | 2.8E+00 | 1.9E+03 |
| **6** | 10.12 | 1.4E+04 | 1.5E+05 | ND | 1.7E+03 | 2.5E+05 | 2.0E+05 | 9.5E+05 | 7.2E+03 | ND | ND | 2.1E+00 | 1.5E+03 |
| **7** | 12.12 | 1.4E+04 | 1.5E+05 | ND | 1.5E+03 | 2.3E+05 | 2.0E+05 | 8.9E+05 | 6.8E+03 | ND | ND | 1.9E+00 | 1.4E+03 |
| **8** | 14.22 | 1.3E+04 | 1.3E+05 | ND | 1.4E+03 | 2.2E+05 | 1.9E+05 | 7.8E+05 | 5.9E+03 | ND | ND | 1.6E+00 | 1.2E+03 |
| **9** | 17.07 | 1.3E+04 | 1.2E+05 | ND | 1.2E+03 | 2.2E+05 | 1.9E+05 | 7.1E+05 | 6.1E+03 | ND | ND | 1.4E+00 | 1.1E+03 |
| **10** | 19.08 | 1.3E+04 | 1.2E+05 | ND | 1.2E+03 | 2.2E+05 | 1.9E+05 | 7.1E+05 | 5.8E+03 | ND | ND | 1.4E+00 | 1.1E+03 |
| **11** | 21.09 | 1.4E+04 | 1.1E+05 | ND | 1.2E+03 | 2.1E+05 | 1.8E+05 | 6.7E+05 | 5.6E+03 | ND | ND | 1.3E+00 | 1.1E+03 |
| **12** | 24.03 | 1.2E+04 | 9.8E+04 | ND | 1.0E+03 | 1.9E+05 | 1.8E+05 | 5.8E+05 | 5.0E+03 | ND | ND | 1.1E+00 | 9.3E+02 |
| **13** | 26.00 | 1.3E+04 | 9.9E+04 | ND | 1.1E+03 | 2.1E+05 | 1.8E+05 | 6.2E+05 | 5.1E+03 | ND | ND | 1.3E+00 | 1.0E+03 |
| **14** | 28.03 | 1.5E+04 | 1.0E+05 | ND | 1.1E+03 | 1.8E+05 | 1.8E+05 | 6.2E+05 | 5.3E+03 | ND | ND | 1.3E+00 | 1.1E+03 |
| **15** | 31.01 | 1.2E+04 | 8.0E+04 | ND | 8.7E+02 | 1.4E+05 | 1.5E+05 | 4.9E+05 | 4.1E+03 | ND | ND | 1.2E+00 | 8.3E+02 |
| **16** | 35.01 | 1.1E+04 | 1.1E+05 | ND | 1.2E+03 | 1.8E+05 | 1.7E+05 | 6.7E+05 | 4.1E+03 | ND | ND | 1.4E+00 | 1.2E+03 |
| **17** | 38.09 | 9.0E+03 | 6.6E+04 | ND | 7.1E+02 | 7.8E+04 | 1.5E+05 | 3.9E+05 | 3.4E+03 | ND | ND | 8.3E-01 | 7.3E+02 |
| **18** | 40.04 | 1.2E+04 | 6.0E+04 | ND | 6.5E+02 | 7.2E+04 | 1.4E+05 | 3.9E+05 | 3.8E+03 | ND | ND | 8.5E-01 | 6.5E+02 |
| **19** | 42.12 | 1.2E+04 | 6.9E+04 | ND | 7.7E+02 | 7.8E+04 | 1.5E+05 | 4.4E+05 | 4.1E+03 | ND | ND | 9.5E-01 | 7.6E+02 |
| **20** | 45.03 | 9.5E+03 | 6.2E+04 | ND | 7.1E+02 | 3.0E+05 | 1.3E+05 | 4.1E+05 | 3.3E+03 | ND | ND | 1.0E+00 | 7.0E+02 |
| **21** | 47.19 | 1.1E+04 | 6.0E+04 | ND | 8.2E+02 | 1.4E+05 | 1.3E+05 | 4.3E+05 | 3.1E+03 | ND | ND | 6.9E-01 | 7.2E+02 |
| **22** | 52.01 | 1.3E+04 | 8.5E+04 | ND | 1.1E+03 | 2.1E+05 | 1.7E+05 | 5.7E+05 | 2.9E+03 | ND | ND | 1.0E+00 | 5.1E+02 |
| **23** | 54.14 | 1.2E+04 | 5.9E+04 | ND | 8.0E+02 | 1.4E+05 | 1.4E+05 | 4.3E+05 | 3.1E+03 | ND | ND | ND | 7.4E+02 |
| **24** | 59.04 | 9.4E+03 | 4.9E+04 | ND | 6.3E+02 | 1.3E+05 | 1.2E+05 | 3.6E+05 | 2.5E+03 | ND | ND | 1.4E+00 | 6.0E+02 |
| **25** | 61.21 | 1.0E+04 | 5.3E+04 | ND | 7.1E+02 | 1.4E+05 | 1.3E+05 | 3.9E+05 | 3.0E+03 | ND | ND | 7.5E-01 | 6.6E+02 |
| **26** | 62.98 | 9.6E+03 | 4.8E+04 | ND | 6.4E+02 | 1.3E+05 | 1.2E+05 | 3.6E+05 | 2.6E+03 | ND | ND | 6.6E-01 | 6.0E+02 |
| **27** | 65.98 | 1.0E+04 | 4.7E+04 | ND | 6.5E+02 | 1.2E+05 | 1.3E+05 | 3.6E+05 | 2.7E+03 | ND | ND | 6.9E-01 | 6.2E+02 |
| **28** | 67.98 | 1.3E+04 | 4.8E+04 | ND | 6.3E+02 | 1.2E+05 | 1.4E+05 | 3.8E+05 | 2.8E+03 | ND | ND | 6.6E-01 | 5.9E+02 |
| **29** | 70.02 | 9.4E+03 | 3.7E+04 | ND | 4.8E+02 | 8.4E+04 | 9.9E+04 | 2.9E+05 | ND | ND | ND | 5.3E-01 | 4.6E+02 |
| **30** | 72.99 | 8.9E+03 | 4.7E+04 | ND | 5.8E+02 | 1.4E+05 | 1.2E+05 | 3.4E+05 | ND | ND | ND | 6.9E-01 | 6.0E+02 |
| **31** | 75.01 | 8.7E+03 | 4.3E+04 | ND | 5.8E+02 | 1.1E+05 | 1.1E+05 | 3.2E+05 | ND | ND | ND | 5.6E-01 | 5.7E+02 |

**Table A.2**. (contd)

| Vial # | Time | Al | B | Ca | Cr | K | Si | Na | Sn | Zn | Zr | Cs | Re |
|---|---|---|---|---|---|---|---|---|---|---|---|---|---|
| | days | µg/L | µg/L | µg/L | µg/L | µg/L | µg/L | µg/L | µg/L | µg/L | µg/L | µg/L | µg/L |
| **32** | 76.97 | 9.0E+03 | 4.2E+04 | ND | 5.2E+02 | 1.3E+05 | 1.1E+05 | 3.1E+05 | ND | ND | ND | 6.3E-01 | 5.7E+02 |
| **33** | 80.01 | 8.5E+03 | 3.9E+04 | ND | 5.5E+02 | 1.4E+05 | 1.1E+05 | 3.0E+05 | ND | ND | ND | 6.0E-01 | 5.5E+02 |
| **34** | 81.96 | 6.0E+03 | 4.8E+04 | ND | 6.7E+02 | 1.4E+05 | 1.2E+05 | 3.2E+05 | ND | ND | ND | 5.7E-01 | 6.1E+02 |
| **35** | 84.05 | 1.0E+04 | 4.8E+04 | ND | 6.8E+02 | 1.3E+05 | 1.4E+05 | 3.8E+05 | 2.8E+03 | ND | ND | 6.5E-01 | 6.0E+02 |
| **36** | 86.97 | 1.0E+04 | 4.0E+04 | ND | 5.5E+02 | 1.3E+05 | 1.2E+05 | 3.3E+05 | 2.3E+03 | ND | ND | 6.5E-01 | 5.3E+02 |
| **37** | 89.01 | 1.0E+04 | 4.1E+04 | ND | 5.9E+02 | 1.4E+05 | 1.2E+05 | 3.3E+05 | 2.5E+03 | ND | ND | 5.3E-01 | 5.3E+02 |
| **38** | 91.09 | 9.8E+03 | 3.9E+04 | ND | 5.0E+02 | 1.2E+05 | 1.1E+05 | 3.1E+05 | ND | ND | ND | 4.9E-01 | 5.2E+02 |
| **39** | 94.03 | 9.7E+03 | 3.8E+04 | ND | 5.0E+02 | 1.2E+05 | 1.1E+05 | 3.1E+05 | 2.5E+03 | ND | ND | 5.5E-01 | 5.1E+02 |
| **40** | 96.04 | 9.9E+03 | 3.8E+04 | ND | 5.4E+02 | 1.2E+05 | 1.1E+05 | 3.2E+05 | 2.2E+03 | ND | ND | 4.4E-01 | 5.2E+02 |
| **41** | 98.03 | 1.0E+04 | 3.7E+04 | ND | 4.8E+02 | 1.2E+05 | 1.1E+05 | 3.2E+05 | ND | ND | ND | 5.3E-01 | 5.2E+02 |
| **42** | 101.00 | 9.7E+03 | 3.6E+04 | ND | 5.1E+02 | 1.4E+05 | 1.1E+05 | 3.1E+05 | 2.4E+03 | ND | ND | 5.6E-01 | 5.0E+02 |
| **43** | 103.12 | 9.3E+03 | 3.6E+04 | ND | 4.8E+02 | 1.3E+05 | 1.1E+05 | 3.0E+05 | 2.3E+03 | ND | ND | 4.6E-01 | 4.9E+02 |
| **44** | 104.99 | 9.5E+03 | 3.5E+04 | ND | 5.3E+02 | 1.2E+05 | 1.1E+05 | 3.0E+05 | ND | ND | ND | 5.2E-01 | 5.1E+02 |
| **45** | 107.48 | 9.5E+03 | 3.4E+04 | ND | 5.0E+02 | 1.3E+05 | 1.1E+05 | 2.9E+05 | 2.2E+03 | ND | ND | 4.7E-01 | 4.9E+02 |
| **46** | 110.32 | 1.2E+04 | 4.1E+04 | ND | 7.0E+02 | 1.2E+05 | 1.1E+05 | 3.2E+05 | 2.5E+03 | ND | ND | 5.3E-01 | 5.5E+02 |
| **47** | 112.23 | 1.2E+04 | 4.1E+04 | ND | 7.3E+02 | 1.5E+05 | 1.2E+05 | 3.3E+05 | 2.5E+03 | ND | ND | 5.1E-01 | 5.7E+02 |
| **48** | 114.99 | 1.1E+04 | 3.7E+04 | ND | 6.5E+02 | 1.3E+05 | 1.1E+05 | 3.0E+05 | 2.5E+03 | ND | ND | 4.5E-01 | 5.1E+02 |
| **49** | 117.00 | 1.4E+04 | 4.1E+04 | ND | 7.4E+02 | 1.2E+05 | 1.2E+05 | 3.4E+05 | 2.9E+03 | ND | ND | 5.1E-01 | 5.8E+02 |
| **50** | 118.97 | 1.2E+04 | 3.3E+04 | ND | 6.1E+02 | 1.3E+05 | 1.1E+05 | 2.8E+05 | 2.3E+03 | ND | ND | 4.8E-01 | 4.9E+02 |
| **51** | 122.03 | 8.8E+03 | 3.4E+04 | ND | 6.3E+02 | 1.2E+05 | 9.2E+04 | 2.5E+05 | 1.8E+03 | ND | ND | 4.4E-01 | 5.1E+02 |
| **52** | 123.97 | 9.3E+03 | 3.8E+04 | ND | 7.2E+02 | 1.2E+05 | 1.0E+05 | 2.7E+05 | 2.1E+03 | ND | ND | 4.4E-01 | 5.7E+02 |
| **53** | 125.96 | 8.2E+03 | 3.4E+04 | ND | 6.6E+02 | 1.2E+05 | 9.2E+04 | 2.6E+05 | 1.9E+03 | ND | ND | 4.7E-01 | 5.2E+02 |
| **54** | 129.13 | 7.8E+03 | 3.3E+04 | ND | 6.5E+02 | 1.4E+05 | 9.0E+04 | 2.5E+05 | 1.7E+03 | ND | ND | 5.0E-01 | 5.1E+02 |
| **55** | 131.20 | 8.0E+03 | 3.4E+04 | ND | 6.7E+02 | 1.3E+05 | 8.8E+04 | 2.6E+05 | 1.7E+03 | ND | ND | 4.4E-01 | 5.3E+02 |
| **56** | 133.13 | 8.7E+03 | 3.6E+04 | ND | 7.1E+02 | 1.5E+05 | 9.8E+04 | 2.8E+05 | 1.9E+03 | ND | ND | 4.7E-01 | 5.6E+02 |
| **57** | 135.97 | 9.2E+03 | 3.8E+04 | ND | 7.7E+02 | 1.6E+05 | 1.1E+05 | 3.0E+05 | 2.0E+03 | ND | ND | 5.4E-01 | 6.1E+02 |
| **58** | 138.11 | 8.2E+03 | 3.4E+04 | ND | 6.8E+02 | 1.3E+05 | 9.3E+04 | 2.6E+05 | 1.8E+03 | ND | ND | 4.1E-01 | 5.3E+02 |
| **59** | 139.96 | 8.0E+03 | 3.1E+04 | ND | 6.5E+02 | 1.3E+05 | 8.8E+04 | 2.6E+05 | 1.7E+03 | ND | ND | 4.5E-01 | 5.0E+02 |

ND indicates “not detected” below quantification level.

**Table A.3**. PUF Results for ORPLB2

| Vial # | Time | Al | B | Ca | Cr | K | Si | Na | V | Zn | Zr | Cs | Re |
|---|---|---|---|---|---|---|---|---|---|---|---|---|---|
| | days | µg/L | µg/L | µg/L | µg/L | µg/L | µg/L | µg/L | µg/L | µg/L | µg/L | µg/L | µg/L |
| **1** | 0.07 | 8.1E+03 | 6.3E+03 | ND | ND | ND | 3.9E+04 | 1.2E+05 | 3.3E+03 | ND | ND | 9.5E+01 | 2.6E+02 |
| **2** | 1.77 | 2.5E+04 | 1.3E+05 | ND | 3.9E+03 | 1.3E+05 | 3.1E+05 | 1.2E+06 | 3.7E+04 | ND | ND | 3.0E+03 | 3.8E+03 |
| **3** | 3.90 | 3.8E+04 | 1.4E+05 | ND | 2.8E+03 | 1.6E+05 | 2.7E+05 | 1.2E+06 | 3.2E+04 | ND | ND | 2.6E+03 | 3.1E+03 |
| **4** | 8.80 | 2.6E+04 | 9.5E+04 | ND | 1.5E+03 | 1.3E+05 | 1.5E+05 | 7.9E+05 | 1.9E+04 | ND | ND | 1.2E+03 | 1.6E+03 |
| **5** | 10.97 | 2.4E+04 | 9.0E+04 | ND | 1.3E+03 | 1.4E+05 | 1.4E+05 | 7.4E+05 | 1.7E+04 | ND | ND | 1.0E+03 | 1.3E+03 |
| **6** | 12.74 | 2.2E+04 | 7.8E+04 | ND | 1.1E+03 | 9.7E+04 | 1.3E+05 | 6.4E+05 | 1.5E+04 | ND | ND | 8.6E+02 | 1.1E+03 |
| **7** | 15.74 | 2.2E+04 | 8.1E+04 | ND | 1.1E+03 | 1.3E+05 | 1.4E+05 | 6.4E+05 | 1.5E+04 | ND | ND | 8.0E+02 | 1.1E+03 |
| **8** | 17.74 | 2.1E+04 | 7.5E+04 | ND | 1.0E+03 | 1.3E+05 | 1.3E+05 | 5.9E+05 | 1.4E+04 | ND | ND | 8.2E+02 | 1.1E+03 |
| **9** | 19.78 | 2.1E+04 | 7.3E+04 | ND | 9.6E+02 | 1.2E+05 | 1.2E+05 | 5.9E+05 | 1.4E+04 | ND | ND | 7.3E+02 | 1.0E+03 |
| **10** | 22.75 | 1.8E+04 | 6.9E+04 | ND | 9.1E+02 | 1.7E+05 | 1.2E+05 | 5.4E+05 | 1.3E+04 | ND | ND | 7.0E+02 | 9.3E+02 |
| **11** | 24.77 | 1.8E+04 | 6.5E+04 | ND | 8.9E+02 | 1.1E+05 | 1.1E+05 | 5.4E+05 | 1.2E+04 | ND | ND | 6.8E+02 | 9.1E+02 |
| **12** | 26.73 | 1.8E+04 | 6.2E+04 | ND | 8.2E+02 | 1.6E+05 | 1.1E+05 | 5.1E+05 | 1.2E+04 | ND | ND | 6.4E+02 | 8.9E+02 |
| **13** | 29.77 | 1.8E+04 | 6.2E+04 | ND | 8.0E+02 | 1.8E+05 | 1.1E+05 | 4.9E+05 | 1.2E+04 | ND | 1.2E+03 | 5.7E+02 | 8.3E+02 |
| **14** | 31.72 | 1.6E+04 | 6.0E+04 | ND | 8.1E+02 | 1.4E+05 | 1.0E+05 | 4.8E+05 | 1.1E+04 | ND | ND | 6.0E+02 | 8.5E+02 |
| **15** | 33.81 | 1.7E+04 | 5.8E+04 | ND | 7.9E+02 | 1.6E+05 | 1.1E+05 | 4.7E+05 | 1.1E+04 | ND | 1.3E+03 | 5.7E+02 | 8.0E+02 |
| **16** | 36.74 | 1.5E+04 | 5.4E+04 | ND | 7.6E+02 | 1.8E+05 | 1.0E+05 | 4.4E+05 | 1.1E+04 | ND | 1.2E+03 | 5.0E+02 | 7.7E+02 |
| **17** | 38.78 | 1.6E+04 | 5.3E+04 | ND | 7.5E+02 | 1.7E+05 | 1.0E+05 | 4.4E+05 | 1.1E+04 | ND | 1.3E+03 | 5.5E+02 | 7.8E+02 |
| **18** | 40.85 | 1.5E+04 | 5.2E+04 | ND | 7.3E+02 | 1.9E+05 | 9.6E+04 | 4.3E+05 | 1.1E+04 | ND | 1.3E+03 | 4.5E+02 | 7.6E+02 |
| **19** | 43.80 | 1.5E+04 | 5.0E+04 | ND | 7.2E+02 | 1.9E+05 | 1.0E+05 | 4.1E+05 | 1.0E+04 | ND | 1.4E+03 | 4.9E+02 | 7.3E+02 |
| **20** | 45.80 | 1.5E+04 | 5.0E+04 | ND | 7.0E+02 | 1.7E+05 | 9.6E+04 | 4.2E+05 | 1.0E+04 | ND | 1.5E+03 | 4.9E+02 | 7.3E+02 |
| **21** | 47.79 | 1.5E+04 | 4.8E+04 | ND | 6.8E+02 | 1.9E+05 | 9.2E+04 | 3.9E+05 | 9.7E+03 | ND | 1.6E+03 | 5.0E+02 | 7.3E+02 |
| **22** | 50.76 | 1.6E+04 | 4.9E+04 | ND | 7.0E+02 | 2.0E+05 | 9.6E+04 | 3.9E+05 | 1.0E+04 | ND | 1.7E+03 | 4.2E+02 | 7.2E+02 |
| **23** | 52.88 | 1.4E+04 | 4.7E+04 | ND | 7.1E+02 | 1.8E+05 | 9.0E+04 | 3.8E+05 | 9.6E+03 | ND | 1.6E+03 | 4.1E+02 | 7.2E+02 |
| **24** | 54.75 | 1.5E+04 | 4.7E+04 | ND | 6.8E+02 | 1.8E+05 | 9.5E+04 | 3.8E+05 | 9.8E+03 | ND | 1.7E+03 | 4.5E+02 | 7.1E+02 |
| **25** | 57.24 | 1.4E+04 | 4.3E+04 | ND | 6.6E+02 | 2.0E+05 | 8.5E+04 | 3.6E+05 | 9.0E+03 | ND | 1.6E+03 | 4.6E+02 | 6.6E+02 |
| **26** | 60.08 | 1.7E+04 | 5.0E+04 | ND | 9.0E+02 | 1.9E+05 | 9.0E+04 | 3.8E+05 | 1.1E+04 | ND | 2.0E+03 | 4.4E+02 | 7.6E+02 |
| **27** | 61.98 | 1.9E+04 | 5.8E+04 | ND | 1.1E+03 | 2.2E+05 | 1.1E+05 | 4.6E+05 | 1.2E+04 | ND | 2.3E+03 | 5.5E+02 | 8.8E+02 |
| **28** | 64.75 | 1.8E+04 | 5.5E+04 | ND | 1.0E+03 | 2.3E+05 | 1.1E+05 | 4.3E+05 | 1.2E+04 | ND | 2.3E+03 | 4.9E+02 | 8.1E+02 |
| **29** | 66.76 | 1.7E+04 | 4.9E+04 | ND | 9.0E+02 | 1.9E+05 | 1.0E+05 | 4.0E+05 | 1.0E+04 | ND | 2.1E+03 | 4.6E+02 | 7.7E+02 |

**Table A.3**. (contd)

| Vial # | Time | Al | B | Ca | Cr | K | Si | Na | V | Zn | Zr | Cs | Re |
|---|---|---|---|---|---|---|---|---|---|---|---|---|---|
| | days | µg/L | µg/L | µg/L | µg/L | µg/L | µg/L | µg/L | µg/L | µg/L | µg/L | µg/L | µg/L |
| **30** | 68.74 | 1.8E+04 | 5.1E+04 | ND | 9.7E+02 | 2.1E+05 | 1.1E+05 | 4.0E+05 | 1.1E+04 | ND | 2.3E+03 | 4.8E+02 | 7.9E+02 |
| **31** | 71.79 | 1.4E+04 | 4.6E+04 | ND | 8.8E+02 | 2.1E+05 | 9.1E+04 | 3.6E+05 | 1.0E+04 | ND | 2.0E+03 | 3.9E+02 | 7.2E+02 |
| **32** | 73.73 | 1.5E+04 | 4.9E+04 | ND | 9.2E+02 | 1.8E+05 | 1.0E+05 | 3.9E+05 | 1.1E+04 | ND | 2.2E+03 | 4.2E+02 | 7.5E+02 |
| **33** | 75.73 | 1.7E+04 | 4.9E+04 | ND | 9.4E+02 | 2.2E+05 | 1.1E+05 | 4.1E+05 | 1.1E+04 | ND | 2.2E+03 | 4.9E+02 | 7.4E+02 |
| **34** | 78.90 | 1.5E+04 | 4.6E+04 | ND | 8.8E+02 | 2.4E+05 | 9.1E+04 | 3.7E+05 | 1.0E+04 | ND | 2.1E+03 | 3.7E+02 | 7.3E+02 |
| **35** | 80.96 | 1.6E+04 | 4.8E+04 | ND | 9.1E+02 | 1.4E+05 | 9.5E+04 | 3.8E+05 | 1.0E+04 | ND | 2.3E+03 | 3.9E+02 | 7.6E+02 |
| **36** | 82.89 | 1.6E+04 | 4.8E+04 | ND | 9.6E+02 | 1.7E+05 | 9.0E+04 | 3.7E+05 | 1.1E+04 | ND | 2.3E+03 | 4.3E+02 | 7.8E+02 |
| **37** | 85.73 | 1.5E+04 | 4.4E+04 | ND | 8.6E+02 | 1.8E+05 | 8.7E+04 | 3.5E+05 | 9.7E+03 | ND | 2.3E+03 | 3.9E+02 | 6.7E+02 |
| **38** | 87.87 | 1.6E+04 | 4.6E+04 | ND | 9.2E+02 | 1.7E+05 | 9.3E+04 | 3.8E+05 | 1.0E+04 | ND | 2.5E+03 | 4.1E+02 | 7.4E+02 |
| **39** | 89.72 | 1.6E+04 | 4.4E+04 | ND | 8.9E+02 | 1.7E+05 | 9.2E+04 | 3.7E+05 | 9.9E+03 | ND | 2.4E+03 | 3.8E+02 | 7.5E+02 |
| **40** | 92.73 | 1.4E+04 | 4.1E+04 | ND | 8.2E+02 | 2.0E+05 | 8.3E+04 | 3.4E+05 | 9.3E+03 | ND | 2.1E+03 | 3.8E+02 | 6.8E+02 |
| **41** | 95.24 | 1.4E+04 | 4.1E+04 | ND | 8.2E+02 | 1.9E+05 | 8.6E+04 | 3.4E+05 | 9.3E+03 | ND | 2.2E+03 | 3.8E+02 | 6.9E+02 |
| **42** | 96.77 | 1.4E+04 | 4.2E+04 | ND | 8.2E+02 | 2.5E+05 | 8.6E+04 | 3.6E+05 | 9.6E+03 | ND | 2.3E+03 | 4.0E+02 | 6.8E+02 |
| **43** | 99.92 | 1.4E+04 | 3.9E+04 | ND | 8.1E+02 | 2.2E+05 | 8.9E+04 | 3.4E+05 | 9.1E+03 | ND | 2.4E+03 | 3.1E+02 | 6.8E+02 |
| **44** | 102.04 | 1.4E+04 | 3.8E+04 | ND | 8.0E+02 | 1.8E+05 | 7.8E+04 | 3.3E+05 | 9.1E+03 | ND | 2.4E+03 | 3.4E+02 | 6.3E+02 |
| **45** | 103.79 | 1.5E+04 | 4.2E+04 | ND | 9.0E+02 | 2.2E+05 | 8.7E+04 | 3.5E+05 | 9.7E+03 | 3.2E+02 | 2.6E+03 | 3.7E+02 | 7.4E+02 |
| **46** | 106.96 | 1.4E+04 | 3.9E+04 | ND | 8.3E+02 | 2.4E+05 | 8.3E+04 | 3.2E+05 | 9.1E+03 | ND | 2.6E+03 | 3.0E+02 | 6.6E+02 |
| **47** | 108.72 | 1.3E+04 | 4.0E+04 | ND | 8.6E+02 | 2.0E+05 | 8.1E+04 | 3.4E+05 | 9.3E+03 | ND | 2.5E+03 | 3.5E+02 | 6.7E+02 |
| **48** | 110.73 | 1.4E+04 | 4.0E+04 | ND | 8.5E+02 | 2.0E+05 | 8.3E+04 | 3.4E+05 | 9.3E+03 | ND | 2.6E+03 | 3.8E+02 | 6.7E+02 |
| **49** | 113.68 | 1.3E+04 | 4.0E+04 | ND | 8.5E+02 | 2.3E+05 | 8.0E+04 | 3.2E+05 | 9.1E+03 | ND | 2.6E+03 | 3.1E+02 | 6.6E+02 |
| **50** | 116.03 | 1.3E+04 | 3.8E+04 | ND | 8.2E+02 | 1.8E+05 | 8.0E+04 | 3.4E+05 | 8.7E+03 | ND | 2.6E+03 | 3.2E+02 | 6.7E+02 |
| **51** | 118.67 | 1.5E+04 | 3.7E+04 | ND | 7.9E+02 | 1.3E+05 | 8.0E+04 | 3.2E+05 | 8.7E+03 | 4.0E+02 | 2.8E+03 | 3.1E+02 | 6.5E+02 |
| **52** | 122.63 | 1.3E+04 | 3.8E+04 | ND | 8.4E+02 | 2.1E+05 | 7.9E+04 | 3.2E+05 | 9.3E+03 | ND | 2.7E+03 | 2.9E+02 | 6.8E+02 |
| **53** | 124.74 | 1.4E+04 | 3.9E+04 | ND | 8.9E+02 | 2.0E+05 | 8.3E+04 | 3.2E+05 | 9.2E+03 | 3.5E+02 | 2.9E+03 | 3.5E+02 | 6.8E+02 |
| **54** | 127.79 | 1.3E+04 | 3.7E+04 | ND | 8.2E+02 | 2.2E+05 | 7.2E+04 | 3.0E+05 | 8.7E+03 | ND | 2.6E+03 | 2.7E+02 | 6.5E+02 |
| **55** | 130.74 | 1.3E+04 | 3.5E+04 | ND | 7.8E+02 | 1.7E+05 | 7.2E+04 | 2.9E+05 | 8.4E+03 | ND | 2.6E+03 | 2.5E+02 | 6.3E+02 |
| **56** | 134.73 | 1.2E+04 | 3.7E+04 | ND | 8.2E+02 | 2.6E+05 | 7.5E+04 | 3.0E+05 | 9.0E+03 | ND | 2.7E+03 | 2.9E+02 | 6.9E+02 |
| **57** | 136.66 | 1.3E+04 | 3.5E+04 | ND | 8.0E+02 | 1.1E+05 | 7.2E+04 | 3.1E+05 | 8.4E+03 | 3.0E+02 | 2.6E+03 | 2.4E+02 | 6.1E+02 |
| **58** | 138.71 | 1.2E+04 | 3.3E+04 | ND | 7.7E+02 | 1.8E+05 | 7.0E+04 | 2.8E+05 | 8.0E+03 | 4.4E+02 | 2.5E+03 | 3.5E+02 | 5.9E+02 |
| **59** | 141.69 | 1.2E+04 | 3.4E+04 | ND | 7.7E+02 | 2.2E+05 | 7.1E+04 | 2.9E+05 | 8.3E+03 | ND | 2.6E+03 | 3.0E+02 | 6.0E+02 |

**Table A.3**. (contd)

| Vial # | Time | Al | B | Ca | Cr | K | Si | Na | V | Zn | Zr | Cs | Re |
|---|---|---|---|---|---|---|---|---|---|---|---|---|---|
| | days | µg/L | µg/L | µg/L | µg/L | µg/L | µg/L | µg/L | µg/L | µg/L | µg/L | µg/L | µg/L |
| **60** | 143.64 | 1.3E+04 | 3.3E+04 | ND | 7.9E+02 | 1.7E+05 | 7.1E+04 | 2.9E+05 | 7.9E+03 | 3.4E+02 | 2.6E+03 | 3.1E+02 | 6.1E+02 |
| **61** | 145.71 | 1.3E+04 | 3.2E+04 | ND | 1.1E+03 | 1.7E+05 | 7.1E+04 | 2.7E+05 | 7.9E+03 | ND | 2.7E+03 | 3.1E+02 | 5.6E+02 |
| **62** | 148.66 | 1.2E+04 | 3.2E+04 | ND | 7.5E+02 | 1.9E+05 | 6.6E+04 | 2.5E+05 | 7.8E+03 | ND | 2.5E+03 | 2.6E+02 | 5.8E+02 |
| **63** | 150.78 | 1.3E+04 | 3.3E+04 | ND | 7.2E+02 | 3.1E+05 | 6.6E+04 | 3.0E+05 | 8.1E+03 | ND | 2.7E+03 | 2.8E+02 | 5.9E+02 |
| **64** | 152.68 | 1.2E+04 | 3.1E+04 | ND | 7.1E+02 | 3.3E+05 | 6.7E+04 | 2.7E+05 | 7.7E+03 | ND | 2.6E+03 | 2.6E+02 | 5.6E+02 |
| **65** | 155.60 | 1.3E+04 | 3.3E+04 | ND | 7.7E+02 | 3.7E+04 | 7.3E+04 | 2.6E+05 | 7.9E+03 | ND | 2.8E+03 | 1.8E+02 | 6.1E+02 |
| **66** | 157.70 | 1.4E+04 | 3.1E+04 | ND | 7.5E+02 | 1.3E+04 | 7.6E+04 | 2.6E+05 | 7.9E+03 | ND | 2.9E+03 | 1.6E+02 | 6.3E+02 |
| **67** | 159.82 | 1.3E+04 | 3.1E+04 | ND | 7.9E+02 | 6.6E+03 | 7.6E+04 | 2.5E+05 | 7.8E+03 | ND | 2.7E+03 | 1.4E+02 | 5.8E+02 |
| **68** | 162.62 | 1.3E+04 | 3.4E+04 | ND | 8.3E+02 | 6.9E+03 | 7.9E+04 | 2.7E+05 | 8.3E+03 | ND | 2.9E+03 | 2.1E+02 | 6.2E+02 |
| **69** | 164.60 | 1.3E+04 | 3.4E+04 | ND | 8.3E+02 | 6.6E+03 | 8.1E+04 | 2.8E+05 | 8.2E+03 | ND | 3.0E+03 | 2.8E+02 | 6.0E+02 |
| **70** | 166.76 | 1.3E+04 | 3.1E+04 | ND | 8.1E+02 | 9.0E+04 | 7.4E+04 | 2.6E+05 | 7.5E+03 | 3.5E+02 | 2.7E+03 | 4.3E+02 | 5.9E+02 |
| **71** | 169.66 | 1.2E+04 | 3.2E+04 | ND | 7.7E+02 | 1.4E+05 | 7.3E+04 | 2.7E+05 | 7.7E+03 | ND | 2.8E+03 | 4.3E+02 | 5.9E+02 |
| **72** | 171.82 | 1.2E+04 | 3.2E+04 | ND | 7.7E+02 | 1.4E+05 | 7.3E+04 | 2.6E+05 | 7.7E+03 | ND | 2.8E+03 | 3.5E+02 | 5.7E+02 |
| **73** | 173.77 | 1.2E+04 | 3.3E+04 | ND | 8.1E+02 | 1.6E+05 | 7.6E+04 | 2.7E+05 | 7.9E+03 | ND | 3.1E+03 | 3.5E+02 | 5.7E+02 |
| **74** | 178.64 | 1.2E+04 | 3.1E+04 | ND | 7.6E+02 | 1.8E+05 | 7.0E+04 | 2.5E+05 | 7.5E+03 | ND | 2.7E+03 | 2.9E+02 | 5.7E+02 |
| **75** | 183.62 | 1.1E+04 | 3.1E+04 | ND | 7.5E+02 | 2.0E+05 | 7.1E+04 | 2.5E+05 | 7.6E+03 | ND | 2.8E+03 | 2.6E+02 | 5.4E+02 |
| **76** | 190.60 | 1.2E+04 | 3.0E+04 | ND | 7.5E+02 | 1.7E+05 | 6.9E+04 | 2.4E+05 | 7.3E+03 | 3.1E+02 | 2.7E+03 | 2.6E+02 | 5.3E+02 |
| **77** | 197.54 | 1.2E+04 | 3.5E+04 | ND | 8.3E+02 | 1.7E+05 | 6.6E+04 | 2.7E+05 | 8.3E+03 | 3.1E+02 | 2.9E+03 | NM | 6.5E+02 |
| **78** | 205.65 | 1.2E+04 | 3.3E+04 | ND | 7.9E+02 | 2.1E+05 | 6.4E+04 | 2.5E+05 | 7.6E+03 | ND | 2.7E+03 | NM | 6.1E+02 |
| **79** | 212.60 | 1.2E+04 | 3.4E+04 | ND | 8.3E+02 | 2.0E+05 | 6.7E+04 | 2.5E+05 | 8.1E+03 | ND | 2.9E+03 | NM | 6.5E+02 |
| **80** | 218.68 | 1.2E+04 | 3.4E+04 | ND | 8.3E+02 | 1.9E+05 | 7.1E+04 | 2.6E+05 | 8.0E+03 | ND | 3.1E+03 | NM | 6.5E+02 |
| **81** | 225.70 | 1.1E+04 | 3.2E+04 | ND | 7.9E+02 | 2.1E+05 | 6.3E+04 | 2.4E+05 | 7.5E+03 | ND | 2.8E+03 | NM | 6.3E+02 |
| **82** | 232.60 | 1.1E+04 | 3.2E+04 | ND | 7.8E+02 | 2.1E+05 | 6.2E+04 | 2.3E+05 | 7.6E+03 | ND | 2.7E+03 | NM | 6.1E+02 |
| **83** | 239.58 | 1.0E+04 | 3.1E+04 | ND | 7.8E+02 | 2.1E+05 | 6.0E+04 | 2.3E+05 | 7.5E+03 | 3.5E+02 | 2.7E+03 | NM | 6.0E+02 |
| **84** | 246.70 | 1.0E+04 | 3.1E+04 | ND | 7.9E+02 | 2.5E+05 | 5.7E+04 | 2.4E+05 | 7.7E+03 | 3.4E+02 | 2.7E+03 | NM | 6.6E+02 |
| **85** | 253.54 | 9.8E+03 | 3.0E+04 | ND | 7.8E+02 | 2.2E+05 | 5.8E+04 | 2.1E+05 | 7.4E+03 | 3.8E+02 | 2.6E+03 | NM | 6.1E+02 |
| **86** | 260.73 | 1.0E+04 | 3.0E+04 | ND | 7.8E+02 | 2.3E+05 | 6.0E+04 | 2.2E+05 | 7.7E+03 | 3.6E+02 | 2.7E+03 | NM | 6.1E+02 |
| **87** | 267.49 | 9.4E+03 | 3.0E+04 | ND | 7.7E+02 | 2.4E+05 | 5.3E+04 | 2.1E+05 | 7.5E+03 | 3.5E+02 | 2.5E+03 | NM | 6.2E+02 |
| **88** | 274.57 | 9.1E+03 | 3.0E+04 | ND | 7.9E+02 | 2.6E+05 | 5.4E+04 | 2.1E+05 | 7.5E+03 | ND | 2.7E+03 | NM | 6.4E+02 |
| **89** | 282.43 | 1.0E+04 | 3.1E+04 | ND | 8.1E+02 | 2.5E+05 | 5.5E+04 | 2.2E+05 | 7.6E+03 | ND | 2.9E+03 | NM | 6.1E+02 |

**Table A.3**. (contd)

| Vial # | Time | Al | B | Ca | Cr | K | Si | Na | V | Zn | Zr | Cs | Re |
|---|---|---|---|---|---|---|---|---|---|---|---|---|---|
| | days | µg/L | µg/L | µg/L | µg/L | µg/L | µg/L | µg/L | µg/L | µg/L | µg/L | µg/L | µg/L |
| **90** | 288.48 | 9.5E+03 | 2.9E+04 | ND | 7.6E+02 | 2.6E+05 | 5.5E+04 | 2.1E+05 | 7.4E+03 | ND | 2.7E+03 | NM | 6.3E+02 |
| **91** | 296.43 | 9.7E+03 | 3.8E+04 | ND | 9.7E+02 | 6.2E+05 | 5.9E+04 | 3.0E+05 | 9.4E+03 | 3.0E+02 | 3.3E+03 | NM | 7.7E+02 |
| **92** | 302.43 | 3.7E+02 | 2.6E+03 | ND | 1.2E+02 | 3.2E+05 | 3.9E+04 | 3.0E+04 | 6.5E+02 | ND | ND | NM | ND |
| **93** | 309.42 | 2.2E+02 | ND | ND | ND | 2.8E+05 | 2.0E+04 | 1.5E+03 | ND | ND | ND | NM | ND |

ND indicates “not detected” below quantification level.

# Appendix B

# PCT (90ºC) Modeling Results

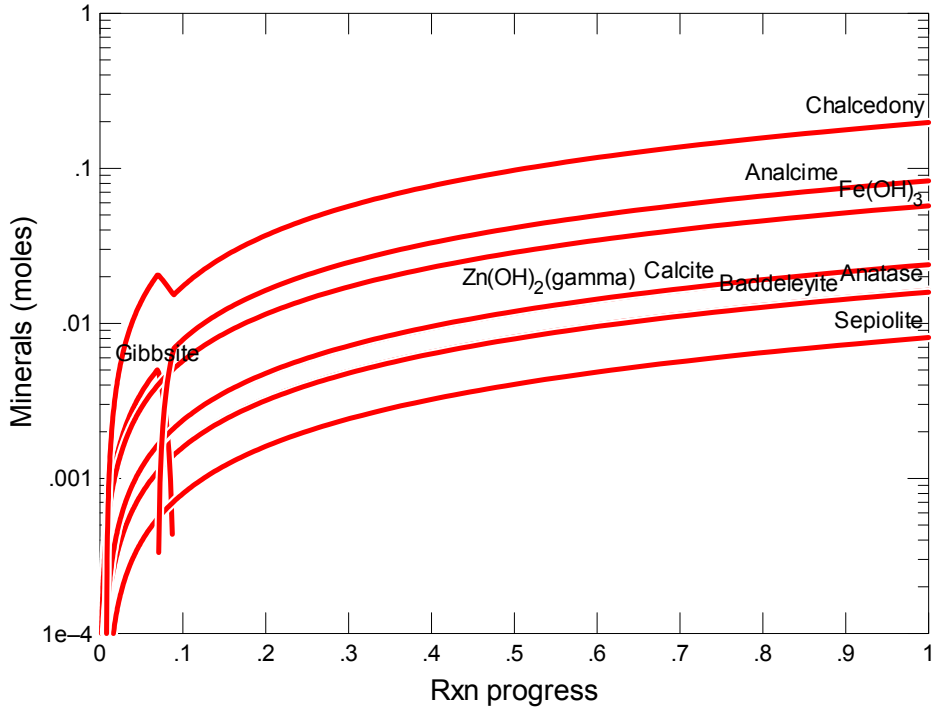


**Figure B.1**. Secondary Phases Calculated to Form as a Function of Reaction Progress (mol-glass/kg) Determined for Glass Sample A1-AN105R2

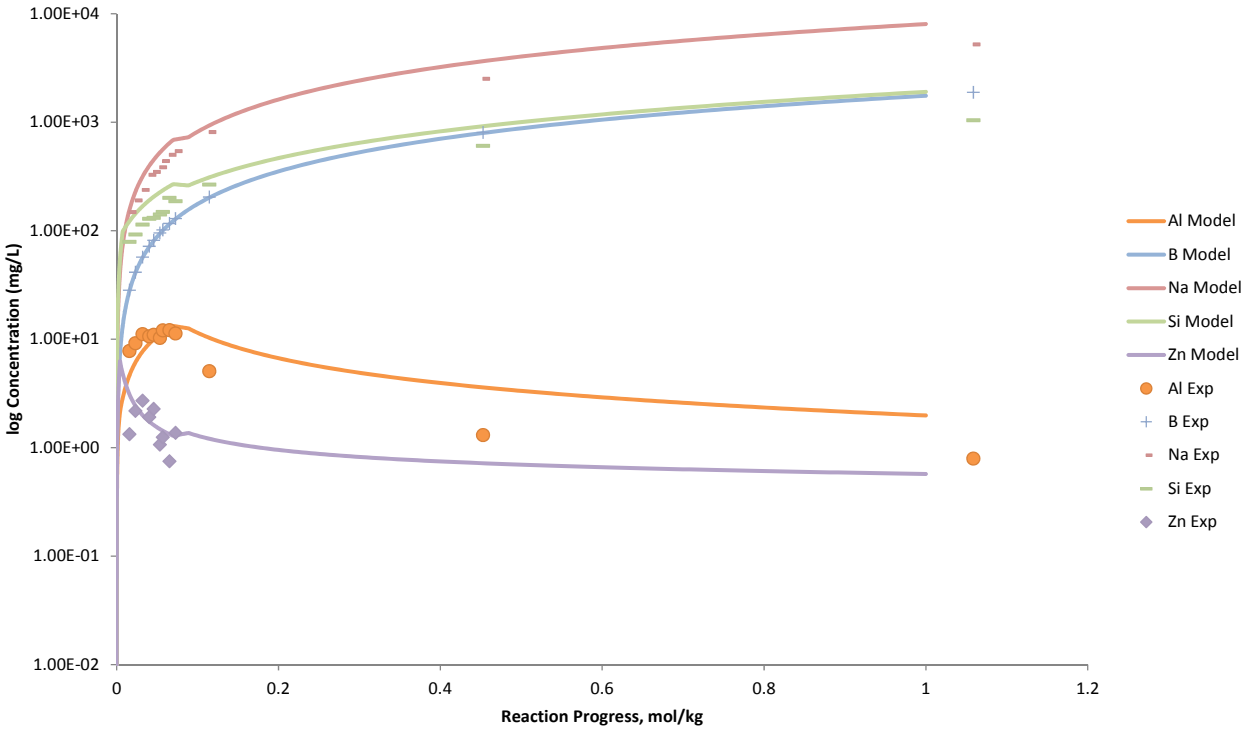


**Figure B.2**. Measured Solution Concentrations (mg/L) and Model Results for Al, B, Na, Si, and Zn, as a Function of Reaction Progress (mol-glass/kg) Determined for Glass Sample A1-AN105R2

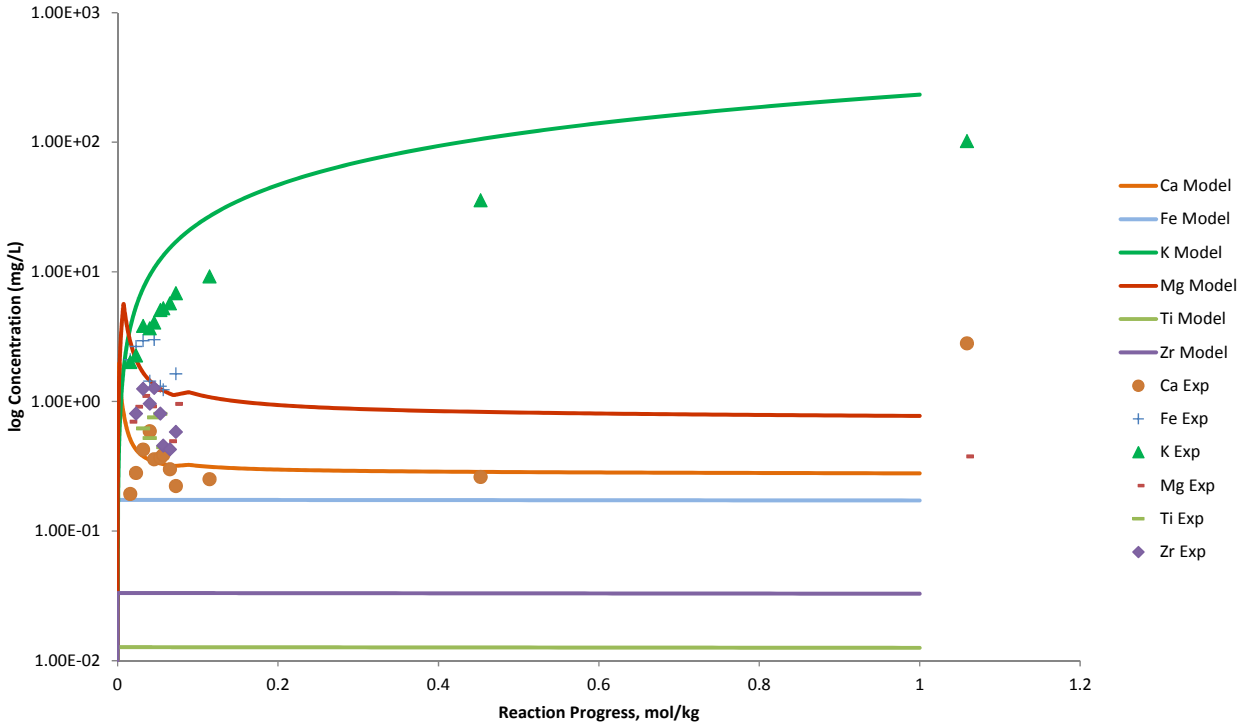


**Figure B.3**. Measured Solution Concentrations (mg/L) and Model Results for Ca, Fe, K, Li, Mg, Ti, and Zr, as a Function of Reaction Progress (mol-glass/kg) Determined for Glass Sample A1-AN105R2

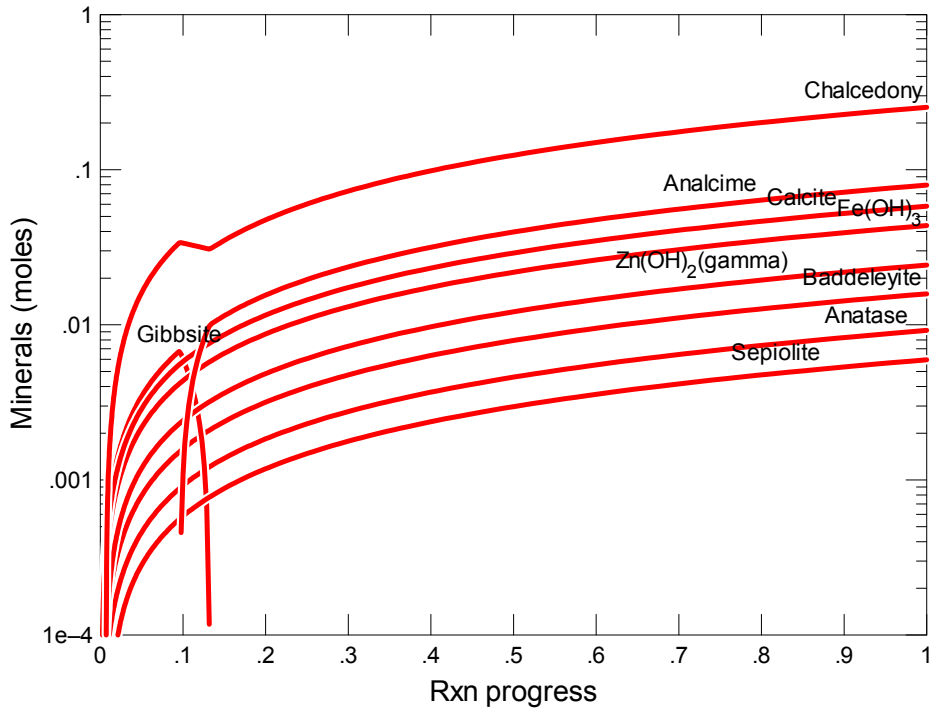


**Figure B.4**. Secondary Phases Calculated to Form as a Function of Reaction Progress (mol-glass/kg) Determined for Glass Sample A100CC

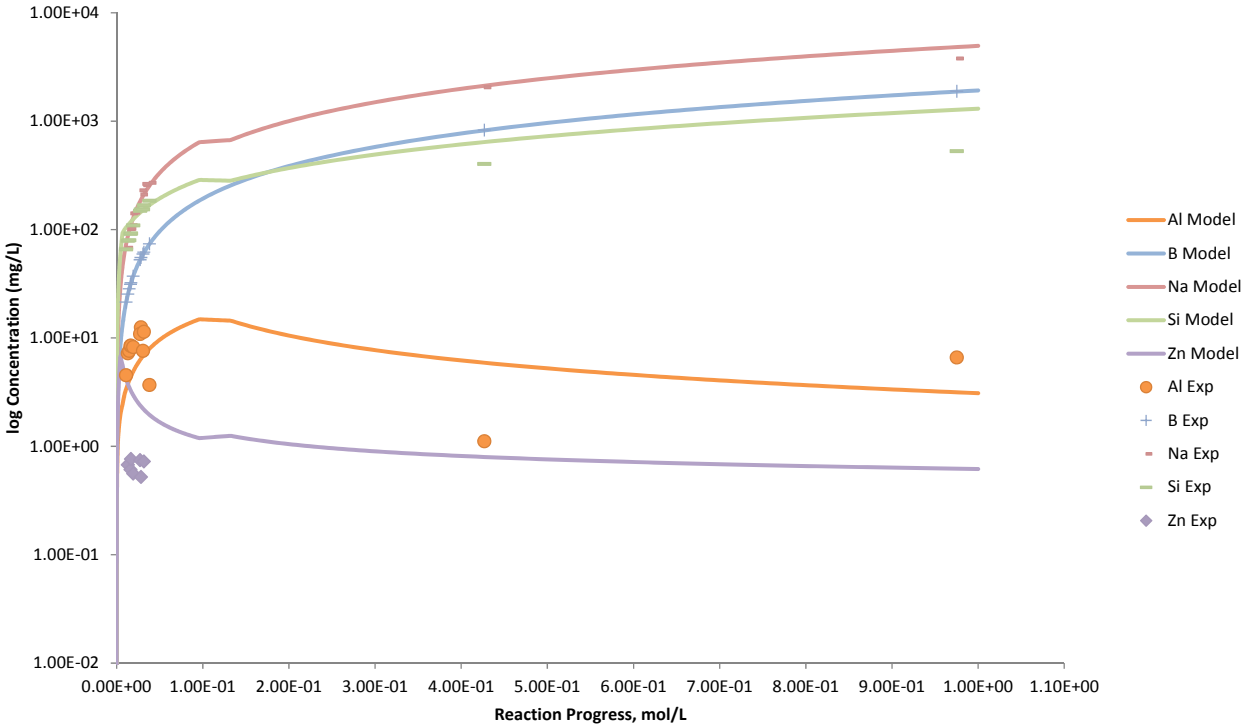


**Figure B.5**. Measured Solution Concentrations (mg/L) and Model Results for Al, B, Na, Si, and Zn, as a Function of Reaction Progress (mol-glass/kg) Determined for Glass Sample A100CC

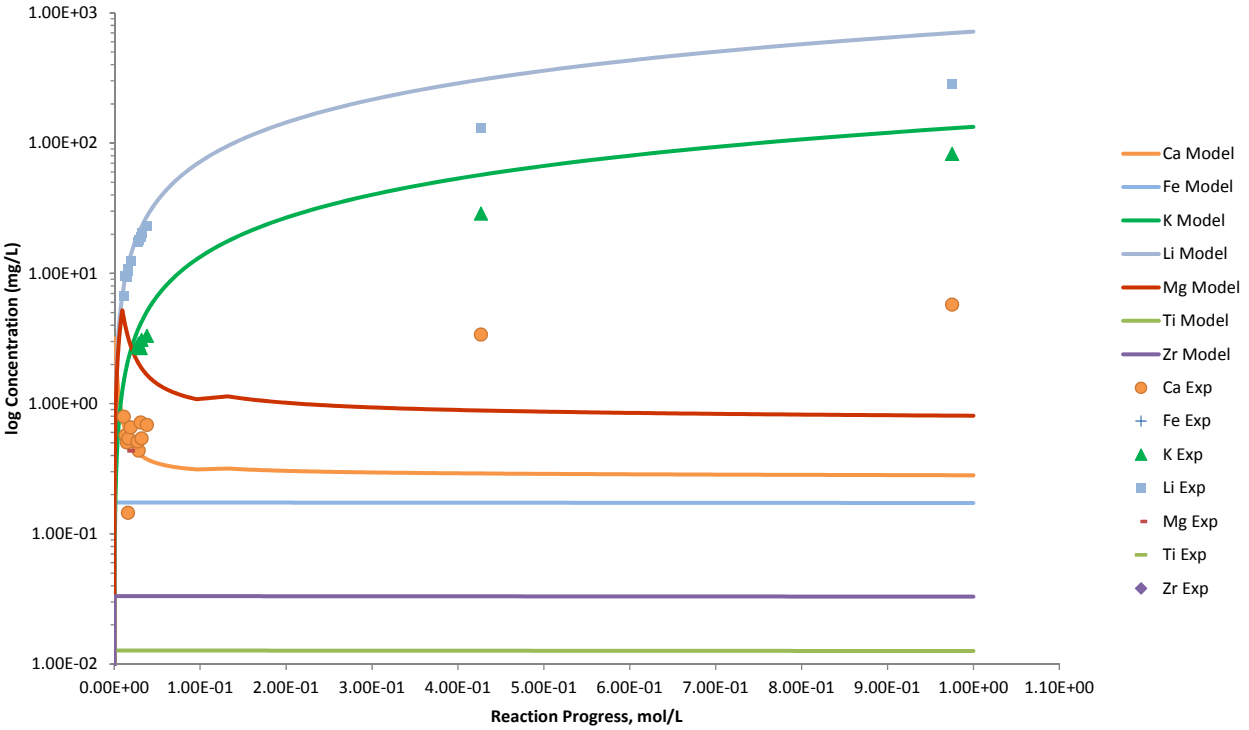


**Figure B.6**. Measured Solution Concentrations (mg/L) and Model Results for Ca, Fe, K, Li, Mg, Ti, and Zr, as a Function of Reaction Progress (mol-glass/kg) Determined for Glass Sample A100CC

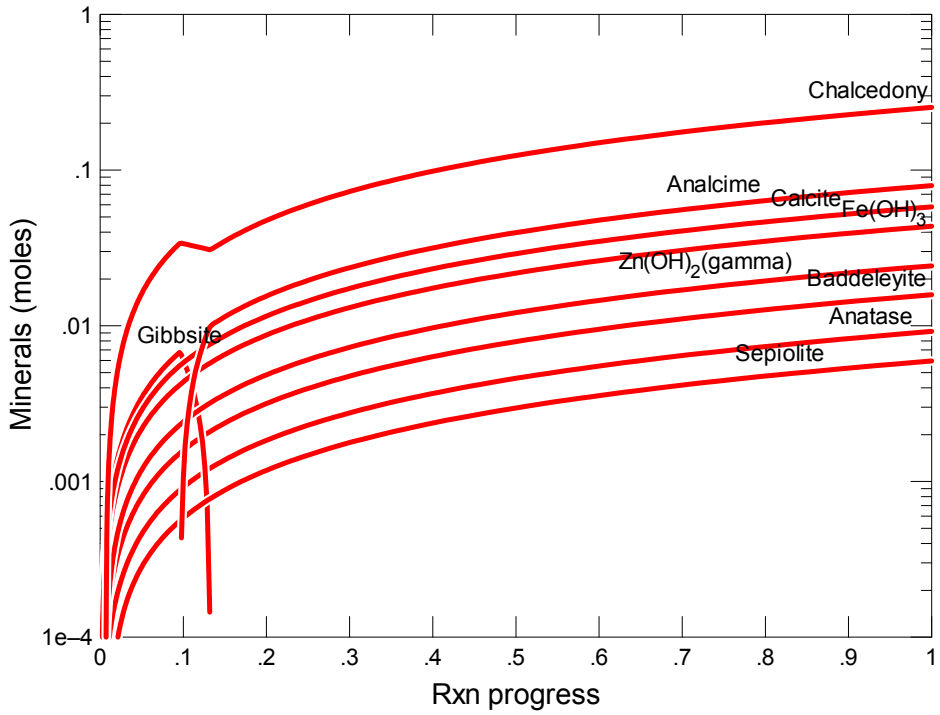


**Figure B.7**. Secondary Phases Calculated to Form as a Function of Reaction Progress (mol-glass/kg) Determined for Glass Sample A100G115A

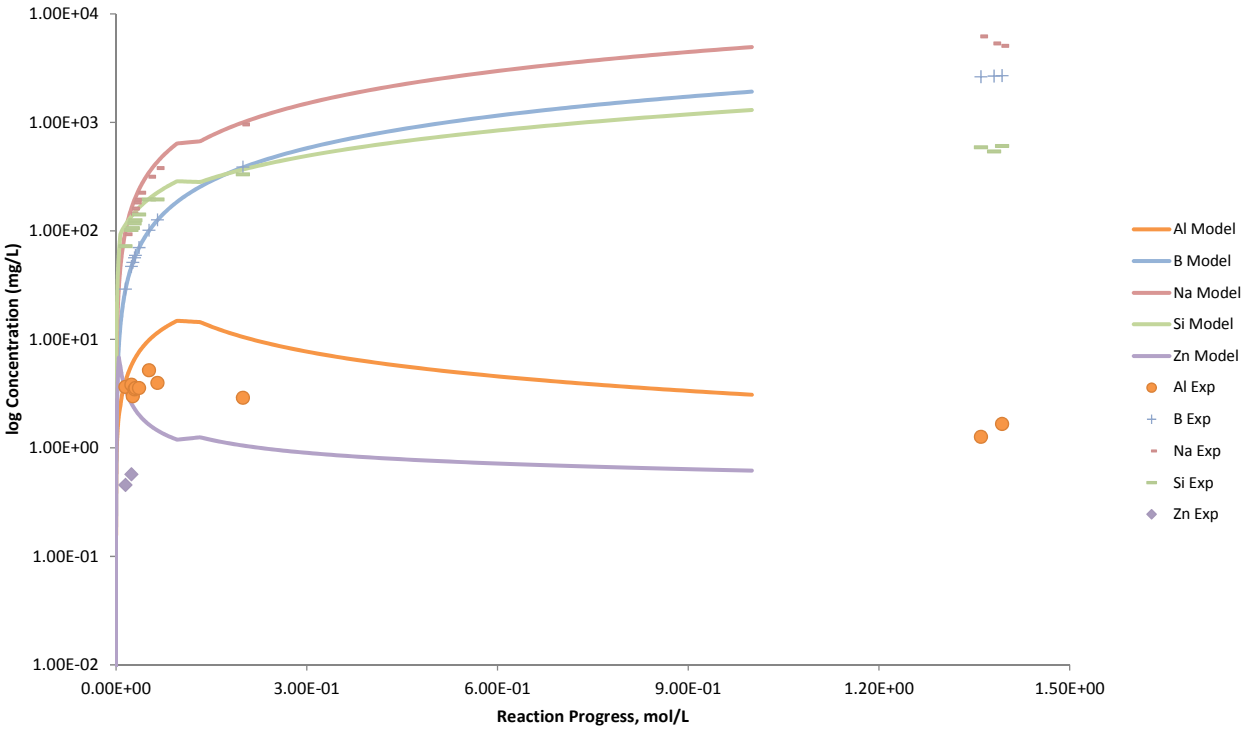


**Figure B.8**. Measured Solution Concentrations (mg/L) and Model Results for Al, B, Na, Si, and Zn, as a Function of Reaction Progress (mol-glass/kg) Determined for Glass Sample A100G115A

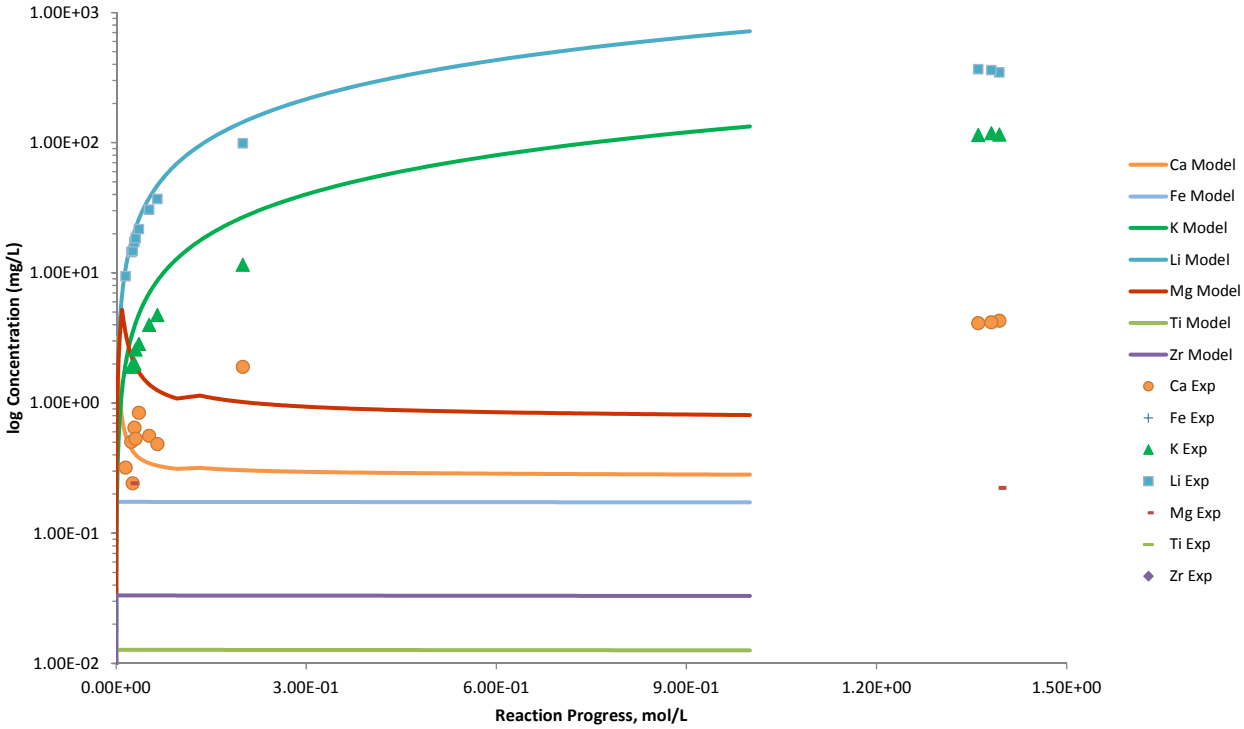


**Figure B.9**. Measured Solution Concentrations (mg/L) and Model Results for Ca, Fe, K, Li, Mg, Ti, and Zr, as a Function of Reaction Progress (mol-glass/kg) Determined for Glass Sample A100G115A

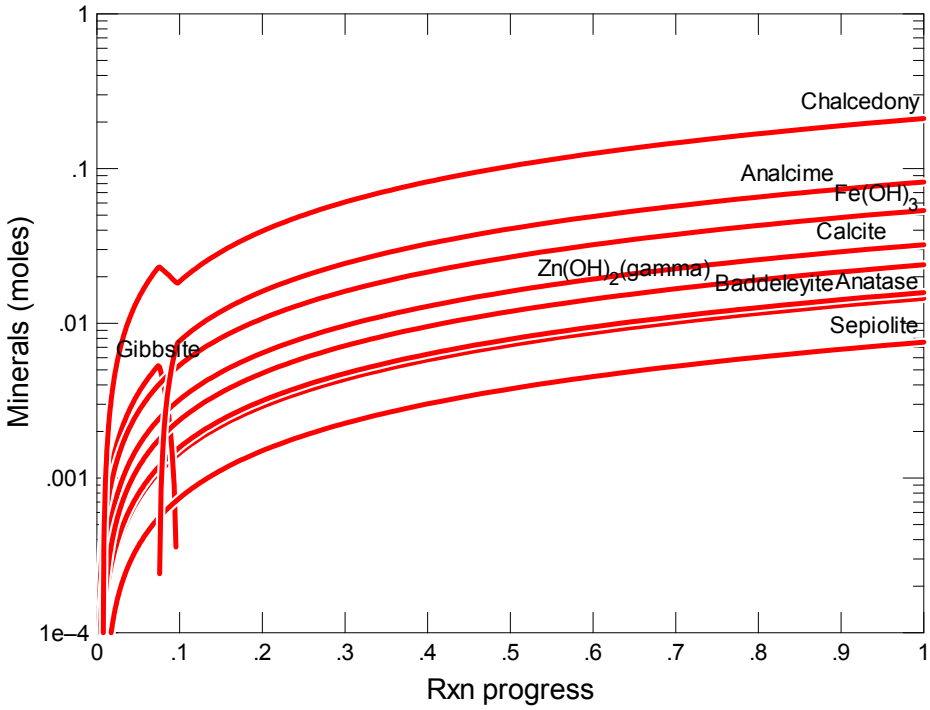


**Figure B.10**. Secondary Phases Calculated to Form as a Function of Reaction Progress (mol-glass/kg) Determined for Glass Sample A1C1-1

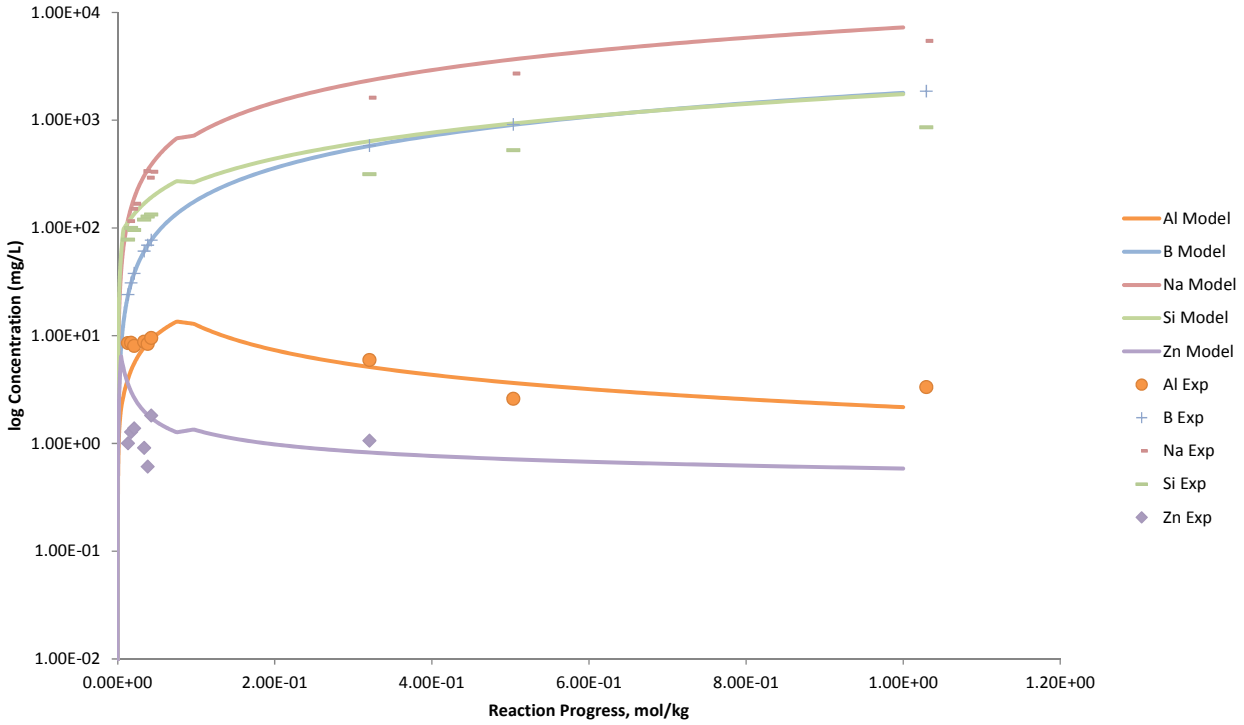


**Figure B.11**. Measured Solution Concentrations (mg/L) and Model Results for Al, B, Na, Si, and Zn, as a Function of Reaction Progress (mol-glass/kg) Determined for Glass Sample A1C1-1

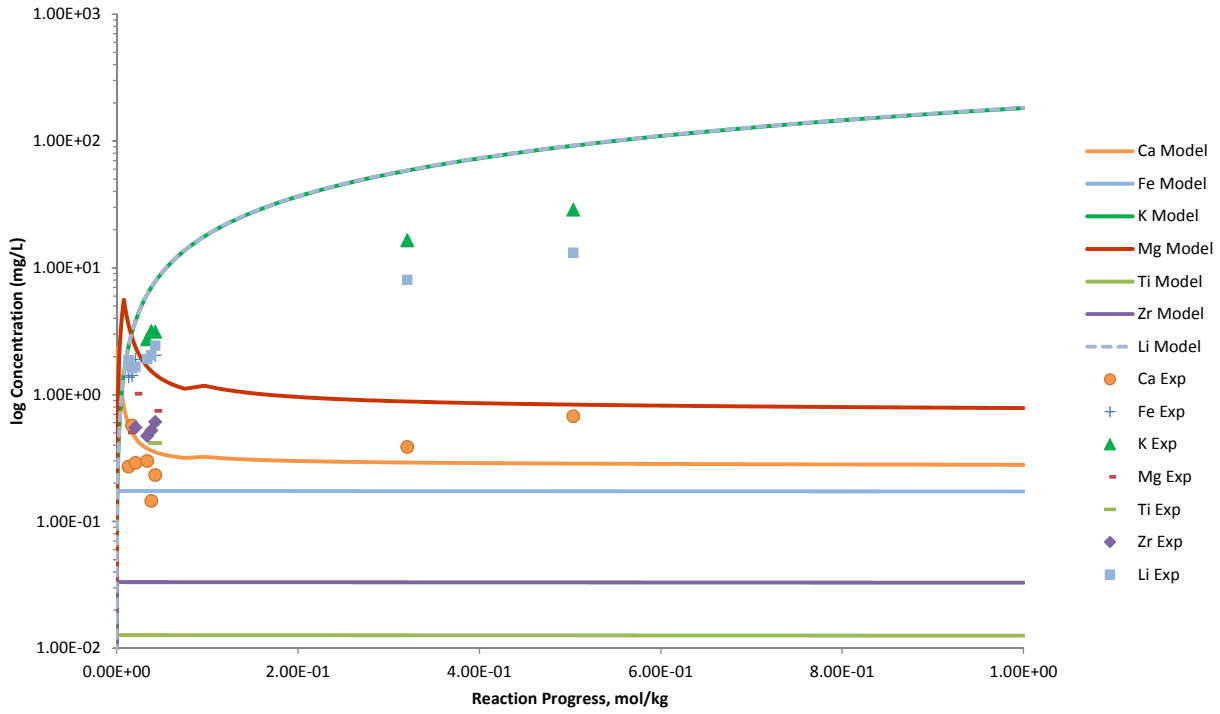


**Figure B.12**. Measured Solution Concentrations (mg/L) and Model Results for Ca, Fe, K, Li, Mg, Ti, and Zr, as a Function of Reaction Progress (mol-glass/kg) Determined for Glass Sample A1C1-1

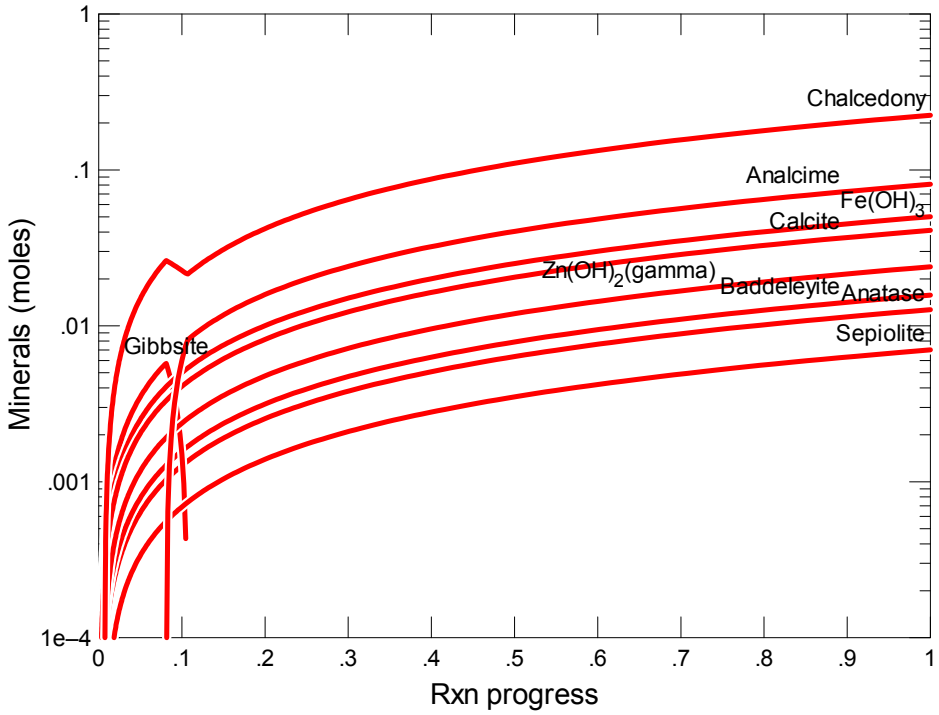


**Figure B.13**. Secondary Phases Calculated to Form as a Function of Reaction Progress (mol-glass/kg) Determined for Glass Sample A1C1-2

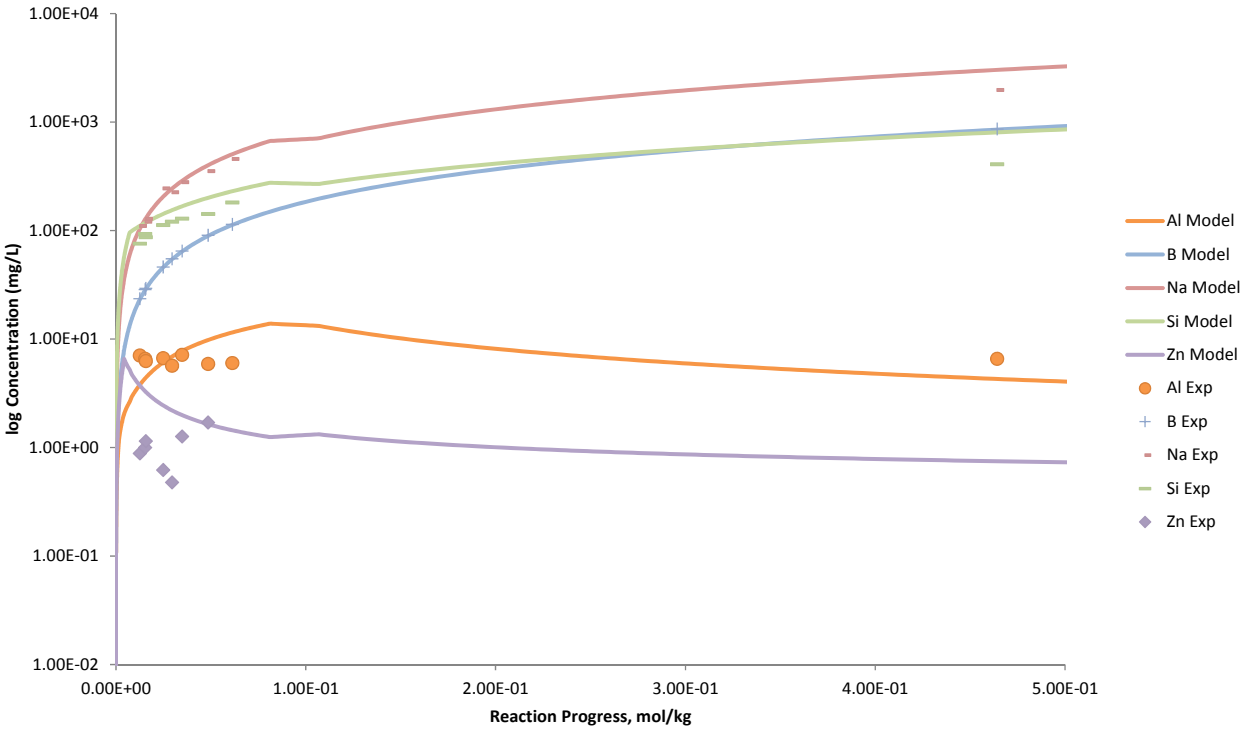


**Figure B.14**. Measured Solution Concentrations (mg/L) and Model Results for Al, B, Na, Si, and Zn, as a Function of Reaction Progress (mol-glass/kg) Determined for Glass Sample A1C1-2

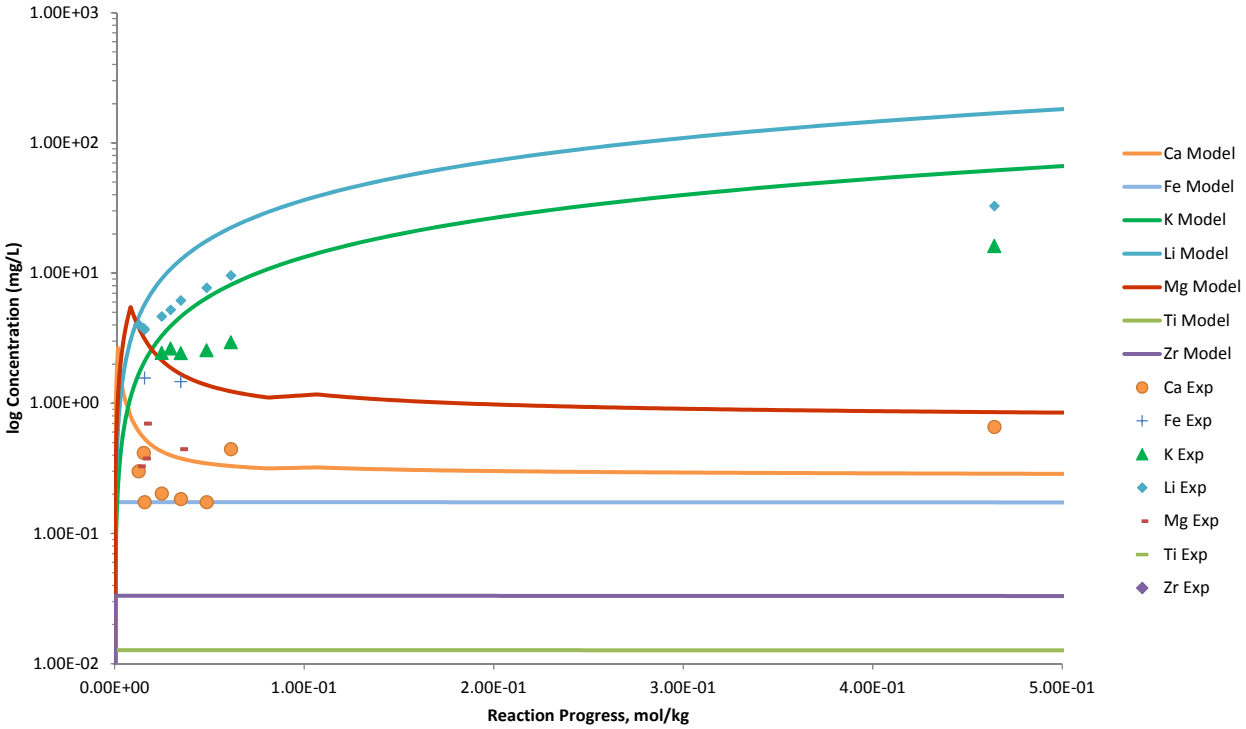


**Figure B.15**. Measured Solution Concentrations (mg/L) and Model Results for Ca, Fe, K, Li, Mg, Ti, and Zr, as a Function of Reaction Progress (mol-glass/kg) Determined for Glass Sample A1C1-2

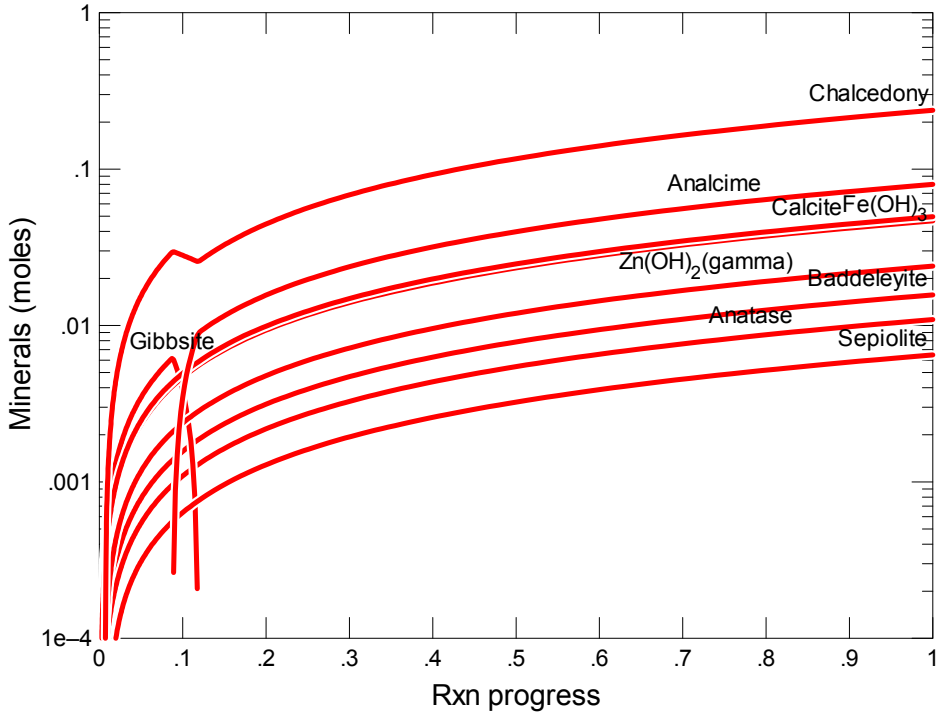


**Figure B.16**. Secondary Phases Calculated to Form as a Function of Reaction Progress (mol-glass/kg) Determined for Glass Sample A1C1-3

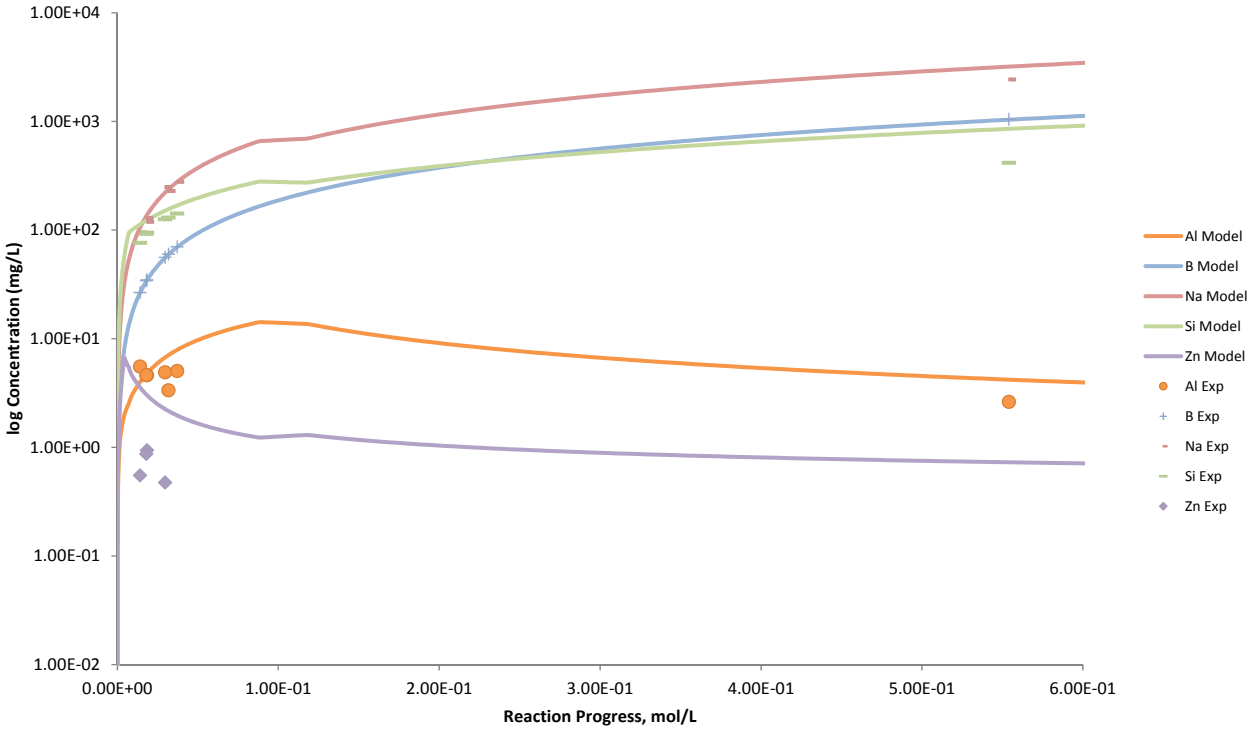


**Figure B.17**. Measured Solution Concentrations (mg/L) and Model Results for Al, B, Na, Si, and Zn, as a Function of Reaction Progress (mol-glass/kg) Determined for Glass Sample A1C1-3

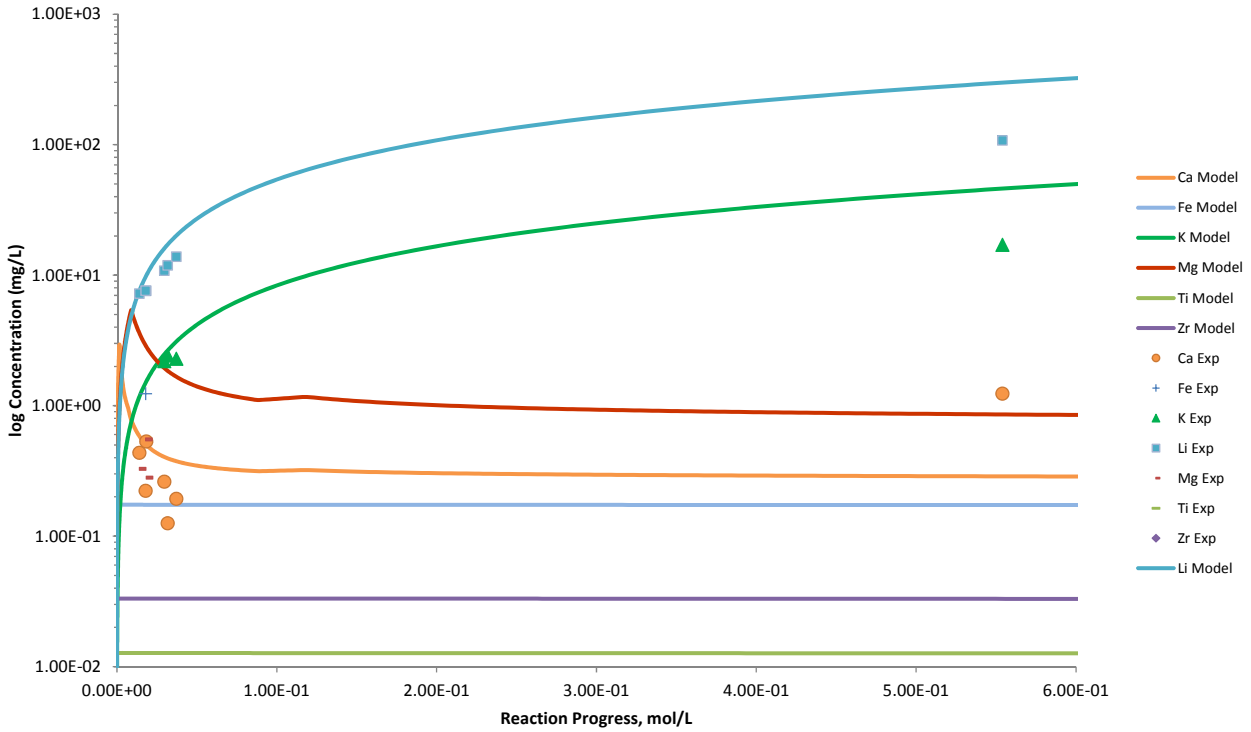


**Figure B.18**. Measured Solution Concentrations (mg/L) and Model Results for Ca, Fe, K, Li, Mg, Ti, and Zr, as a Function of Reaction Progress (mol-glass/kg) Determined for Glass Sample A1C1-3

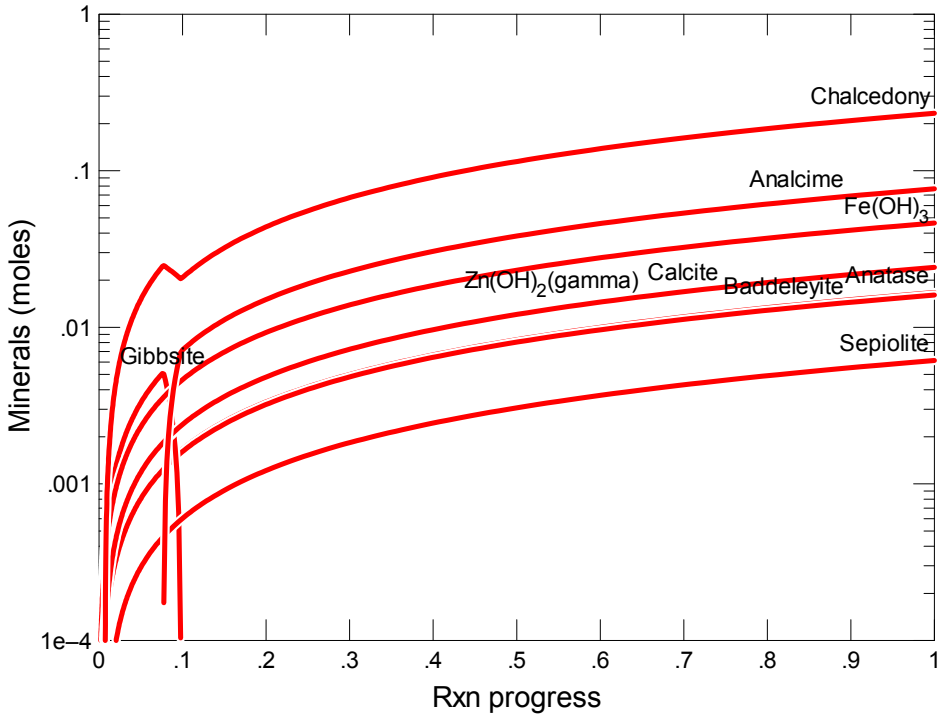


**Figure B.19**. Secondary Phases Calculated to Form as a Function of Reaction Progress (mol-glass/kg) Determined for Glass Sample A2-AP101

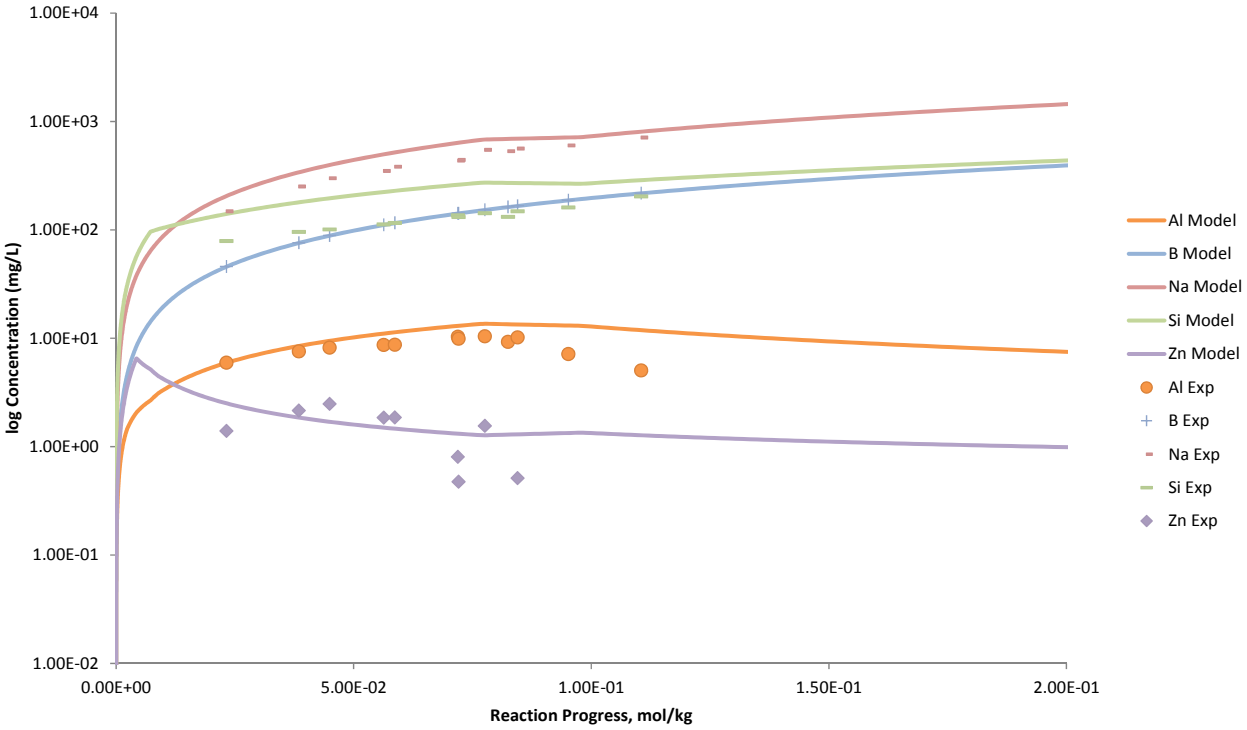


**Figure B.20**. Measured Solution Concentrations (mg/L) and Model Results for Al, B, Na, Si, and Zn, as a Function of Reaction Progress (mol-glass/kg) Determined for Glass Sample A2-AP101

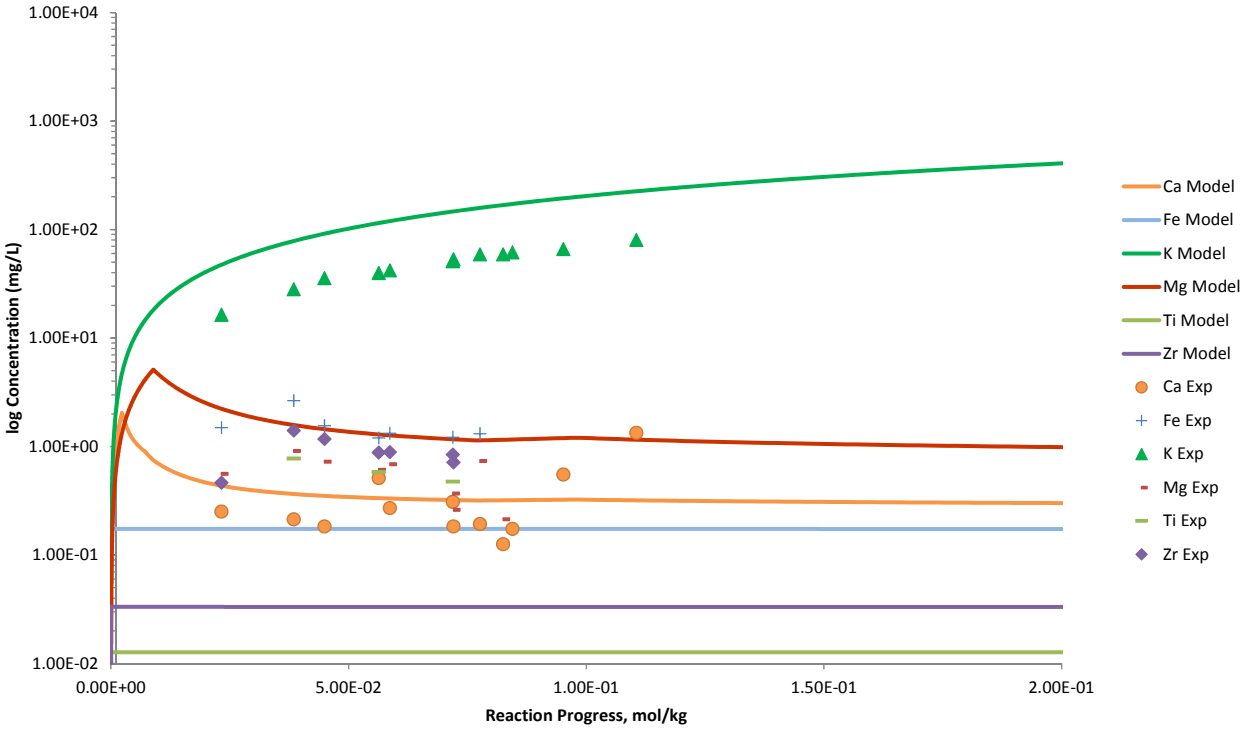


**Figure B.21**. Measured Solution Concentrations (mg/L) and Model Results for Ca, Fe, K, Li, Mg, Ti, and Zr, as a Function of Reaction Progress (mol-glass/kg) Determined for Glass Sample A2-AP101

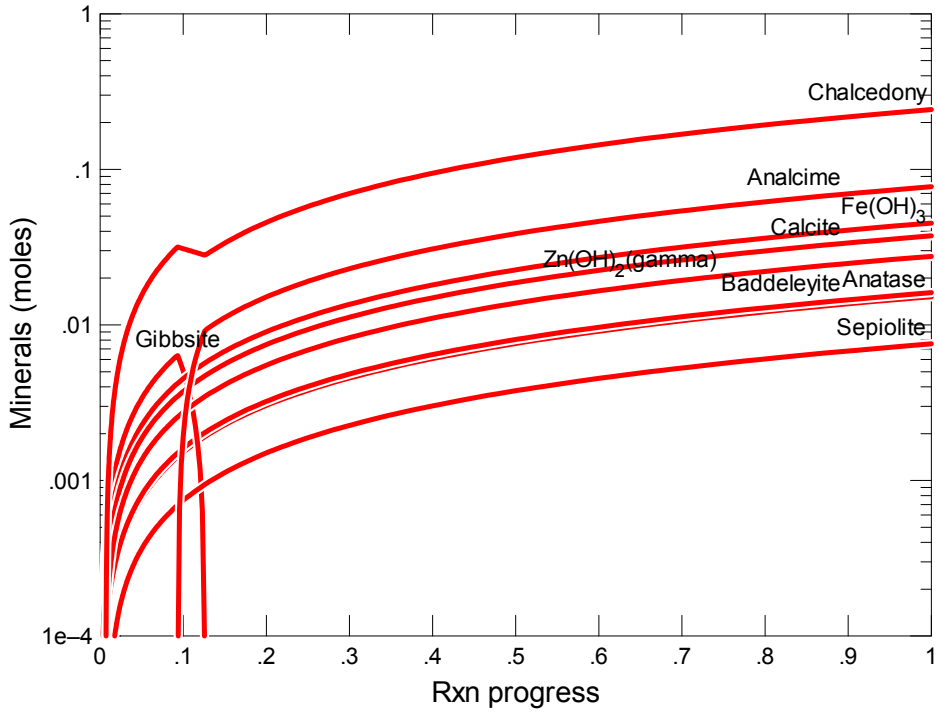


**Figure B.22**. Secondary Phases Calculated to Form as a Function of Reaction Progress (mol-glass/kg) Determined for Glass Sample A2B1-1

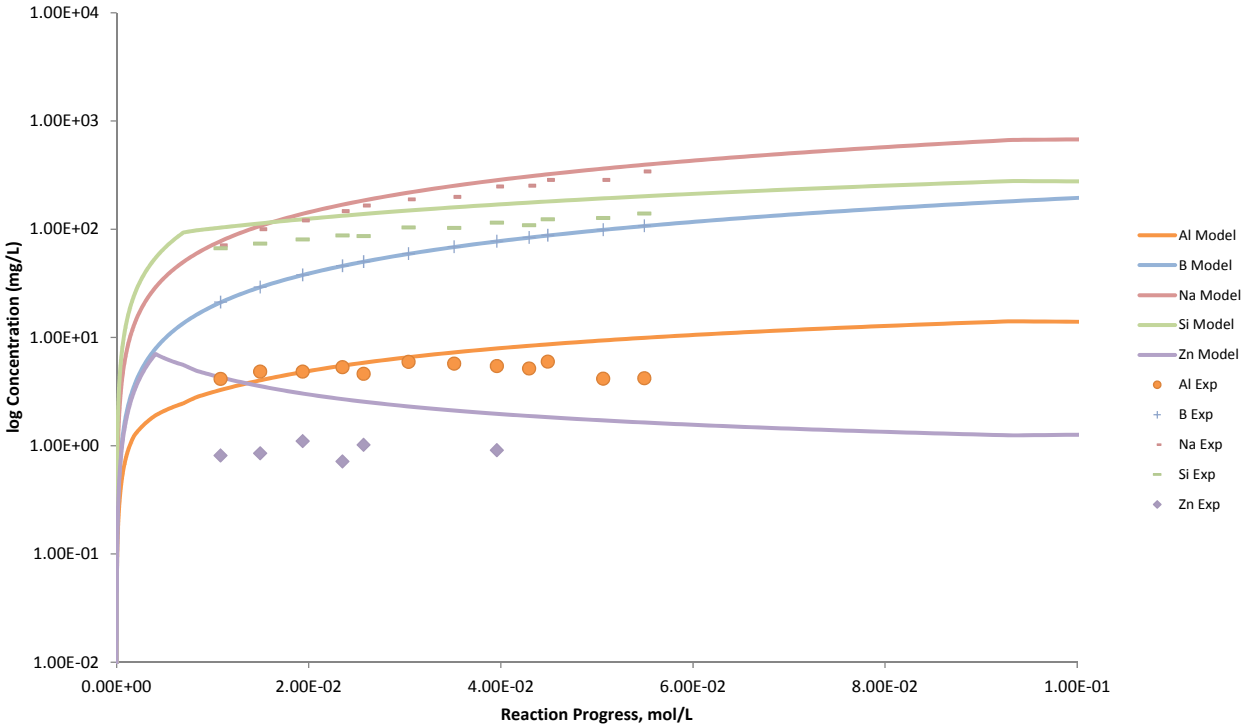


**Figure B.23**. Measured Solution Concentrations (mg/L) and Model Results for Al, B, Na, Si, and Zn, as a Function of Reaction Progress (mol-glass/kg) Determined for Glass Sample A2B1-1

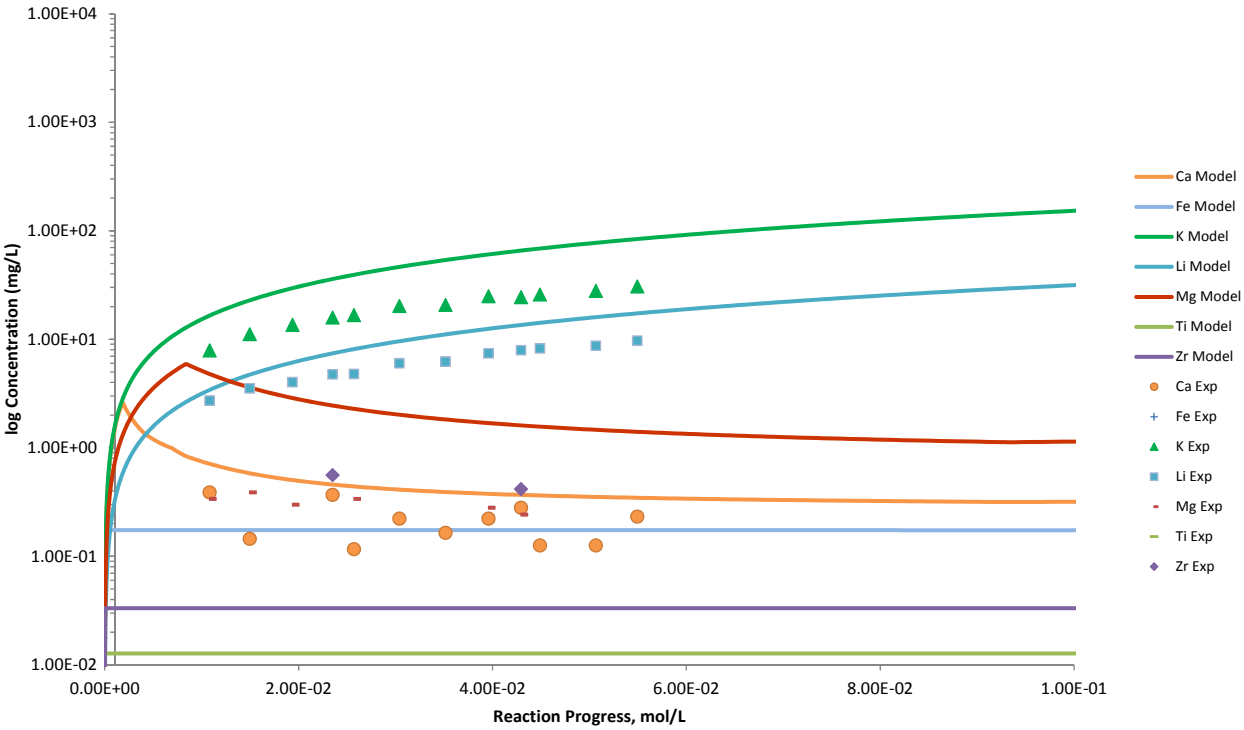


**Figure B.24**. Measured Solution Concentrations (mg/L) and Model Results for Ca, Fe, K, Li, Mg, Ti, and Zr, as a Function of Reaction Progress (mol-glass/kg) Determined for Glass Sample A2B1-1

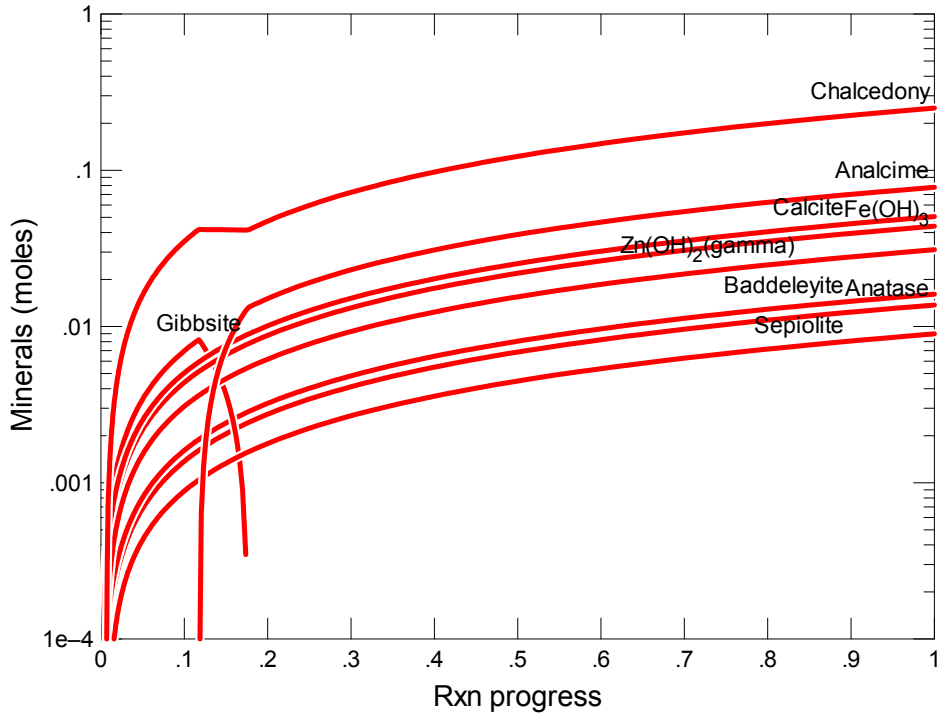


**Figure B.25**. Secondary Phases Calculated to Form as a Function of Reaction Progress (mol-glass/kg) Determined for Glass Sample A2B1-2

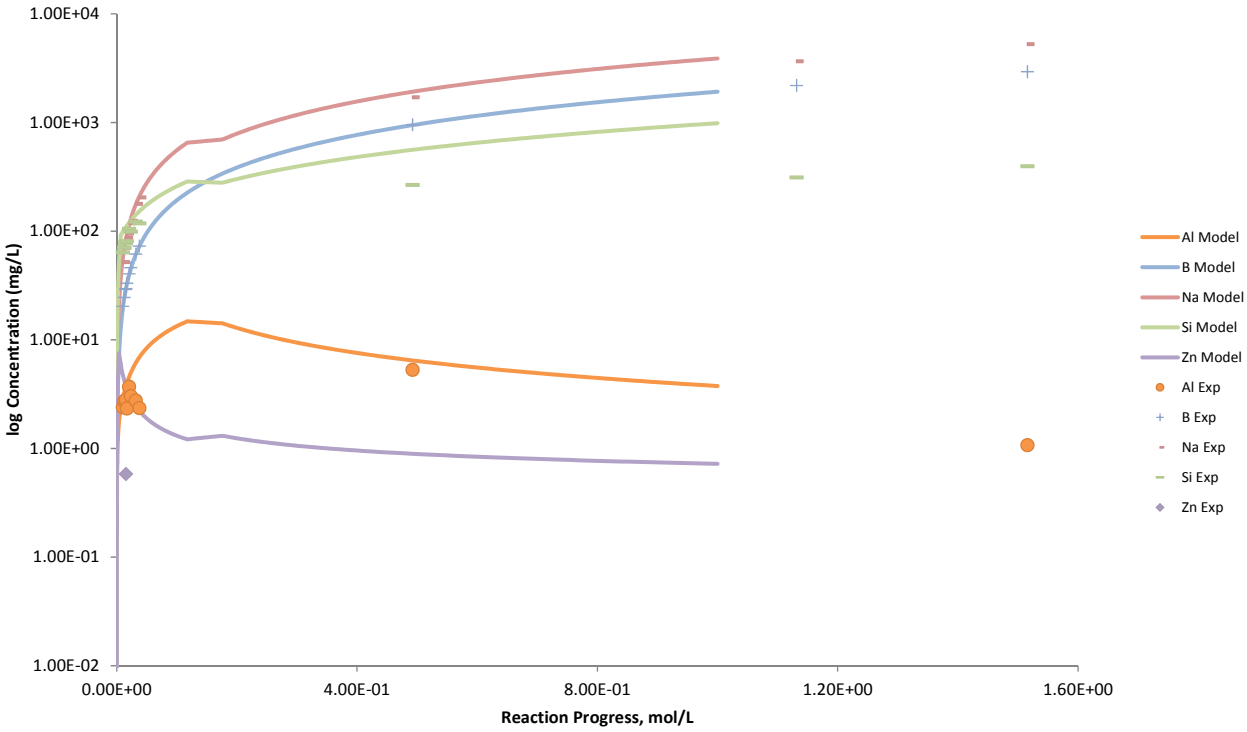


**Figure B.26**. Measured Solution Concentrations (mg/L) and Model Results for Al, B, Na, Si, and Zn, as a Function of Reaction Progress (mol-glass/kg) Determined for Glass Sample A2B1-2

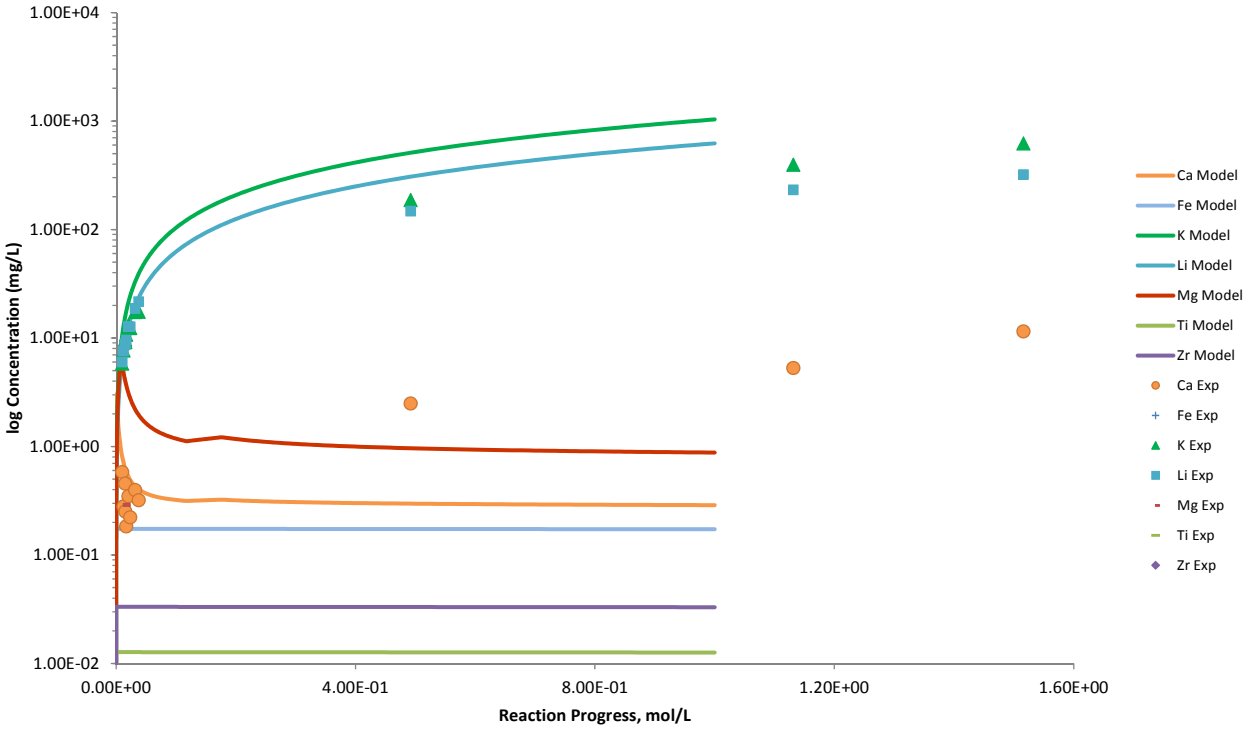


**Figure B.27**. Measured Solution Concentrations (mg/L) and Model Results for Ca, Fe, K, Li, Mg, Ti, and Zr, as a Function of Reaction Progress (mol-glass/kg) Determined for Glass Sample A2B1-2

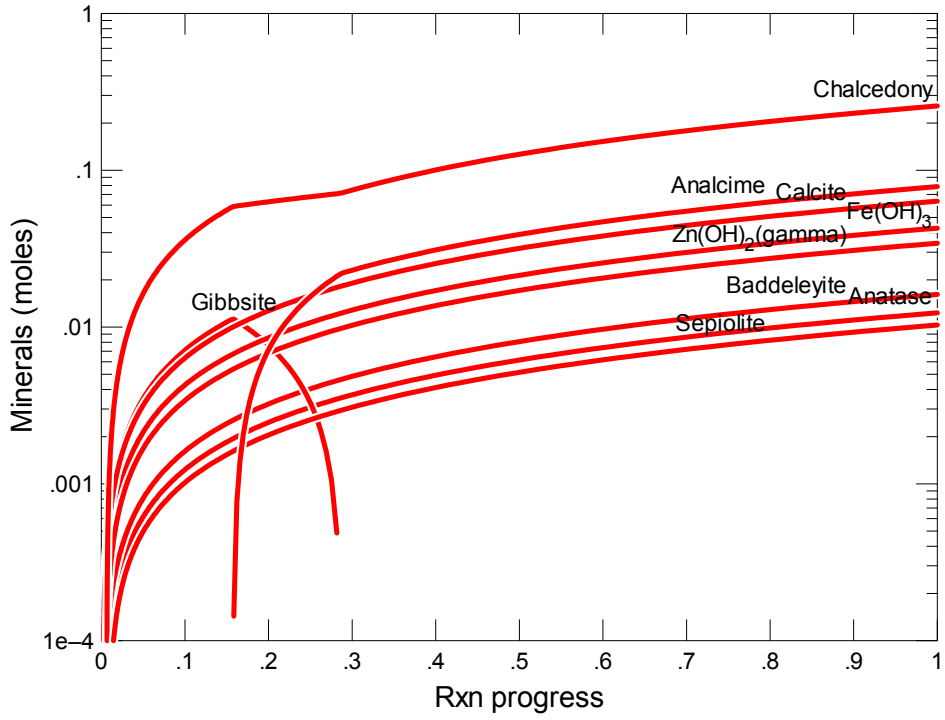


**Figure B.28**. Secondary Phases Calculated to Form as a Function of Reaction Progress (mol-glass/kg) Determined for Glass Sample A2B1-3

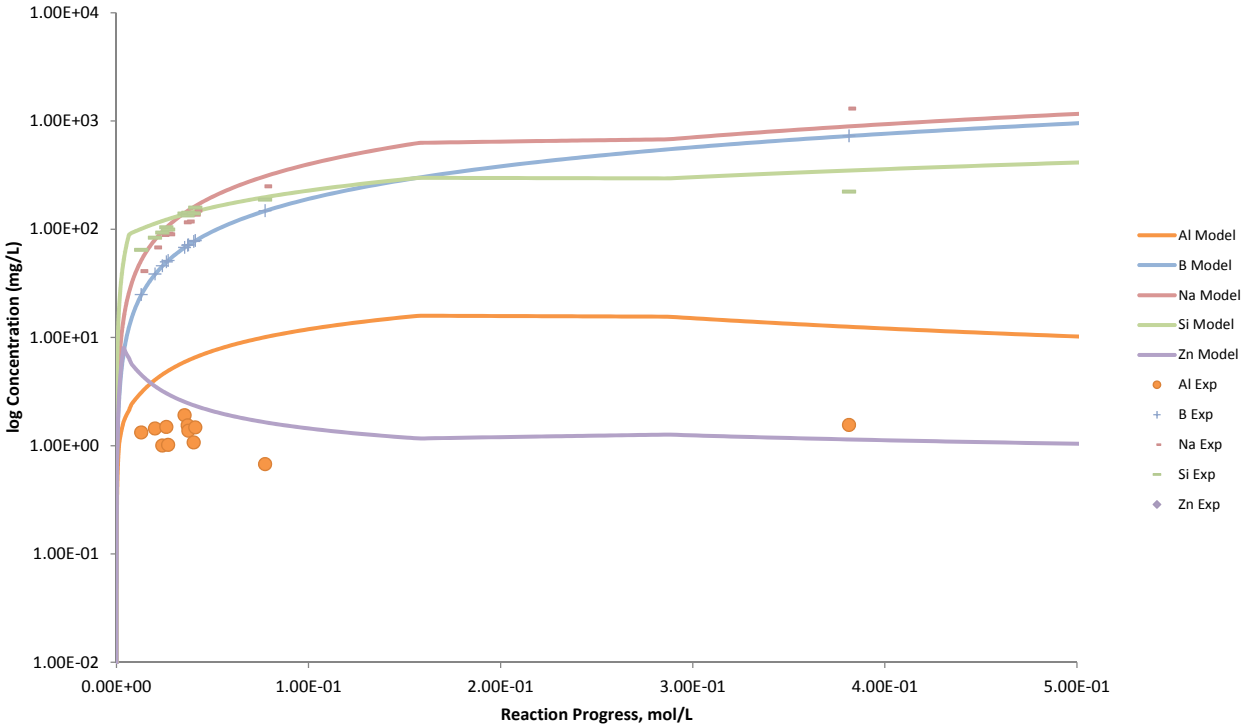


**Figure B.29**. Measured Solution Concentrations (mg/L) and Model Results for Al, B, Na, Si, and Zn, as a Function of Reaction Progress (mol-glass/kg) Determined for Glass Sample A2B1-3

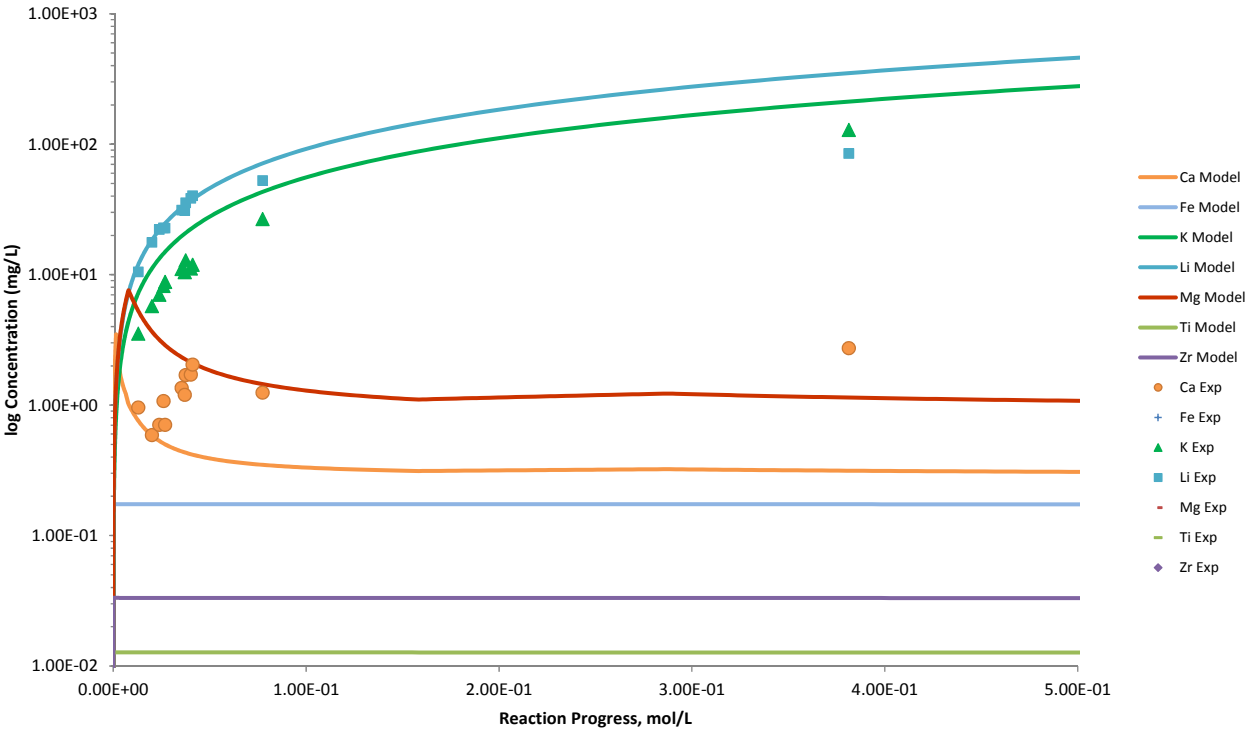


**Figure B.30**. Measured Solution Concentrations (mg/L) and Model Results for Ca, Fe, K, Li, Mg, Ti, and Zr, as a Function of Reaction Progress (mol-glass/kg) Determined for Glass Sample A2B1-3

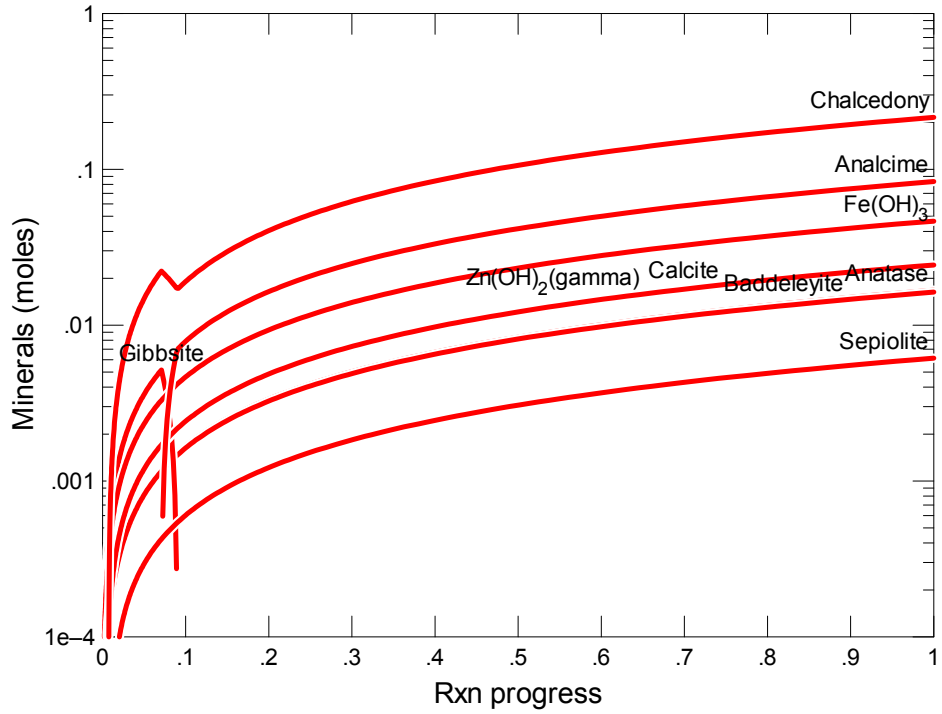


**Figure B.31**. Secondary Phases Calculated to Form as a Function of Reaction Progress (mol-glass/kg) Determined for Glass Sample A88AP101R1

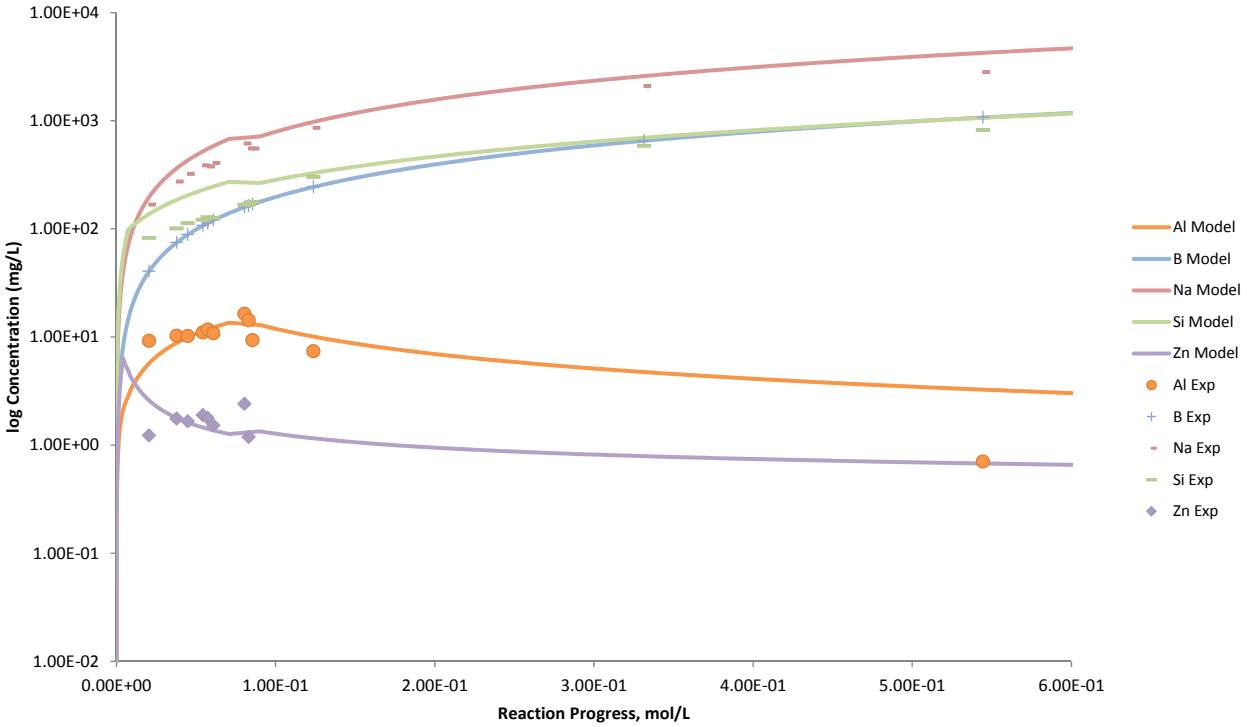


**Figure B.32**. Measured Solution Concentrations (mg/L) and Model Results for Al, B, Na, Si, and Zn, as a Function of Reaction Progress (mol-glass/kg) Determined for Glass Sample A88AP101R1

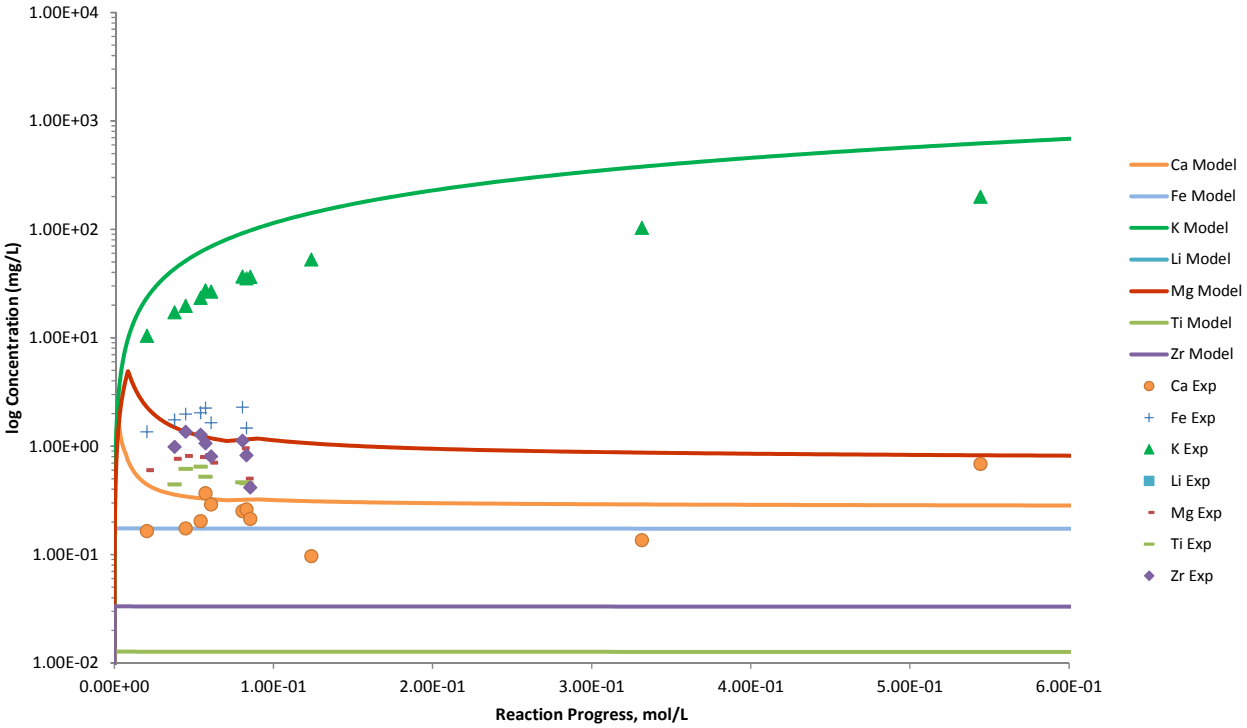


**Figure B.33**. Measured Solution Concentrations (mg/L) and Model Results for Ca, Fe, K, Li, Mg, Ti, and Zr, as a Function of Reaction Progress (mol-glass/kg) Determined for Glass Sample A88AP101R1

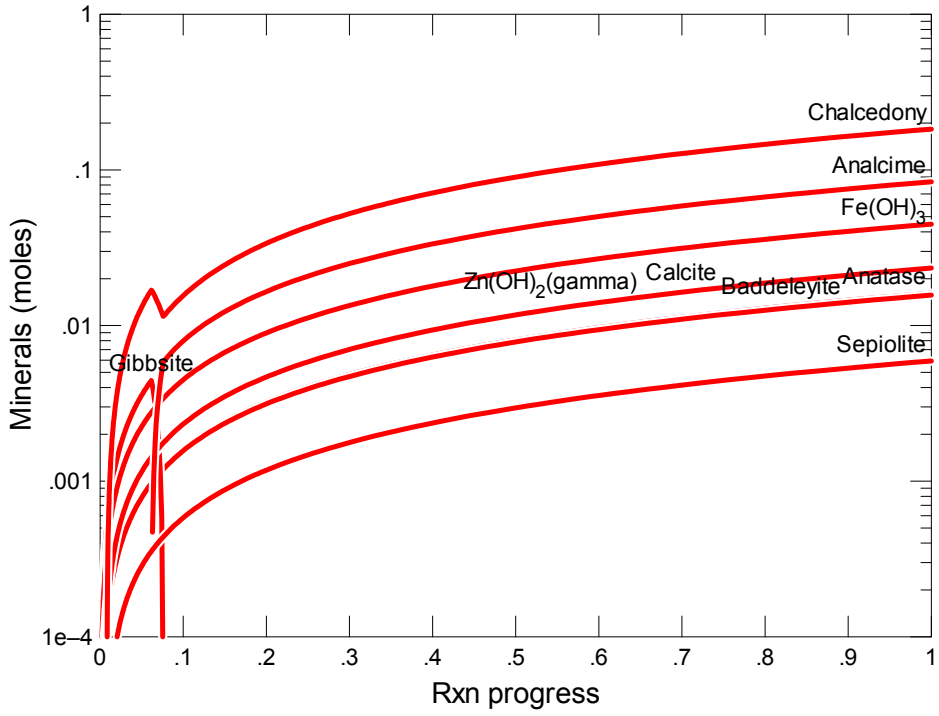


**Figure B.34**. Secondary Phases Calculated to Form as a Function of Reaction Progress (mol-glass/kg) Determined for Glass Sample A88Si+15

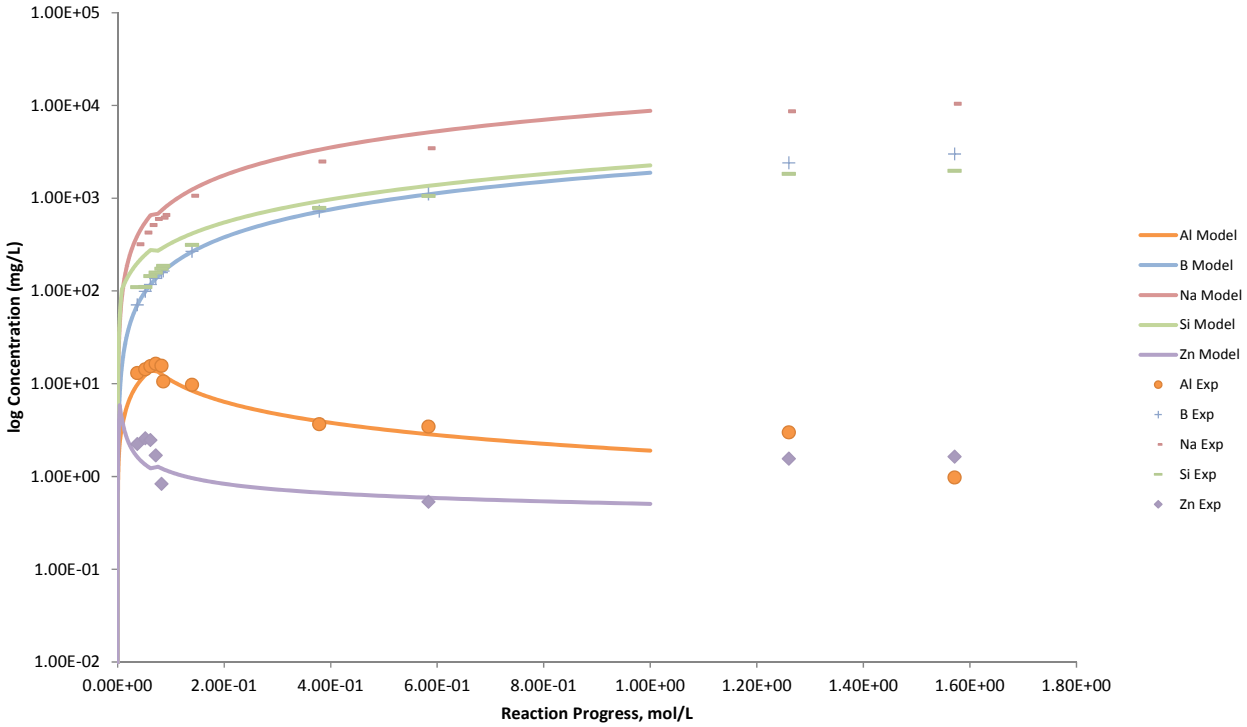


**Figure B.35**. Measured Solution Concentrations (mg/L) and Model Results for Al, B, Na, Si, and Zn, as a Function of Reaction Progress (mol-glass/kg) Determined for Glass Sample A88Si+15

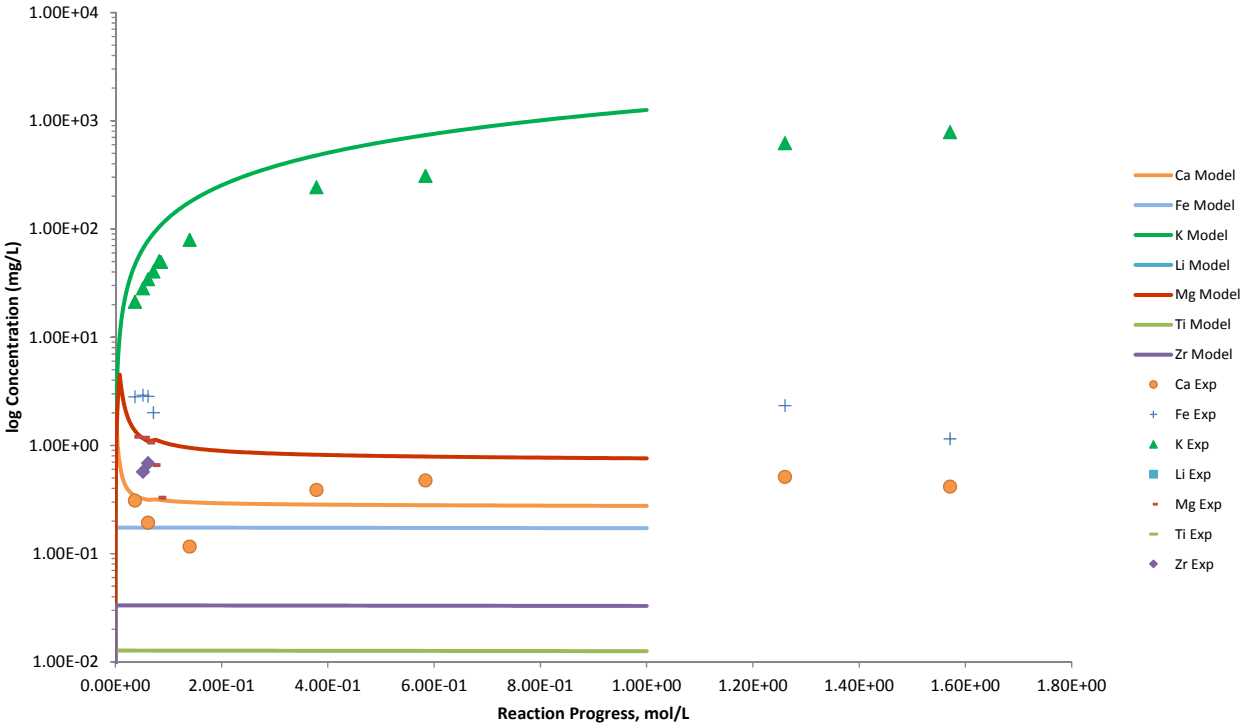


**Figure B.36**. Measured Solution Concentrations (mg/L) and Model Results for Ca, Fe, K, Li, Mg, Ti, and Zr, as a Function of Reaction Progress (mol-glass/kg) Determined for Glass Sample A88Si+15

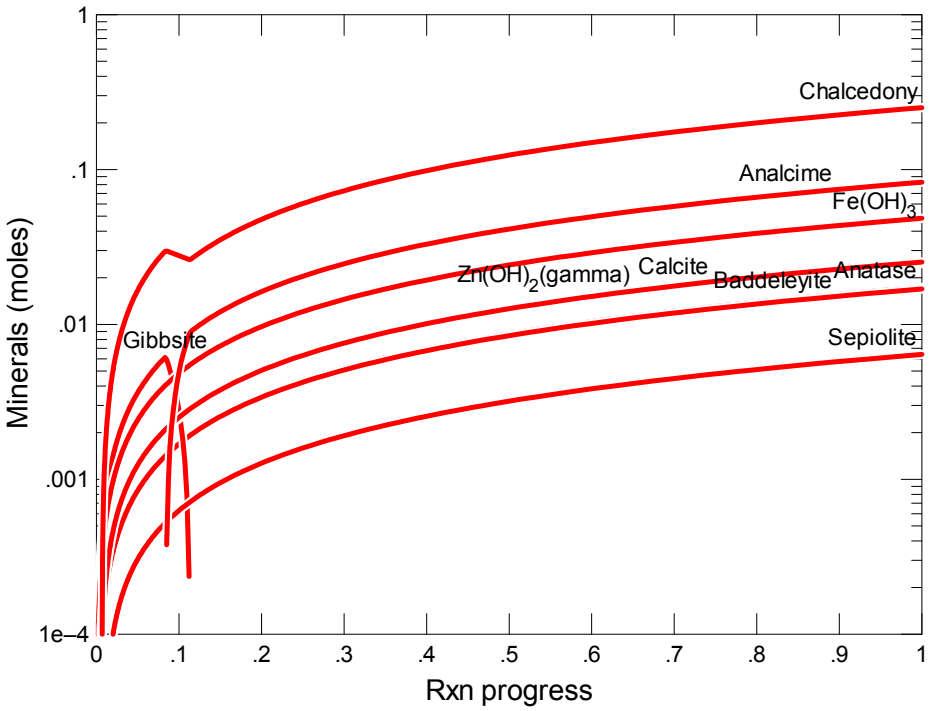


**Figure B.37**. Secondary Phases Calculated to Form as a Function of Reaction Progress (mol-glass/kg) Determined for Glass Sample A88Si-15

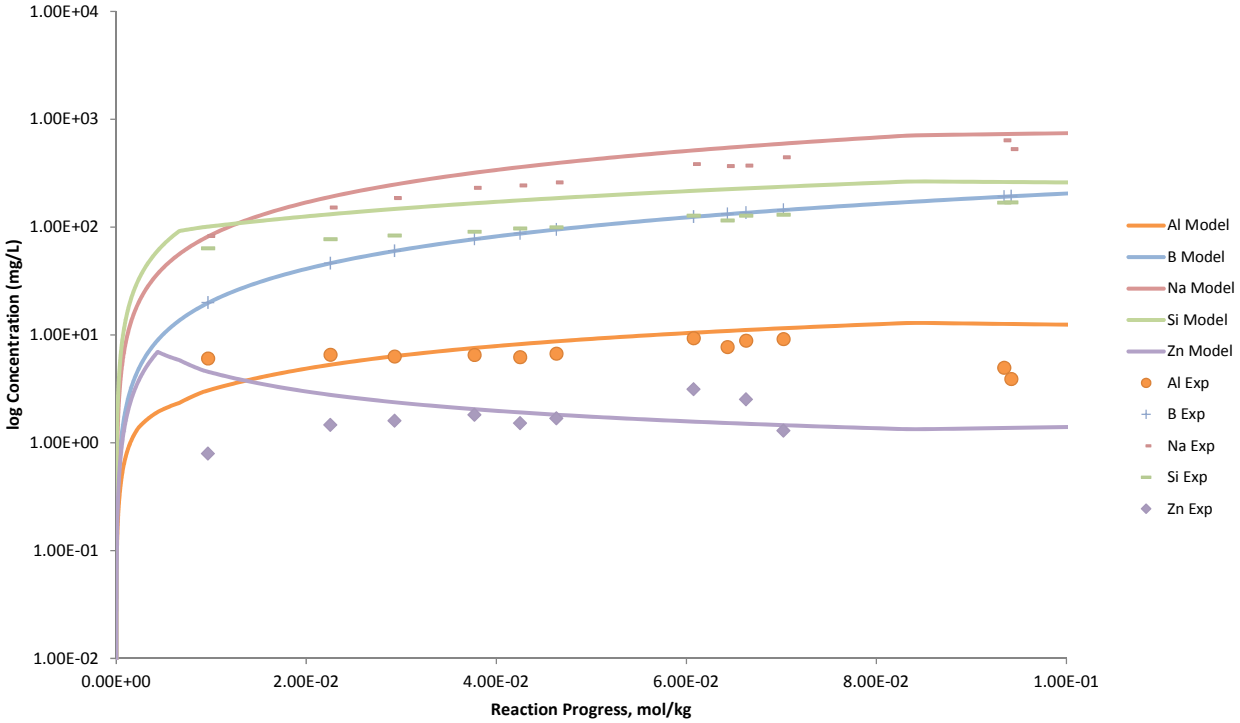


**Figure B.38**. Measured Solution Concentrations (mg/L) and Model Results for Al, B, Na, Si, and Zn, as a Function of Reaction Progress (mol-glass/kg) Determined for Glass Sample A88Si-15

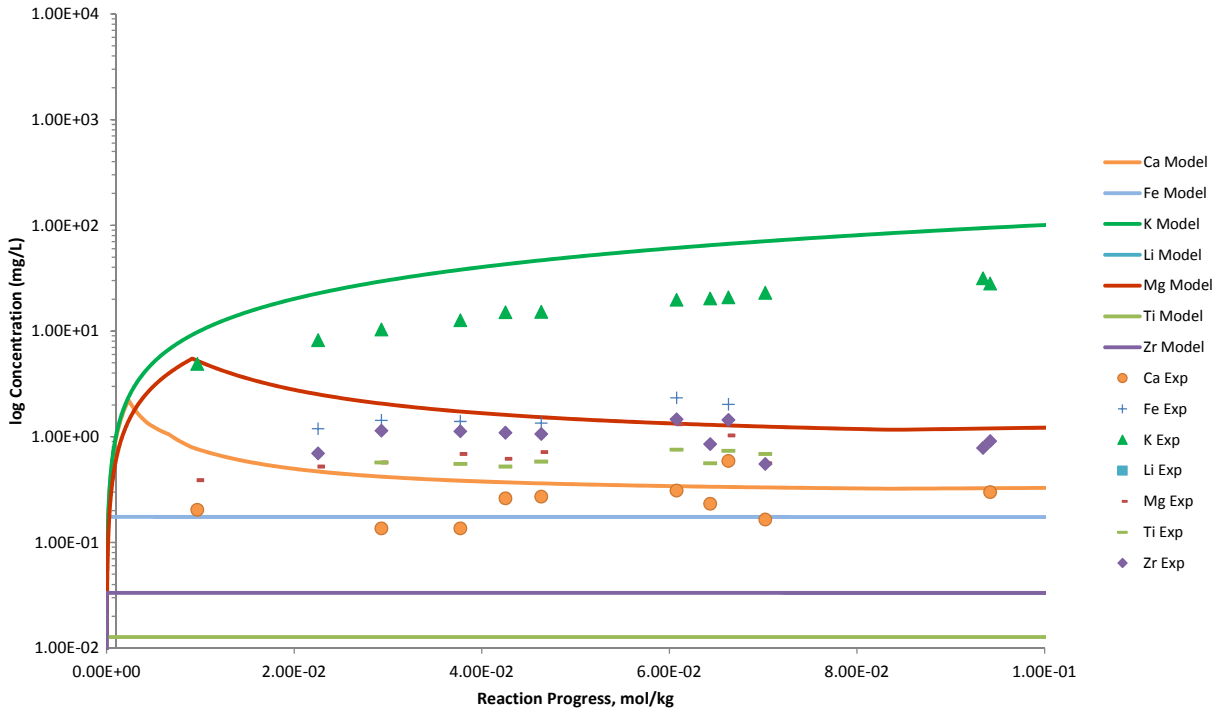


**Figure B.39**. Measured Solution Concentrations (mg/L) and Model Results for Ca, Fe, K, Li, Mg, Ti, and Zr, as a Function of Reaction Progress (mol-glass/kg) Determined for Glass Sample A88Si-15

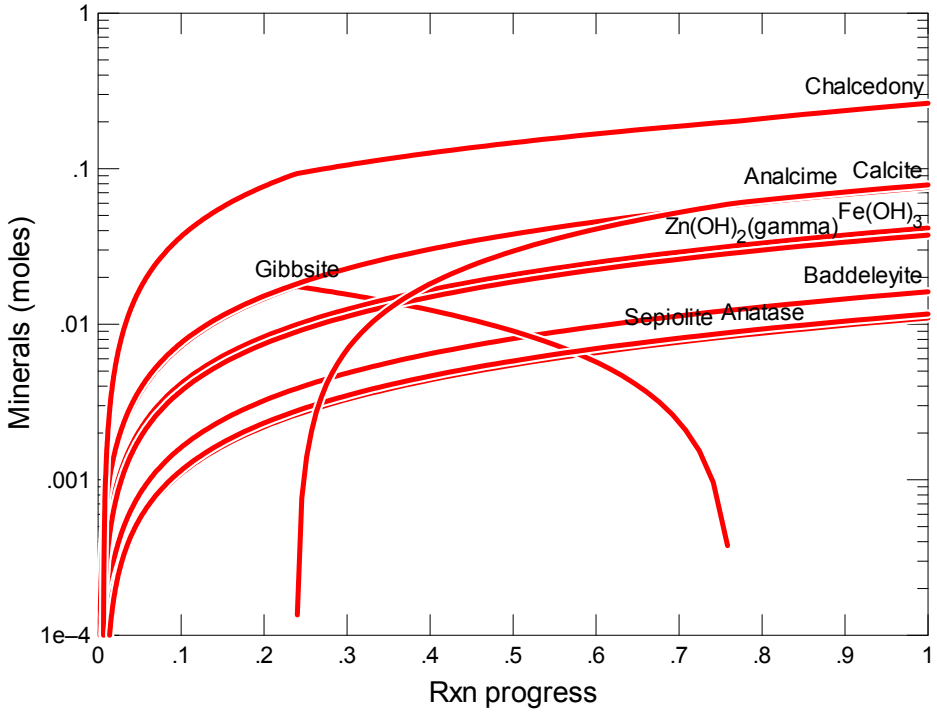


**Figure B.40**. Secondary Phases Calculated to Form as a Function of Reaction Progress (mol-glass/kg) Determined for Glass Sample B1-AZ101

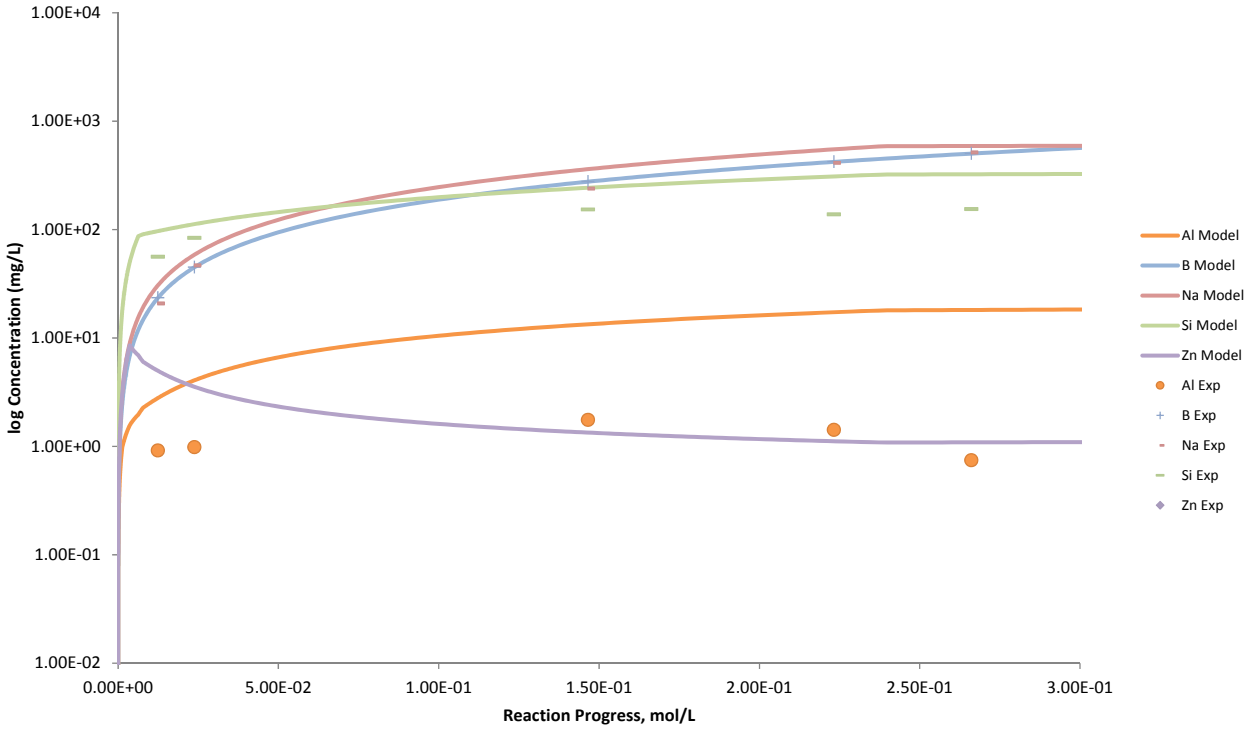


**Figure B.41**. Measured Solution Concentrations (mg/L) and Model Results for Al, B, Na, Si, and Zn, as a Function of Reaction Progress (mol-glass/kg) Determined for Glass Sample B1-AZ101

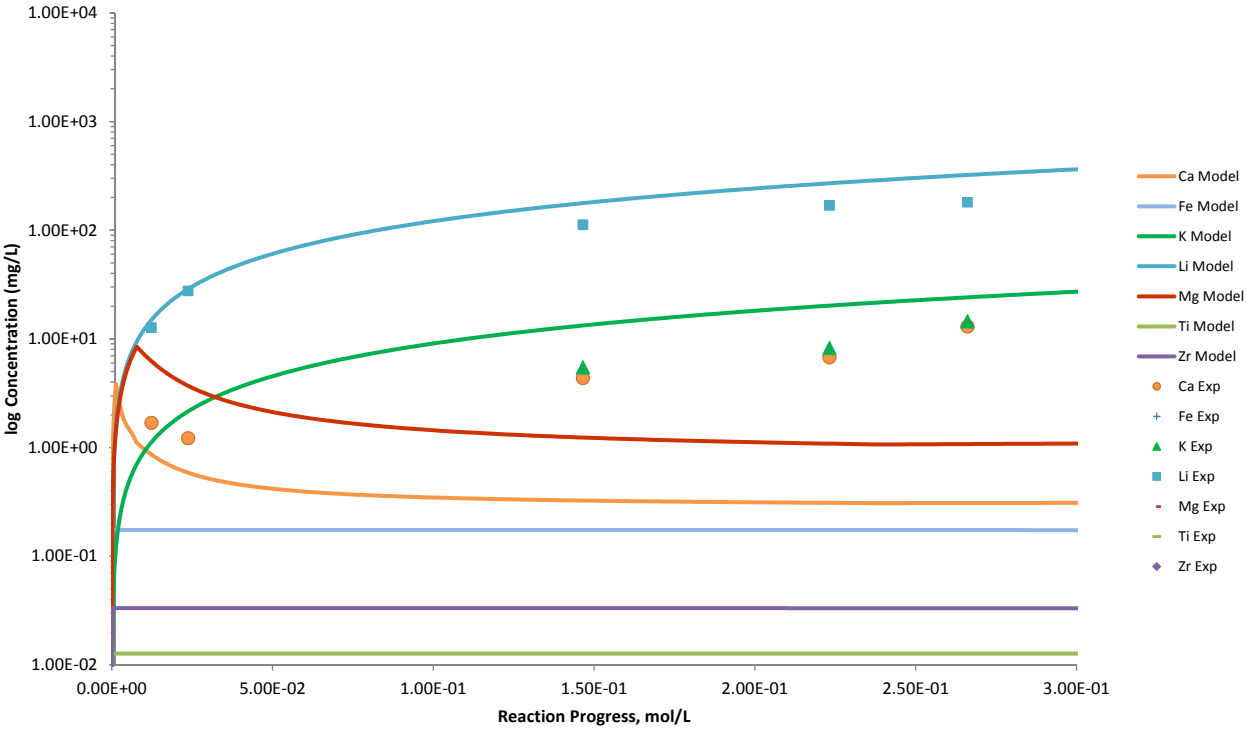


**Figure B.42**. Measured Solution Concentrations (mg/L) and Model Results for Ca, Fe, K, Li, Mg, Ti, and Zr, as a Function of Reaction Progress (mol-glass/kg) Determined for Glass Sample B1-AZ101

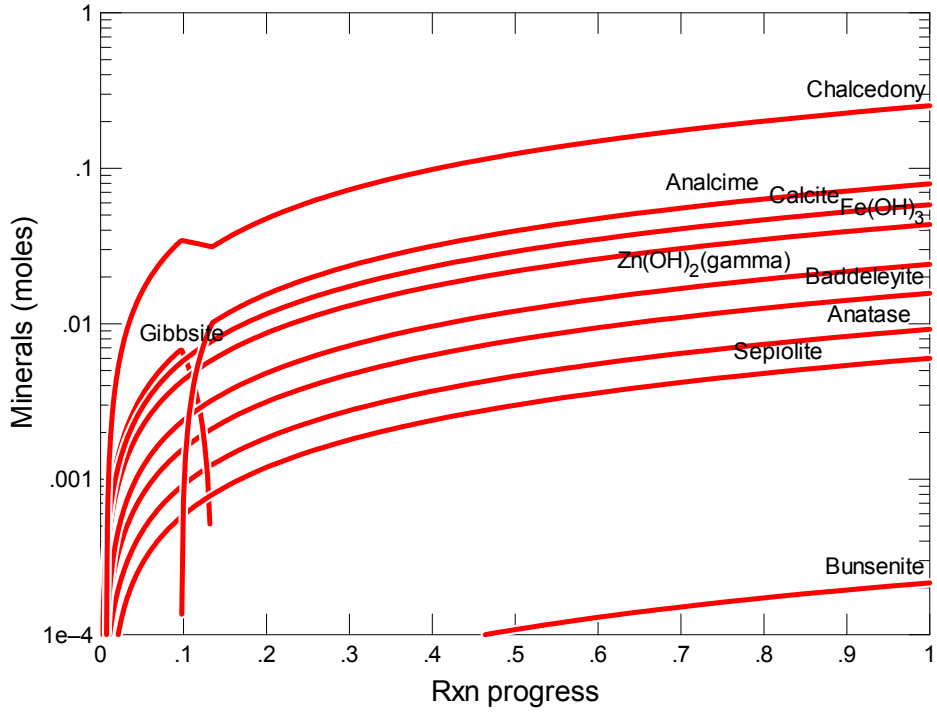


**Figure B.43**. Secondary Phases Calculated to Form as a Function of Reaction Progress (mol-glass/kg) Determined for Glass Sample C1-AN107

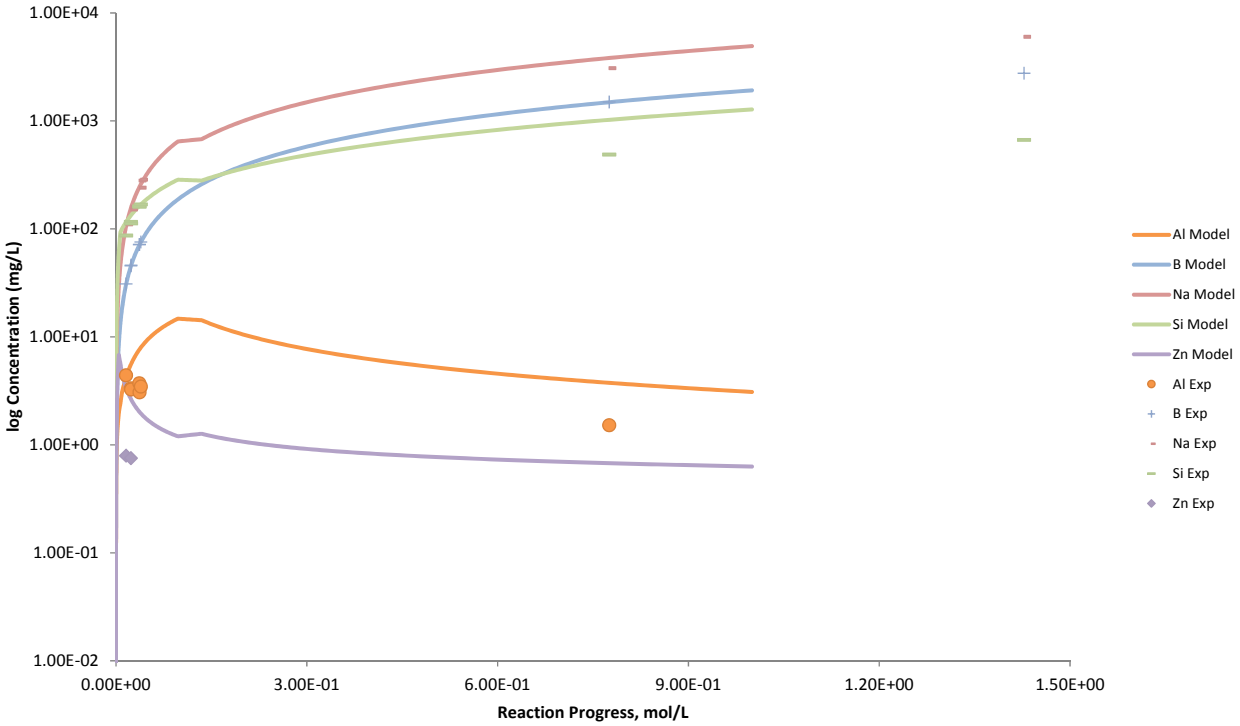


**Figure B.44**. Measured Solution Concentrations (mg/L) and Model Results for Al, B, Na, Si, and Zn, as a Function of Reaction Progress (mol-glass/kg) Determined for Glass Sample C1-AN107

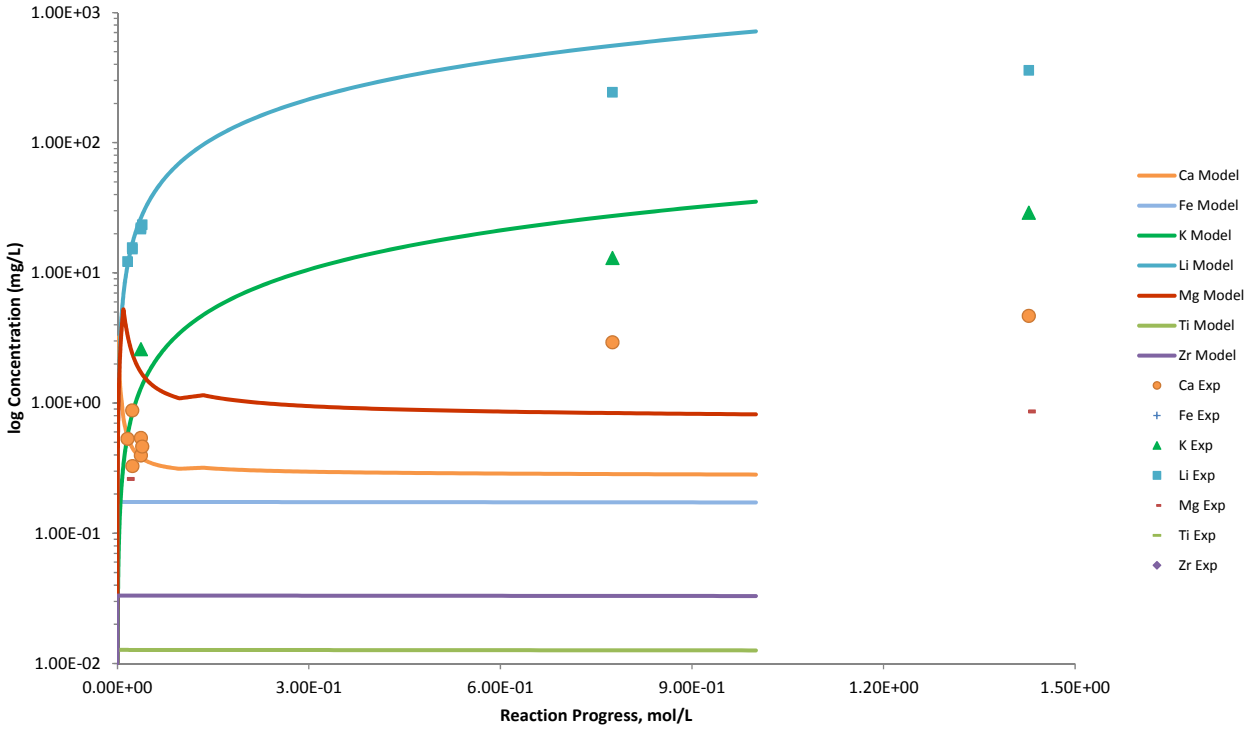


**Figure B.45**. Measured Solution Concentrations (mg/L) and Model Results for Ca, Fe, K, Li, Mg, Ti, and Zr, as a Function of Reaction Progress (mol-glass/kg) Determined for Glass Sample C1-AN107

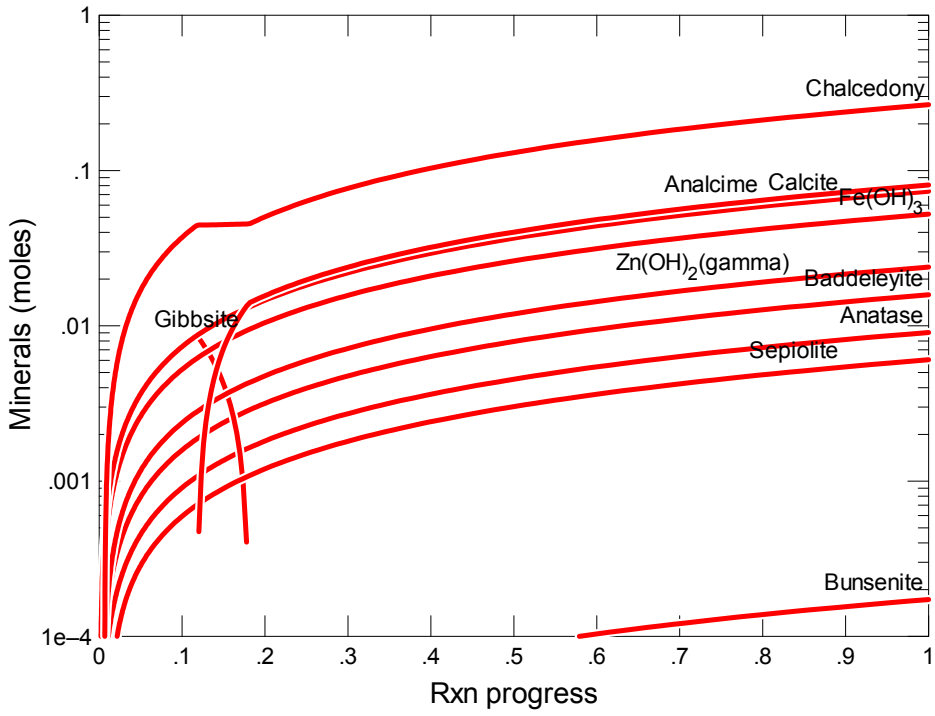


**Figure B.46**. Secondary Phases Calculated to Form as a Function of Reaction Progress (mol-glass/kg) Determined for Glass Sample C100-G-136B

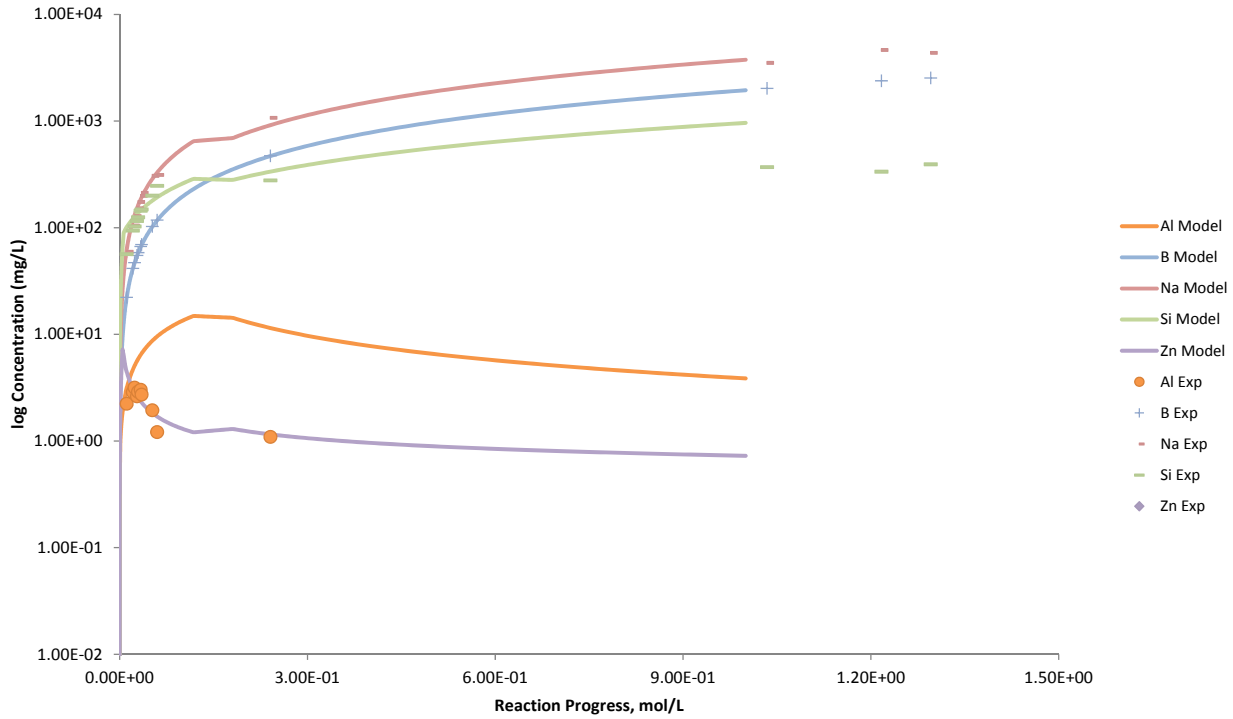


**Figure B.47**. Measured Solution Concentrations (mg/L) and Model Results for Al, B, Na, Si, and Zn, as a Function of Reaction Progress (mol-glass/kg) Determined for Glass Sample C100-G-136B

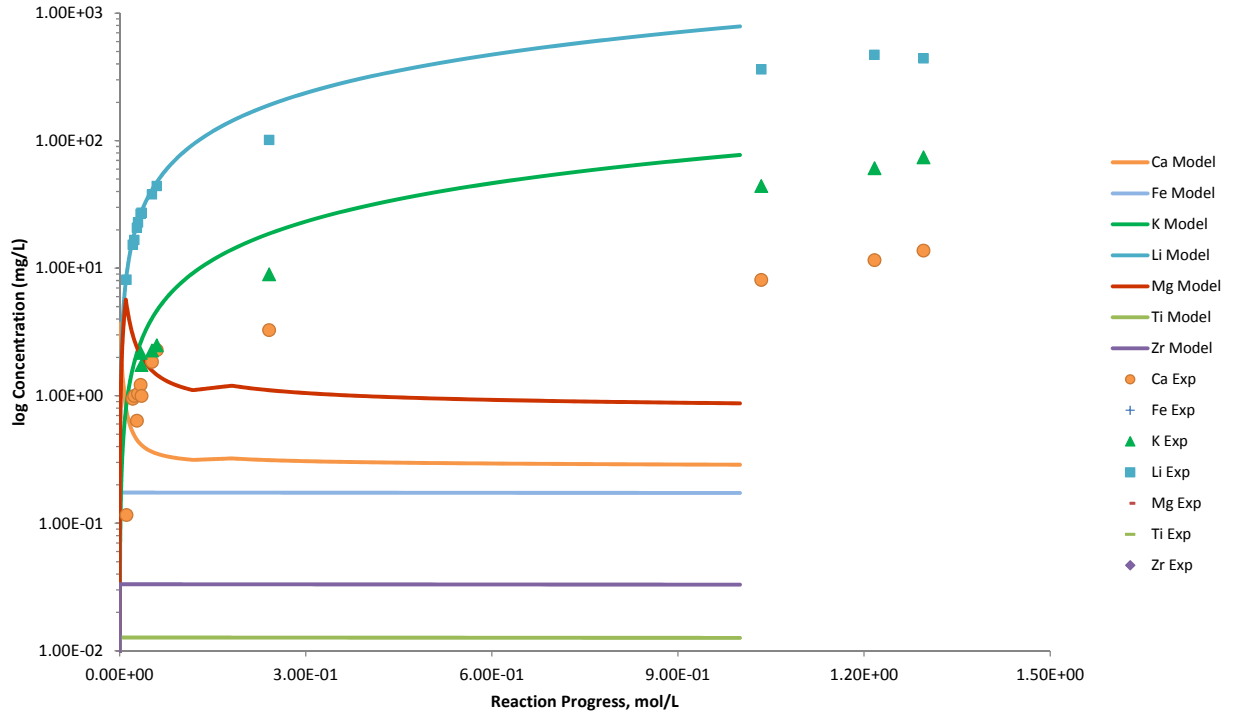


**Figure B.48**. Measured Solution Concentrations (mg/L) and Model Results for Ca, Fe, K, Li, Mg, Ti, and Zr, as a Function of Reaction Progress (mol-glass/kg) Determined for Glass Sample C100-G-136B

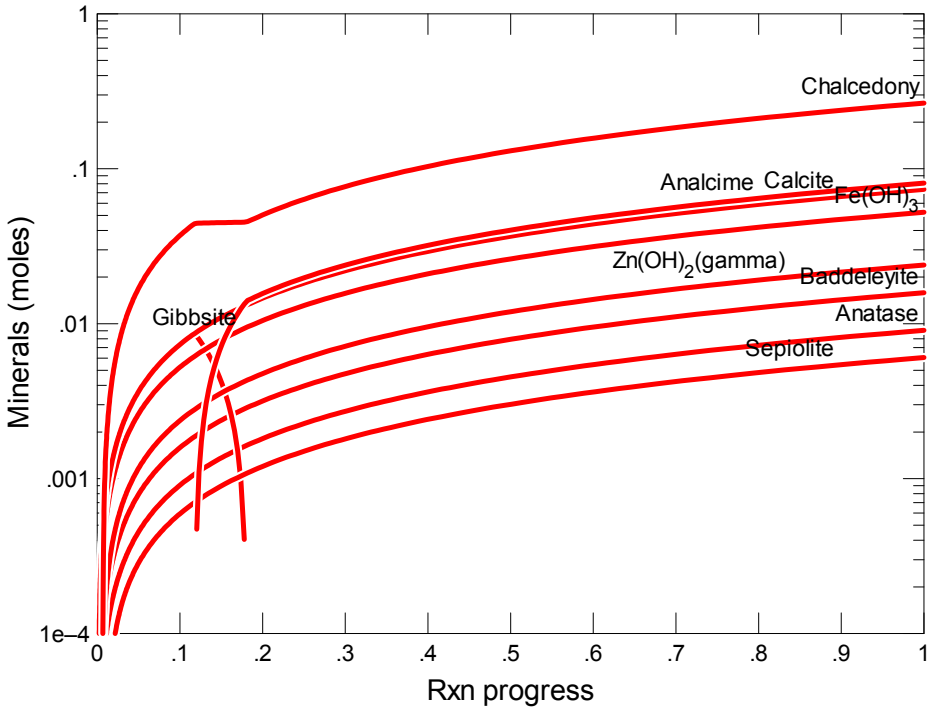


**Figure B.49**. Secondary Phases Calculated to Form as a Function of Reaction Progress (mol-glass/kg) Determined for Glass Sample C100GCC

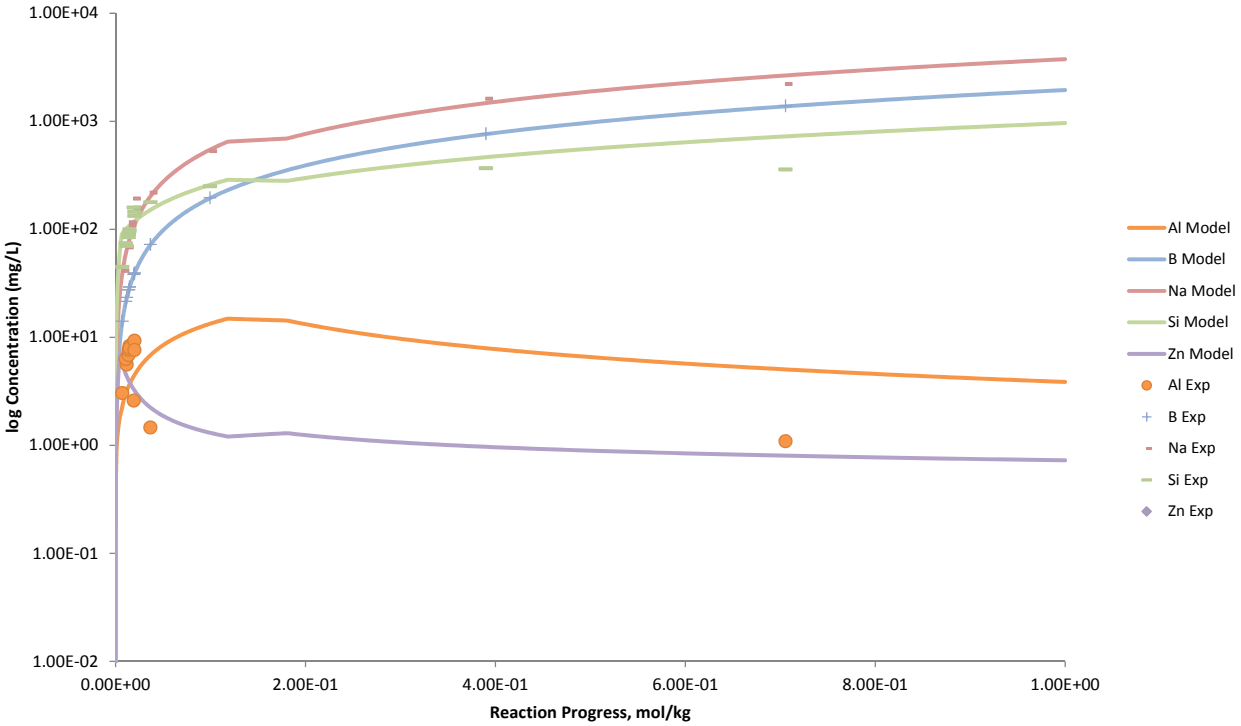


**Figure B.50**. Measured Solution Concentrations (mg/L) and Model Results for Al, B, Na, Si, and Zn, as a Function of Reaction Progress (mol-glass/kg) Determined for Glass Sample C100GCC

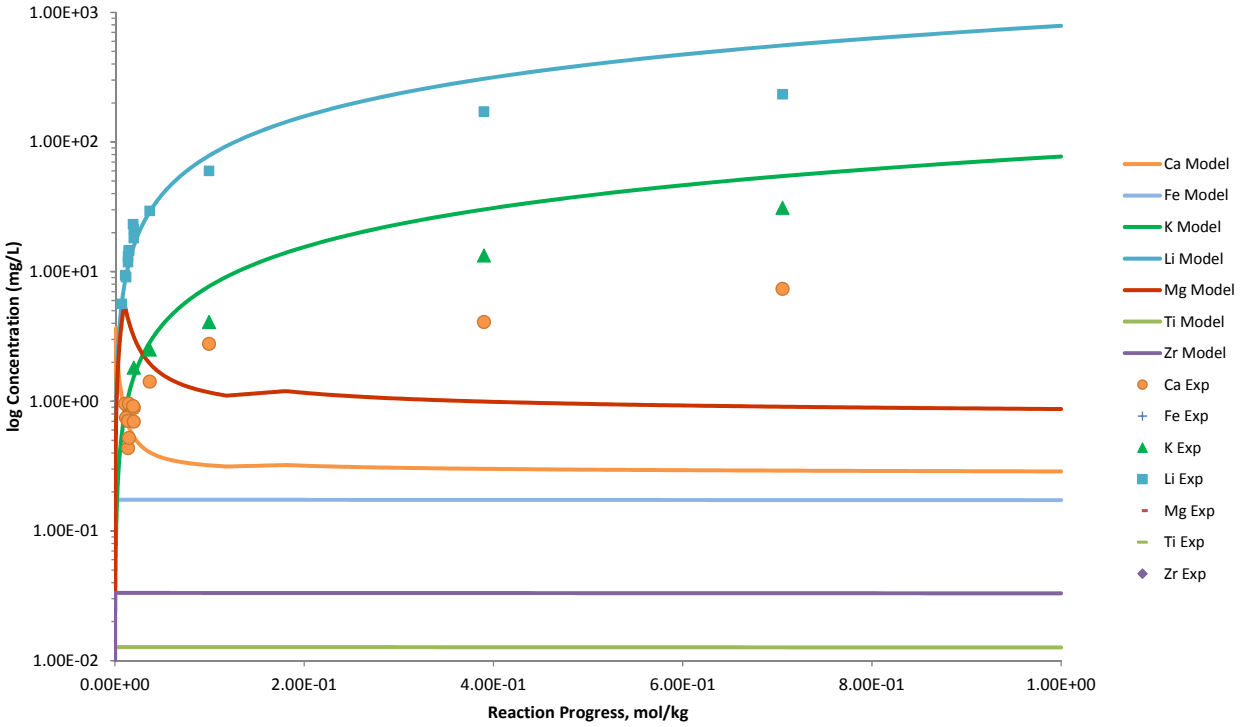


**Figure B.51**. Measured Solution Concentrations (mg/L) and Model Results for Ca, Fe, K, Li, Mg, Ti, and Zr, as a Function of Reaction Progress (mol-glass/kg) Determined for Glass Sample C100GCC

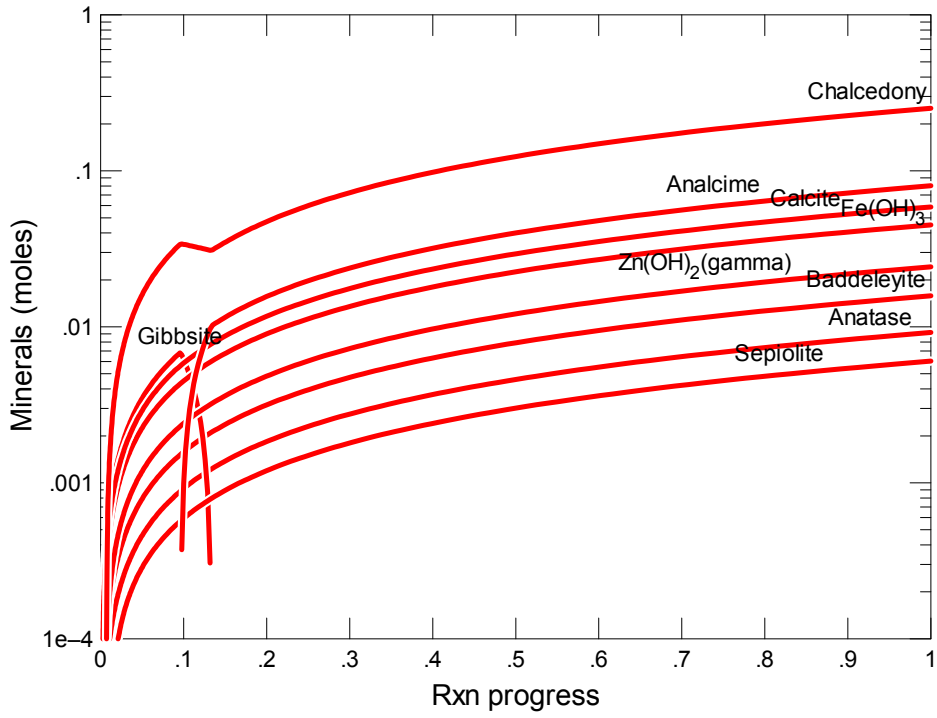


**Figure B.52**. Secondary Phases Calculated to Form as a Function of Reaction Progress (mol-glass/kg) Determined for Glass Sample C22AN107

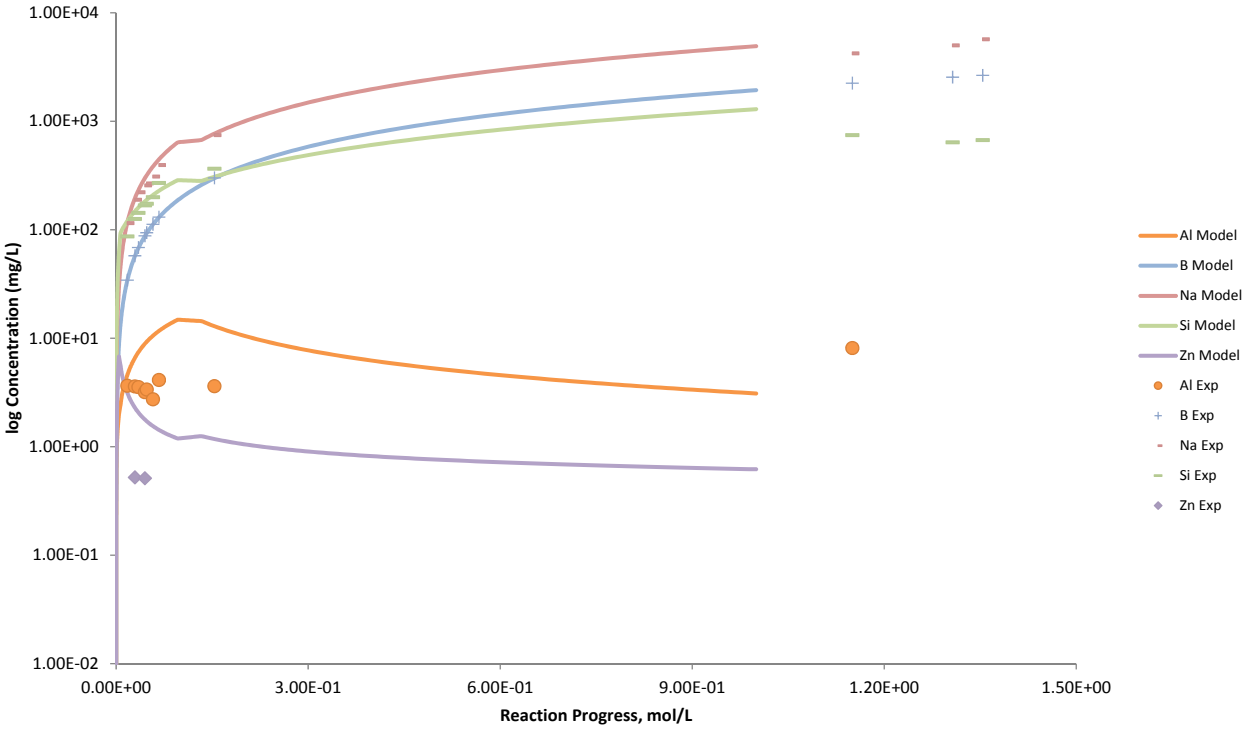


**Figure B.53**. Measured Solution Concentrations (mg/L) and Model Results for Al, B, Na, Si, and Zn, as a Function of Reaction Progress (mol-glass/kg) Determined for Glass Sample C22AN107

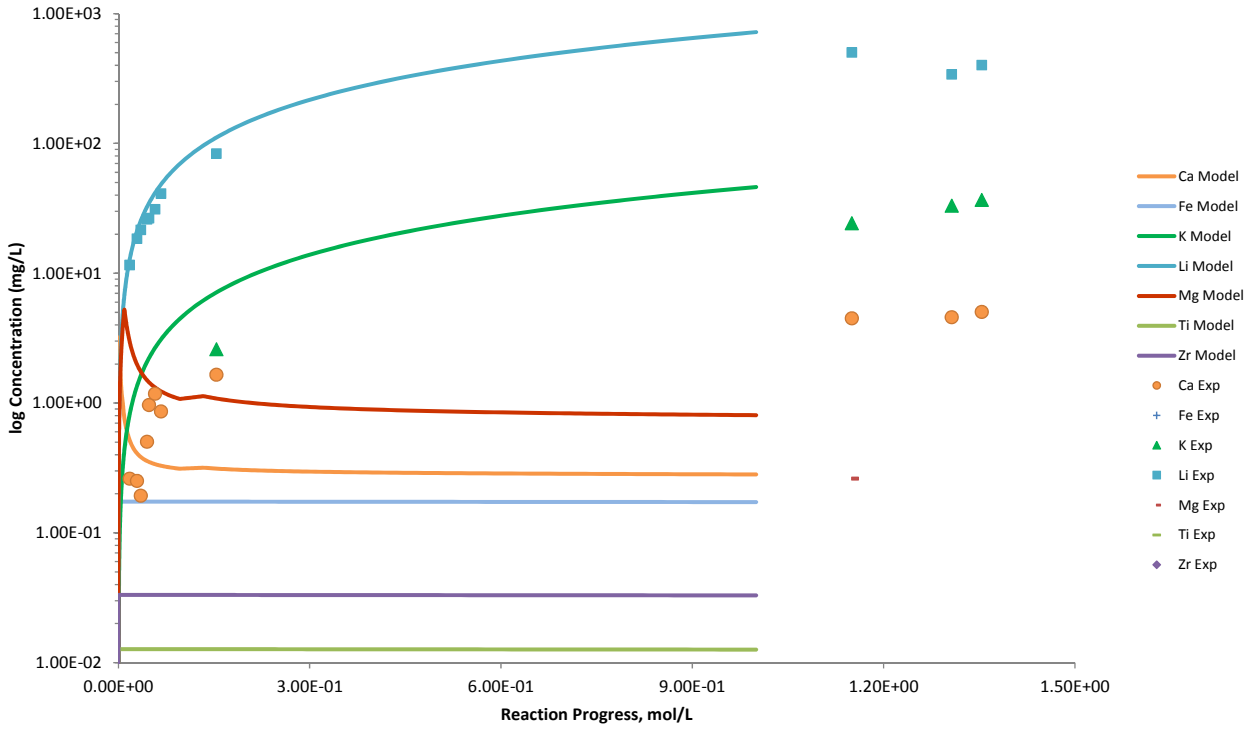


**Figure B.54**. Measured Solution Concentrations (mg/L) and Model Results for Ca, Fe, K, Li, Mg, Ti, and Zr, as a Function of Reaction Progress (mol-glass/kg) Determined for Glass Sample C22AN107

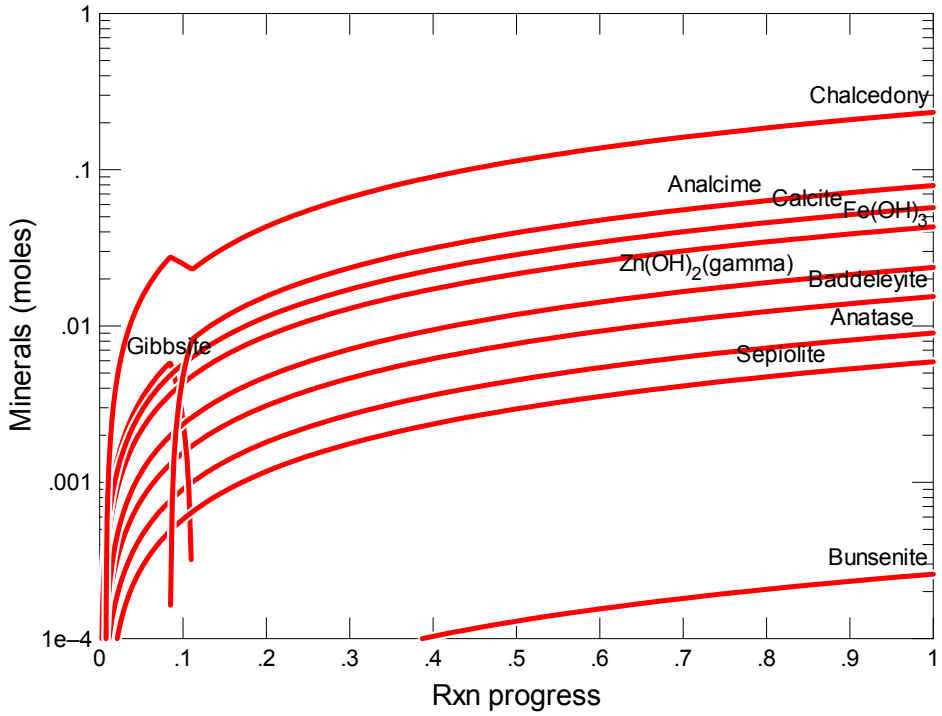


**Figure B.55**. Secondary Phases Calculated to Form as a Function of Reaction Progress (mol-glass/kg) Determined for Glass Sample C22Si+15

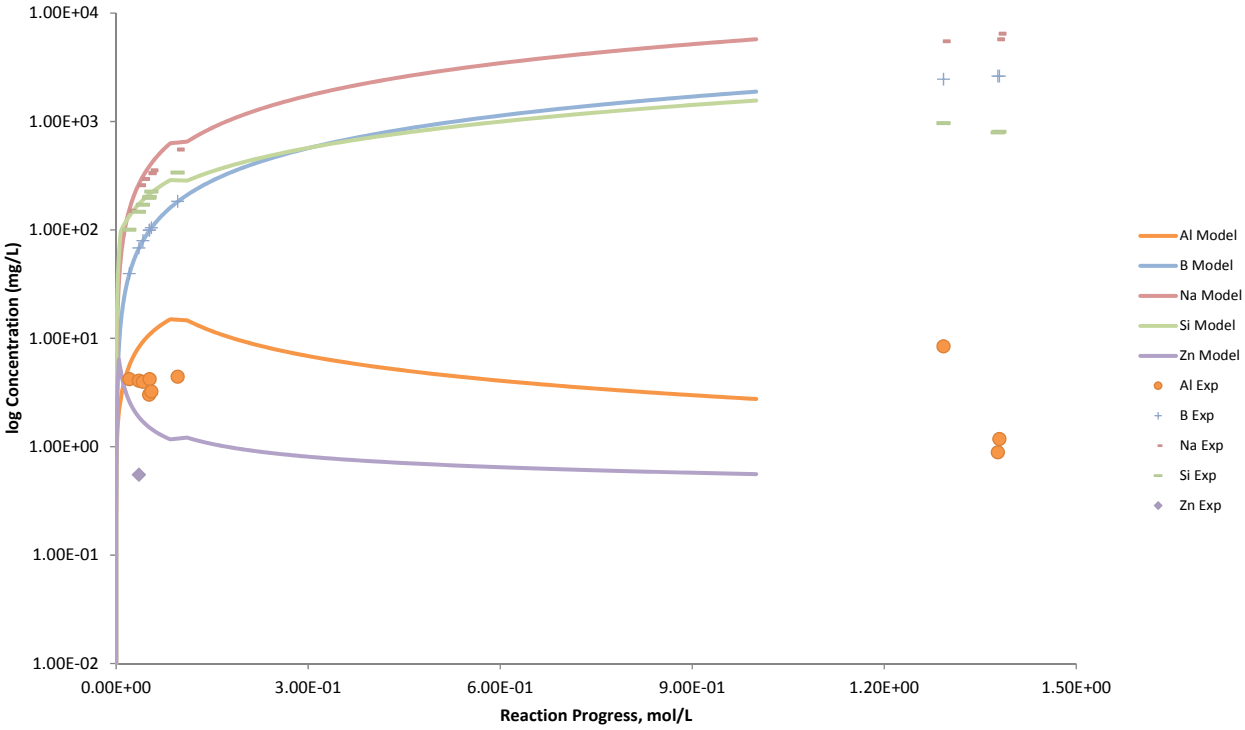


**Figure B.56**. Measured Solution Concentrations (mg/L) and Model Results for Al, B, Na, Si, and Zn, as a Function of Reaction Progress (mol-glass/kg) Determined for Glass Sample C22Si+15

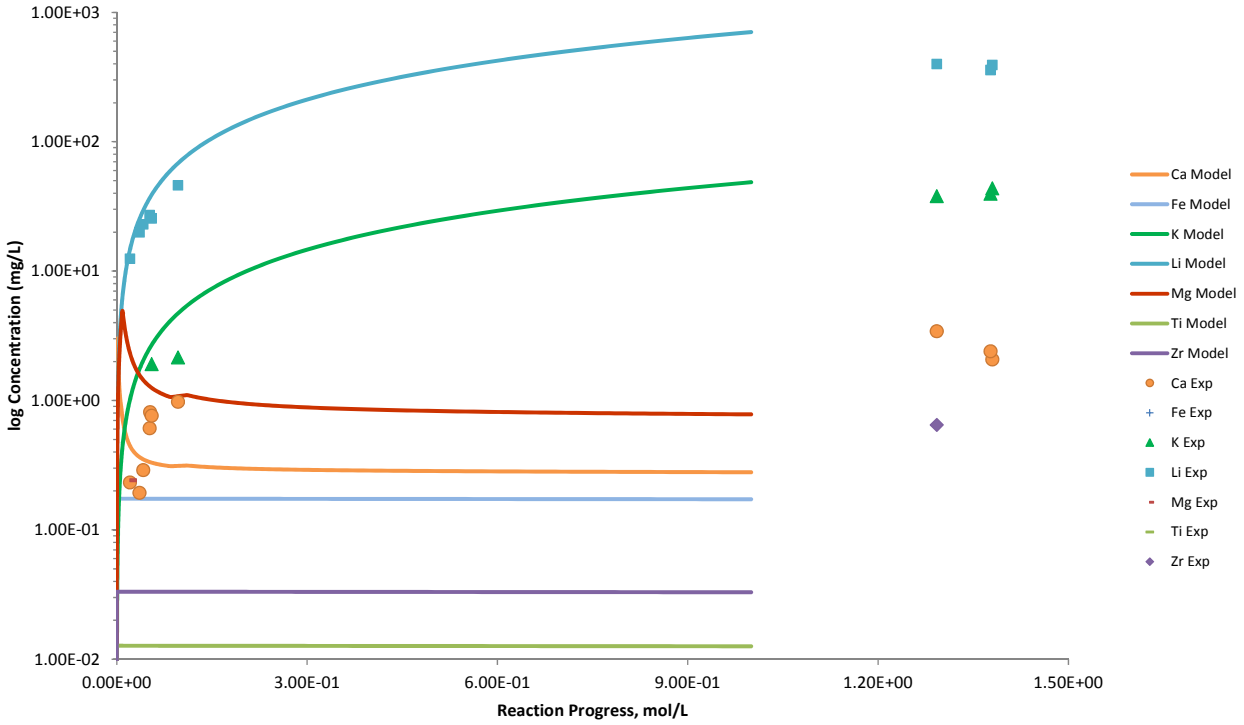


**Figure B.57**. Measured Solution Concentrations (mg/L) and Model Results for Ca, Fe, K, Li, Mg, Ti, and Zr, as a Function of Reaction Progress (mol-glass/kg) Determined for Glass Sample C22Si+15

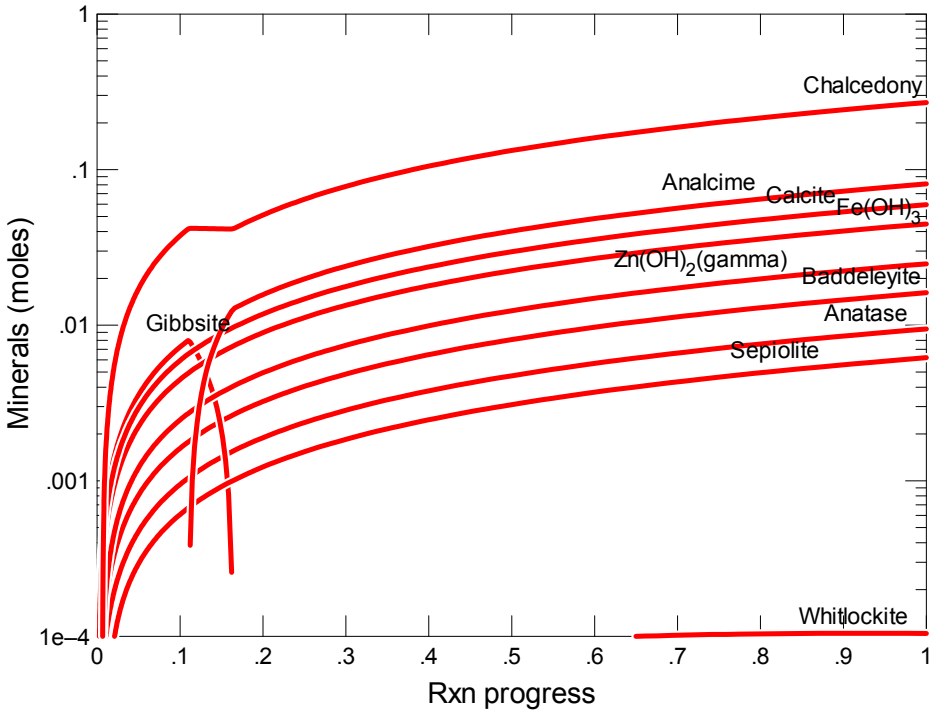


**Figure B.58**. Secondary Phases Calculated to Form as a Function of Reaction Progress (mol-glass/kg) Determined for Glass Sample C22Si-15

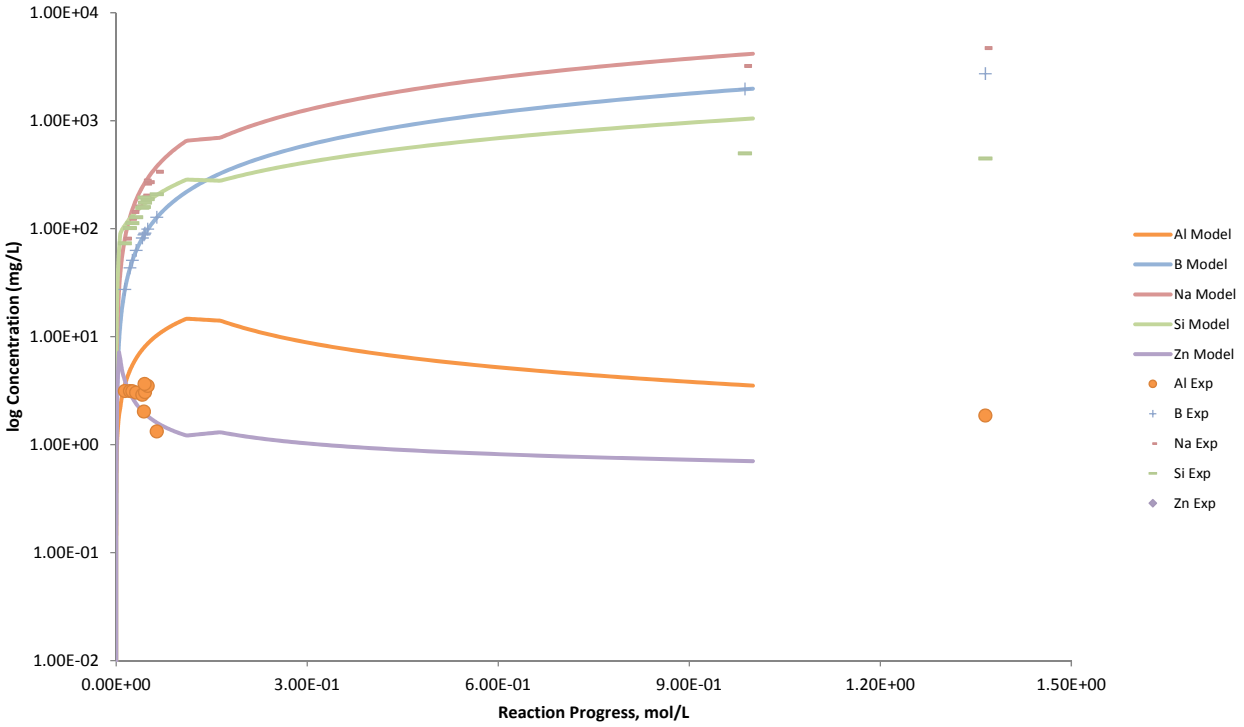


**Figure B.59**. Measured Solution Concentrations (mg/L) and Model Results for Al, B, Na, Si, and Zn, as a Function of Reaction Progress (mol-glass/kg) Determined for Glass Sample C22Si-15

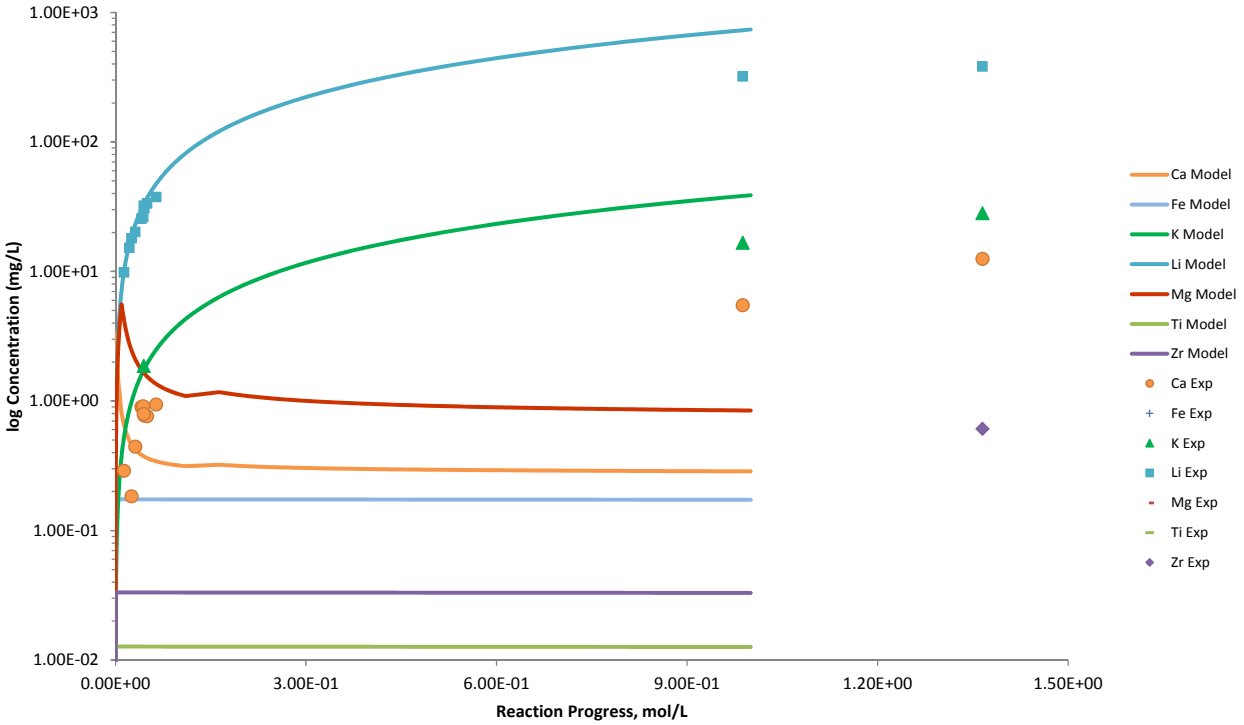


**Figure B.60**. Measured Solution Concentrations (mg/L) and Model Results for Ca, Fe, K, Li, Mg, Ti, and Zr, as a Function of Reaction Progress (mol-glass/kg) Determined for Glass Sample C22Si-15

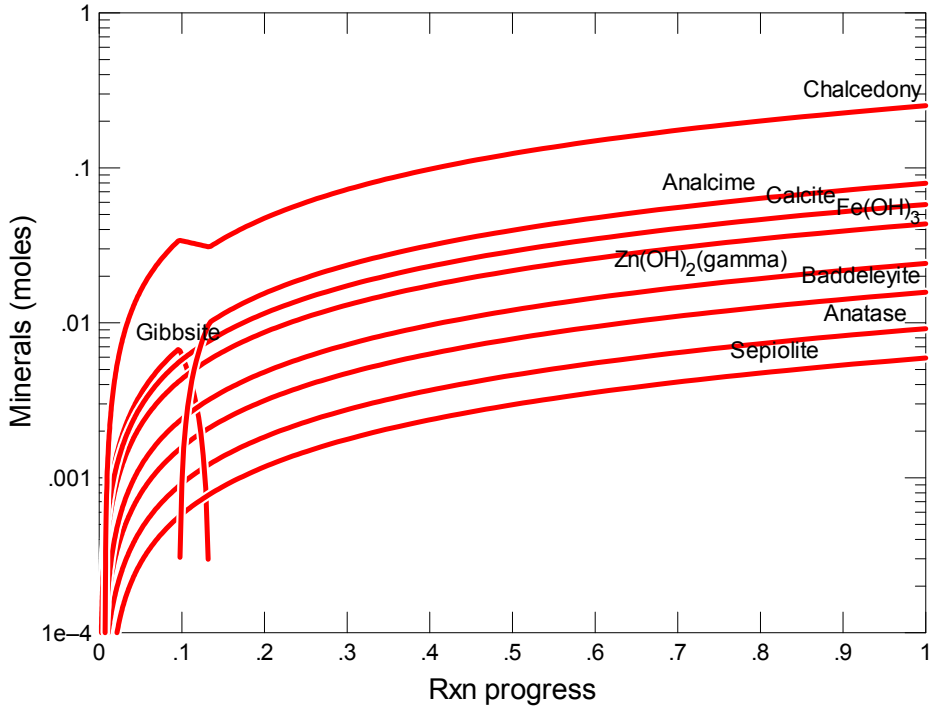


**Figure B.61**. Secondary Phases Calculated to Form as a Function of Reaction Progress (mol-glass/kg) Determined for Glass Sample LAWA102R1

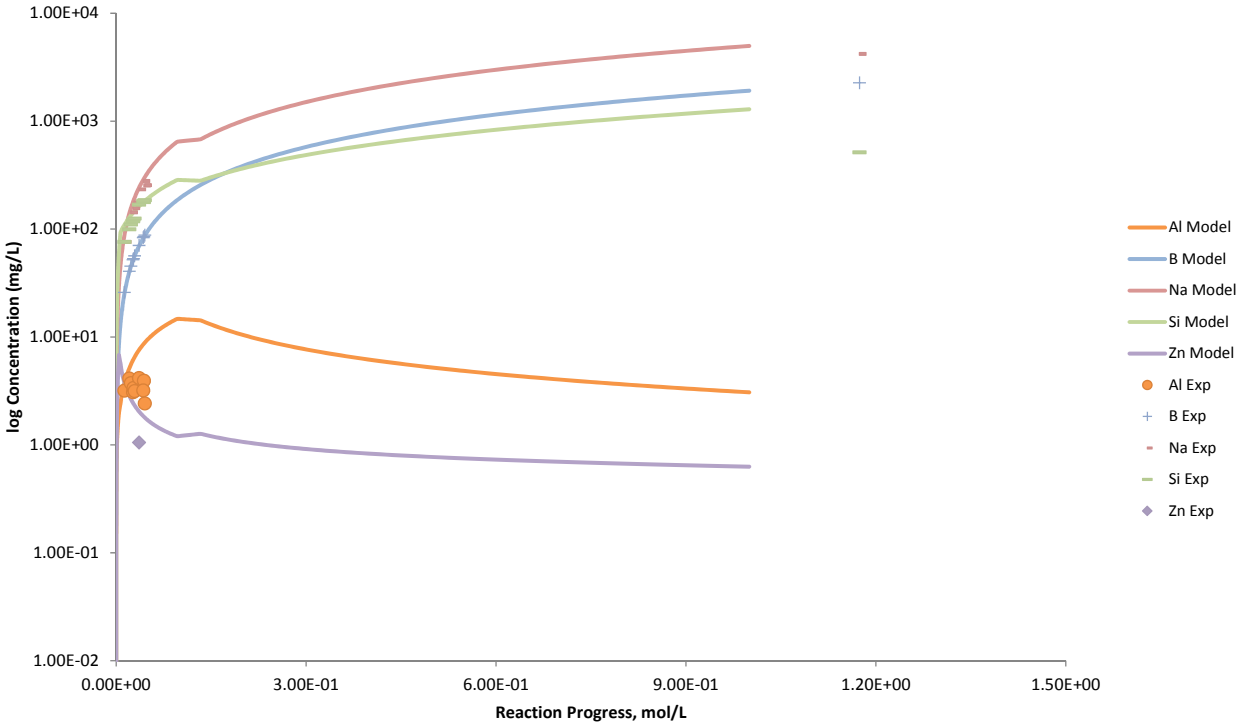


**Figure B.62**. Measured Solution Concentrations (mg/L) and Model Results for Al, B, Na, Si, and Zn, as a Function of Reaction Progress (mol-glass/kg) Determined for Glass Sample LAWA102R1

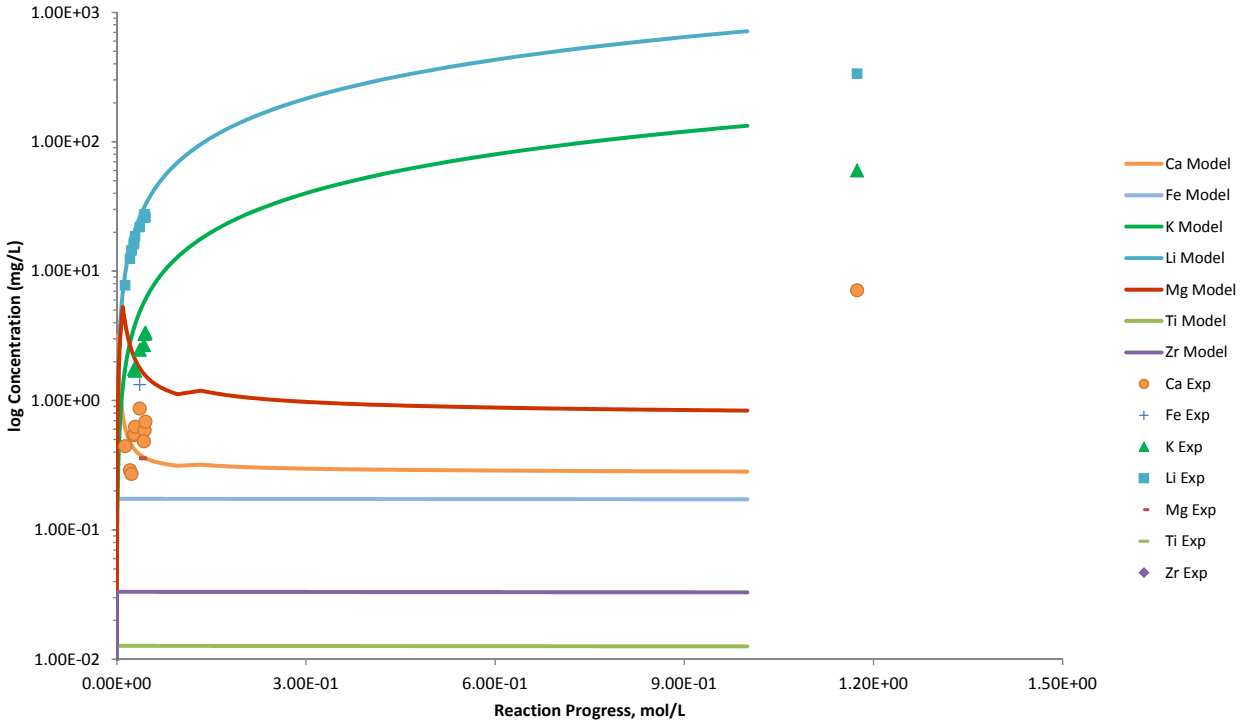


**Figure B.63**. Measured Solution Concentrations (mg/L) and Model Results for Ca, Fe, K, Li, Mg, Ti, and Zr, as a Function of Reaction Progress (mol-glass/kg) Determined for Glass Sample LAWA102R1

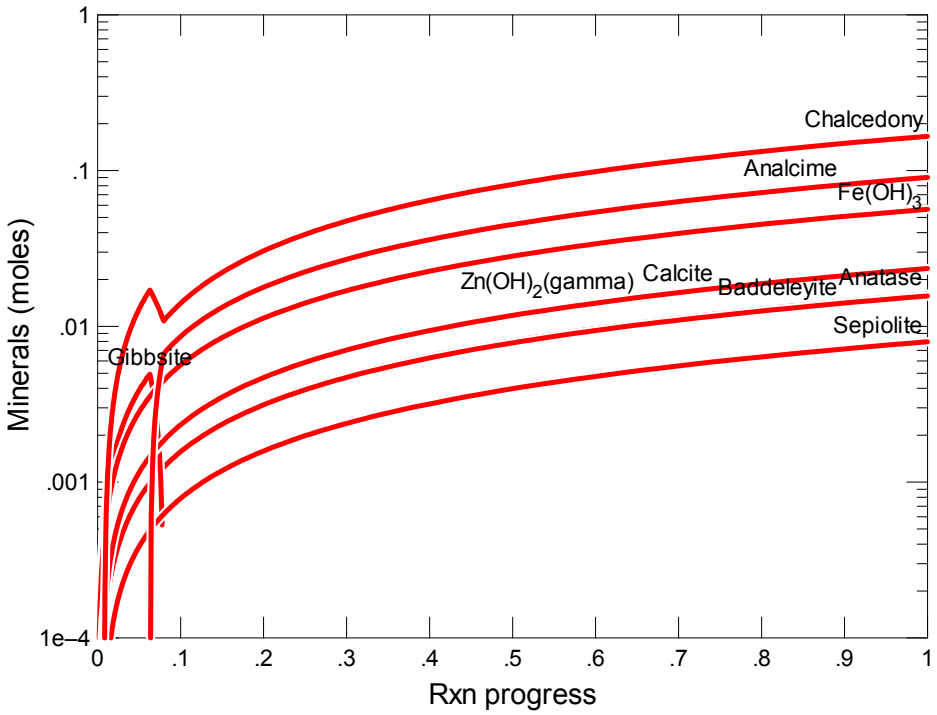


**Figure B.64**. Secondary Phases Calculated to Form as a Function of Reaction Progress (mol-glass/kg) Determined for Glass Sample LAWA104

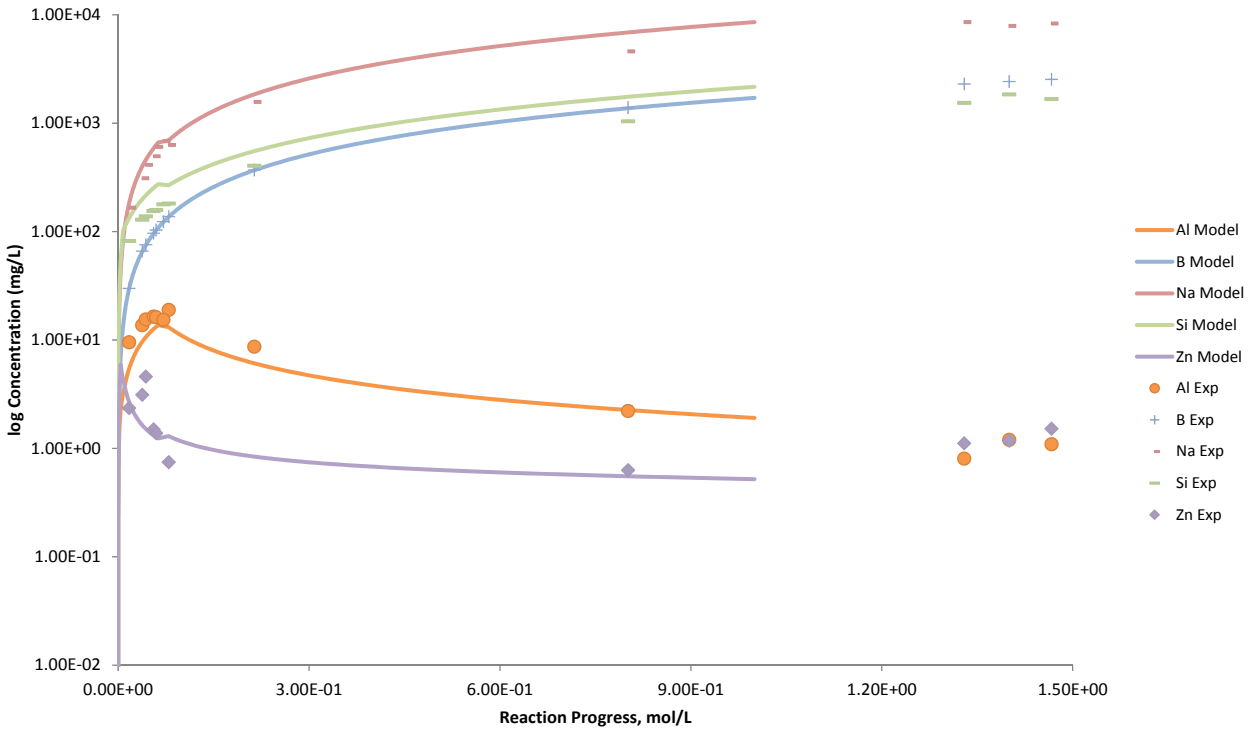


**Figure B.65**. Measured Solution Concentrations (mg/L) and Model Results for Al, B, Na, Si, and Zn, as a Function of Reaction Progress (mol-glass/kg) Determined for Glass Sample LAWA104

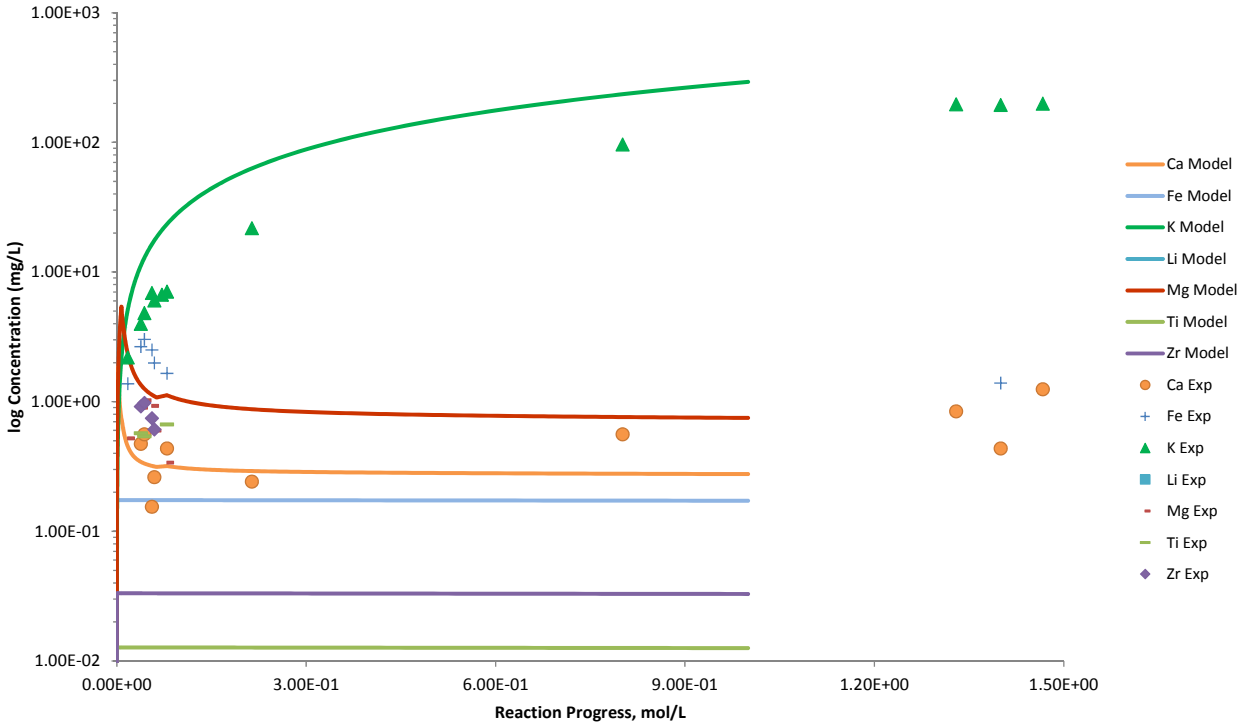


**Figure B.66**. Measured Solution Concentrations (mg/L) and Model Results for Ca, Fe, K, Li, Mg, Ti, and Zr, as a Function of Reaction Progress (mol-glass/kg) Determined for Glass Sample LAWA104

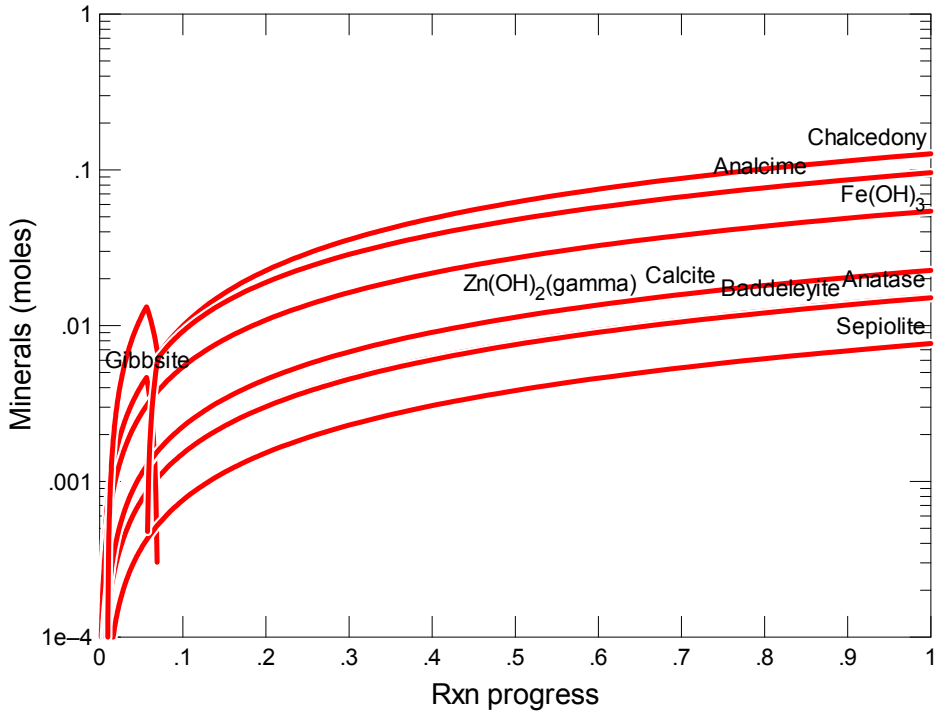


**Figure B.67**. Secondary Phases Calculated to Form as a Function of Reaction Progress (mol-glass/kg) Determined for Glass Sample LAWA105

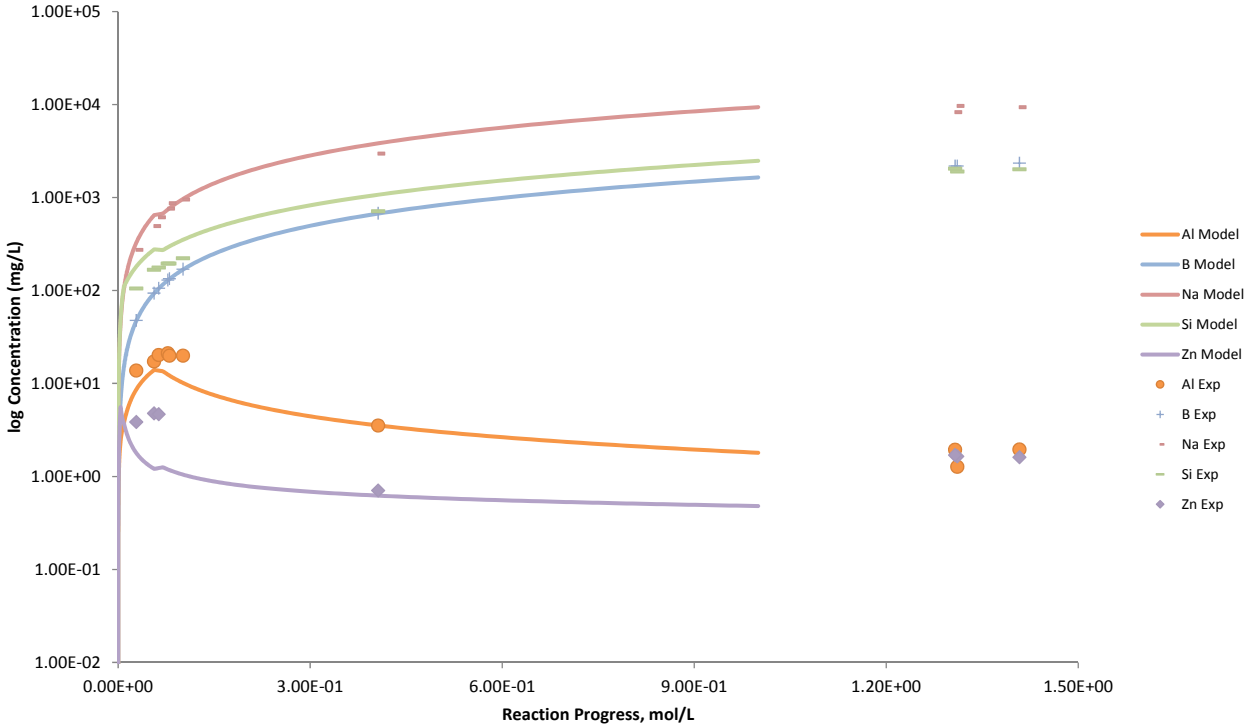


**Figure B.68**. Measured Solution Concentrations (mg/L) and Model Results for Al, B, Na, Si, and Zn, as a Function of Reaction Progress (mol-glass/kg) Determined for Glass Sample LAWA105

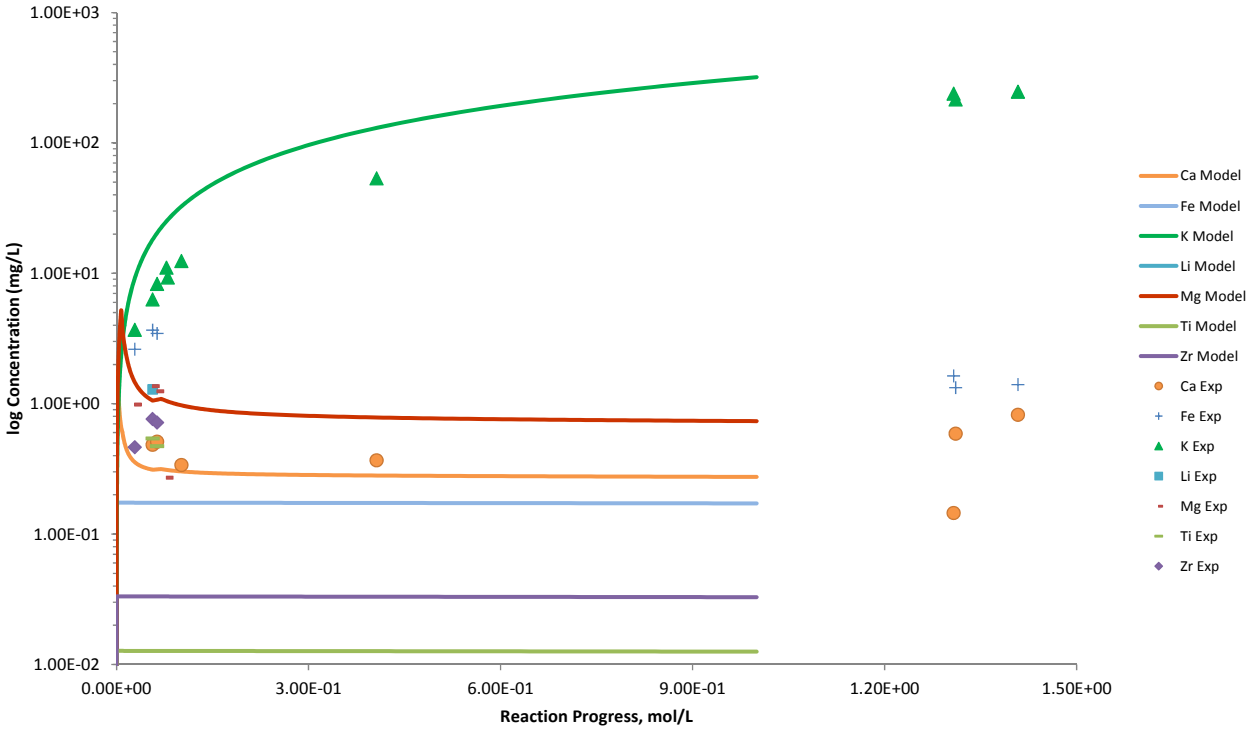


**Figure B.69**. Measured Solution Concentrations (mg/L) and Model Results for Ca, Fe, K, Li, Mg, Ti, and Zr, as a Function of Reaction Progress (mol-glass/kg) Determined for Glass Sample LAWA105

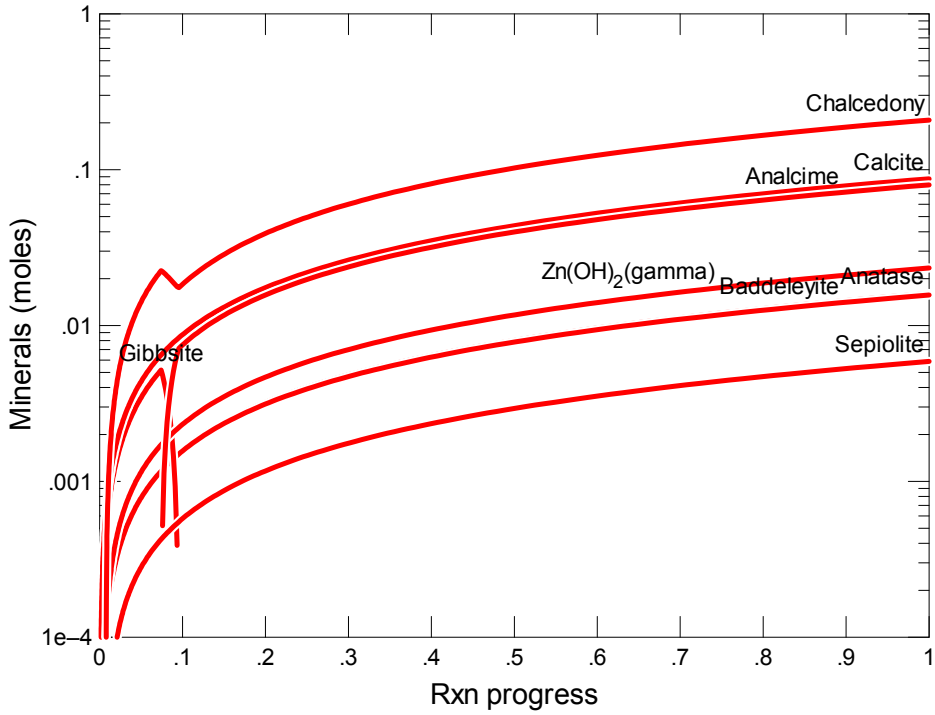


**Figure B.70**. Secondary Phases Calculated to Form as a Function of Reaction Progress (mol-glass/kg) Determined for Glass Sample LAWA112B14

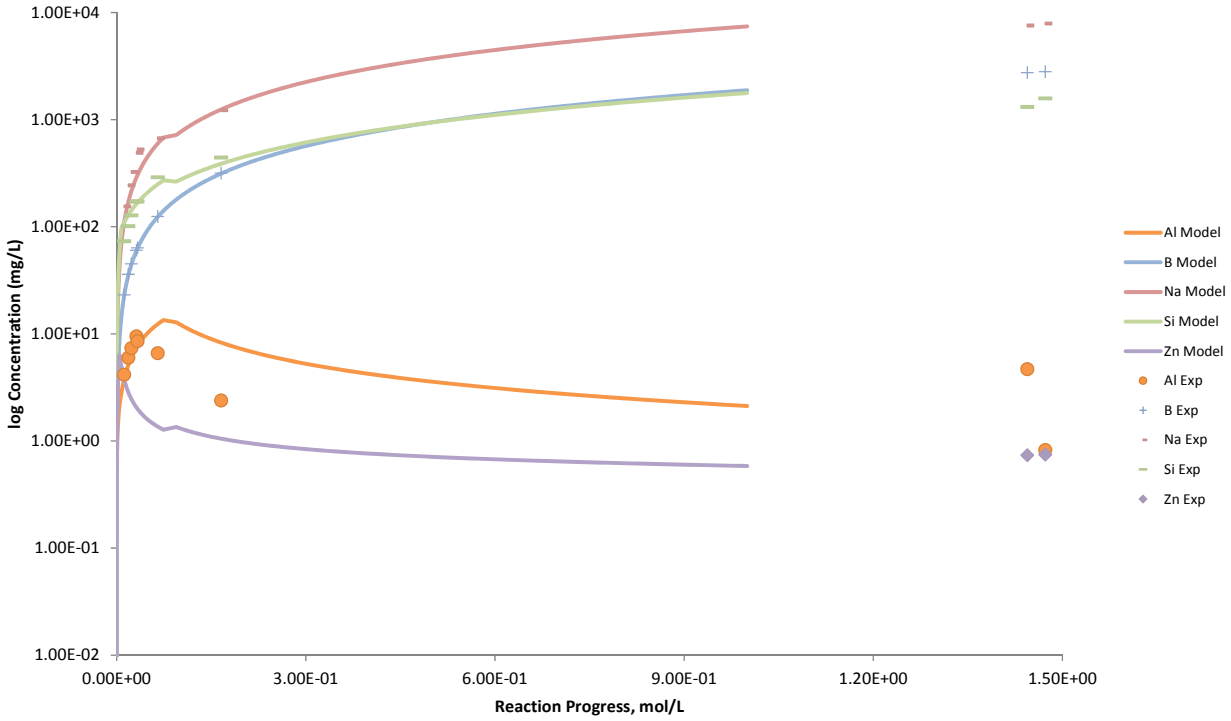


**Figure B.71**. Measured Solution Concentrations (mg/L) and Model Results for Al, B, Na, Si, and Zn, as a Function of Reaction Progress (mol-glass/kg) Determined for Glass Sample LAWA112B14

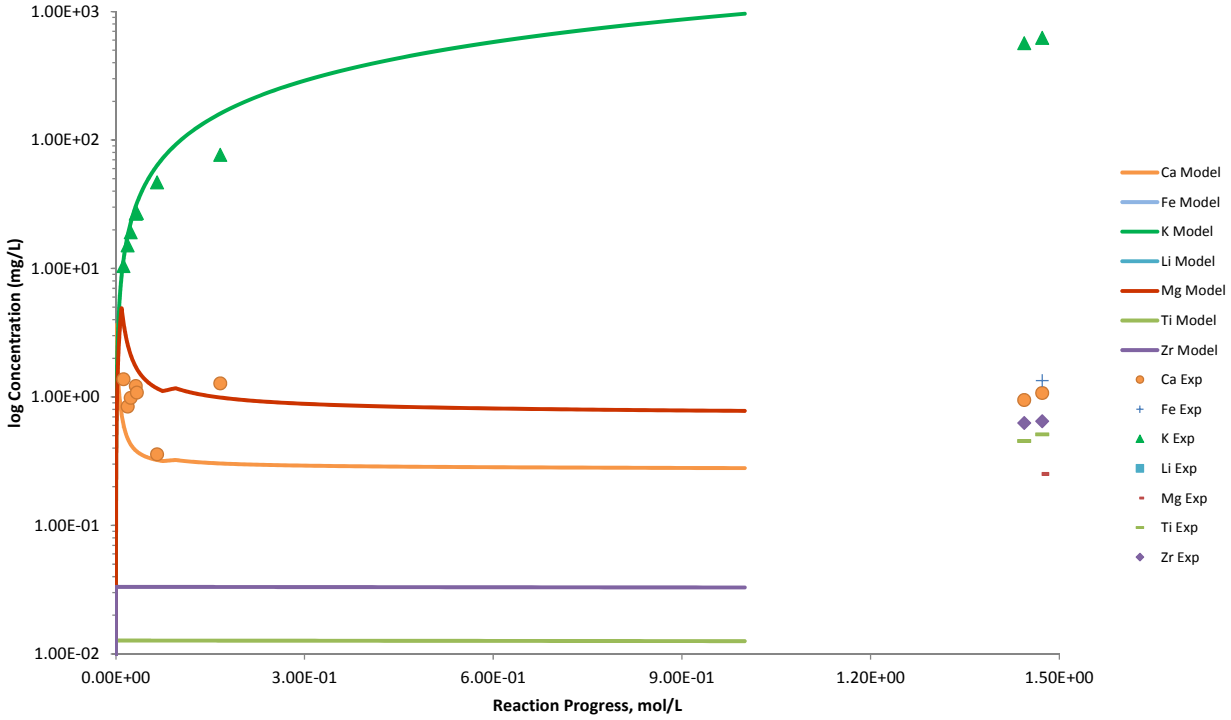


**Figure B.72**. Measured Solution Concentrations (mg/L) and Model Results for Ca, Fe, K, Li, Mg, Ti, and Zr, as a Function of Reaction Progress (mol-glass/kg) Determined for Glass Sample LAWA112B14

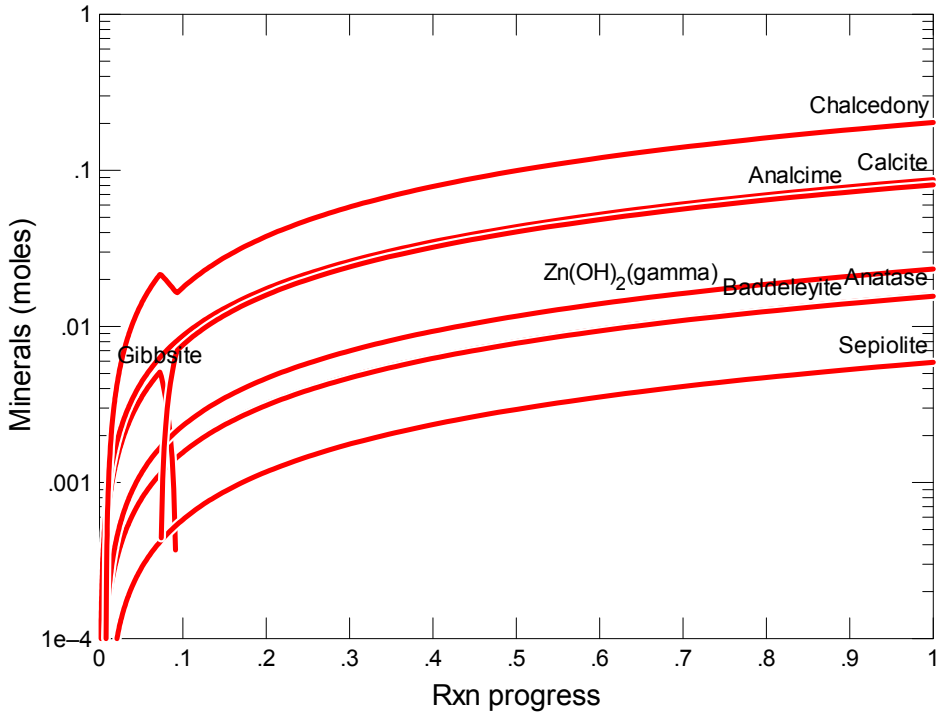


**Figure B.73**. Secondary Phases Calculated to Form as a Function of Reaction Progress (mol-glass/kg) Determined for Glass Sample LAWA112B15

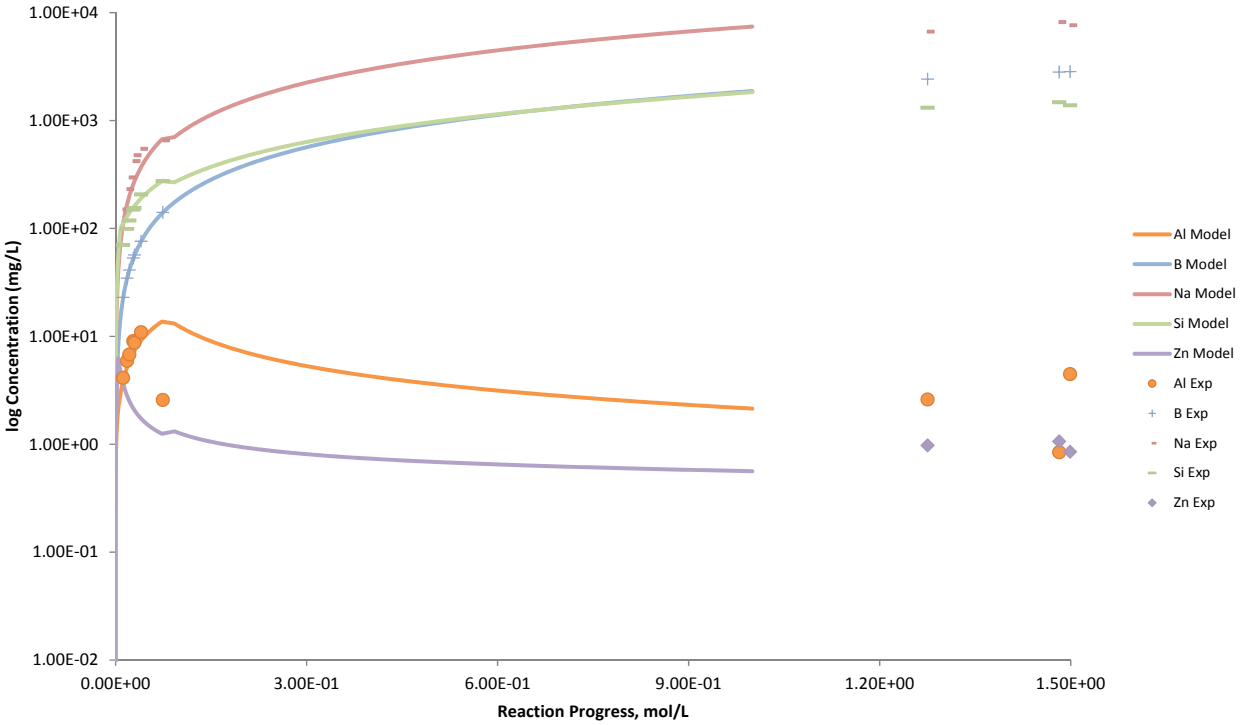


**Figure B.74**. Measured Solution Concentrations (mg/L) and Model Results for Al, B, Na, Si, and Zn, as a Function of Reaction Progress (mol-glass/kg) Determined for Glass Sample LAWA112B15

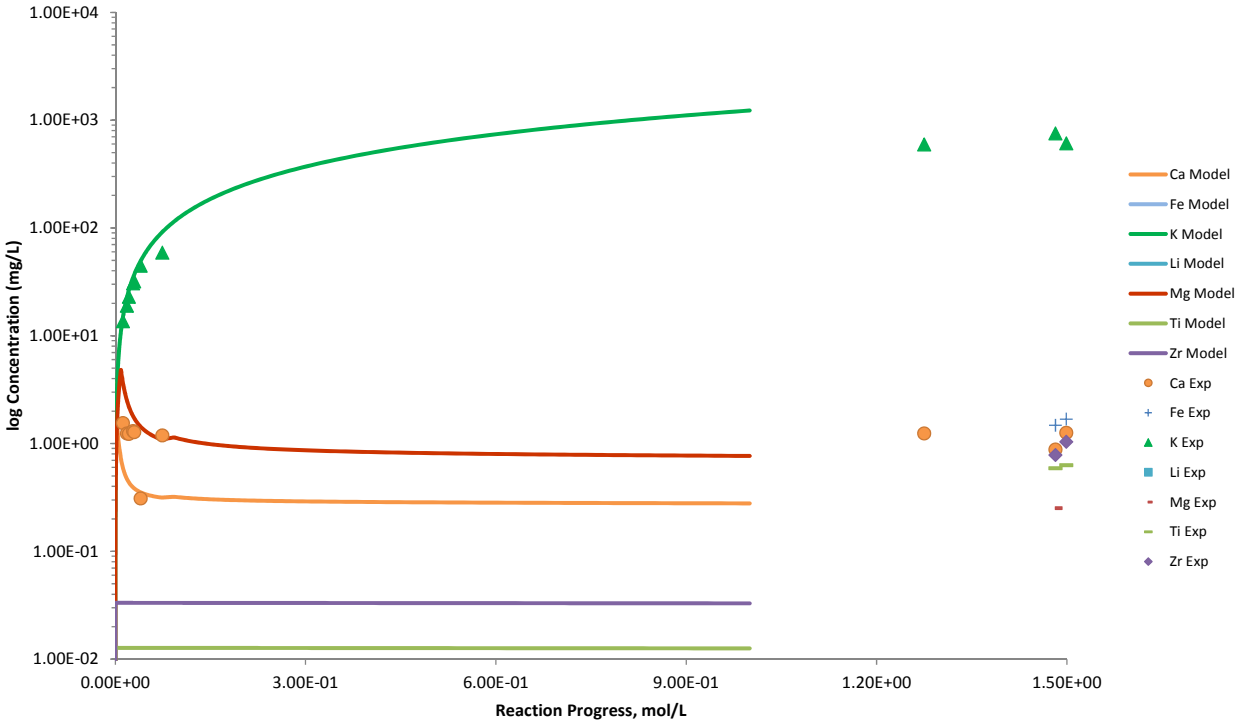


**Figure B.75**. Measured Solution Concentrations (mg/L) and Model Results for Ca, Fe, K, Li, Mg, Ti, and Zr, as a Function of Reaction Progress (mol-glass/kg) Determined for Glass Sample LAWA112B15

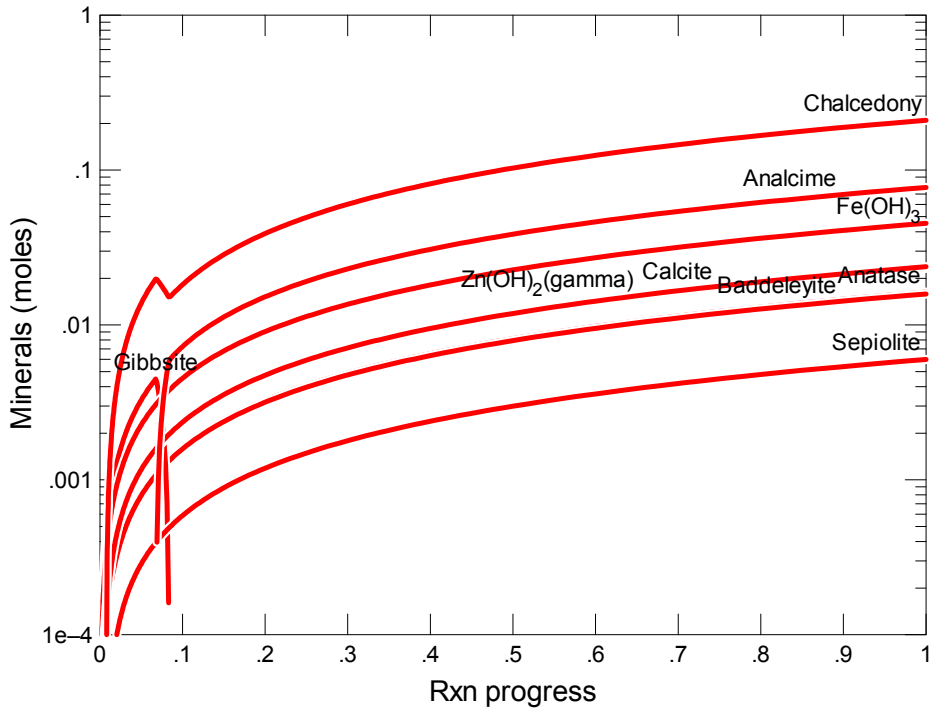


**Figure B.76**. Secondary Phases Calculated to Form as a Function of Reaction Progress (mol-glass/kg) Determined for Glass Sample LAWA125

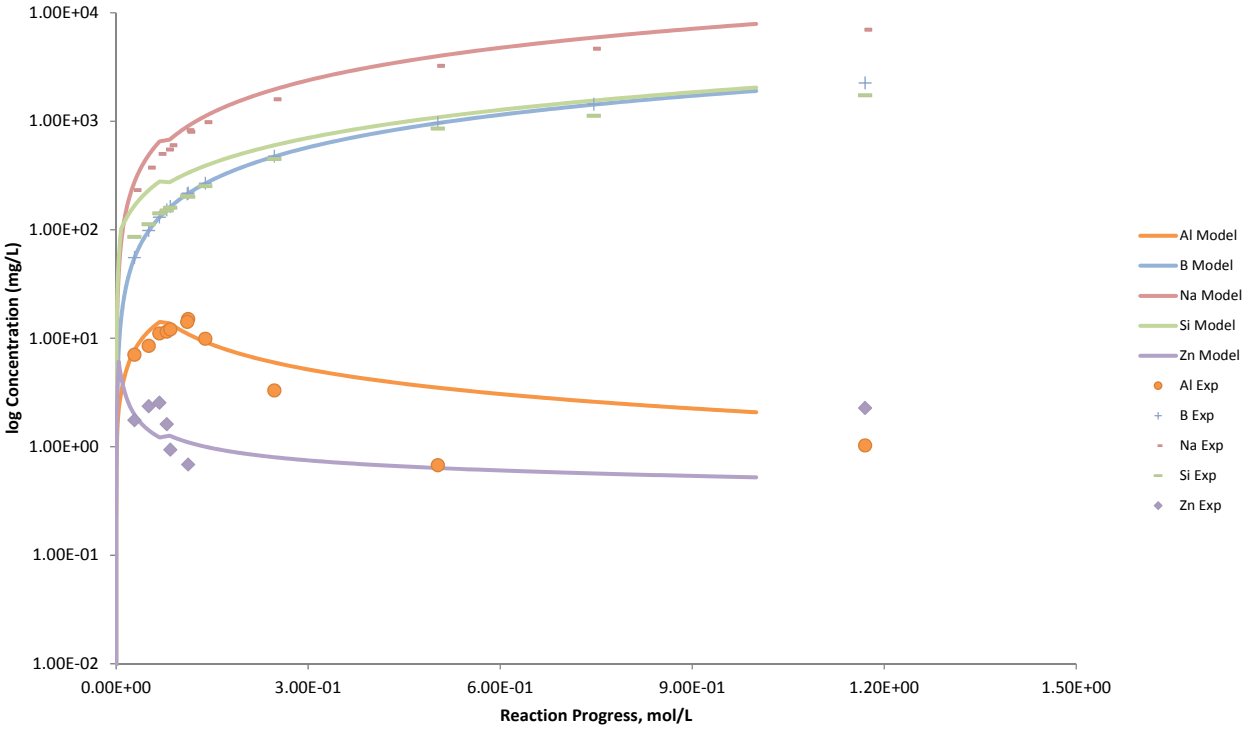


**Figure B.77**. Measured Solution Concentrations (mg/L) and Model Results for Al, B, Na, Si, and Zn, as a Function of Reaction Progress (mol-glass/kg) Determined for Glass Sample LAWA125

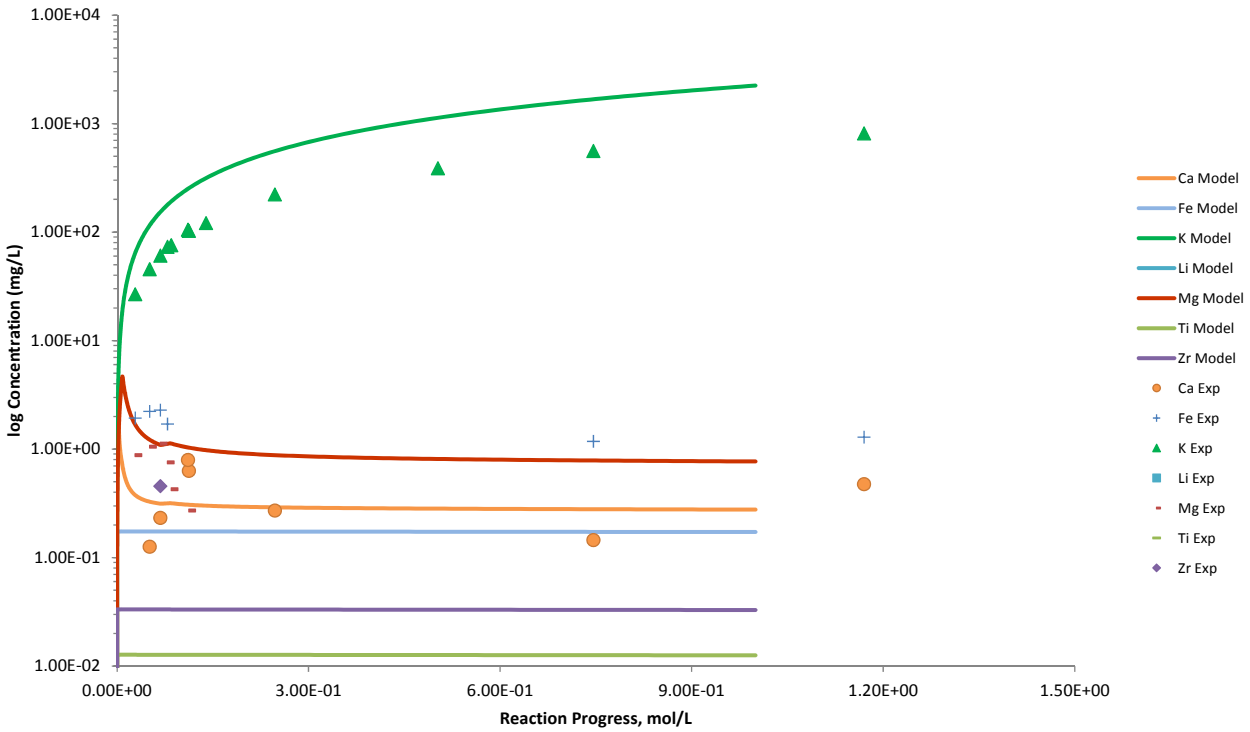


**Figure B.78**. Measured Solution Concentrations (mg/L) and Model Results for Ca, Fe, K, Li, Mg, Ti, and Zr, as a Function of Reaction Progress (mol-glass/kg) Determined for Glass Sample LAWA125

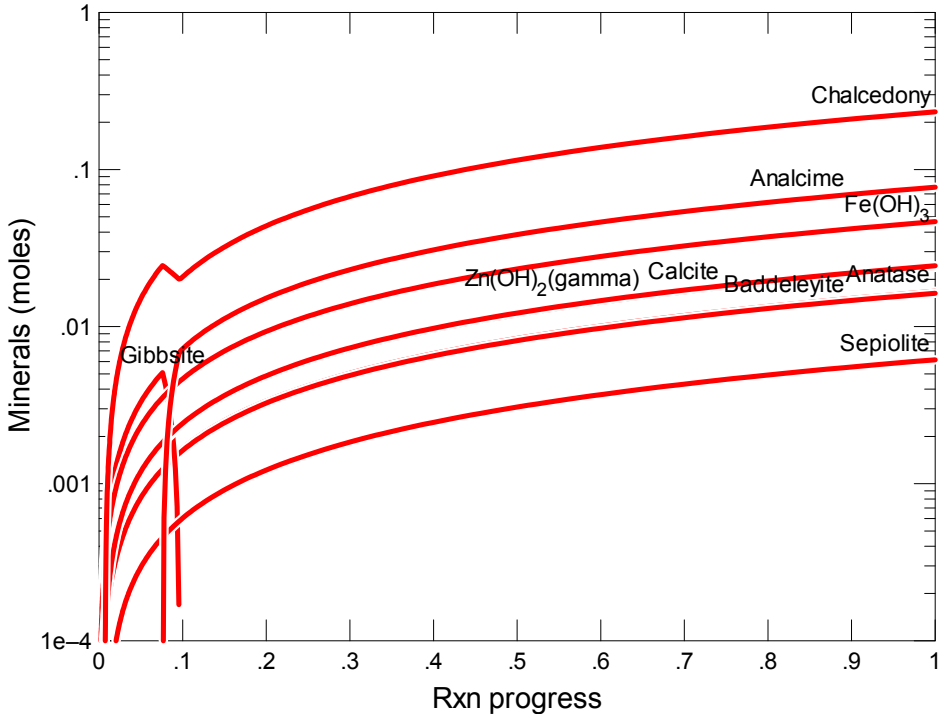


**Figure B.79**. Secondary Phases Calculated to Form as a Function of Reaction Progress (mol-glass/kg) Determined for Glass Sample LAWA126

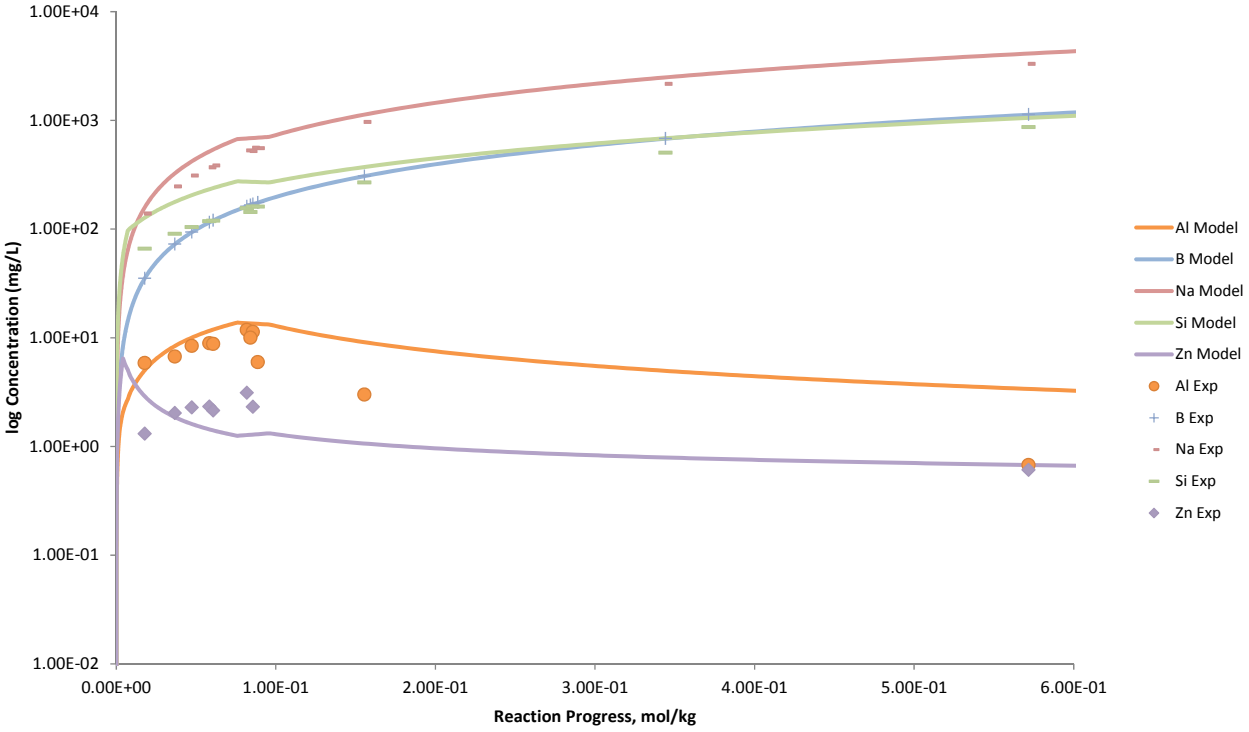


**Figure B.80**. Measured Solution Concentrations (mg/L) and Model Results for Al, B, Na, Si, and Zn, as a Function of Reaction Progress (mol-glass/kg) Determined for Glass Sample LAWA126

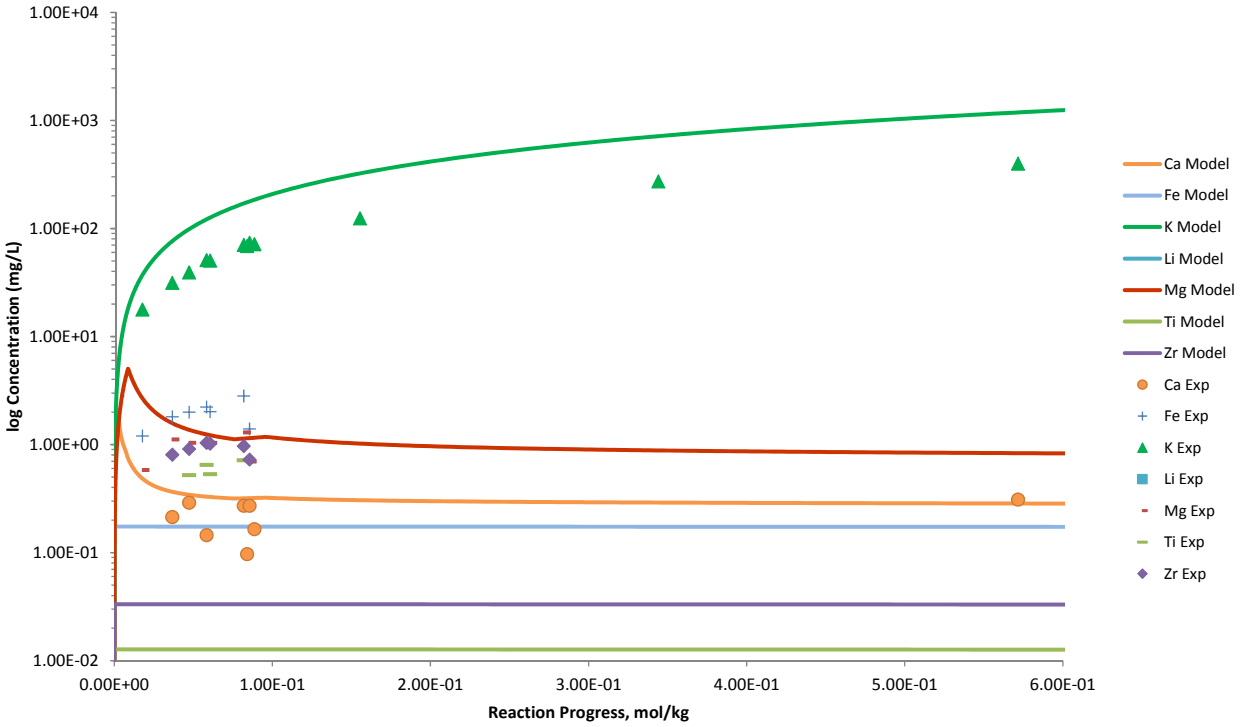


**Figure B.81**. Measured Solution Concentrations (mg/L) and Model Results for Ca, Fe, K, Li, Mg, Ti, and Zr, as a Function of Reaction Progress (mol-glass/kg) Determined for Glass Sample LAWA126

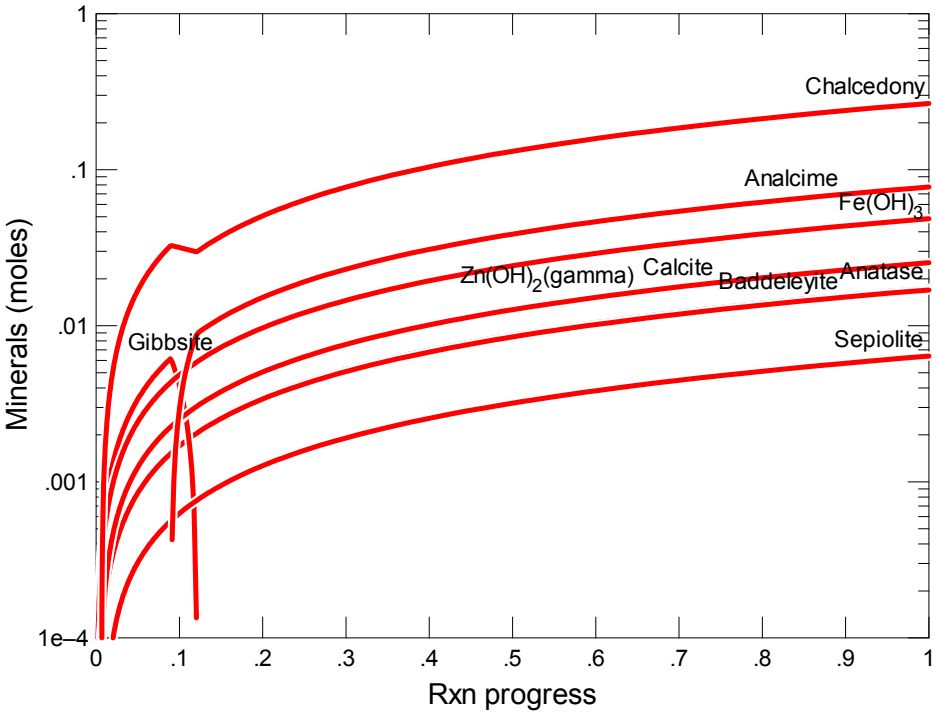


**Figure B.82**. Secondary Phases Calculated to Form as a Function of Reaction Progress (mol-glass/kg) Determined for Glass Sample LAWA127R1

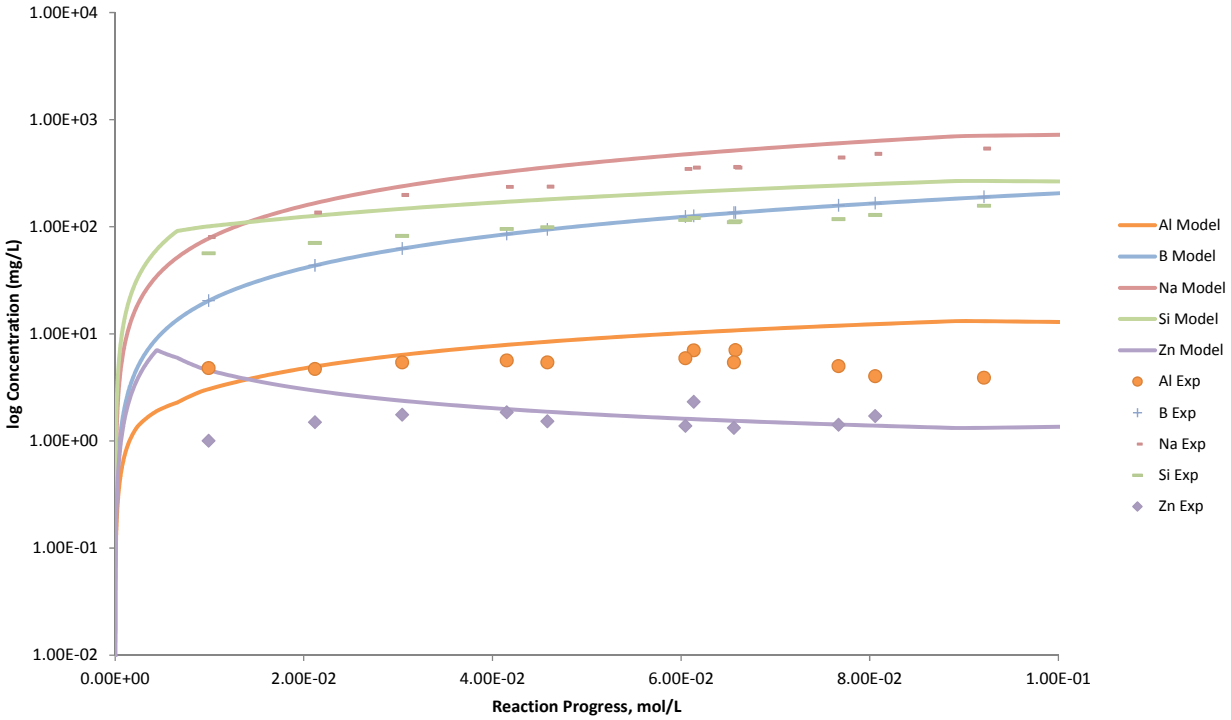


**Figure B.83**. Measured Solution Concentrations (mg/L) and Model Results for Al, B, Na, Si, and Zn, as a Function of Reaction Progress (mol-glass/kg) Determined for Glass Sample LAWA127R1

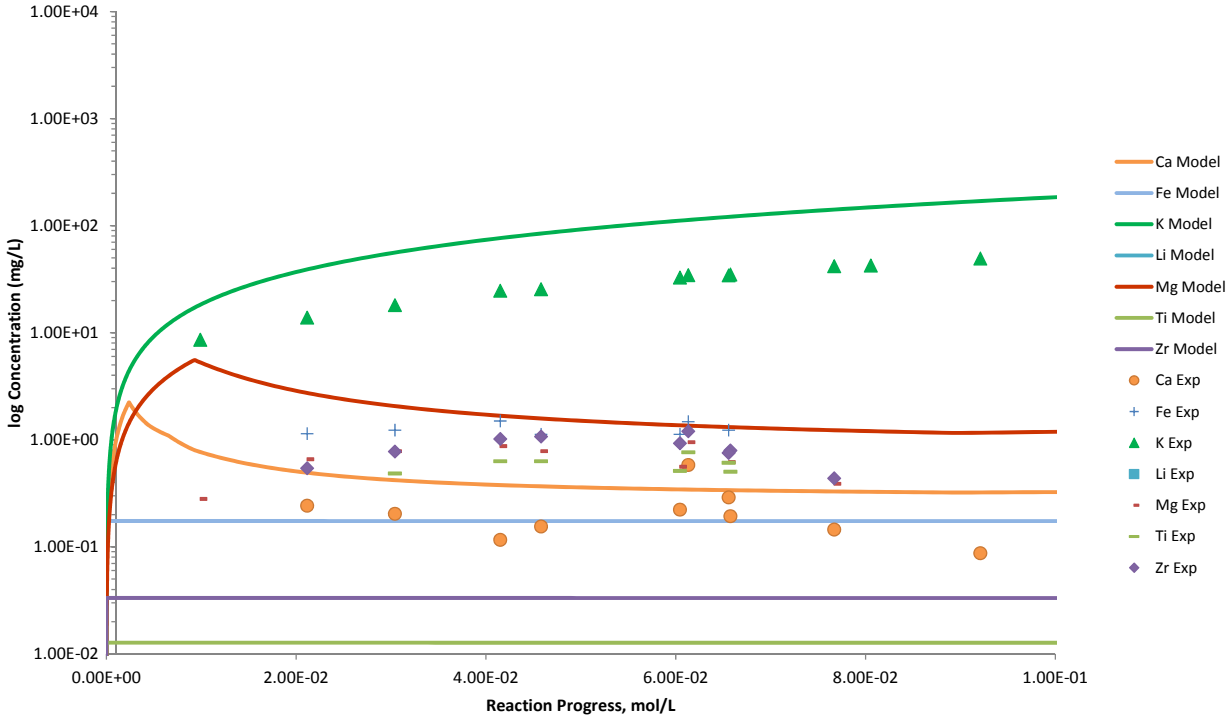


**Figure B.84**. Measured Solution Concentrations (mg/L) and Model Results for Ca, Fe, K, Li, Mg, Ti, and Zr, as a Function of Reaction Progress (mol-glass/kg) Determined for Glass Sample LAWA127R1

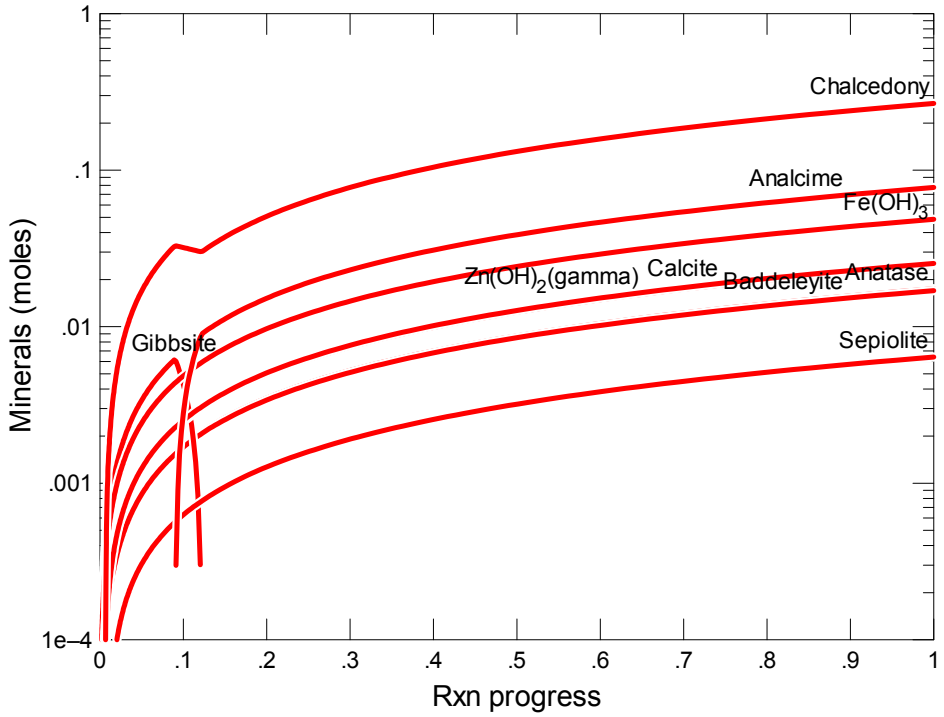


**Figure B.85**. Secondary Phases Calculated to Form as a Function of Reaction Progress (mol-glass/kg) Determined for Glass Sample LAWA127R2

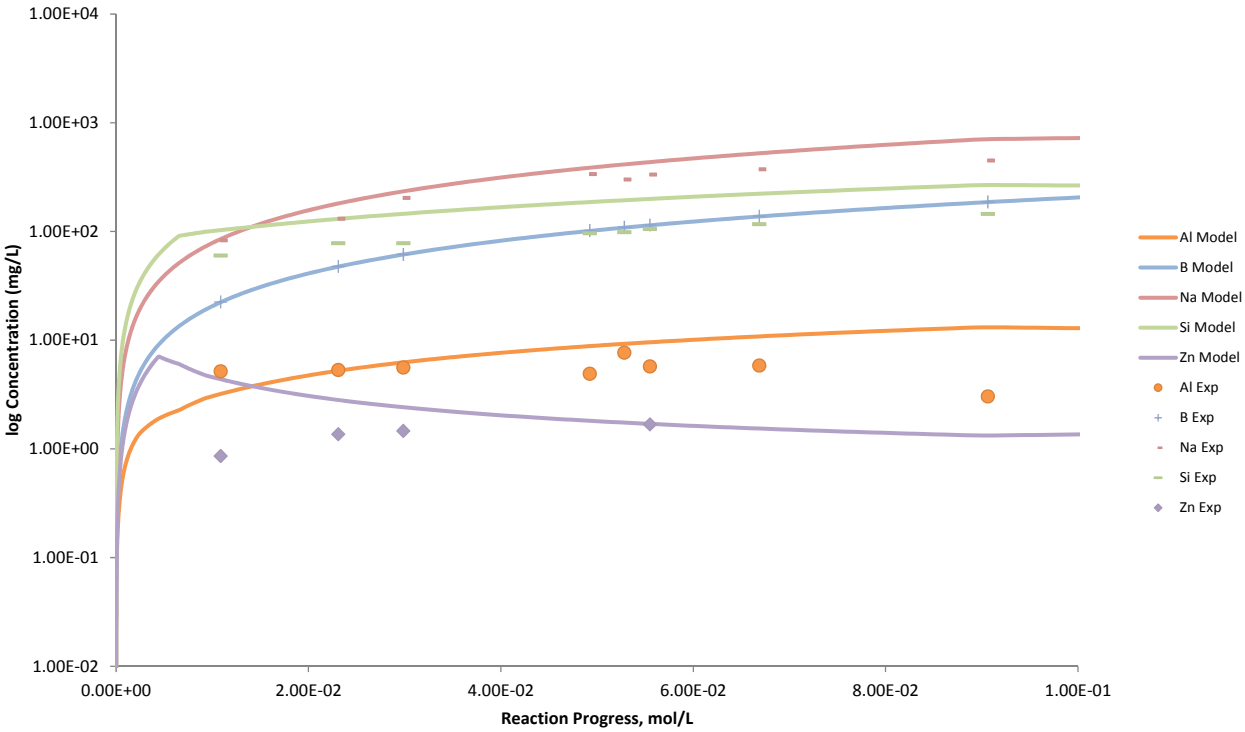


**Figure B.86**. Measured Solution Concentrations (mg/L) and Model Results for Al, B, Na, Si, and Zn, as a Function of Reaction Progress (mol-glass/kg) Determined for Glass Sample LAWA127R2

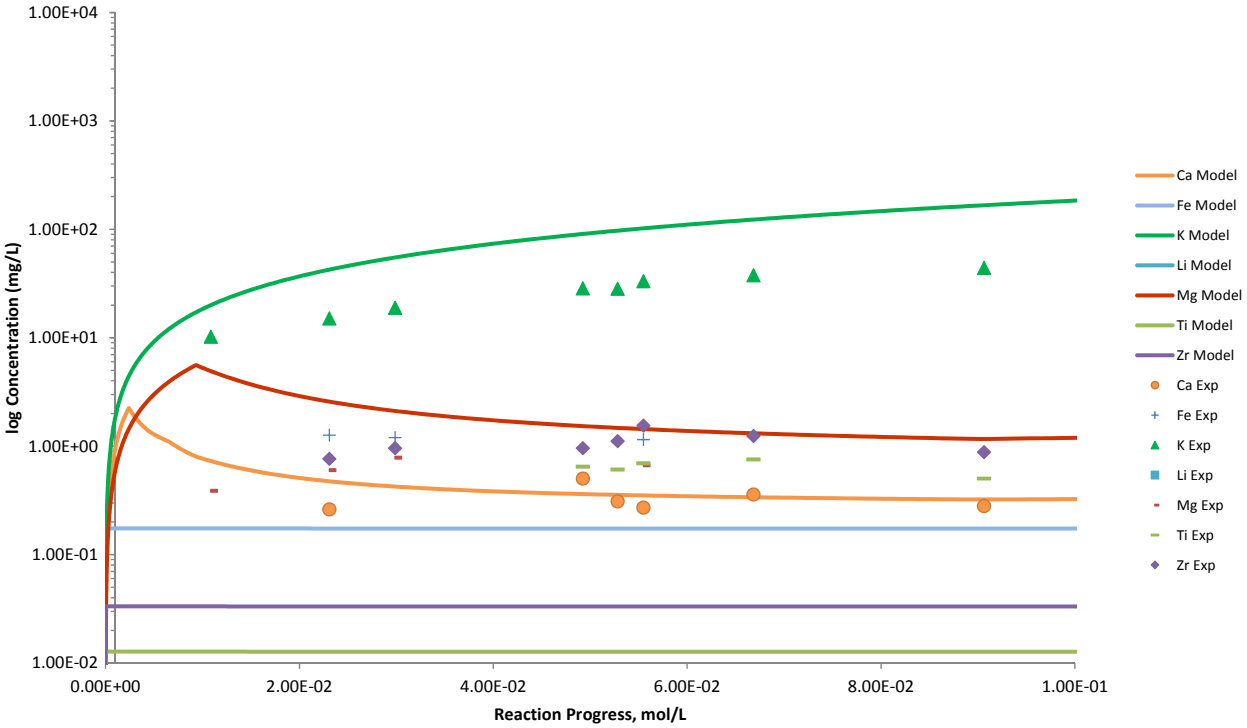


**Figure B.87**. Measured Solution Concentrations (mg/L) and Model Results for Ca, Fe, K, Li, Mg, Ti, and Zr, as a Function of Reaction Progress (mol-glass/kg) Determined for Glass Sample LAWA127R2

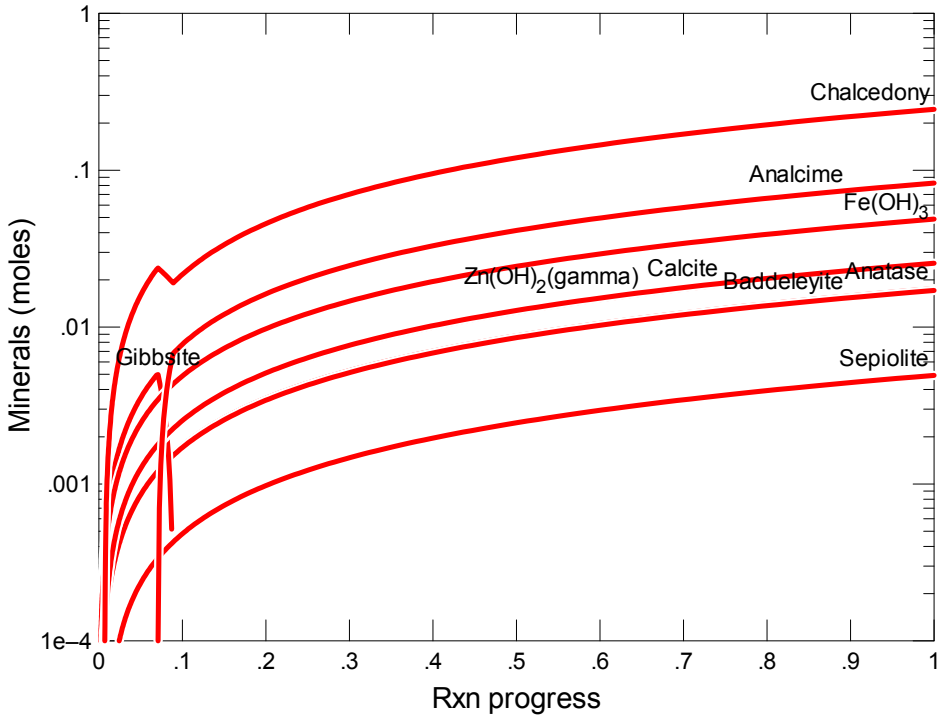


**Figure B.88**. Secondary Phases Calculated to Form as a Function of Reaction Progress (mol-glass/kg) Determined for Glass Sample LAWA128

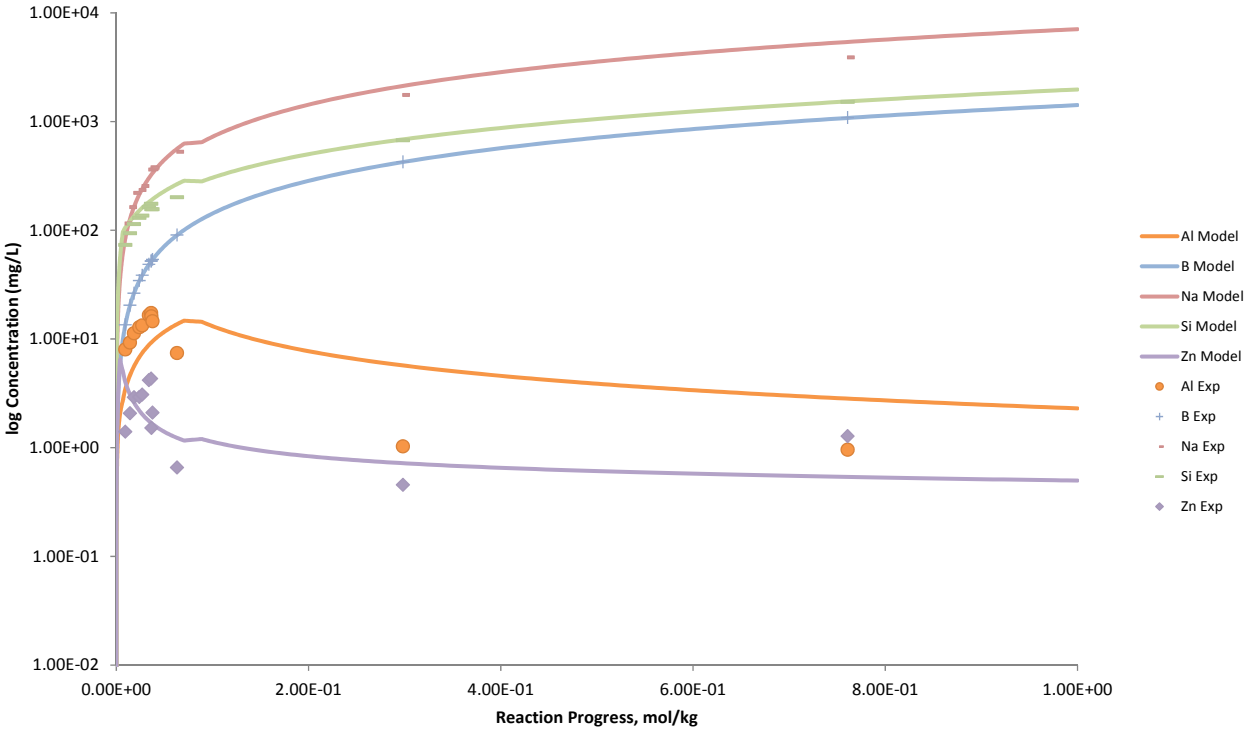


**Figure B.89**. Measured Solution Concentrations (mg/L) and Model Results for Al, B, Na, Si, and Zn, as a Function of Reaction Progress (mol-glass/kg) Determined for Glass Sample LAWA128

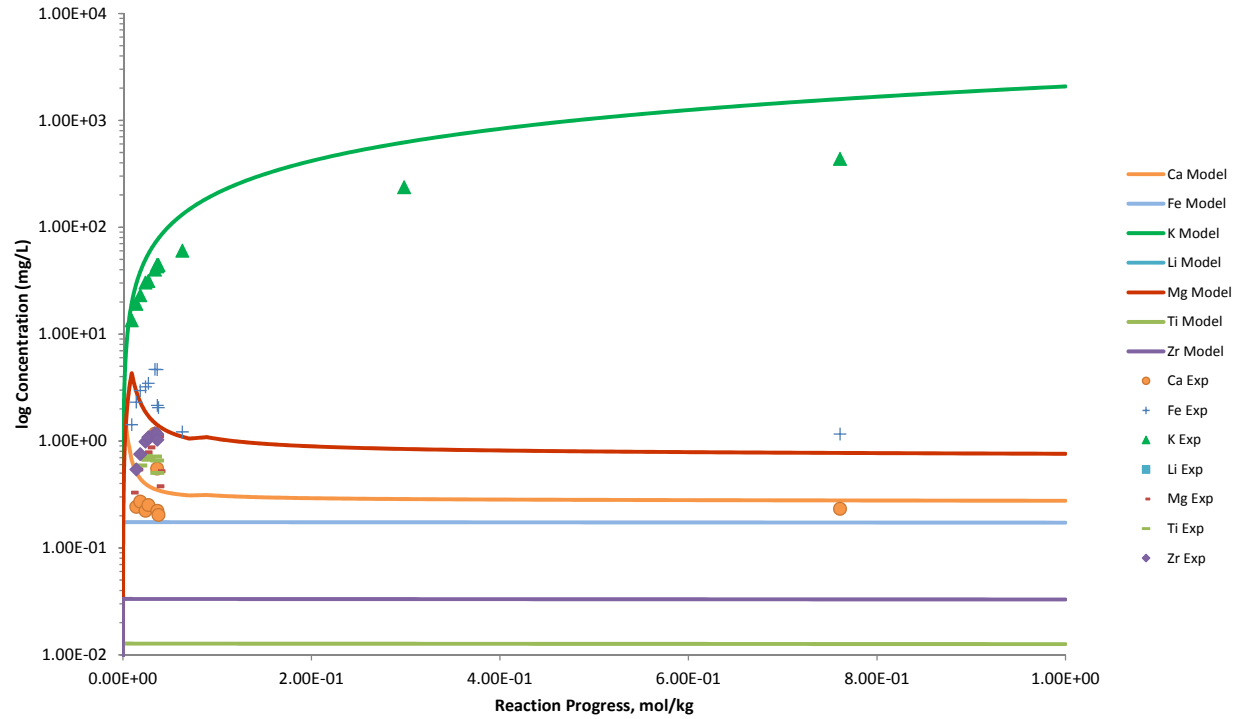


**Figure B.90**. Measured Solution Concentrations (mg/L) and Model Results for Ca, Fe, K, Li, Mg, Ti, and Zr, as a Function of Reaction Progress (mol-glass/kg) Determined for Glass Sample LAWA128

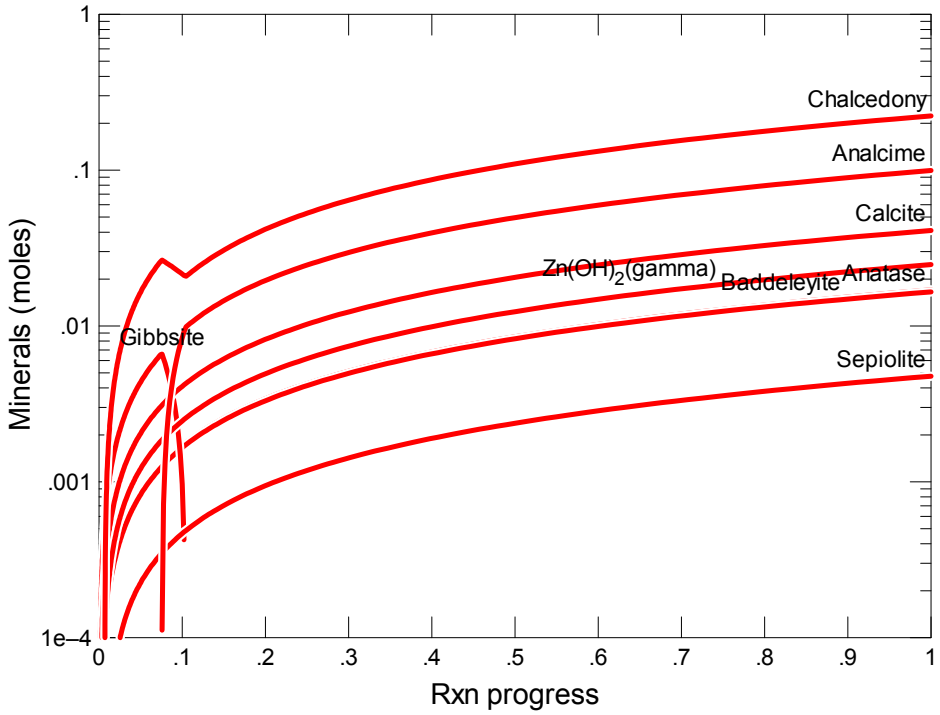


**Figure B.91**. Secondary Phases Calculated to Form as a Function of Reaction Progress (mol-glass/kg) Determined for Glass Sample LAWA129

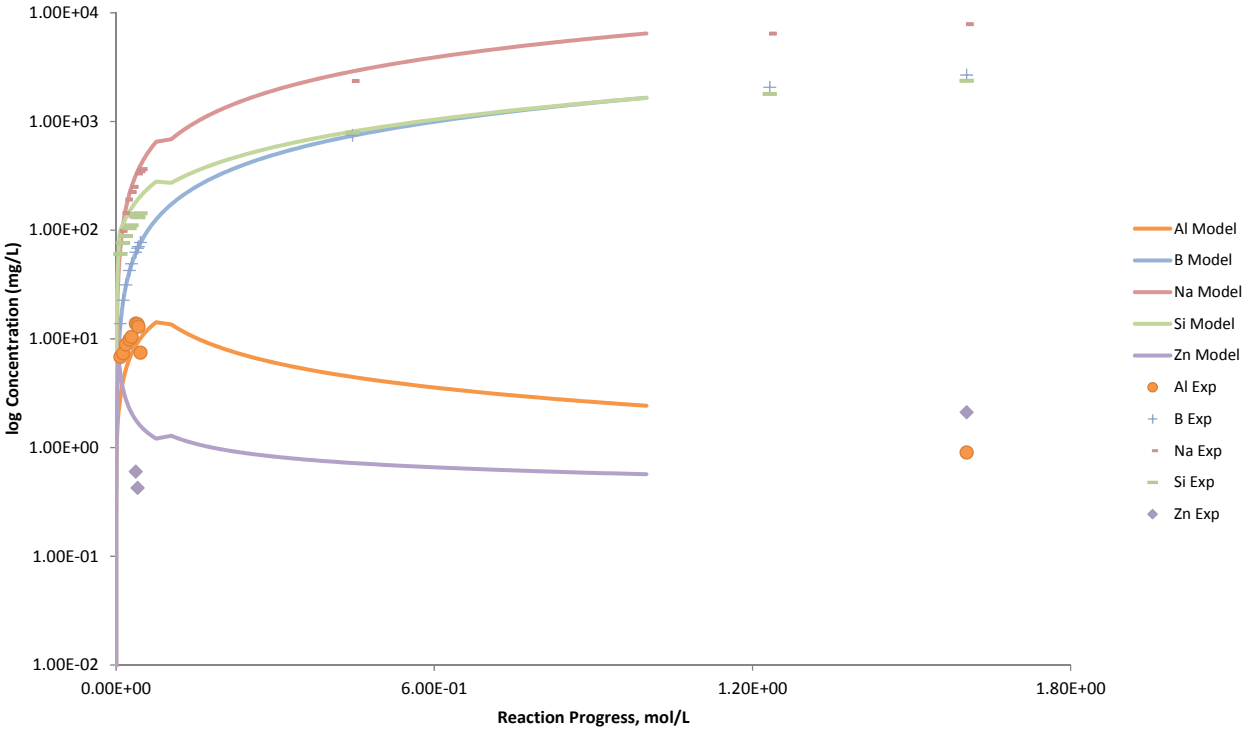


**Figure B.92**. Measured Solution Concentrations (mg/L) and Model Results for Al, B, Na, Si, and Zn, as a Function of Reaction Progress (mol-glass/kg) Determined for Glass Sample LAWA129

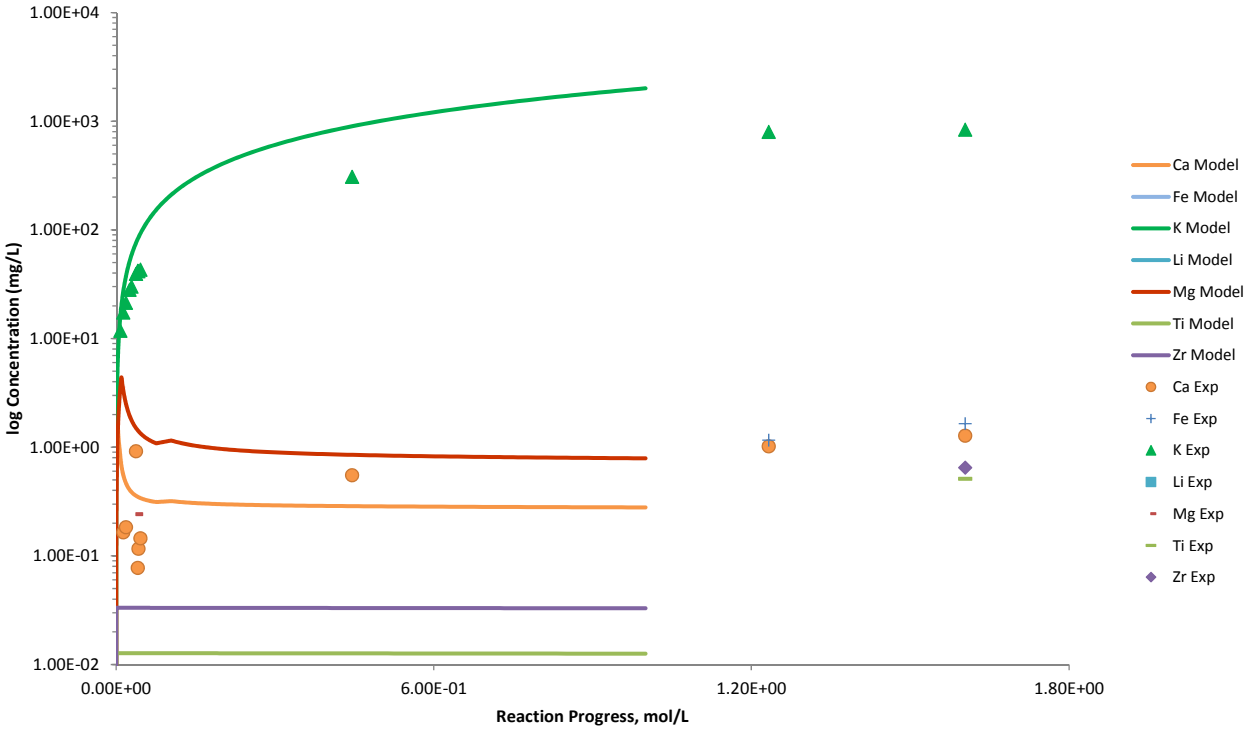


**Figure B.93**. Measured Solution Concentrations (mg/L) and Model Results for Ca, Fe, K, Li, Mg, Ti, and Zr, as a Function of Reaction Progress (mol-glass/kg) Determined for Glass Sample LAWA129

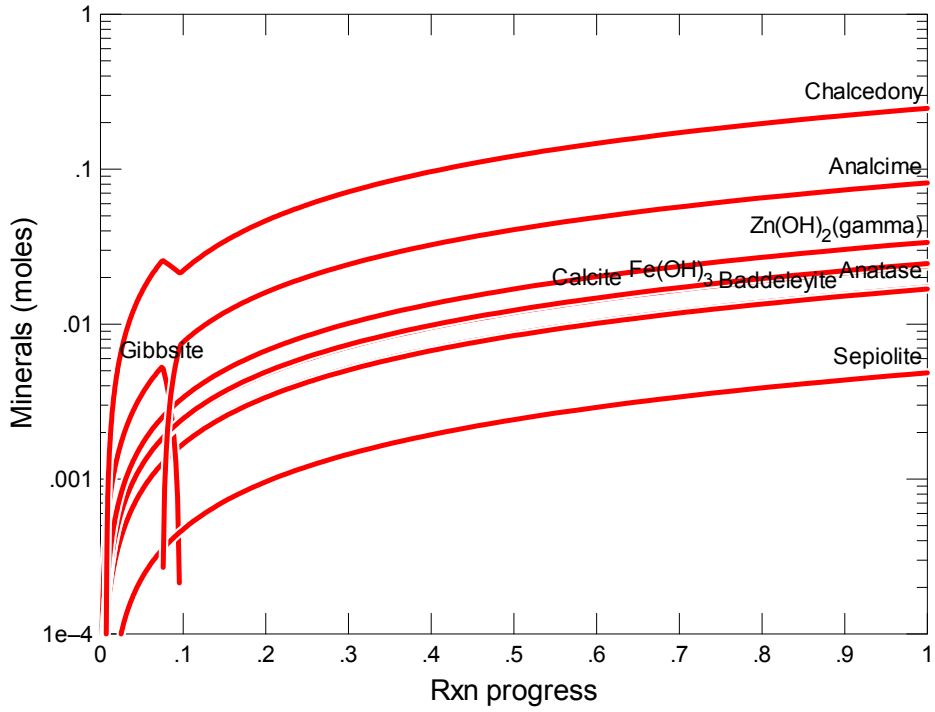


**Figure B.94**. Secondary Phases Calculated to Form as a Function of Reaction Progress (mol-glass/kg) Determined for Glass Sample LAWA130

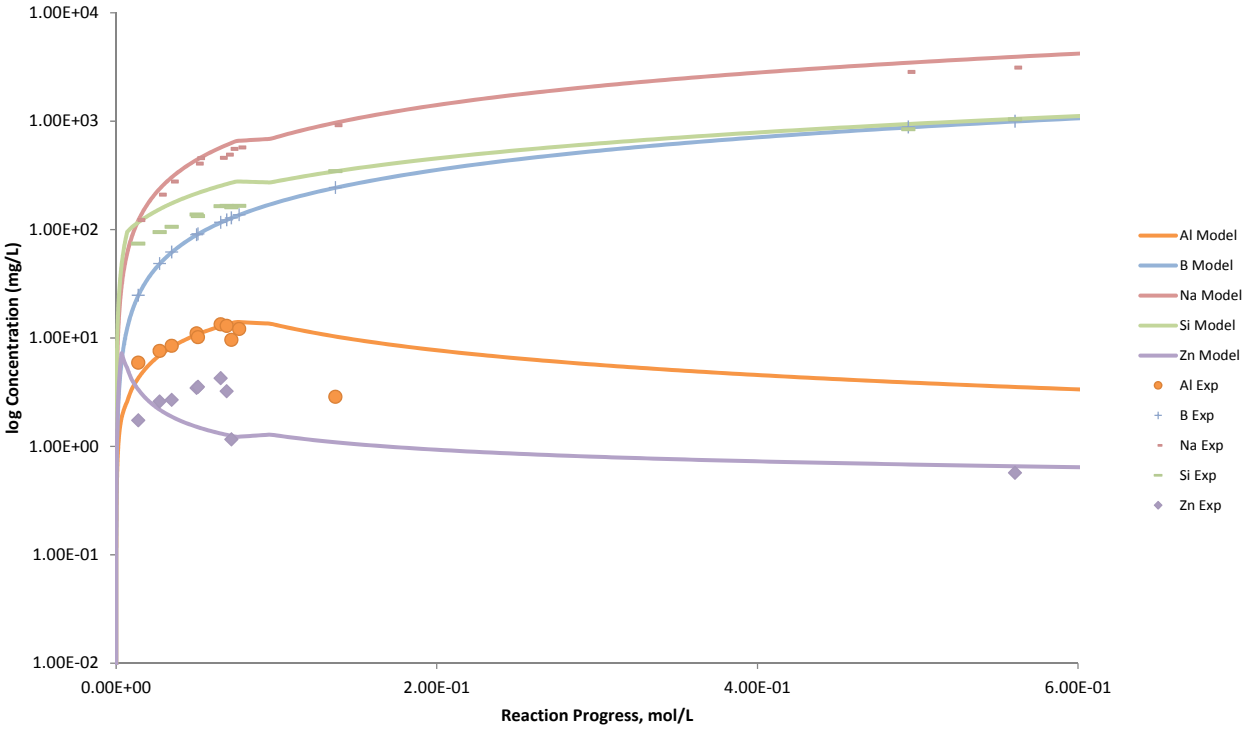


**Figure B.95**. Measured Solution Concentrations (mg/L) and Model Results for Al, B, Na, Si, and Zn, as a Function of Reaction Progress (mol-glass/kg) Determined for Glass Sample LAWA130

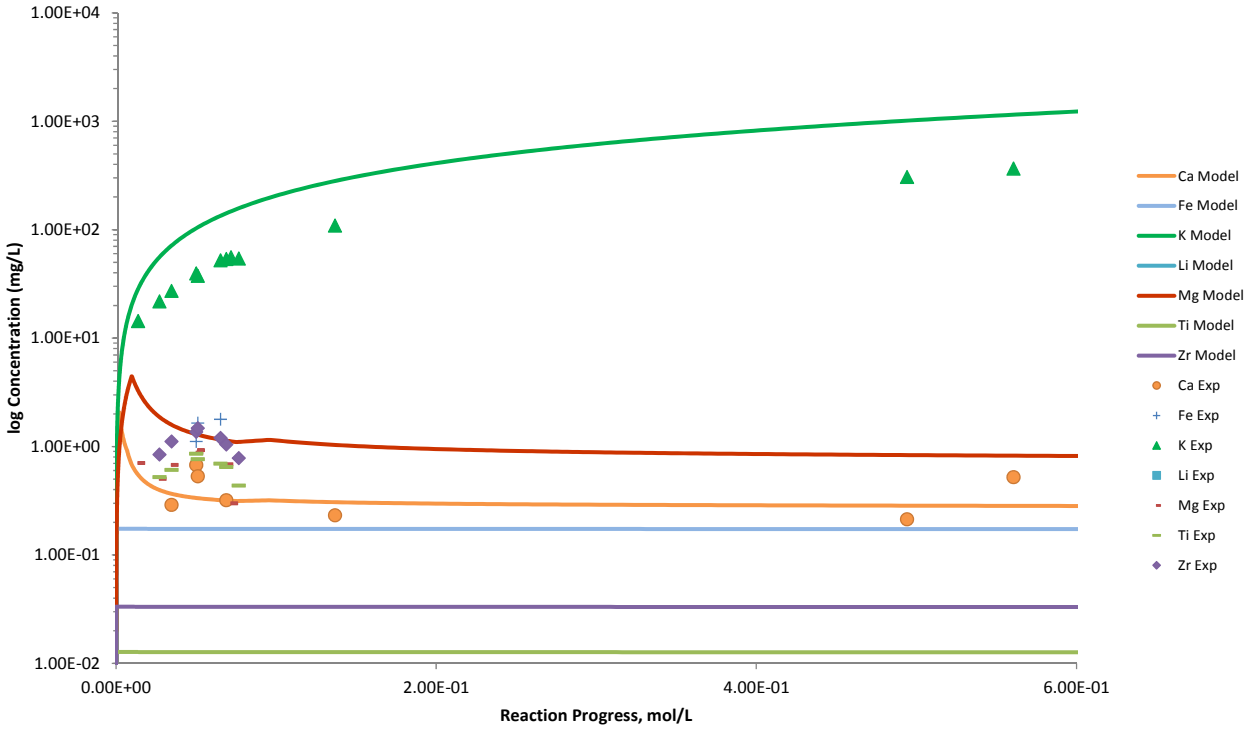


**Figure B.96**. Measured Solution Concentrations (mg/L) and Model Results for Ca, Fe, K, Li, Mg, Ti, and Zr, as a Function of Reaction Progress (mol-glass/kg) Determined for Glass Sample LAWA130

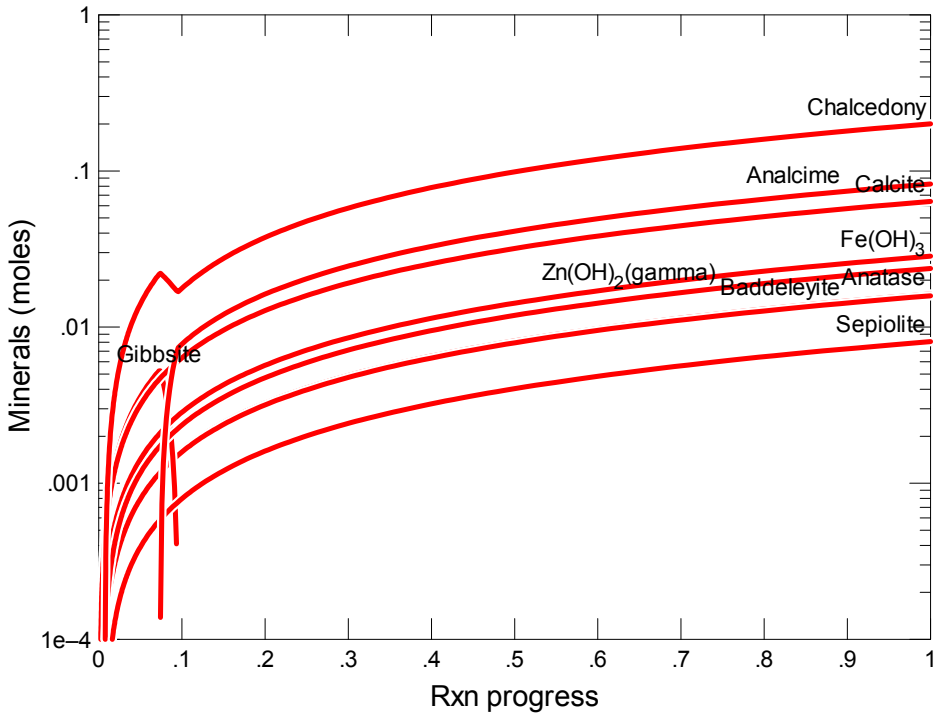


**Figure B.97**. Secondary Phases Calculated to Form as a Function of Reaction Progress (mol-glass/kg) Determined for Glass Sample LAWA133

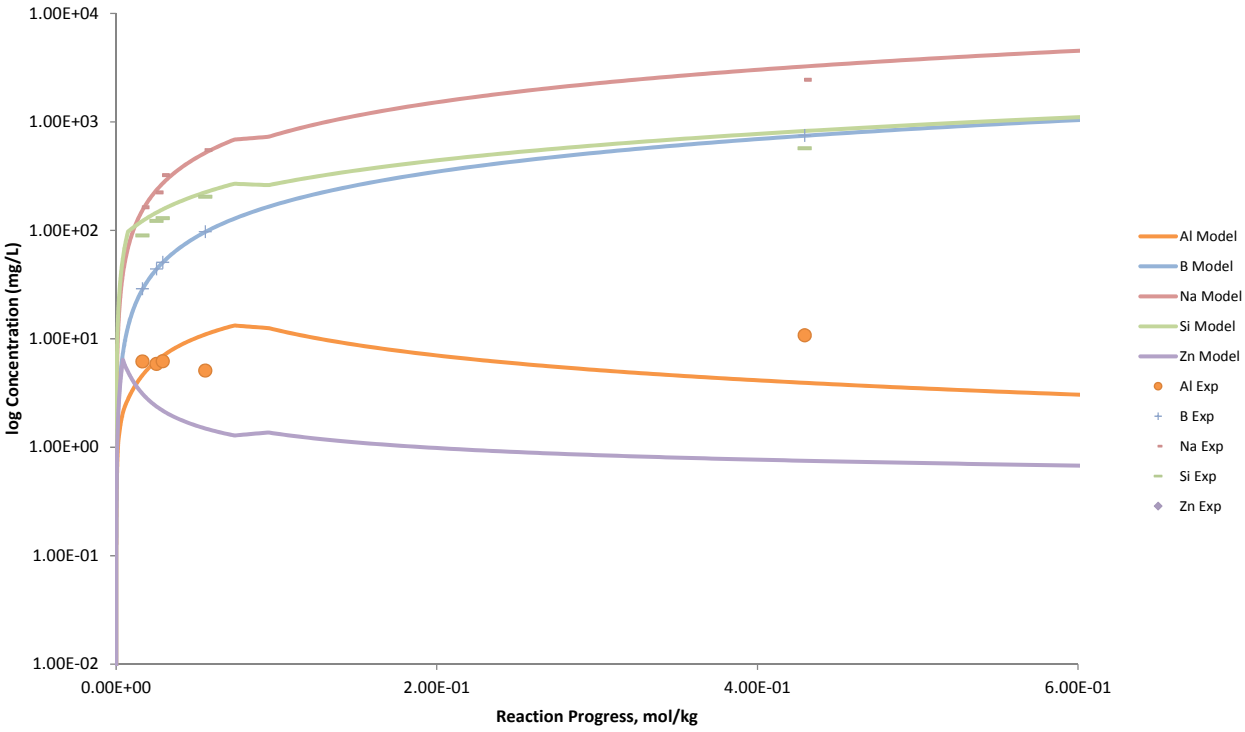


**Figure B.98**. Measured Solution Concentrations (mg/L) and Model Results for Al, B, Na, Si, and Zn, as a Function of Reaction Progress (mol-glass/kg) Determined for Glass Sample LAWA133

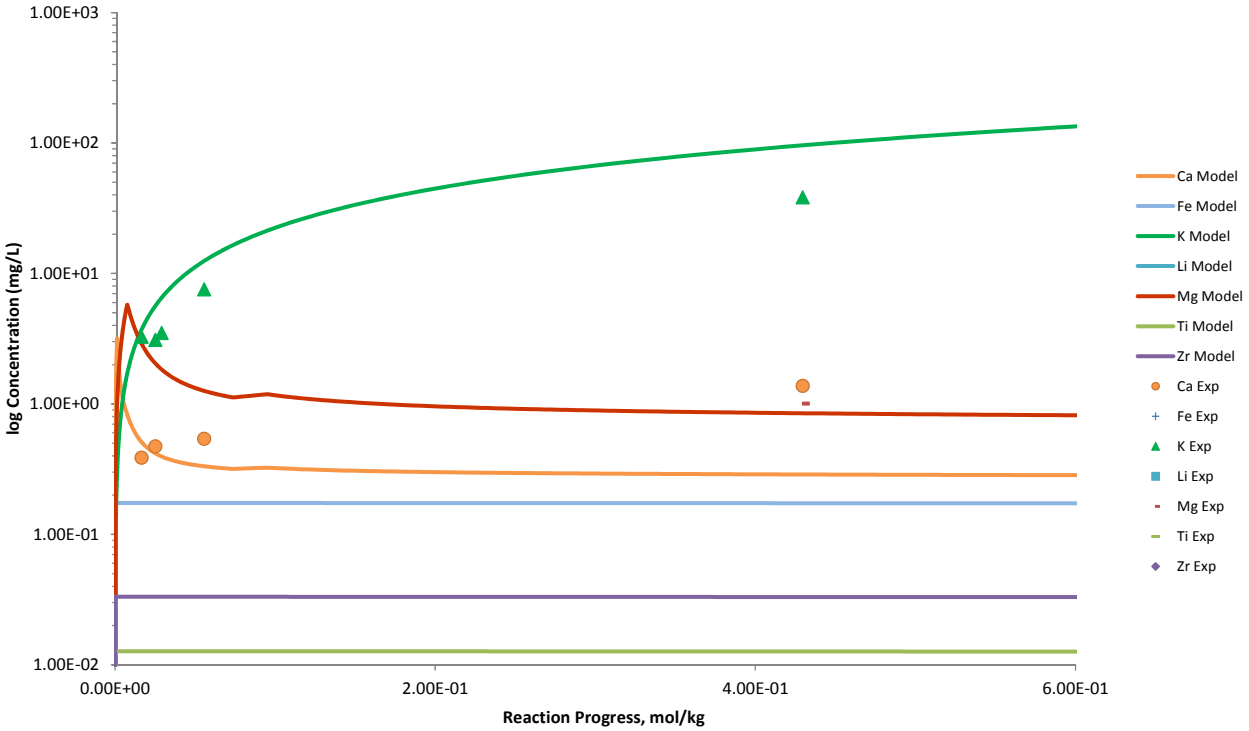


**Figure B.99**. Measured Solution Concentrations (mg/L) and Model Results for Ca, Fe, K, Li, Mg, Ti, and Zr, as a Function of Reaction Progress (mol-glass/kg) Determined for Glass Sample LAWA133

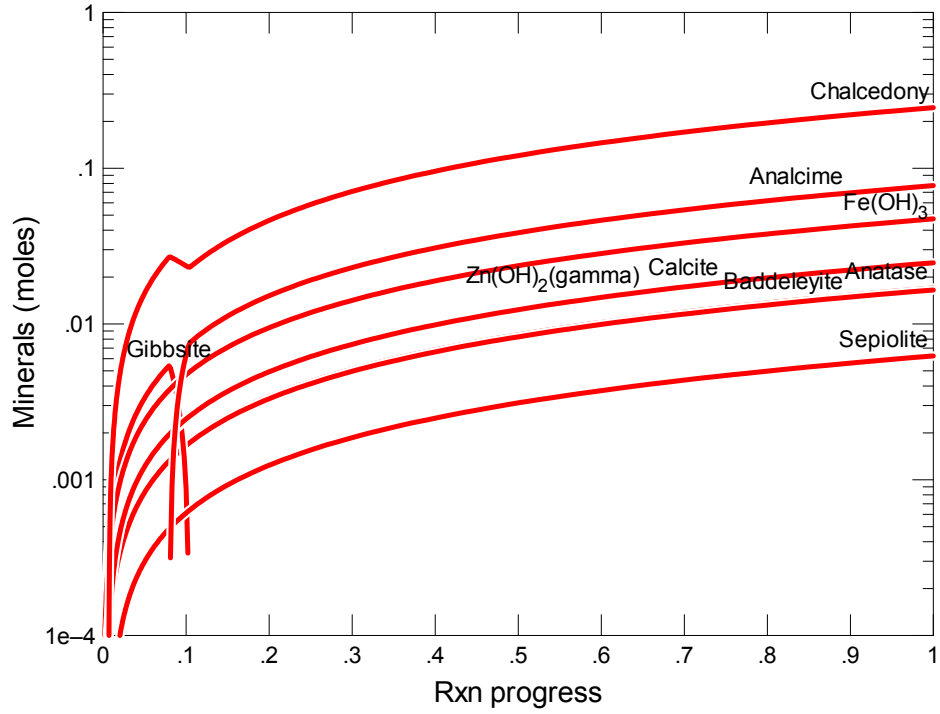


**Figure B.100**. Secondary Phases Calculated to Form as a Function of Reaction Progress (mol-glass/kg) Determined for Glass Sample LAWA134

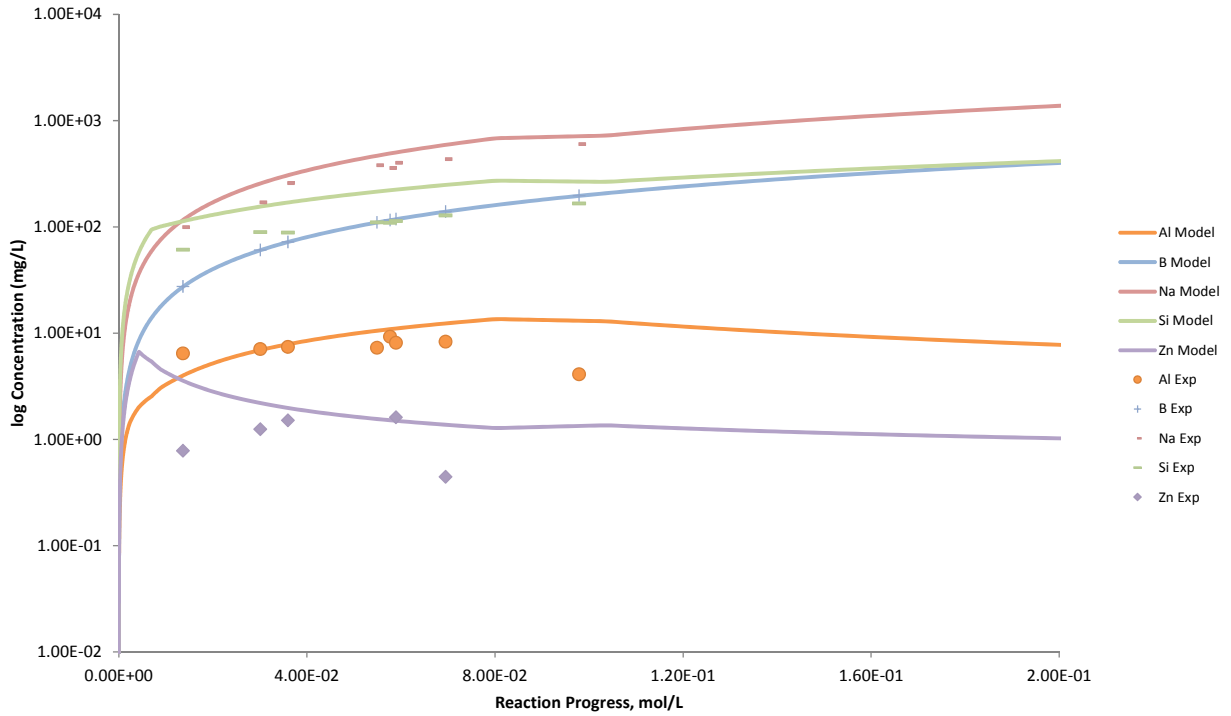


**Figure B.101**. Measured Solution Concentrations (mg/L) and Model Results for Al, B, Na, Si, and Zn, as a Function of Reaction Progress (mol-glass/kg) Determined for Glass Sample LAWA134

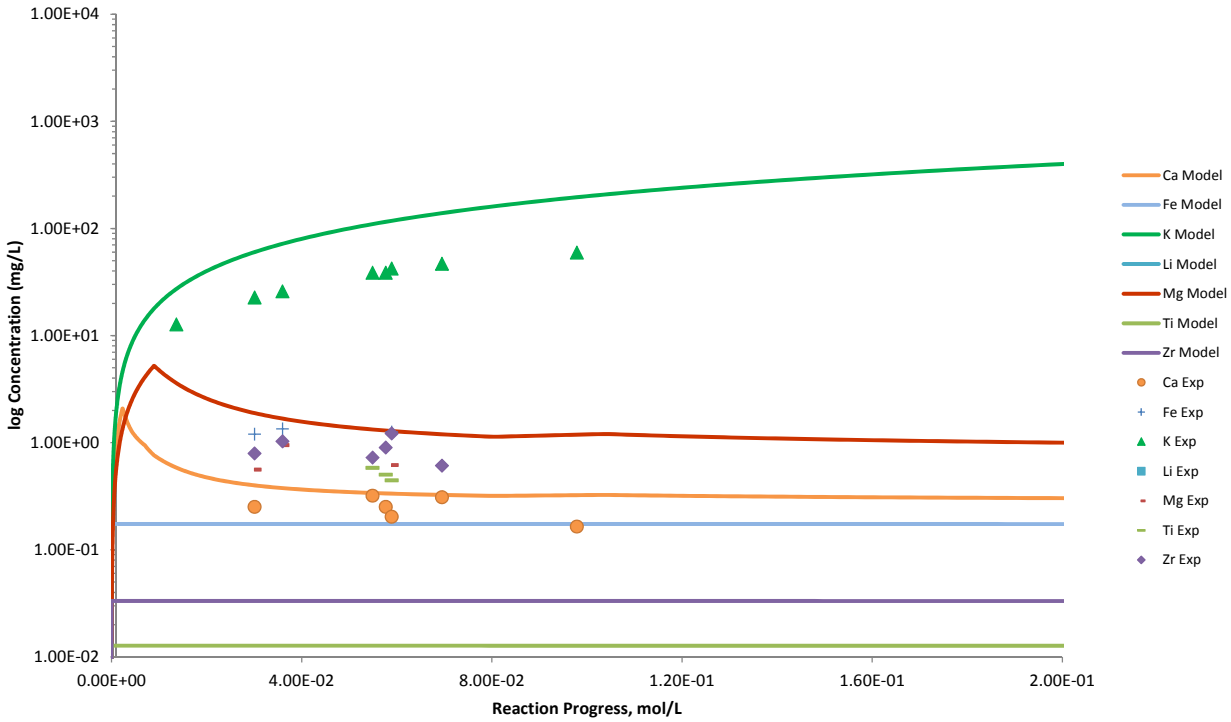


**Figure B.102**. Measured Solution Concentrations (mg/L) and Model Results for Ca, Fe, K, Li, Mg, Ti, and Zr, as a Function of Reaction Progress (mol-glass/kg) Determined for Glass Sample LAWA134

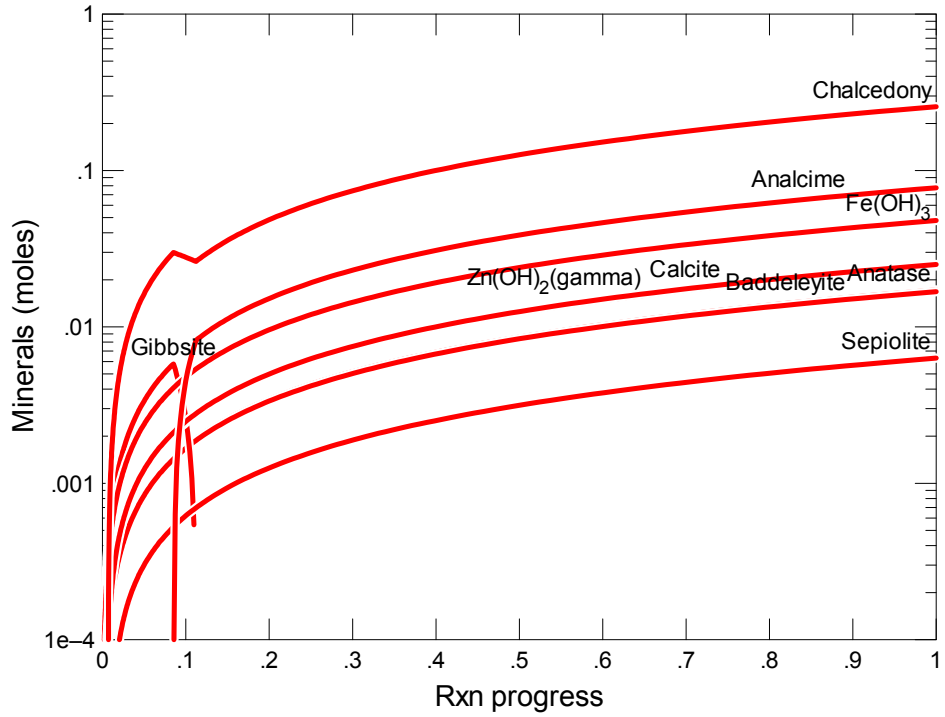


**Figure B.103**. Secondary Phases Calculated to Form as a Function of Reaction Progress (mol-glass/kg) Determined for Glass Sample LAWA135

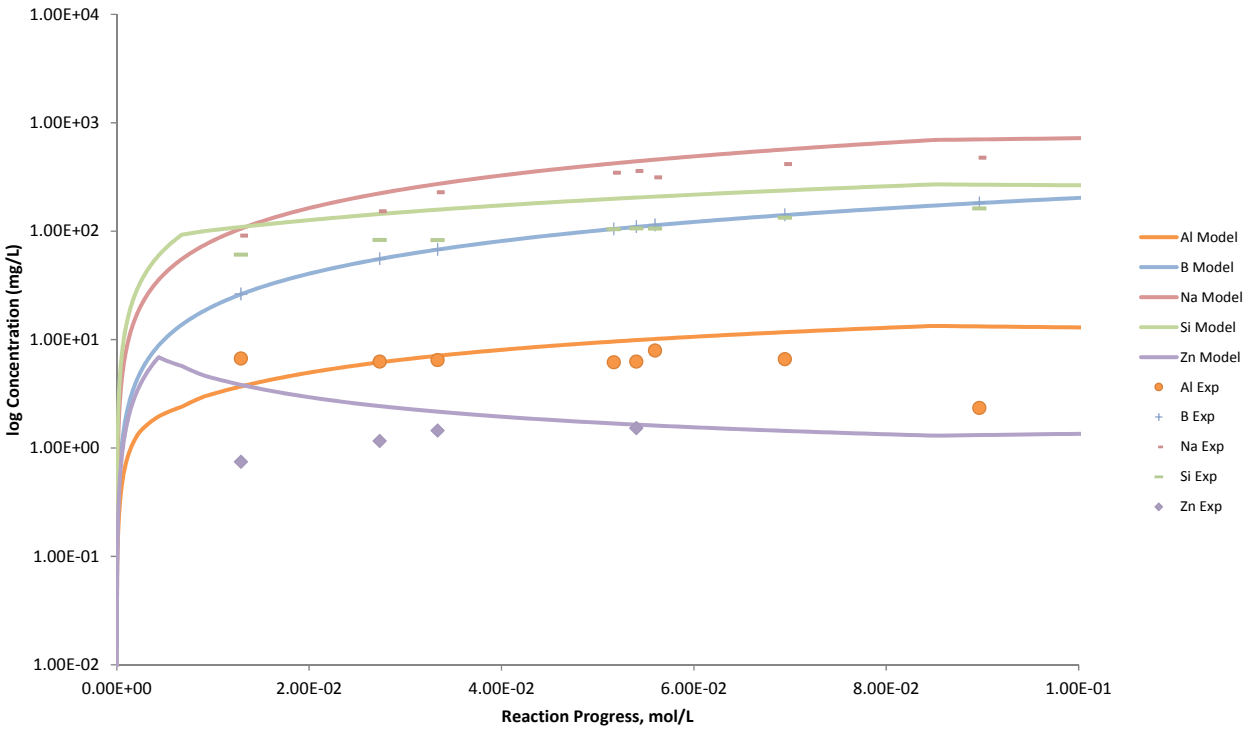


**Figure B.104**. Measured Solution Concentrations (mg/L) and Model Results for Al, B, Na, Si, and Zn, as a Function of Reaction Progress (mol-glass/kg) Determined for Glass Sample LAWA135

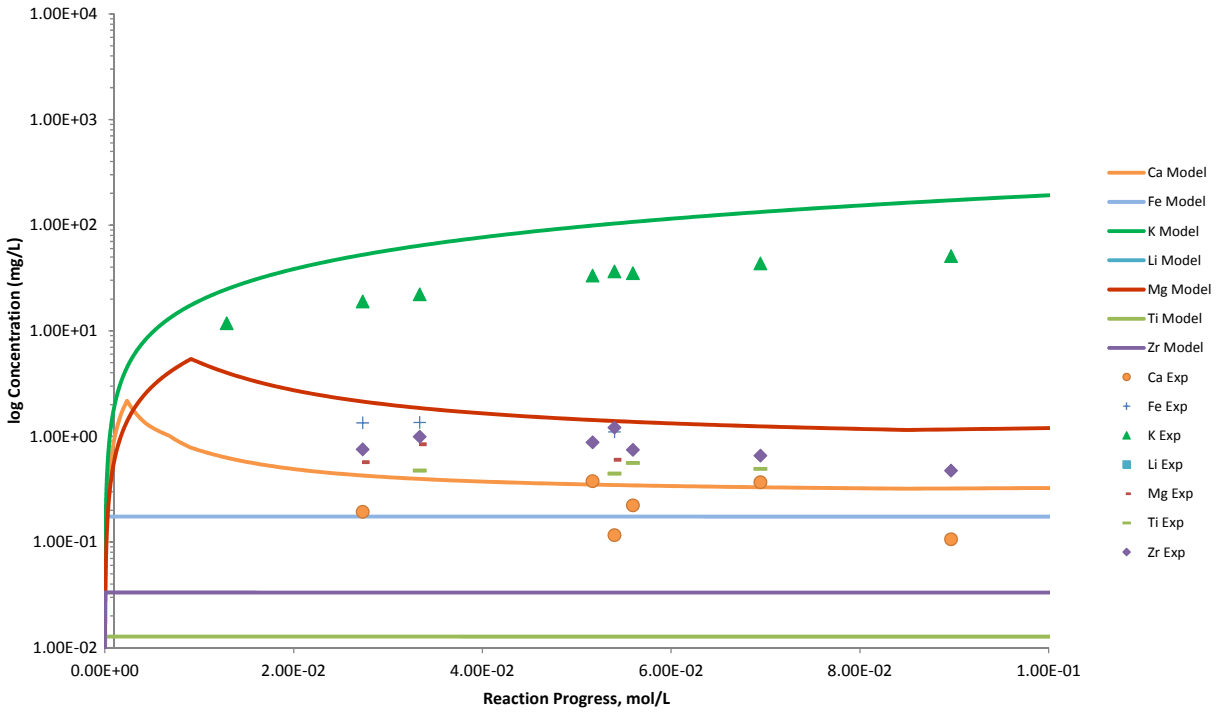


**Figure B.105**. Measured Solution Concentrations (mg/L) and Model Results for Ca, Fe, K, Li, Mg, Ti, and Zr, as a Function of Reaction Progress (mol-glass/kg) Determined for Glass Sample LAWA135

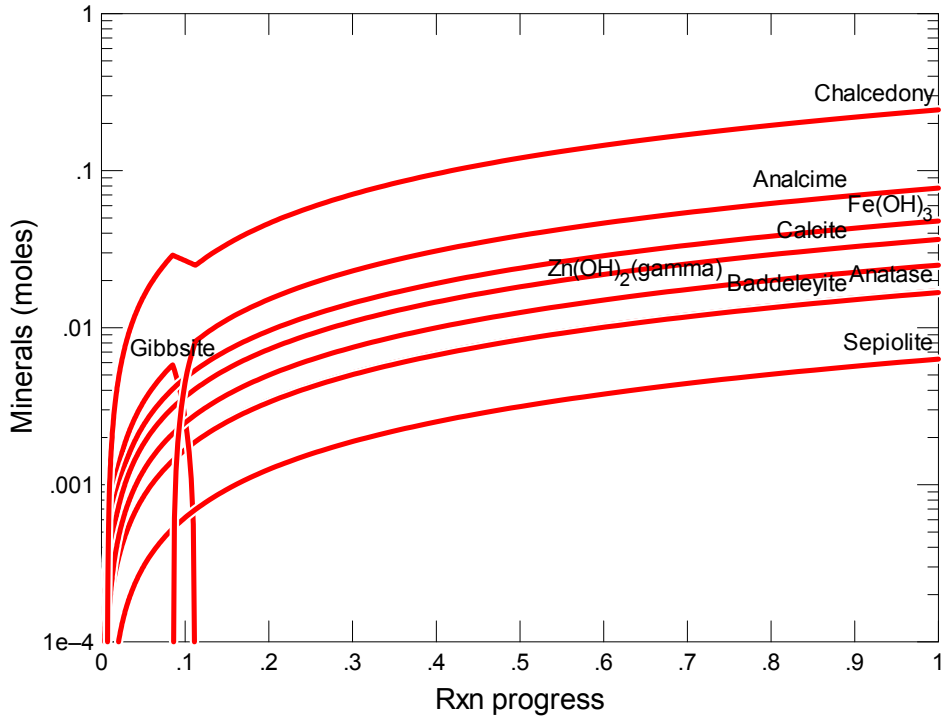


**Figure B.106**. Secondary Phases Calculated to Form as a Function of Reaction Progress (mol-glass/kg) Determined for Glass Sample LAWA136

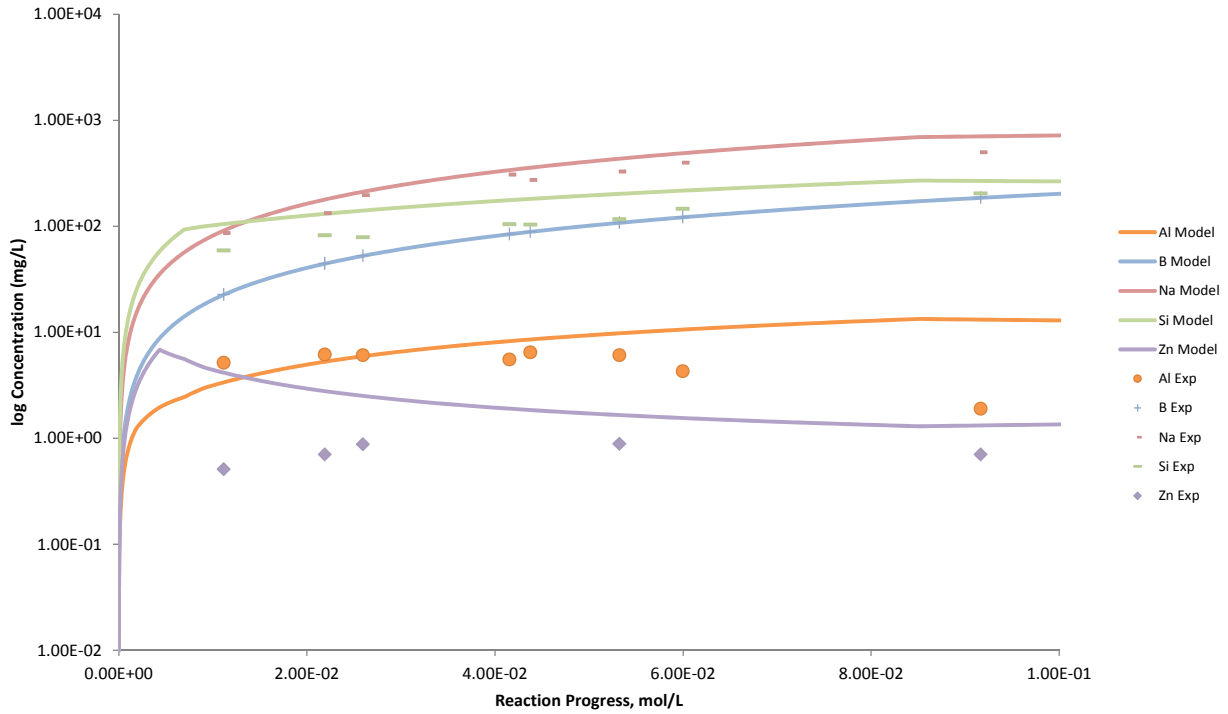


**Figure B.107**. Measured Solution Concentrations (mg/L) and Model Results for Al, B, Na, Si, and Zn, as a Function of Reaction Progress (mol-glass/kg) Determined for Glass Sample LAWA136

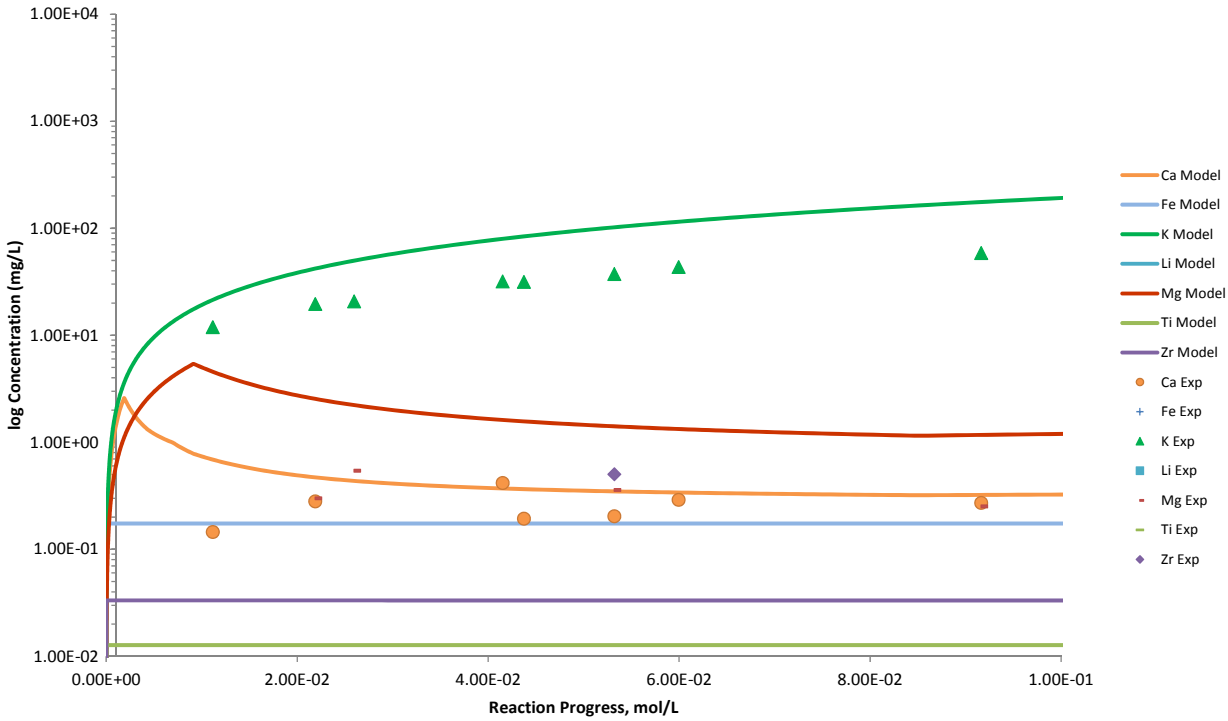


**Figure B.108**. Measured Solution Concentrations (mg/L) and Model Results for Ca, Fe, K, Li, Mg, Ti, and Zr, as a Function of Reaction Progress (mol-glass/kg) Determined for Glass Sample LAWA136

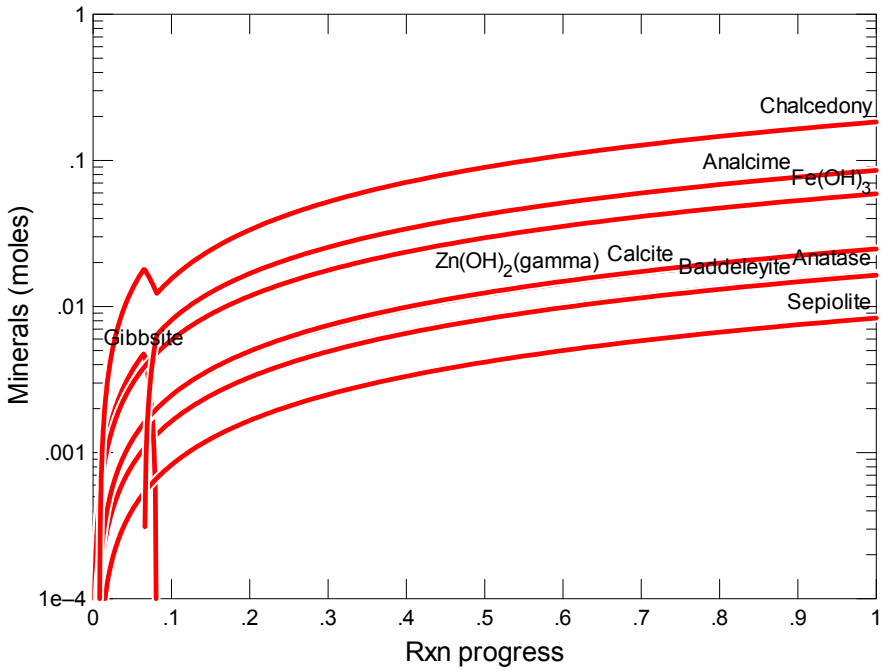


**Figure B.109**. Secondary Phases Calculated to Form as a Function of Reaction Progress (mol-glass/kg) Determined for Glass Sample LAWA41

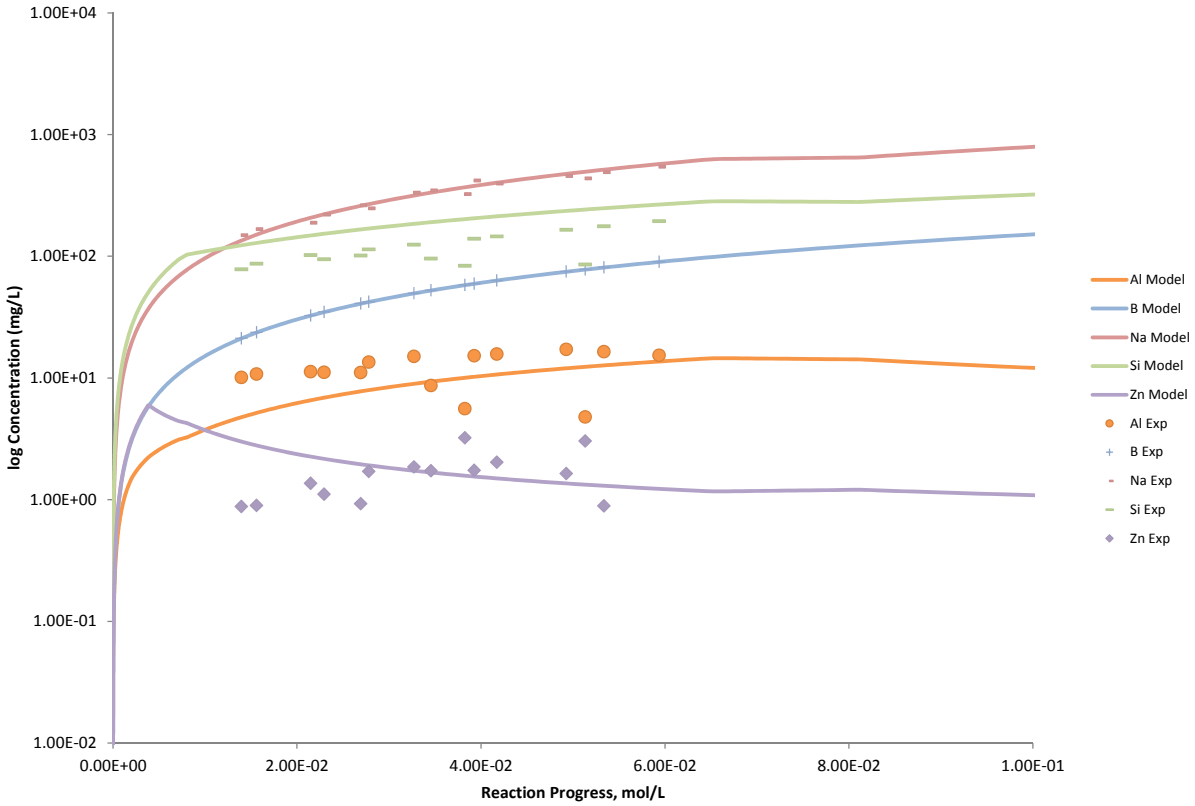


**Figure B.110**. Measured Solution Concentrations (mg/L) and Model Results for Al, B, Na, Si, and Zn, as a Function of Reaction Progress (mol-glass/kg) Determined for Glass Sample LAWA41

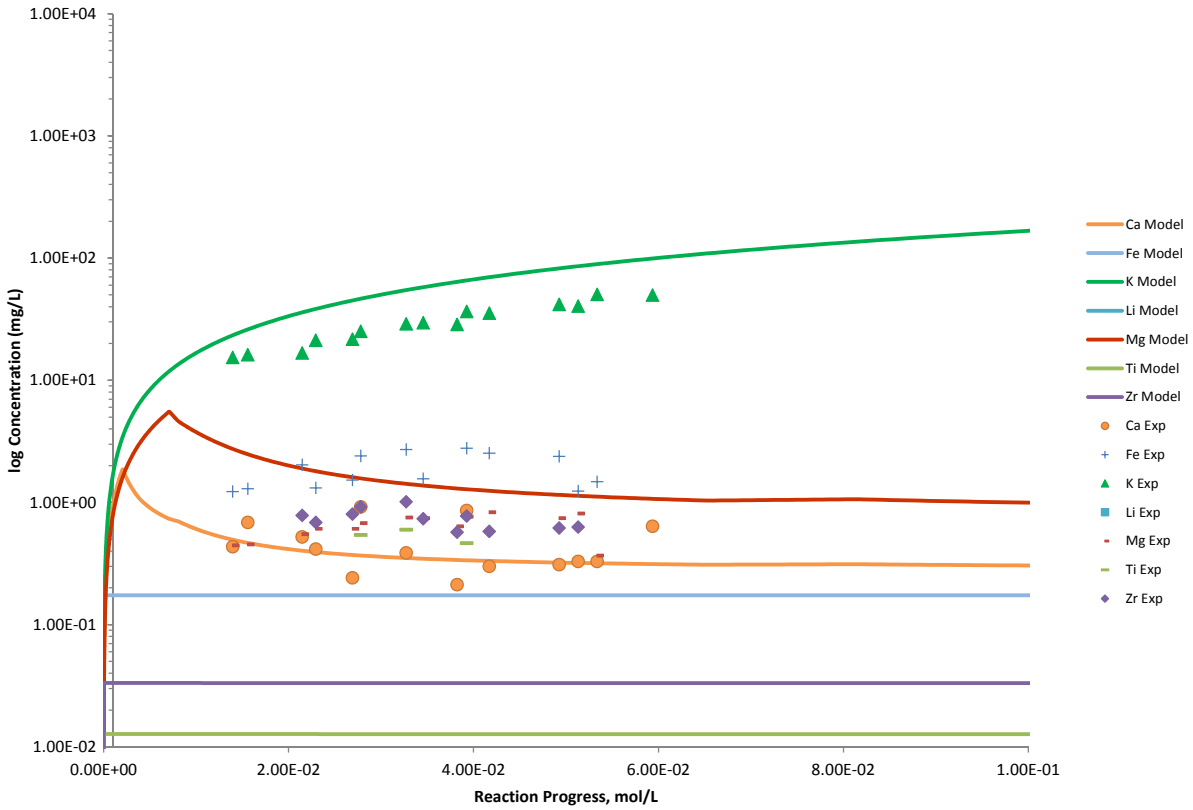


**Figure B.111**. Measured Solution Concentrations (mg/L) and Model Results for Ca, Fe, K, Li, Mg, Ti, and Zr, as a Function of Reaction Progress (mol-glass/kg) Determined for Glass Sample LAWA41

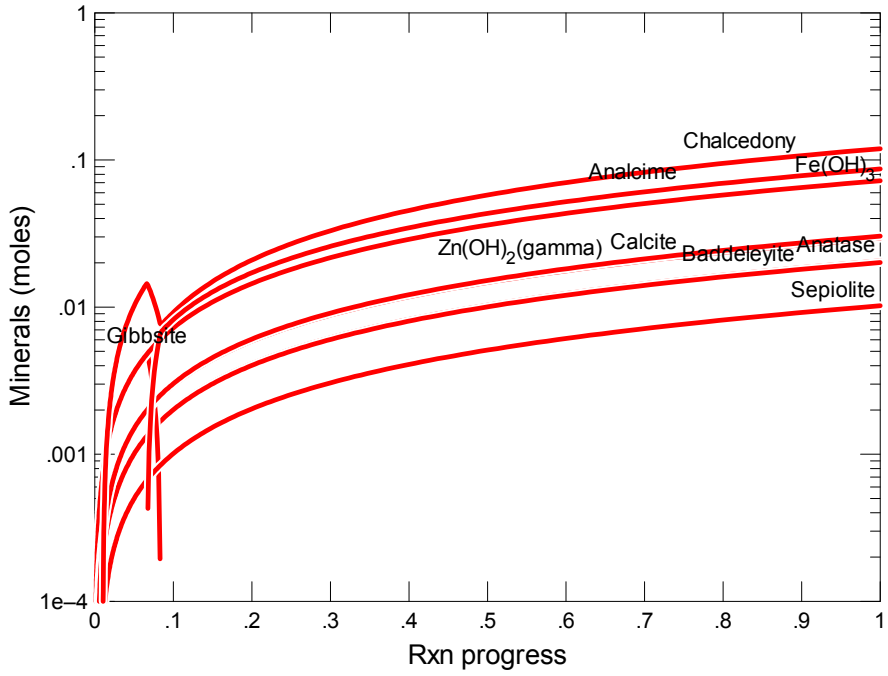


**Figure B.112**. Secondary Phases Calculated to Form as a Function of Reaction Progress (mol-glass/kg) Determined for Glass Sample LAWA42

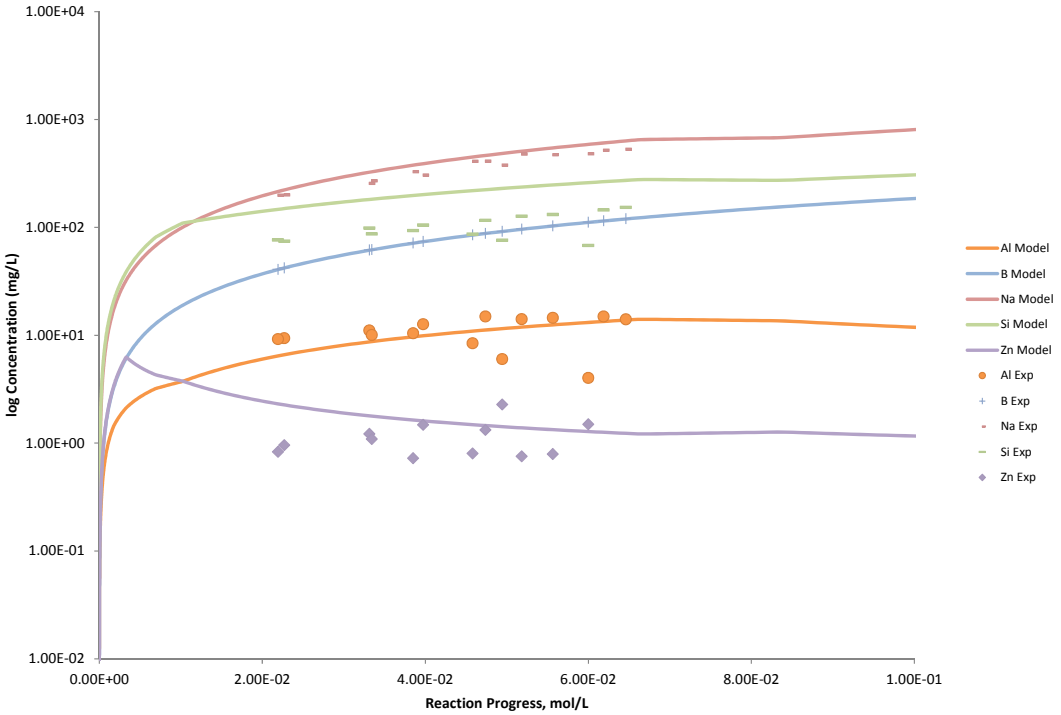


**Figure B.113**. Measured Solution Concentrations (mg/L) and Model Results for Al, B, Na, Si, and Zn, as a Function of Reaction Progress (mol-glass/kg) Determined for Glass Sample LAWA42

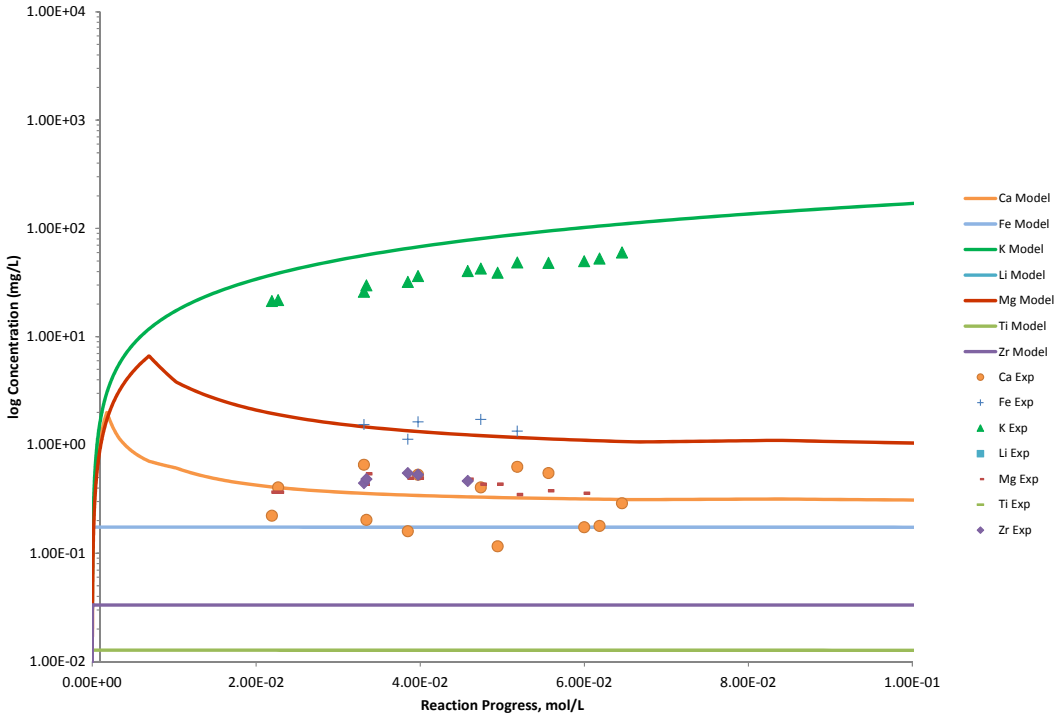


**Figure B.114**. Measured Solution Concentrations (mg/L) and Model Results for Ca, Fe, K, Li, Mg, Ti, and Zr, as a Function of Reaction Progress (mol-glass/kg) Determined for Glass Sample LAWA42

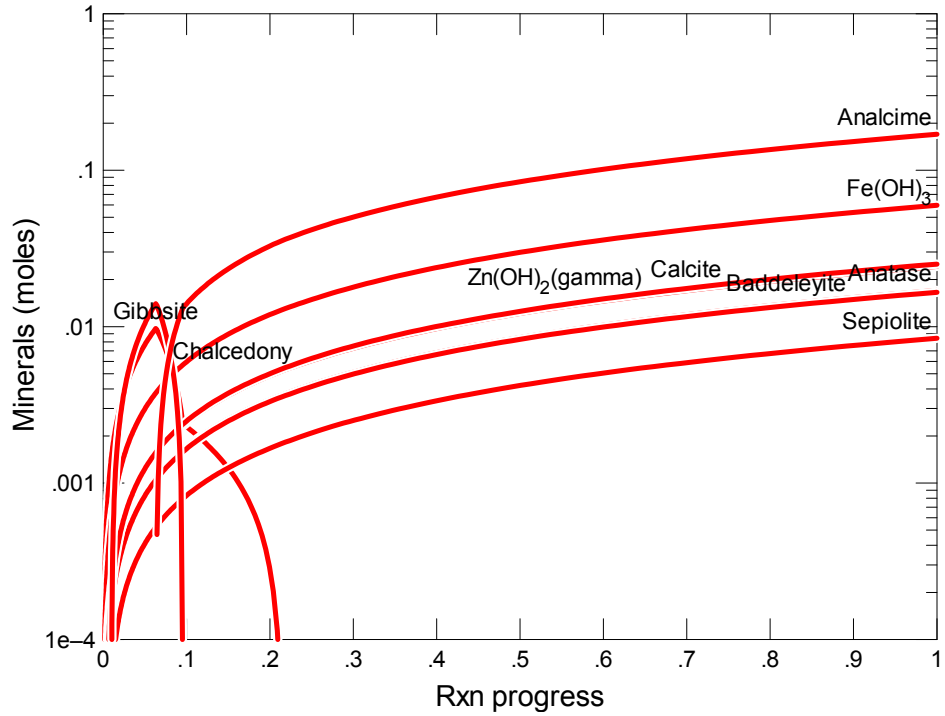


**Figure B.115**. Secondary Phases Calculated to Form as a Function of Reaction Progress (mol-glass/kg) Determined for Glass Sample LAWA43-1

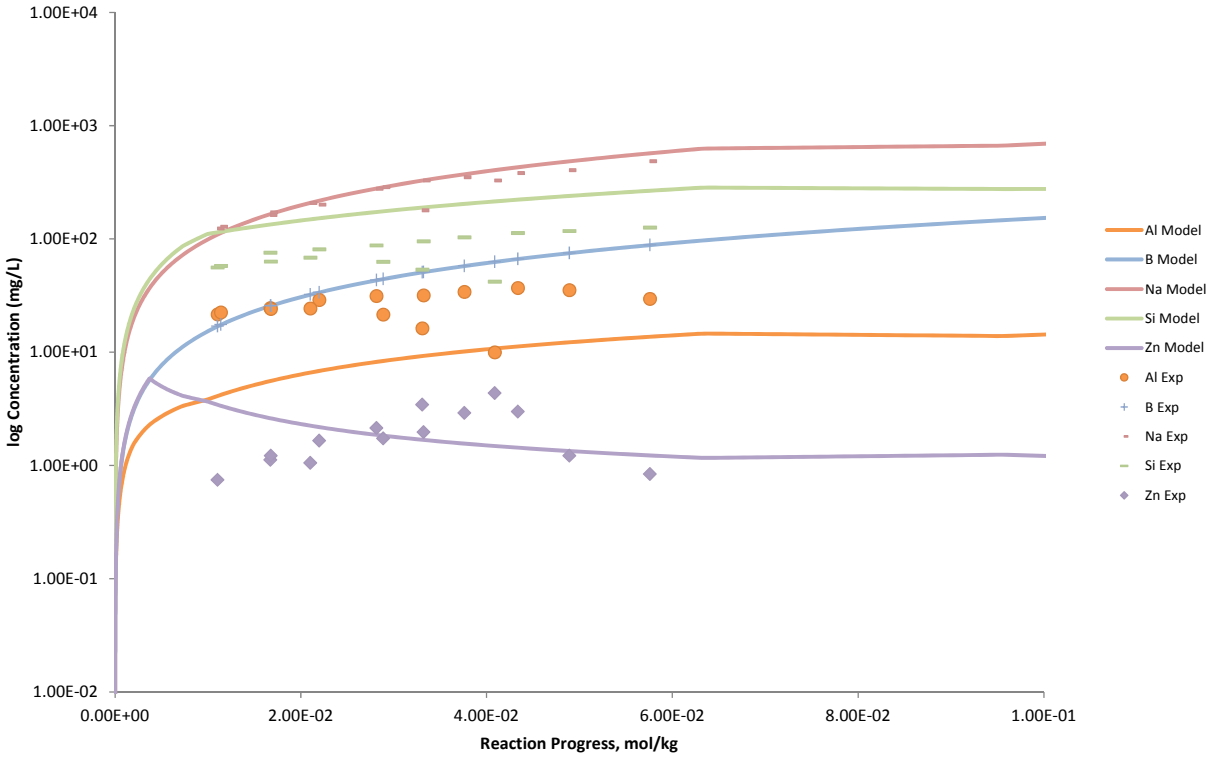


**Figure B.116**. Measured Solution Concentrations (mg/L) and Model Results for Al, B, Na, Si, and Zn, as a Function of Reaction Progress (mol-glass/kg) Determined for Glass Sample LAWA43-1

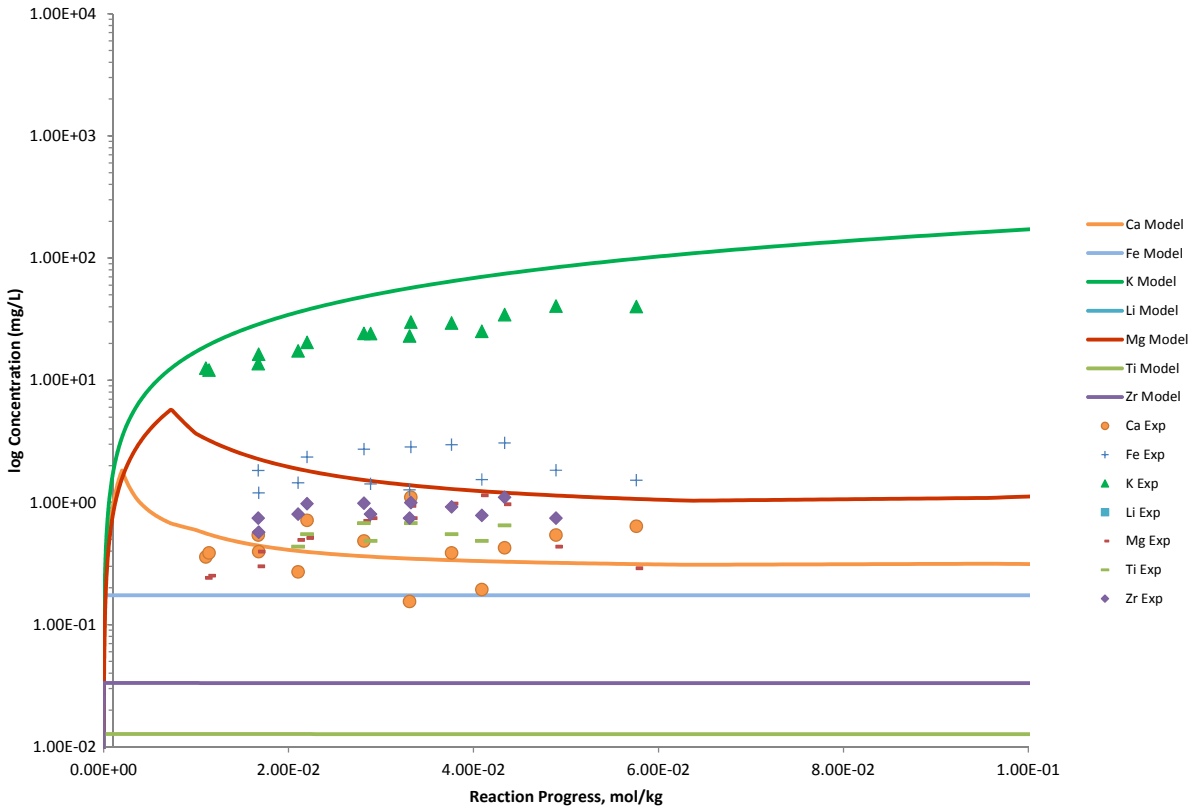


**Figure B.117**. Measured Solution Concentrations (mg/L) and Model Results for Ca, Fe, K, Li, Mg, Ti, and Zr, as a Function of Reaction Progress (mol-glass/kg) Determined for Glass Sample LAWA43-1

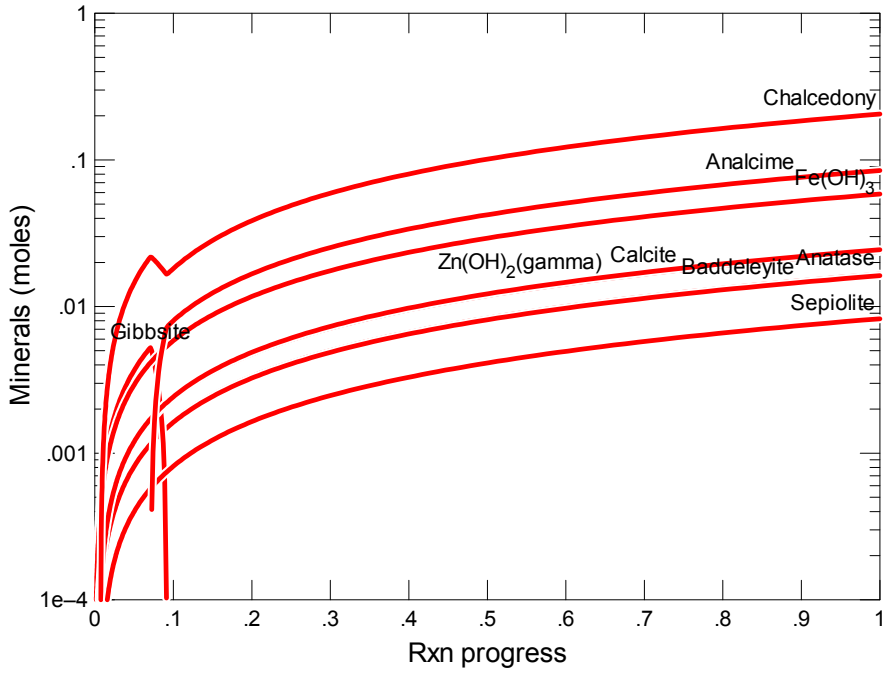


**Figure B.118**. Secondary Phases Calculated to Form as a Function of Reaction Progress (mol-glass/kg) Determined for Glass Sample LAWA44

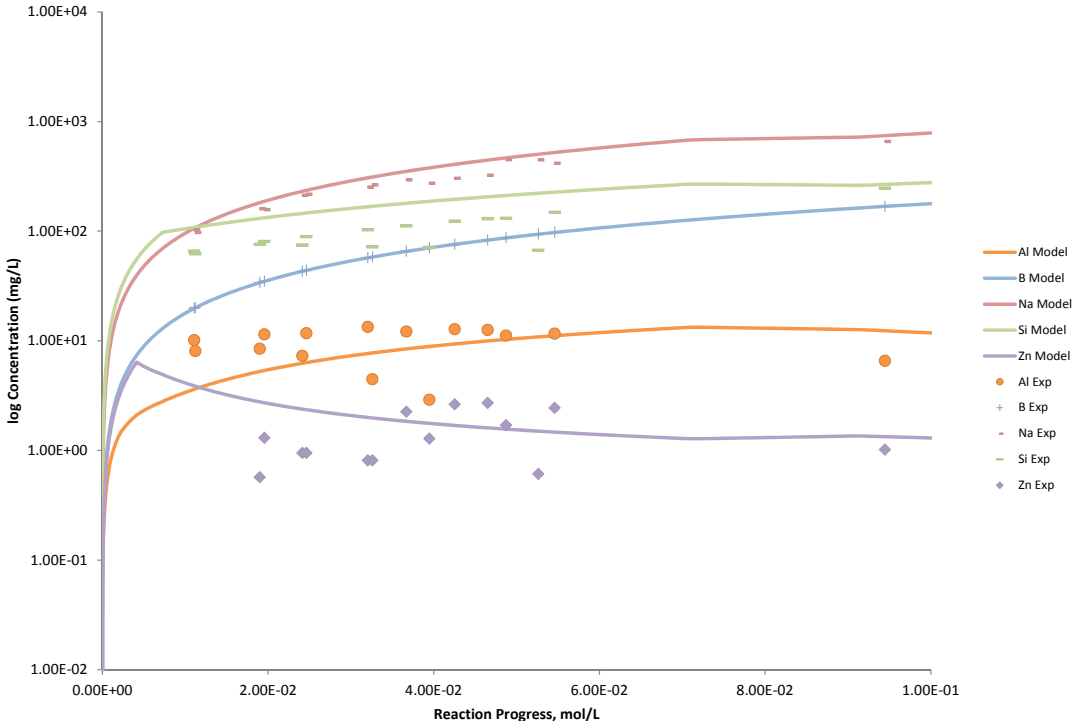


**Figure B.119**. Measured Solution Concentrations (mg/L) and Model Results for Al, B, Na, Si, and Zn, as a Function of Reaction Progress (mol-glass/kg) Determined for Glass Sample LAWA44

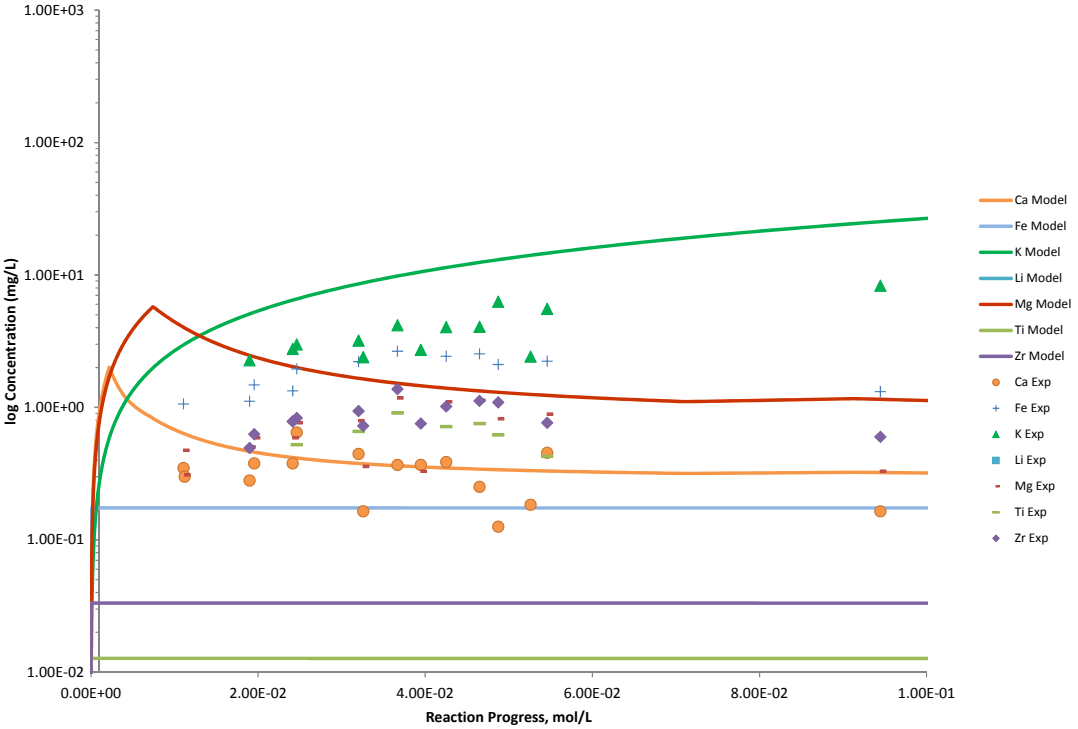


**Figure B.120**. Measured Solution Concentrations (mg/L) and Model Results for Ca, Fe, K, Li, Mg, Ti, and Zr, as a Function of Reaction Progress (mol-glass/kg) Determined for Glass Sample LAWA44

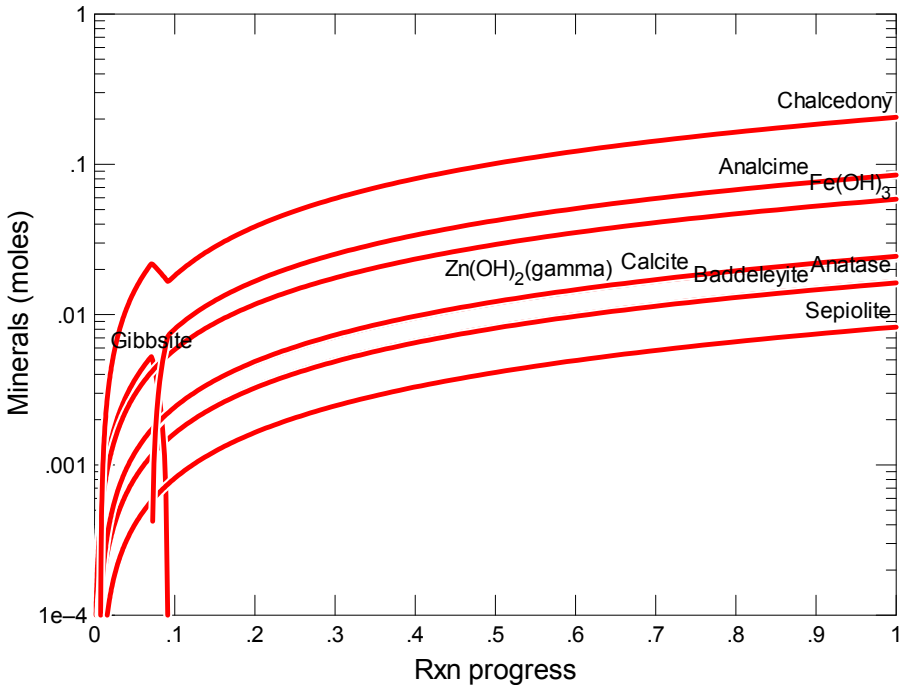


**Figure B.121**. Secondary Phases Calculated to Form as a Function of Reaction Progress (mol-glass/kg) Determined for Glass Sample LAWA44R10

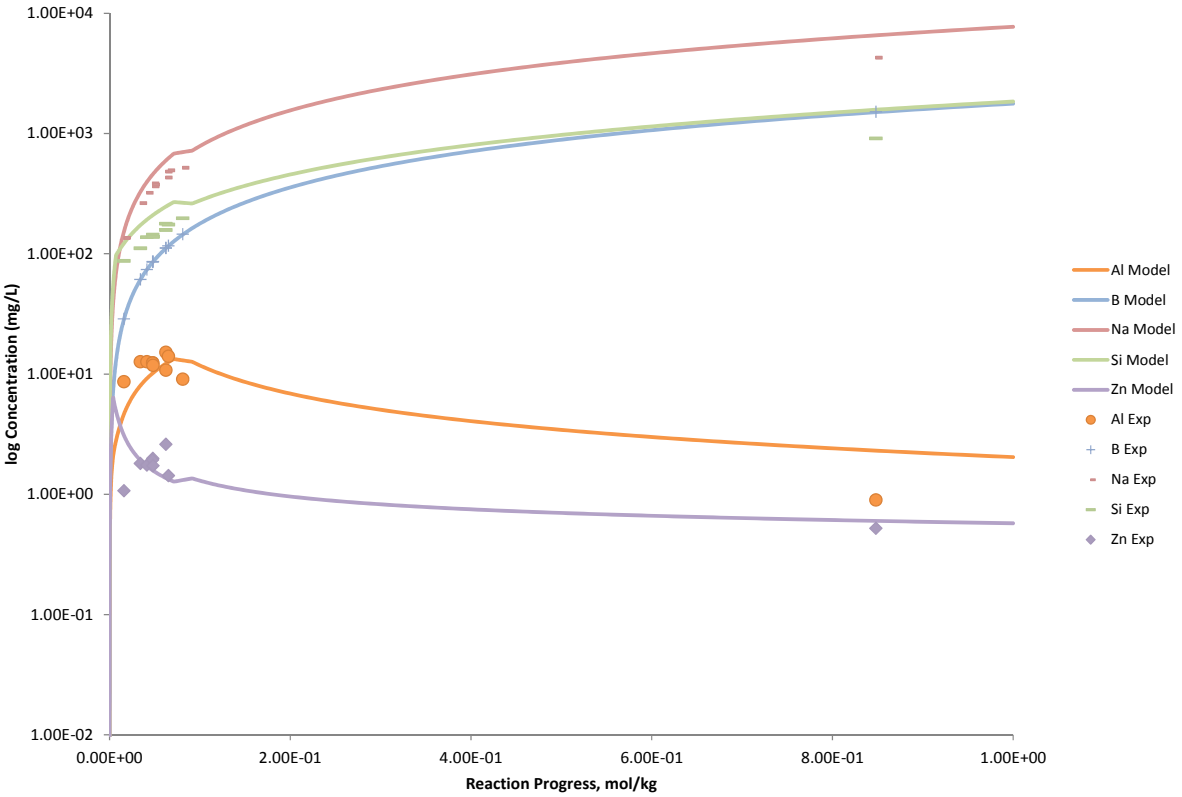


**Figure B.122**. Measured Solution Concentrations (mg/L) and Model Results for Al, B, Na, Si, and Zn, as a Function of Reaction Progress (mol-glass/kg) Determined for Glass Sample LAWA44R10

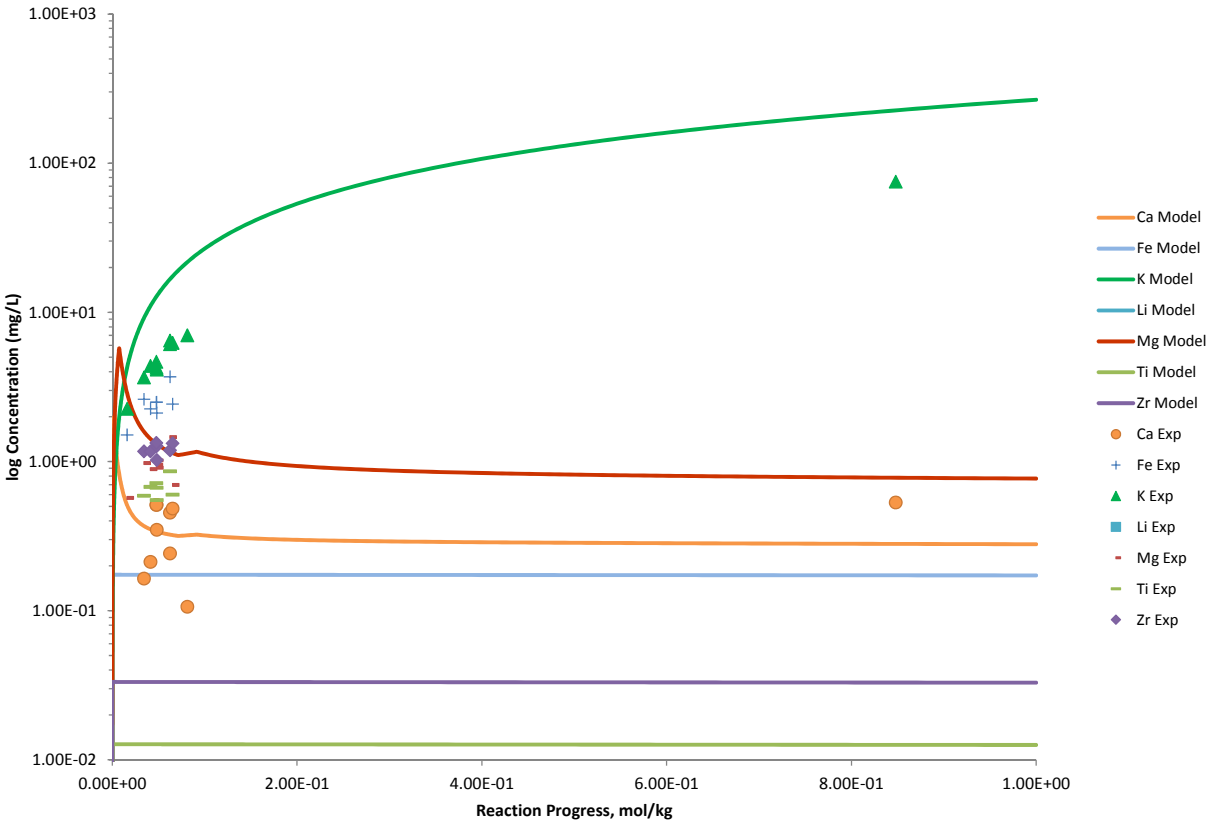


**Figure B.123**. Measured Solution Concentrations (mg/L) and Model Results for Ca, Fe, K, Li, Mg, Ti, and Zr, as a Function of Reaction Progress (mol-glass/kg) Determined for Glass Sample LAWA44R10

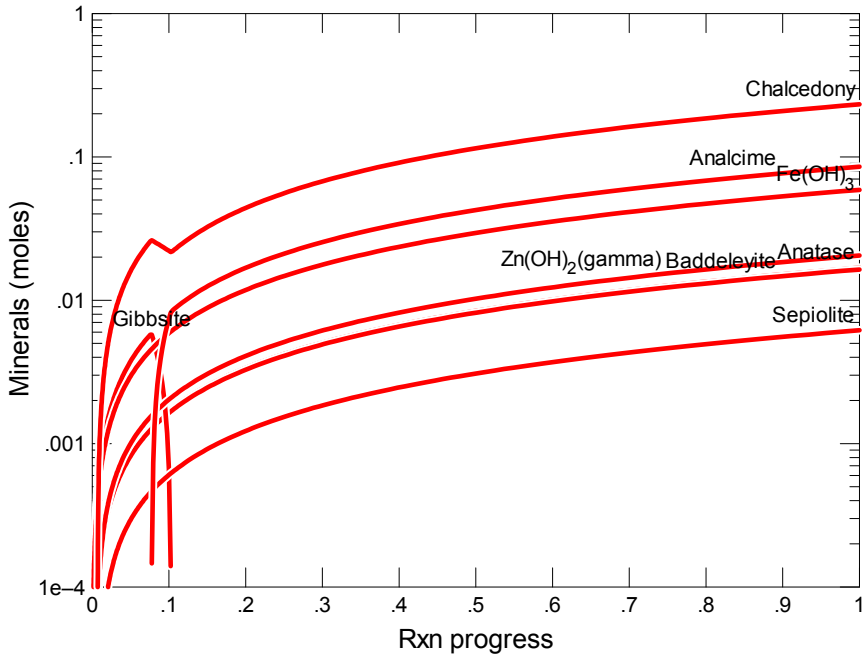


**Figure B.124**. Secondary Phases Calculated to Form as a Function of Reaction Progress (mol-glass/kg) Determined for Glass Sample LAWA45

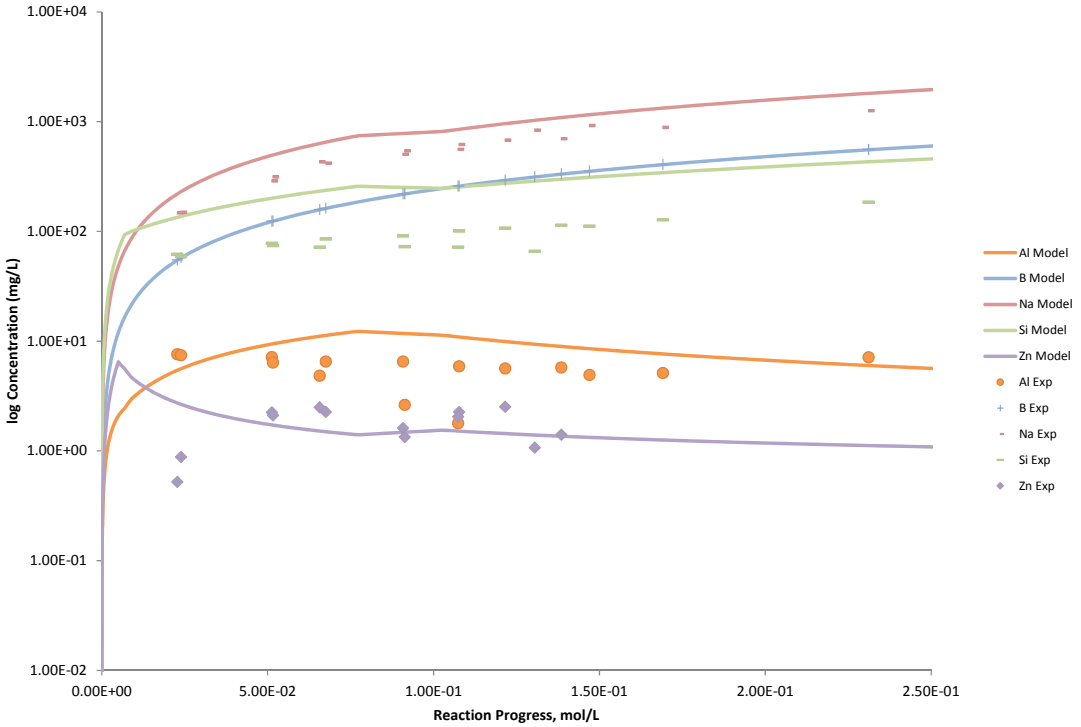


**Figure B.125**. Measured Solution Concentrations (mg/L) and Model Results for Al, B, Na, Si, and Zn, as a Function of Reaction Progress (mol-glass/kg) Determined for Glass Sample LAWA45

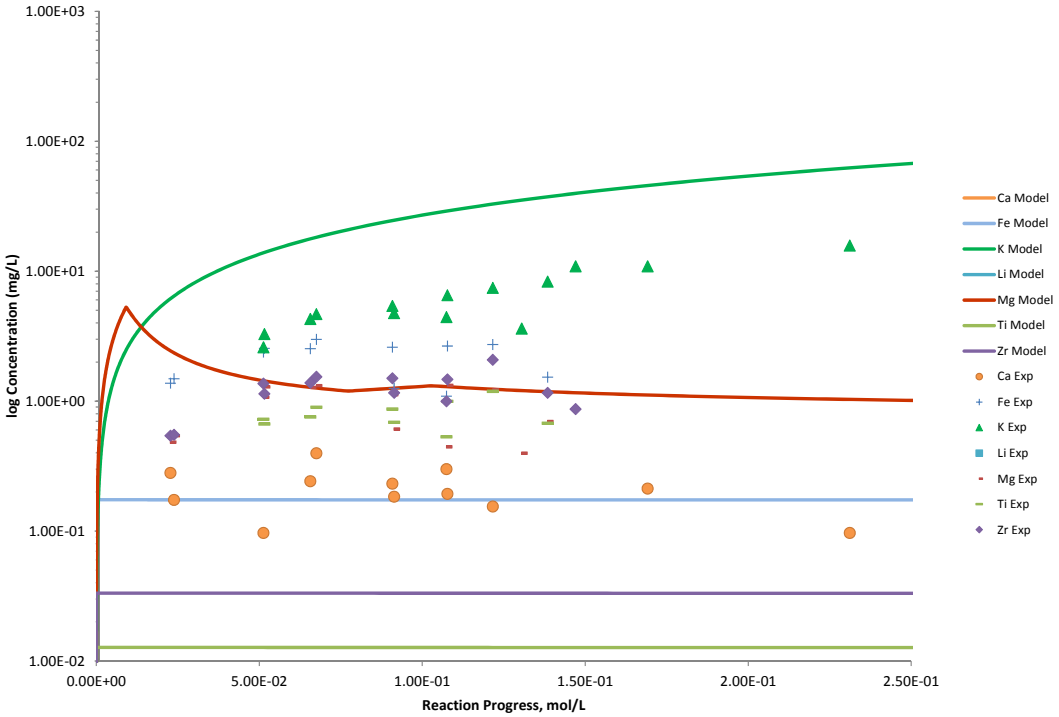


**Figure B.126**. Measured Solution Concentrations (mg/L) and Model Results for Ca, Fe, K, Li, Mg, Ti, and Zr, as a Function of Reaction Progress (mol-glass/kg) Determined for Glass Sample LAWA45

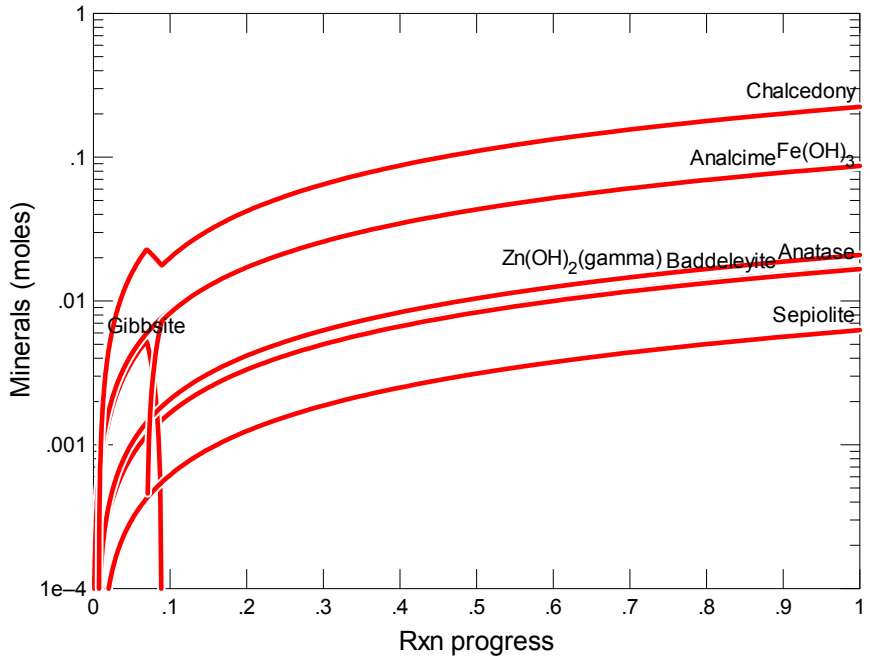


**Figure B.127**. Secondary Phases Calculated to Form as a Function of Reaction Progress (mol-glass/kg) Determined for Glass Sample LAWA49

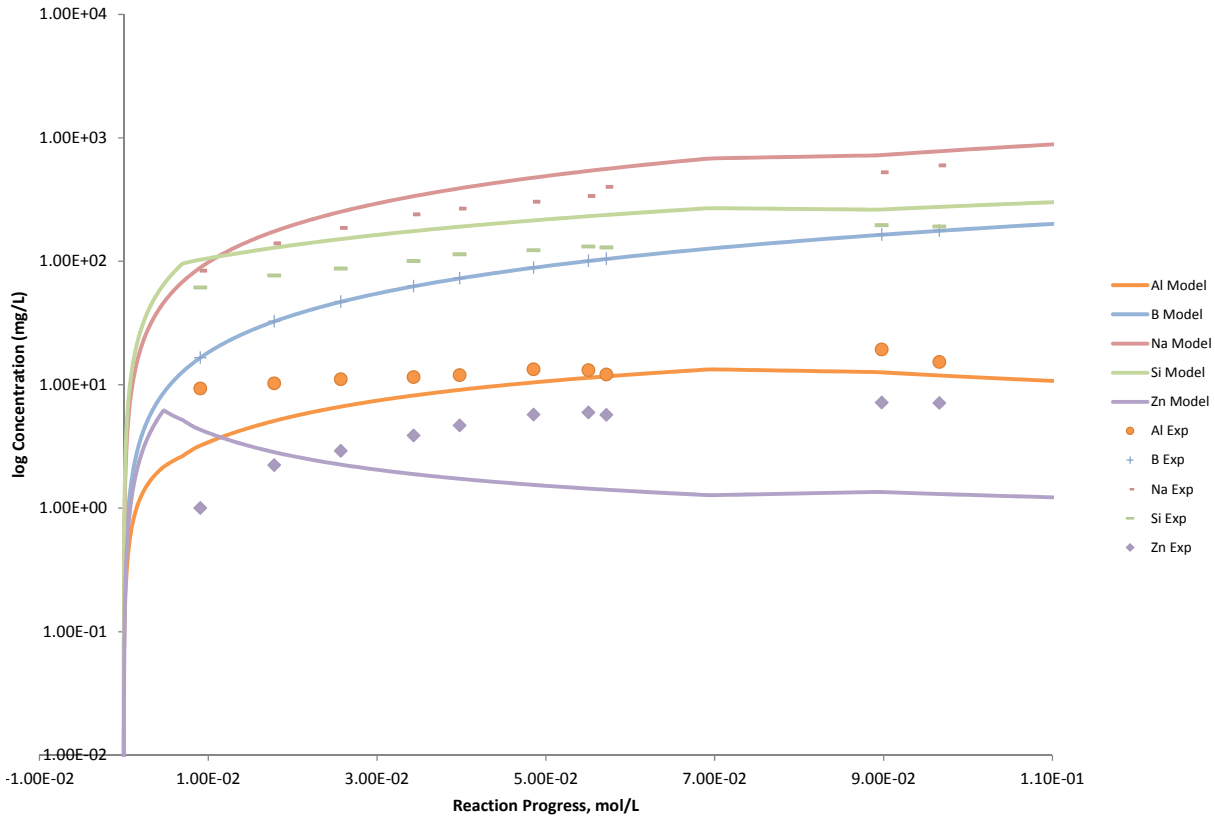


**Figure B.128**. Measured Solution Concentrations (mg/L) and Model Results for Al, B, Na, Si, and Zn, as a Function of Reaction Progress (mol-glass/kg) Determined for Glass Sample LAWA49

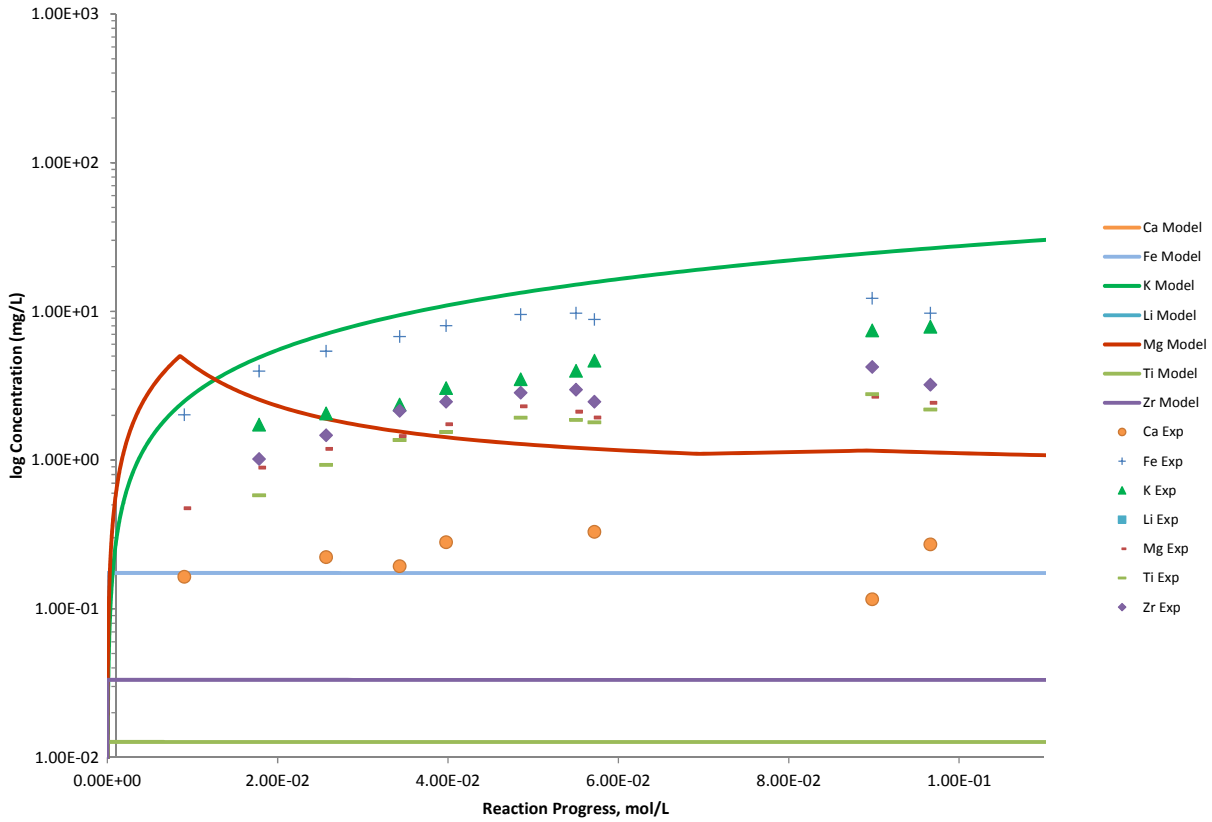


**Figure B.129**. Measured Solution Concentrations (mg/L) and Model Results for Ca, Fe, K, Li, Mg, Ti, and Zr, as a Function of Reaction Progress (mol-glass/kg) Determined for Glass Sample LAWA49

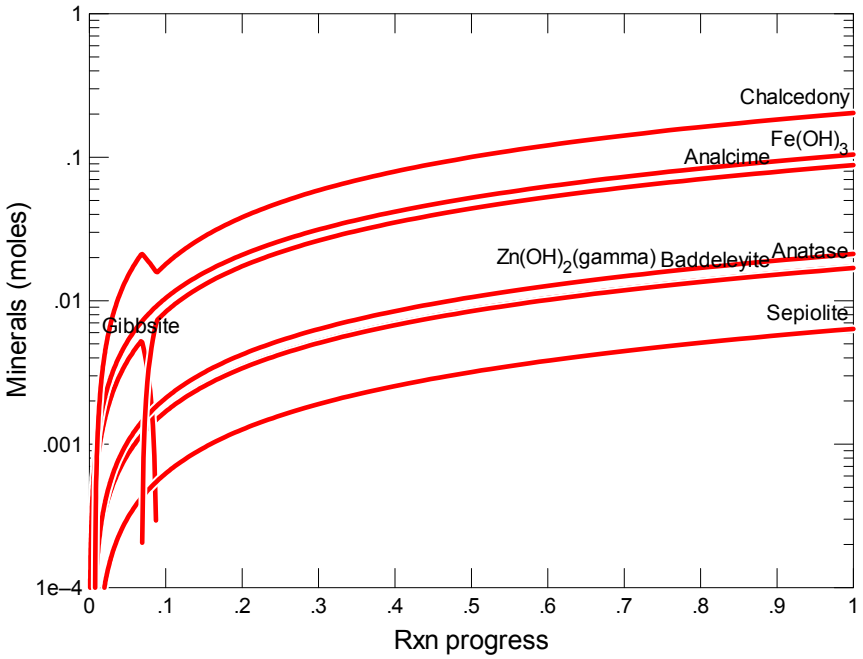


**Figure B.130**. Secondary Phases Calculated to Form as a Function of Reaction Progress (mol-glass/kg) Determined for Glass Sample LAWA50

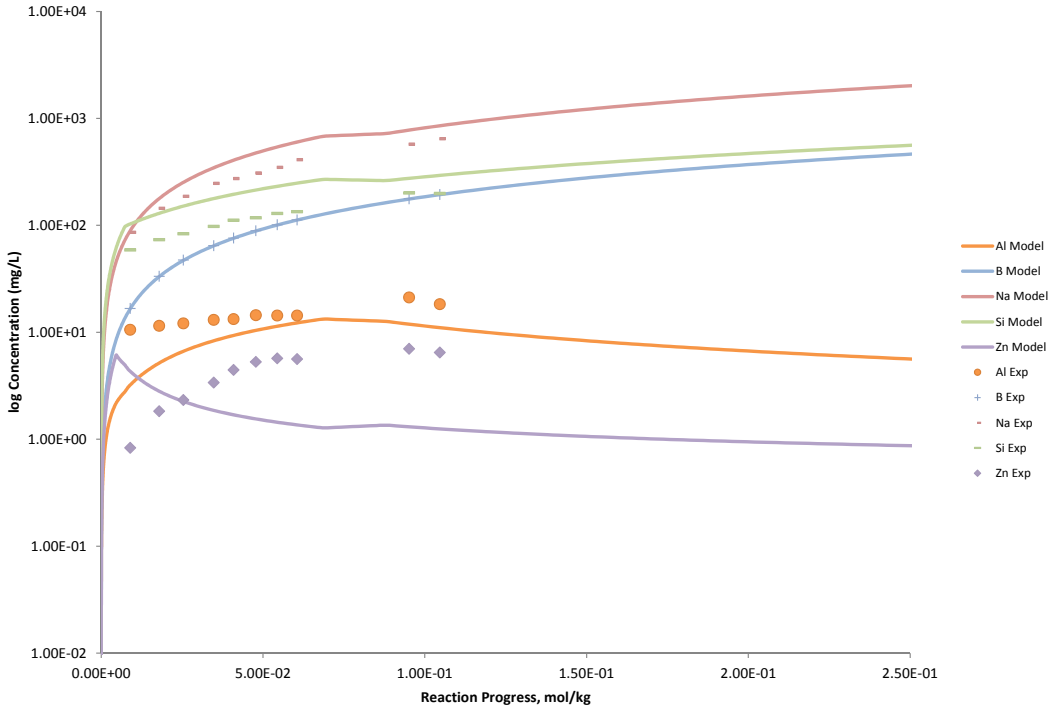


**Figure B.131**. Measured Solution Concentrations (mg/L) and Model Results for Al, B, Na, Si, and Zn, as a Function of Reaction Progress (mol-glass/kg) Determined for Glass Sample LAWA50

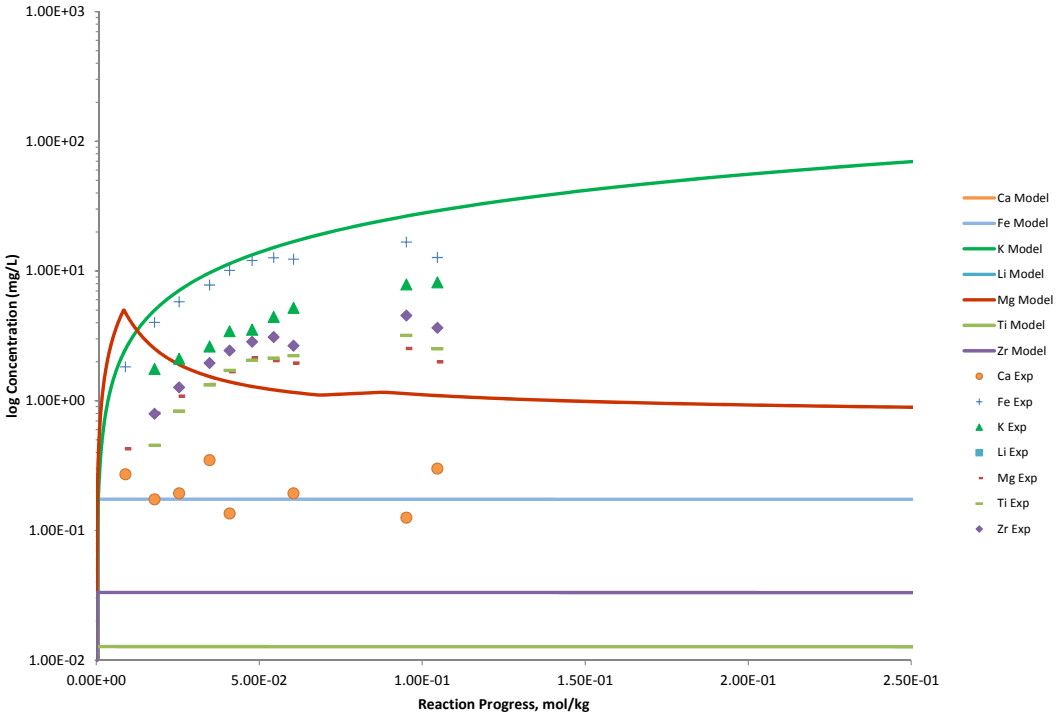


**Figure B.132**. Measured Solution Concentrations (mg/L) and Model Results for Ca, Fe, K, Li, Mg, Ti, and Zr, as a Function of Reaction Progress (mol-glass/kg) Determined for Glass Sample LAWA50

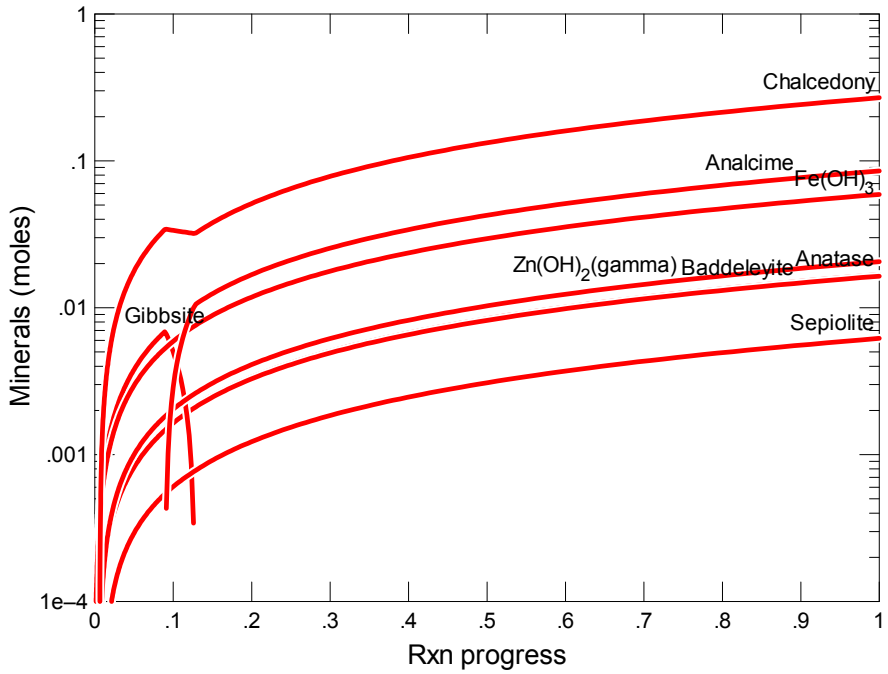


**Figure B.133**. Secondary Phases Calculated to Form as a Function of Reaction Progress (mol-glass/kg) Determined for Glass Sample LAWA51

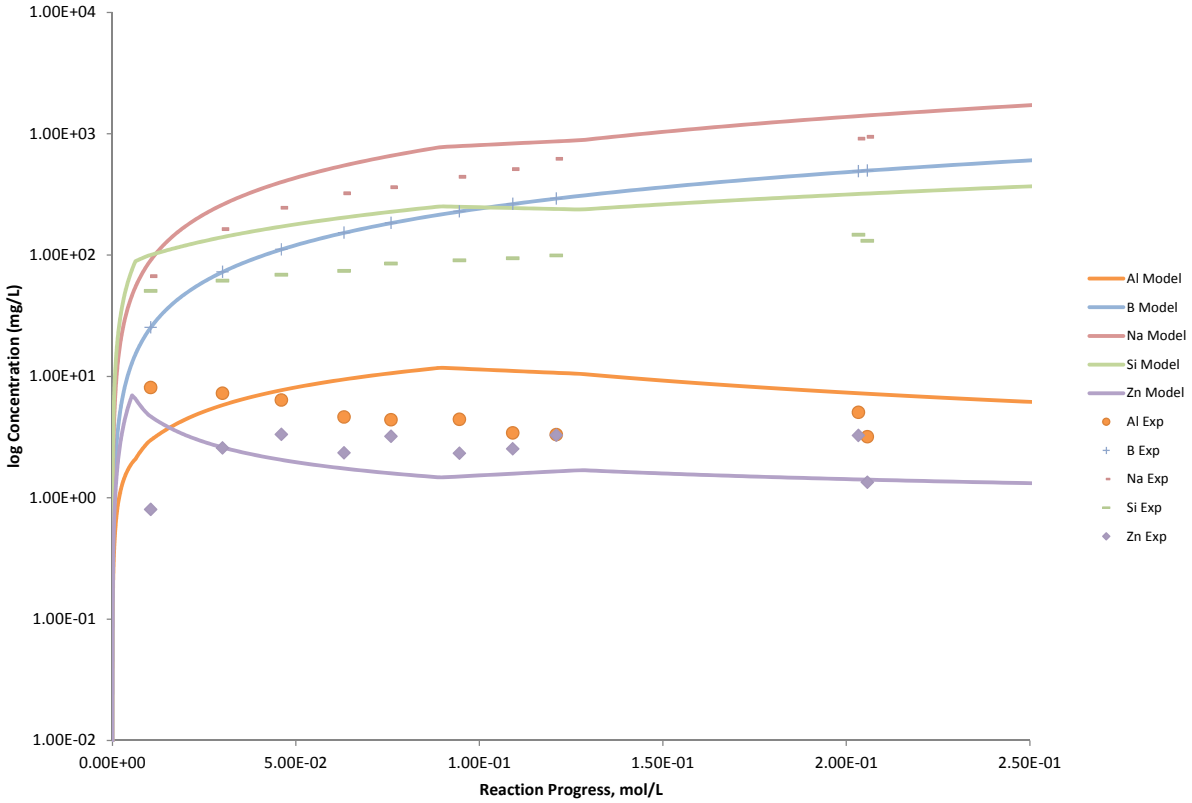


**Figure B.134**. Measured Solution Concentrations (mg/L) and Model Results for Al, B, Na, Si, and Zn, as a Function of Reaction Progress (mol-glass/kg) Determined for Glass Sample LAWA51

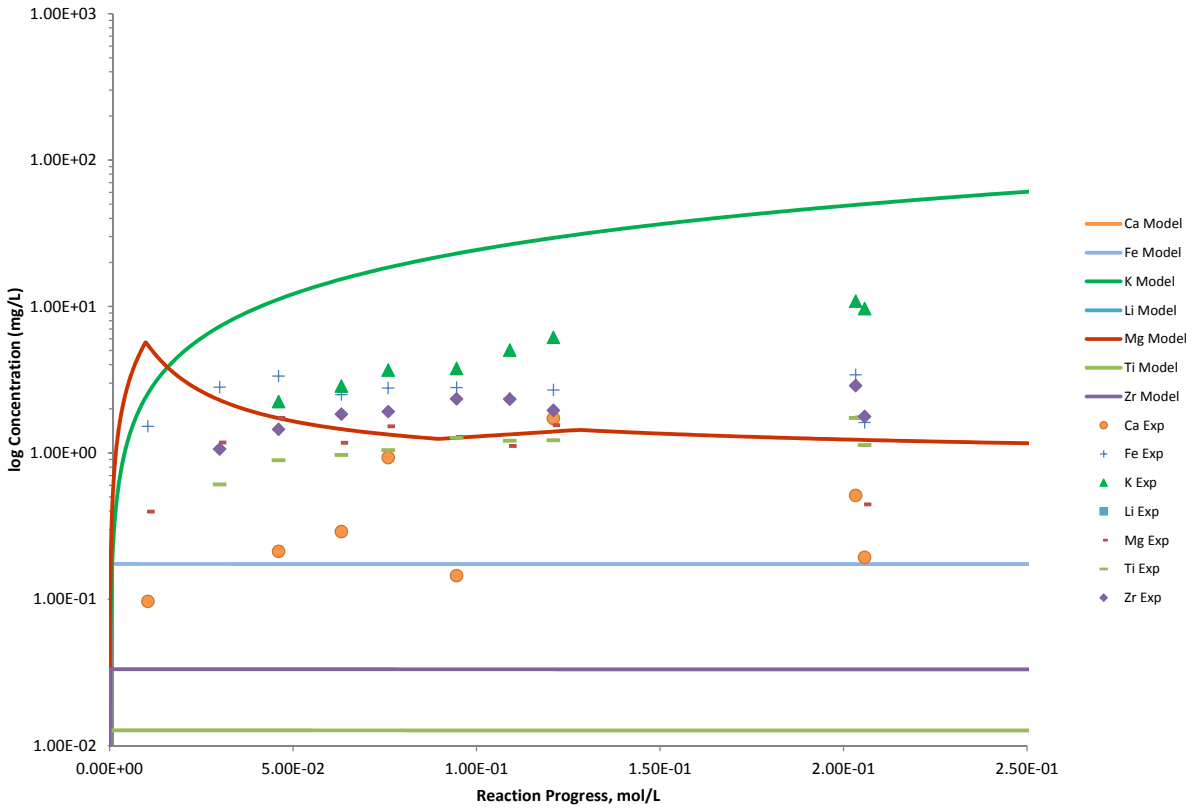


**Figure B.135**. Measured Solution Concentrations (mg/L) and Model Results for Ca, Fe, K, Li, Mg, Ti, and Zr, as a Function of Reaction Progress (mol-glass/kg) Determined for Glass Sample LAWA51

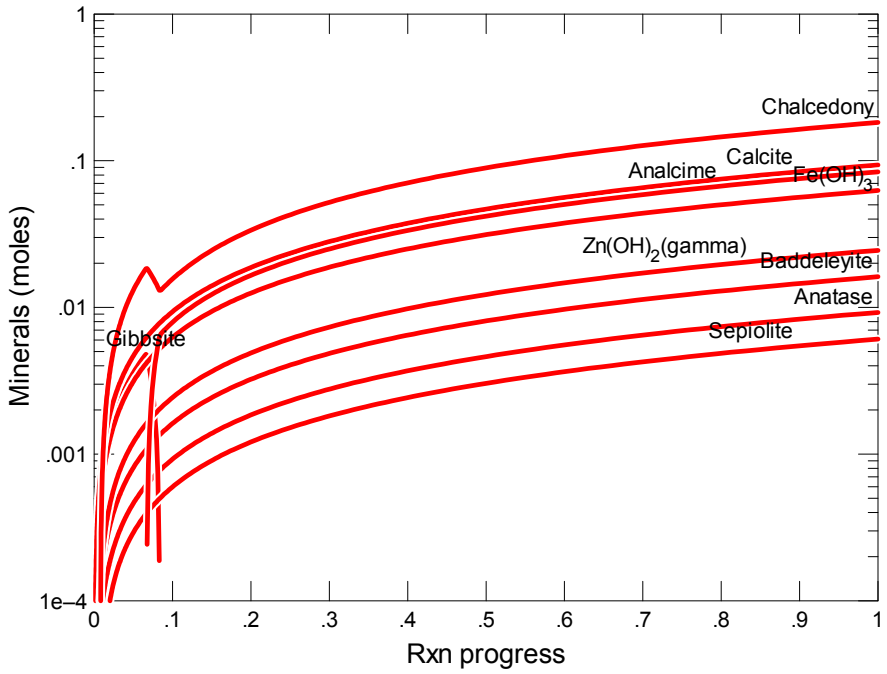


**Figure B.136**. Secondary Phases Calculated to Form as a Function of Reaction Progress (mol-glass/kg) Determined for Glass Sample LAWA52

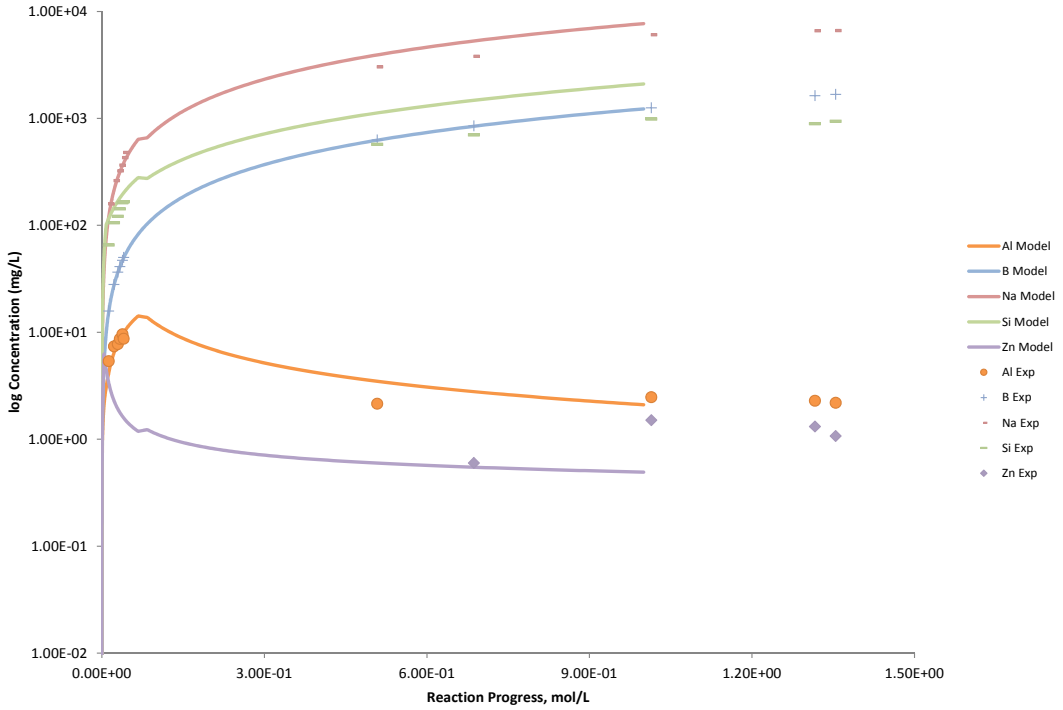


**Figure B.137**. Measured Solution Concentrations (mg/L) and Model Results for Al, B, Na, Si, and Zn, as a Function of Reaction Progress (mol-glass/kg) Determined for Glass Sample LAWA52

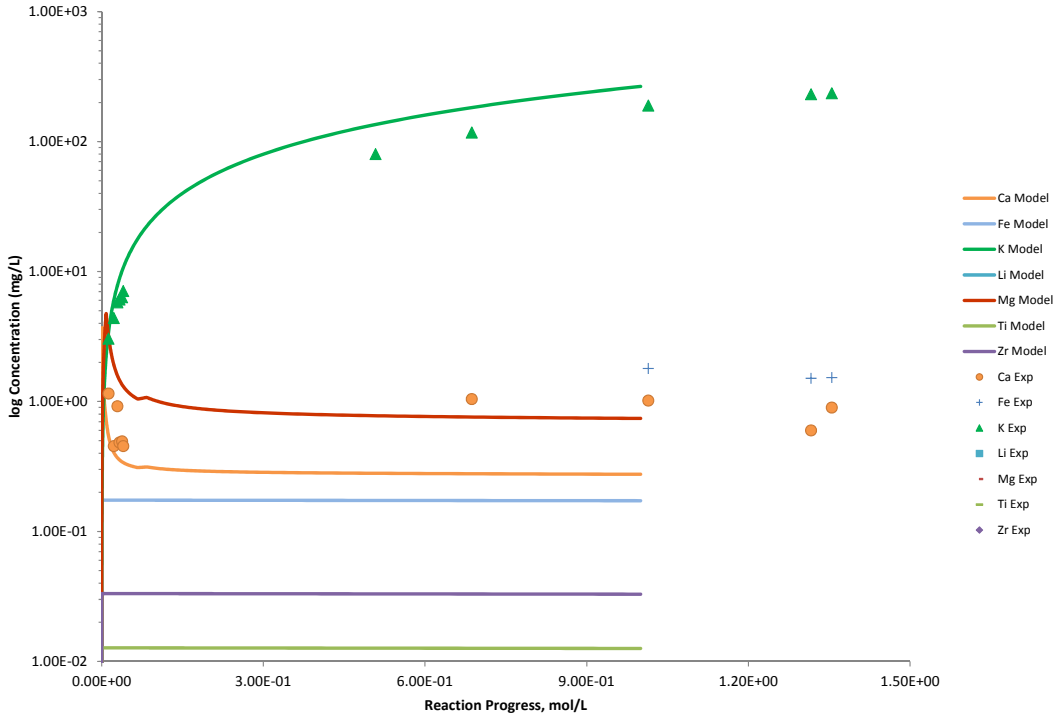


**Figure B.138**. Measured Solution Concentrations (mg/L) and Model Results for Ca, Fe, K, Li, Mg, Ti, and Zr, as a Function of Reaction Progress (mol-glass/kg) Determined for Glass Sample LAWA52

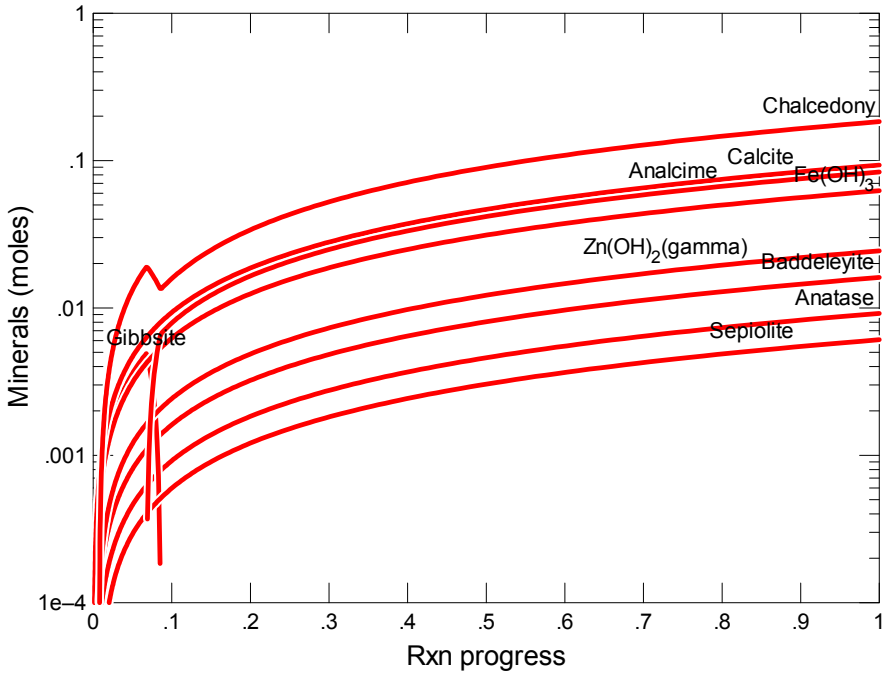


**Figure B.139**. Secondary Phases Calculated to Form as a Function of Reaction Progress (mol-glass/kg) Determined for Glass Sample LAWA53

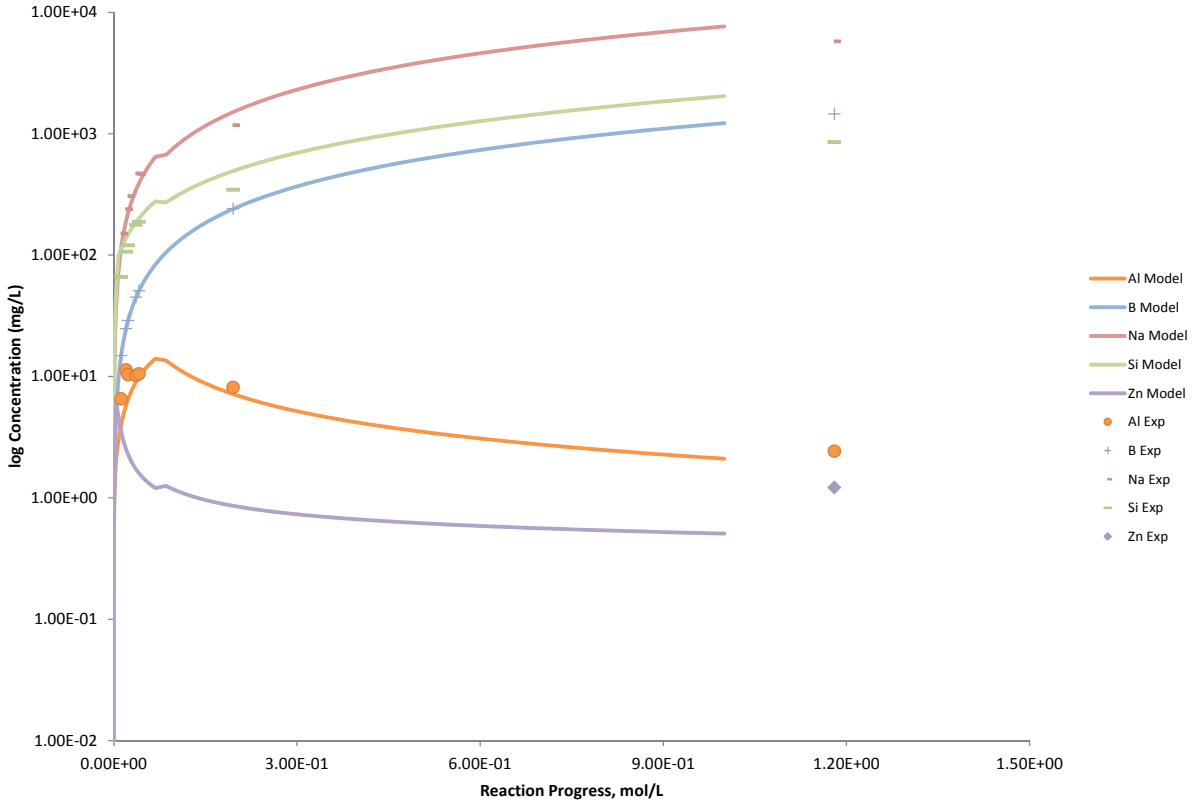


**Figure B.140**. Measured Solution Concentrations (mg/L) and Model Results for Al, B, Na, Si, and Zn, as a Function of Reaction Progress (mol-glass/kg) Determined for Glass Sample LAWA53

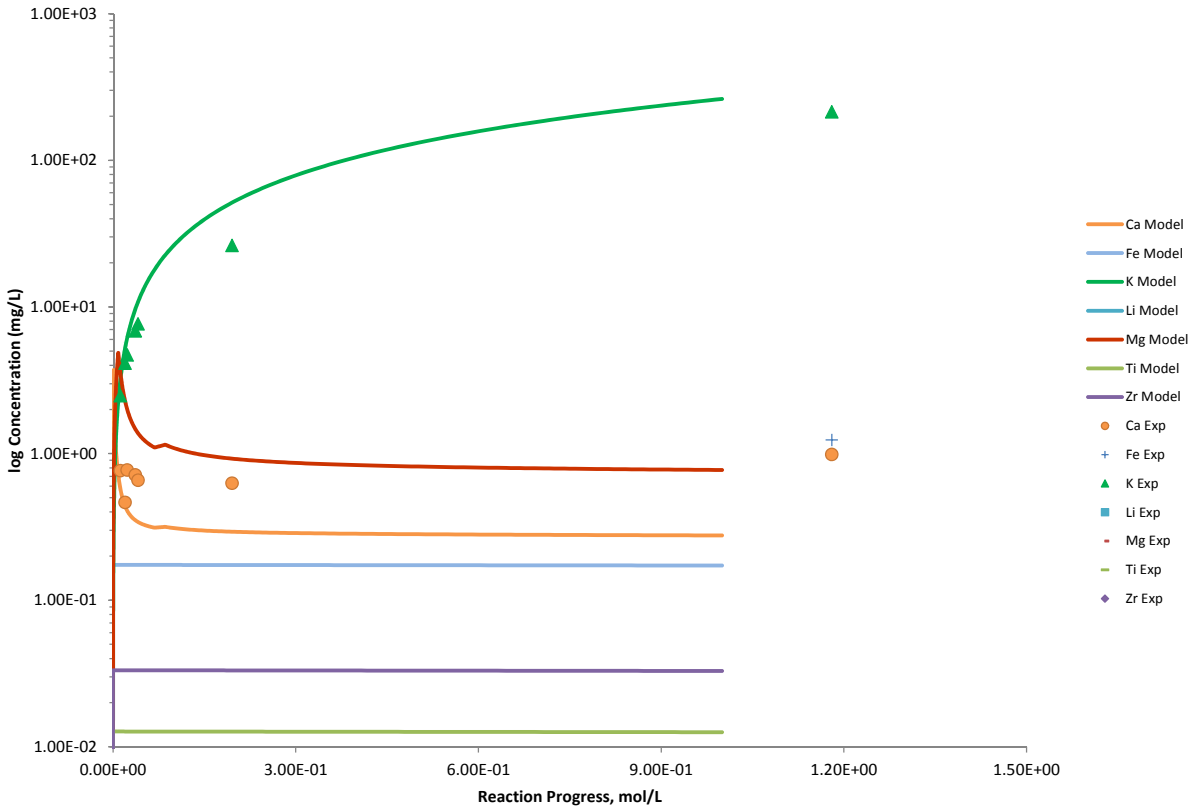


**Figure B.141**. Measured Solution Concentrations (mg/L) and Model Results for Ca, Fe, K, Li, Mg, Ti, and Zr, as a Function of Reaction Progress (mol-glass/kg) Determined for Glass Sample LAWA53

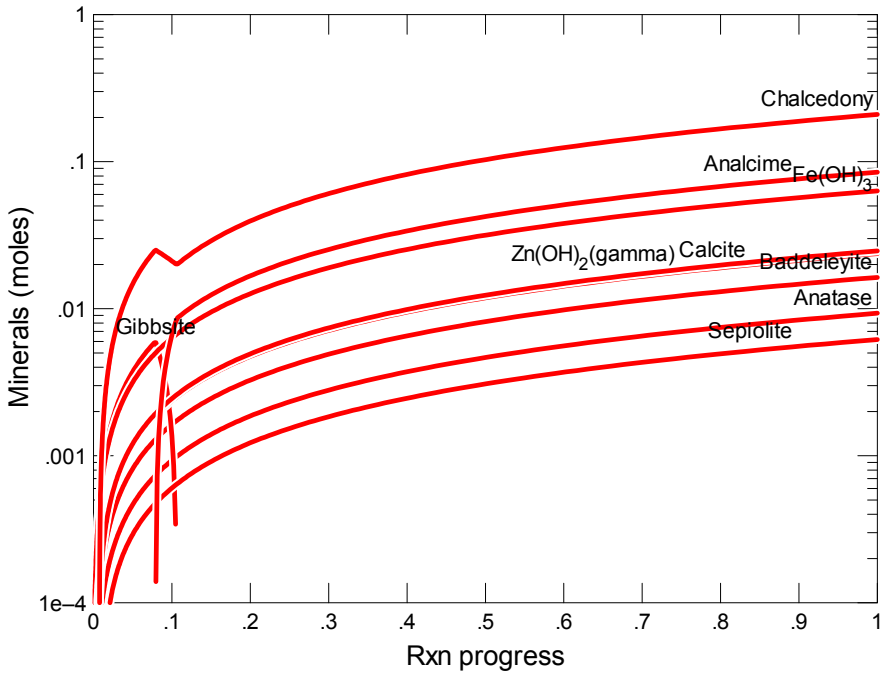


**Figure B.142**. Secondary Phases Calculated to Form as a Function of Reaction Progress (mol-glass/kg) Determined for Glass Sample LAWA56

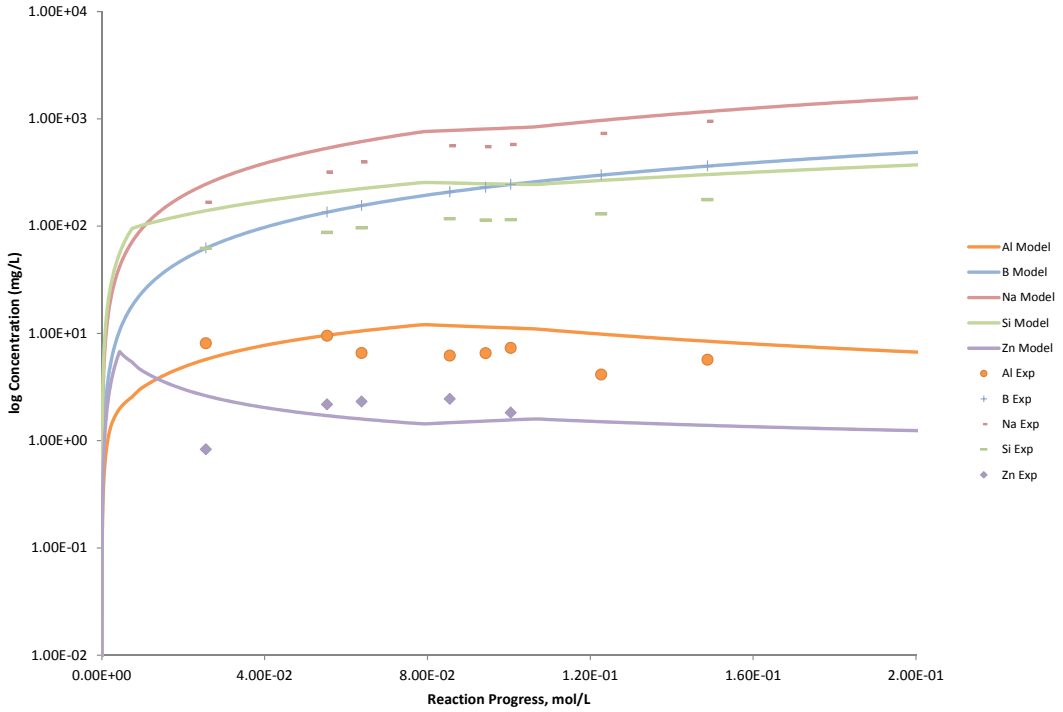


**Figure B.143**. Measured Solution Concentrations (mg/L) and Model Results for Al, B, Na, Si, and Zn, as a Function of Reaction Progress (mol-glass/kg) Determined for Glass Sample LAWA56

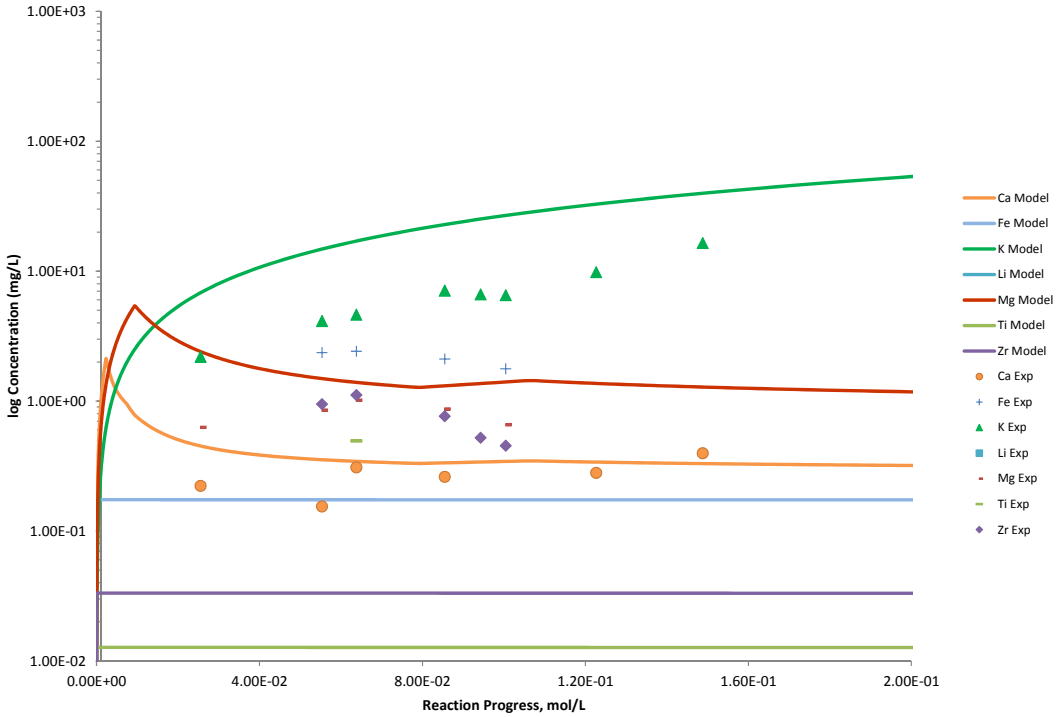


**Figure B.144**. Measured Solution Concentrations (mg/L) and Model Results for Ca, Fe, K, Li, Mg, Ti, and Zr, as a Function of Reaction Progress (mol-glass/kg) Determined for Glass Sample LAWA56

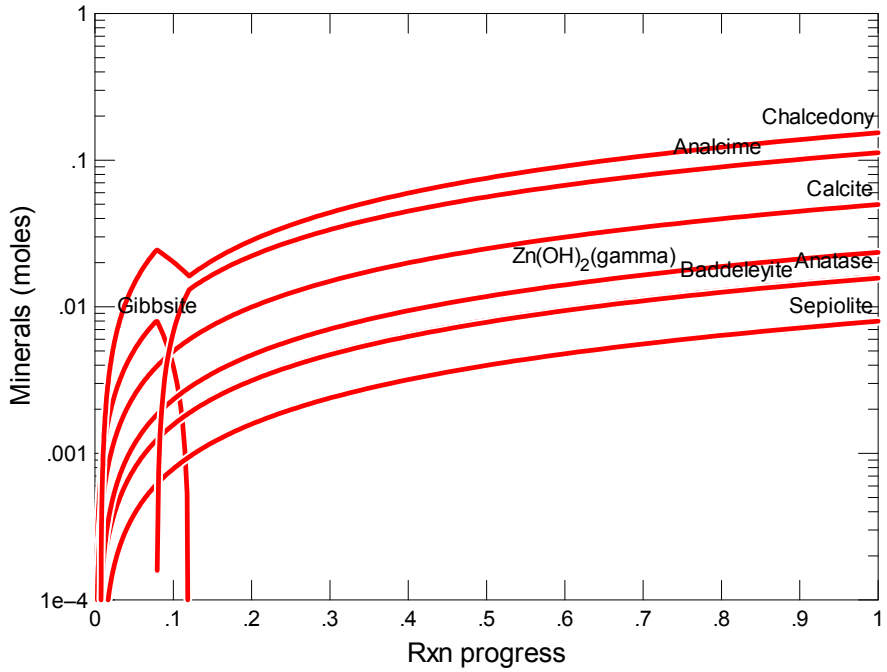


**Figure B.145**. Secondary Phases Calculated to Form as a Function of Reaction Progress (mol-glass/kg) Determined for Glass Sample LAWA60

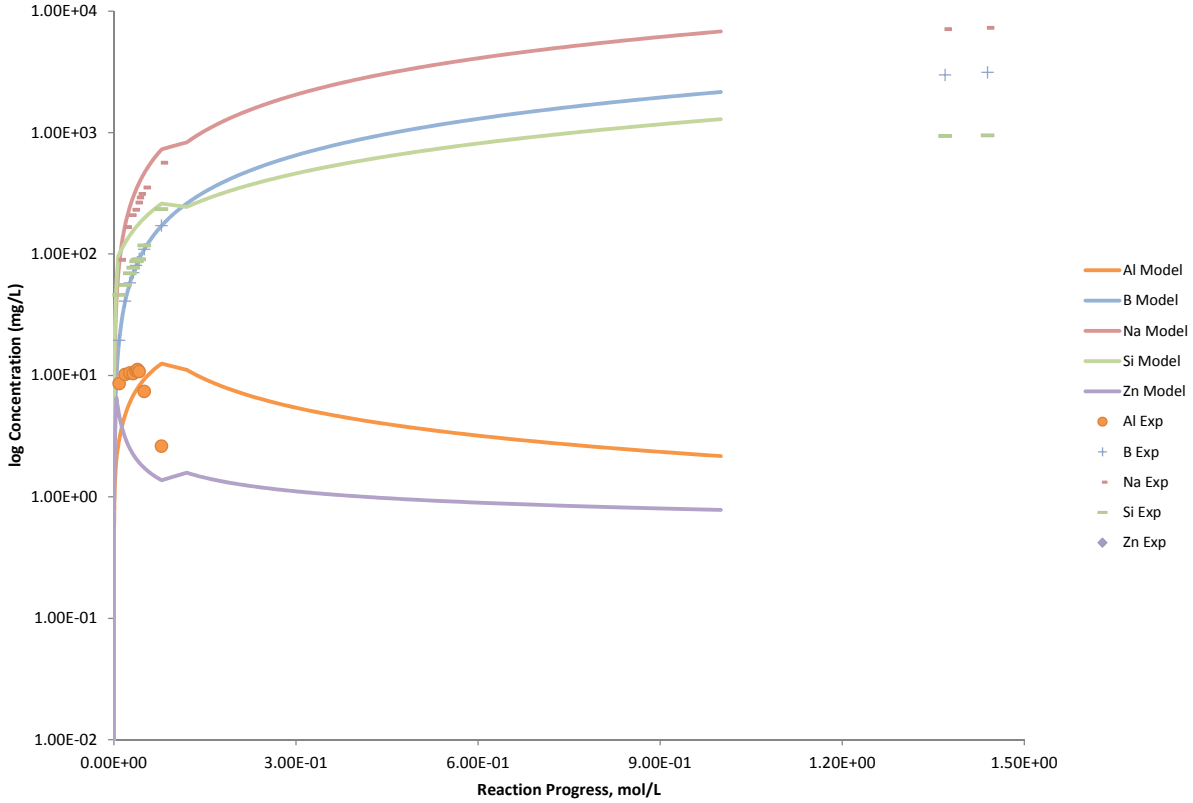


**Figure B.146**. Measured Solution Concentrations (mg/L) and Model Results for Al, B, Na, Si, and Zn, as a Function of Reaction Progress (mol-glass/kg) Determined for Glass Sample LAWA60

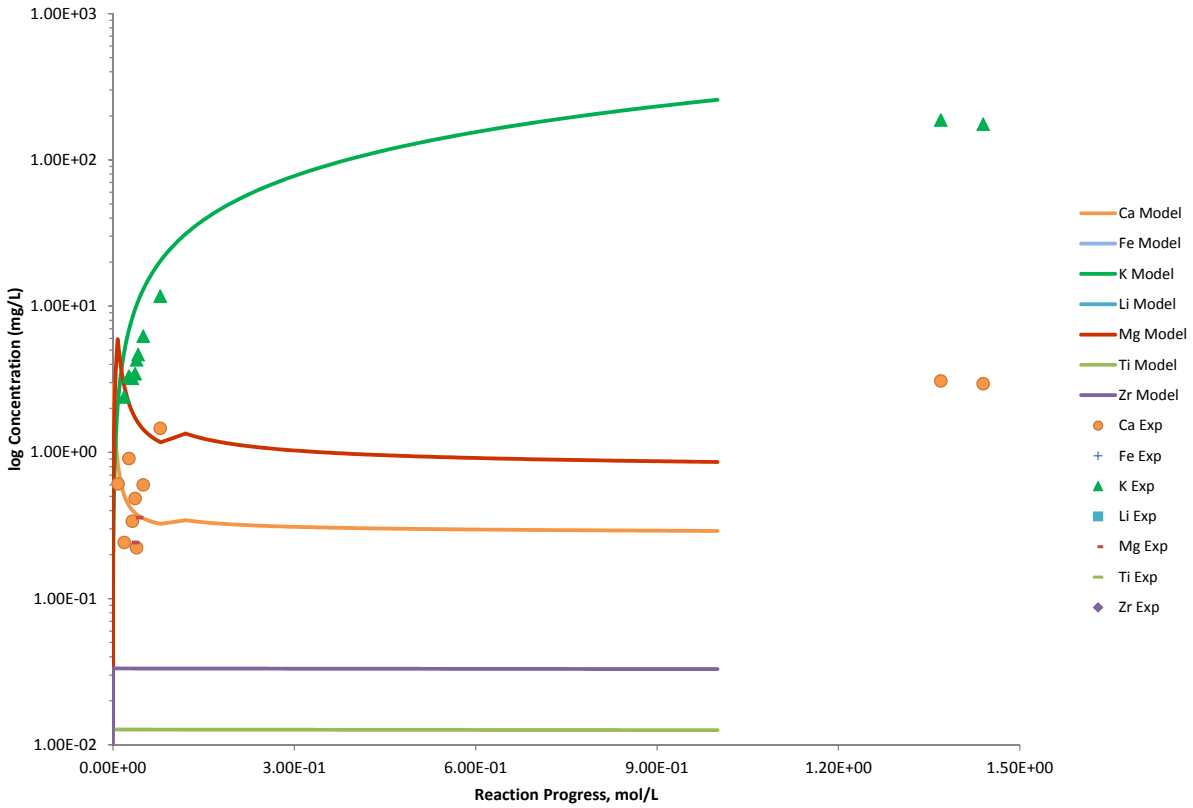


**Figure B.147**. Measured Solution Concentrations (mg/L) and Model Results for Ca, Fe, K, Li, Mg, Ti, and Zr, as a Function of Reaction Progress (mol-glass/kg) Determined for Glass Sample LAWA60

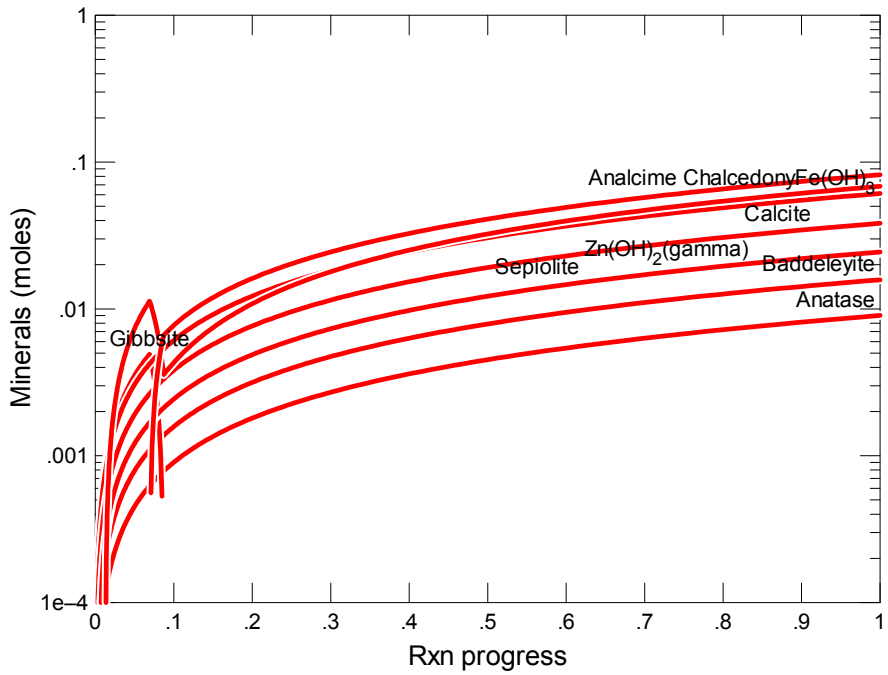


**Figure B.148**. Secondary Phases Calculated to Form as a Function of Reaction Progress (mol-glass/kg) Determined for Glass Sample LAWA65

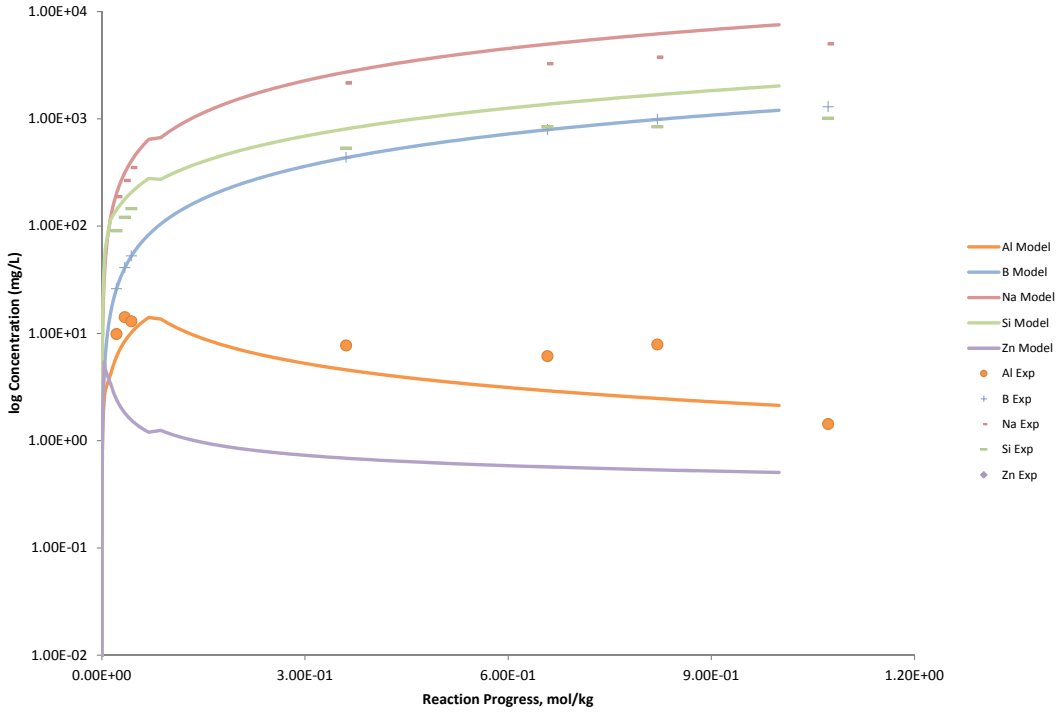


**Figure B.149**. Measured Solution Concentrations (mg/L) and Model Results for Al, B, Na, Si, and Zn, as a Function of Reaction Progress (mol-glass/kg) Determined for Glass Sample LAWA65

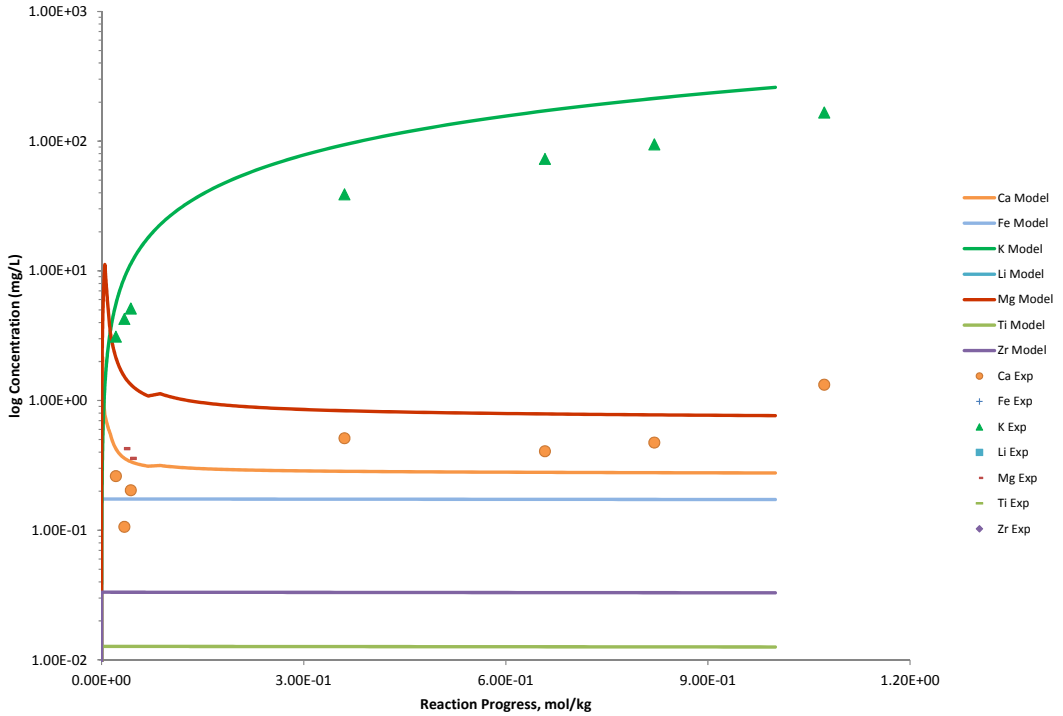


**Figure B.150**. Measured Solution Concentrations (mg/L) and Model Results for Ca, Fe, K, Li, Mg, Ti, and Zr, as a Function of Reaction Progress (mol-glass/kg) Determined for Glass Sample LAWA65

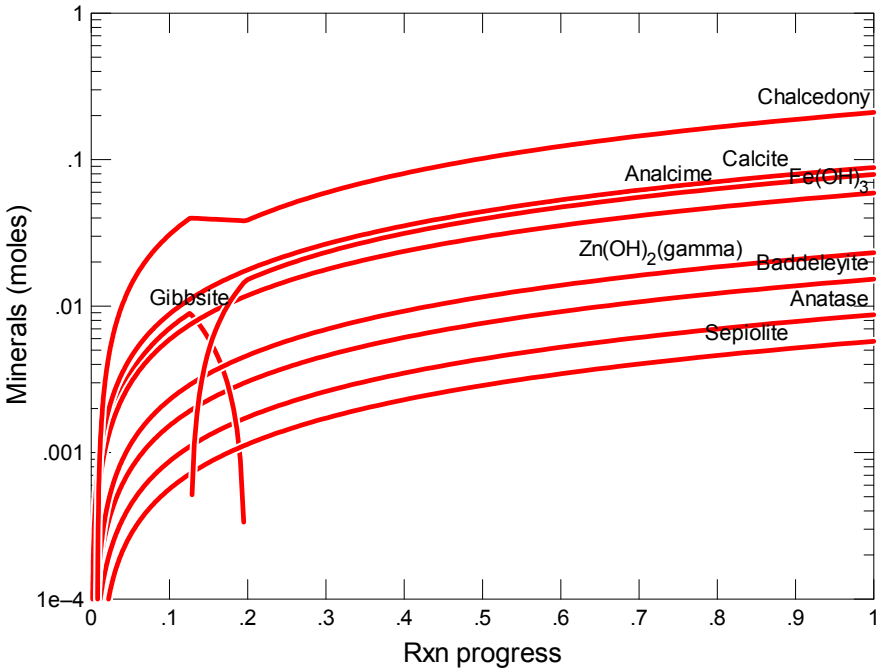


**Figure B.151**. Secondary Phases Calculated to Form as a Function of Reaction Progress (mol-glass/kg) Determined for Glass Sample LAWA76

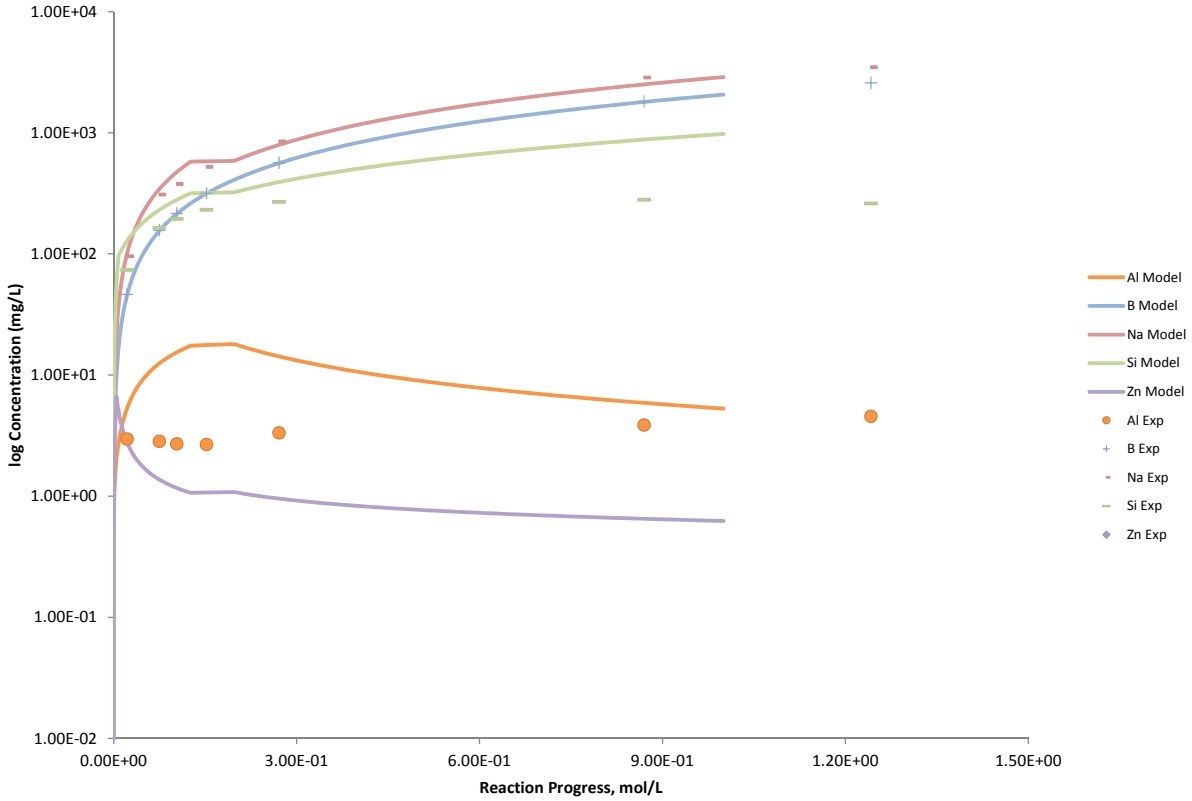


**Figure B.152**. Measured Solution Concentrations (mg/L) and Model Results for Al, B, Na, Si, and Zn, as a Function of Reaction Progress (mol-glass/kg) Determined for Glass Sample LAWA76

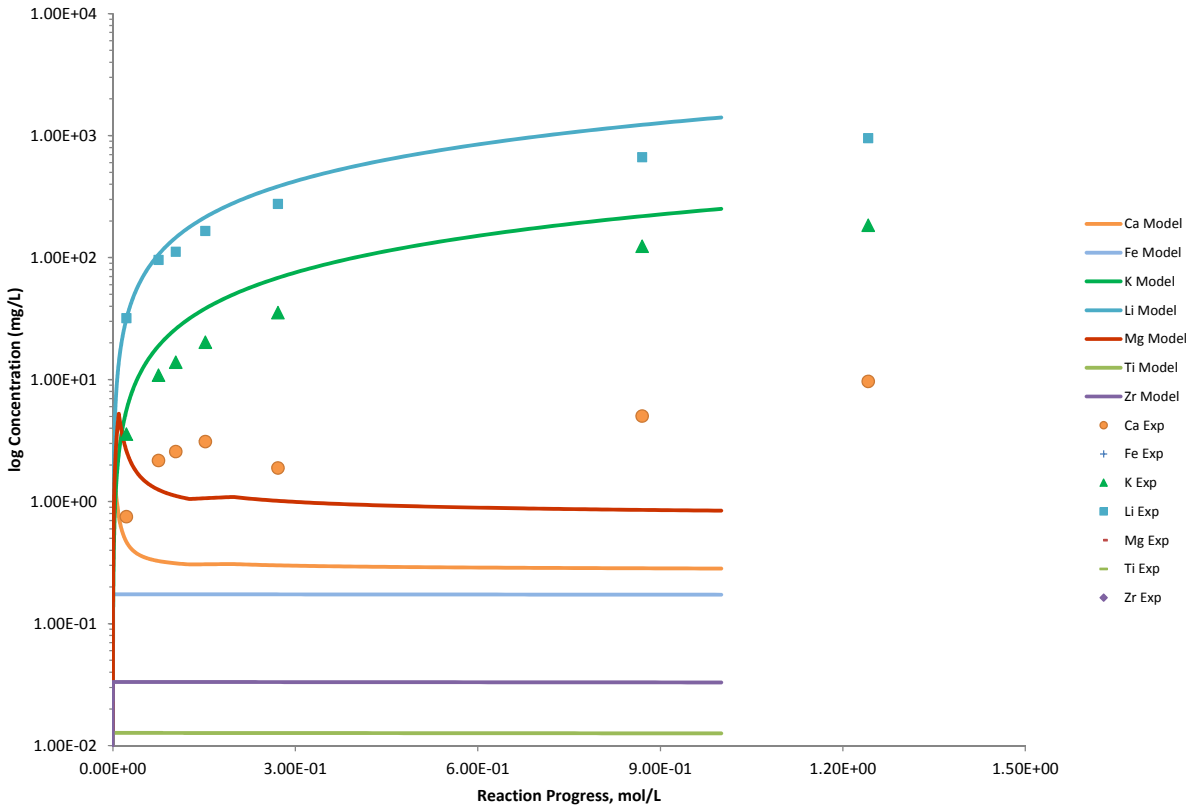


**Figure B.153**. Measured Solution Concentrations (mg/L) and Model Results for Ca, Fe, K, Li, Mg, Ti, and Zr, as a Function of Reaction Progress (mol-glass/kg) Determined for Glass Sample LAWA76

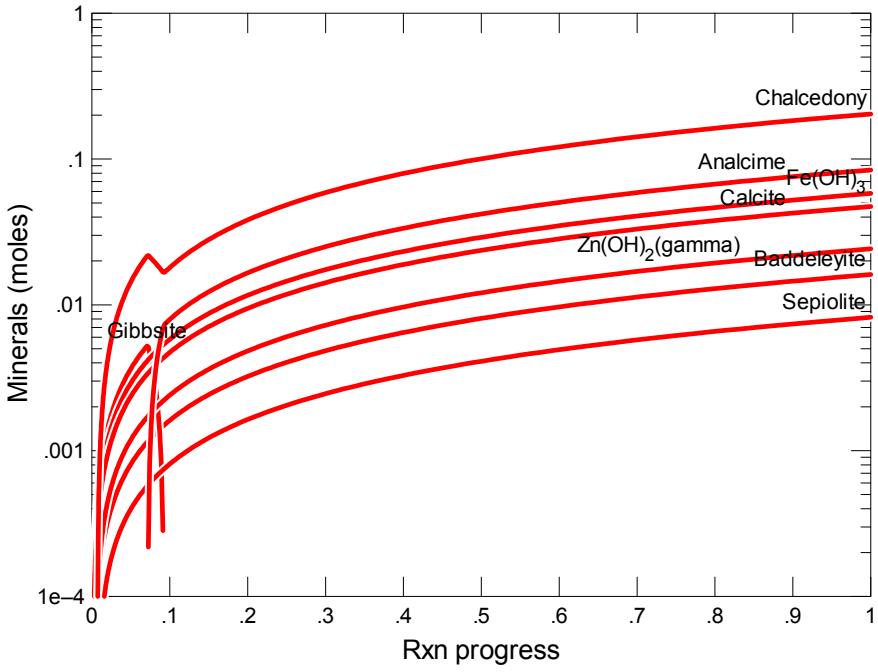


**Figure B.154**. Secondary Phases Calculated to Form as a Function of Reaction Progress (mol-glass/kg) Determined for Glass Sample LAWA81

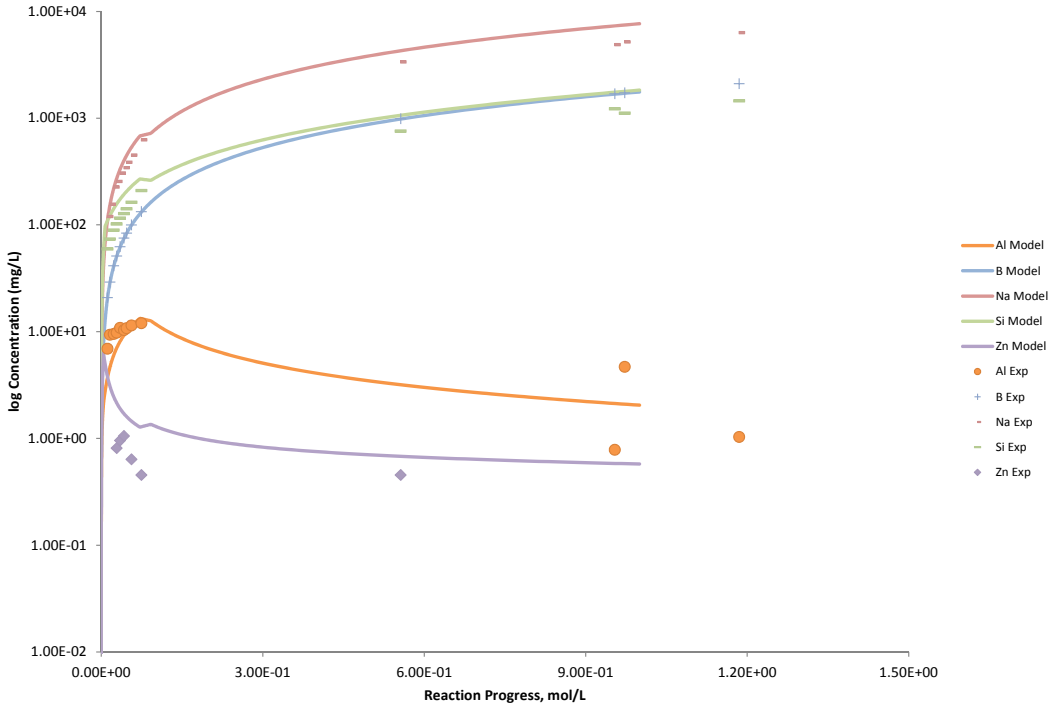


**Figure B.155**. Measured Solution Concentrations (mg/L) and Model Results for Al, B, Na, Si, and Zn, as a Function of Reaction Progress (mol-glass/kg) Determined for Glass Sample LAWA81

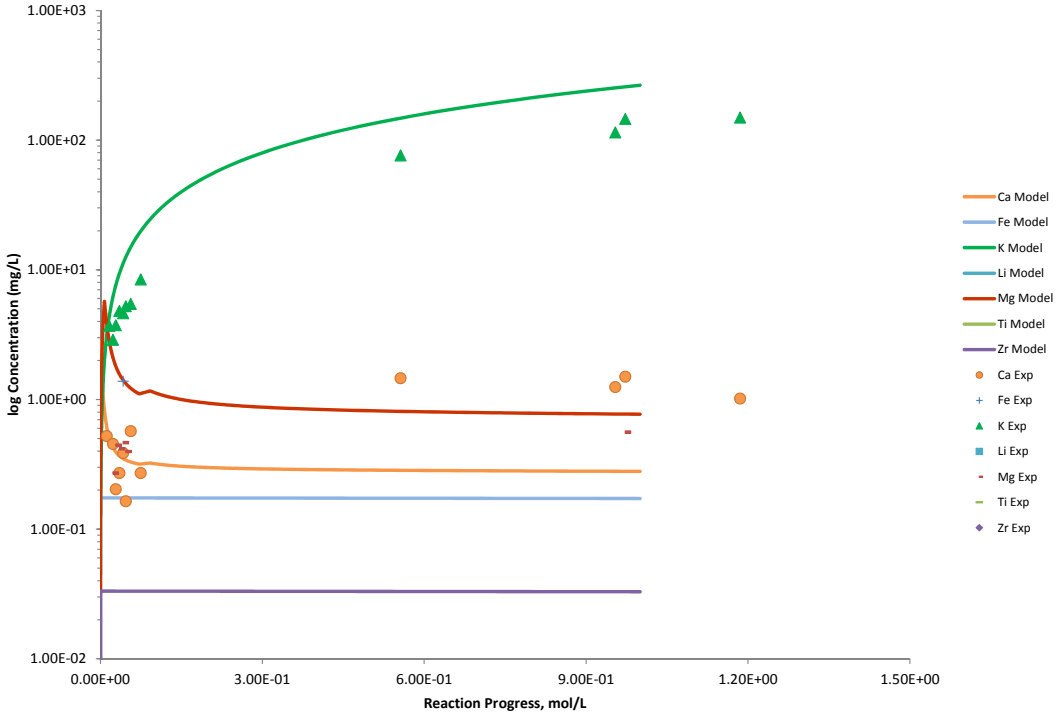


**Figure B.156**. Measured Solution Concentrations (mg/L) and Model Results for Ca, Fe, K, Li, Mg, Ti, and Zr, as a Function of Reaction Progress (mol-glass/kg) Determined for Glass Sample LAWA81

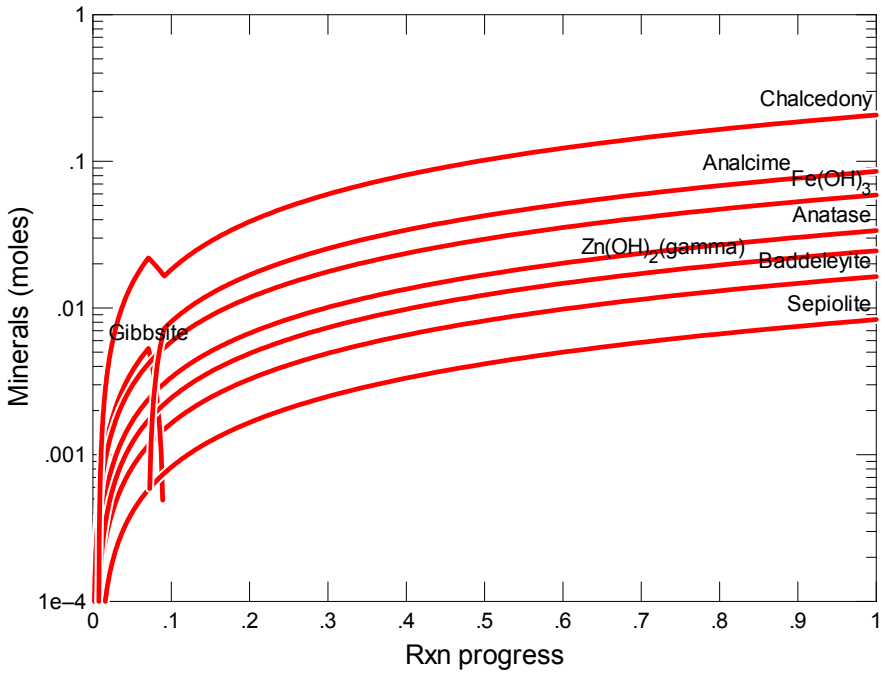


**Figure B.157**. Secondary Phases Calculated to Form as a Function of Reaction Progress (mol-glass/kg) Determined for Glass Sample LAWA82

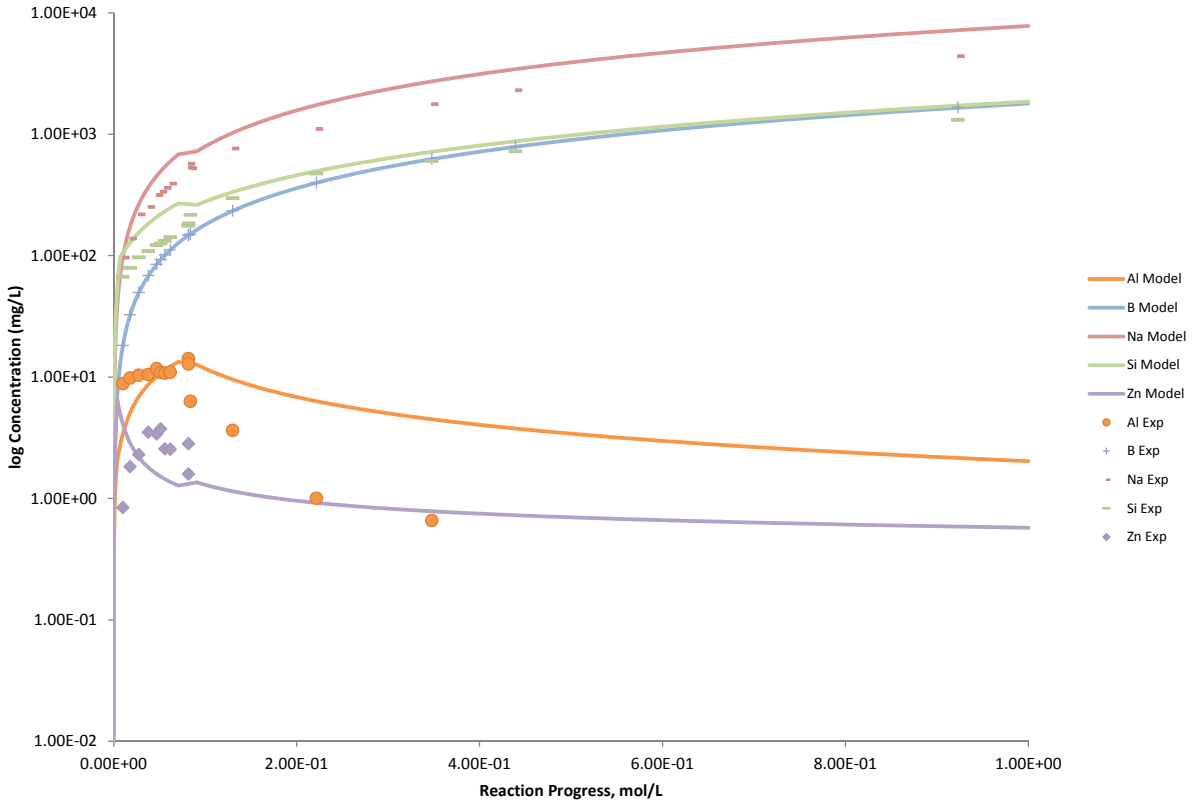


**Figure B.158**. Measured Solution Concentrations (mg/L) and Model Results for Al, B, Na, Si, and Zn, as a Function of Reaction Progress (mol-glass/kg) Determined for Glass Sample LAWA82

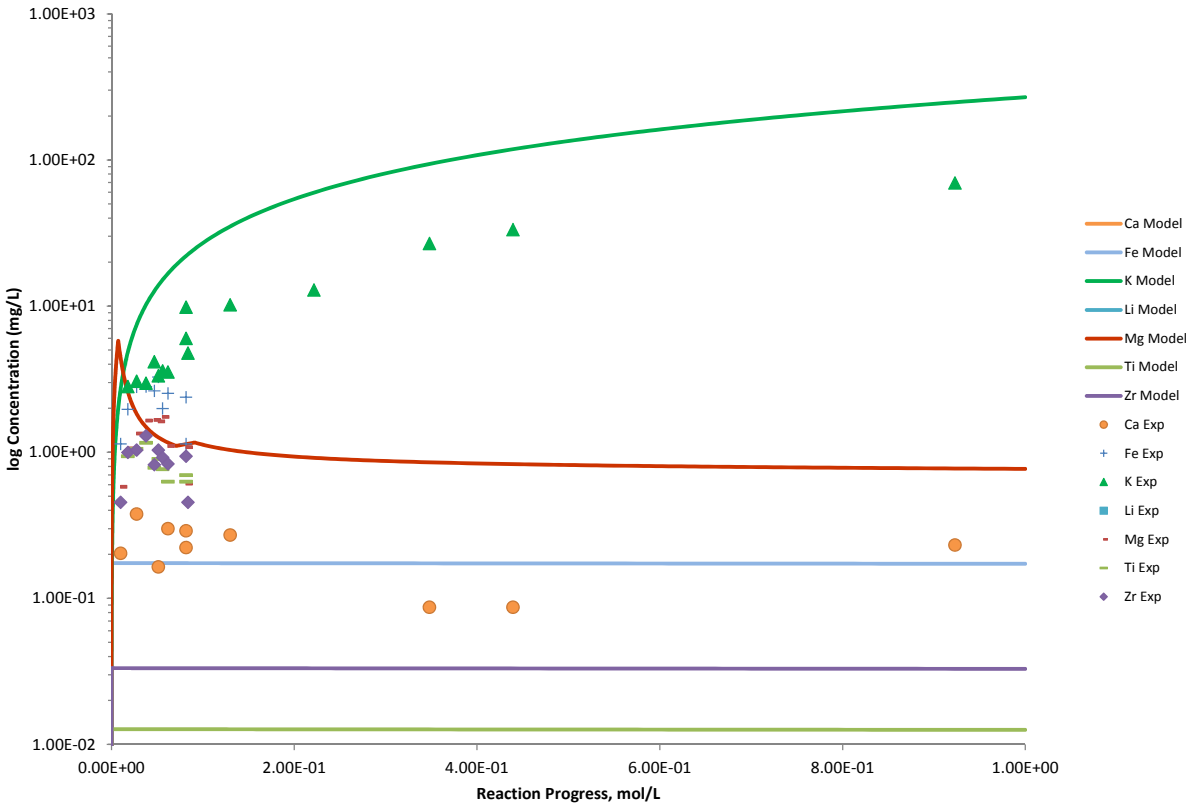


**Figure B.159**. Measured Solution Concentrations (mg/L) and Model Results for Ca, Fe, K, Li, Mg, Ti, and Zr, as a Function of Reaction Progress (mol-glass/kg) Determined for Glass Sample LAWA82

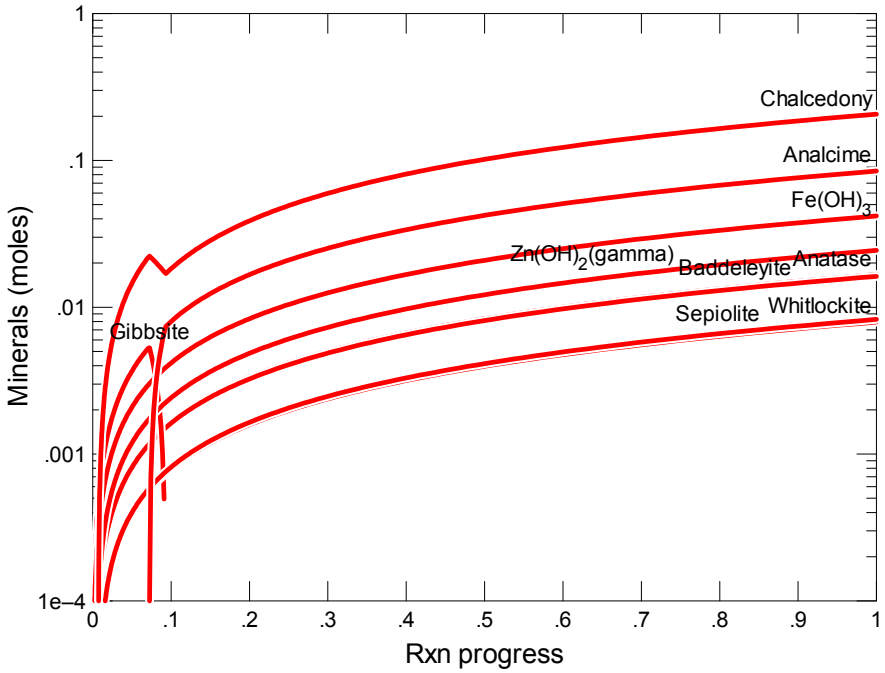


**Figure B.160**. Secondary Phases Calculated to Form as a Function of Reaction Progress (mol-glass/kg) Determined for Glass Sample LAWA83

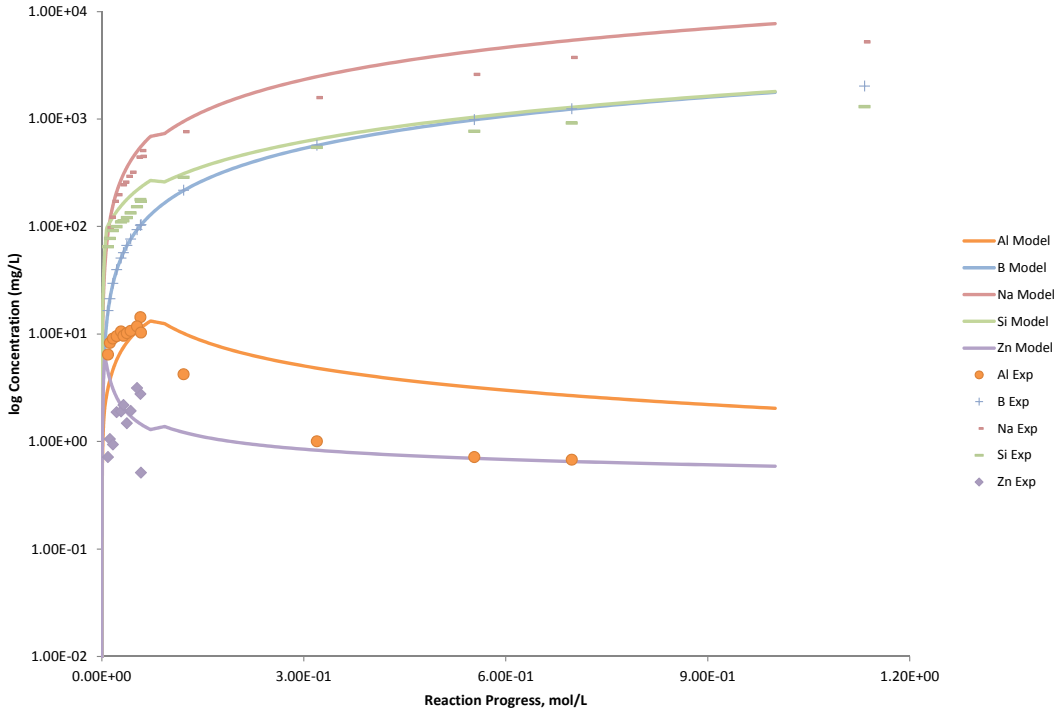


**Figure B.161**. Measured Solution Concentrations (mg/L) and Model Results for Al, B, Na, Si, and Zn, as a Function of Reaction Progress (mol-glass/kg) Determined for Glass Sample LAWA83

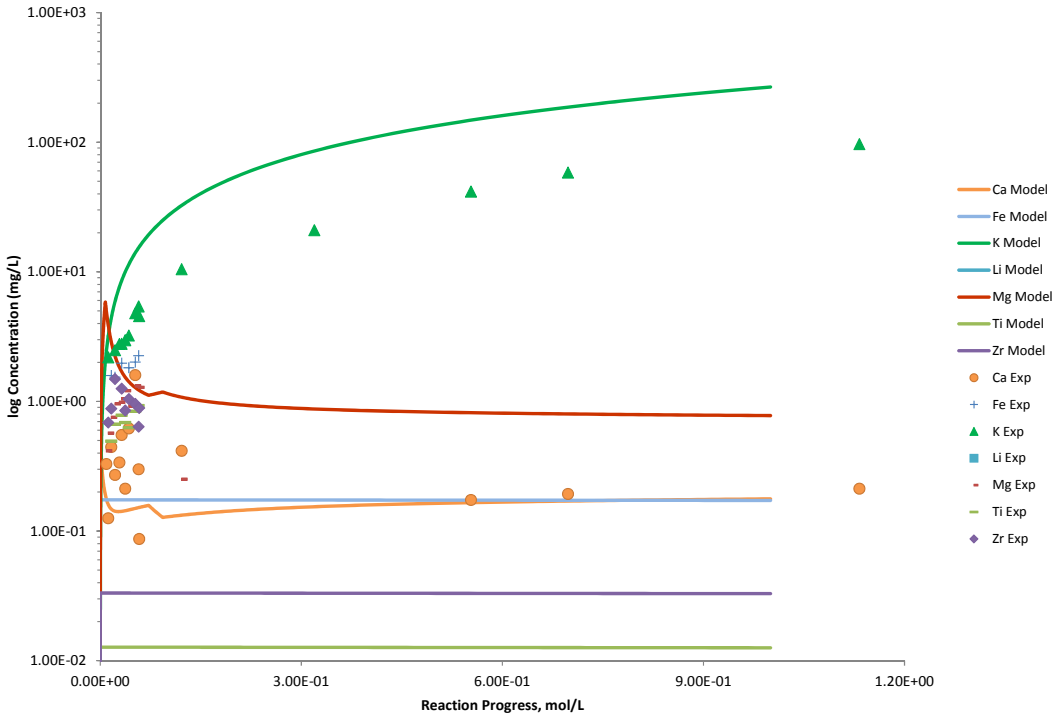


**Figure B.162**. Measured Solution Concentrations (mg/L) and Model Results for Ca, Fe, K, Li, Mg, Ti, and Zr, as a Function of Reaction Progress (mol-glass/kg) Determined for Glass Sample LAWA83

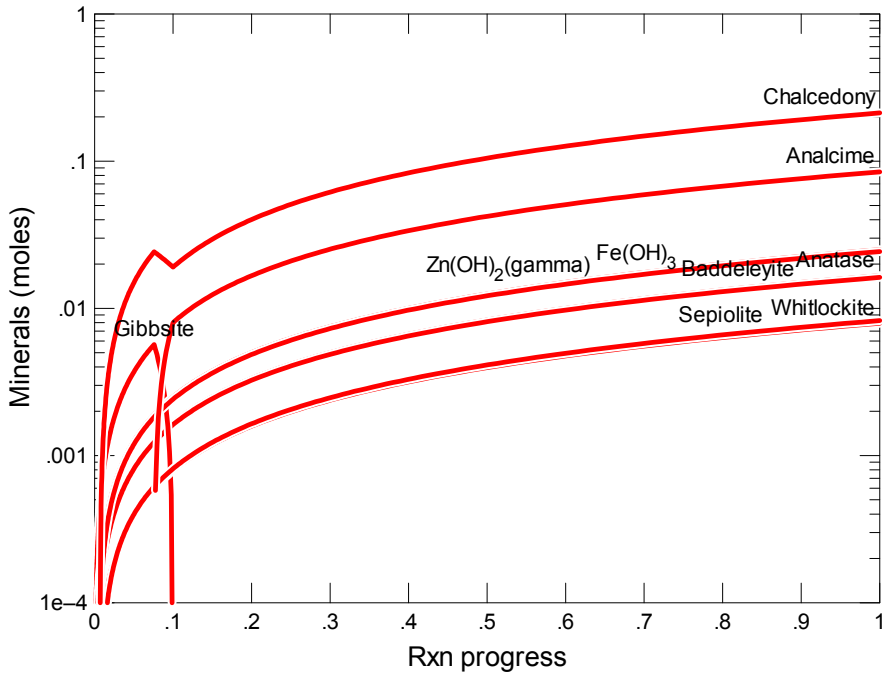


**Figure B.163**. Secondary Phases Calculated to Form as a Function of Reaction Progress (mol-glass/kg) Determined for Glass Sample LAWA84

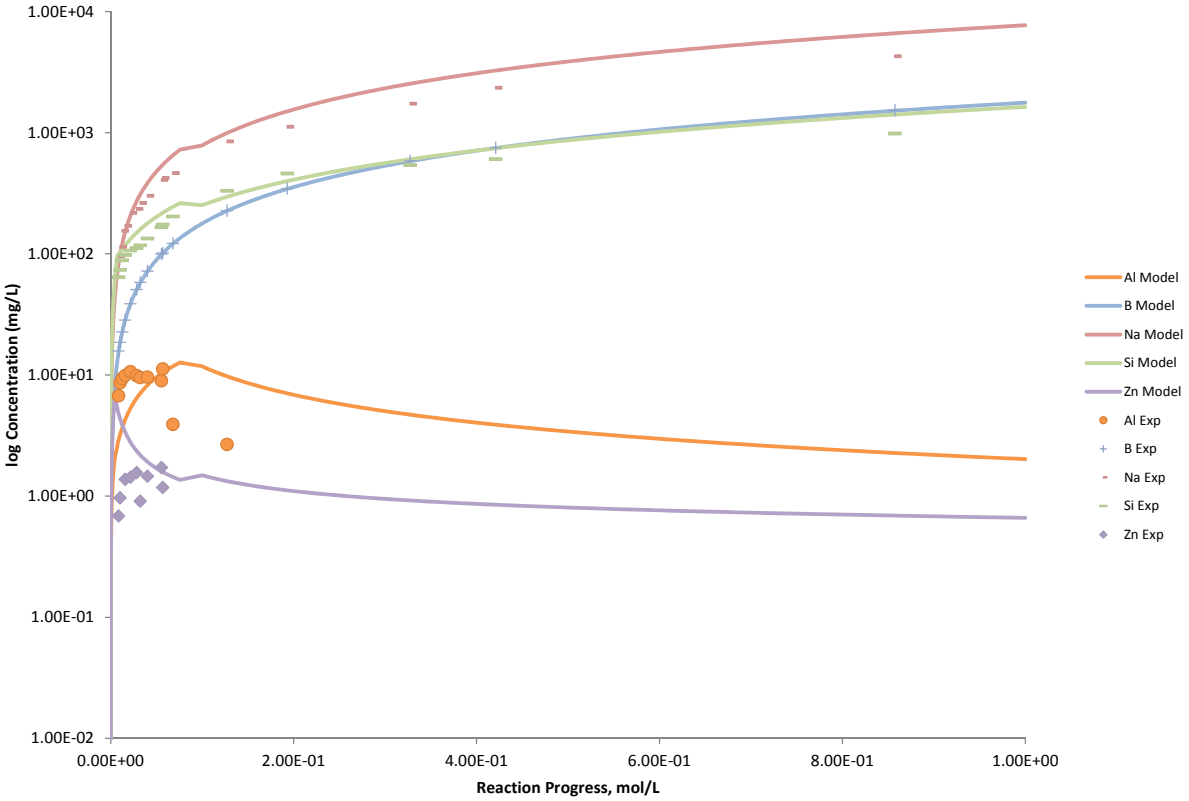


**Figure B.164**. Measured Solution Concentrations (mg/L) and Model Results for Al, B, Na, Si, and Zn, as a Function of Reaction Progress (mol-glass/kg) Determined for Glass Sample LAWA84

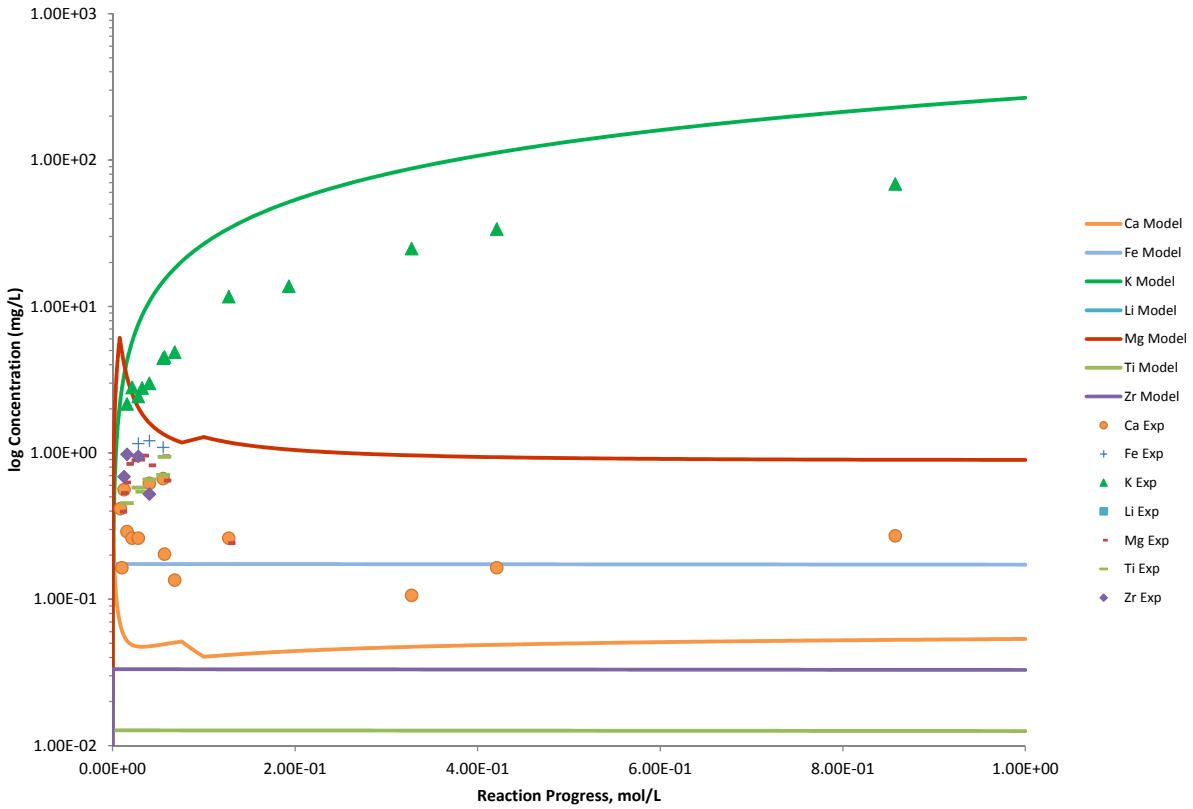


**Figure B.165**. Measured Solution Concentrations (mg/L) and Model Results for Ca, Fe, K, Li, Mg, Ti, and Zr, as a Function of Reaction Progress (mol-glass/kg) Determined for Glass Sample LAWA84

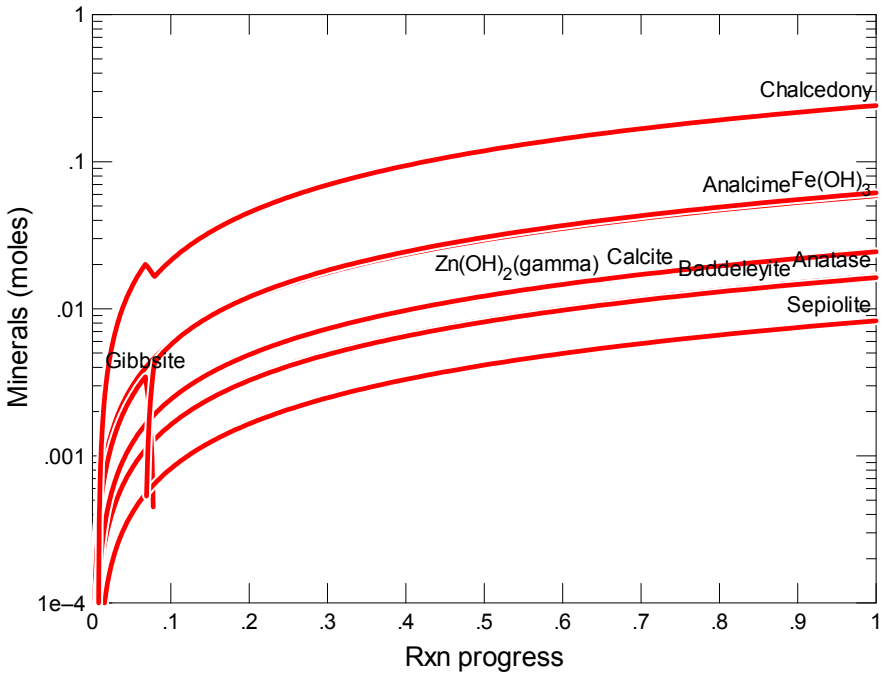


**Figure B.166**. Secondary Phases Calculated to Form as a Function of Reaction Progress (mol-glass/kg) Determined for Glass Sample LAWA87

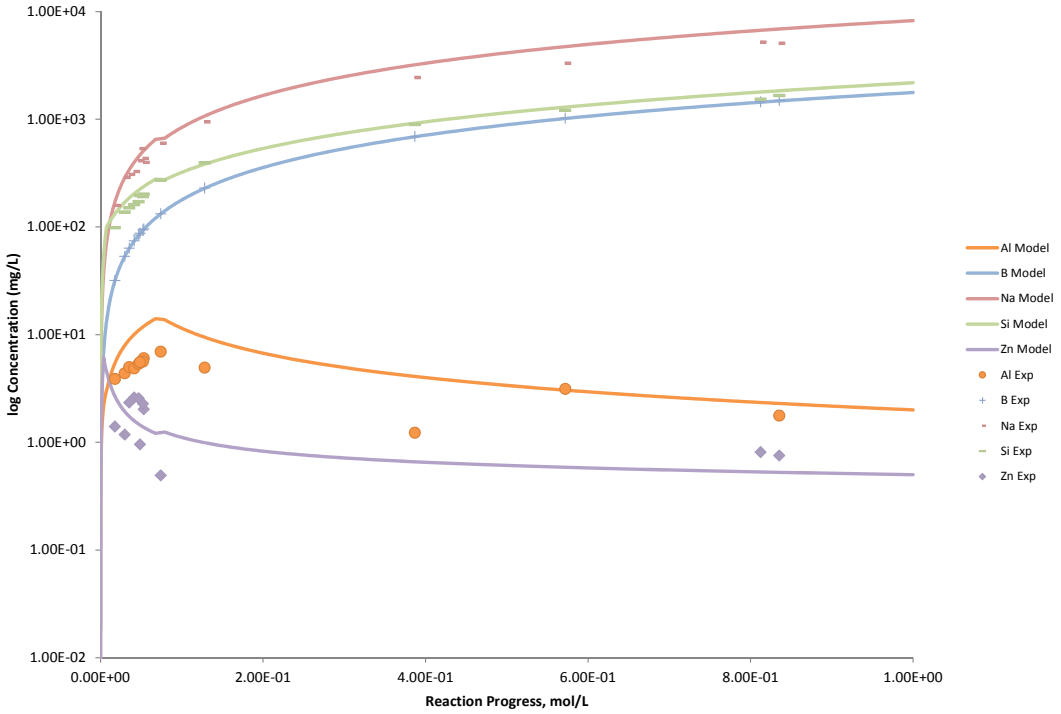


**Figure B.167**. Measured Solution Concentrations (mg/L) and Model Results for Al, B, Na, Si, and Zn, as a Function of Reaction Progress (mol-glass/kg) Determined for Glass Sample LAWA87

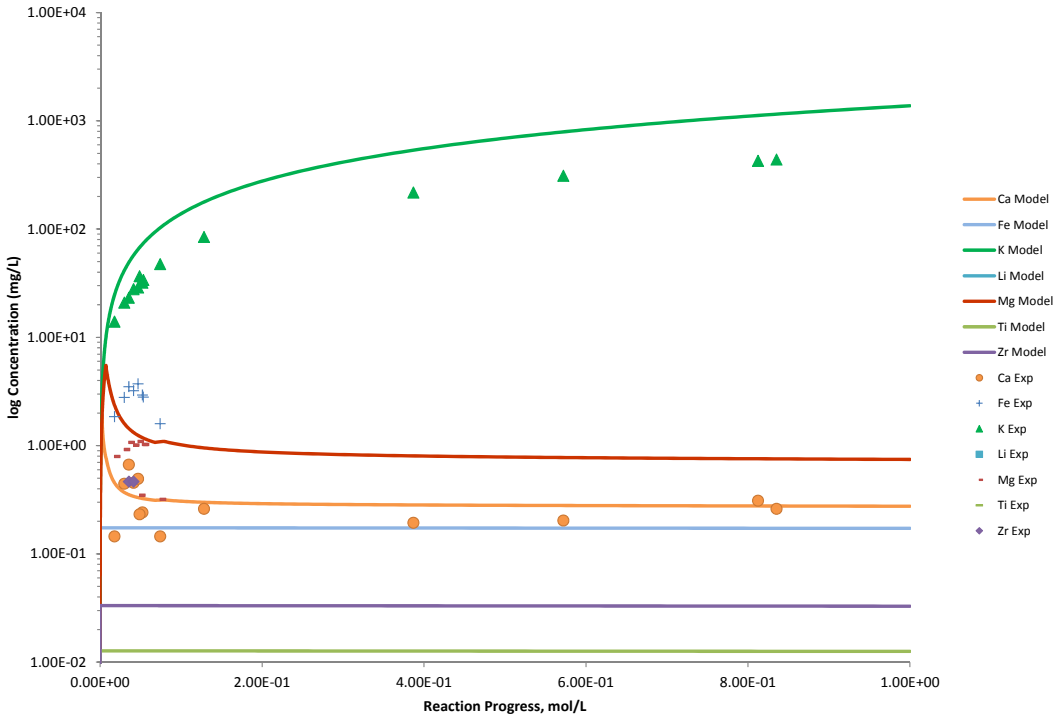


**Figure B.168**. Measured Solution Concentrations (mg/L) and Model Results for Ca, Fe, K, Li, Mg, Ti, and Zr, as a Function of Reaction Progress (mol-glass/kg) Determined for Glass Sample LAWA87

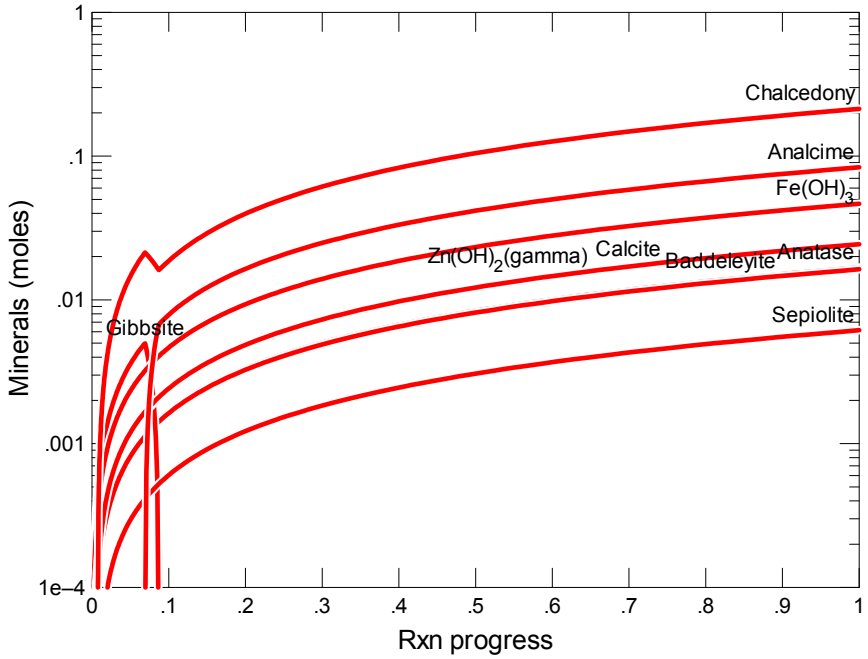


**Figure B.169**. Secondary Phases Calculated to Form as a Function of Reaction Progress (mol-glass/kg) Determined for Glass Sample LAWA88

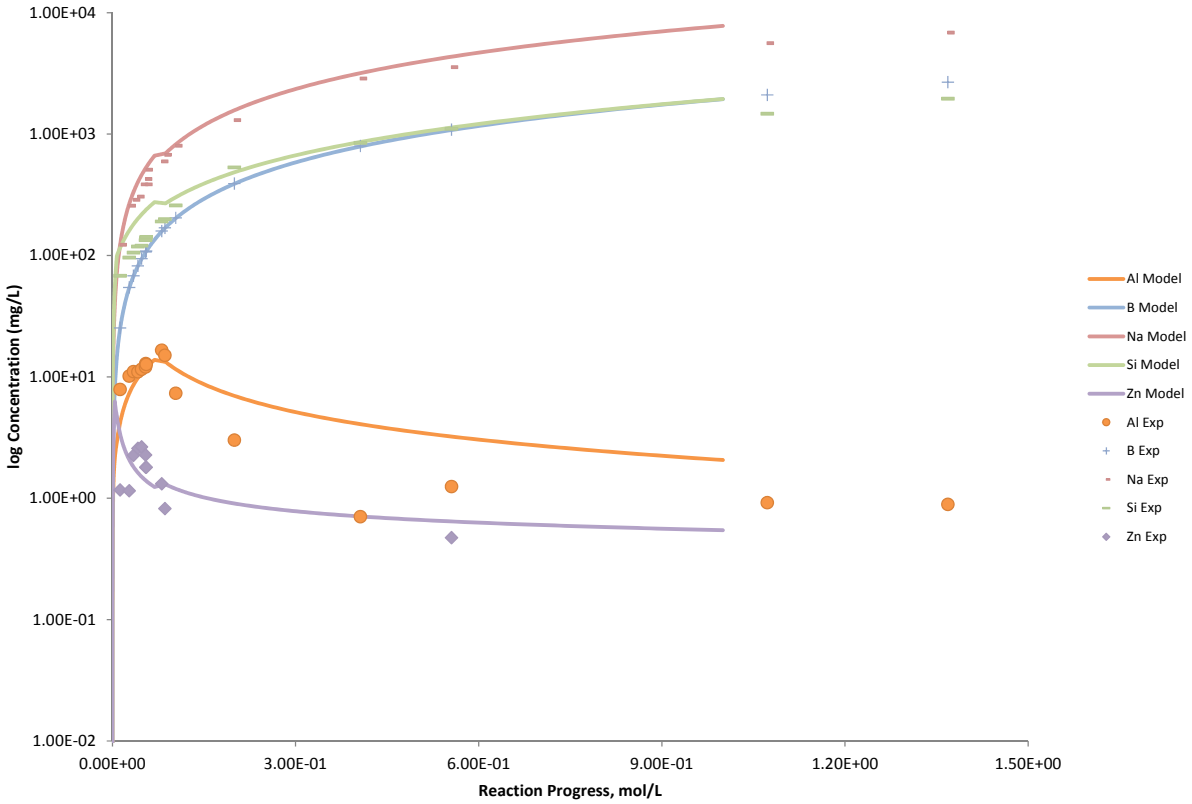


**Figure B.170**. Measured Solution Concentrations (mg/L) and Model Results for Al, B, Na, Si, and Zn, as a Function of Reaction Progress (mol-glass/kg) Determined for Glass Sample LAWA88

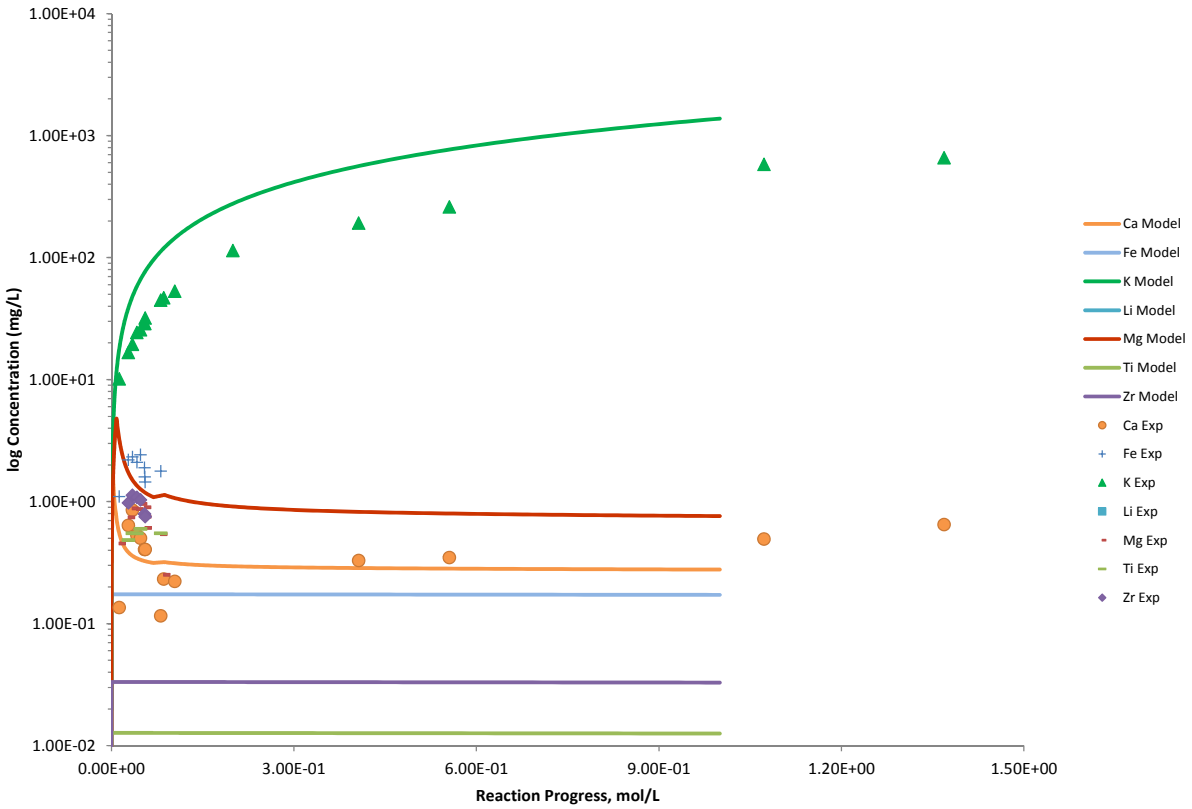


**Figure B.171**. Measured Solution Concentrations (mg/L) and Model Results for Ca, Fe, K, Li, Mg, Ti, and Zr, as a Function of Reaction Progress (mol-glass/kg) Determined for Glass Sample LAWA88

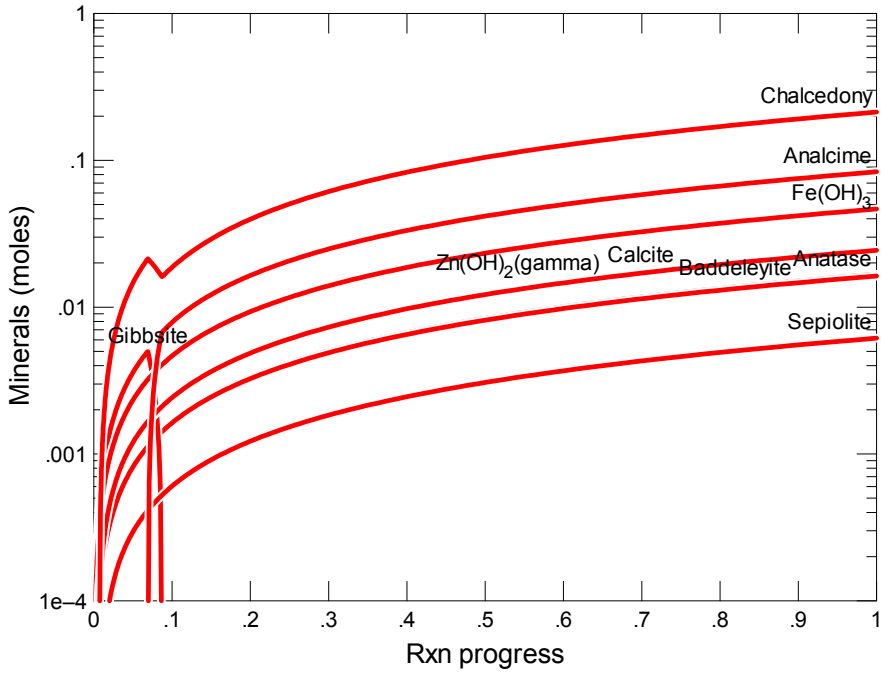


**Figure B.172**. Secondary Phases Calculated to Form as a Function of Reaction Progress (mol-glass/kg) Determined for Glass Sample LAWA88R1

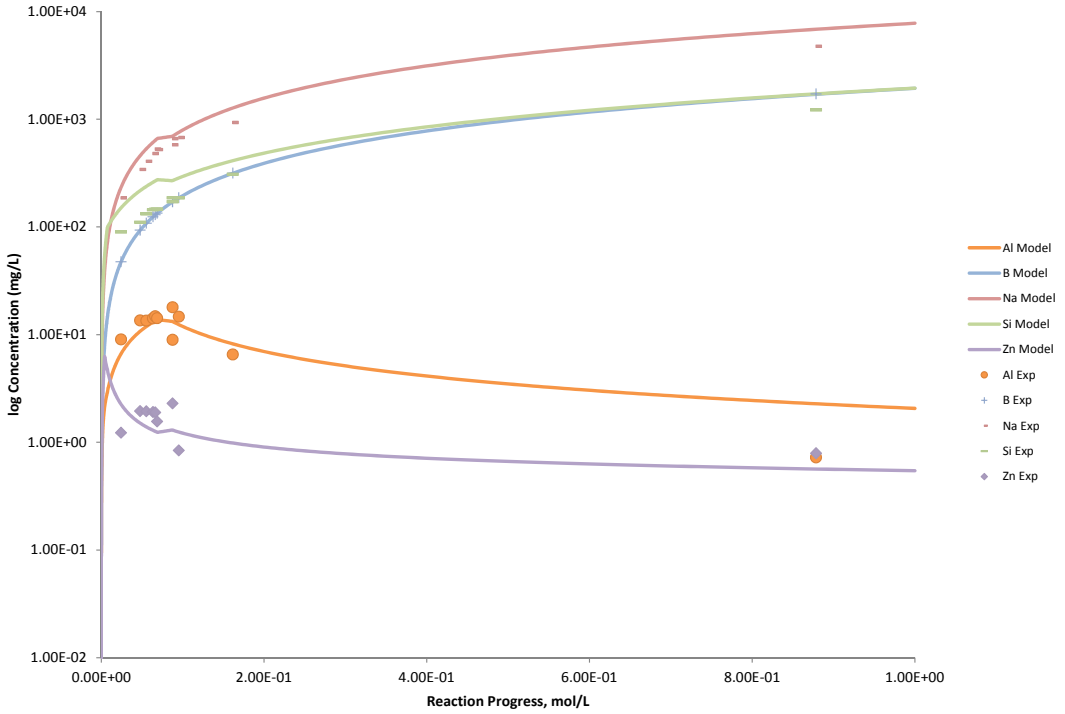


**Figure B.173**. Measured Solution Concentrations (mg/L) and Model Results for Al, B, Na, Si, and Zn, as a Function of Reaction Progress (mol-glass/kg) Determined for Glass Sample LAWA88R1

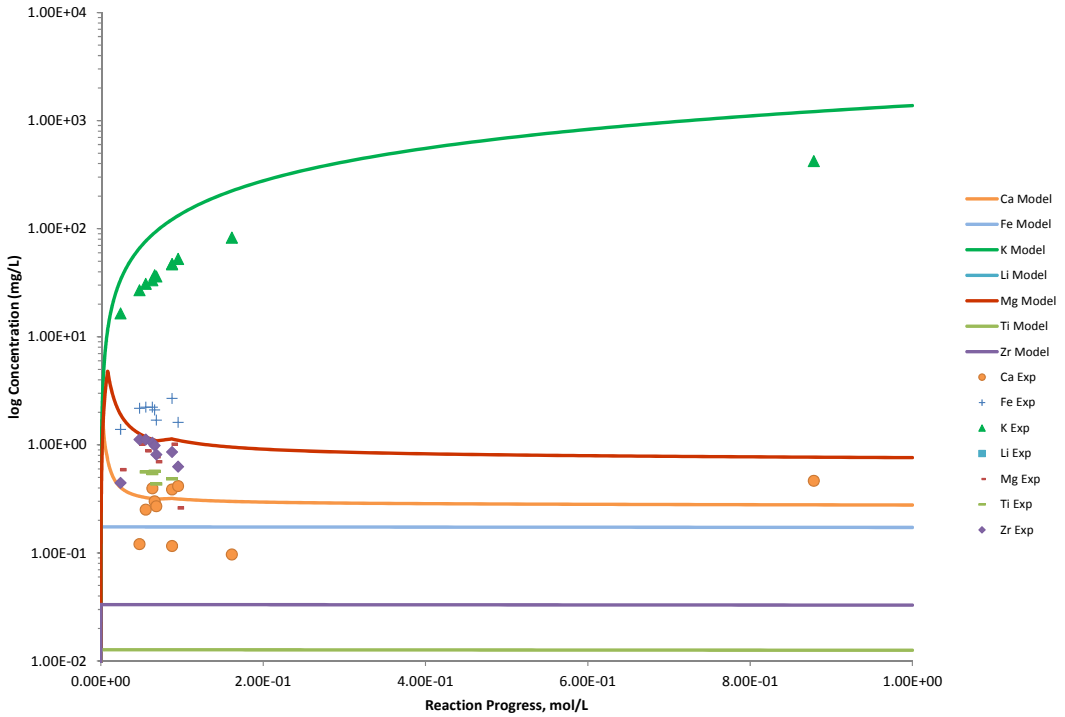


**Figure B.174**. Measured Solution Concentrations (mg/L) and Model Results for Ca, Fe, K, Li, Mg, Ti, and Zr, as a Function of Reaction Progress (mol-glass/kg) Determined for Glass Sample LAWA88R1

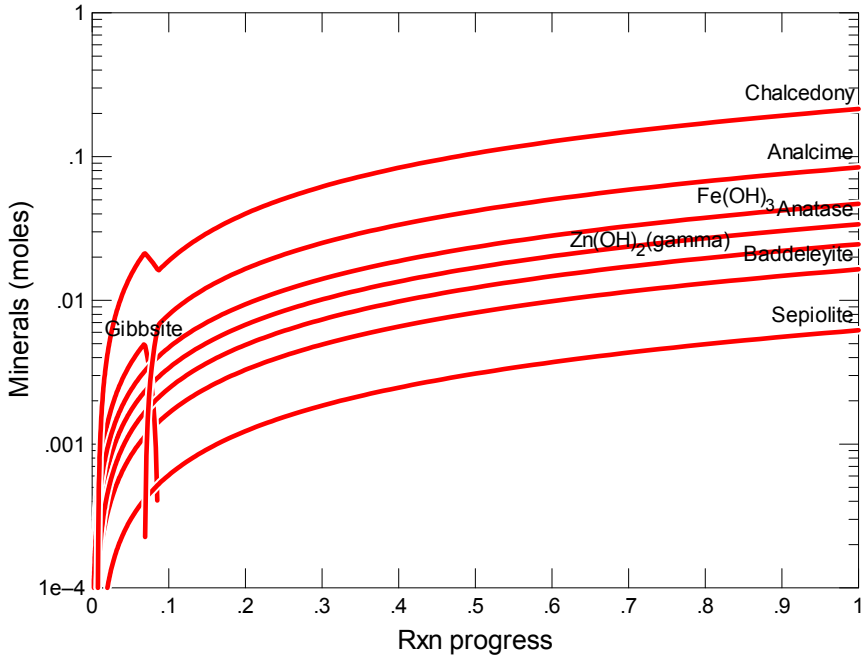


**Figure B.175**. Secondary Phases Calculated to Form as a Function of Reaction Progress (mol-glass/kg) Determined for Glass Sample LAWA89

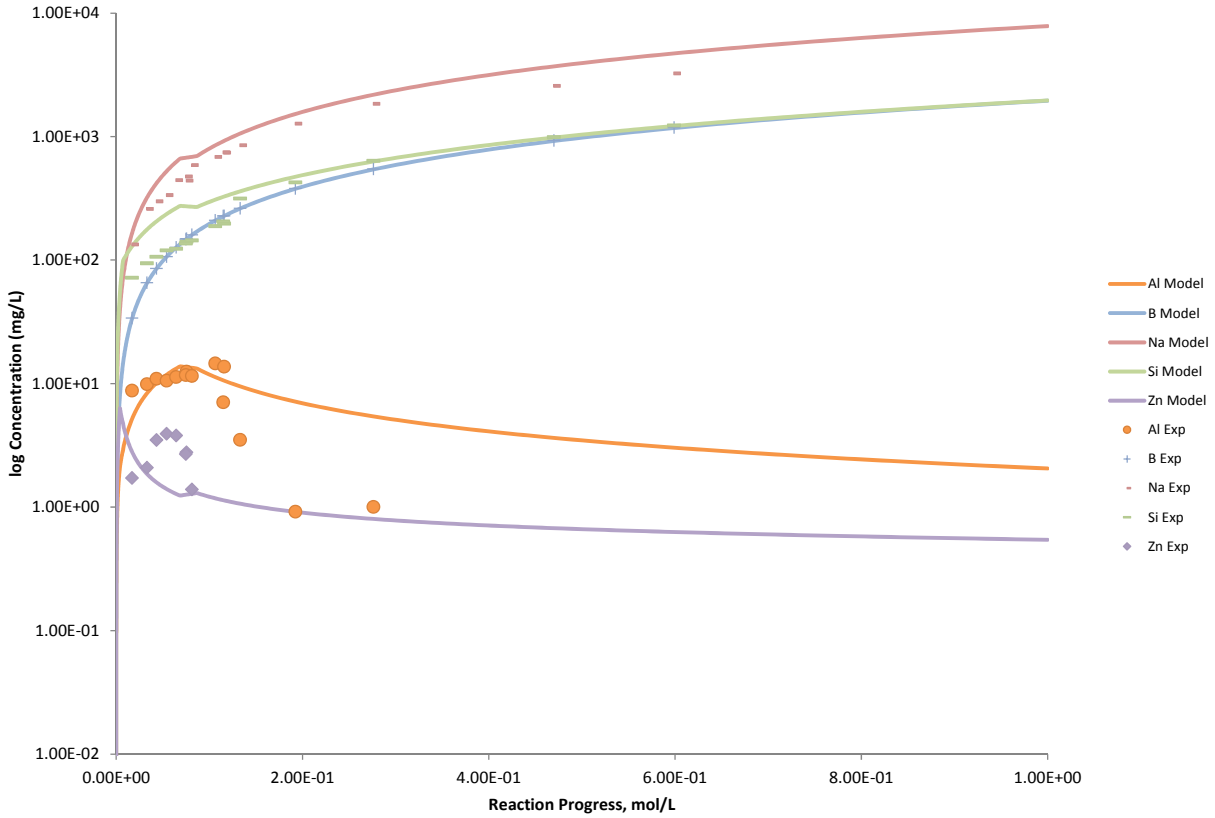


**Figure B.176**. Measured Solution Concentrations (mg/L) and Model Results for Al, B, Na, Si, and Zn, as a Function of Reaction Progress (mol-glass/kg) Determined for Glass Sample LAWA89

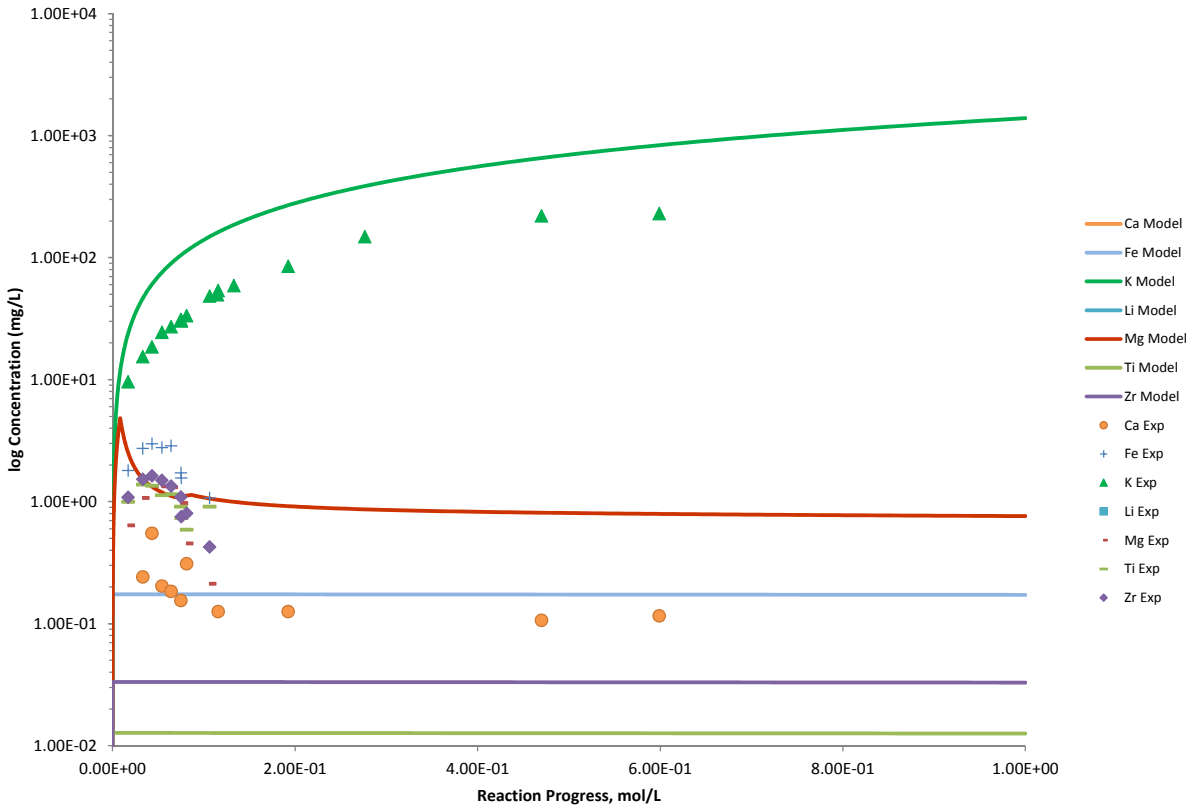


**Figure B.177**. Measured Solution Concentrations (mg/L) and Model Results for Ca, Fe, K, Li, Mg, Ti, and Zr, as a Function of Reaction Progress (mol-glass/kg) Determined for Glass Sample LAWA89

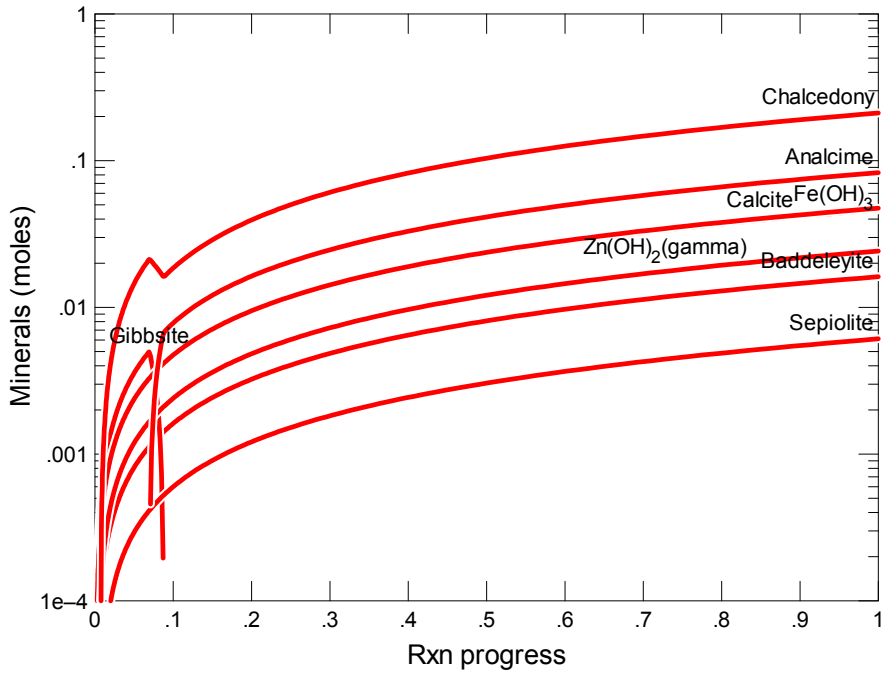


**Figure B.178**. Secondary Phases Calculated to Form as a Function of Reaction Progress (mol-glass/kg) Determined for Glass Sample LAWA90

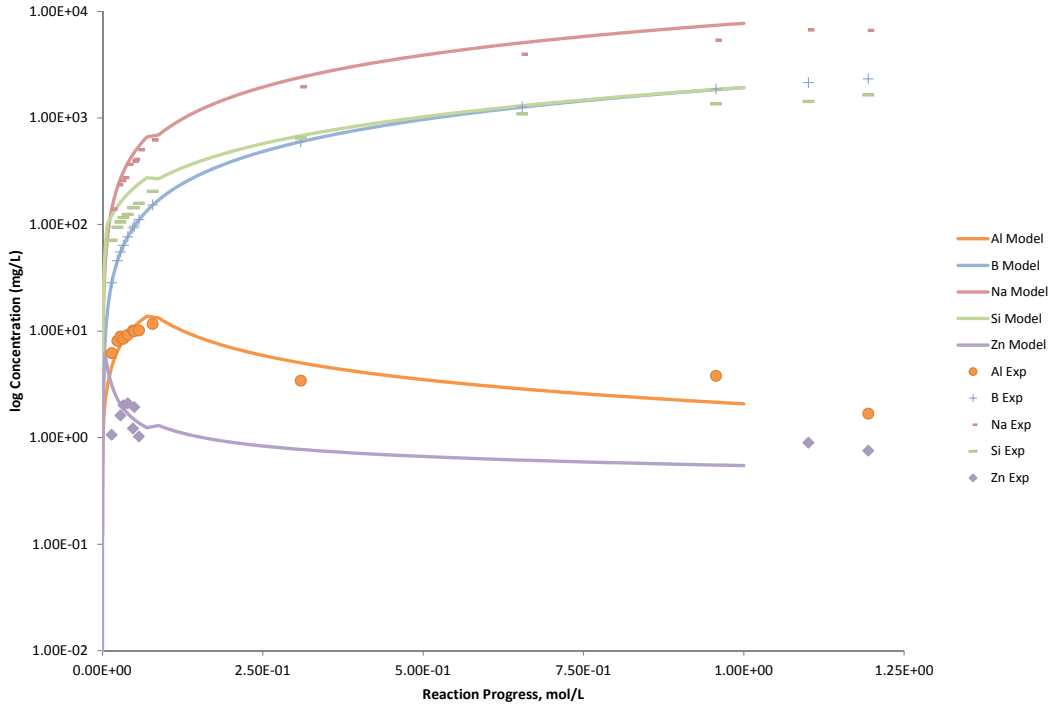


**Figure B.179**. Measured Solution Concentrations (mg/L) and Model Results for Al, B, Na, Si, and Zn, as a Function of Reaction Progress (mol-glass/kg) Determined for Glass Sample LAWA90

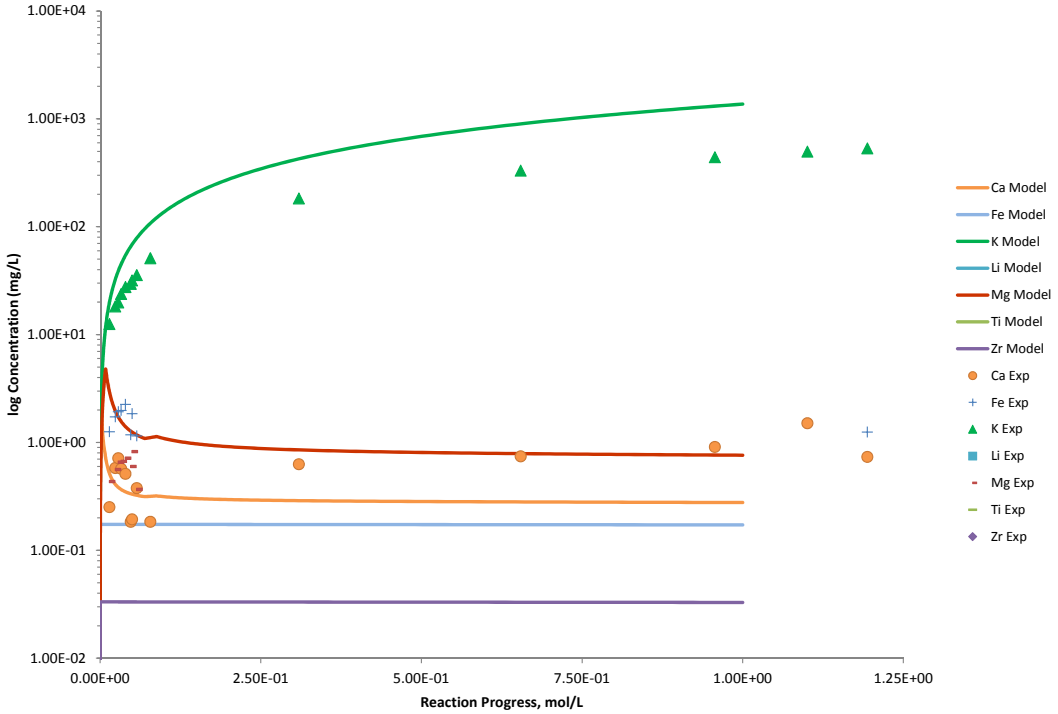


**Figure B.180**. Measured Solution Concentrations (mg/L) and Model Results for Ca, Fe, K, Li, Mg, Ti, and Zr, as a Function of Reaction Progress (mol-glass/kg) Determined for Glass Sample LAWA90

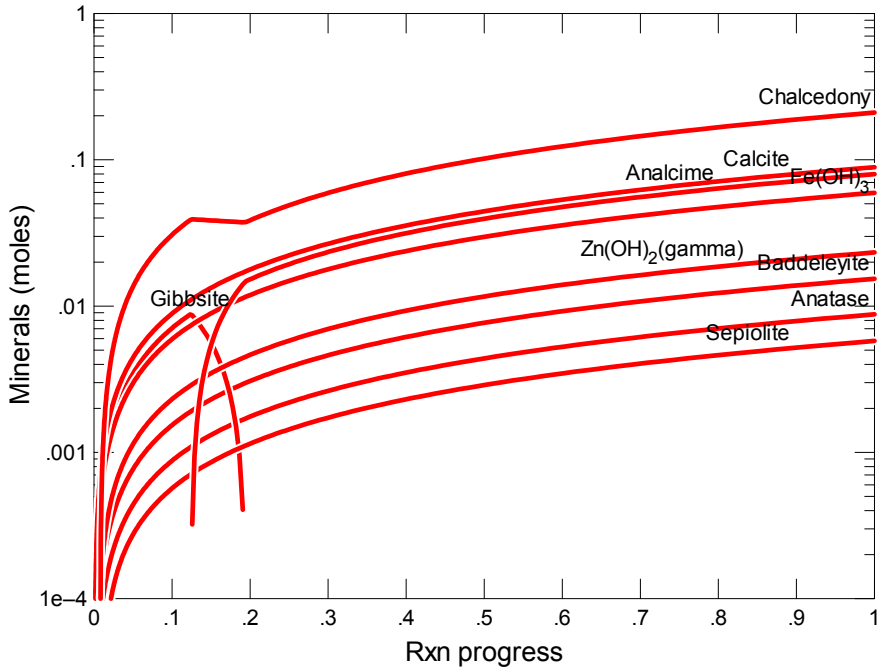


**Figure B.181**. Secondary Phases Calculated to Form as a Function of Reaction Progress (mol-glass/kg) Determined for Glass Sample LAWA93

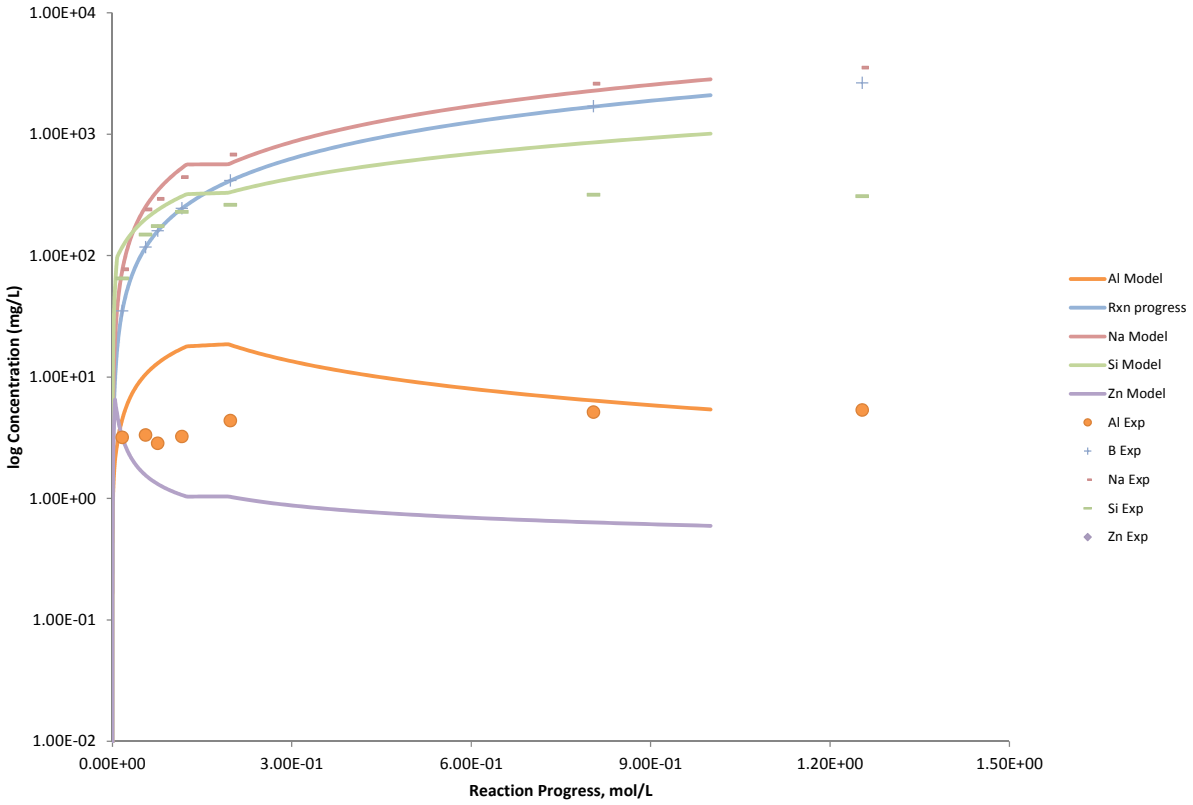


**Figure B.182**. Measured Solution Concentrations (mg/L) and Model Results for Al, B, Na, Si, and Zn, as a Function of Reaction Progress (mol-glass/kg) Determined for Glass Sample LAWA93

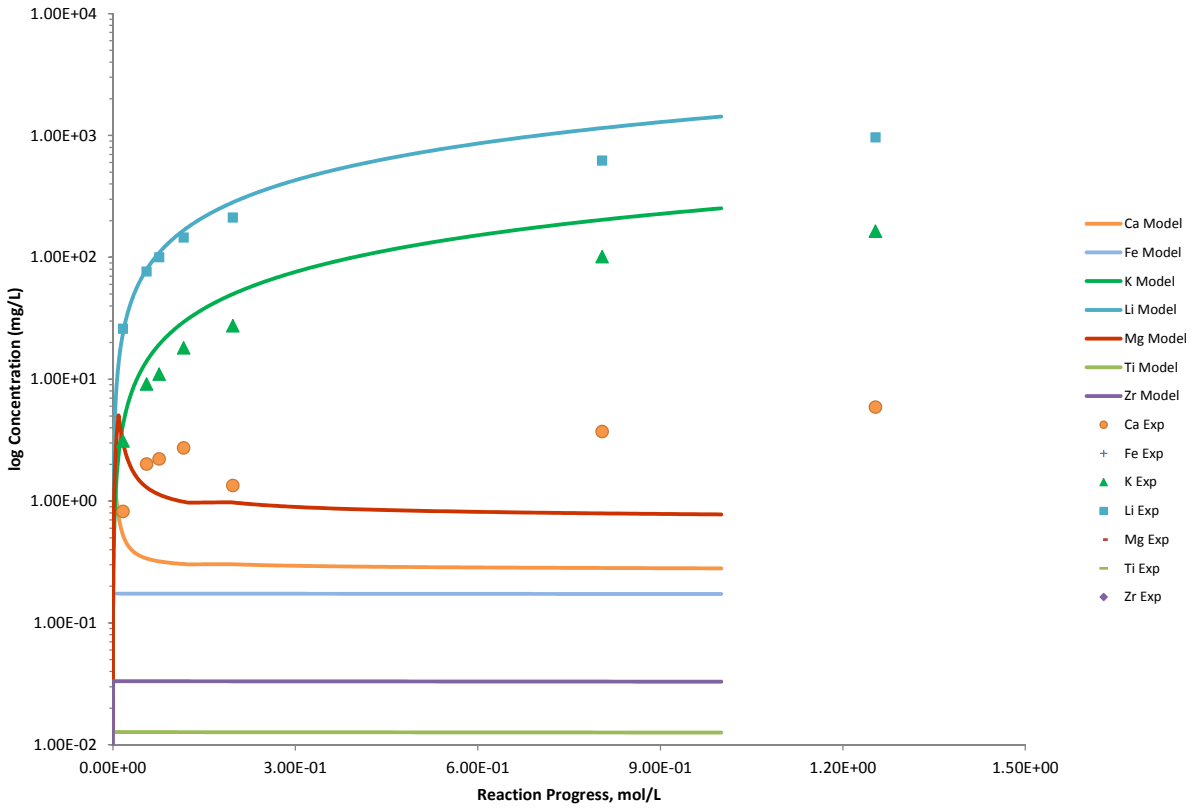


**Figure B.183**. Measured Solution Concentrations (mg/L) and Model Results for Ca, Fe, K, Li, Mg, Ti, and Zr, as a Function of Reaction Progress (mol-glass/kg) Determined for Glass Sample LAWA93

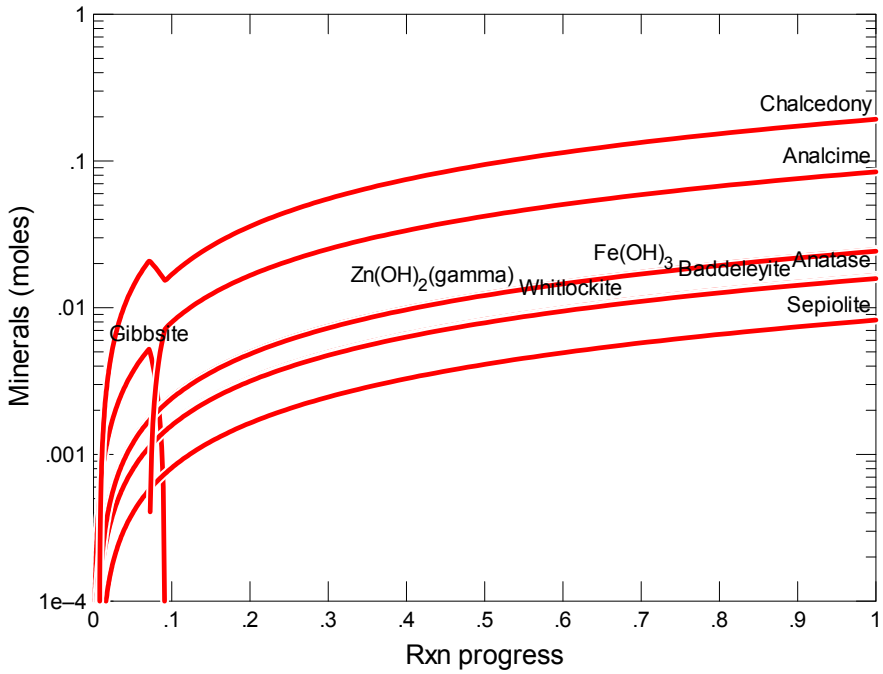


**Figure B.184**. Secondary Phases Calculated to Form as a Function of Reaction Progress (mol-glass/kg) Determined for Glass Sample LAWA96

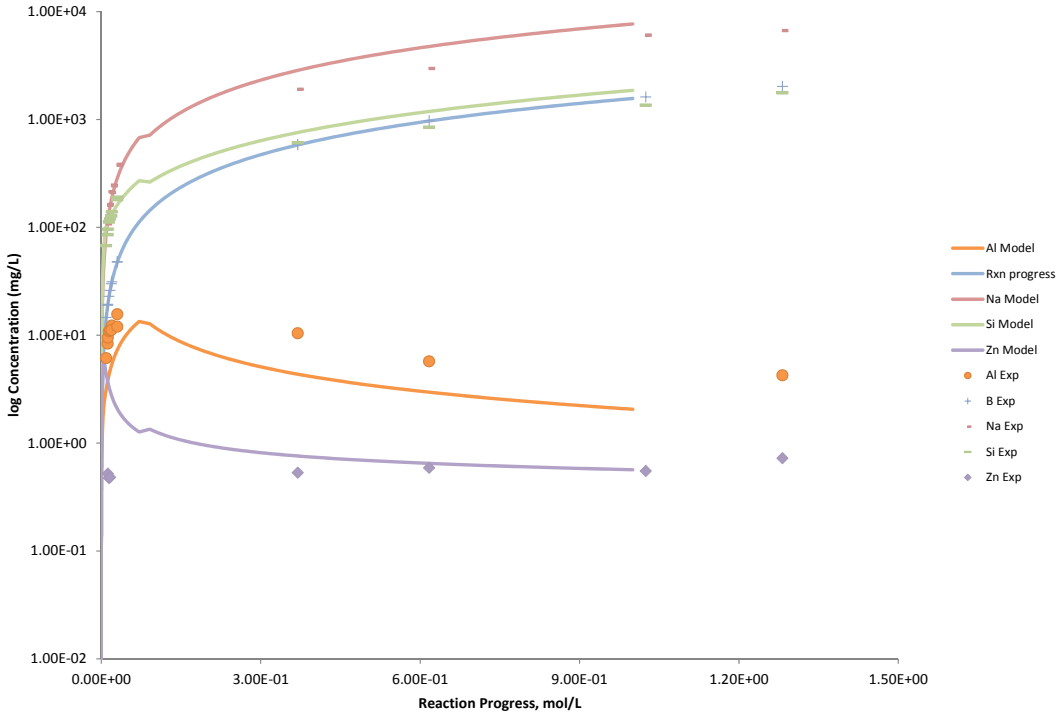


**Figure B.185**. Measured Solution Concentrations (mg/L) and Model Results for Al, B, Na, Si, and Zn, as a Function of Reaction Progress (mol-glass/kg) Determined for Glass Sample LAWA96

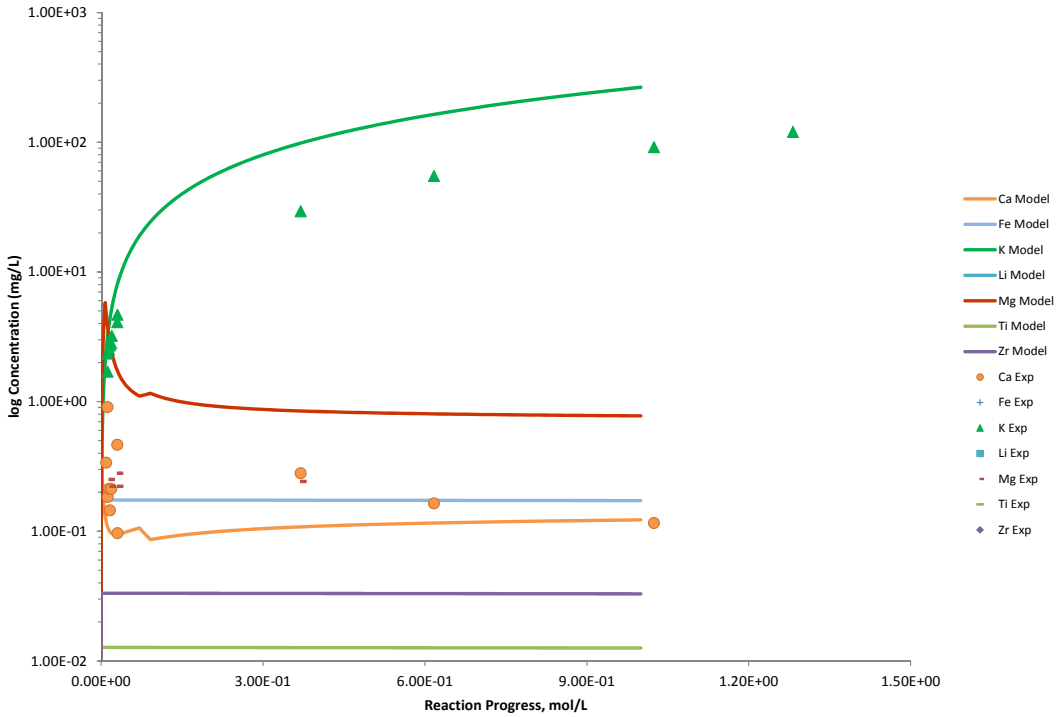


**Figure B.186**. Measured Solution Concentrations (mg/L) and Model Results for Ca, Fe, K, Li, Mg, Ti, and Zr, as a Function of Reaction Progress (mol-glass/kg) Determined for Glass Sample LAWA96

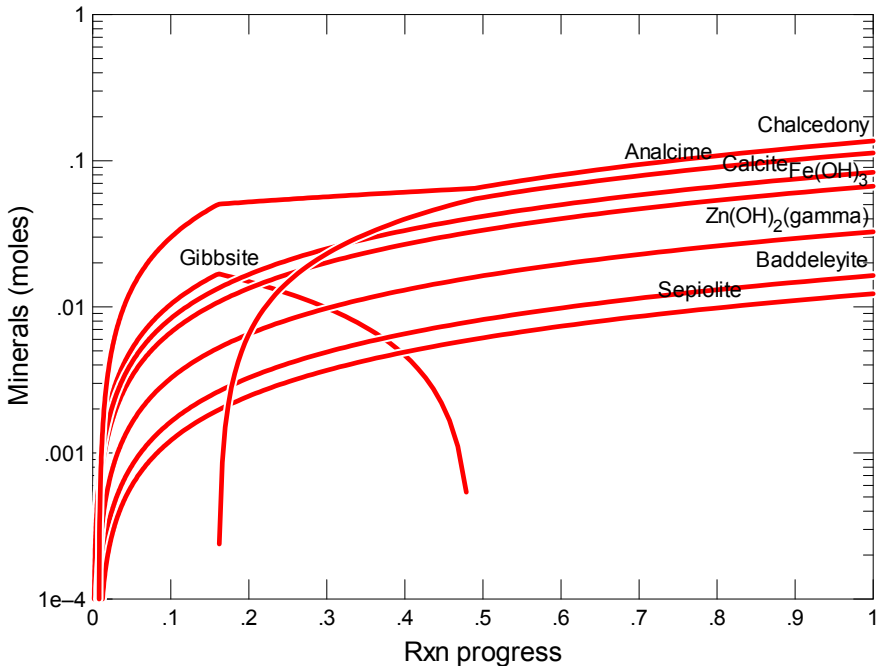


**Figure B.187**. Secondary Phases Calculated to Form as a Function of Reaction Progress (mol-glass/kg) Determined for Glass Sample LAWB30

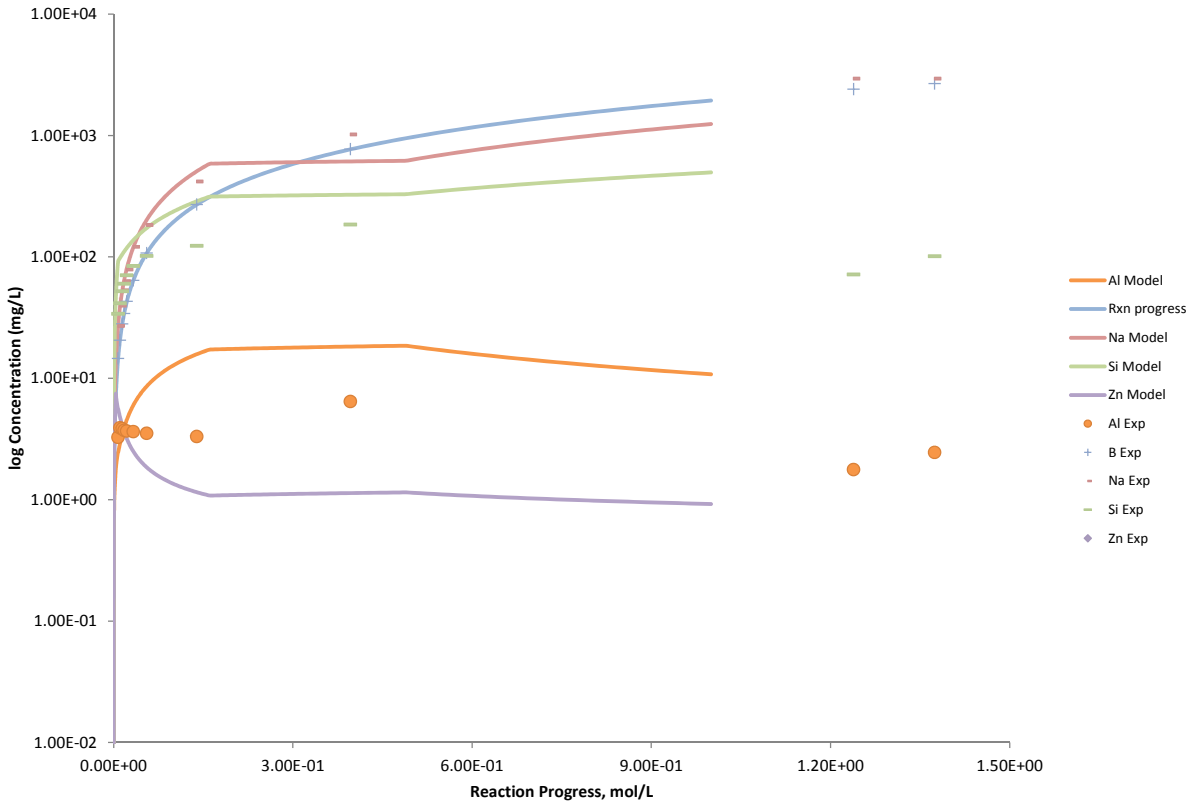


**Figure B.188**. Measured Solution Concentrations (mg/L) and Model Results for Al, B, Na, Si, and Zn, as a Function of Reaction Progress (mol-glass/kg) Determined for Glass Sample LAWB30

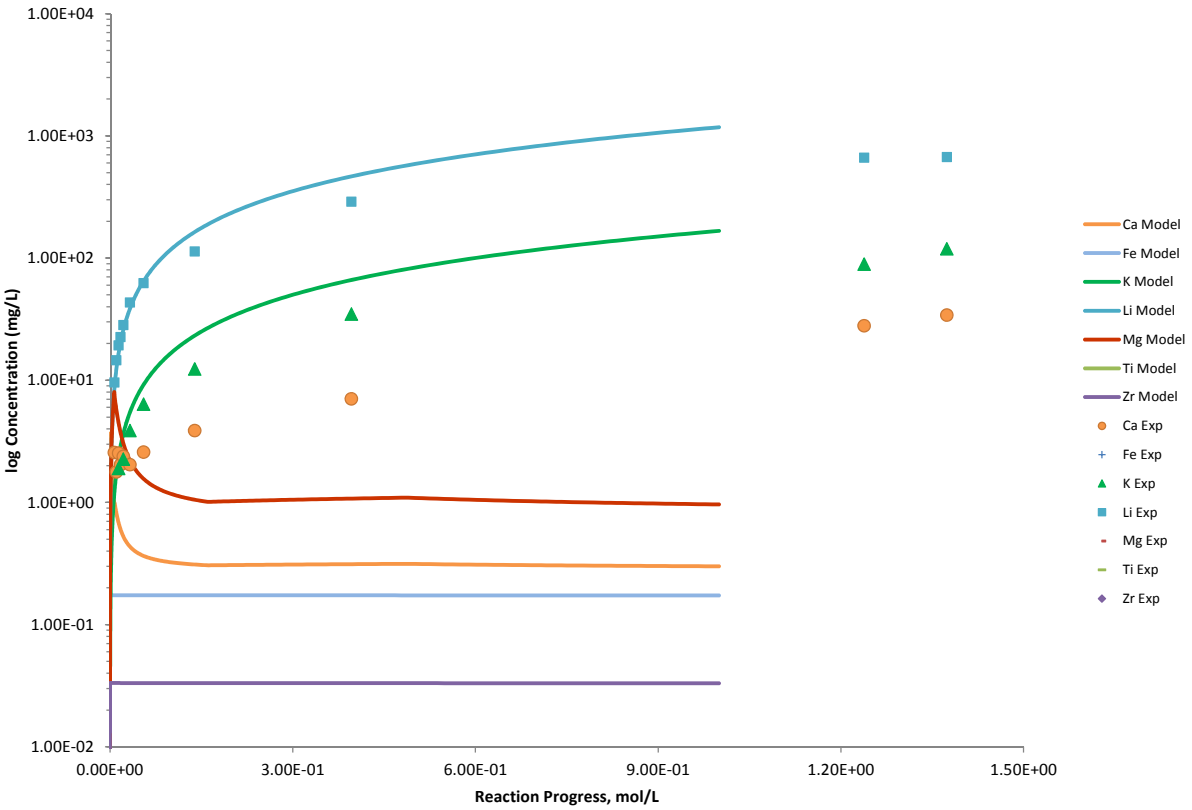


**Figure B.189**. Measured Solution Concentrations (mg/L) and Model Results for Ca, Fe, K, Li, Mg, Ti, and Zr, as a Function of Reaction Progress (mol-glass/kg) Determined for Glass Sample LAWB30

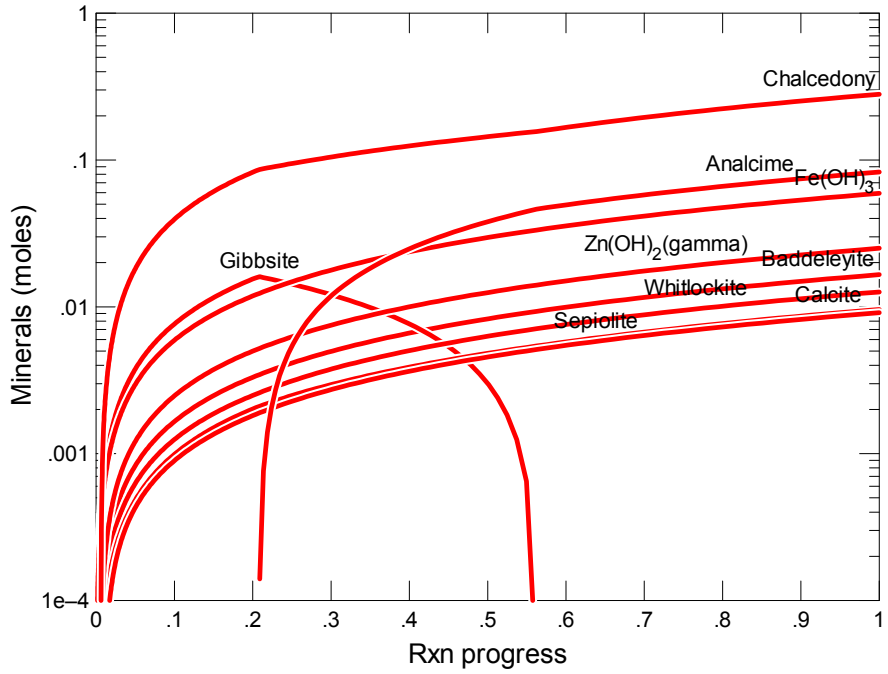


**Figure B.190**. Secondary Phases Calculated to Form as a Function of Reaction Progress (mol-glass/kg) Determined for Glass Sample LAWB31

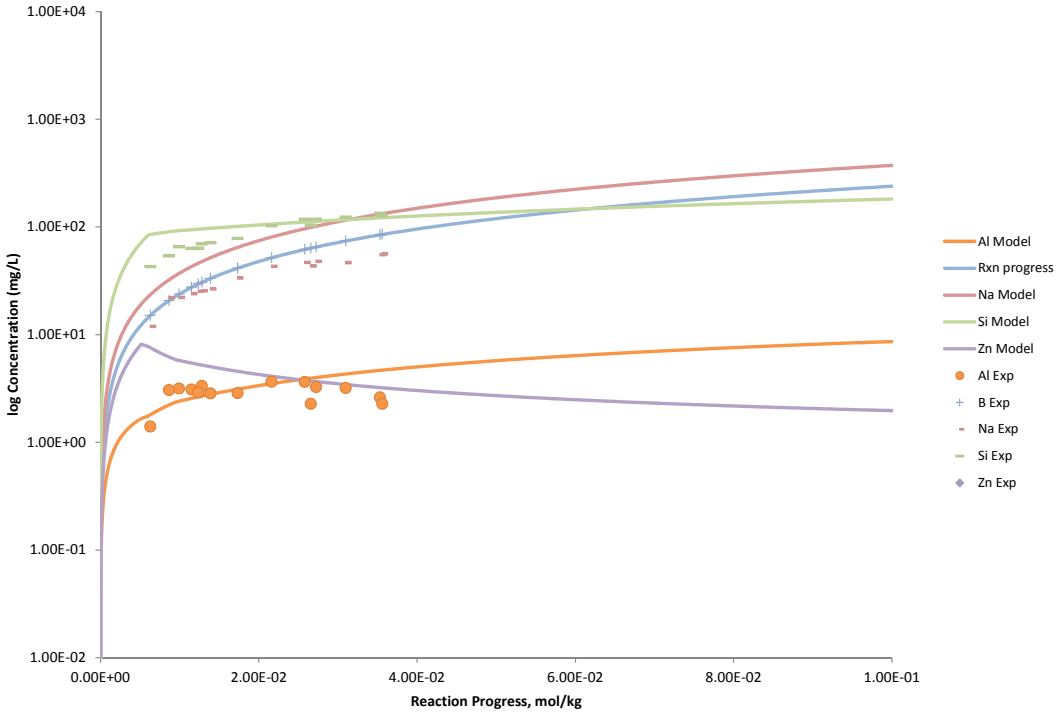


**Figure B.191**. Measured Solution Concentrations (mg/L) and Model Results for Al, B, Na, Si, and Zn, as a Function of Reaction Progress (mol-glass/kg) Determined for Glass Sample LAWB31

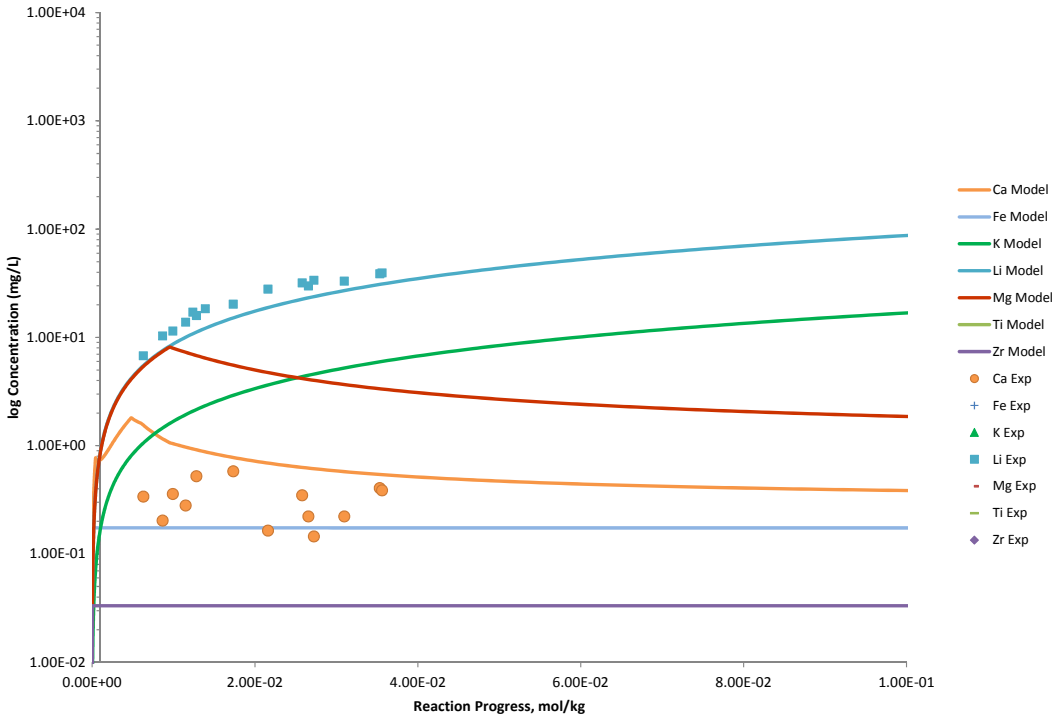


**Figure B.192**. Measured Solution Concentrations (mg/L) and Model Results for Ca, Fe, K, Li, Mg, Ti, and Zr, as a Function of Reaction Progress (mol-glass/kg) Determined for Glass Sample LAWB31

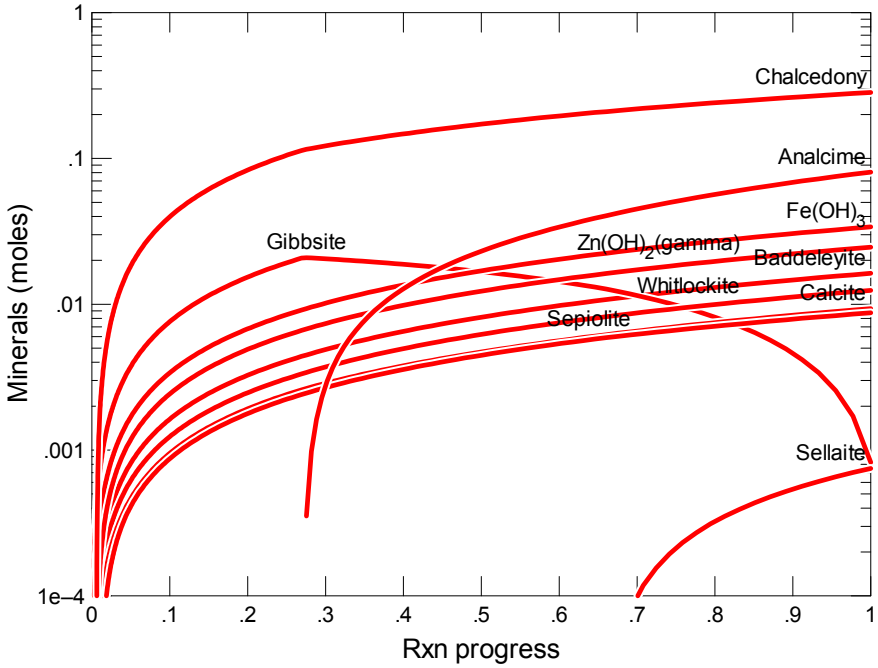


**Figure B.193**. Secondary Phases Calculated to Form as a Function of Reaction Progress (mol-glass/kg) Determined for Glass Sample LAWB32

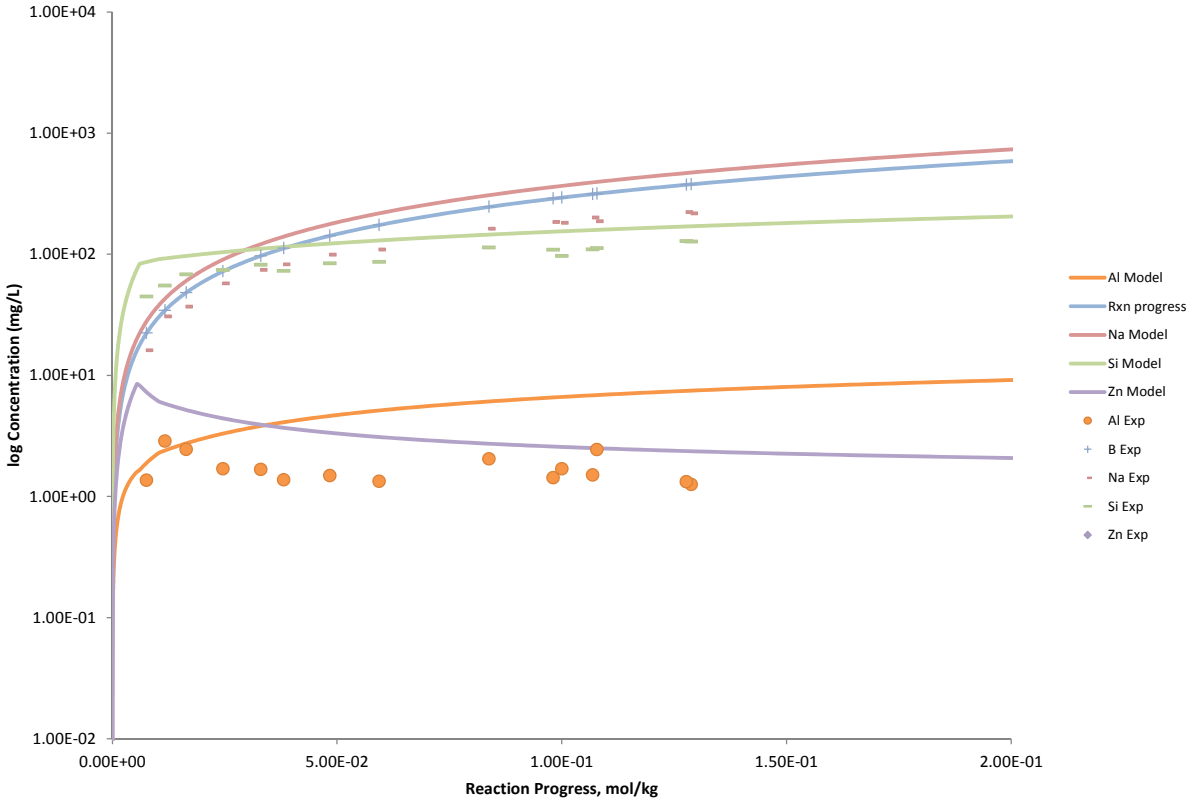


**Figure B.194**. Measured Solution Concentrations (mg/L) and Model Results for Al, B, Na, Si, and Zn, as a Function of Reaction Progress (mol-glass/kg) Determined for Glass Sample LAWB32

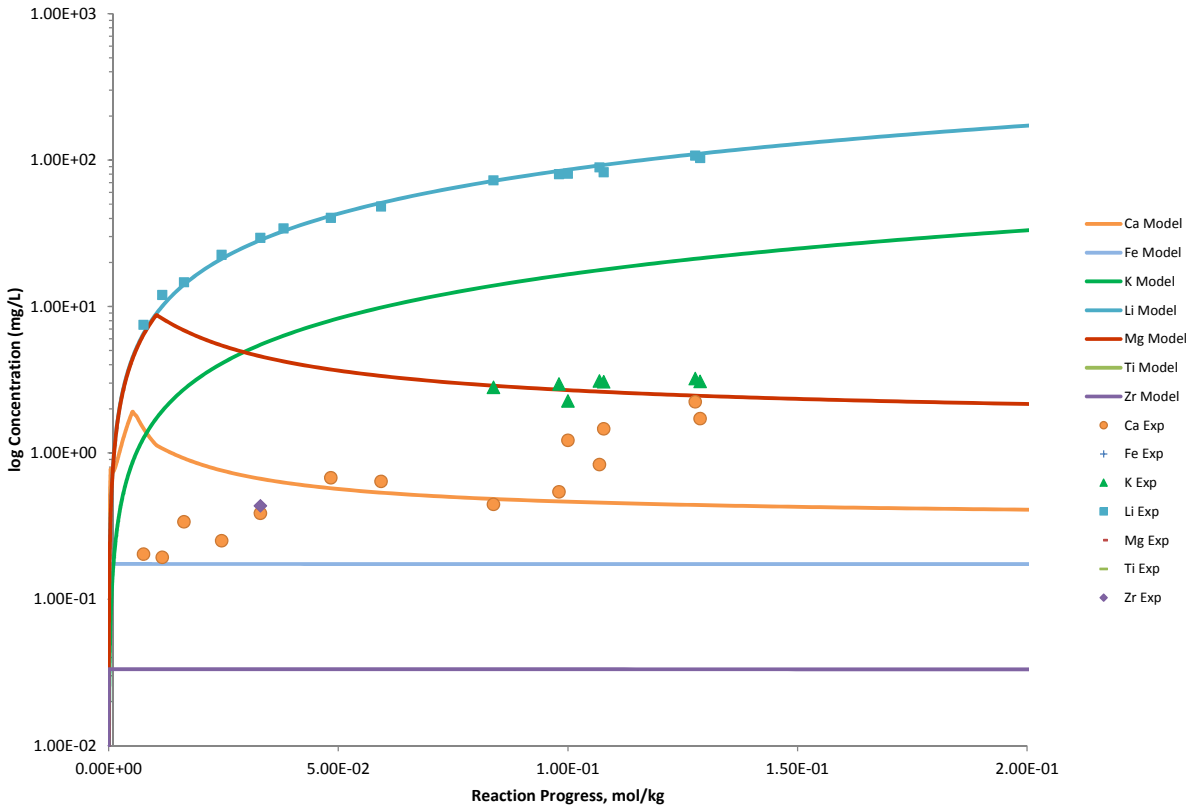


**Figure B.195**. Measured Solution Concentrations (mg/L) and Model Results for Ca, Fe, K, Li, Mg, Ti, and Zr, as a Function of Reaction Progress (mol-glass/kg) Determined for Glass Sample LAWB32

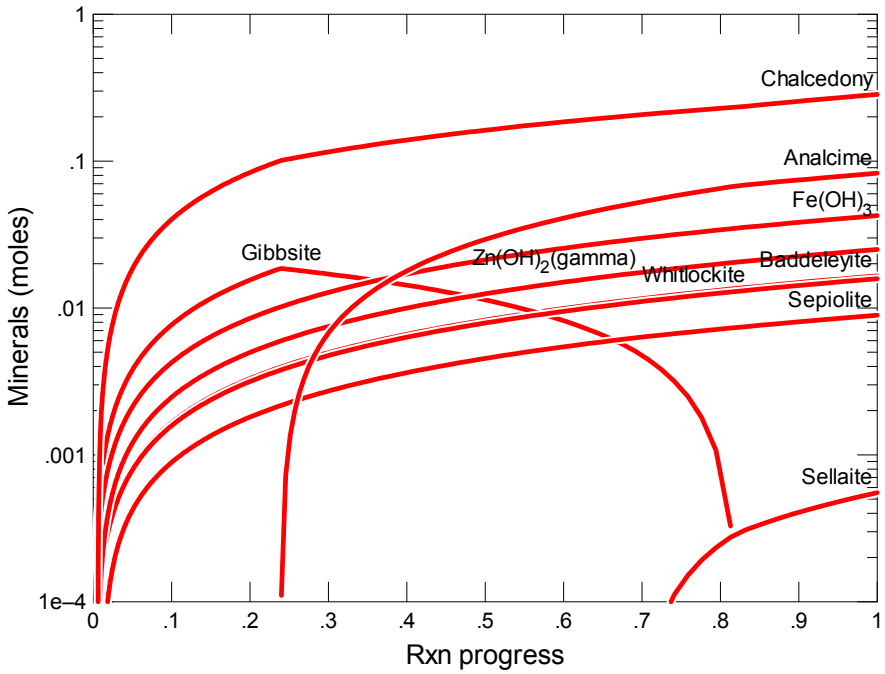


**Figure B.196**. Secondary Phases Calculated to Form as a Function of Reaction Progress (mol-glass/kg) Determined for Glass Sample LAWB33

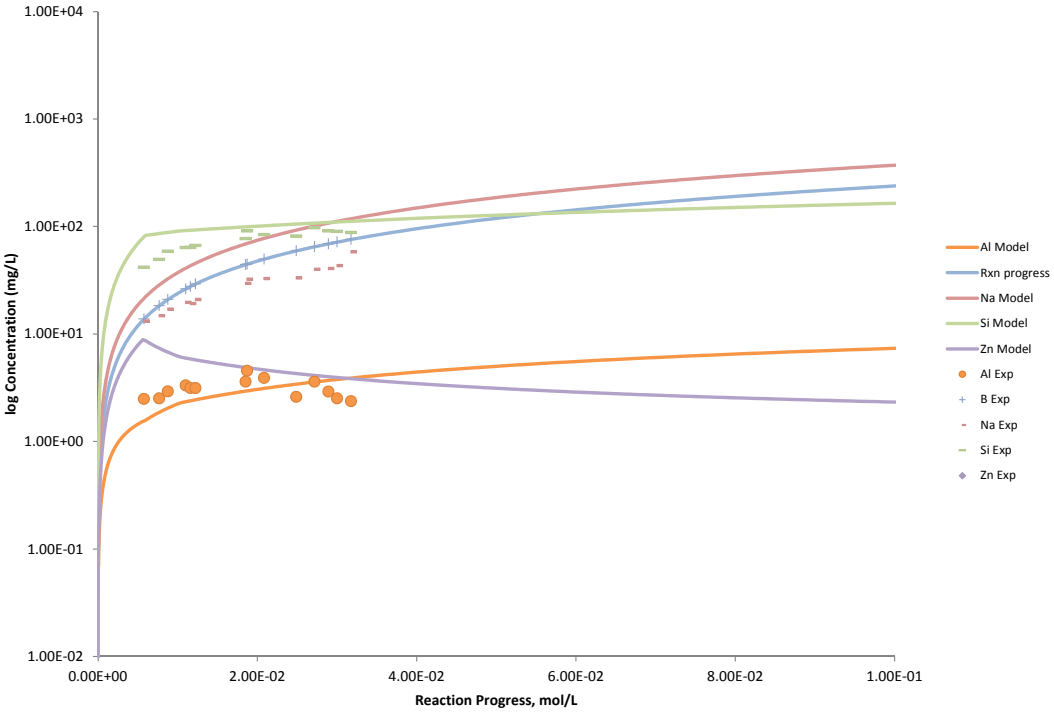


**Figure B.197**. Measured Solution Concentrations (mg/L) and Model Results for Al, B, Na, Si, and Zn, as a Function of Reaction Progress (mol-glass/kg) Determined for Glass Sample LAWB33

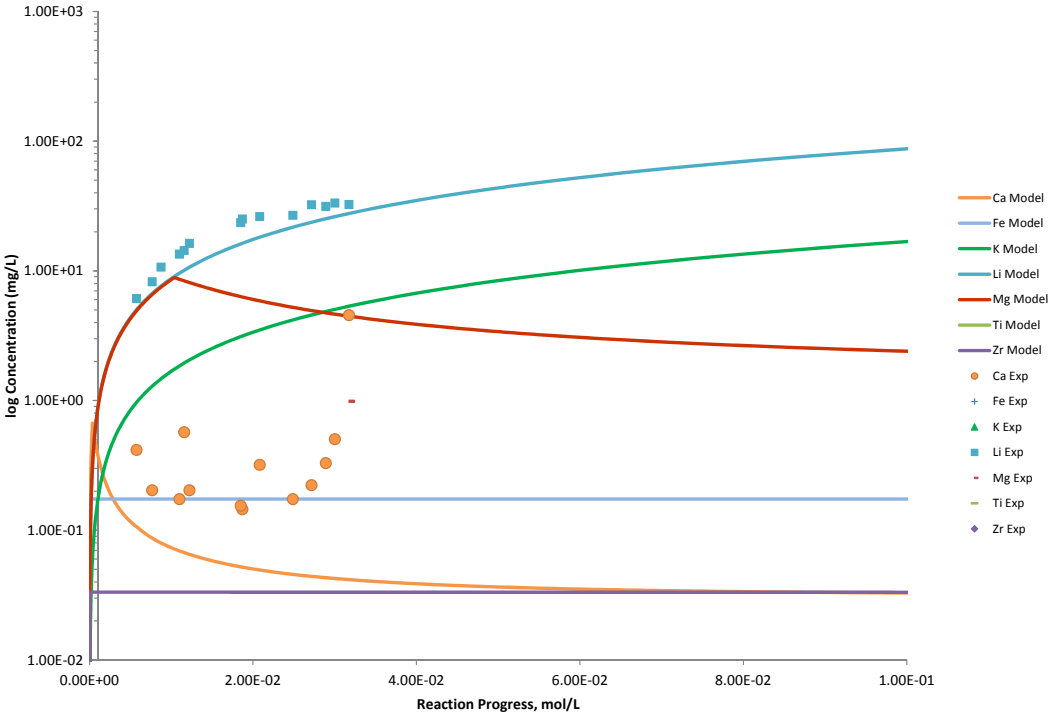


**Figure B.198**. Measured Solution Concentrations (mg/L) and Model Results for Ca, Fe, K, Li, Mg, Ti, and Zr, as a Function of Reaction Progress (mol-glass/kg) Determined for Glass Sample LAWB33

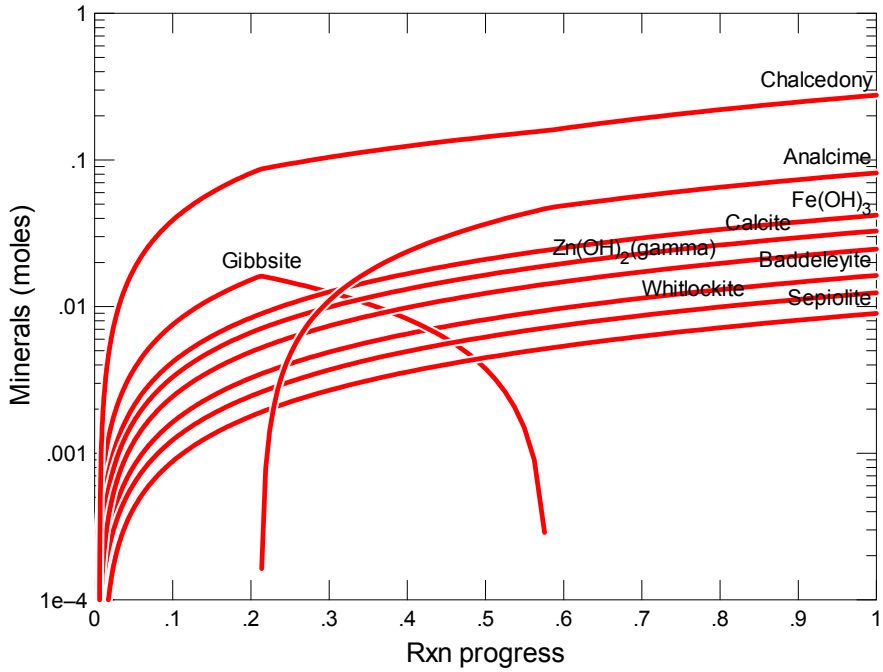


**Figure B.199**. Secondary Phases Calculated to Form as a Function of Reaction Progress (mol-glass/kg) Determined for Glass Sample LAWB34

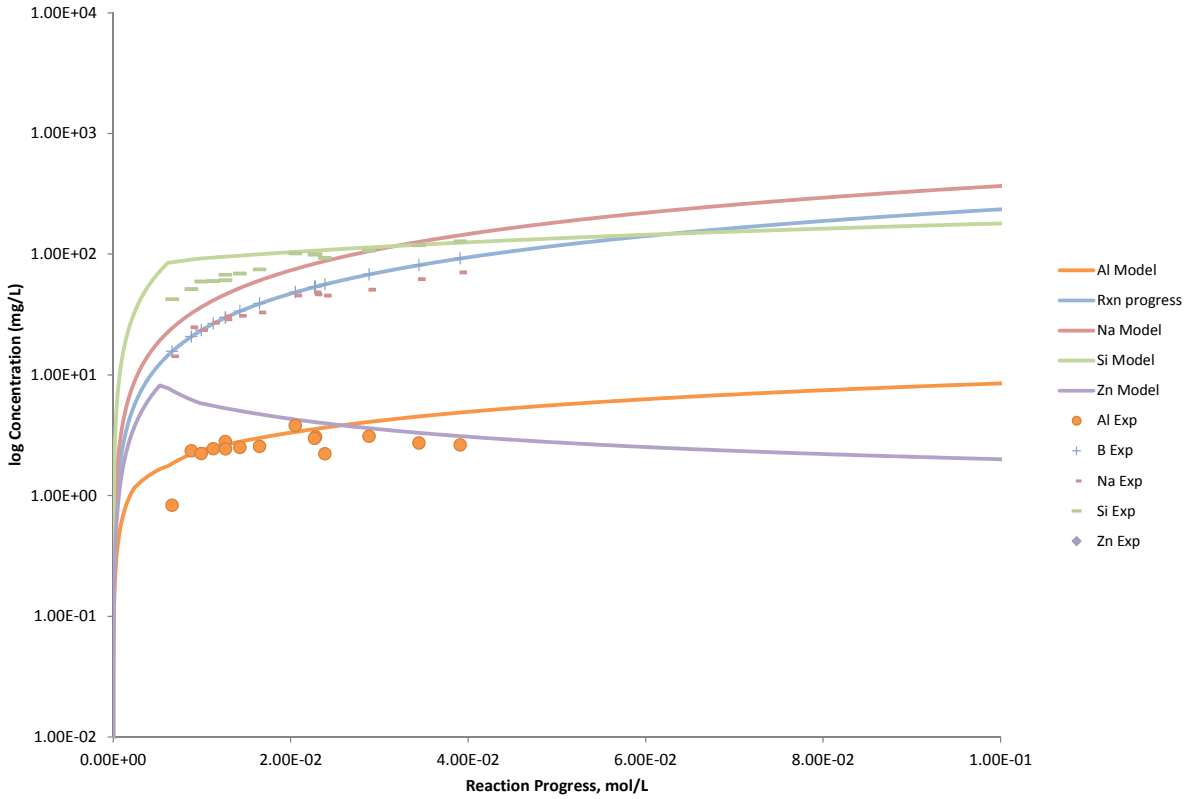


**Figure B.200**. Measured Solution Concentrations (mg/L) and Model Results for Al, B, Na, Si, and Zn, as a Function of Reaction Progress (mol-glass/kg) Determined for Glass Sample LAWB34

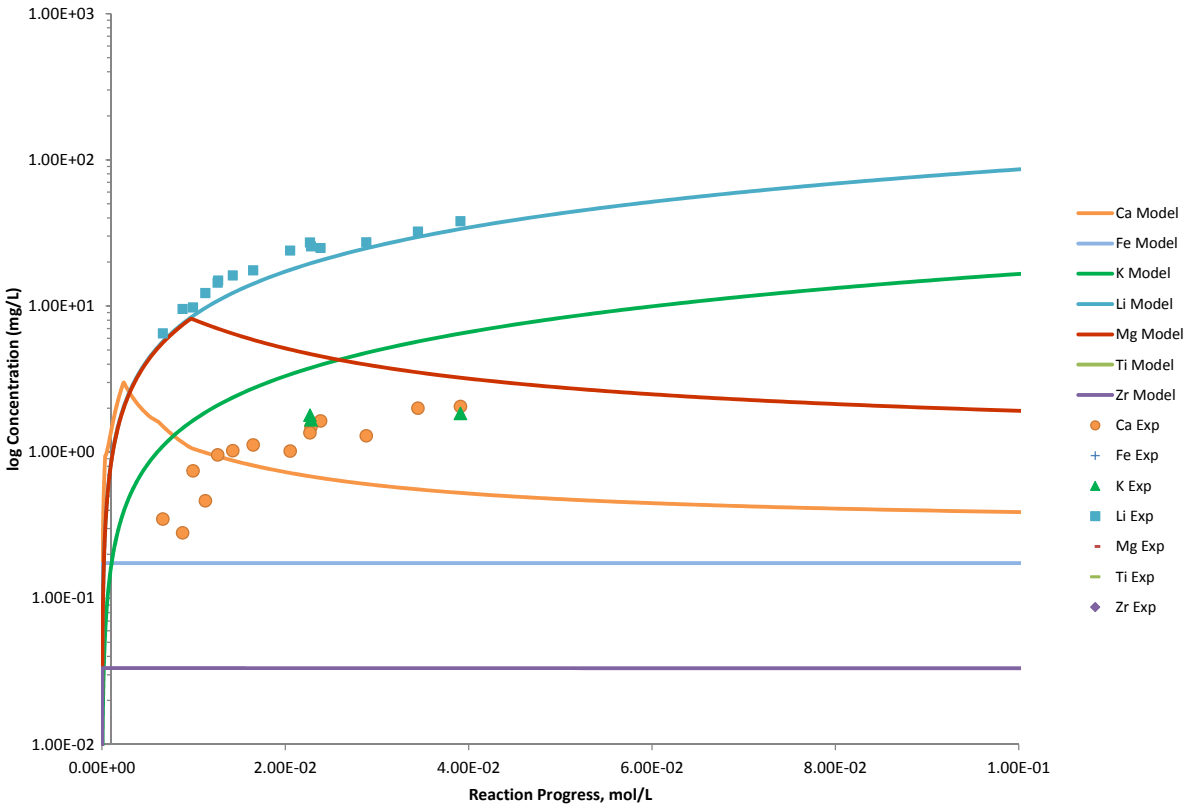


**Figure B.201**. Measured Solution Concentrations (mg/L) and Model Results for Ca, Fe, K, Li, Mg, Ti, and Zr, as a Function of Reaction Progress (mol-glass/kg) Determined for Glass Sample LAWB34

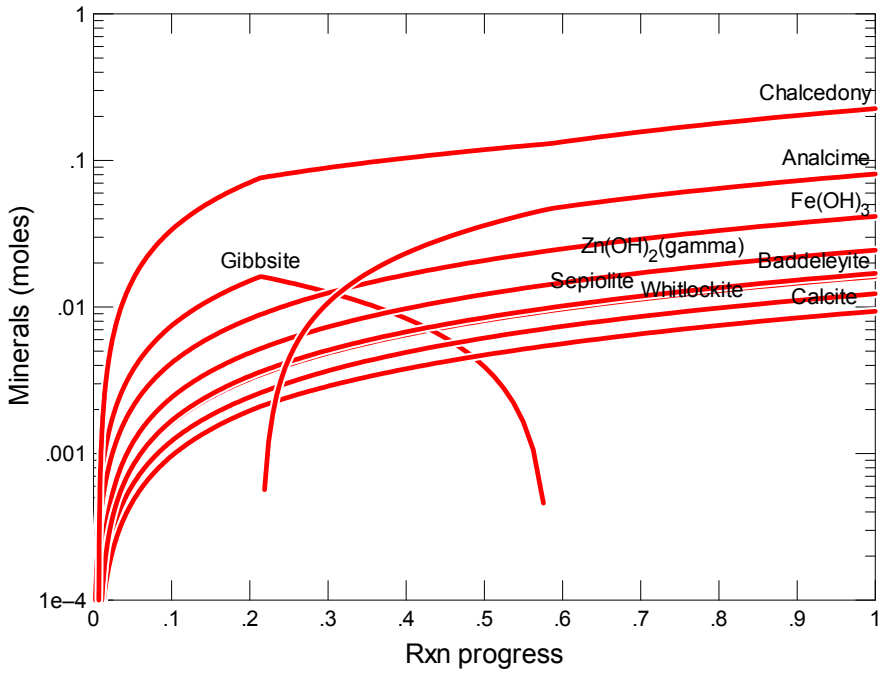


**Figure B.202**. Secondary Phases Calculated to Form as a Function of Reaction Progress (mol-glass/kg) Determined for Glass Sample LAWB35

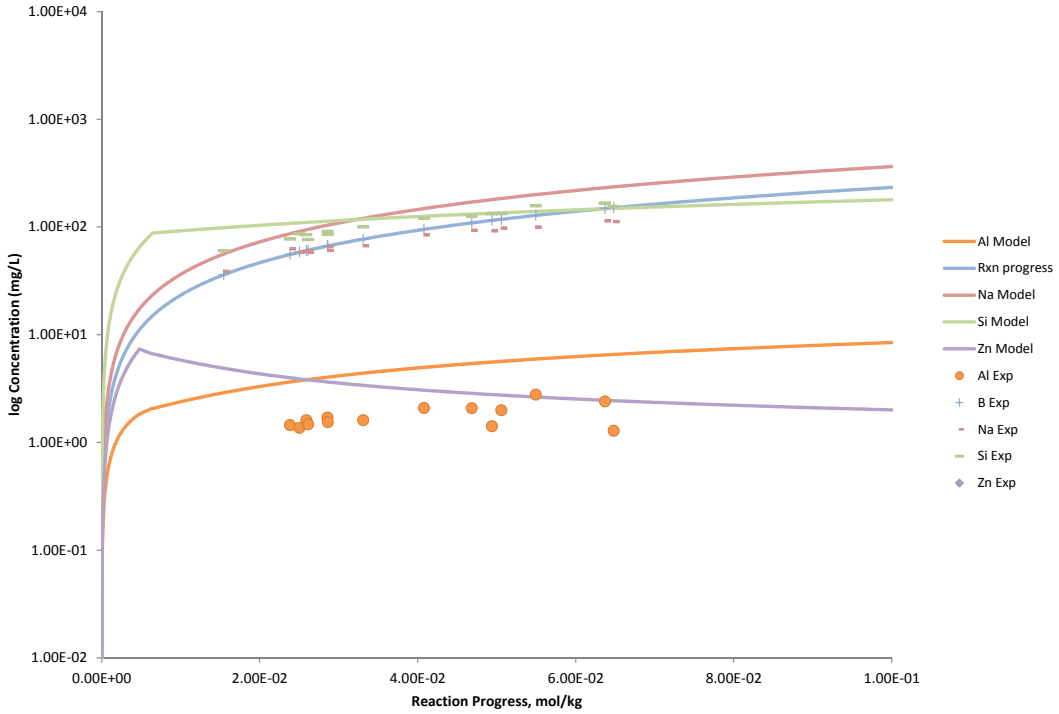


**Figure B.203**. Measured Solution Concentrations (mg/L) and Model Results for Al, B, Na, Si, and Zn, as a Function of Reaction Progress (mol-glass/kg) Determined for Glass Sample LAWB35

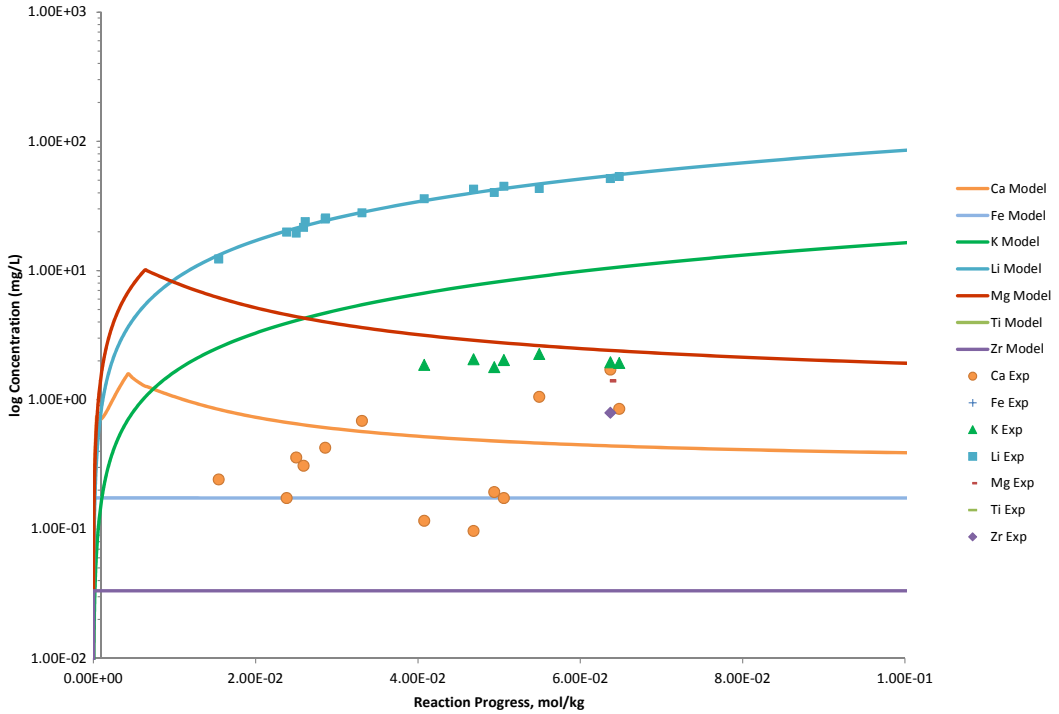


**Figure B.204**. Measured Solution Concentrations (mg/L) and Model Results for Ca, Fe, K, Li, Mg, Ti, and Zr, as a Function of Reaction Progress (mol-glass/kg) Determined for Glass Sample LAWB35

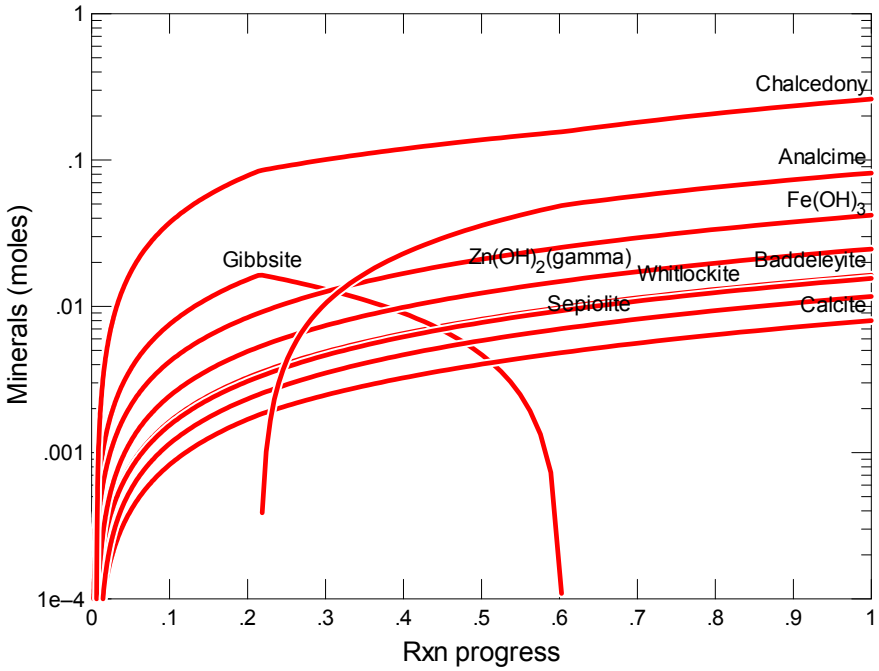


**Figure B.205**. Secondary Phases Calculated to Form as a Function of Reaction Progress (mol-glass/kg) Determined for Glass Sample LAWB37

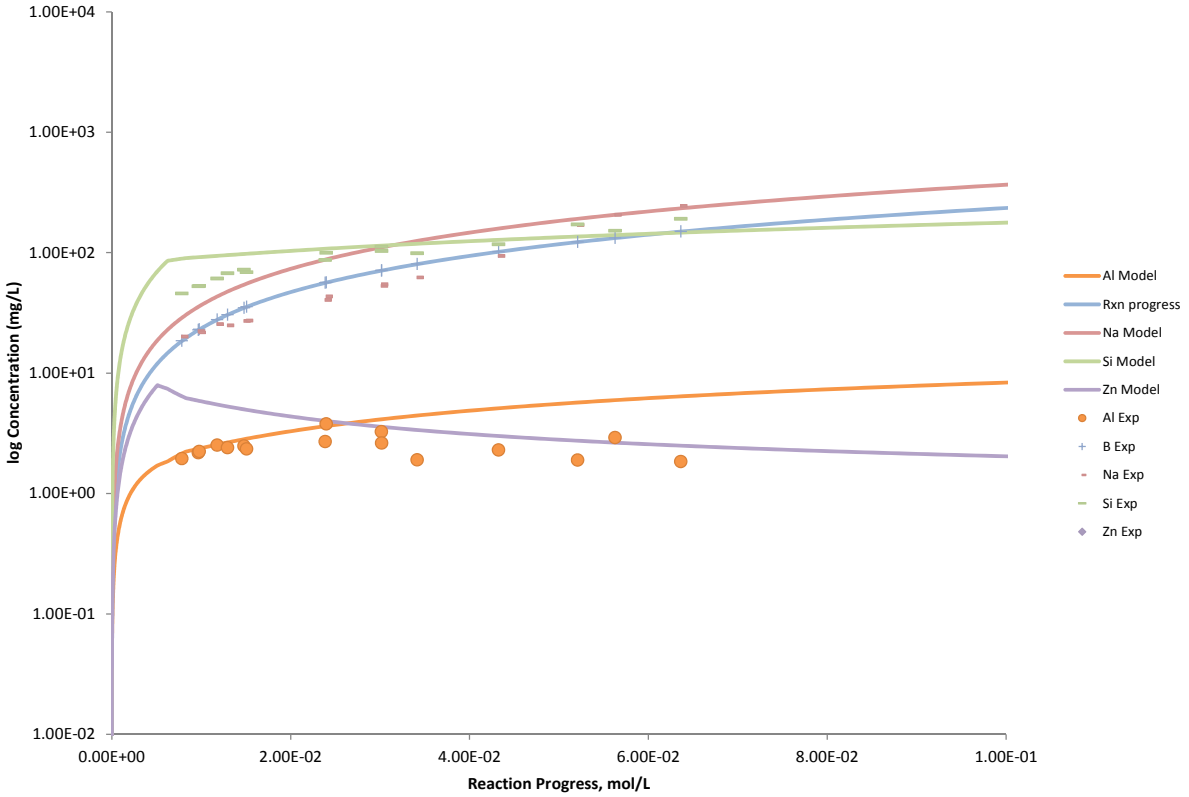


**Figure B.206**. Measured Solution Concentrations (mg/L) and Model Results for Al, B, Na, Si, and Zn, as a Function of Reaction Progress (mol-glass/kg) Determined for Glass Sample LAWB37

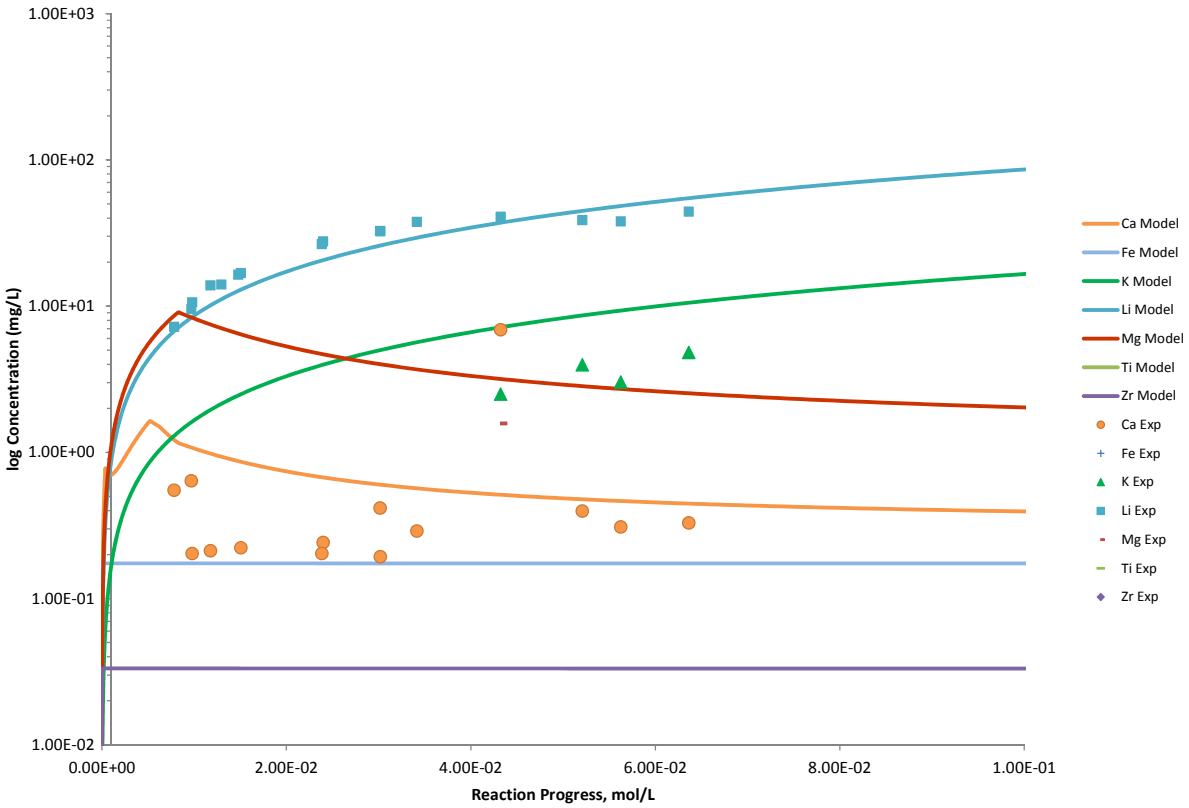


**Figure B.207**. Measured Solution Concentrations (mg/L) and Model Results for Ca, Fe, K, Li, Mg, Ti, and Zr, as a Function of Reaction Progress (mol-glass/kg) Determined for Glass Sample LAWB37

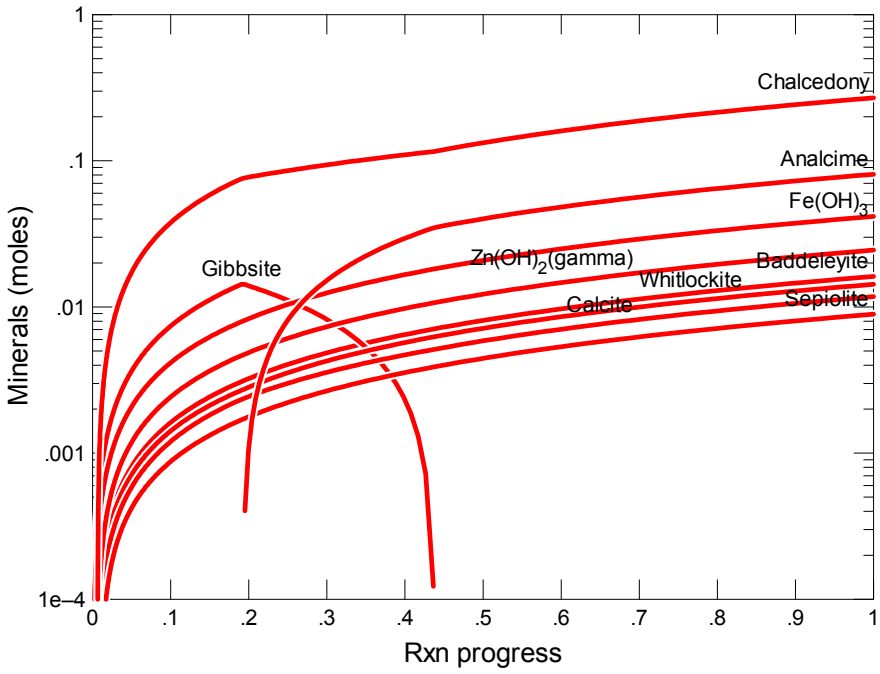


**Figure B.208**. Secondary Phases Calculated to Form as a Function of Reaction Progress (mol-glass/kg) Determined for Glass Sample LAWB38

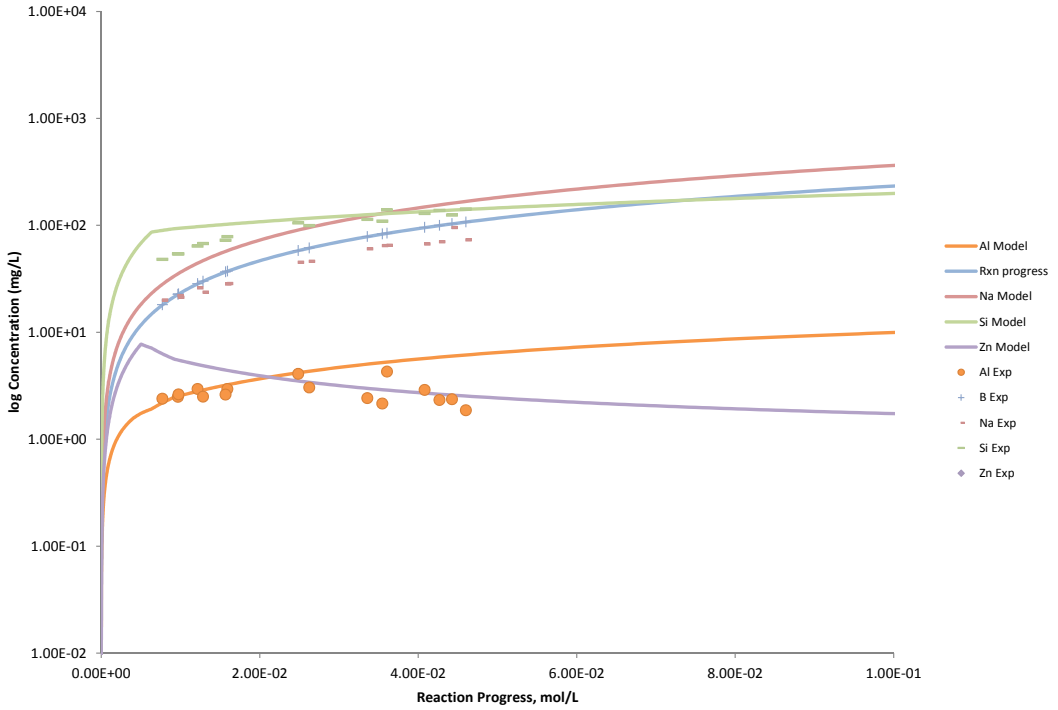


**Figure B.209**. Measured Solution Concentrations (mg/L) and Model Results for Al, B, Na, Si, and Zn, as a Function of Reaction Progress (mol-glass/kg) Determined for Glass Sample LAWB38

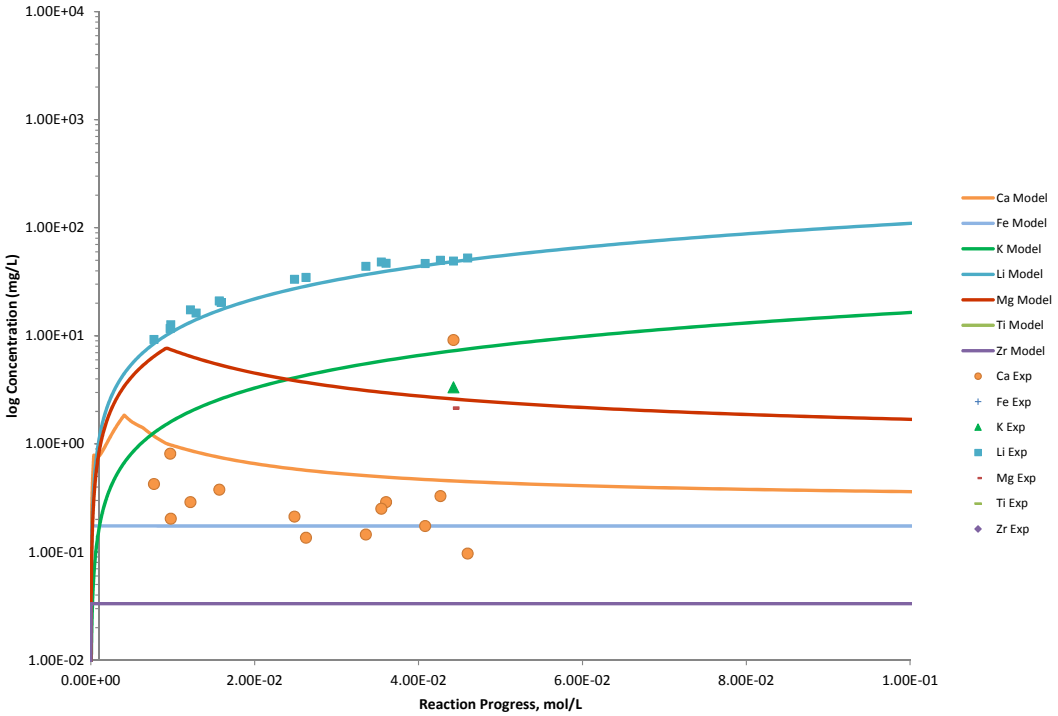


**Figure B.210**. Measured Solution Concentrations (mg/L) and Model Results for Ca, Fe, K, Li, Mg, Ti, and Zr, as a Function of Reaction Progress (mol-glass/kg) Determined for Glass Sample LAWB38

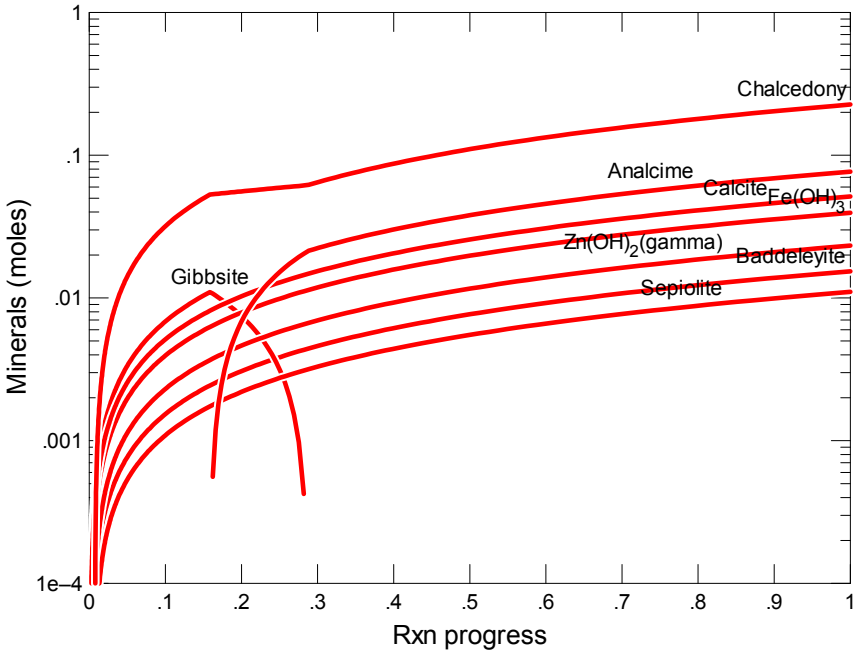


**Figure B.211**. Secondary Phases Calculated to Form as a Function of Reaction Progress (mol-glass/kg) Determined for Glass Sample LAWB40

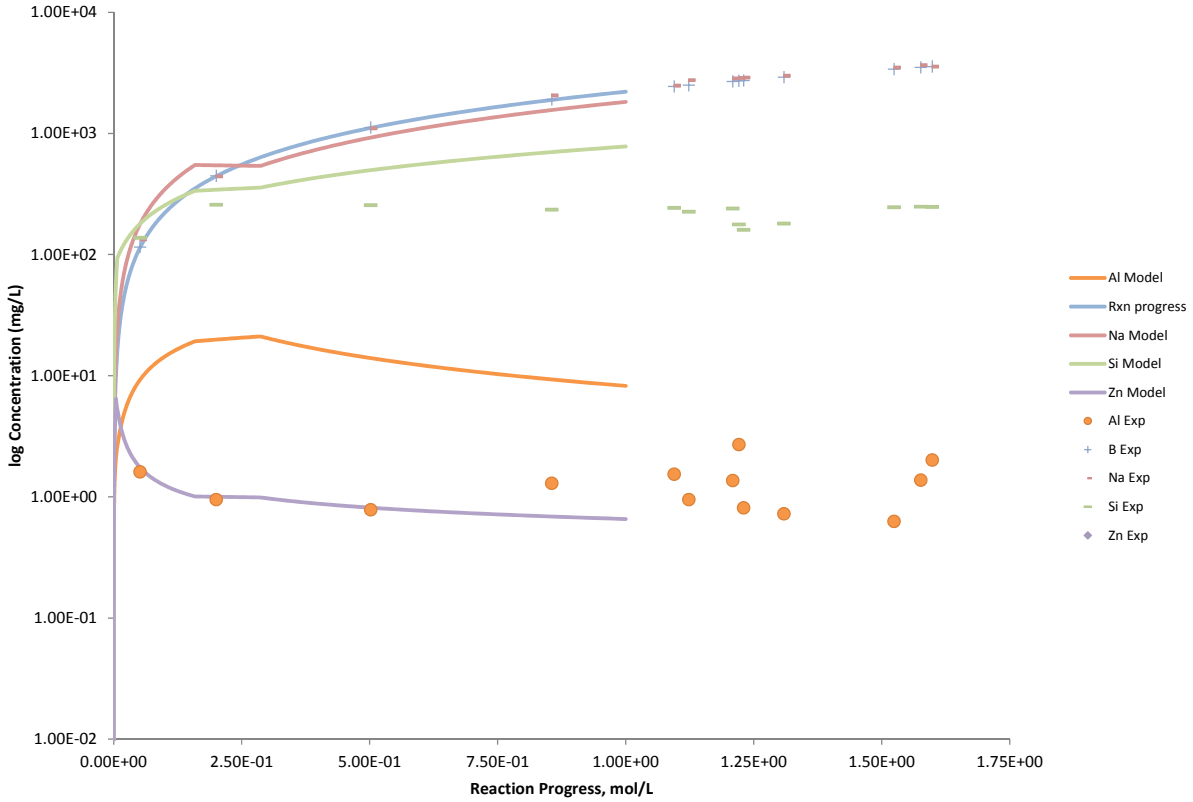


**Figure B.212**. Measured Solution Concentrations (mg/L) and Model Results for Al, B, Na, Si, and Zn, as a Function of Reaction Progress (mol-glass/kg) Determined for Glass Sample LAWB40

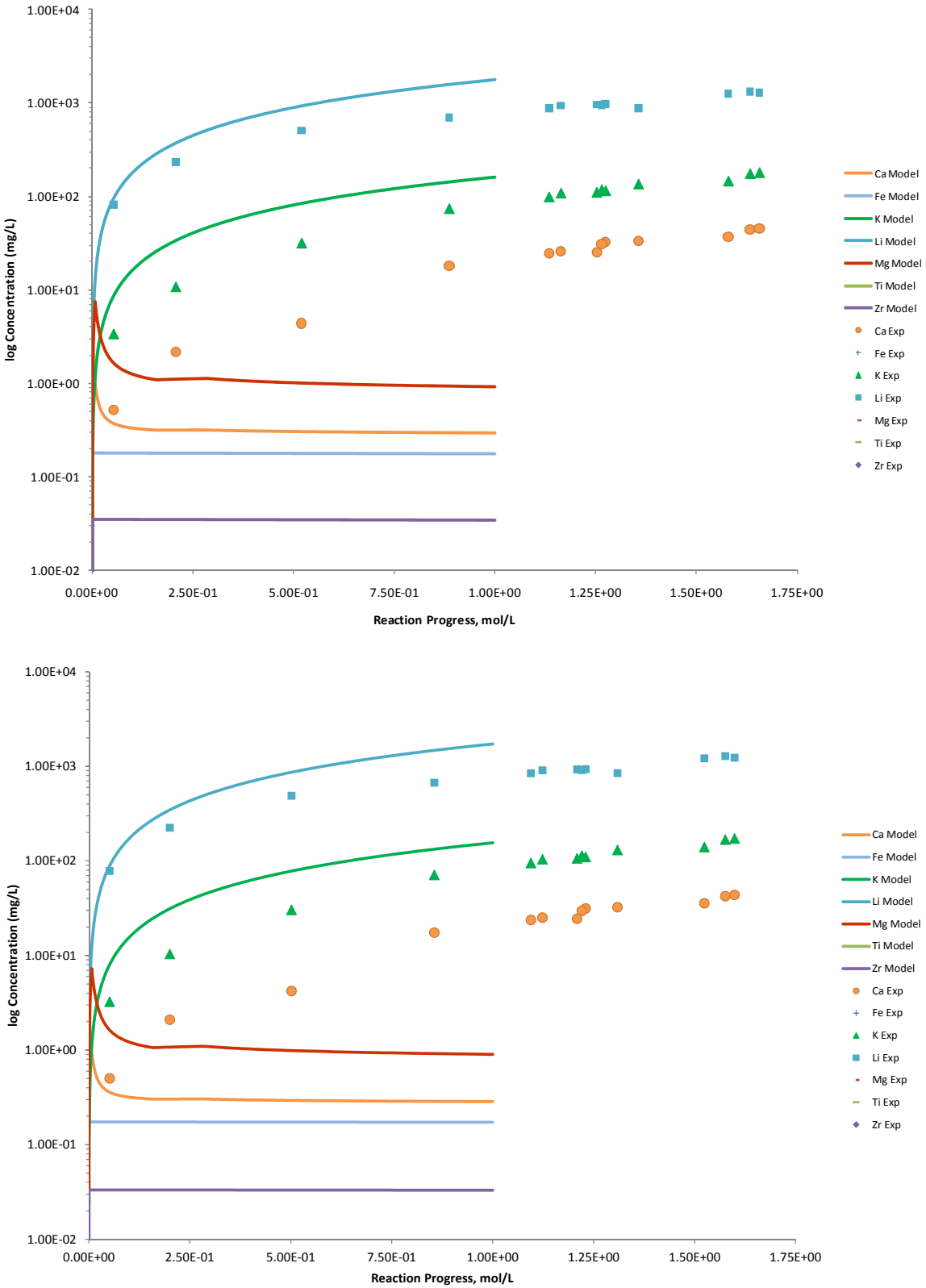


**Figure B.213**. Measured Solution Concentrations (mg/L) and Model Results for Ca, Fe, K, Li, Mg, Ti, and Zr, as a Function of Reaction Progress (mol-glass/kg) Determined for Glass Sample LAWB40

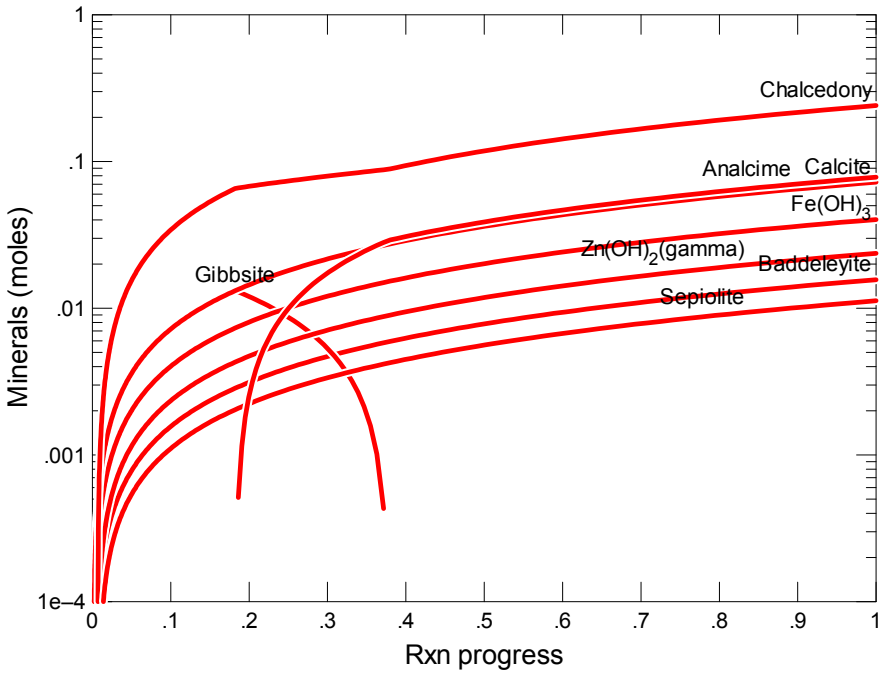


**Figure B.214**. Secondary Phases Calculated to Form as a Function of Reaction Progress (mol-glass/kg) Determined for Glass Sample LAWB41

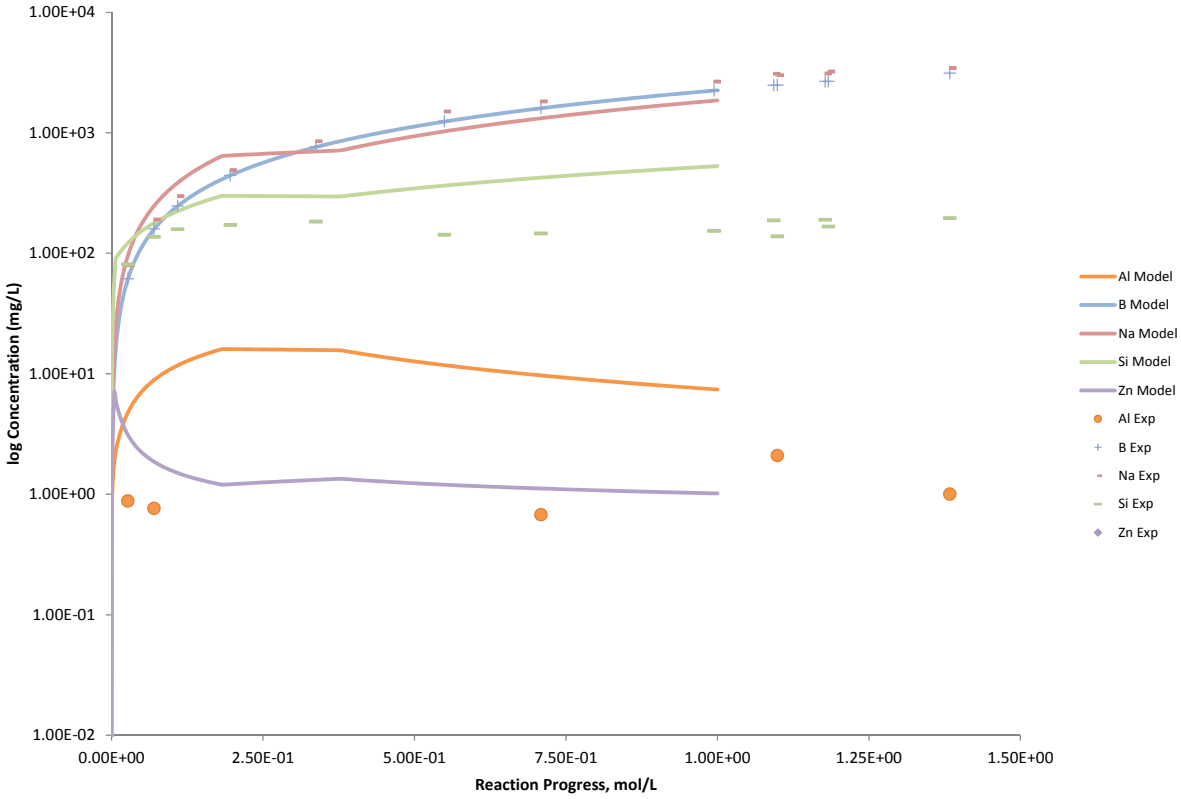


**Figure B.215**. Measured Solution Concentrations (mg/L) and Model Results for Al, B, Na, Si, and Zn, as a Function of Reaction Progress (mol-glass/kg) Determined for Glass Sample LAWB41

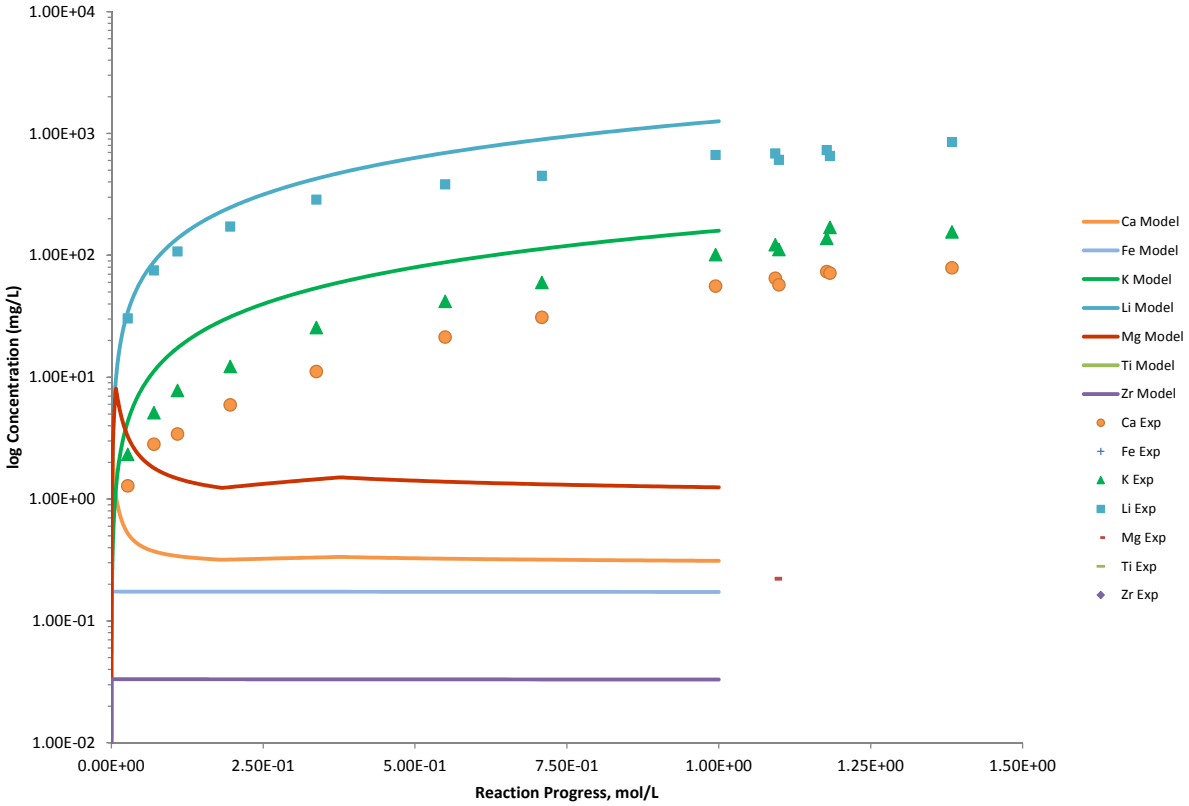


**Figure B.216**. Measured Solution Concentrations (mg/L) and Model Results for Ca, Fe, K, Li, Mg, Ti, and Zr, as a Function of Reaction Progress (mol-glass/kg) Determined for Glass Sample LAWB41

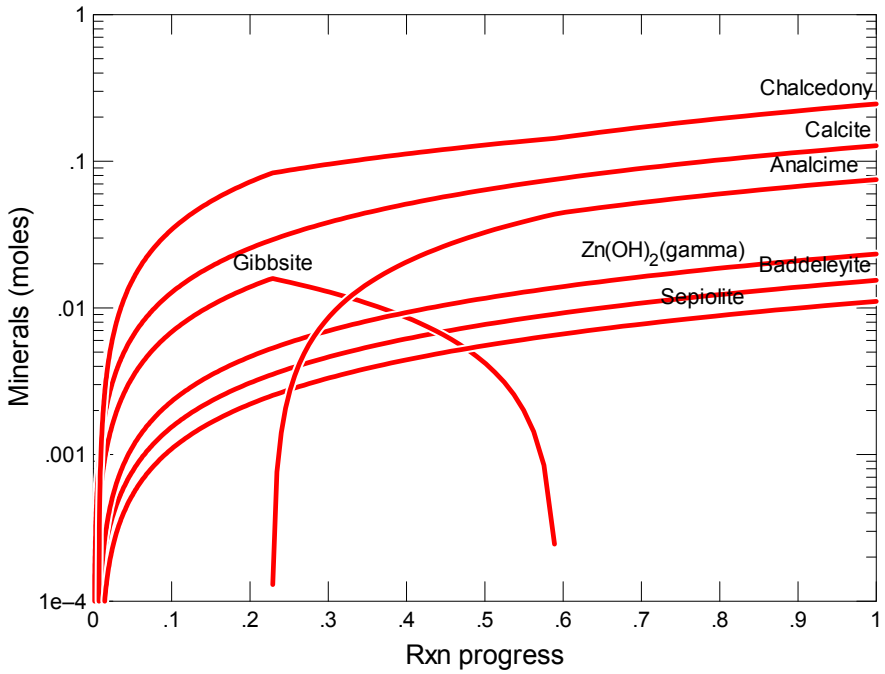


**Figure B.217**. Secondary Phases Calculated to Form as a Function of Reaction Progress (mol-glass/kg) Determined for Glass Sample LAWB60

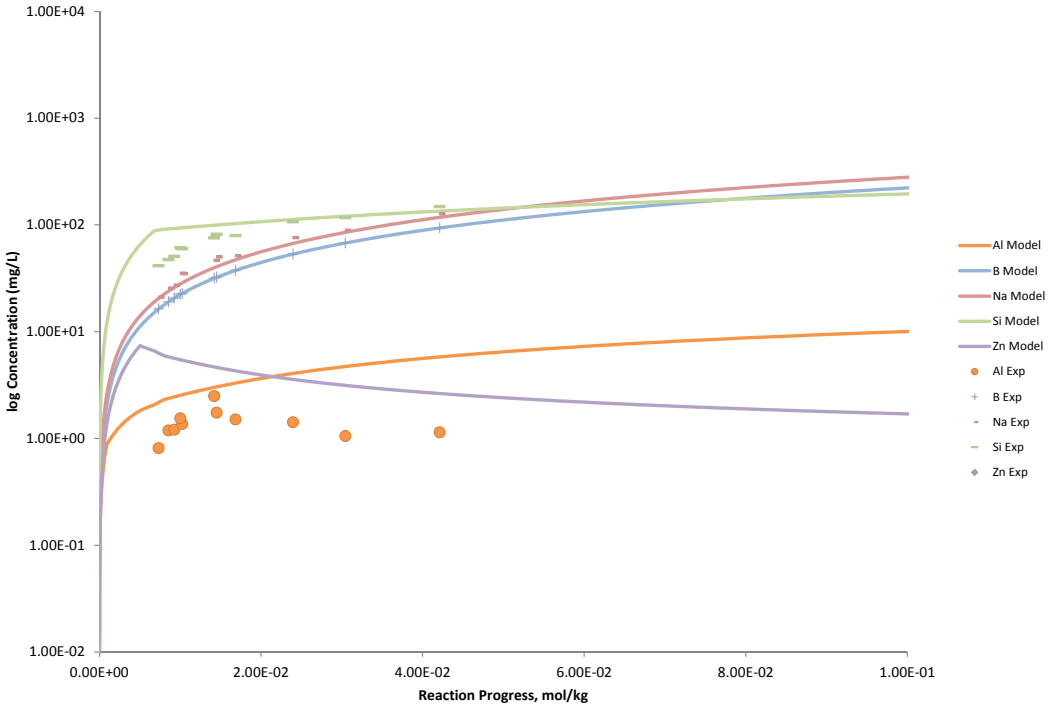


**Figure B.218**. Measured Solution Concentrations (mg/L) and Model Results for Al, B, Na, Si, and Zn, as a Function of Reaction Progress (mol-glass/kg) Determined for Glass Sample LAWB60

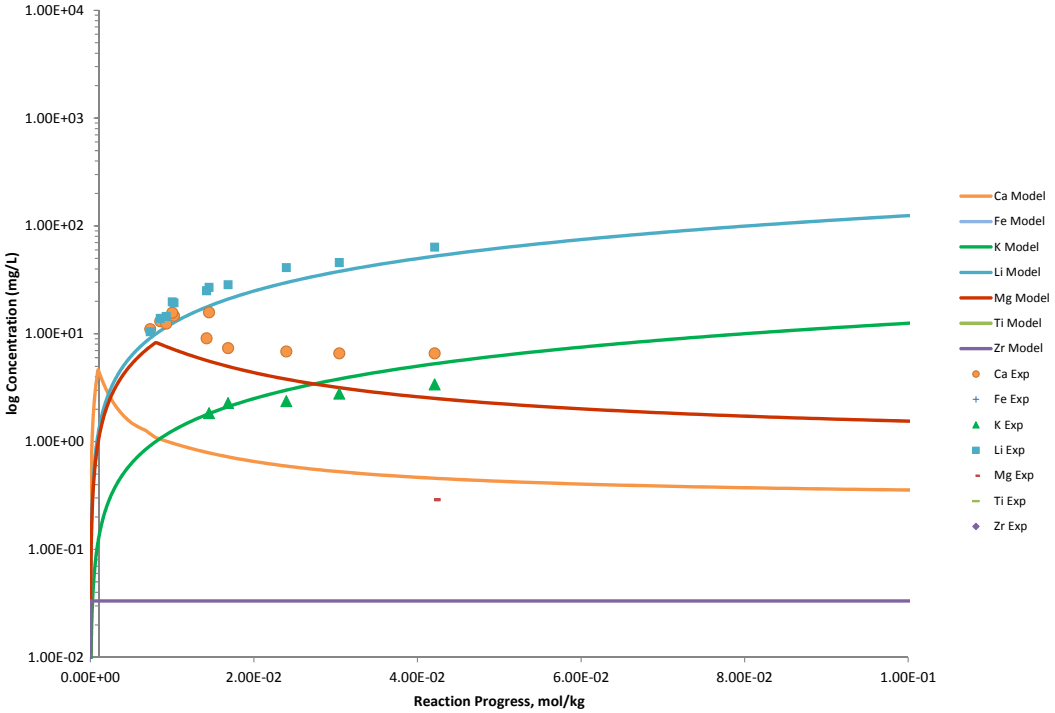


**Figure B.219**. Measured Solution Concentrations (mg/L) and Model Results for Ca, Fe, K, Li, Mg, Ti, and Zr, as a Function of Reaction Progress (mol-glass/kg) Determined for Glass Sample LAWB60

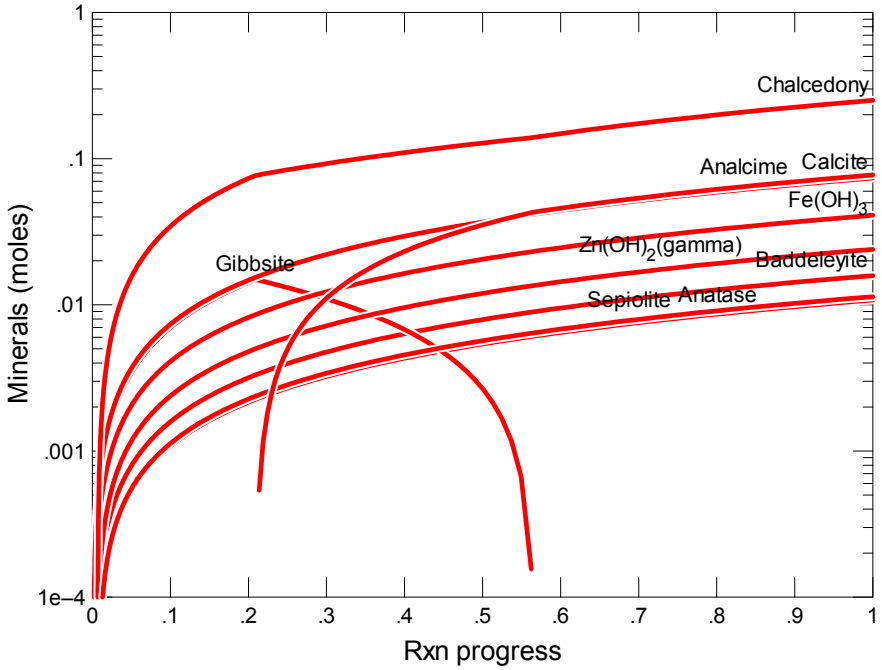


**Figure B.220**. Secondary Phases Calculated to Form as a Function of Reaction Progress (mol-glass/kg) Determined for Glass Sample LAWB61

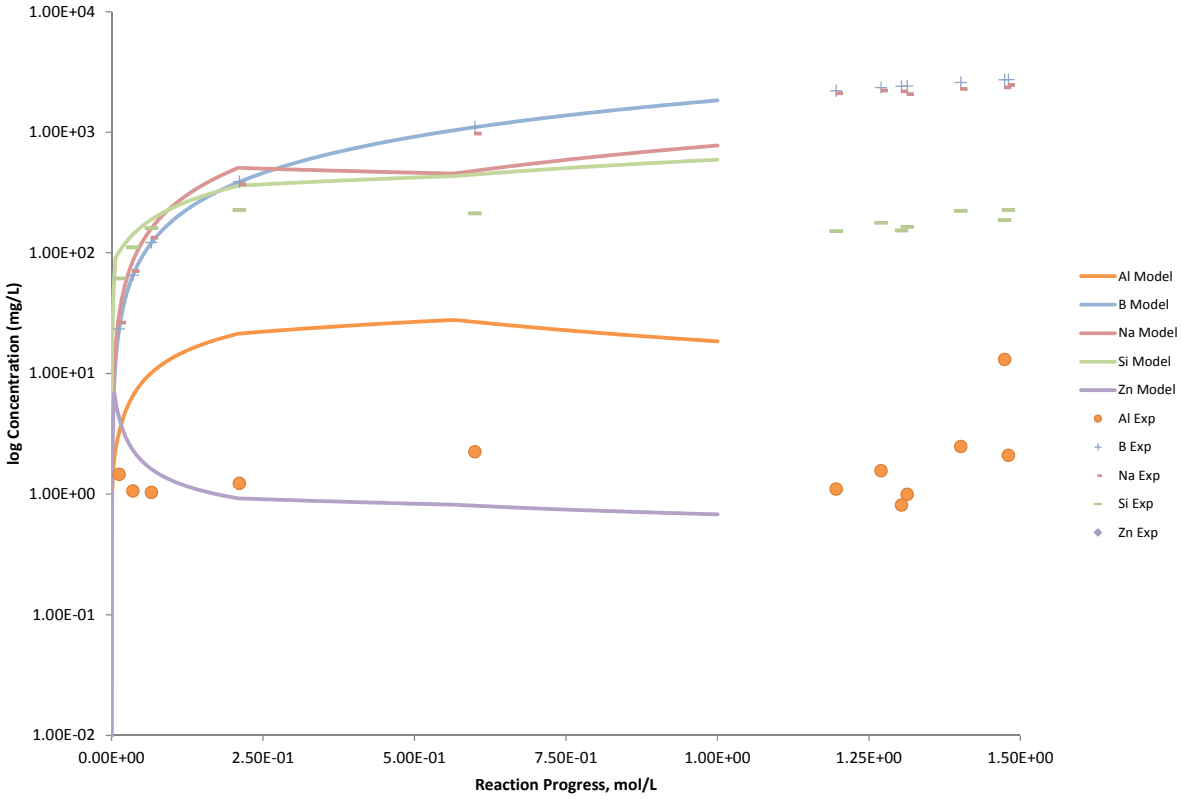


**Figure B.221**. Measured Solution Concentrations (mg/L) and Model Results for Al, B, Na, Si, and Zn, as a Function of Reaction Progress (mol-glass/kg) Determined for Glass Sample LAWB61

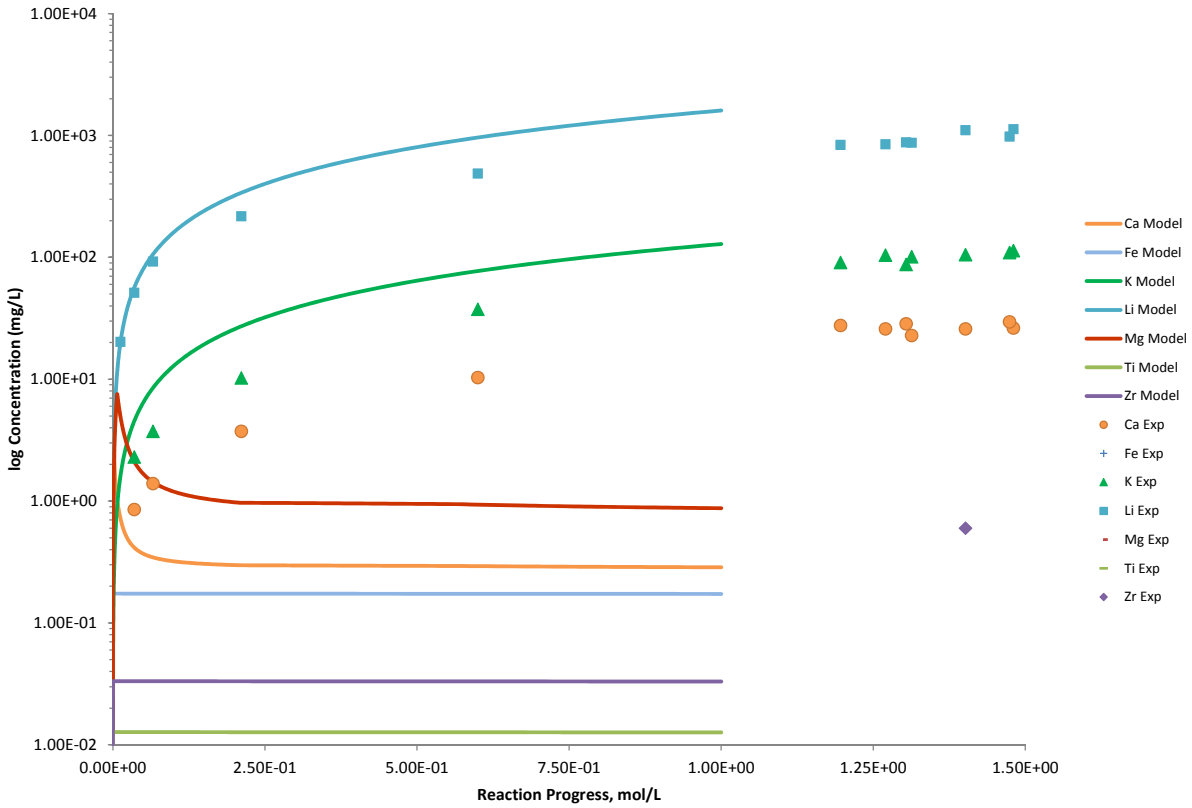


**Figure B.222**. Measured Solution Concentrations (mg/L) and Model Results for Ca, Fe, K, Li, Mg, Ti, and Zr, as a Function of Reaction Progress (mol-glass/kg) Determined for Glass Sample LAWB61

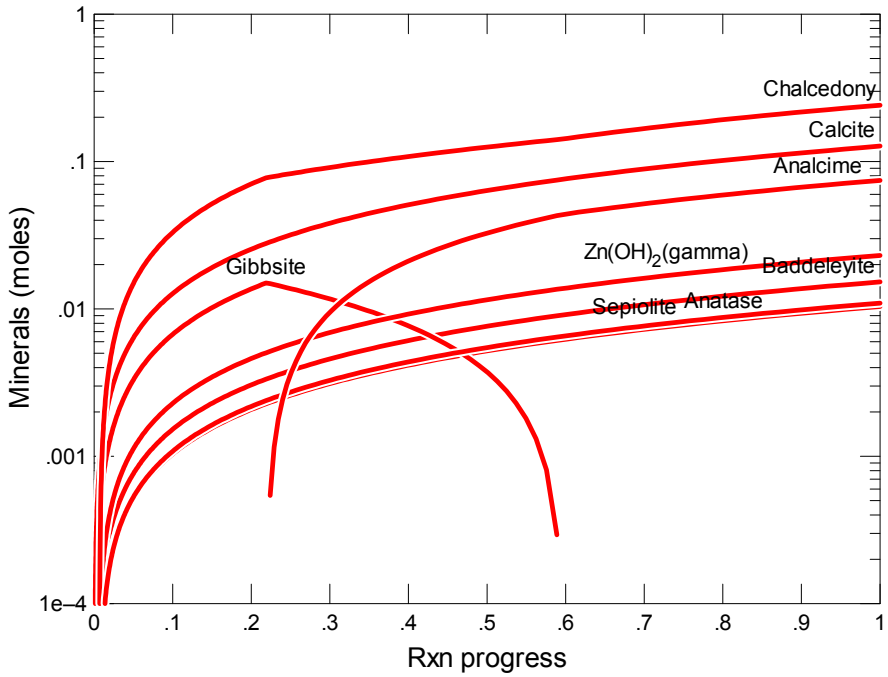


**Figure B.223**. Secondary Phases Calculated to Form as a Function of Reaction Progress (mol-glass/kg) Determined for Glass Sample LAWB62

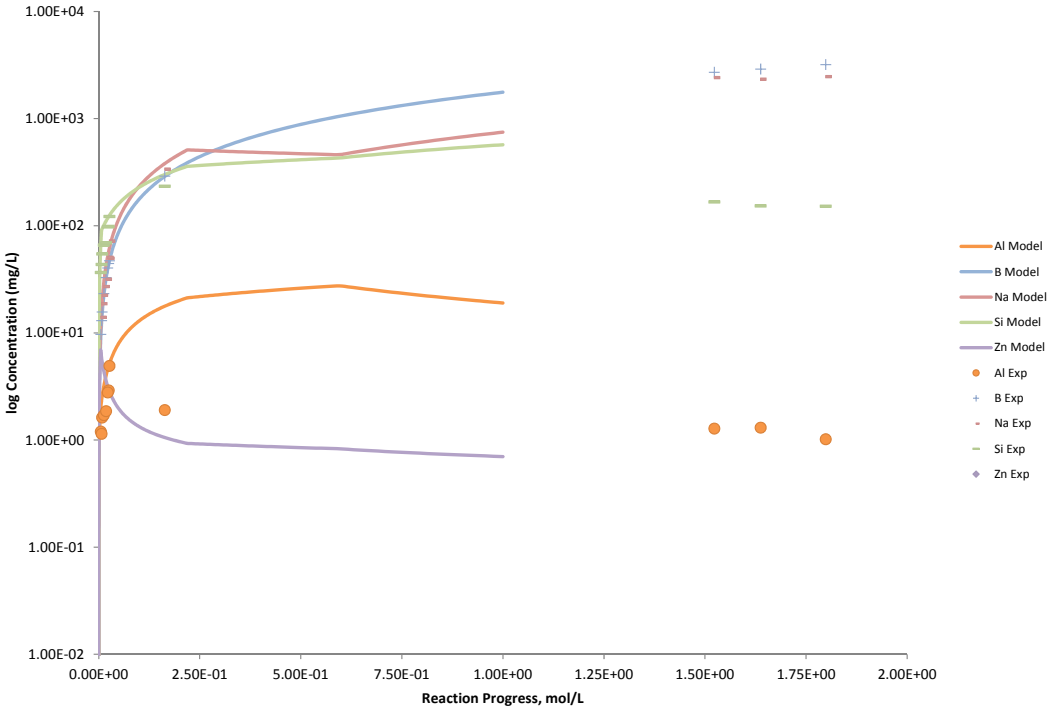


**Figure B.224**. Measured Solution Concentrations (mg/L) and Model Results for Al, B, Na, Si, and Zn, as a Function of Reaction Progress (mol-glass/kg) Determined for Glass Sample LAWB62

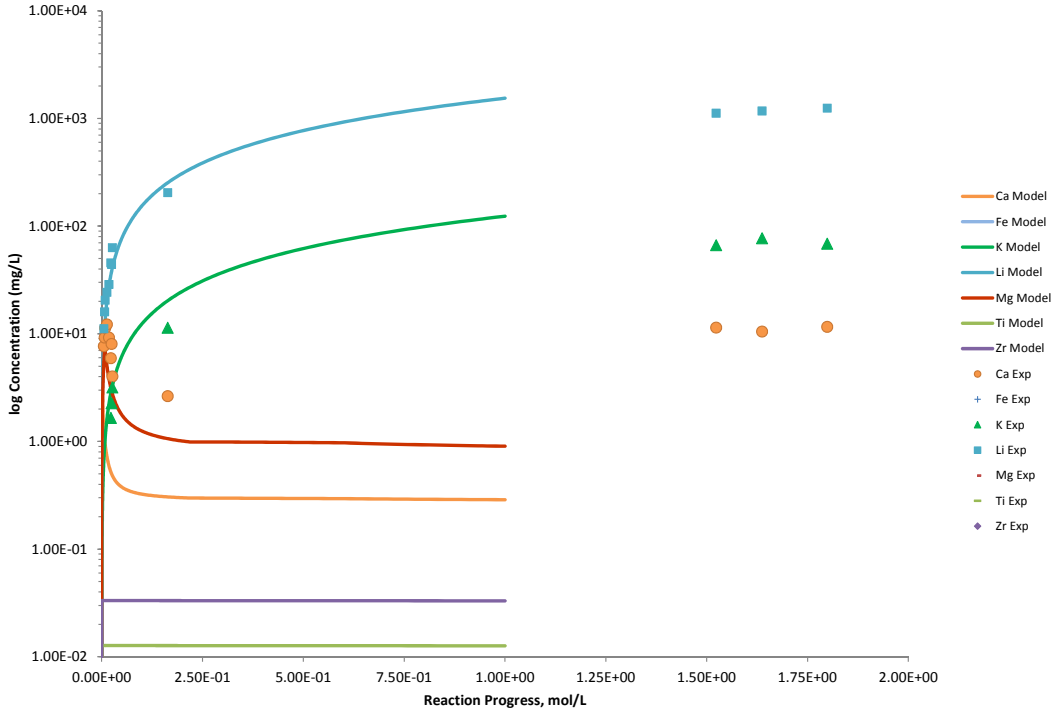


**Figure B.225**. Measured Solution Concentrations (mg/L) and Model Results for Ca, Fe, K, Li, Mg, Ti, and Zr, as a Function of Reaction Progress (mol-glass/kg) Determined for Glass Sample LAWB62

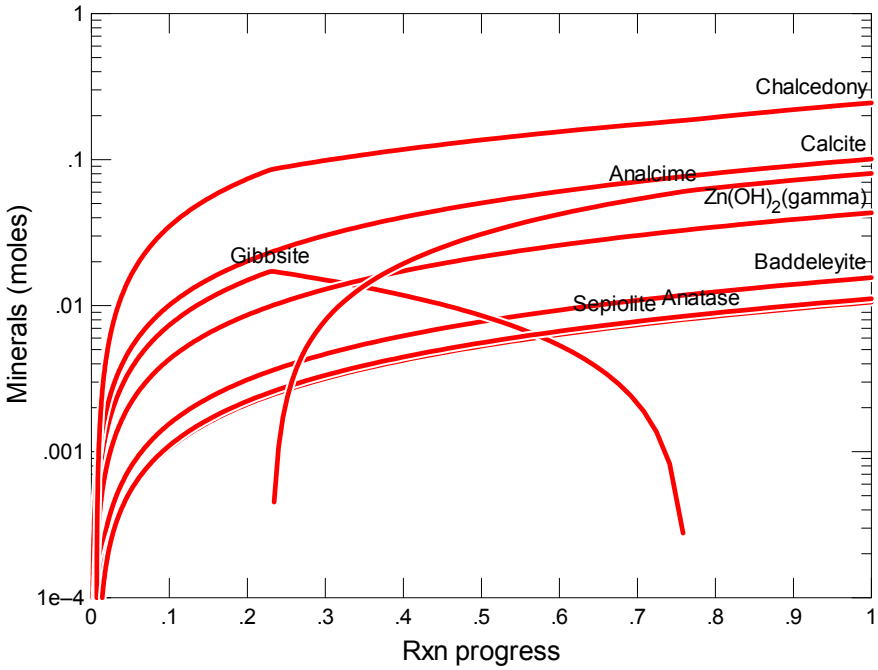


**Figure B.226**. Secondary Phases Calculated to Form as a Function of Reaction Progress (mol-glass/kg) Determined for Glass Sample LAWB63

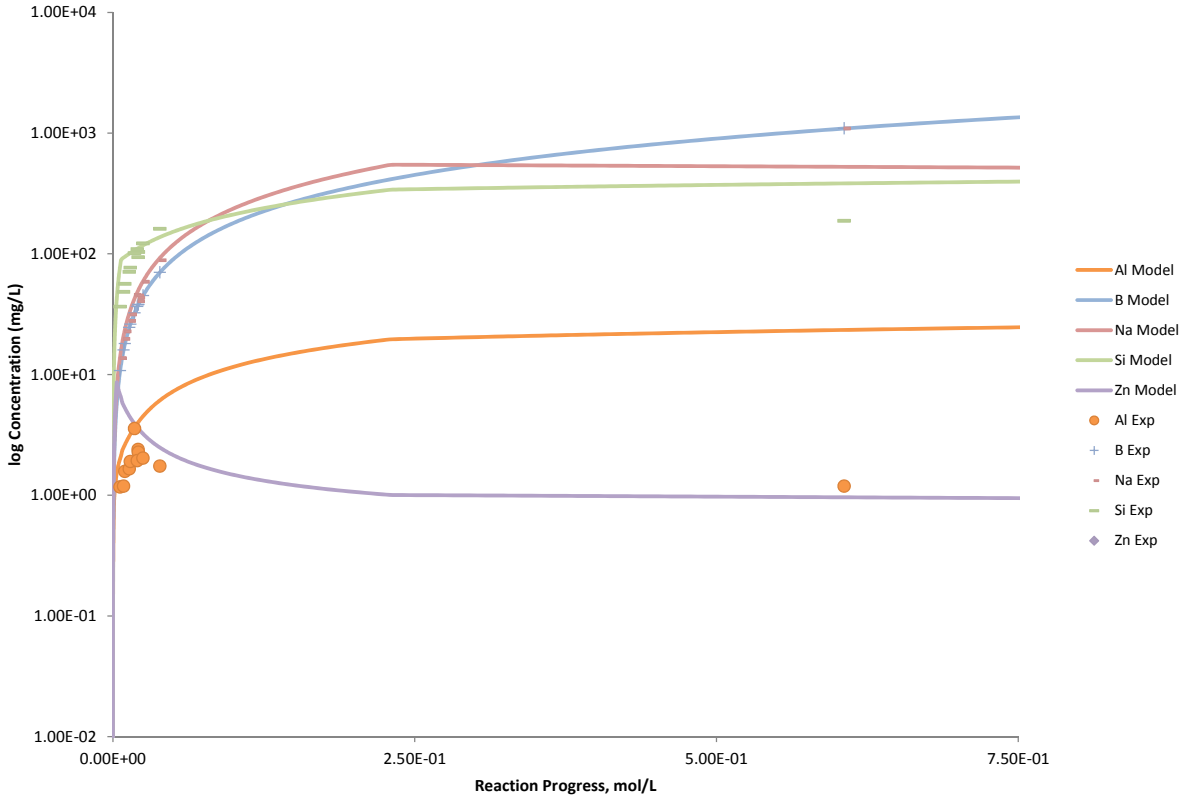


**Figure B.227**. Measured Solution Concentrations (mg/L) and Model Results for Al, B, Na, Si, and Zn, as a Function of Reaction Progress (mol-glass/kg) Determined for Glass Sample LAWB63

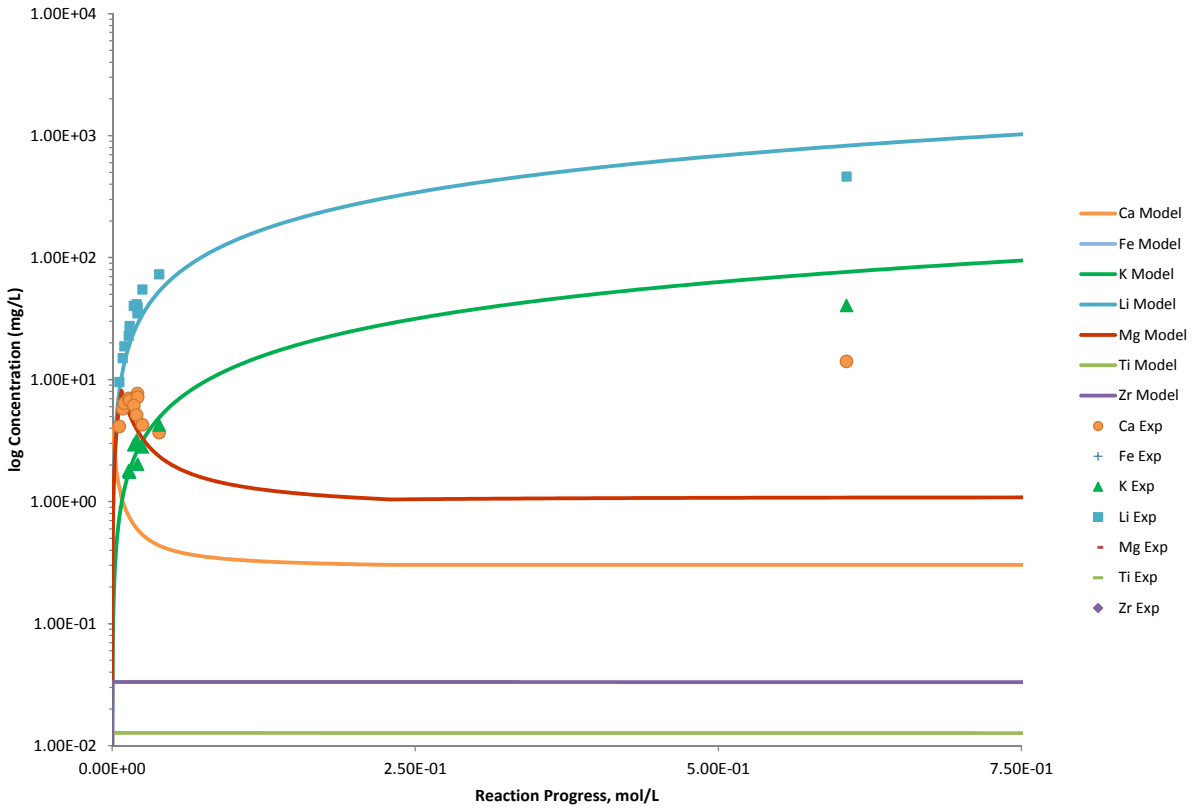


**Figure B.228**. Measured Solution Concentrations (mg/L) and Model Results for Ca, Fe, K, Li, Mg, Ti, and Zr, as a Function of Reaction Progress (mol-glass/kg) Determined for Glass Sample LAWB63

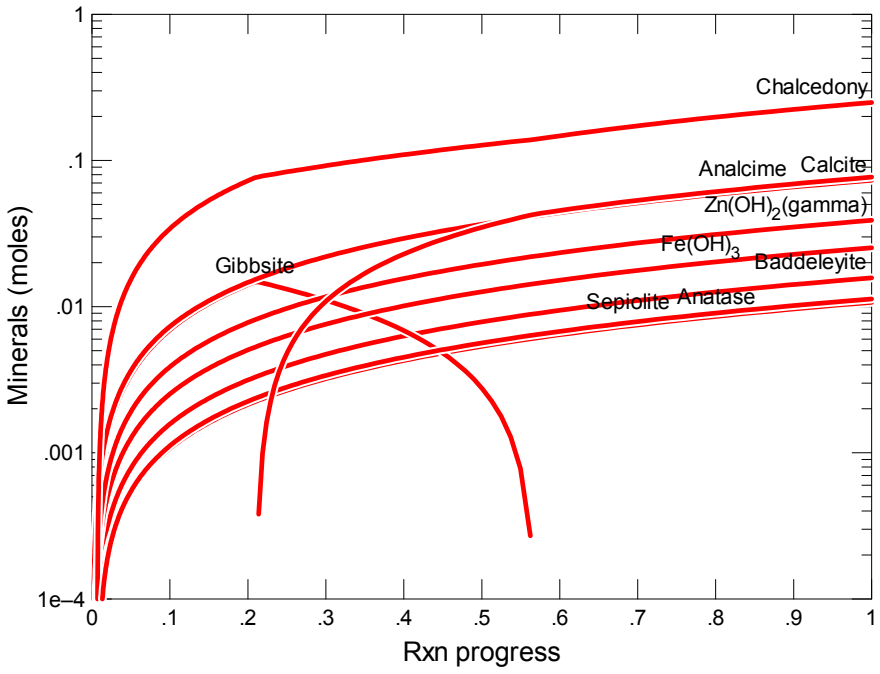


**Figure B.229**. Secondary Phases Calculated to Form as a Function of Reaction Progress (mol-glass/kg) Determined for Glass Sample LAWB64

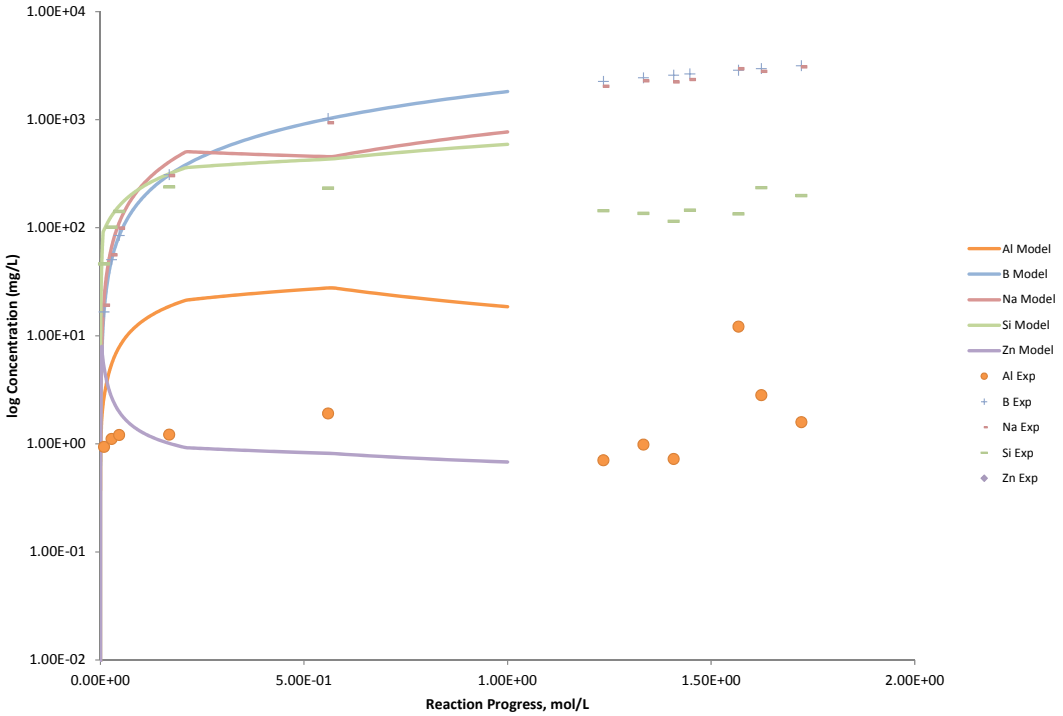


**Figure B.230**. Measured Solution Concentrations (mg/L) and Model Results for Al, B, Na, Si, and Zn, as a Function of Reaction Progress (mol-glass/kg) Determined for Glass Sample LAWB64

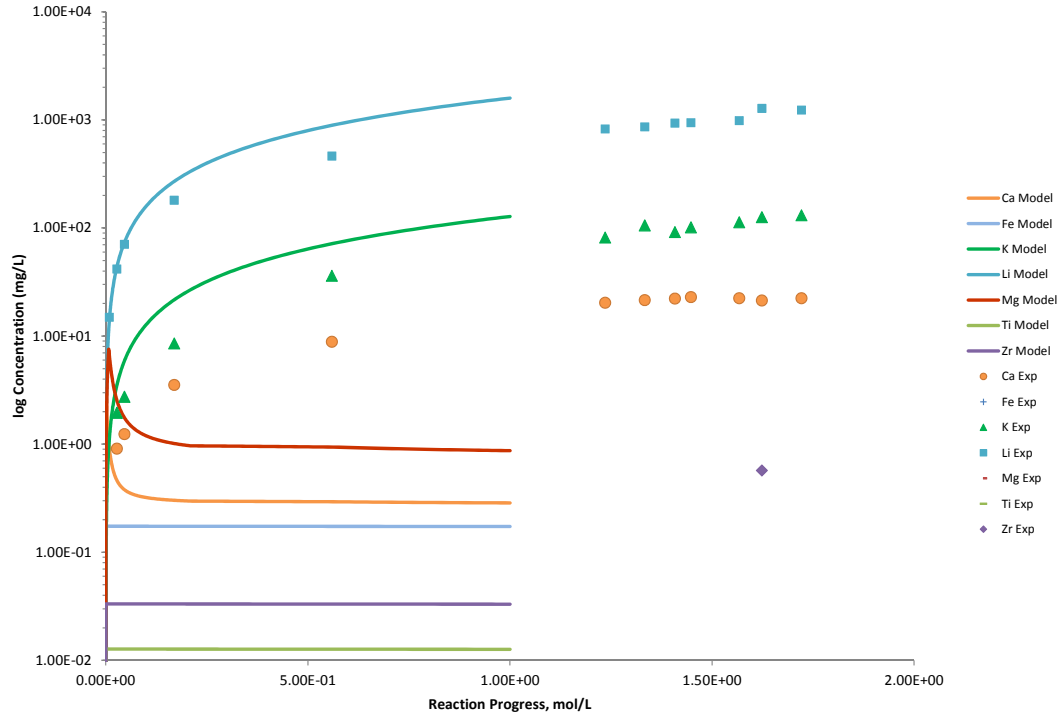


**Figure B.231**. Measured Solution Concentrations (mg/L) and Model Results for Ca, Fe, K, Li, Mg, Ti, and Zr, as a Function of Reaction Progress (mol-glass/kg) Determined for Glass Sample LAWB64

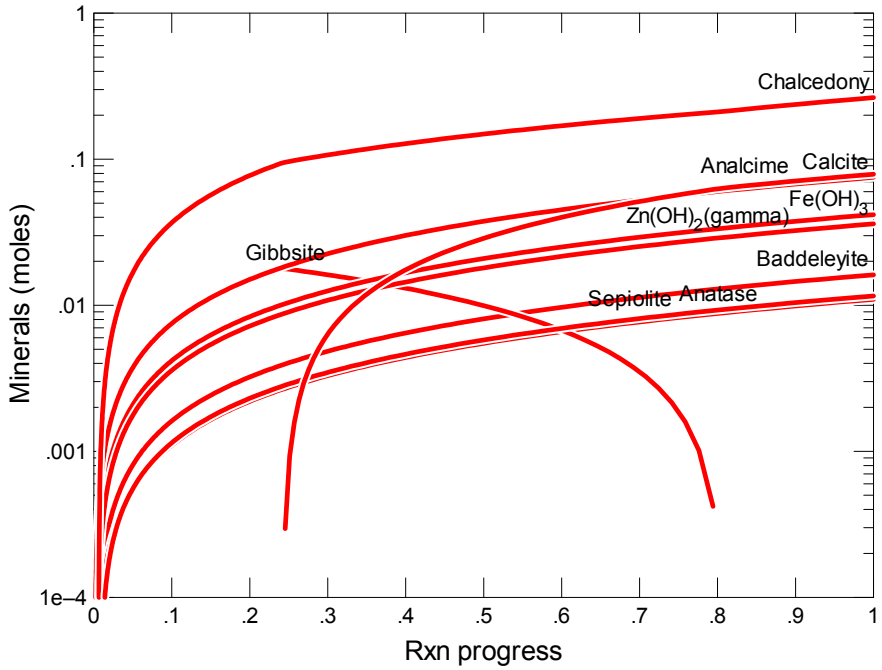


**Figure B.232**. Secondary Phases Calculated to Form as a Function of Reaction Progress (mol-glass/kg) Determined for Glass Sample LAWB65

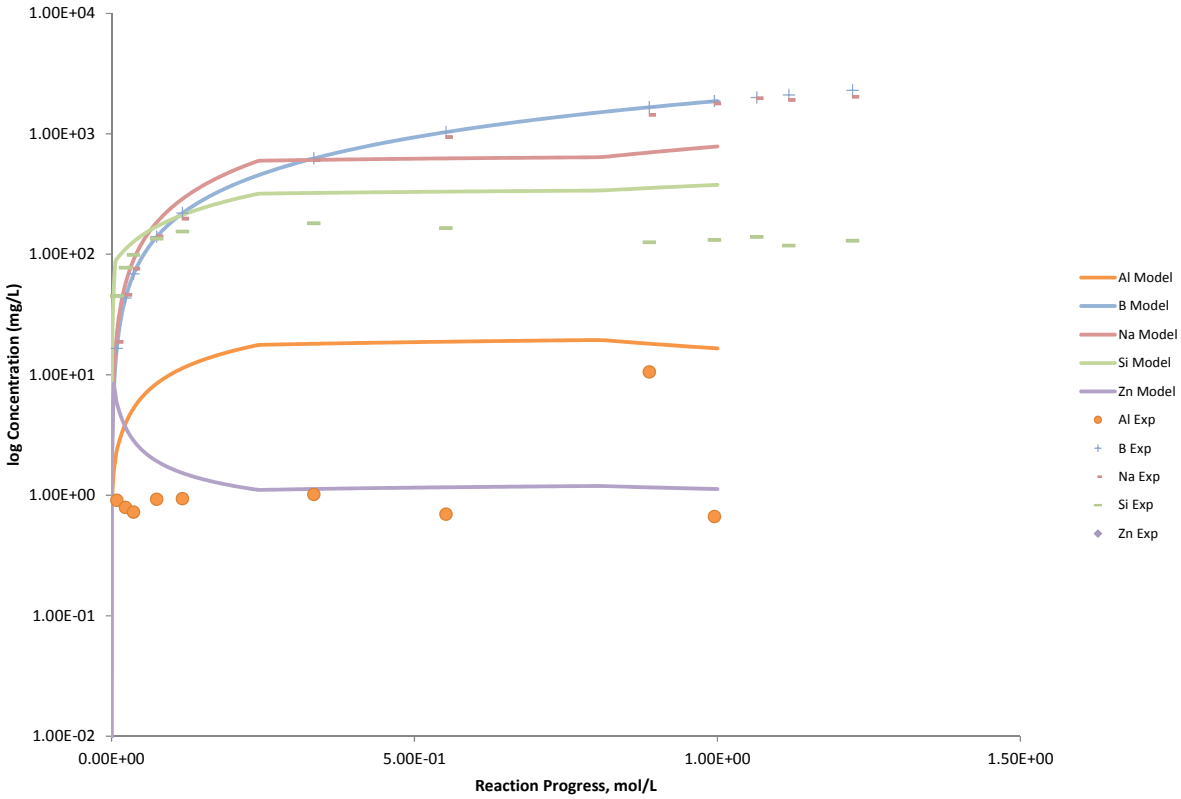


**Figure B.233**. Measured Solution Concentrations (mg/L) and Model Results for Al, B, Na, Si, and Zn, as a Function of Reaction Progress (mol-glass/kg) Determined for Glass Sample LAWB65

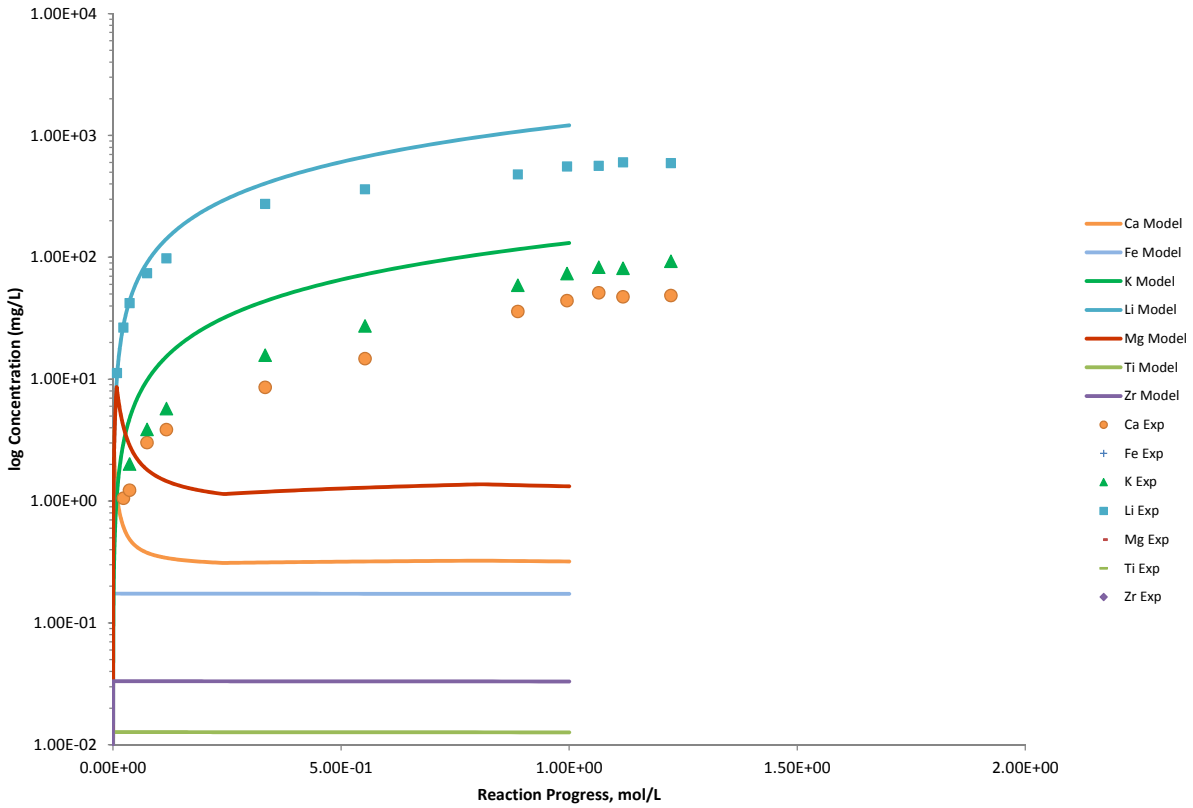


**Figure B.234**. Measured Solution Concentrations (mg/L) and Model Results for Ca, Fe, K, Li, Mg, Ti, and Zr, as a Function of Reaction Progress (mol-glass/kg) Determined for Glass Sample LAWB65

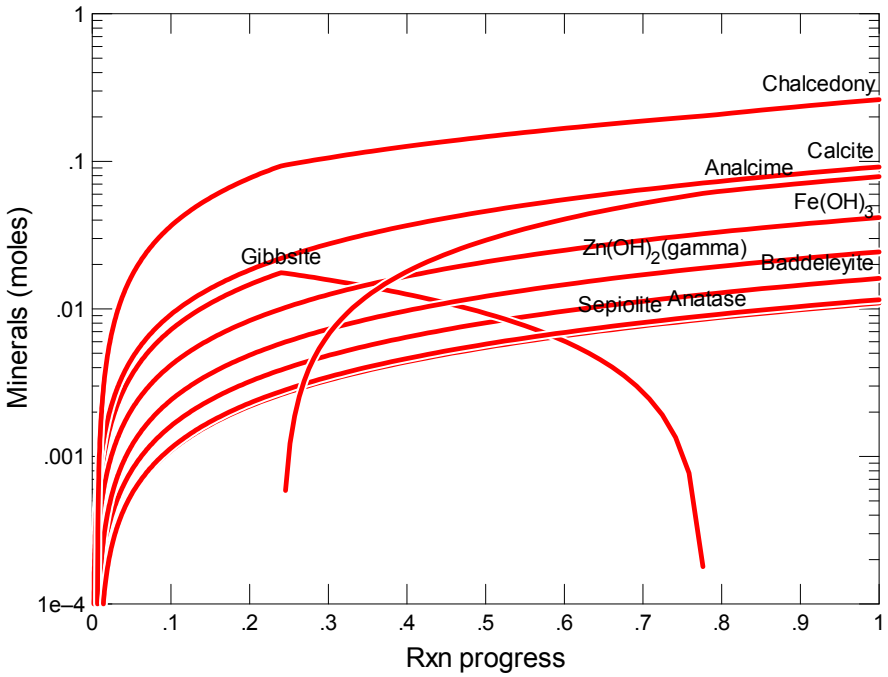


**Figure B.235**. Secondary Phases Calculated to Form as a Function of Reaction Progress (mol-glass/kg) Determined for Glass Sample LAWB66

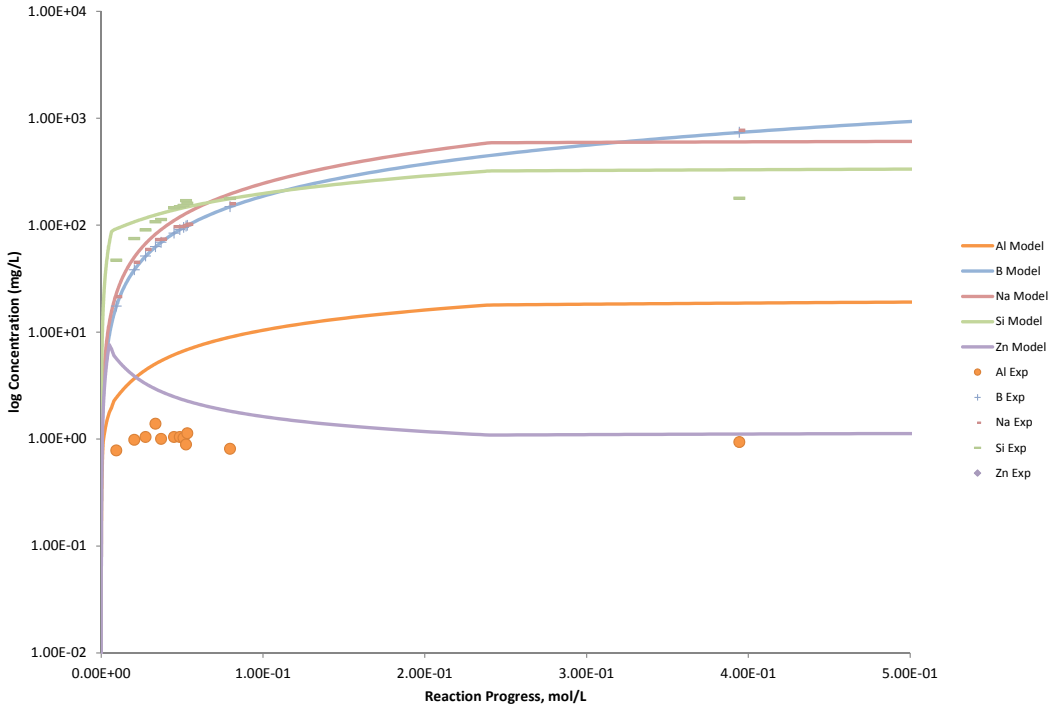


**Figure B.236**. Measured Solution Concentrations (mg/L) and Model Results for Al, B, Na, Si, and Zn, as a Function of Reaction Progress (mol-glass/kg) Determined for Glass Sample LAWB66

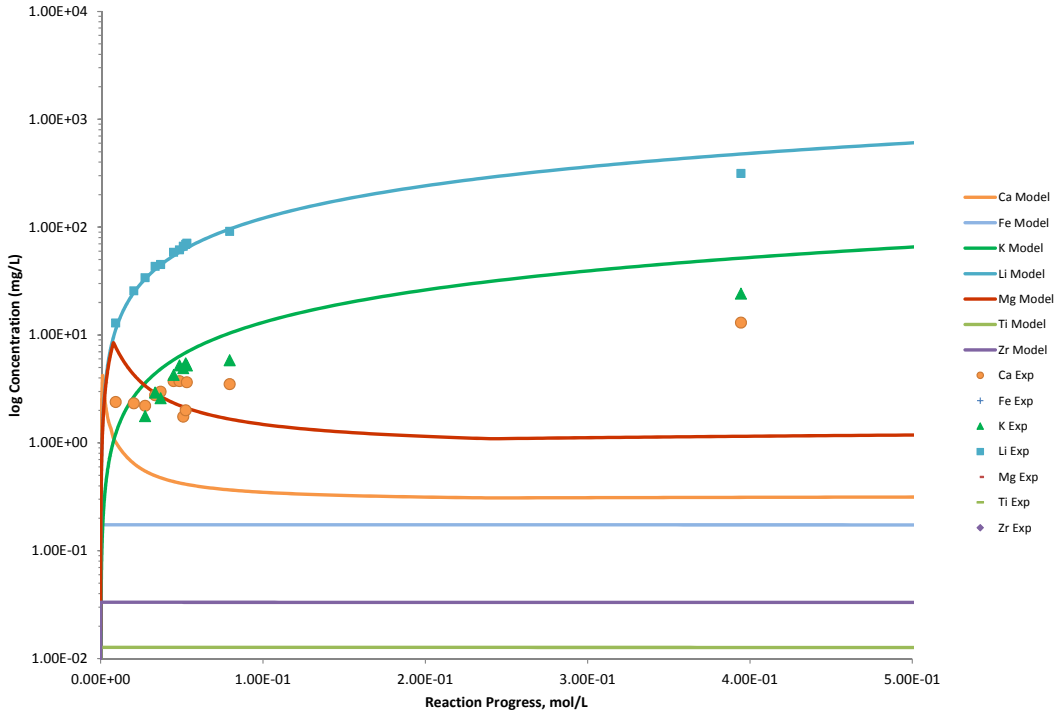


**Figure B.237**. Measured Solution Concentrations (mg/L) and Model Results for Ca, Fe, K, Li, Mg, Ti, and Zr, as a Function of Reaction Progress (mol-glass/kg) Determined for Glass Sample LAWB66

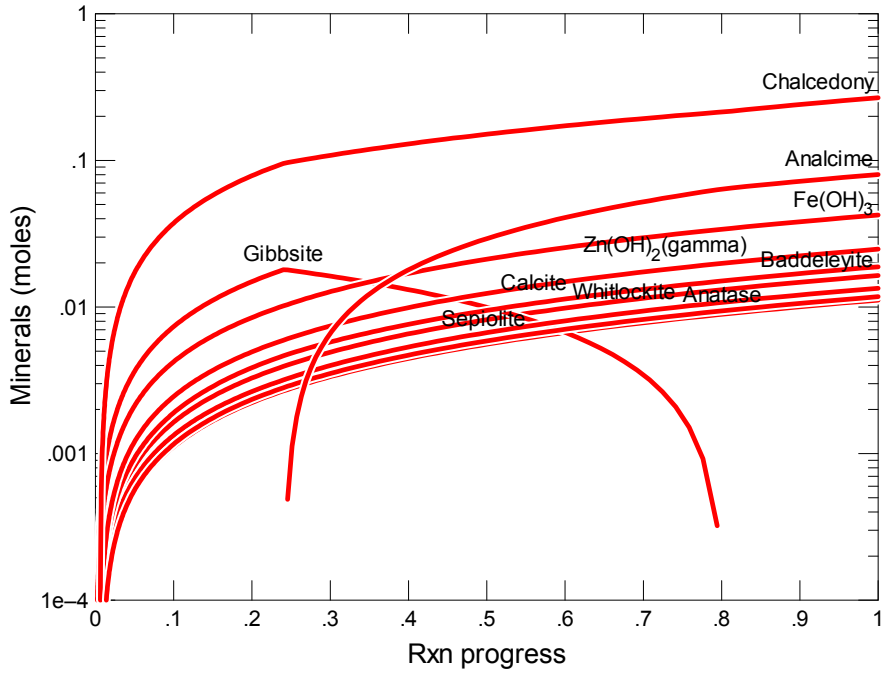


**Figure B.238**. Secondary Phases Calculated to Form as a Function of Reaction Progress (mol-glass/kg) Determined for Glass Sample LAWB67

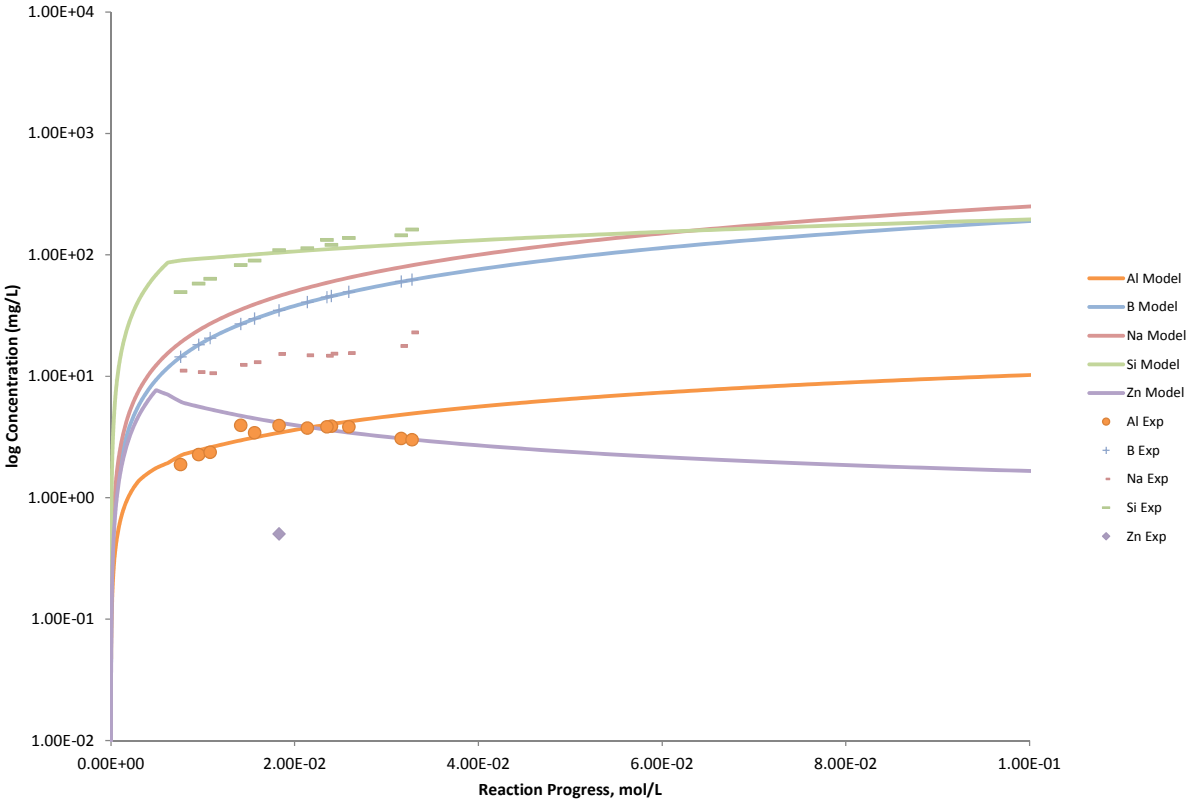


**Figure B.239**. Measured Solution Concentrations (mg/L) and Model Results for Al, B, Na, Si, and Zn, as a Function of Reaction Progress (mol-glass/kg) Determined for Glass Sample LAWB67

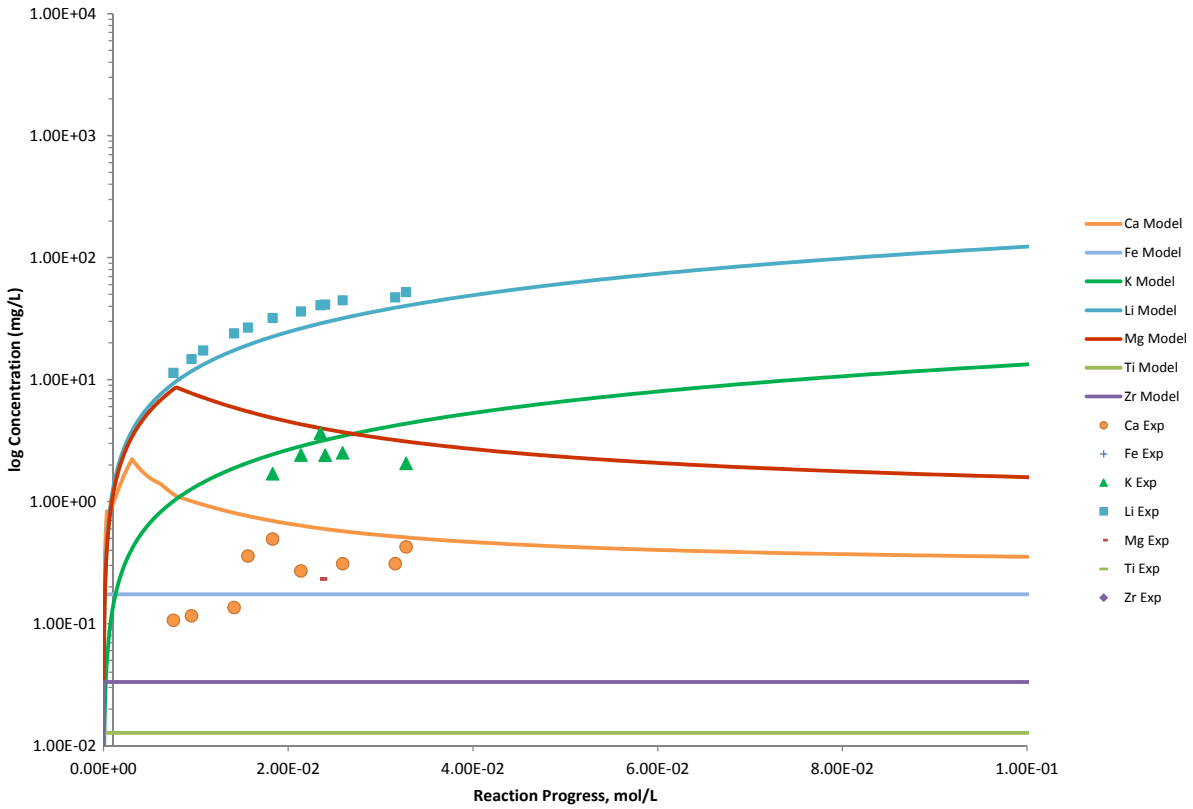


**Figure B.240**. Measured Solution Concentrations (mg/L) and Model Results for Ca, Fe, K, Li, Mg, Ti, and Zr, as a Function of Reaction Progress (mol-glass/kg) Determined for Glass Sample LAWB67

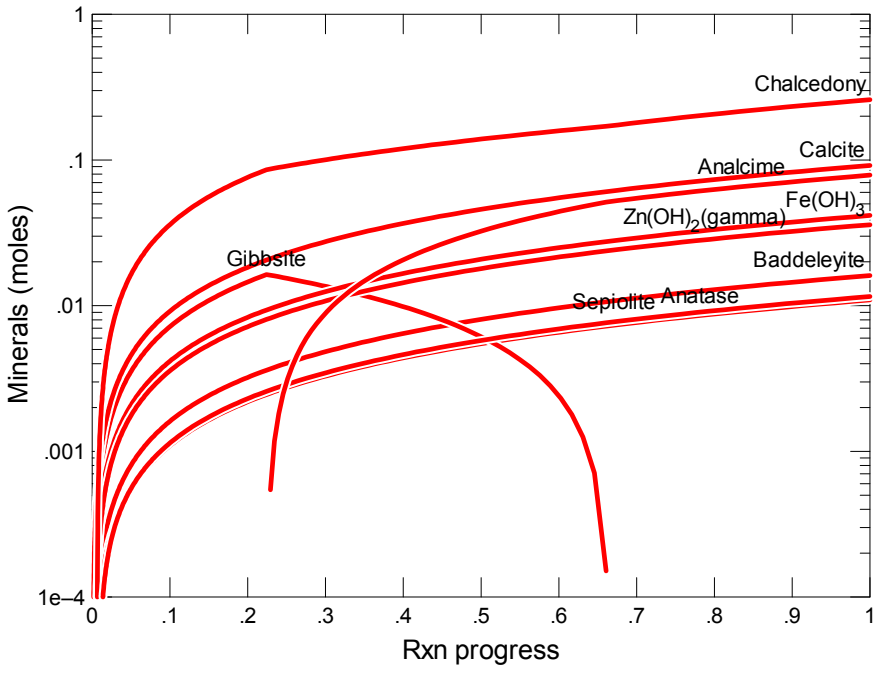


**Figure B.241**. Secondary Phases Calculated to Form as a Function of Reaction Progress (mol-glass/kg) Determined for Glass Sample LAWB68

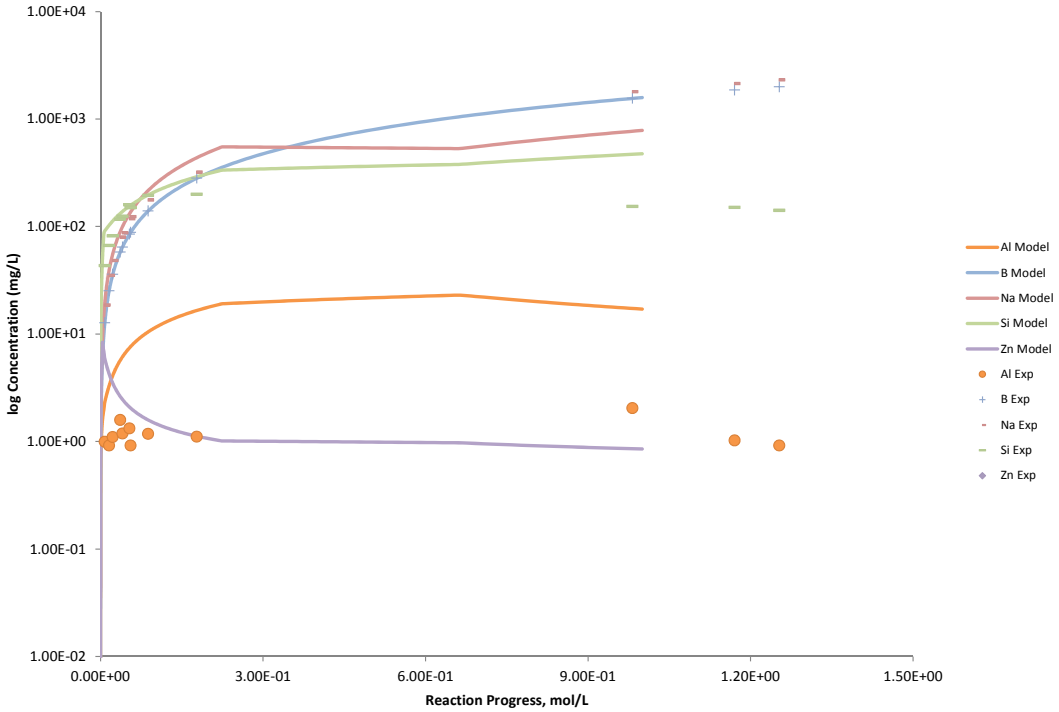


**Figure B.242**. Measured Solution Concentrations (mg/L) and Model Results for Al, B, Na, Si, and Zn, as a Function of Reaction Progress (mol-glass/kg) Determined for Glass Sample LAWB68

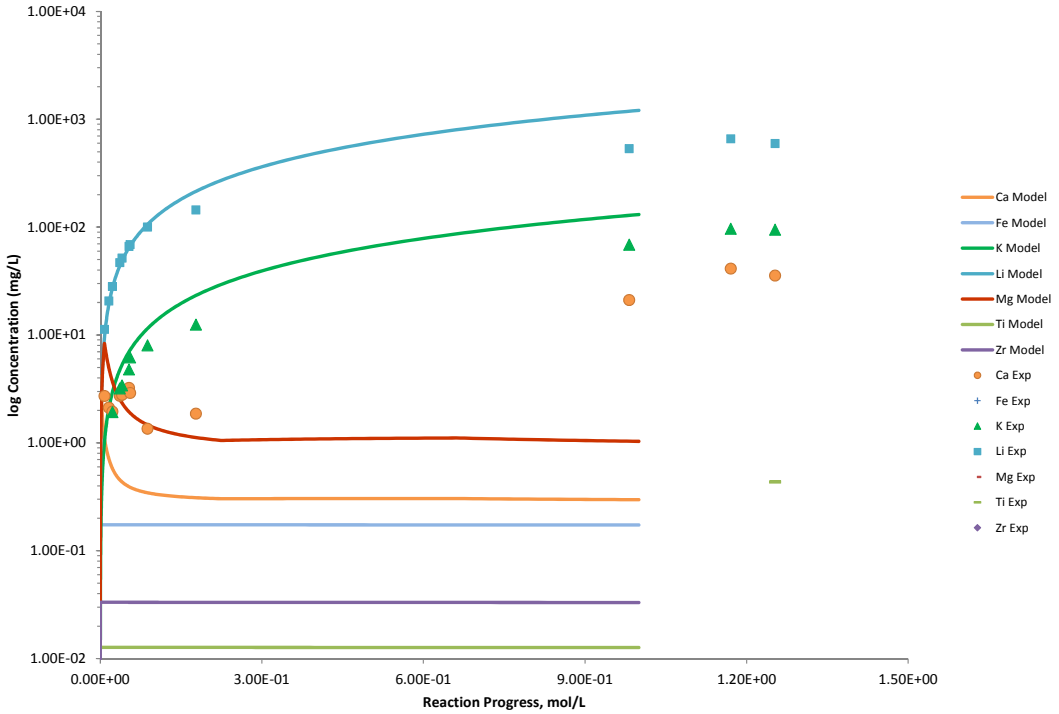


**Figure B.243**. Measured Solution Concentrations (mg/L) and Model Results for Ca, Fe, K, Li, Mg, Ti, and Zr, as a Function of Reaction Progress (mol-glass/kg) Determined for Glass Sample LAWB68

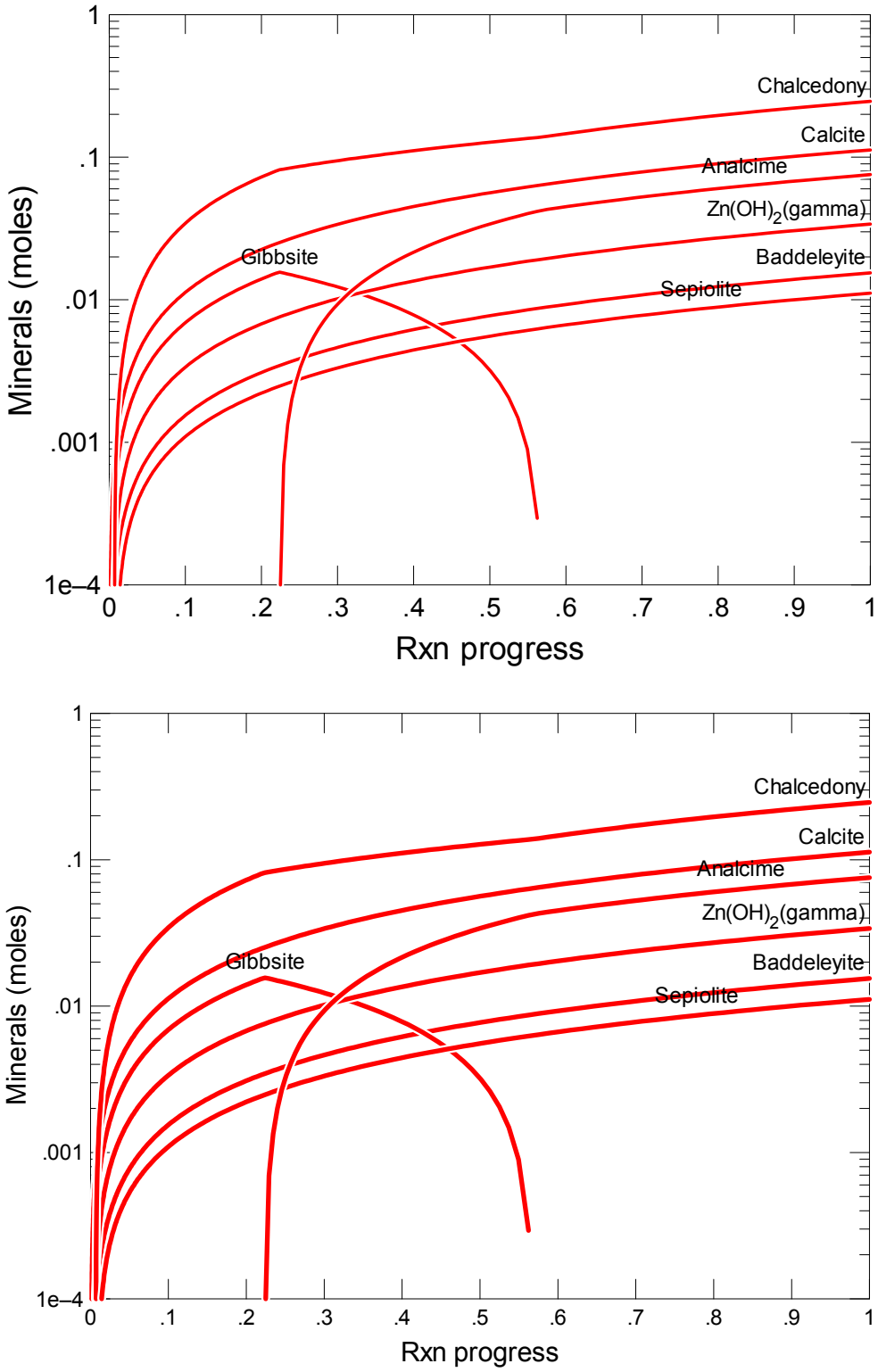


**Figure B.244**. Secondary Phases Calculated to Form as a Function of Reaction Progress (mol-glass/kg) Determined for Glass Sample LAWB69

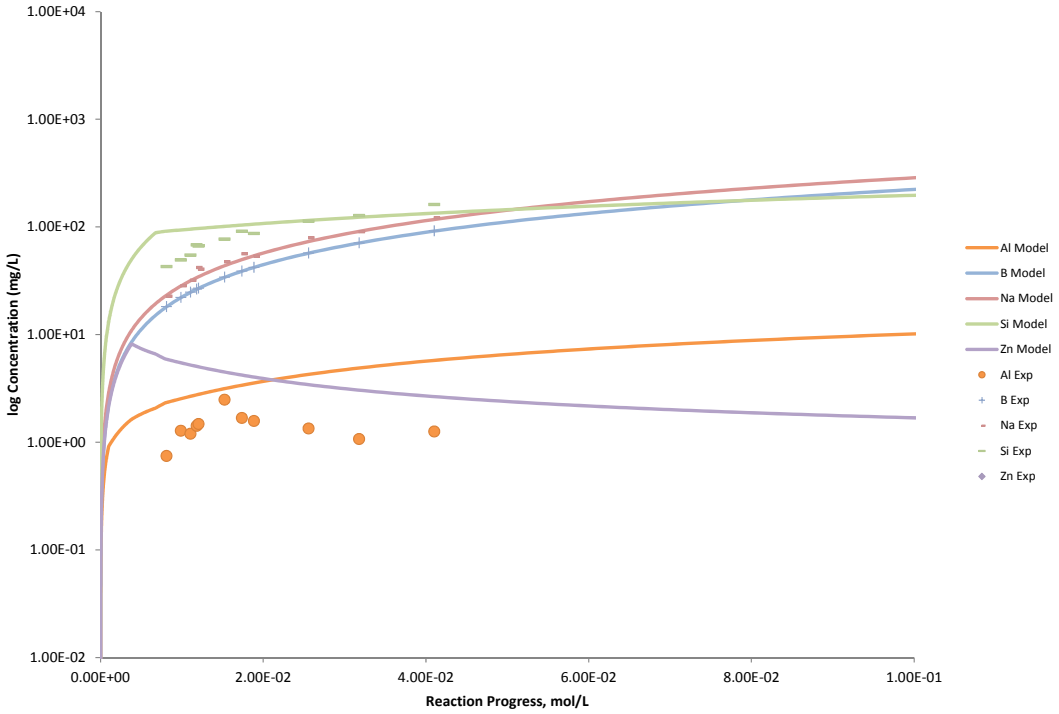


**Figure B.245**. Measured Solution Concentrations (mg/L) and Model Results for Al, B, Na, Si, and Zn, as a Function of Reaction Progress (mol-glass/kg) Determined for Glass Sample LAWB69

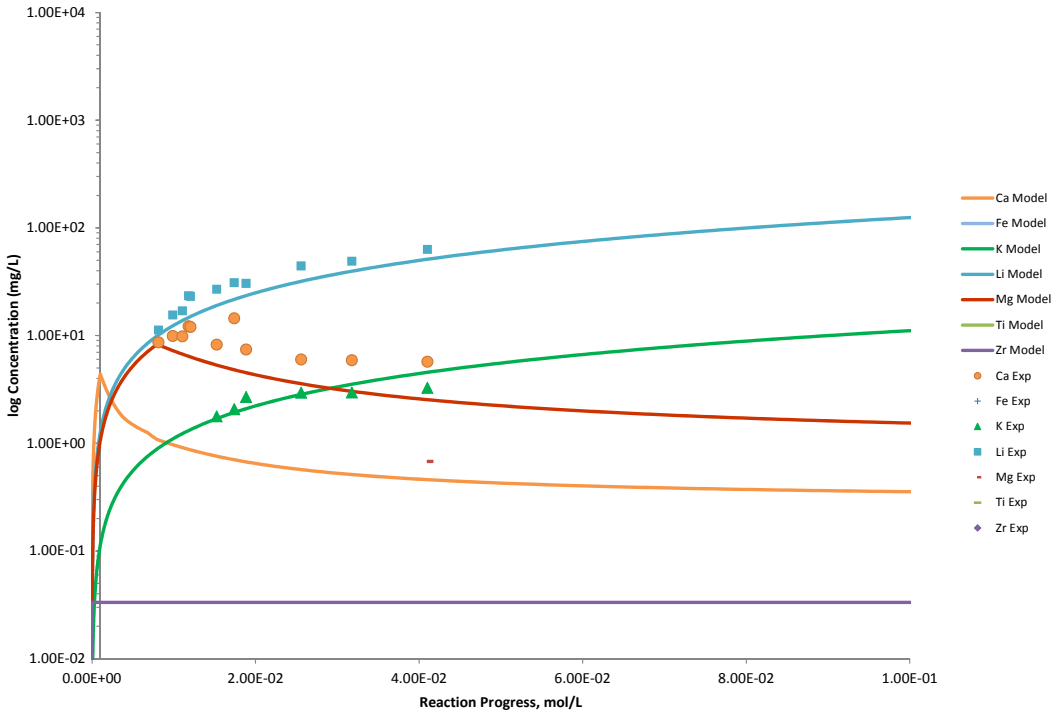


**Figure B.246**. Measured Solution Concentrations (mg/L) and Model Results for Ca, Fe, K, Li, Mg, Ti, and Zr, as a Function of Reaction Progress (mol-glass/kg) Determined for Glass Sample LAWB69

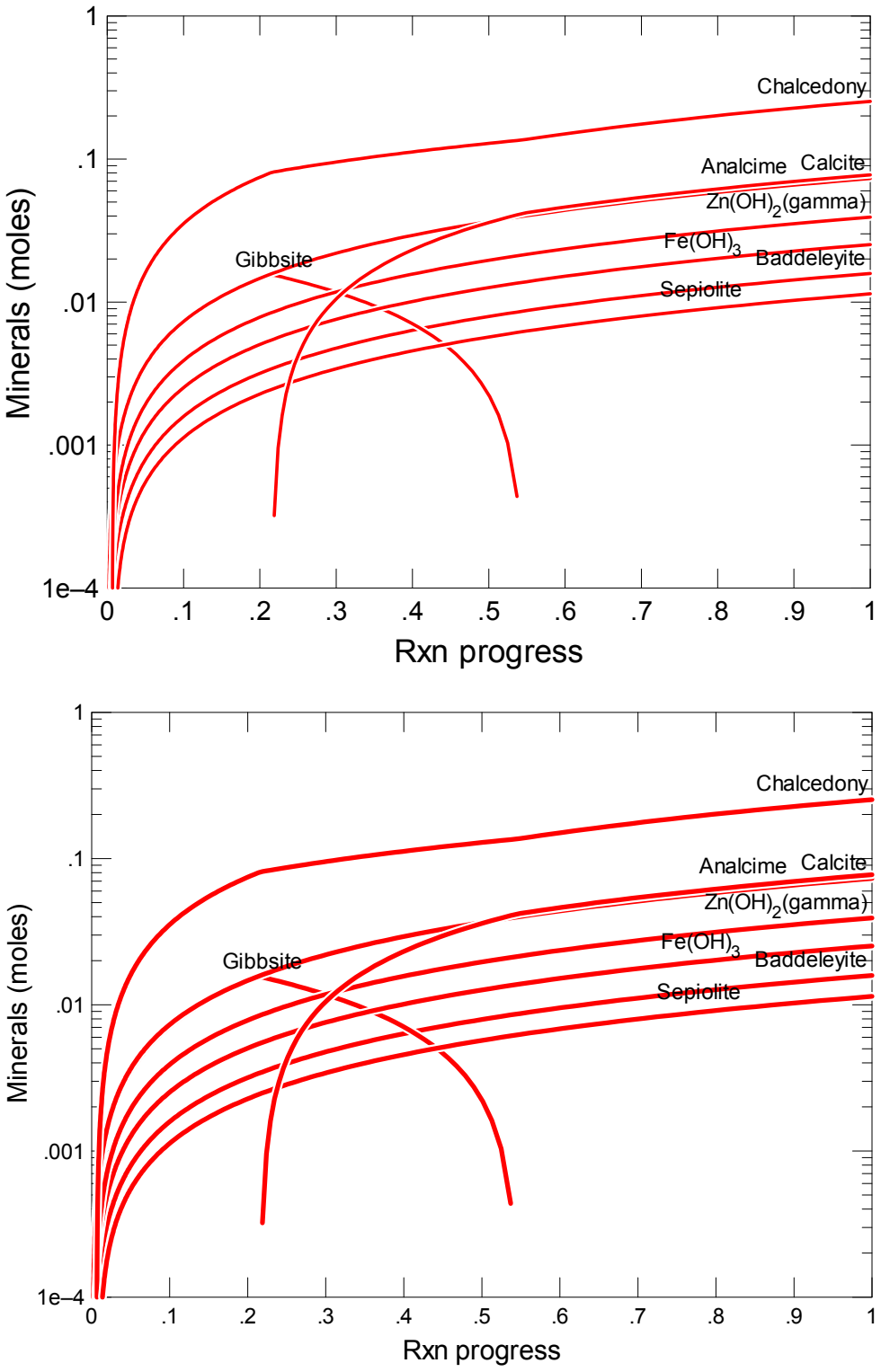


**Figure B.247**. Secondary Phases Calculated to Form as a Function of Reaction Progress (mol-glass/kg) Determined for Glass Sample LAWB70

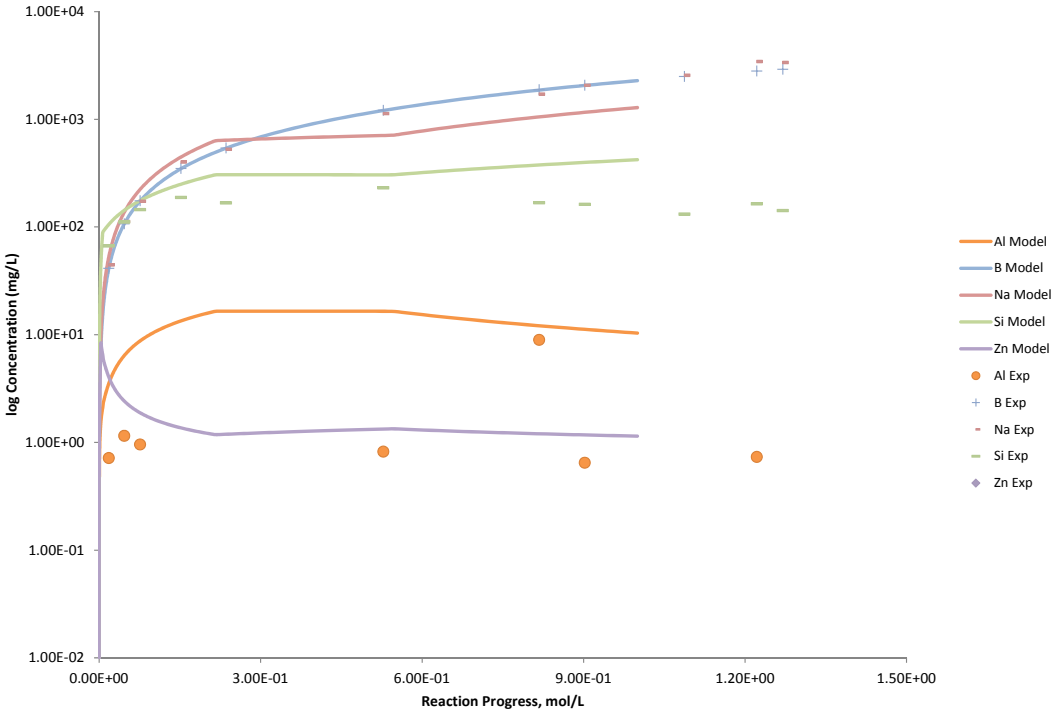


**Figure B.248**. Measured Solution Concentrations (mg/L) and Model Results for Al, B, Na, Si, and Zn, as a Function of Reaction Progress (mol-glass/kg) Determined for Glass Sample LAWB70

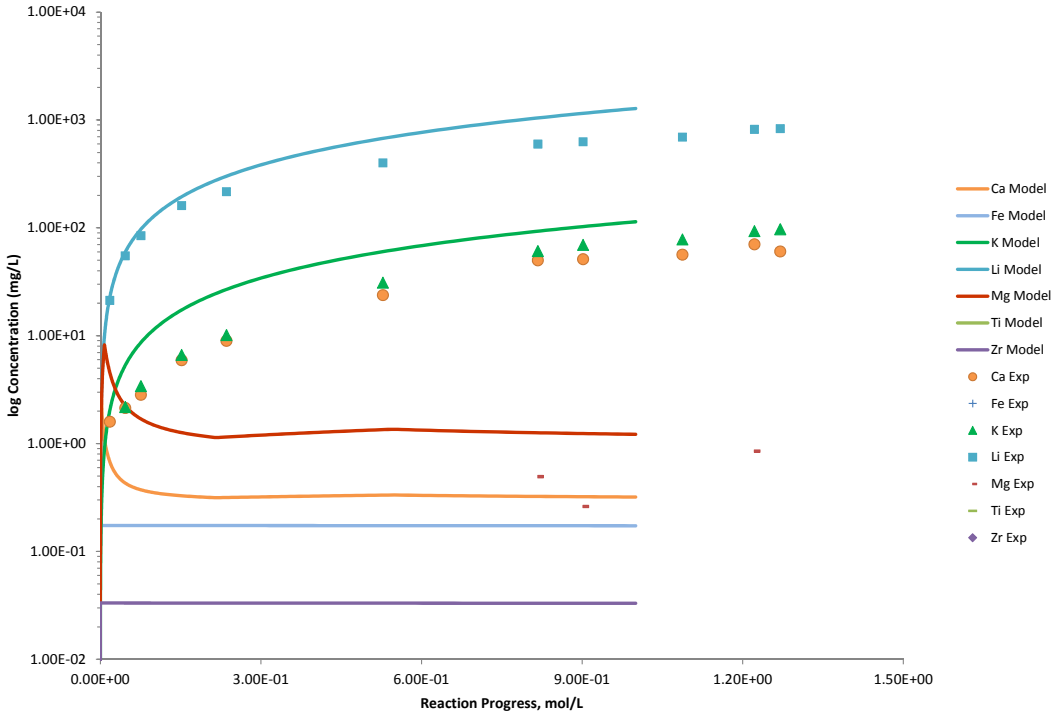


**Figure B.249**. Measured Solution Concentrations (mg/L) and Model Results for Ca, Fe, K, Li, Mg, Ti, and Zr, as a Function of Reaction Progress (mol-glass/kg) Determined for Glass Sample LAWB70

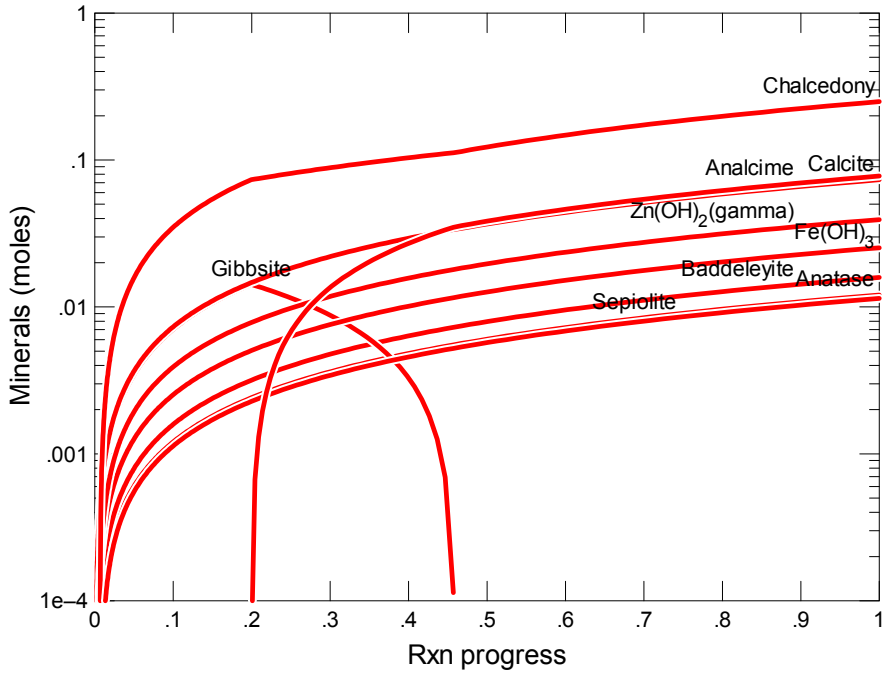


**Figure B.250**. Secondary Phases Calculated to Form as a Function of Reaction Progress (mol-glass/kg) Determined for Glass Sample LAWB71

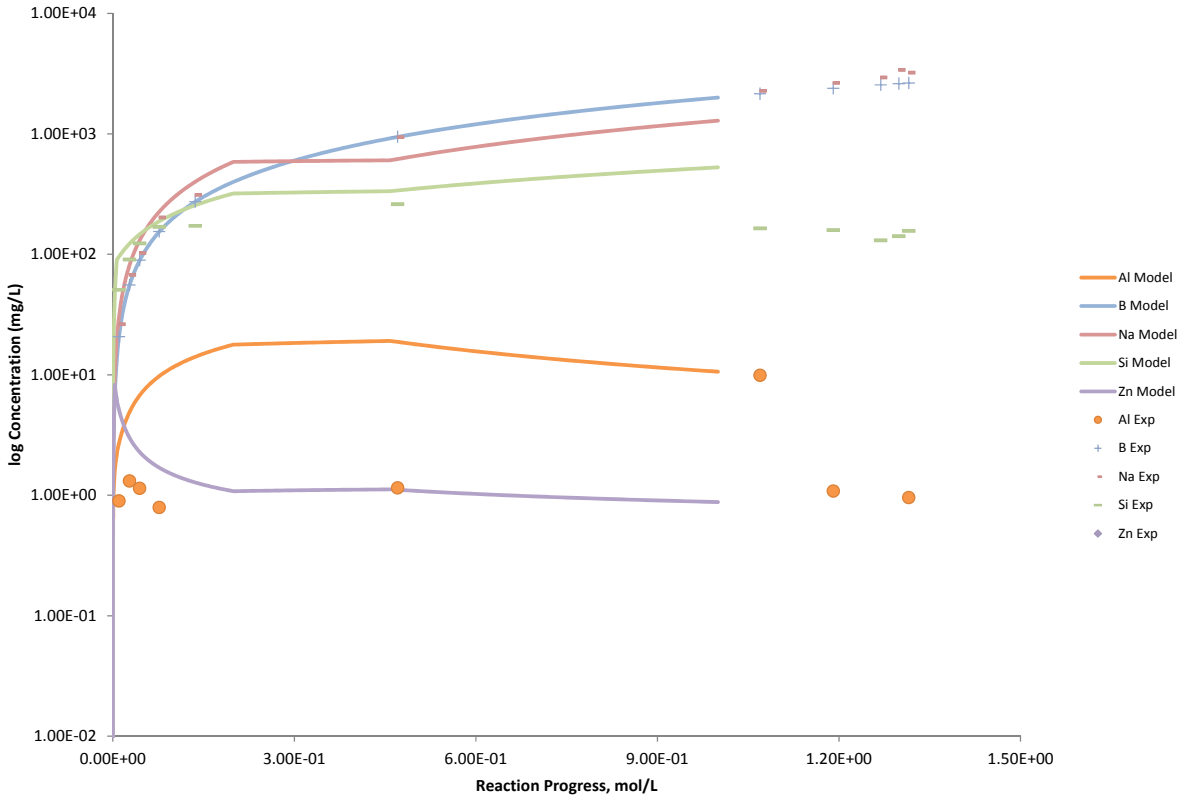


**Figure B.251**. Measured Solution Concentrations (mg/L) and Model Results for Al, B, Na, Si, and Zn, as a Function of Reaction Progress (mol-glass/kg) Determined for Glass Sample LAWB71

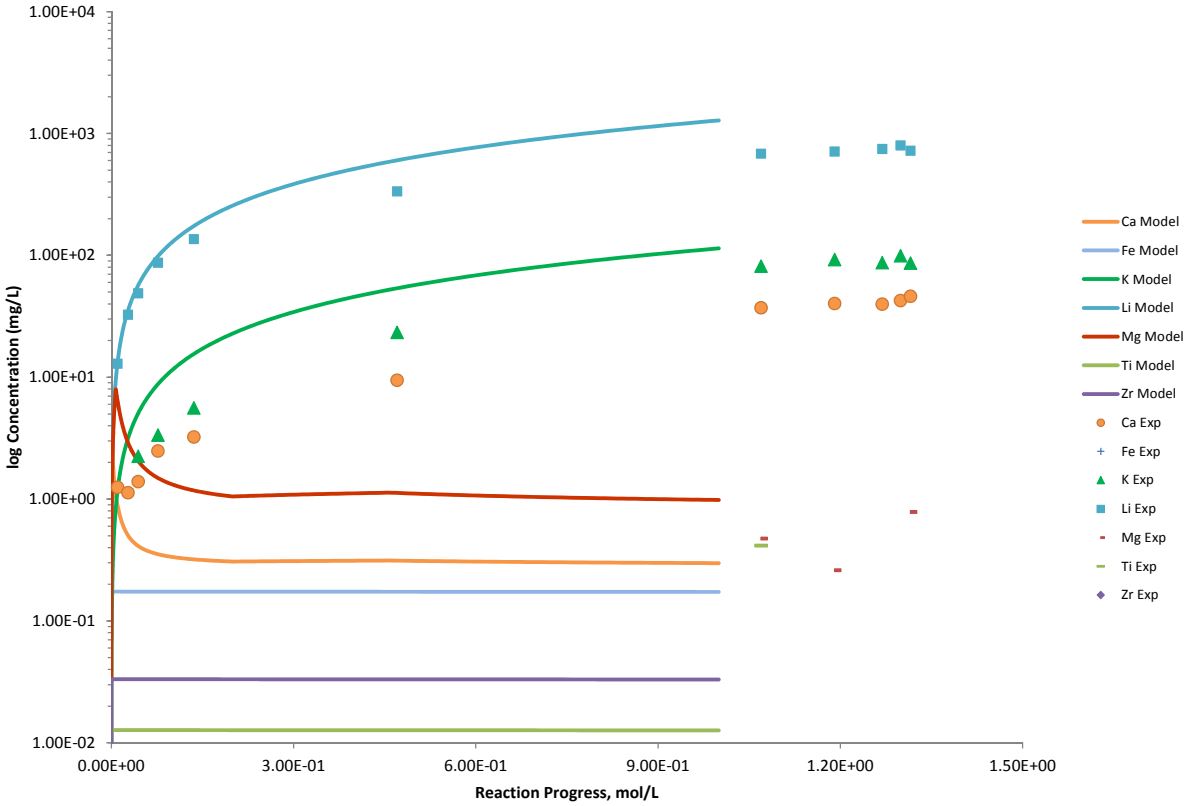


**Figure B.252**. Measured Solution Concentrations (mg/L) and Model Results for Ca, Fe, K, Li, Mg, Ti, and Zr, as a Function of Reaction Progress (mol-glass/kg) Determined for Glass Sample LAWB71

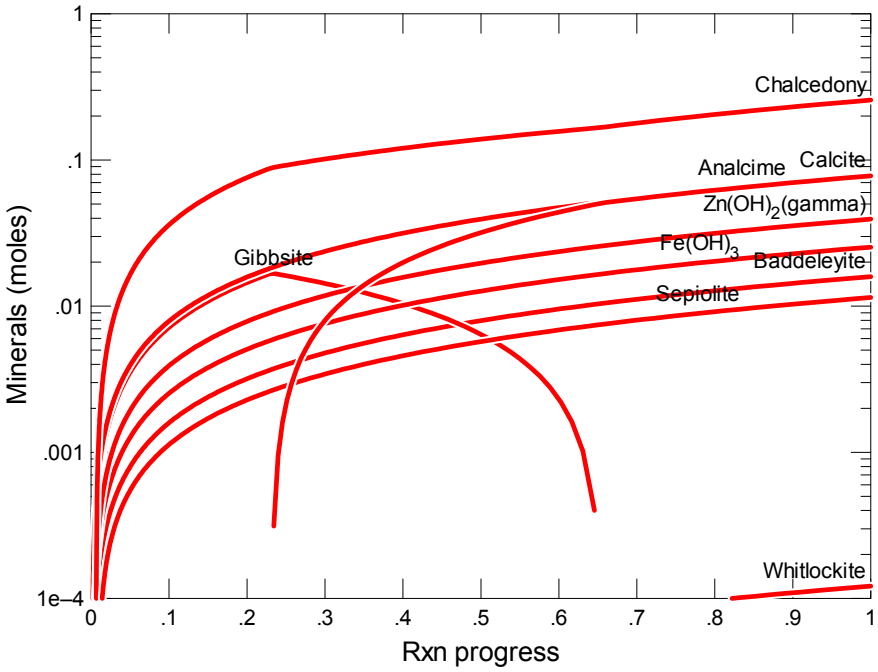


**Figure B.253**. Secondary Phases Calculated to Form as a Function of Reaction Progress (mol-glass/kg) Determined for Glass Sample LAWB72

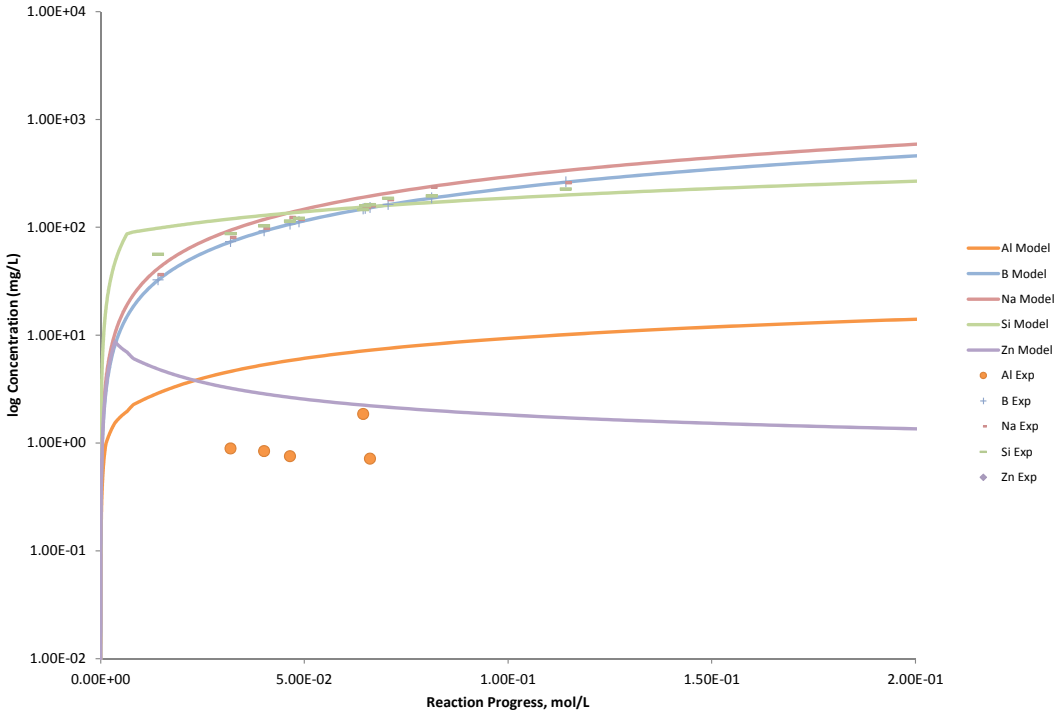


**Figure B.254**. Measured Solution Concentrations (mg/L) and Model Results for Al, B, Na, Si, and Zn, as a Function of Reaction Progress (mol-glass/kg) Determined for Glass Sample LAWB72

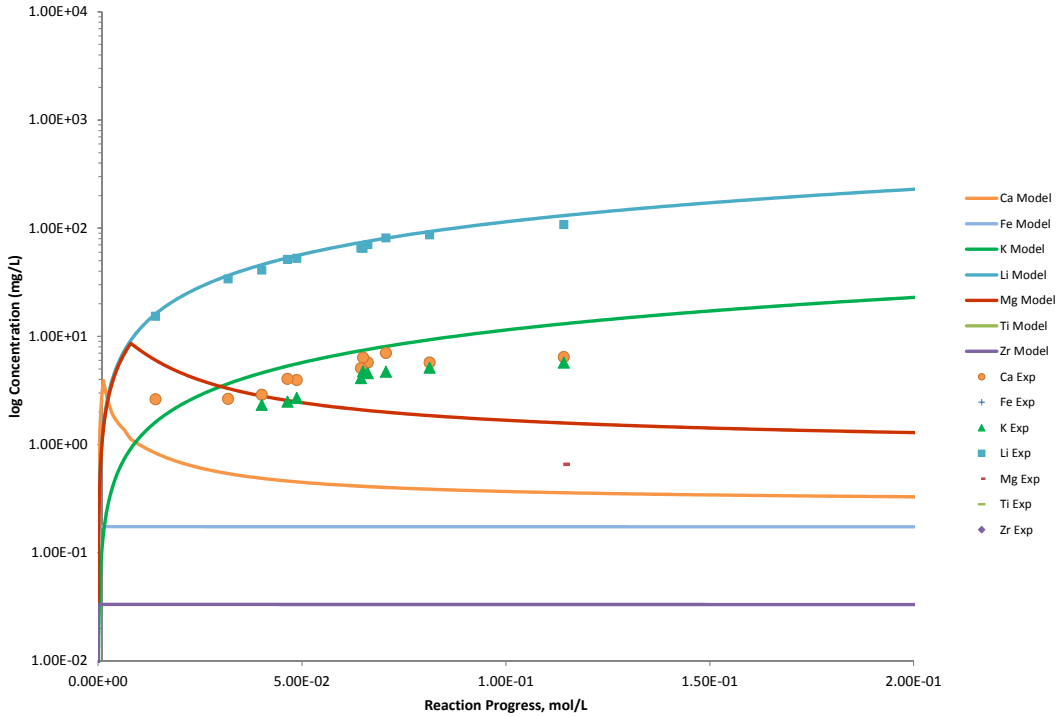


**Figure B.255**. Measured Solution Concentrations (mg/L) and Model Results for Ca, Fe, K, Li, Mg, Ti, and Zr, as a Function of Reaction Progress (mol-glass/kg) Determined for Glass Sample LAWB72

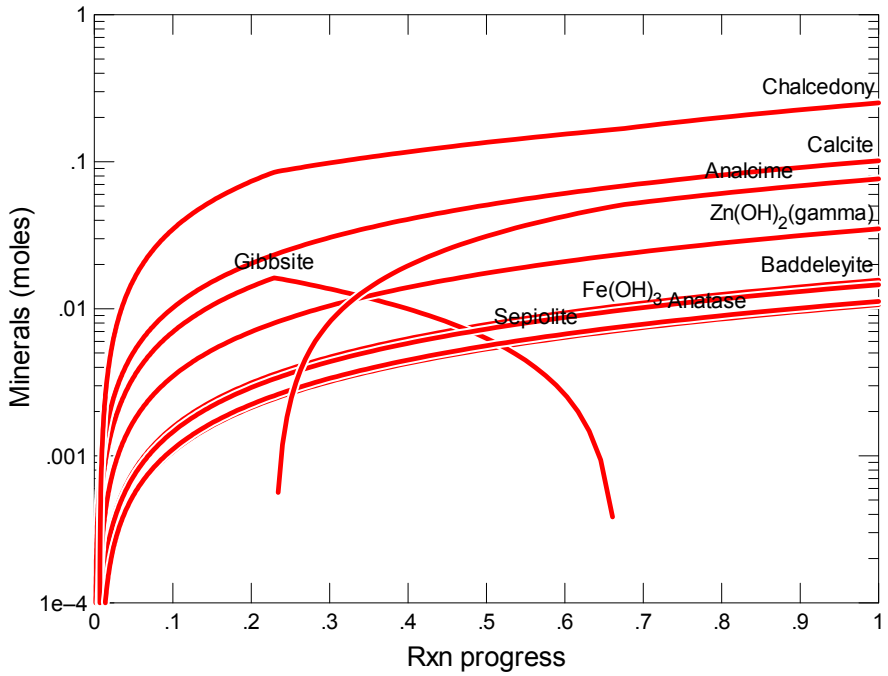


**Figure B.256**. Secondary Phases Calculated to Form as a Function of Reaction Progress (mol-glass/kg) Determined for Glass Sample LAWB73

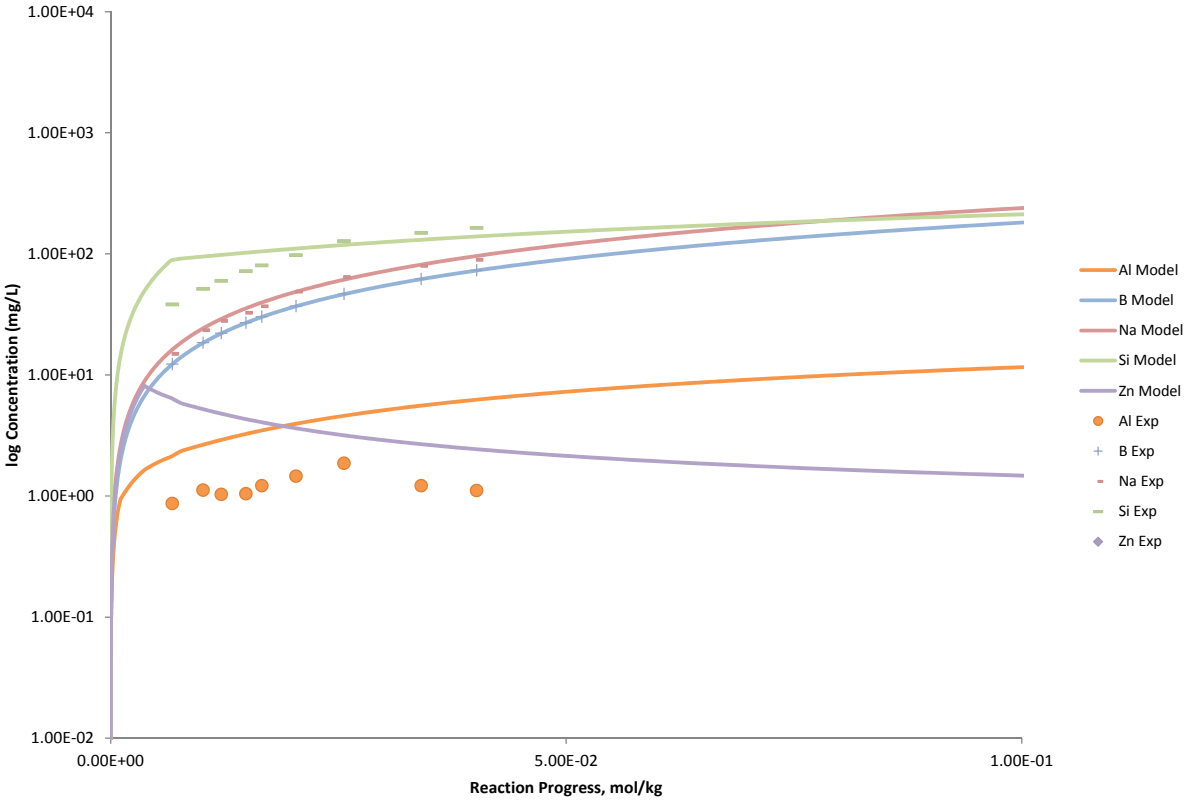


**Figure B.257**. Measured Solution Concentrations (mg/L) and Model Results for Al, B, Na, Si, and Zn, as a Function of Reaction Progress (mol-glass/kg) Determined for Glass Sample LAWB73

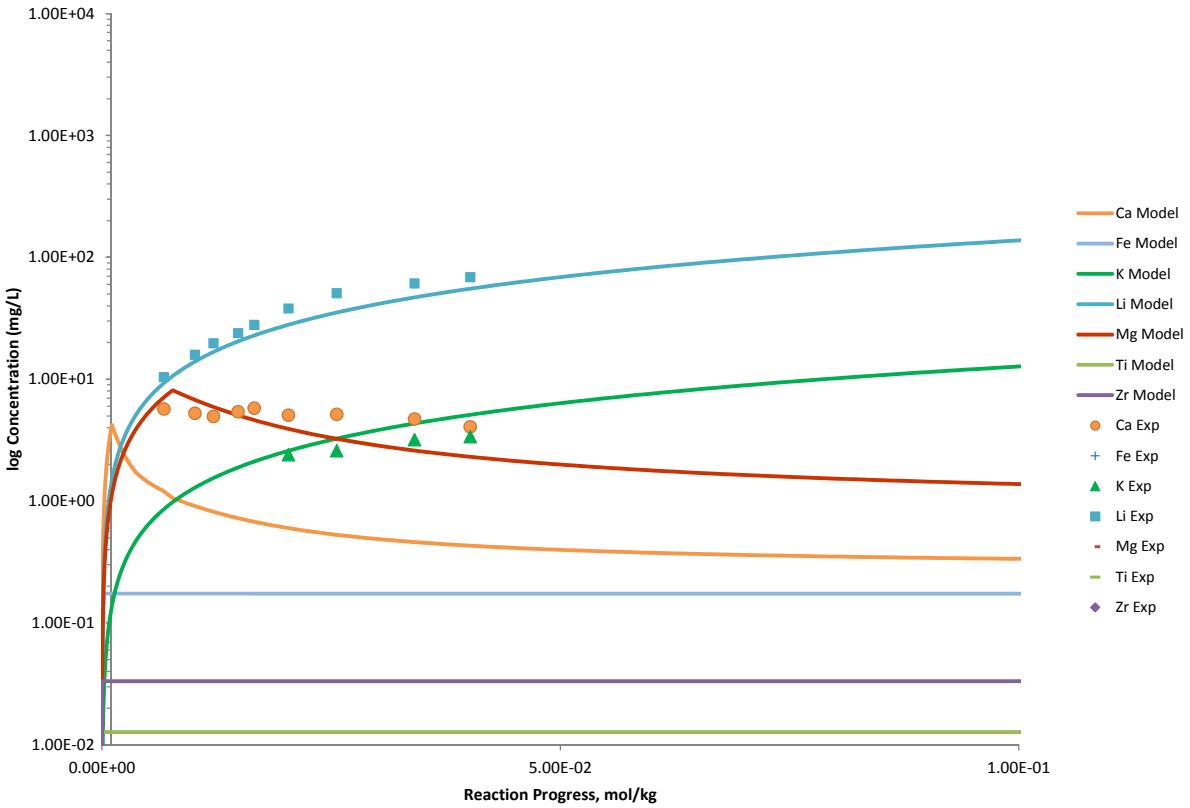


**Figure B.258**. Measured Solution Concentrations (mg/L) and Model Results for Ca, Fe, K, Li, Mg, Ti, and Zr, as a Function of Reaction Progress (mol-glass/kg) Determined for Glass Sample LAWB73

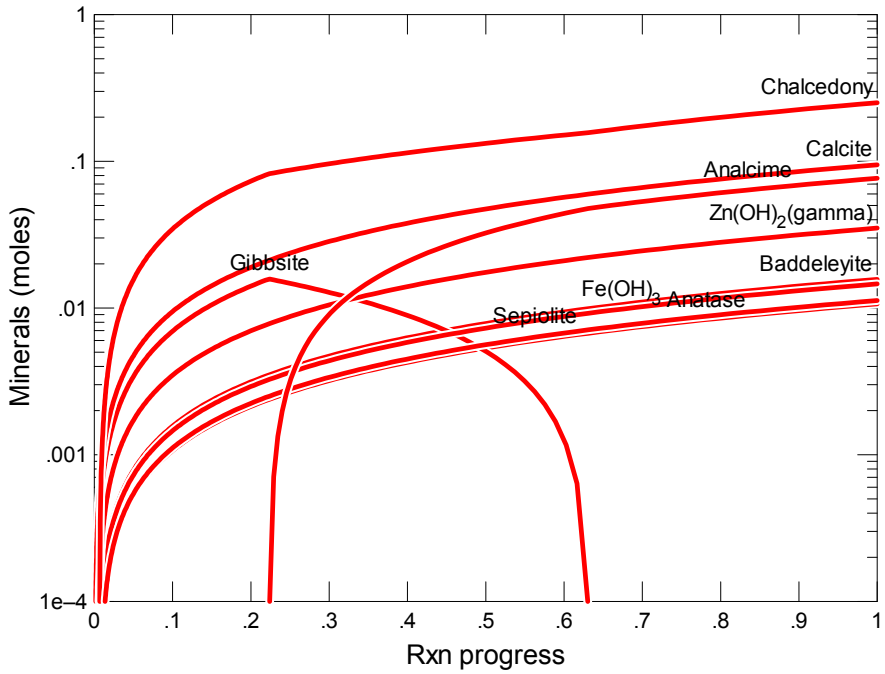


**Figure B.259**. Secondary Phases Calculated to Form as a Function of Reaction Progress (mol-glass/kg) Determined for Glass Sample LAWB74

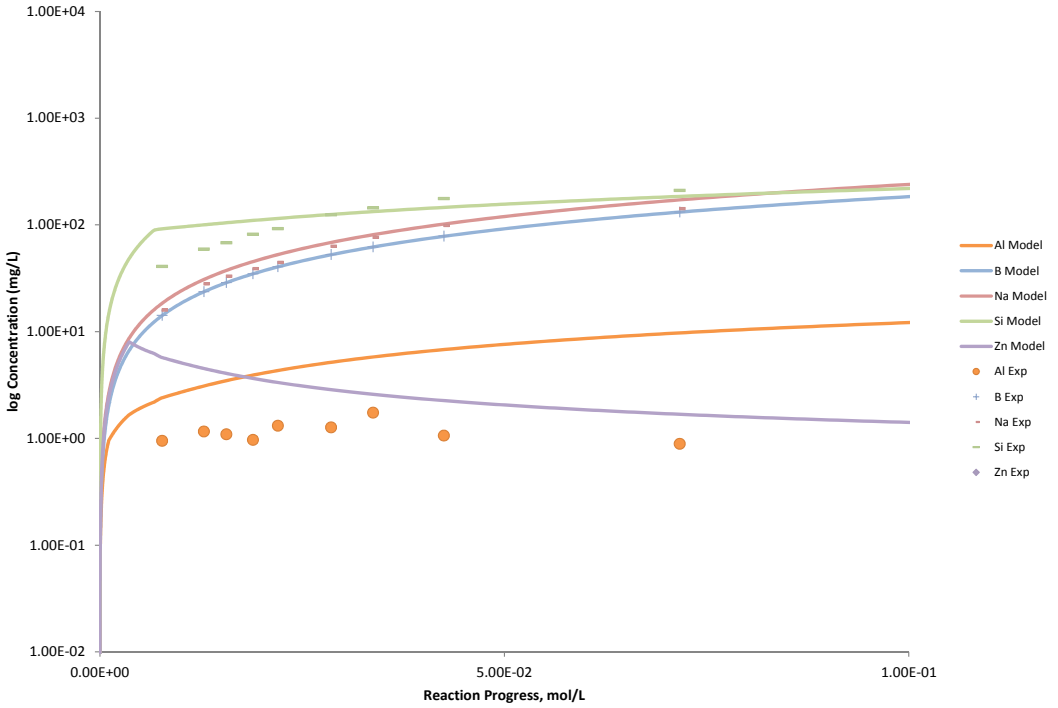


**Figure B.260**. Measured Solution Concentrations (mg/L) and Model Results for Al, B, Na, Si, and Zn, as a Function of Reaction Progress (mol-glass/kg) Determined for Glass Sample LAWB74

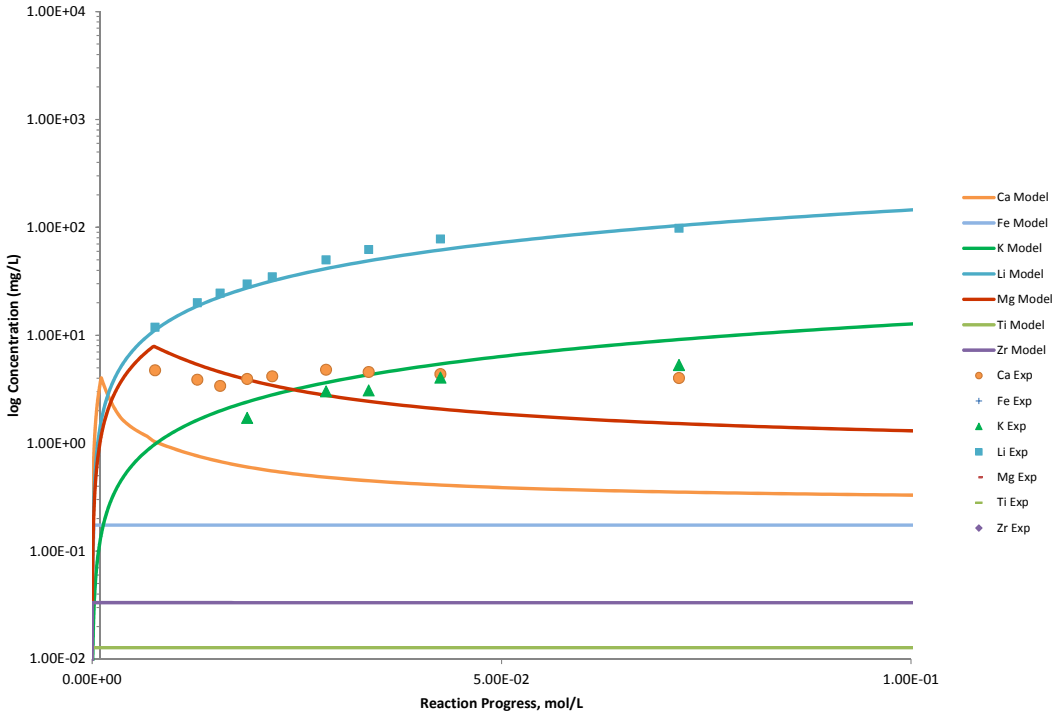


**Figure B.261**. Measured Solution Concentrations (mg/L) and Model Results for Ca, Fe, K, Li, Mg, Ti, and Zr, as a Function of Reaction Progress (mol-glass/kg) Determined for Glass Sample LAWB74

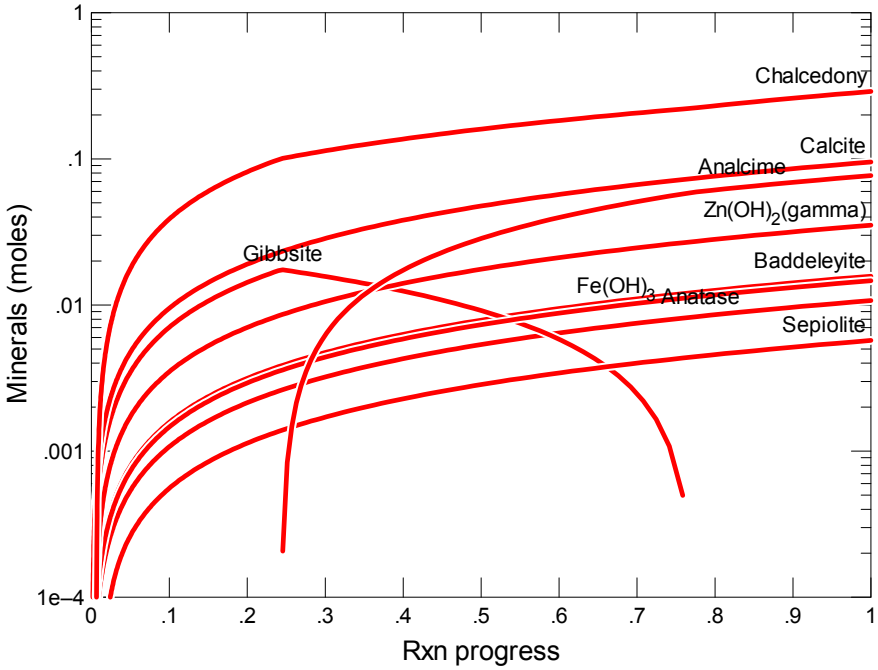


**Figure B.262**. Secondary Phases Calculated to Form as a Function of Reaction Progress (mol-glass/kg) Determined for Glass Sample LAWB75

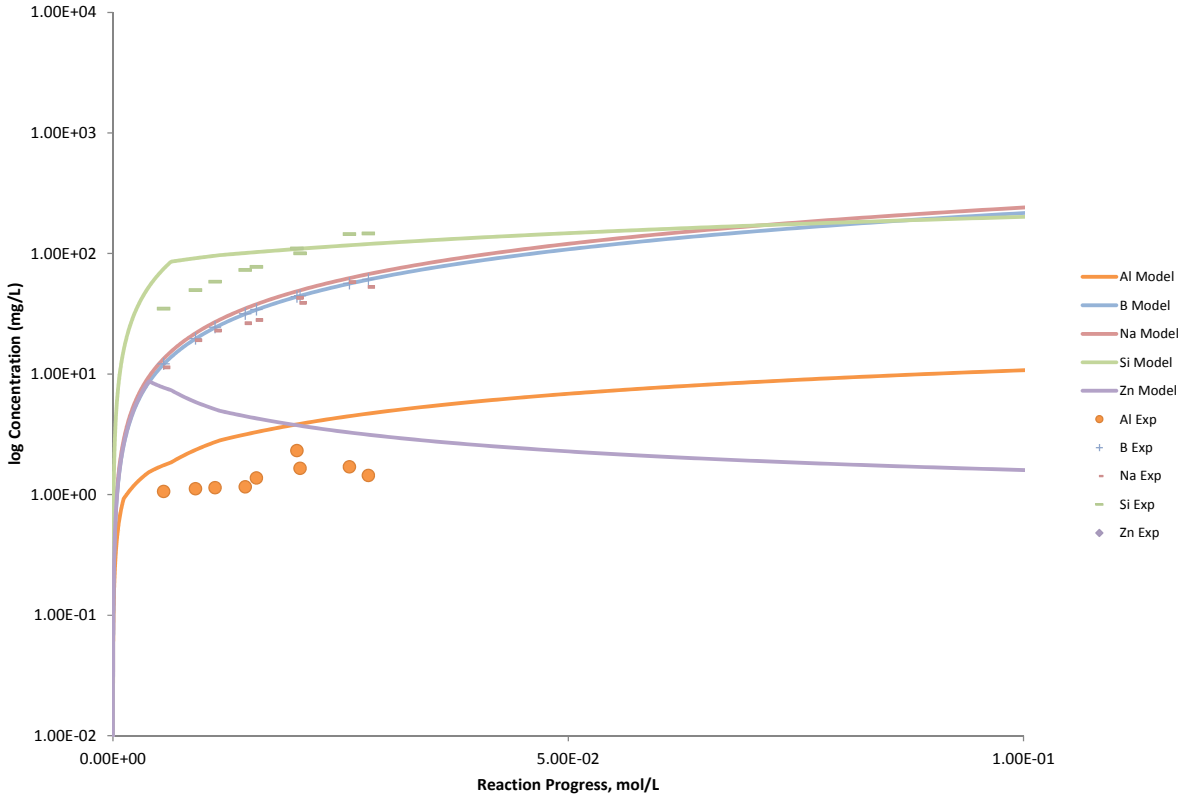


**Figure B.263**. Measured Solution Concentrations (mg/L) and Model Results for Al, B, Na, Si, and Zn, as a Function of Reaction Progress (mol-glass/kg) Determined for Glass Sample LAWB75

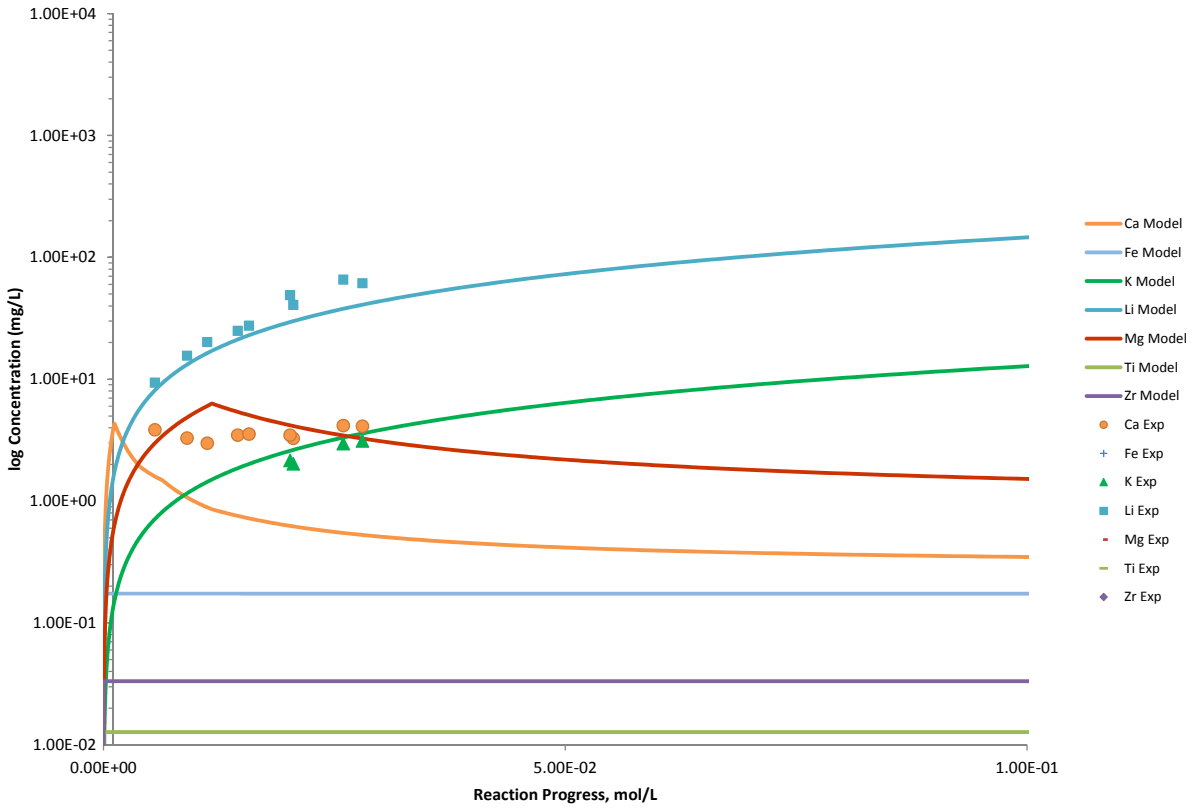


**Figure B.264**. Measured Solution Concentrations (mg/L) and Model Results for Ca, Fe, K, Li, Mg, Ti, and Zr, as a Function of Reaction Progress (mol-glass/kg) Determined for Glass Sample LAWB75

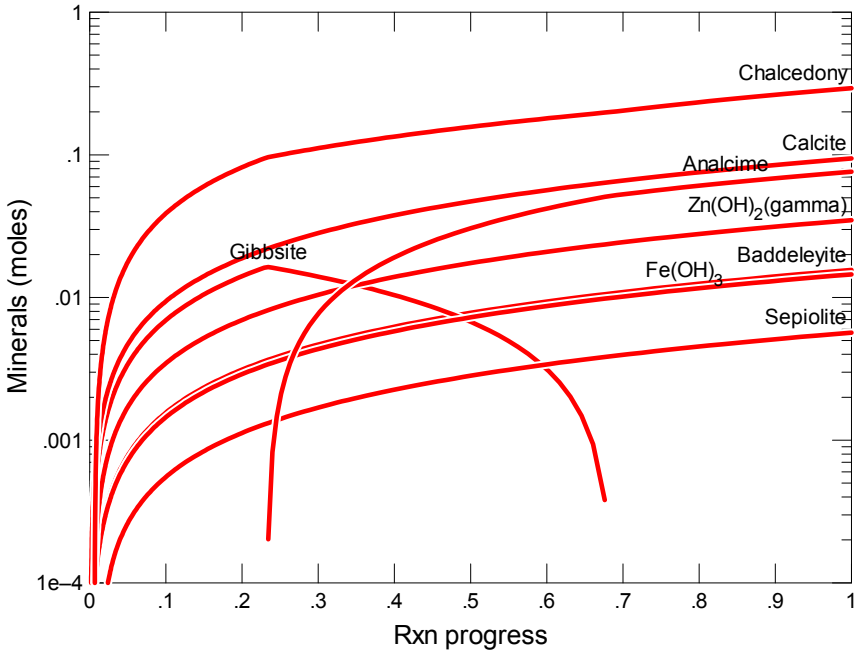


**Figure B.265**. Secondary Phases Calculated to Form as a Function of Reaction Progress (mol-glass/kg) Determined for Glass Sample LAWB76

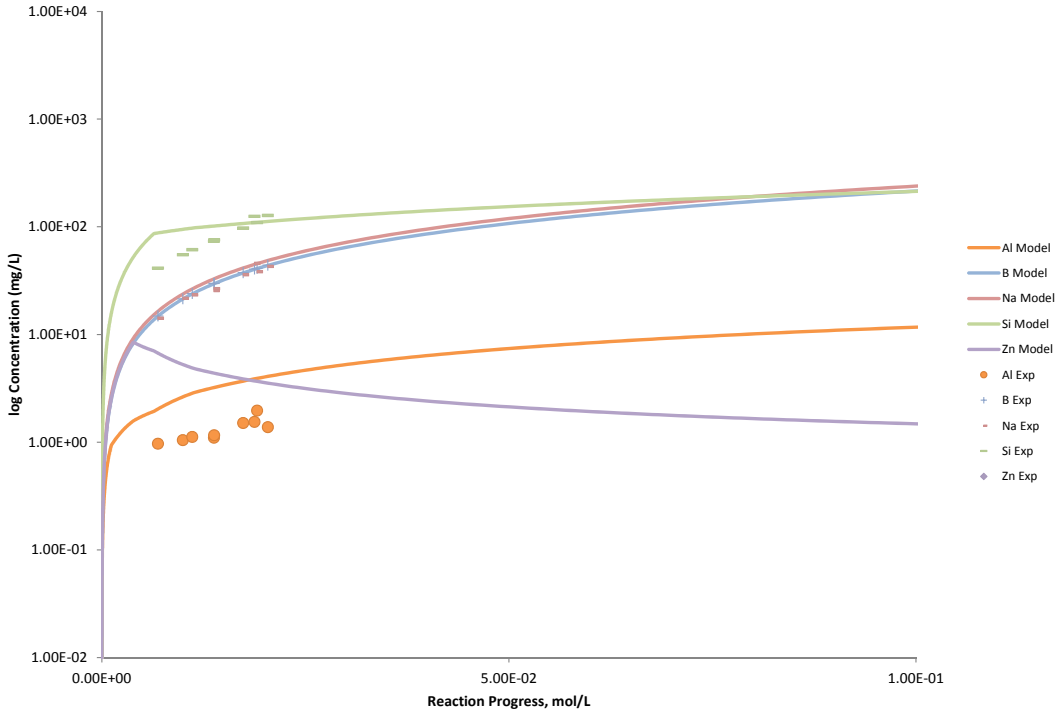


**Figure B.266**. Measured Solution Concentrations (mg/L) and Model Results for Al, B, Na, Si, and Zn, as a Function of Reaction Progress (mol-glass/kg) Determined for Glass Sample LAWB76

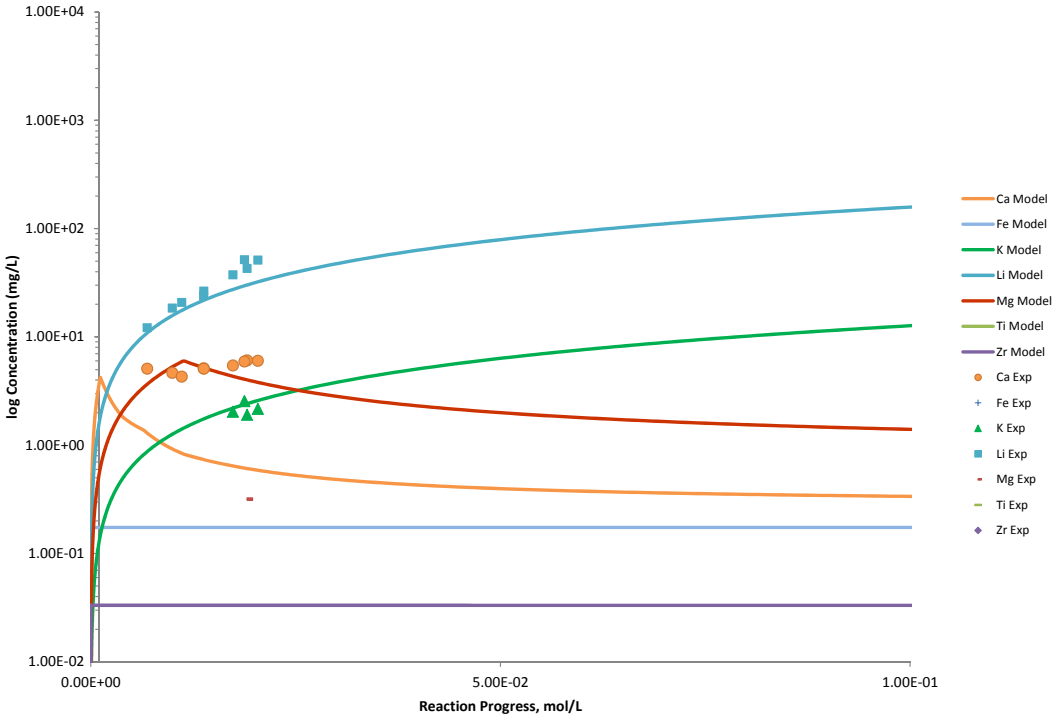


**Figure B.267**. Measured Solution Concentrations (mg/L) and Model Results for Ca, Fe, K, Li, Mg, Ti, and Zr, as a Function of Reaction Progress (mol-glass/kg) Determined for Glass Sample LAWB76

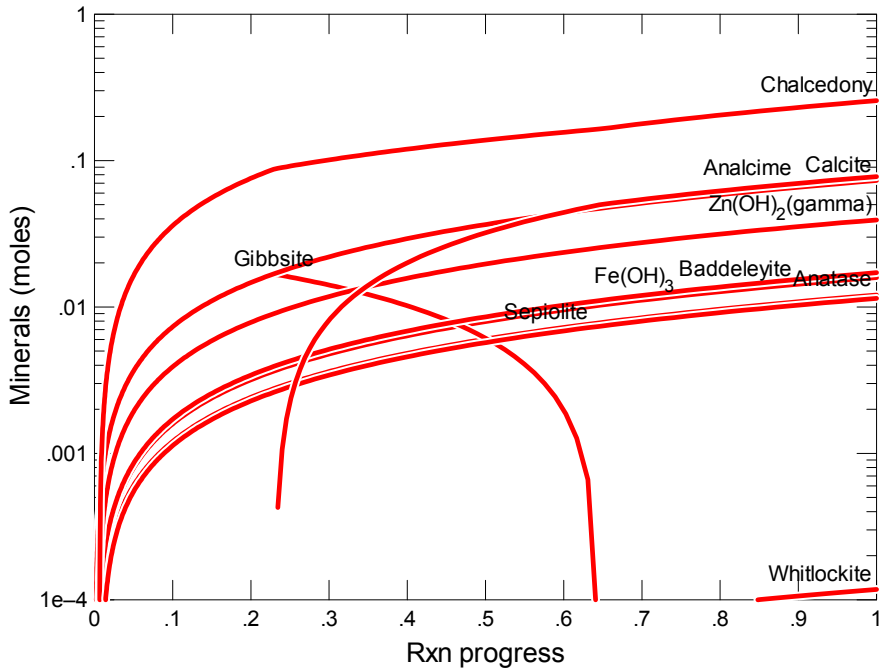


**Figure B.268**. Secondary Phases Calculated to Form as a Function of Reaction Progress (mol-glass/kg) Determined for Glass Sample LAWB77

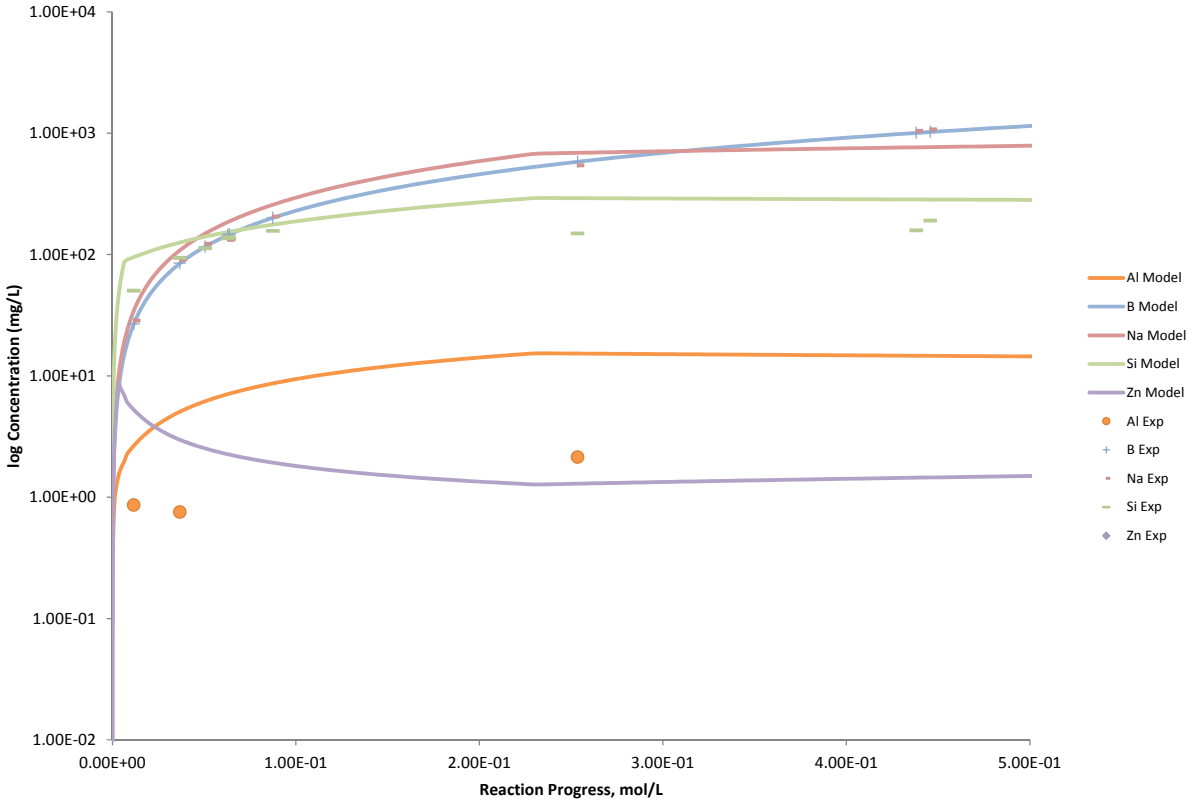


**Figure B.269**. Measured Solution Concentrations (mg/L) and Model Results for Al, B, Na, Si, and Zn, as a Function of Reaction Progress (mol-glass/kg) Determined for Glass Sample LAWB77

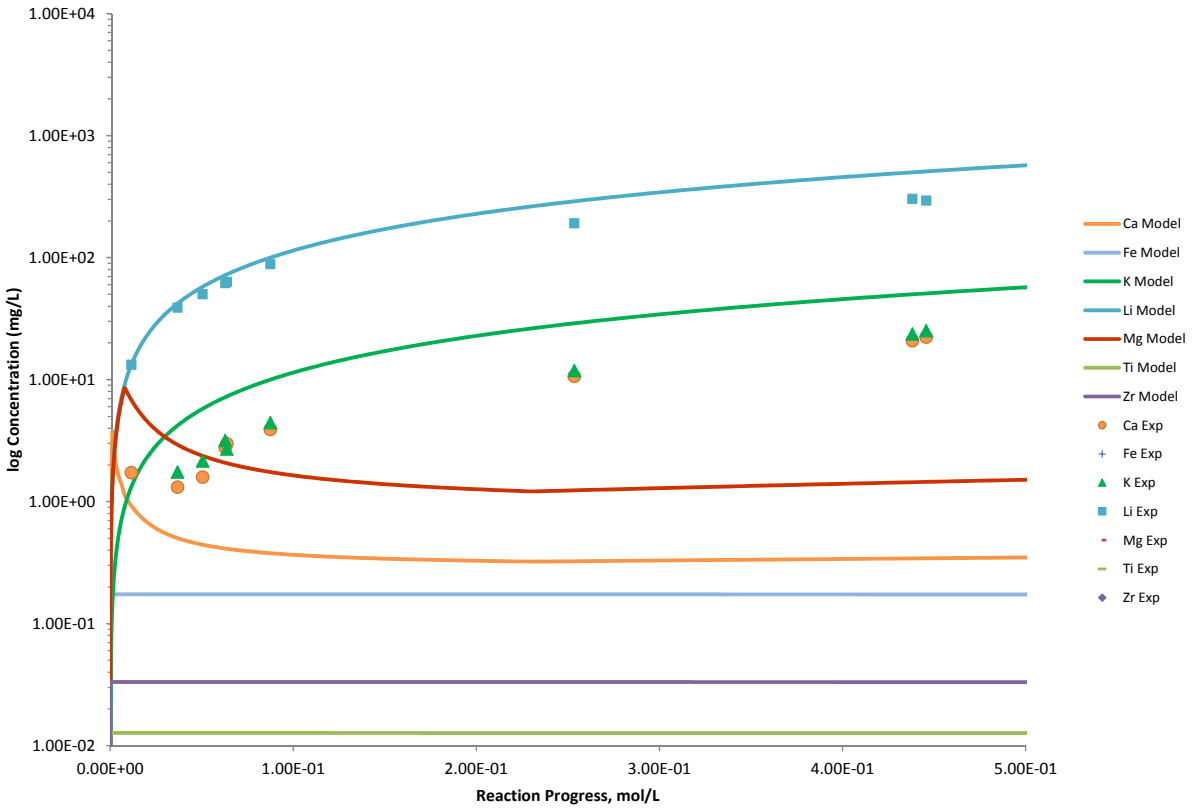


**Figure B.270**. Measured Solution Concentrations (mg/L) and Model Results for Ca, Fe, K, Li, Mg, Ti, and Zr, as a Function of Reaction Progress (mol-glass/kg) Determined for Glass Sample LAWB77

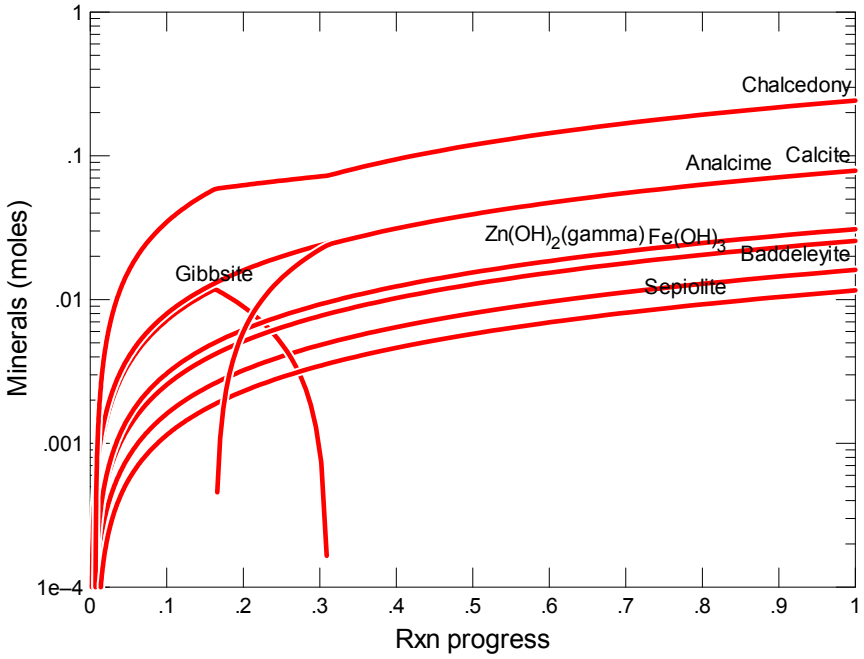


**Figure B.271**. Secondary Phases Calculated to Form as a Function of Reaction Progress (mol-glass/kg) Determined for Glass Sample LAWB78

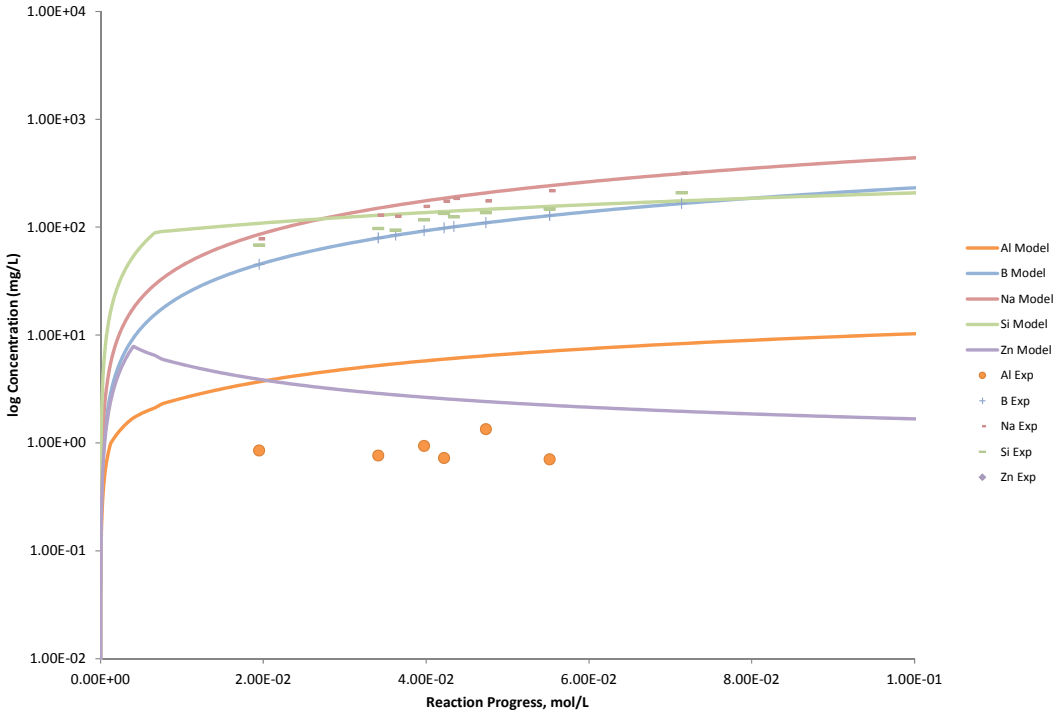


**Figure B.272**. Measured Solution Concentrations (mg/L) and Model Results for Al, B, Na, Si, and Zn, as a Function of Reaction Progress (mol-glass/kg) Determined for Glass Sample LAWB78

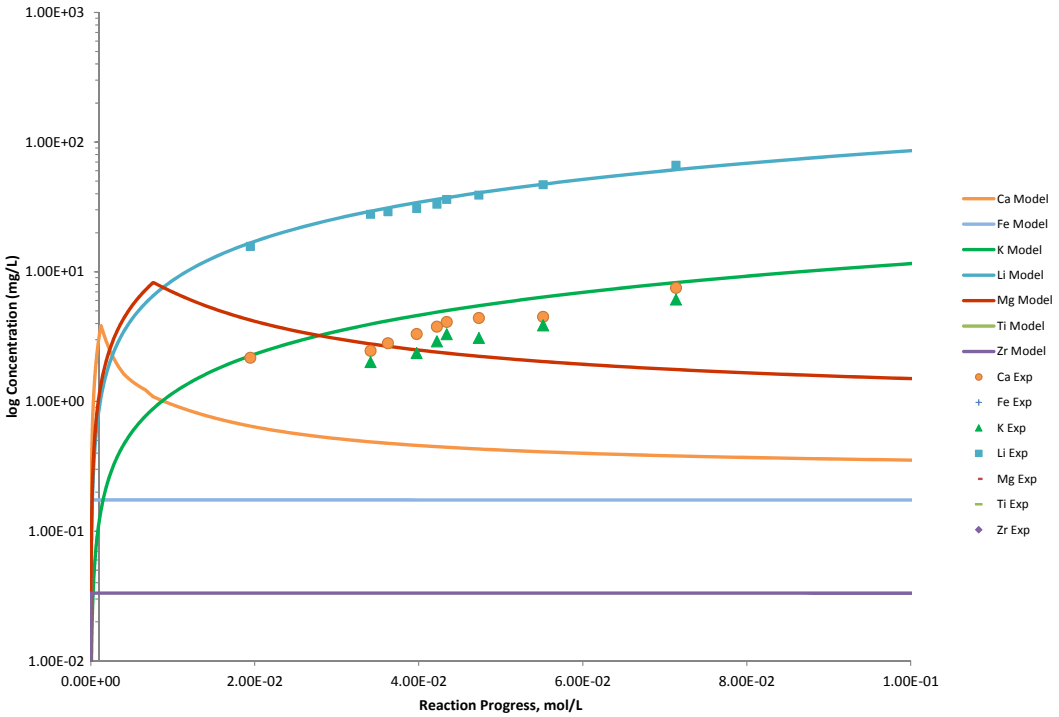


**Figure B.273**. Measured Solution Concentrations (mg/L) and Model Results for Ca, Fe, K, Li, Mg, Ti, and Zr, as a Function of Reaction Progress (mol-glass/kg) Determined for Glass Sample LAWB78

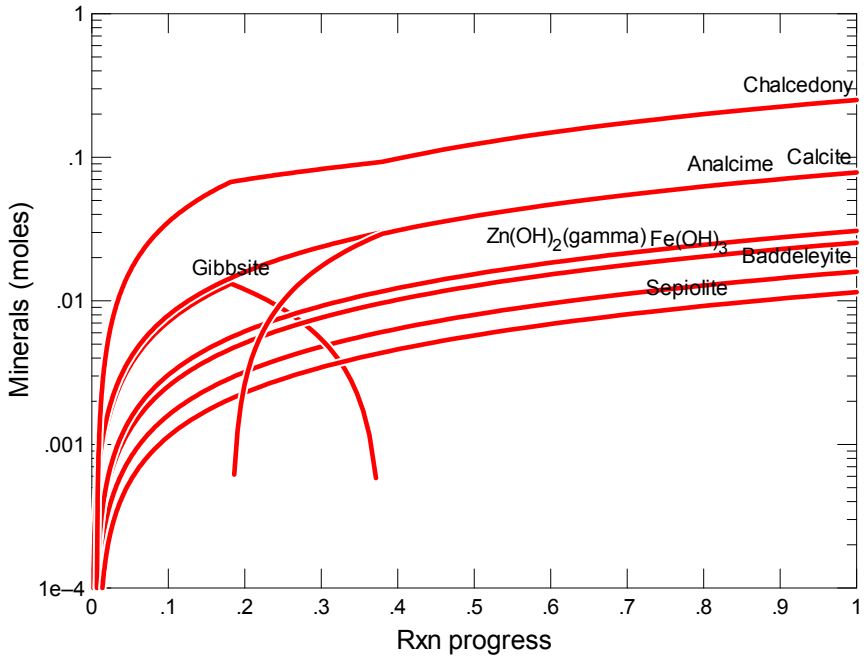


**Figure B.274**. Secondary Phases Calculated to Form as a Function of Reaction Progress (mol-glass/kg) Determined for Glass Sample LAWB79

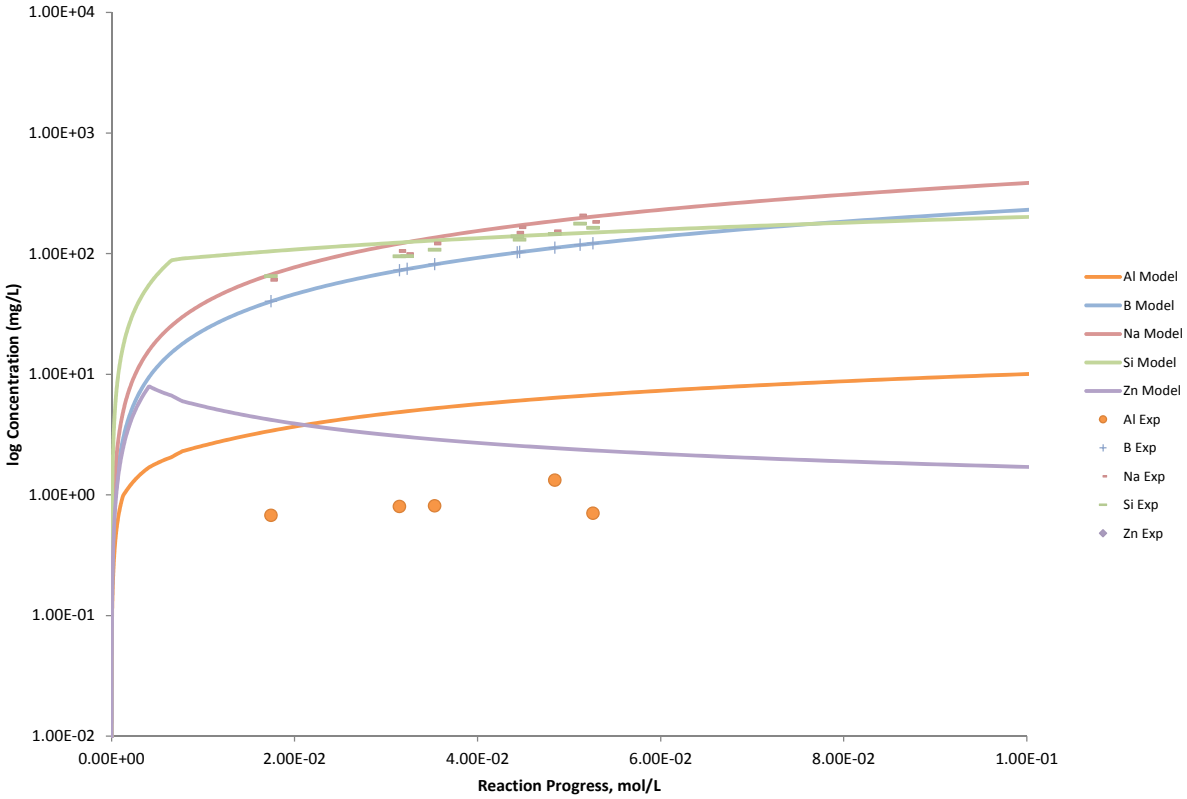


**Figure B.275**. Measured Solution Concentrations (mg/L) and Model Results for Al, B, Na, Si, and Zn, as a Function of Reaction Progress (mol-glass/kg) Determined for Glass Sample LAWB79

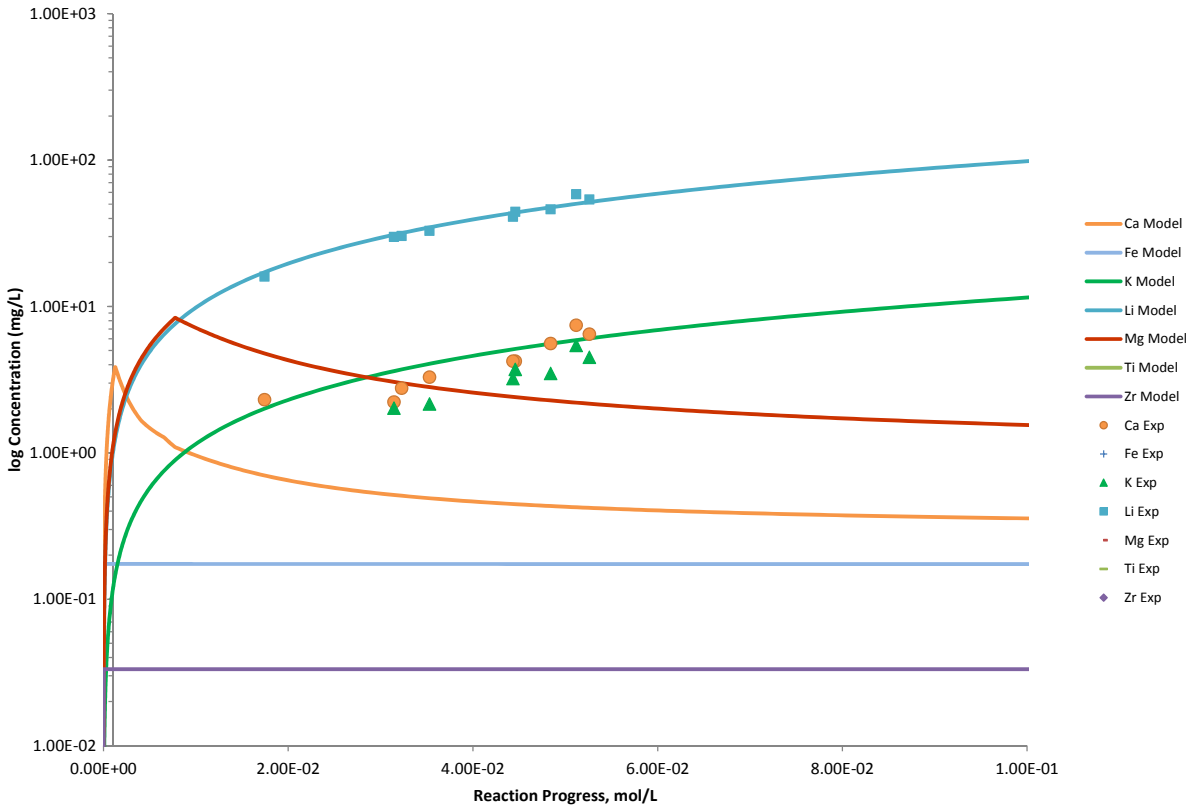


**Figure B.276**. Measured Solution Concentrations (mg/L) and Model Results for Ca, Fe, K, Li, Mg, Ti, and Zr, as a Function of Reaction Progress (mol-glass/kg) Determined for Glass Sample LAWB79

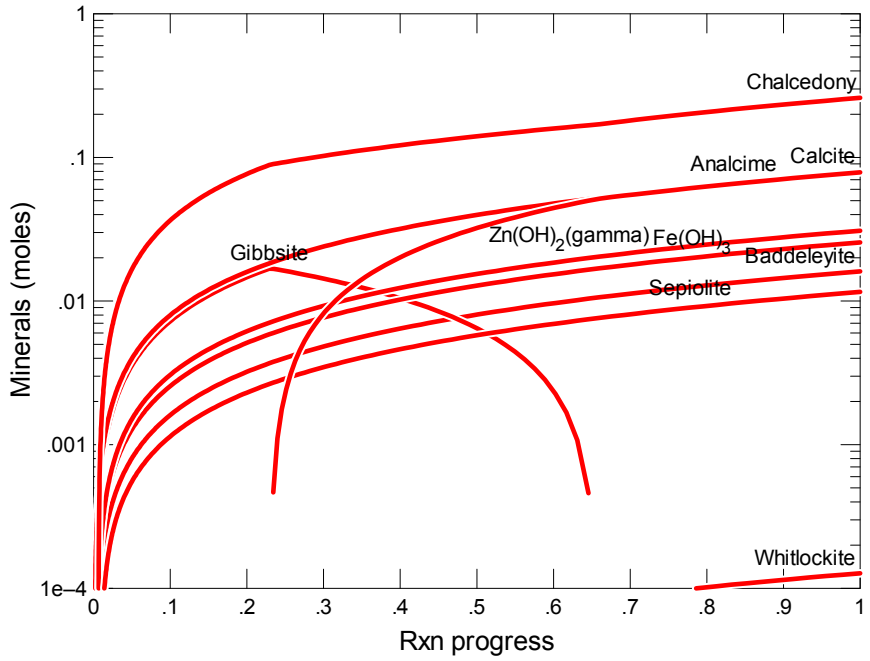


**Figure B.277**. Secondary Phases Calculated to Form as a Function of Reaction Progress (mol-glass/kg) Determined for Glass Sample LAWB80

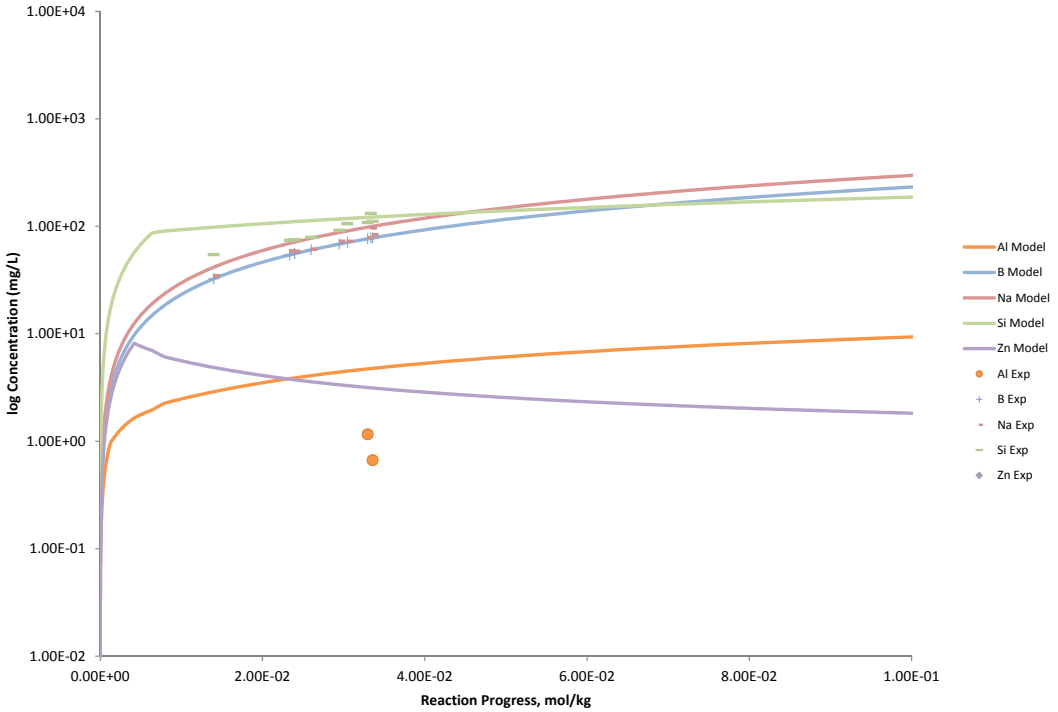


**Figure B.278**. Measured Solution Concentrations (mg/L) and Model Results for Al, B, Na, Si, and Zn, as a Function of Reaction Progress (mol-glass/kg) Determined for Glass Sample LAWB80

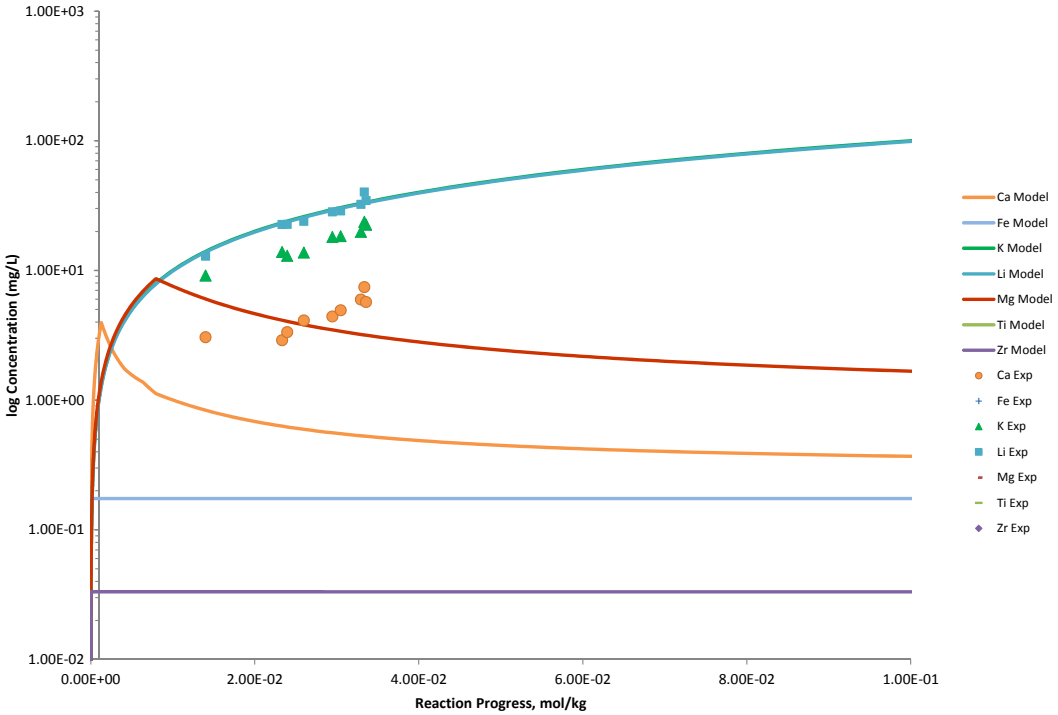


**Figure B.279**. Measured Solution Concentrations (mg/L) and Model Results for Ca, Fe, K, Li, Mg, Ti, and Zr, as a Function of Reaction Progress (mol-glass/kg) Determined for Glass Sample LAWB80

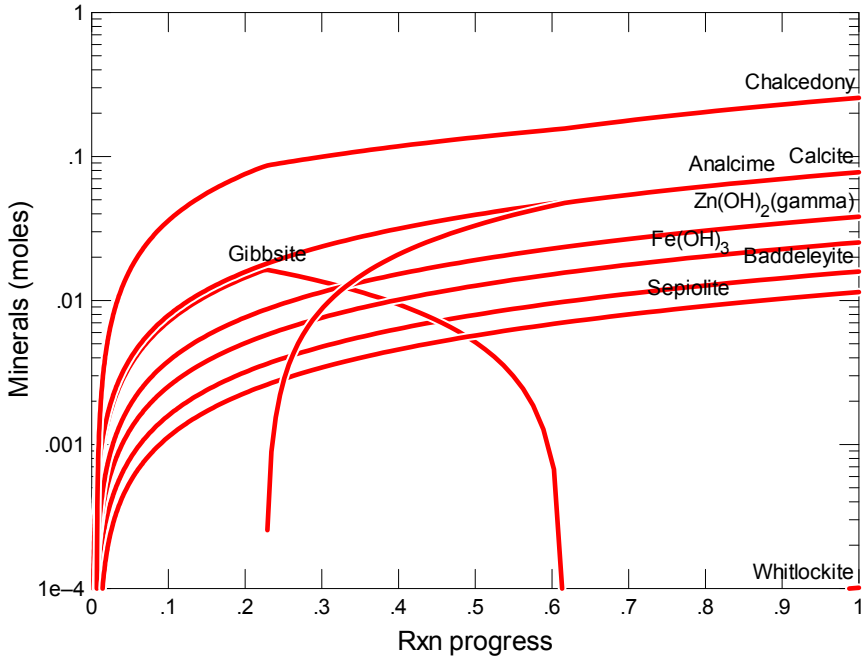


**Figure B.280**. Secondary Phases Calculated to Form as a Function of Reaction Progress (mol-glass/kg) Determined for Glass Sample LAWB81

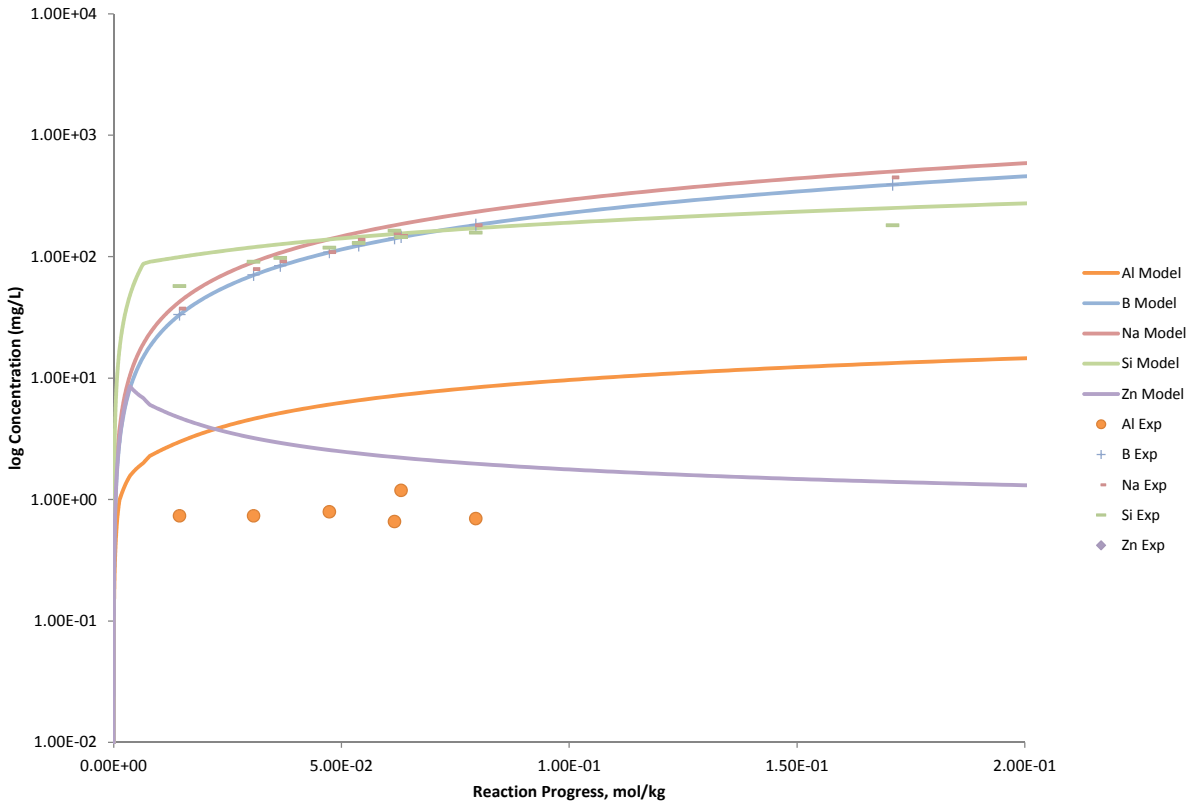


**Figure B.281**. Measured Solution Concentrations (mg/L) and Model Results for Al, B, Na, Si, and Zn, as a Function of Reaction Progress (mol-glass/kg) Determined for Glass Sample LAWB81

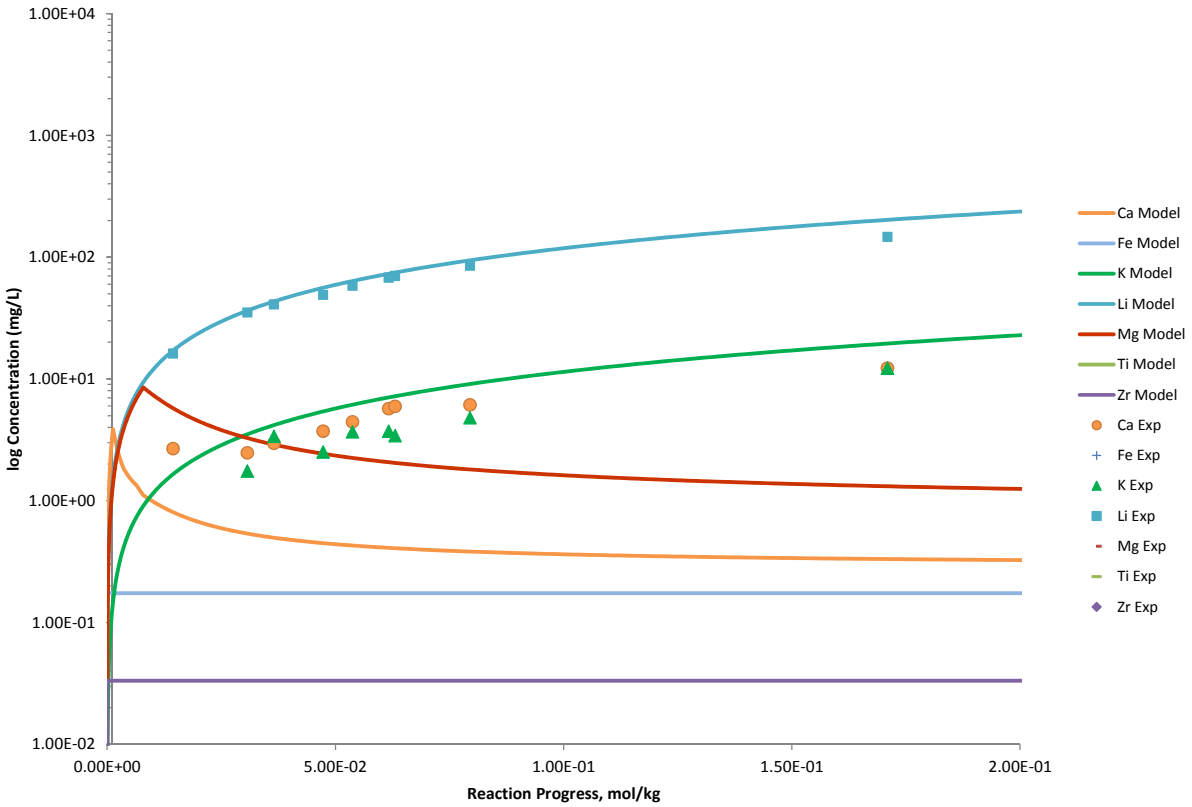


**Figure B.282**. Measured Solution Concentrations (mg/L) and Model Results for Ca, Fe, K, Li, Mg, Ti, and Zr, as a Function of Reaction Progress (mol-glass/kg) Determined for Glass Sample LAWB81

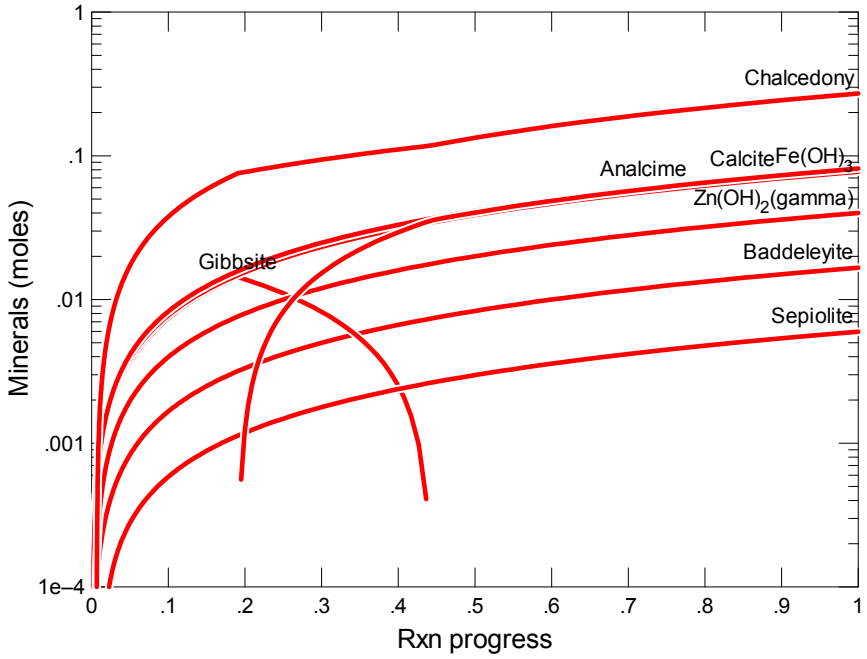


**Figure B.283**. Secondary Phases Calculated to Form as a Function of Reaction Progress (mol-glass/kg) Determined for Glass Sample LAWB82

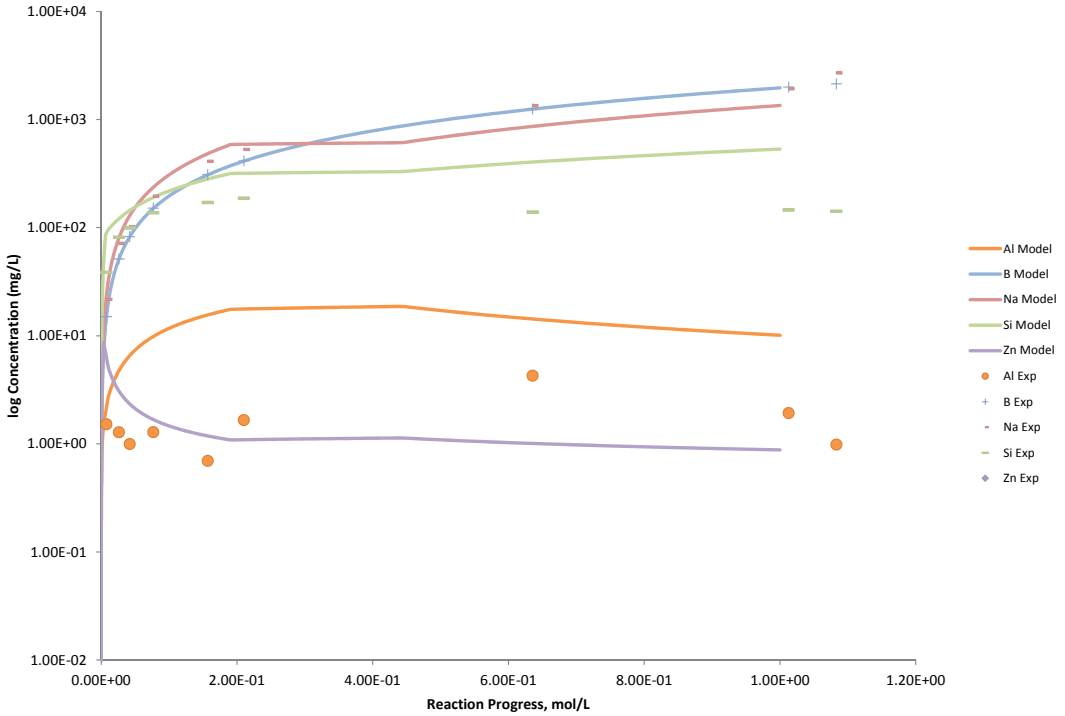


**Figure B.284**. Measured Solution Concentrations (mg/L) and Model Results for Al, B, Na, Si, and Zn, as a Function of Reaction Progress (mol-glass/kg) Determined for Glass Sample LAWB82

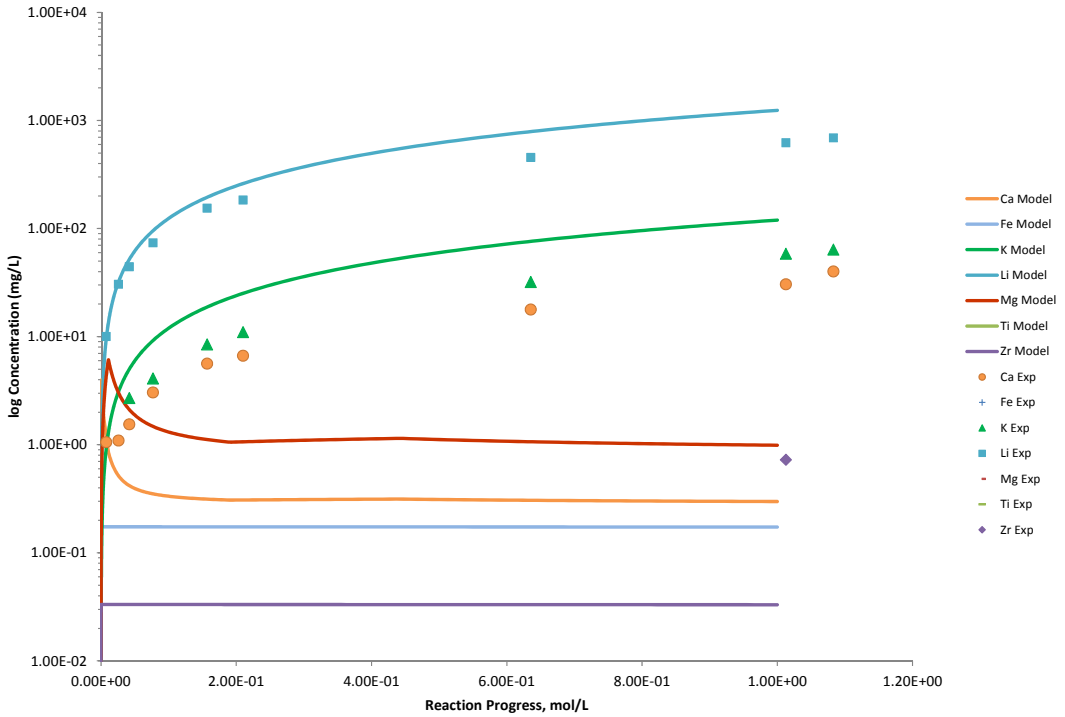


**Figure B.285**. Measured Solution Concentrations (mg/L) and Model Results for Ca, Fe, K, Li, Mg, Ti, and Zr, as a Function of Reaction Progress (mol-glass/kg) Determined for Glass Sample LAWB82

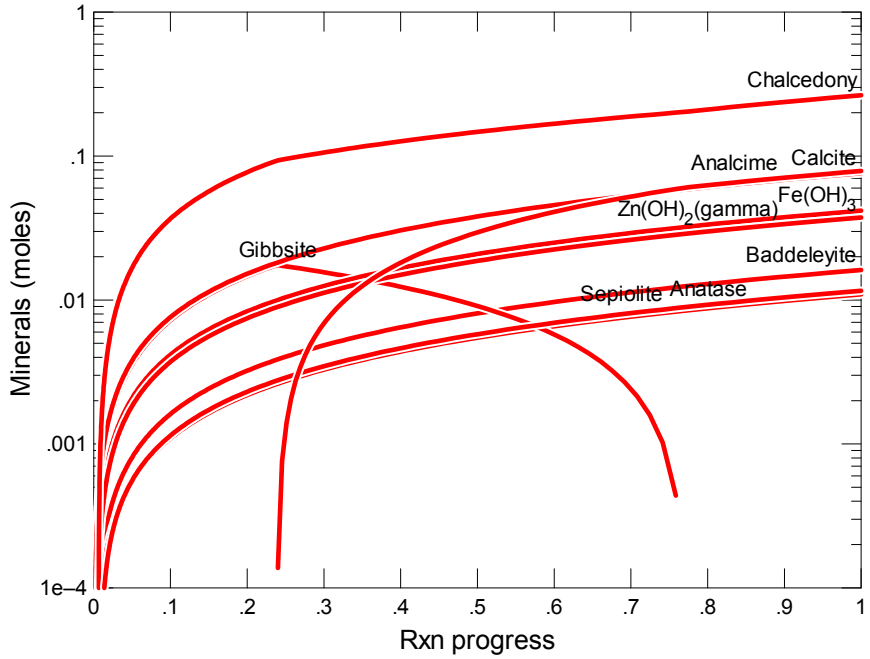


**Figure B.286**. Secondary Phases Calculated to Form as a Function of Reaction Progress (mol-glass/kg) Determined for Glass Sample LAWB83

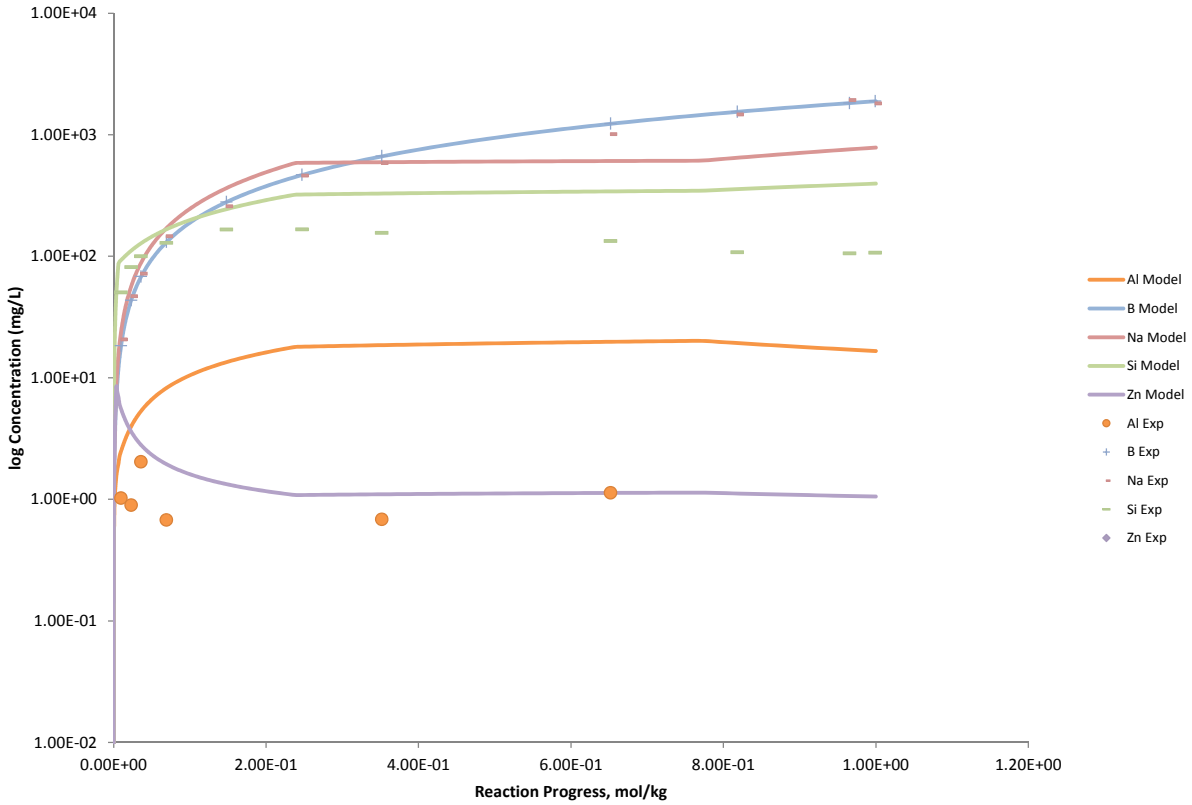


**Figure B.287**. Measured Solution Concentrations (mg/L) and Model Results for Al, B, Na, Si, and Zn, as a Function of Reaction Progress (mol-glass/kg) Determined for Glass Sample LAWB83

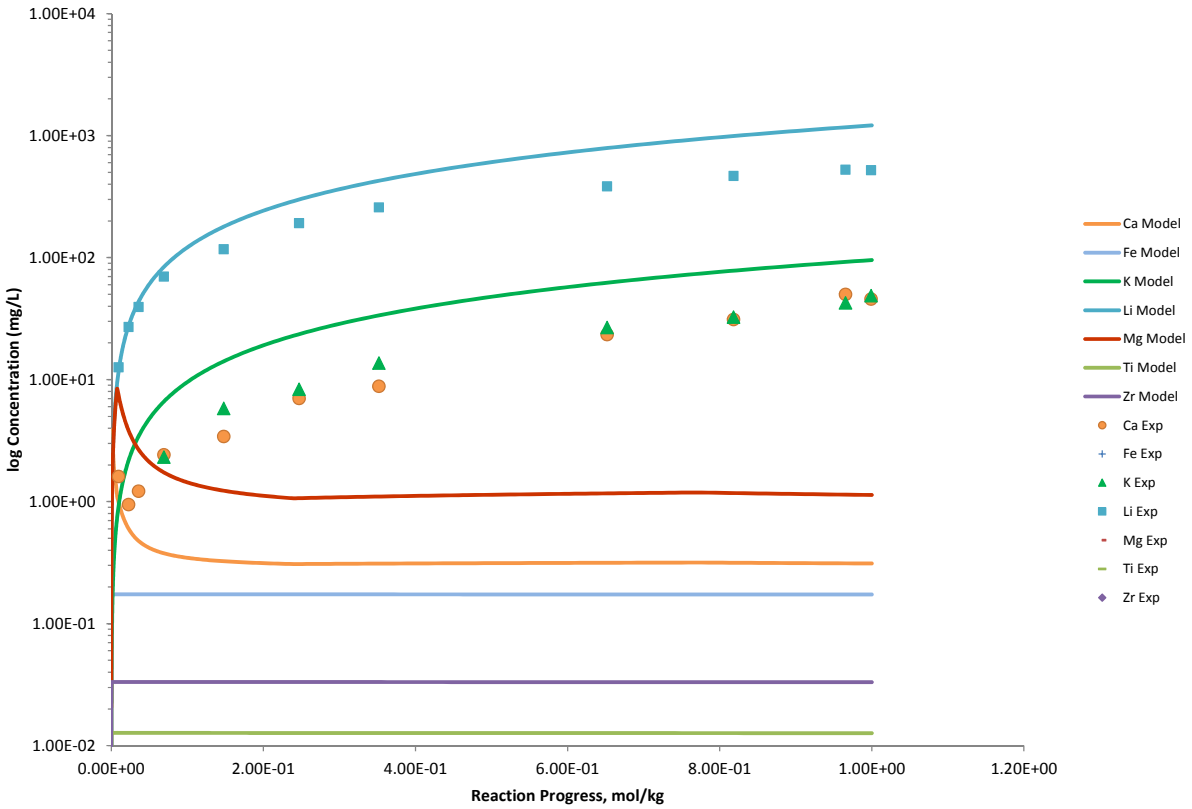


**Figure B.288**. Measured Solution Concentrations (mg/L) and Model Results for Ca, Fe, K, Li, Mg, Ti, and Zr, as a Function of Reaction Progress (mol-glass/kg) Determined for Glass Sample LAWB83

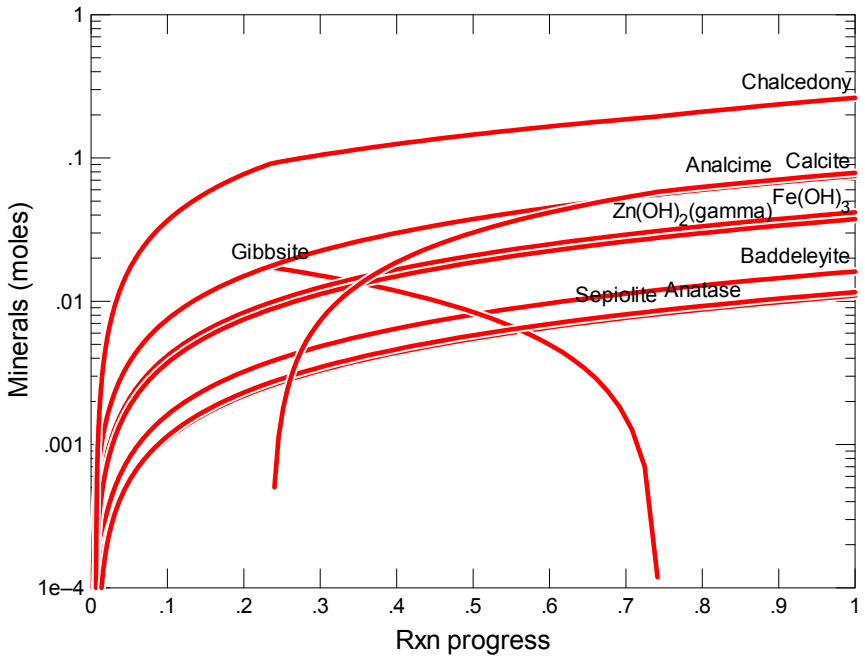


**Figure B.289**. Secondary Phases Calculated to Form as a Function of Reaction Progress (mol-glass/kg) Determined for Glass Sample LAWB84

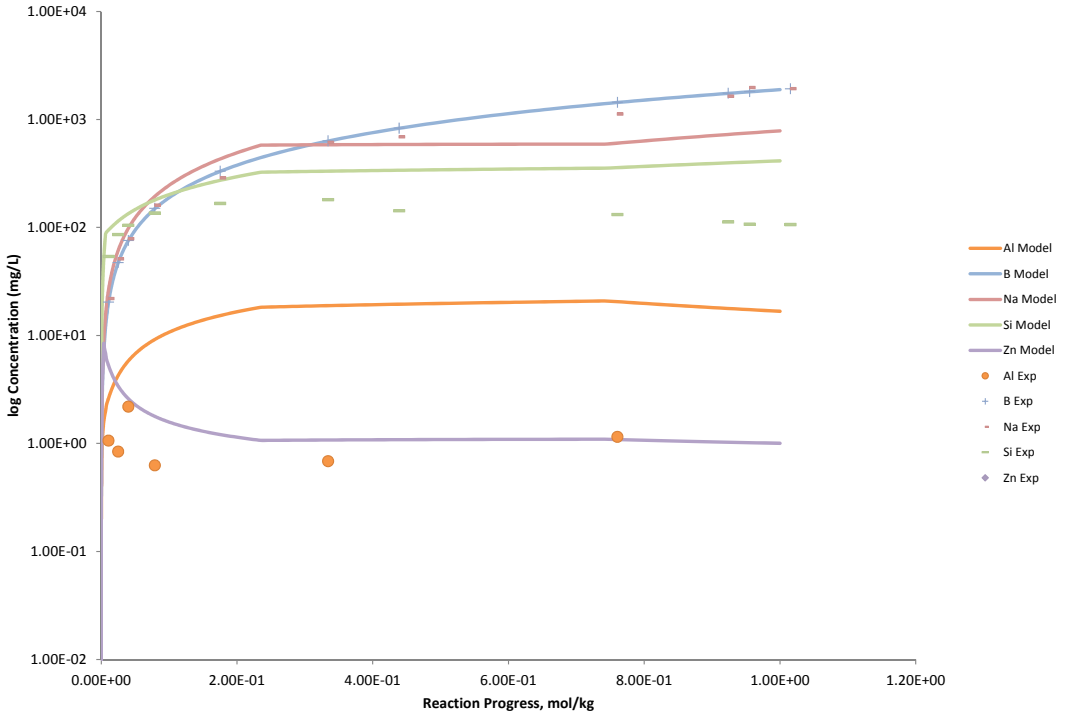


**Figure B.290**. Measured Solution Concentrations (mg/L) and Model Results for Al, B, Na, Si, and Zn, as a Function of Reaction Progress (mol-glass/kg) Determined for Glass Sample LAWB84

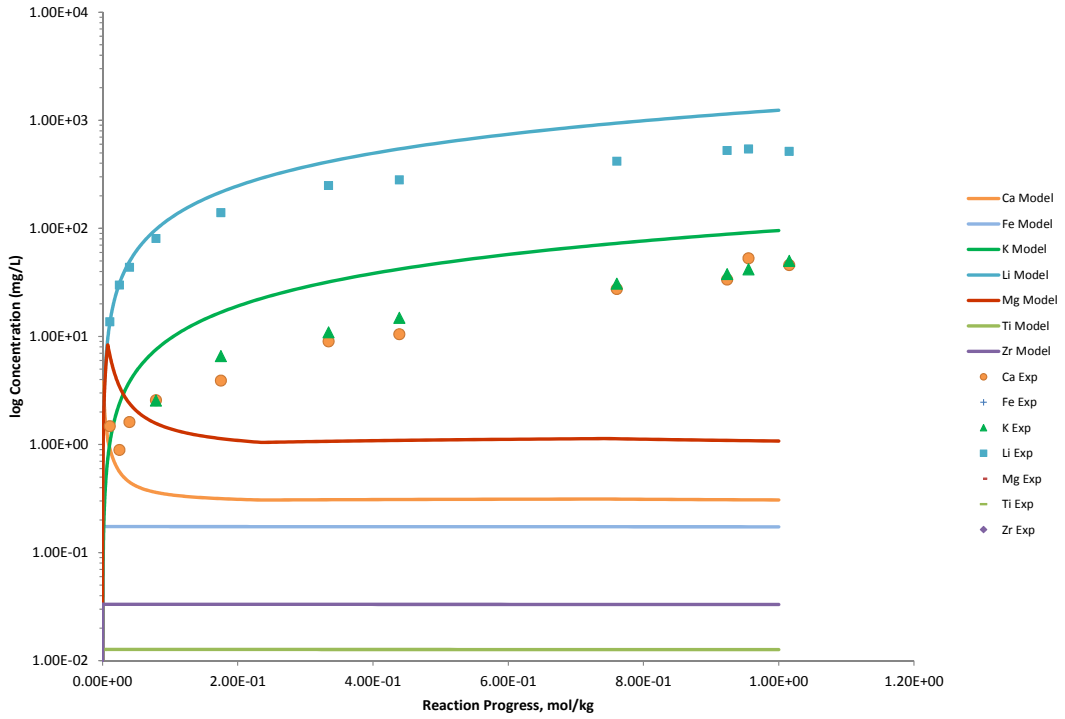


**Figure B.291**. Measured Solution Concentrations (mg/L) and Model Results for Ca, Fe, K, Li, Mg, Ti, and Zr, as a Function of Reaction Progress (mol-glass/kg) Determined for Glass Sample LAWB84

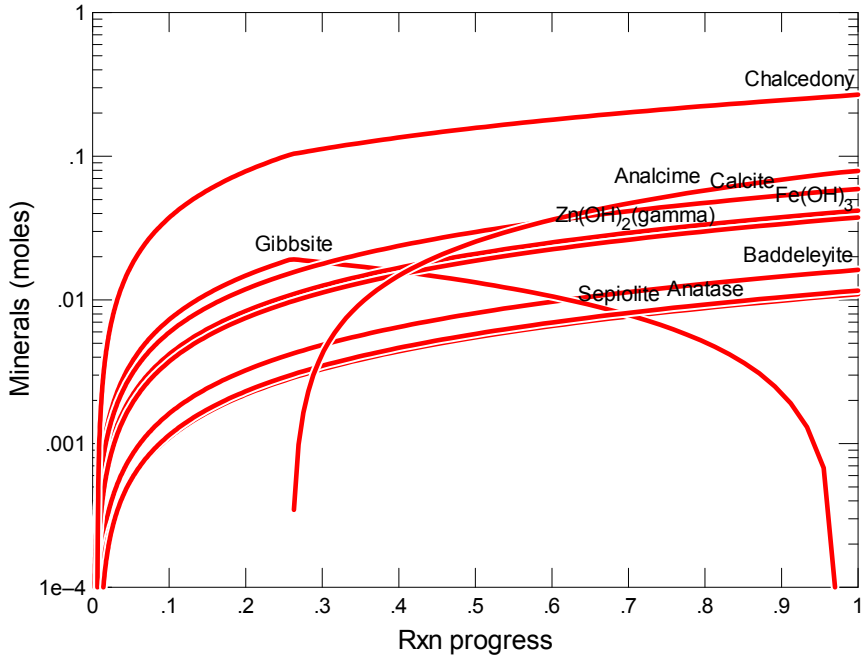


**Figure B.292**. Secondary Phases Calculated to Form as a Function of Reaction Progress (mol-glass/kg) Determined for Glass Sample LAWB85

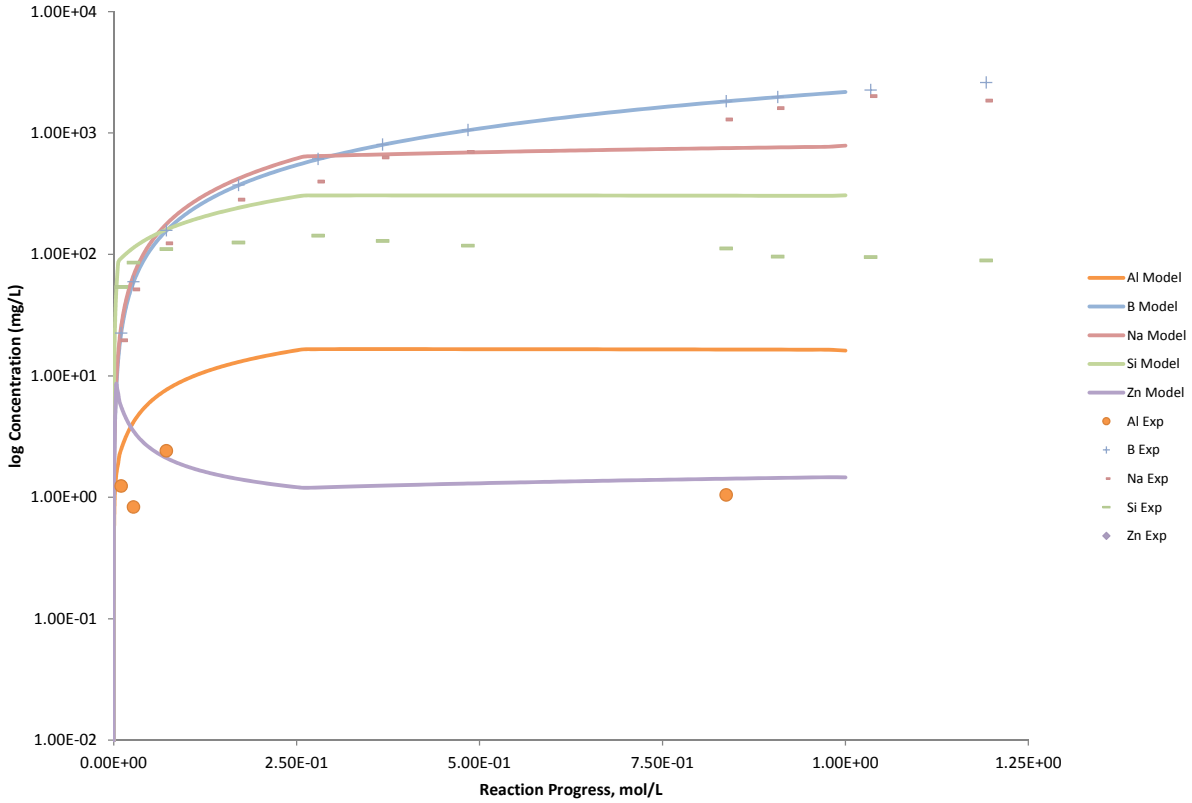


**Figure B.293**. Measured Solution Concentrations (mg/L) and Model Results for Al, B, Na, Si, and Zn, as a Function of Reaction Progress (mol-glass/kg) Determined for Glass Sample LAWB85

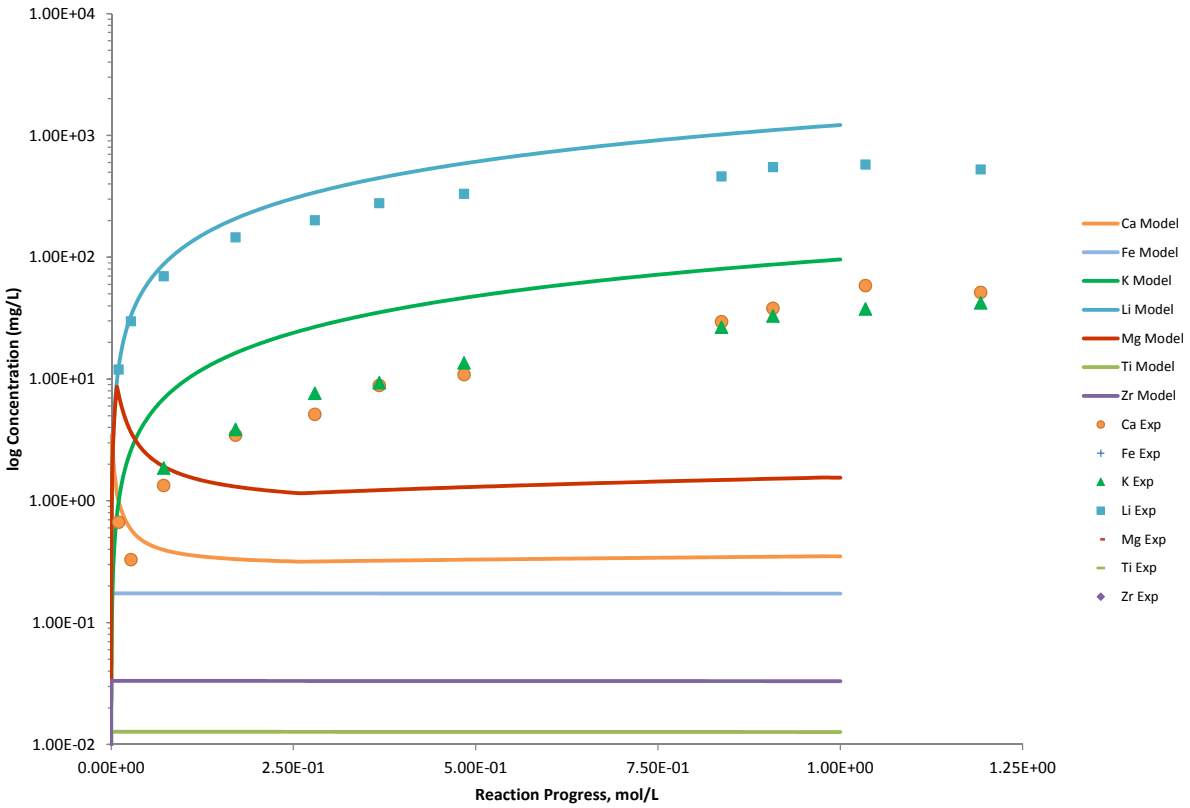


**Figure B.294**. Measured Solution Concentrations (mg/L) and Model Results for Ca, Fe, K, Li, Mg, Ti, and Zr, as a Function of Reaction Progress (mol-glass/kg) Determined for Glass Sample LAWB85

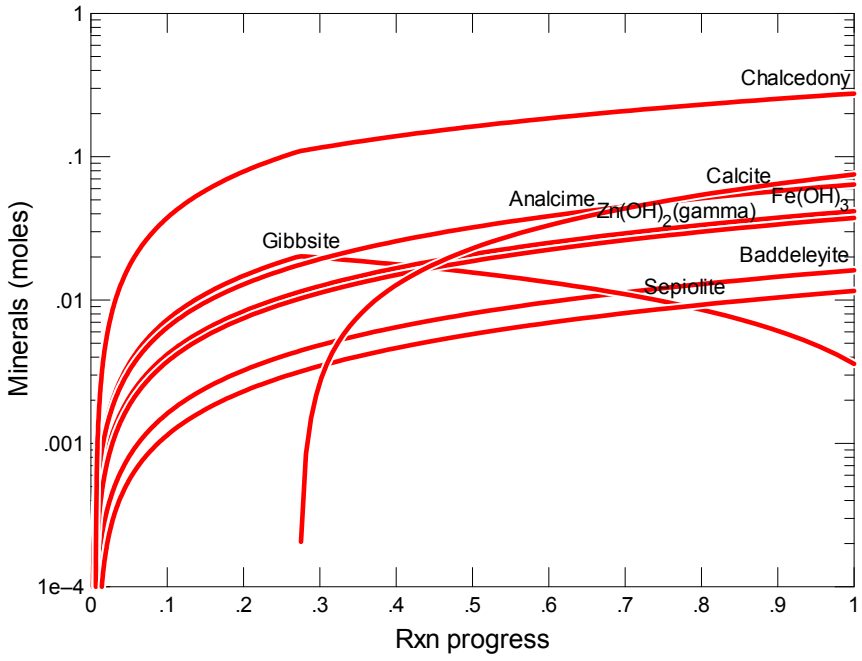


**Figure B.295**. Secondary Phases Calculated to Form as a Function of Reaction Progress (mol-glass/kg) Determined for Glass Sample LAWB86

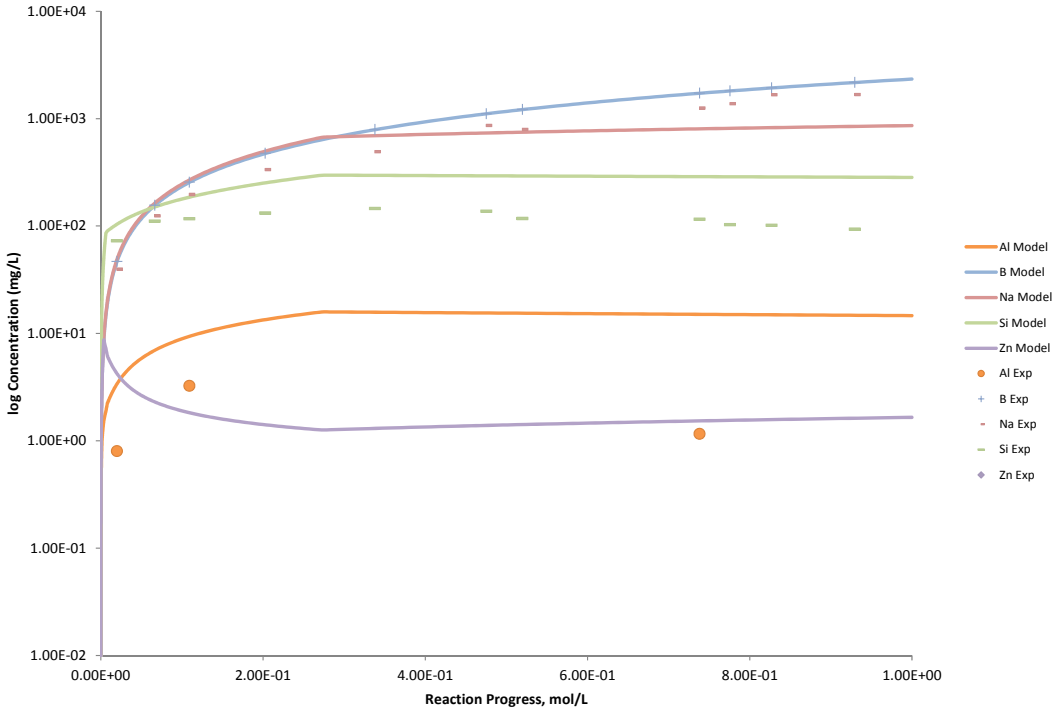


**Figure B.296**. Measured Solution Concentrations (mg/L) and Model Results for Al, B, Na, Si, and Zn, as a Function of Reaction Progress (mol-glass/kg) Determined for Glass Sample LAWB86

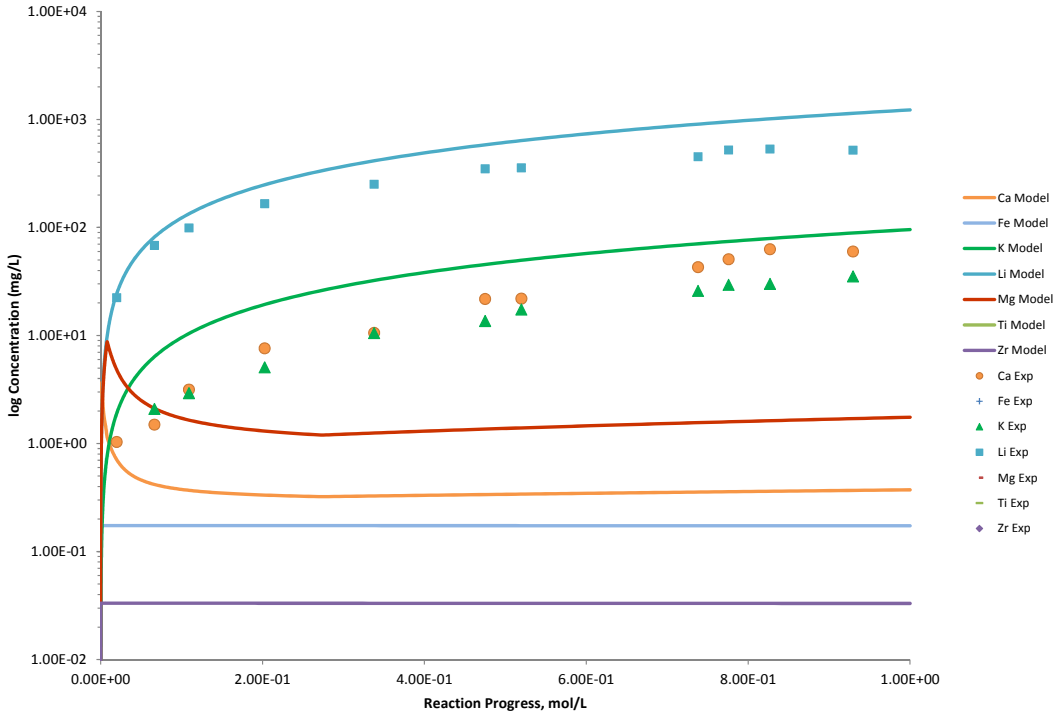


**Figure B.297**. Measured Solution Concentrations (mg/L) and Model Results for Ca, Fe, K, Li, Mg, Ti, and Zr, as a Function of Reaction Progress (mol-glass/kg) Determined for Glass Sample LAWB86

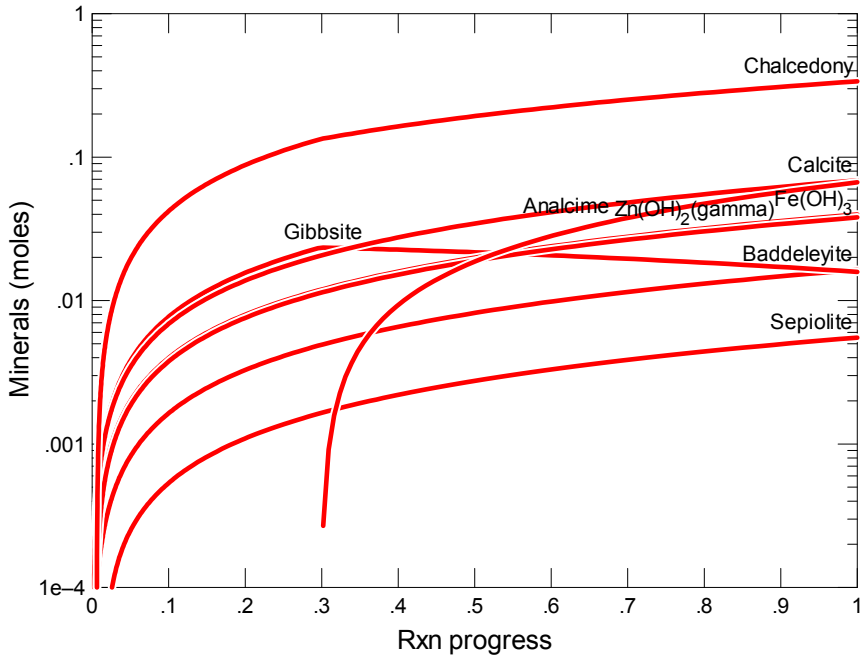


**Figure B.298**. Secondary Phases Calculated to Form as a Function of Reaction Progress (mol-glass/kg) Determined for Glass Sample LAWB87

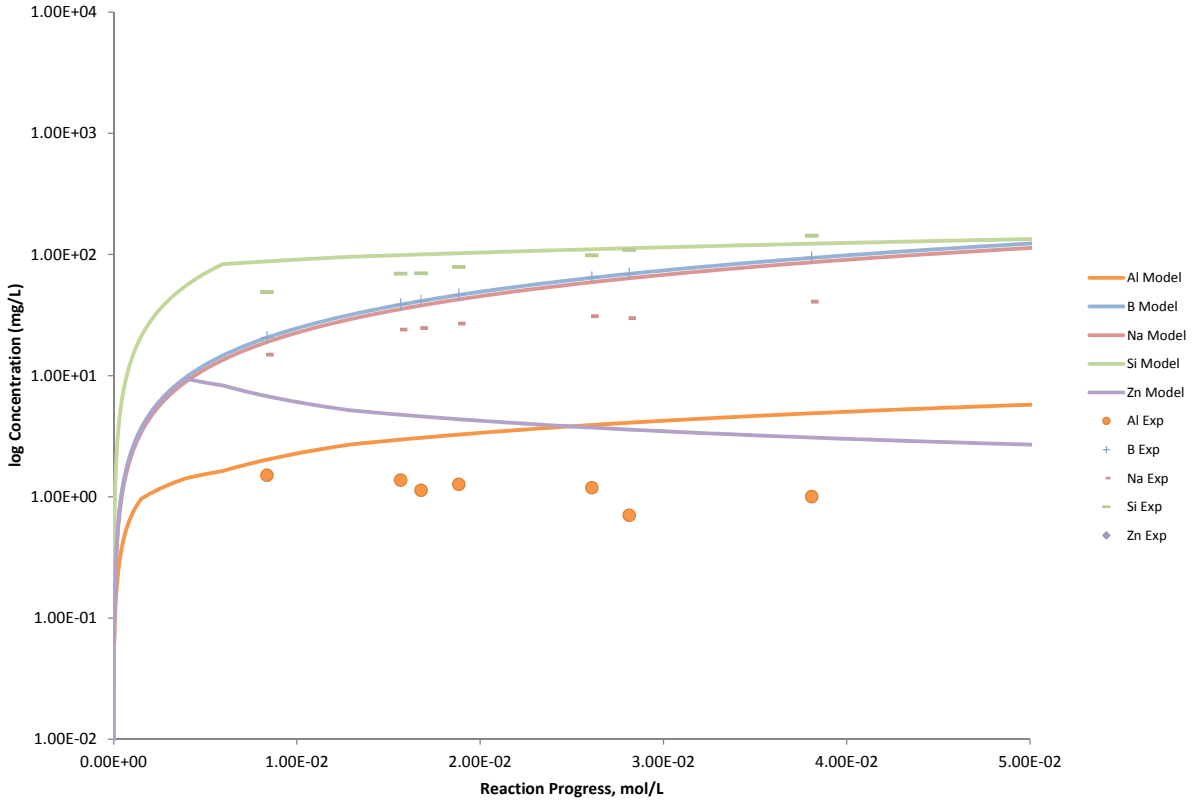


**Figure B.299**. Measured Solution Concentrations (mg/L) and Model Results for Al, B, Na, Si, and Zn, as a Function of Reaction Progress (mol-glass/kg) Determined for Glass Sample LAWB87

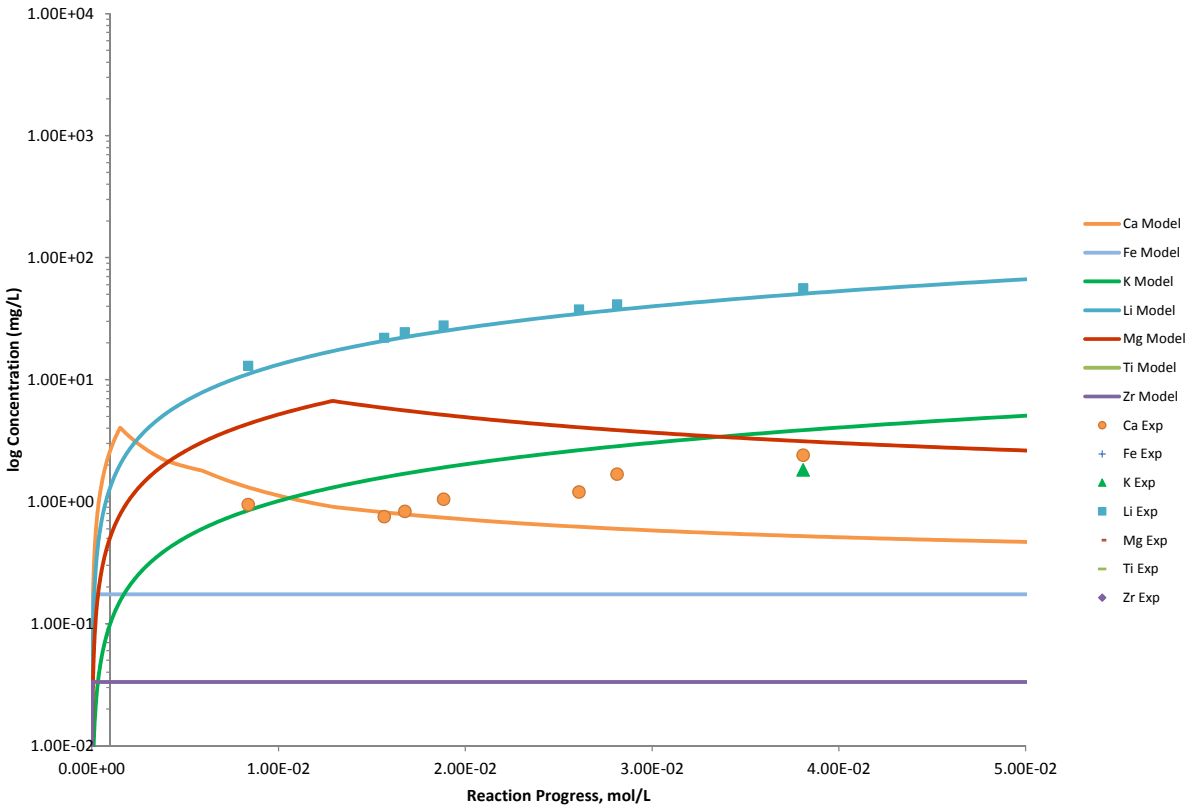


**Figure B.300**. Measured Solution Concentrations (mg/L) and Model Results for Ca, Fe, K, Li, Mg, Ti, and Zr, as a Function of Reaction Progress (mol-glass/kg) Determined for Glass Sample LAWB87

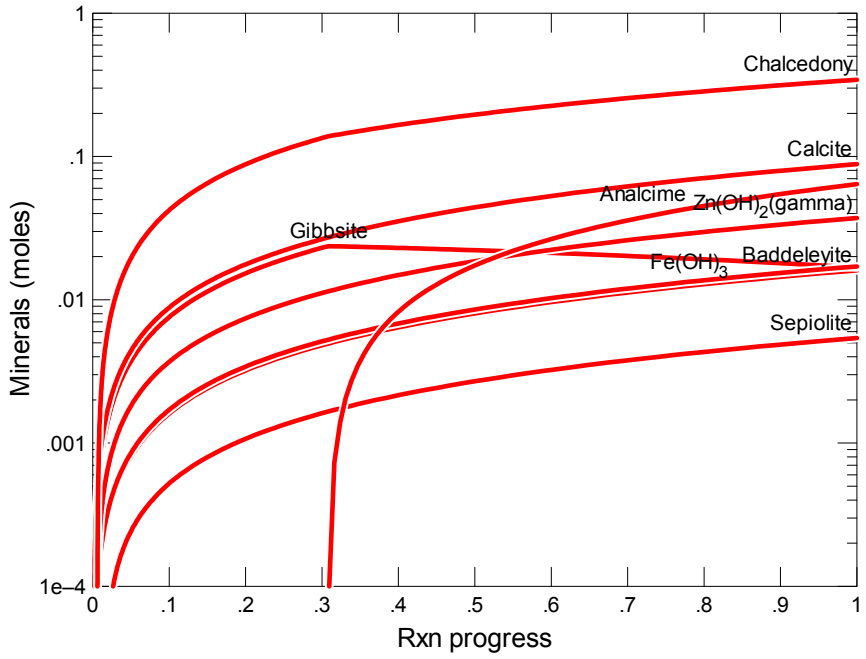


**Figure B.301**. Secondary Phases Calculated to Form as a Function of Reaction Progress (mol-glass/kg) Determined for Glass Sample LAWB88

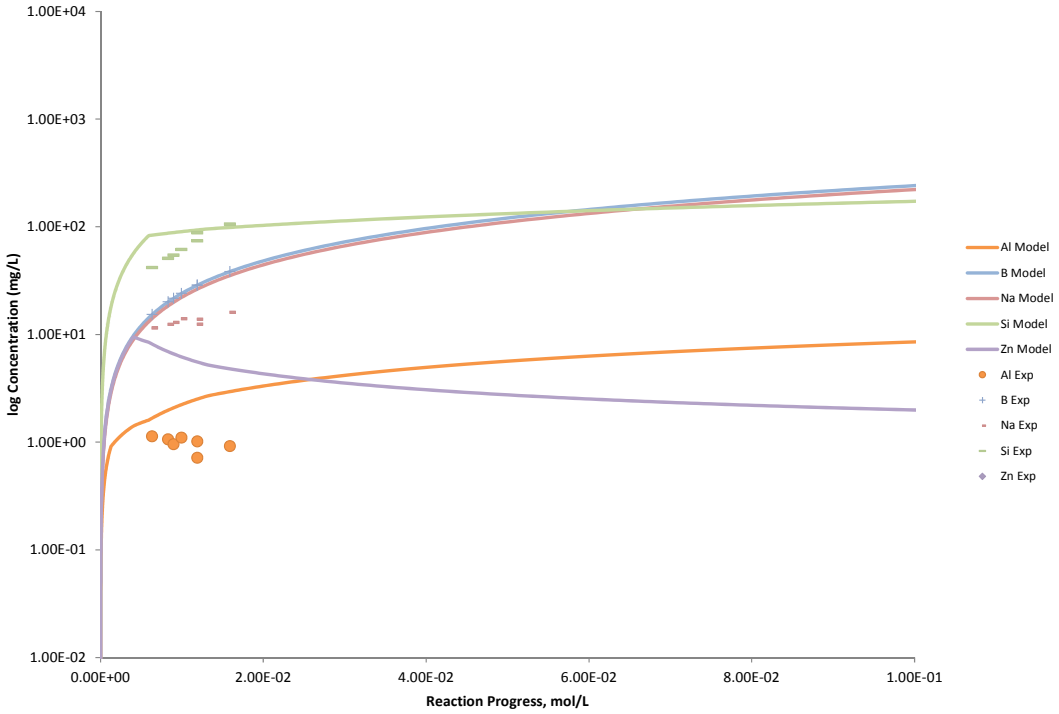


**Figure B.302**. Measured Solution Concentrations (mg/L) and Model Results for Al, B, Na, Si, and Zn, as a Function of Reaction Progress (mol-glass/kg) Determined for Glass Sample LAWB88

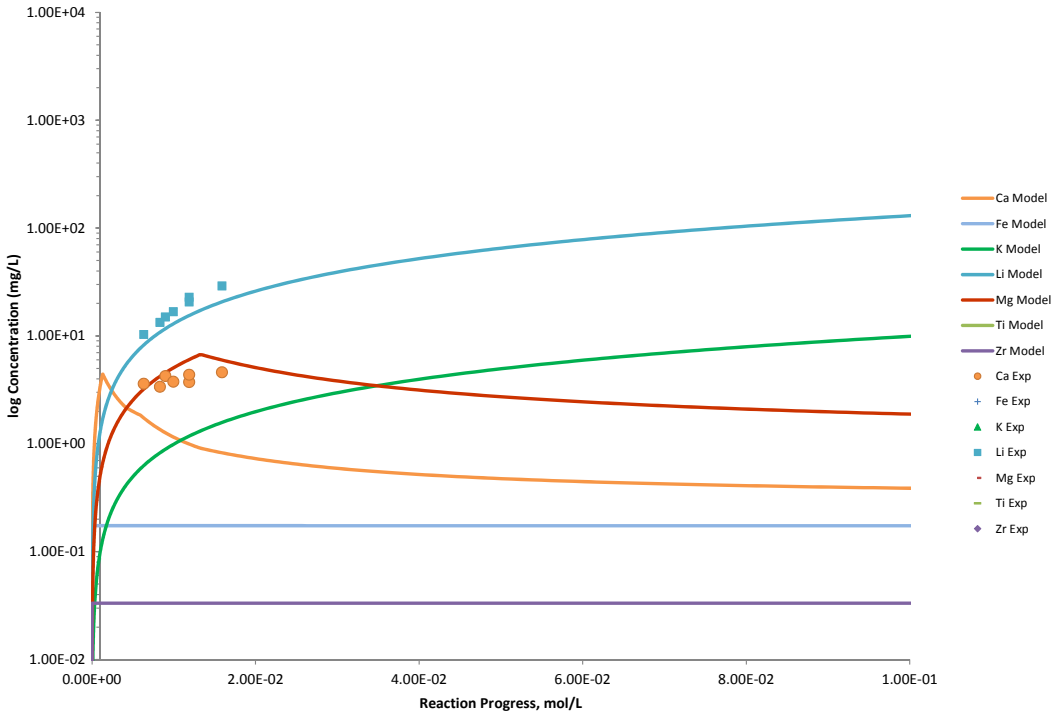


**Figure B.303**. Measured Solution Concentrations (mg/L) and Model Results for Ca, Fe, K, Li, Mg, Ti, and Zr, as a Function of Reaction Progress (mol-glass/kg) Determined for Glass Sample LAWB88

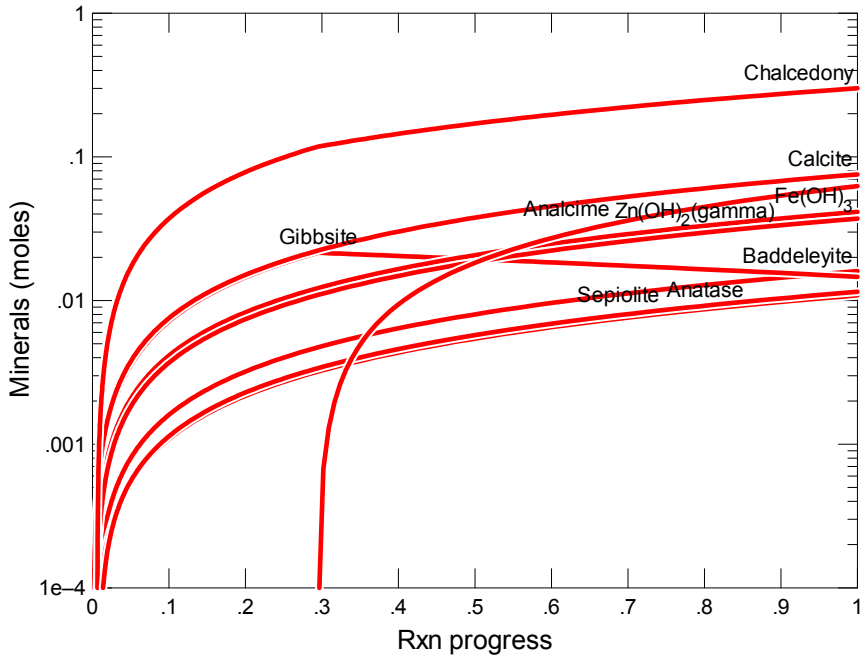


**Figure B.304**. Secondary Phases Calculated to Form as a Function of Reaction Progress (mol-glass/kg) Determined for Glass Sample LAWB89

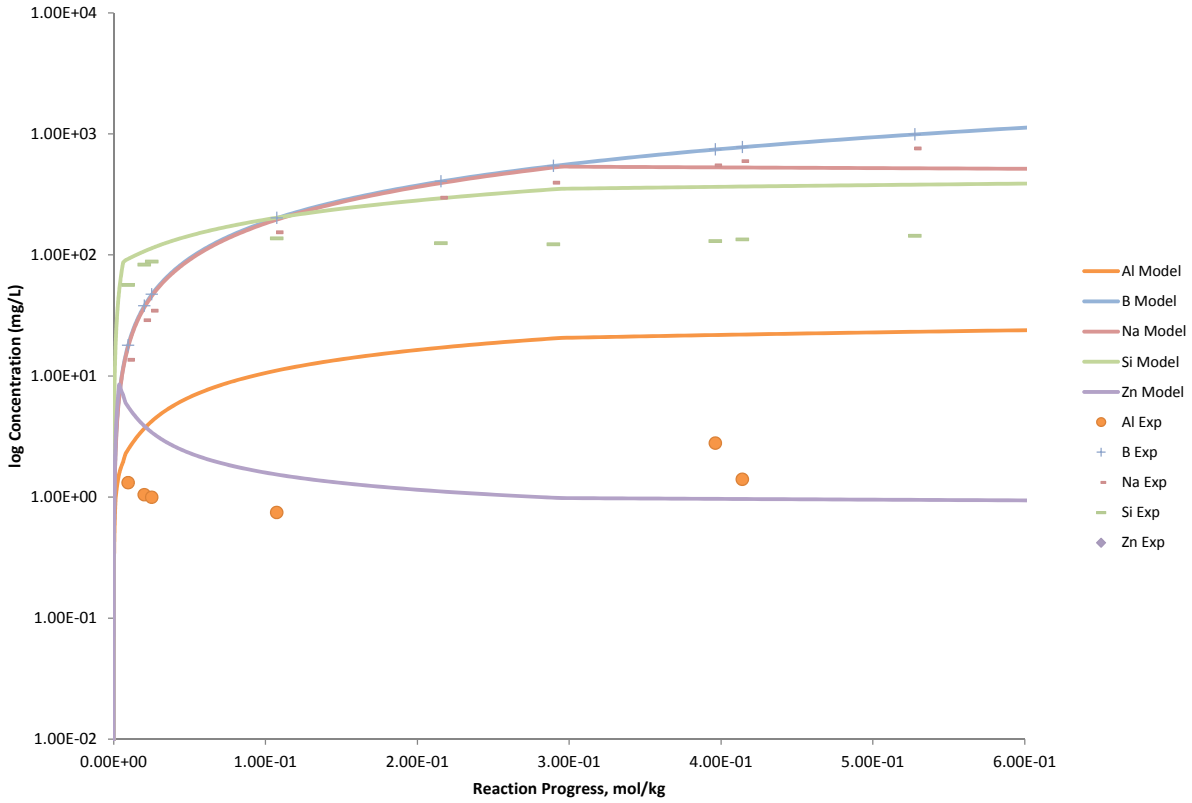


**Figure B.305**. Measured Solution Concentrations (mg/L) and Model Results for Al, B, Na, Si, and Zn, as a Function of Reaction Progress (mol-glass/kg) Determined for Glass Sample LAWB89

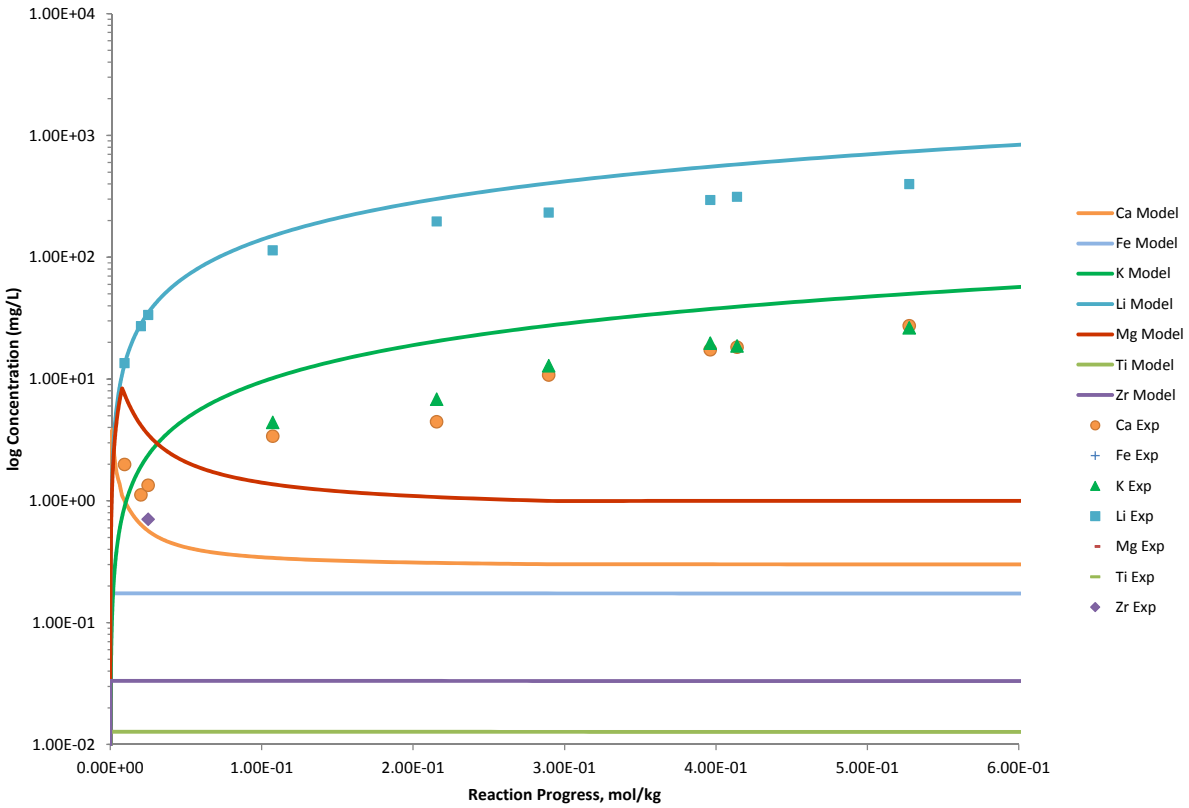


**Figure B.306**. Measured Solution Concentrations (mg/L) and Model Results for Ca, Fe, K, Li, Mg, Ti, and Zr, as a Function of Reaction Progress (mol-glass/kg) Determined for Glass Sample LAWB89

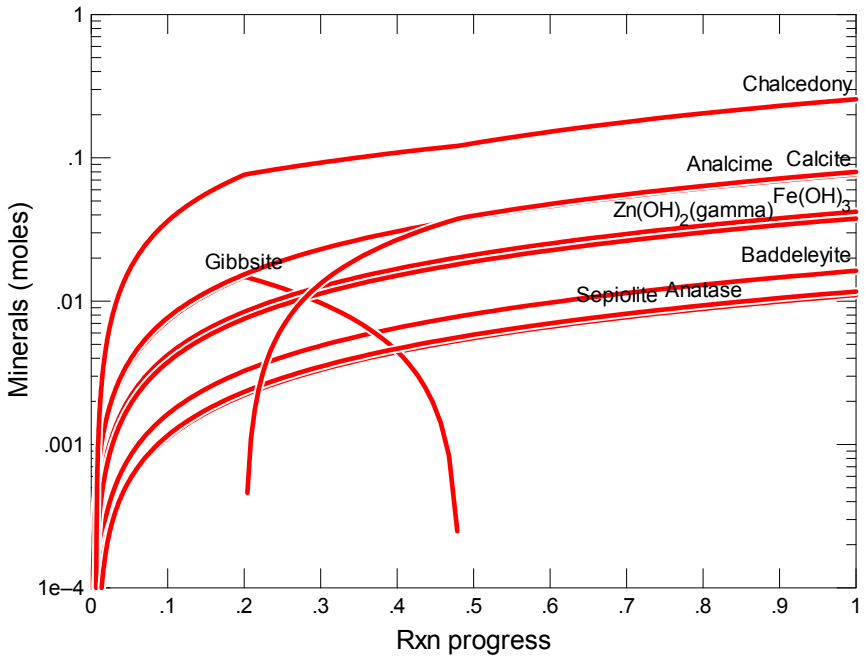


**Figure B.307**. Secondary Phases Calculated to Form as a Function of Reaction Progress (mol-glass/kg) Determined for Glass Sample LAWB90

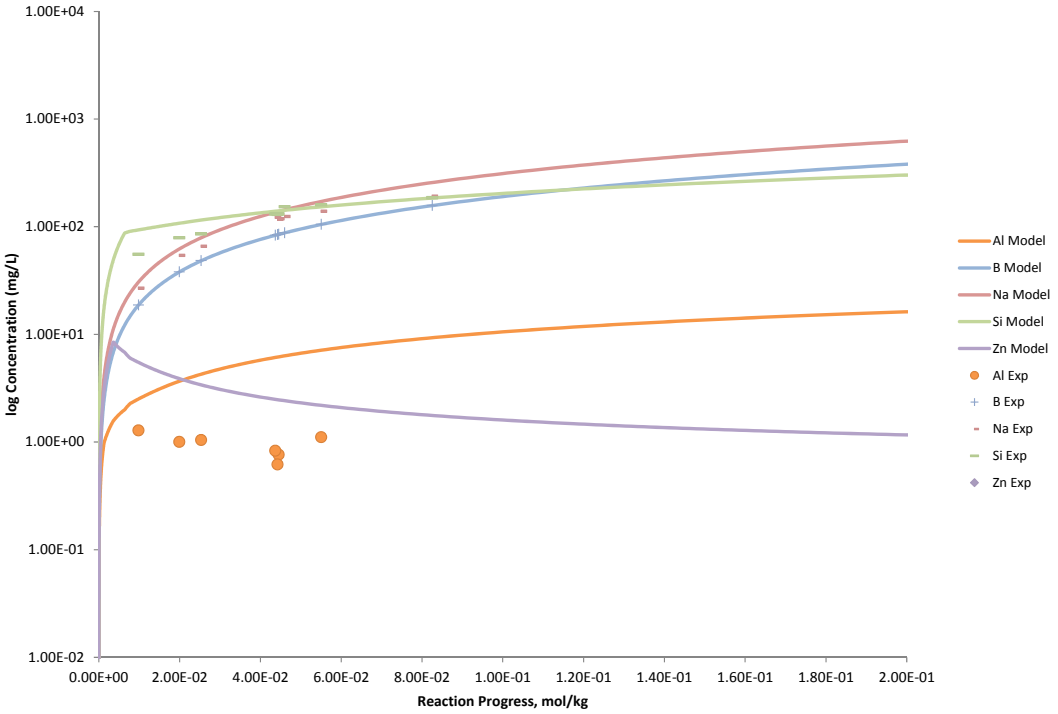


**Figure B.308**. Measured Solution Concentrations (mg/L) and Model Results for Al, B, Na, Si, and Zn, as a Function of Reaction Progress (mol-glass/kg) Determined for Glass Sample LAWB90

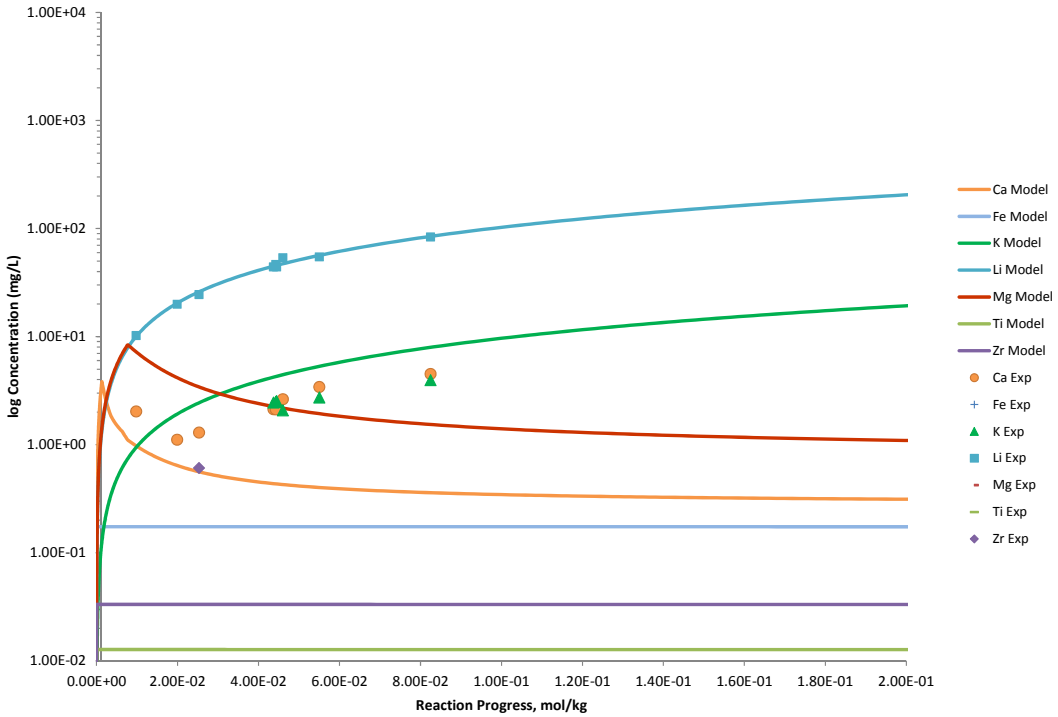


**Figure B.309**. Measured Solution Concentrations (mg/L) and Model Results for Ca, Fe, K, Li, Mg, Ti, and Zr, as a Function of Reaction Progress (mol-glass/kg) Determined for Glass Sample LAWB90

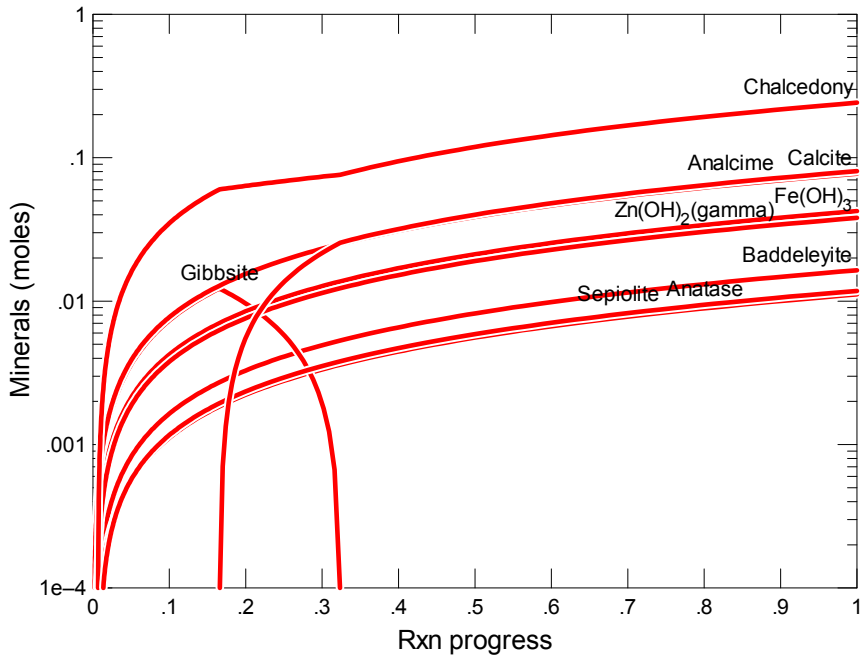


**Figure B.310**. Secondary Phases Calculated to Form as a Function of Reaction Progress (mol-glass/kg) Determined for Glass Sample LAWB91

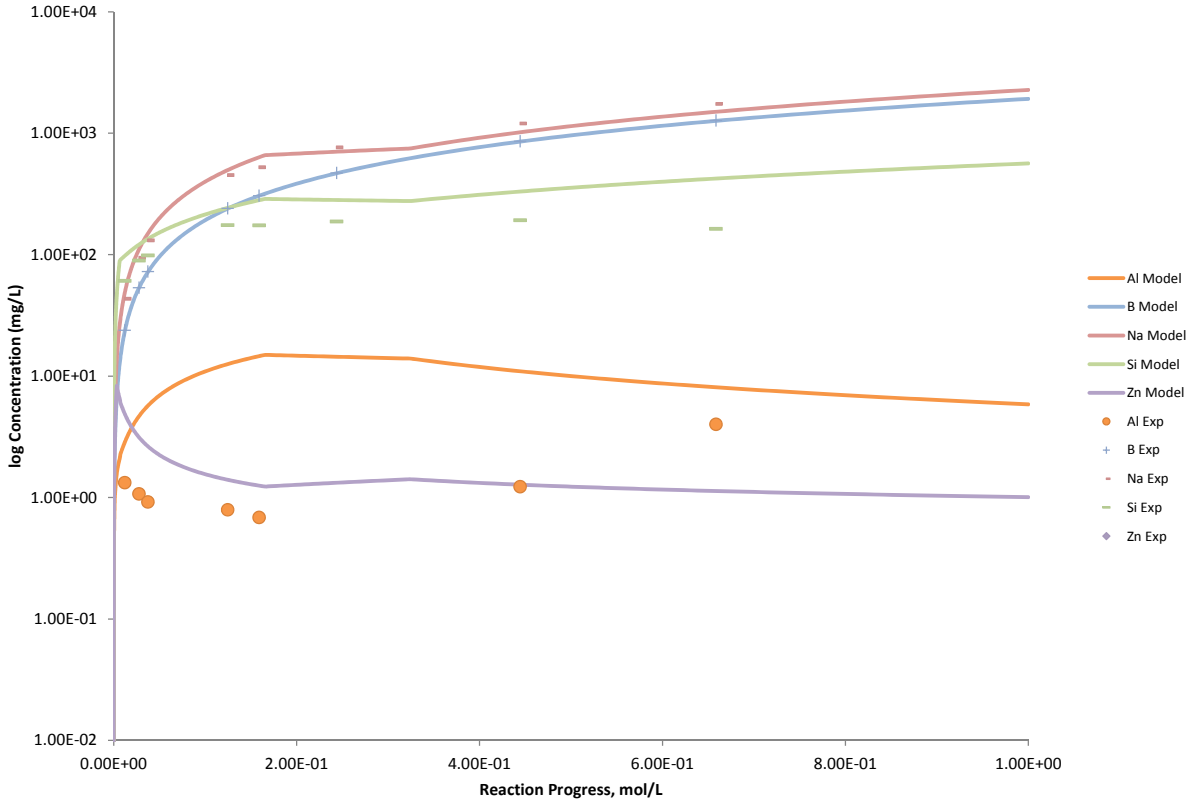


**Figure B.311**. Measured Solution Concentrations (mg/L) and Model Results for Al, B, Na, Si, and Zn, as a Function of Reaction Progress (mol-glass/kg) Determined for Glass Sample LAWB91

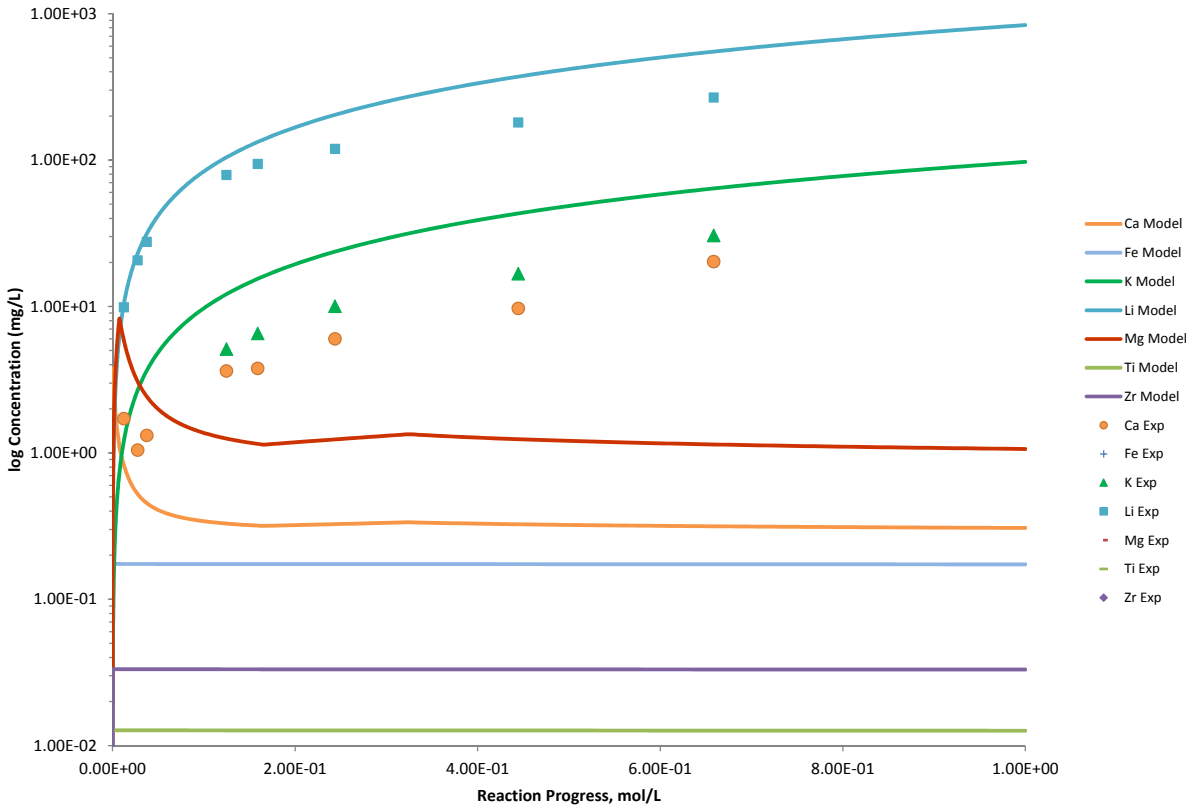


**Figure B.312**. Measured Solution Concentrations (mg/L) and Model Results for Ca, Fe, K, Li, Mg, Ti, and Zr, as a Function of Reaction Progress (mol-glass/kg) Determined for Glass Sample LAWB91

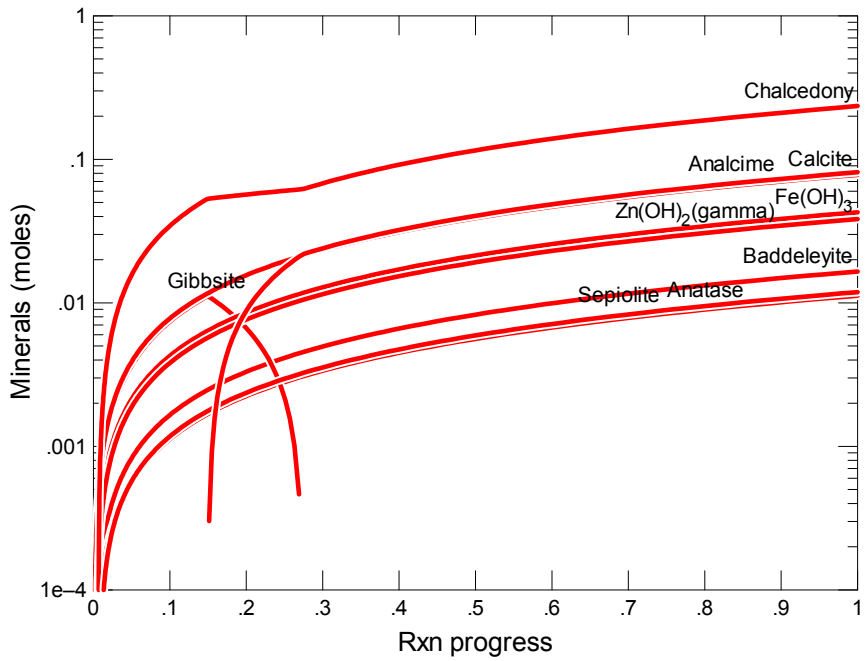


**Figure B.313**. Secondary Phases Calculated to Form as a Function of Reaction Progress (mol-glass/kg) Determined for Glass Sample LAWB92

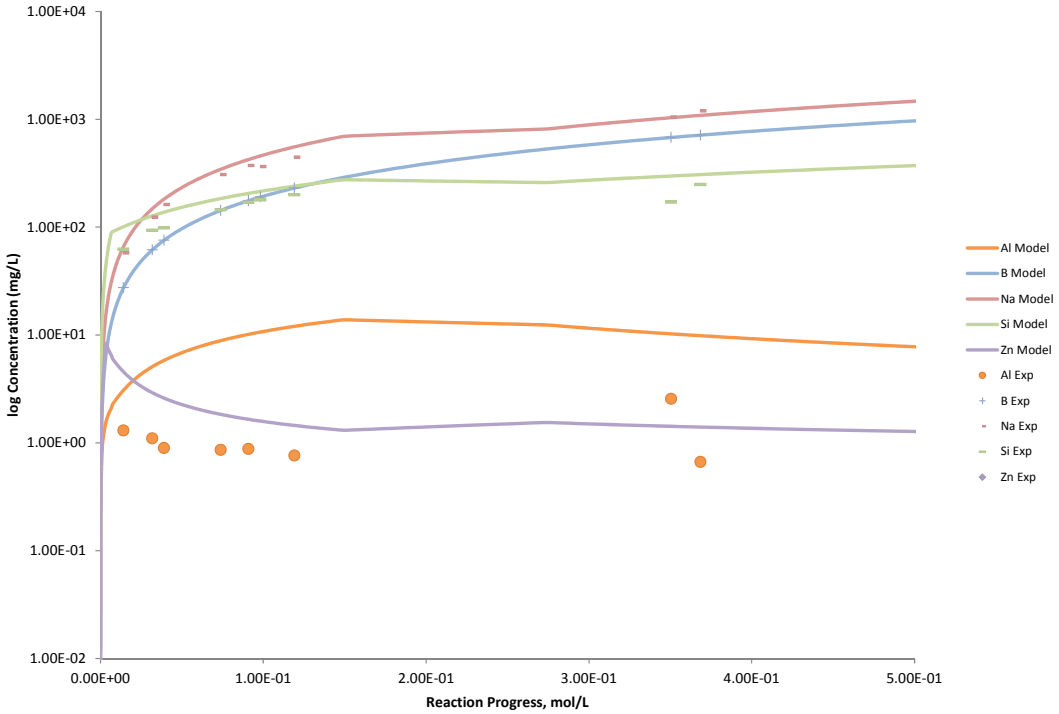


**Figure B.314**. Measured Solution Concentrations (mg/L) and Model Results for Al, B, Na, Si, and Zn, as a Function of Reaction Progress (mol-glass/kg) Determined for Glass Sample LAWB92

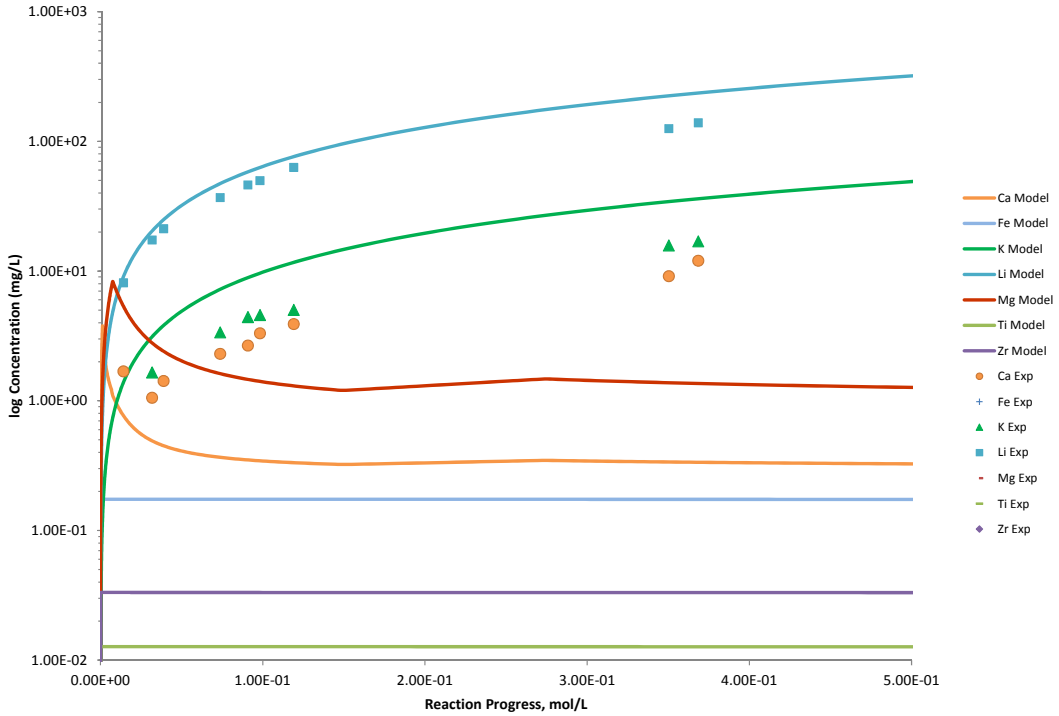


**Figure B.315**. Measured Solution Concentrations (mg/L) and Model Results for Ca, Fe, K, Li, Mg, Ti, and Zr, as a Function of Reaction Progress (mol-glass/kg) Determined for Glass Sample LAWB92

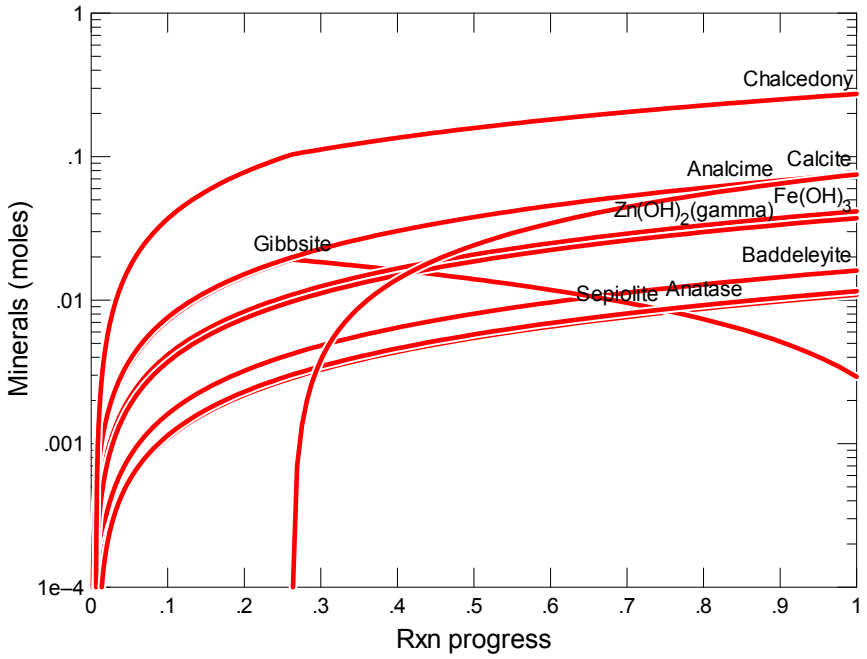


**Figure B.316**. Secondary Phases Calculated to Form as a Function of Reaction Progress (mol-glass/kg) Determined for Glass Sample LAWB93

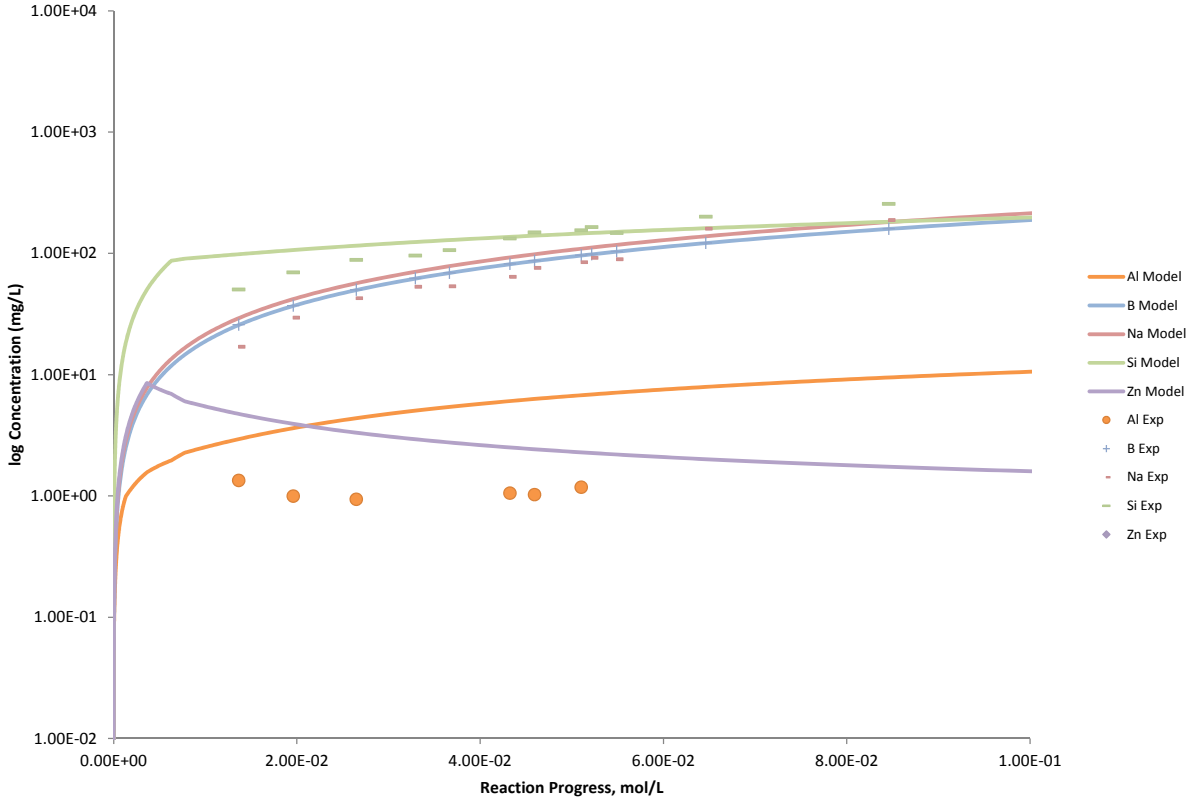


**Figure B.317**. Measured Solution Concentrations (mg/L) and Model Results for Al, B, Na, Si, and Zn, as a Function of Reaction Progress (mol-glass/kg) Determined for Glass Sample LAWB93

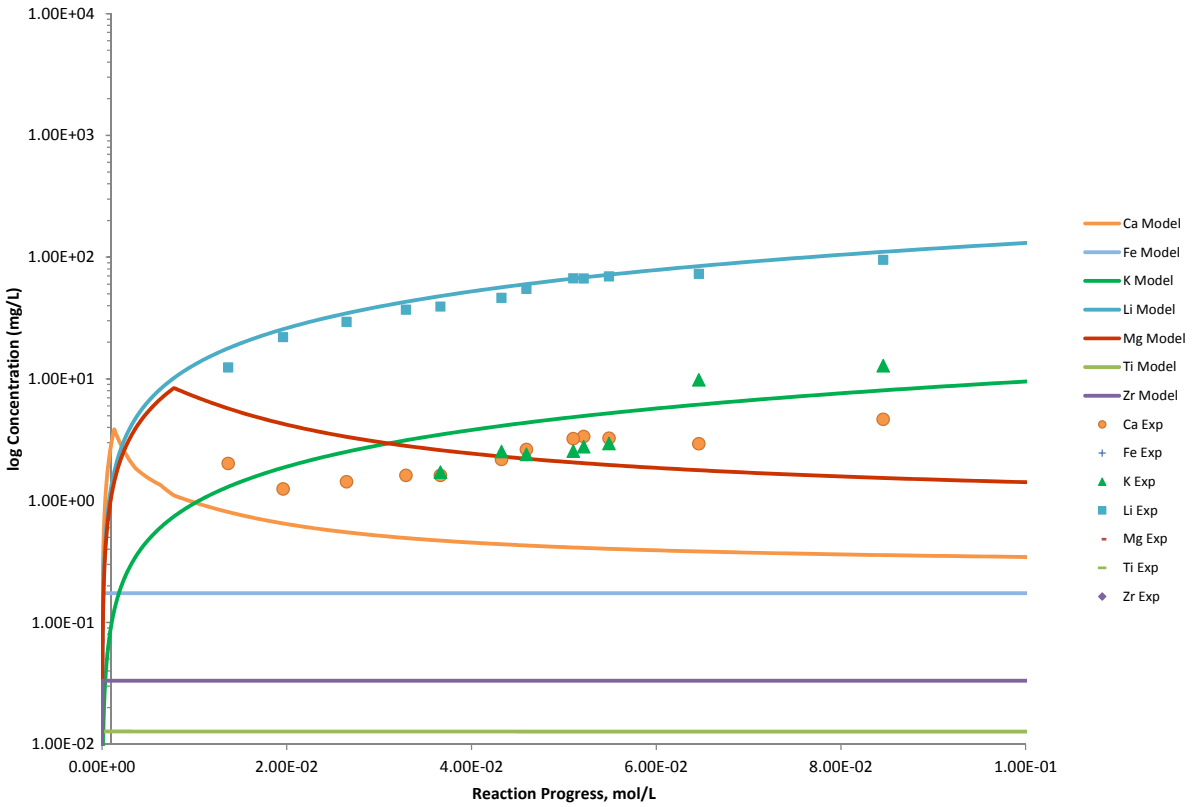


**Figure B.318**. Measured Solution Concentrations (mg/L) and Model Results for Ca, Fe, K, Li, Mg, Ti, and Zr, as a Function of Reaction Progress (mol-glass/kg) Determined for Glass Sample LAWB93

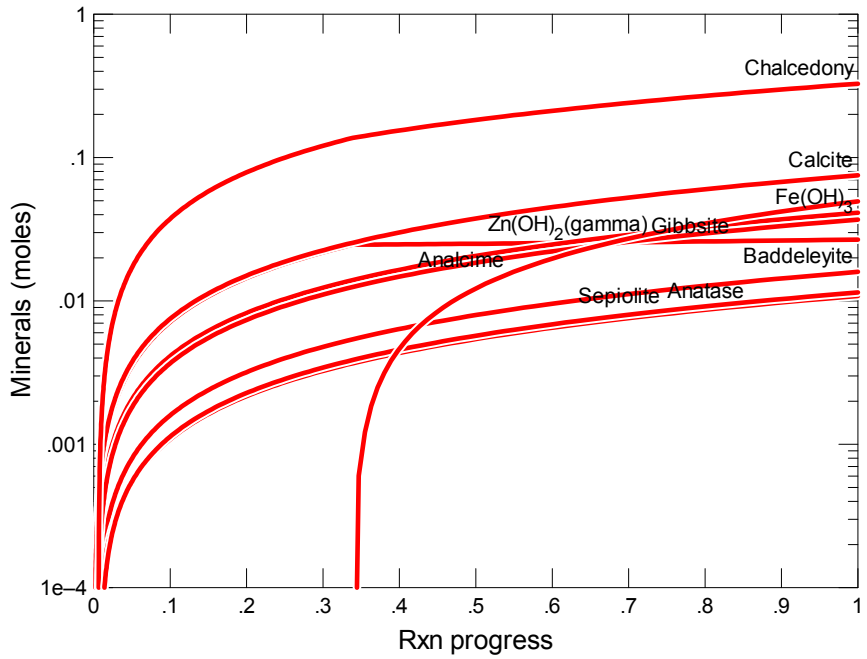


**Figure B.319**. Secondary Phases Calculated to Form as a Function of Reaction Progress (mol-glass/kg) Determined for Glass Sample LAWB94

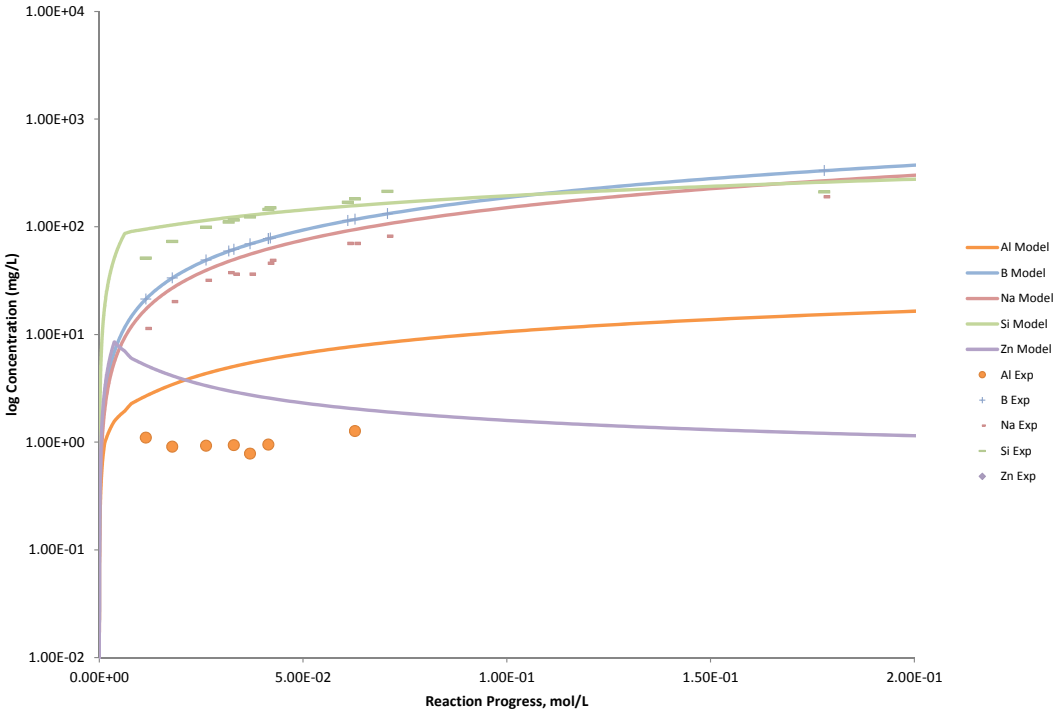


**Figure B.320**. Measured Solution Concentrations (mg/L) and Model Results for Al, B, Na, Si, and Zn, as a Function of Reaction Progress (mol-glass/kg) Determined for Glass Sample LAWB94

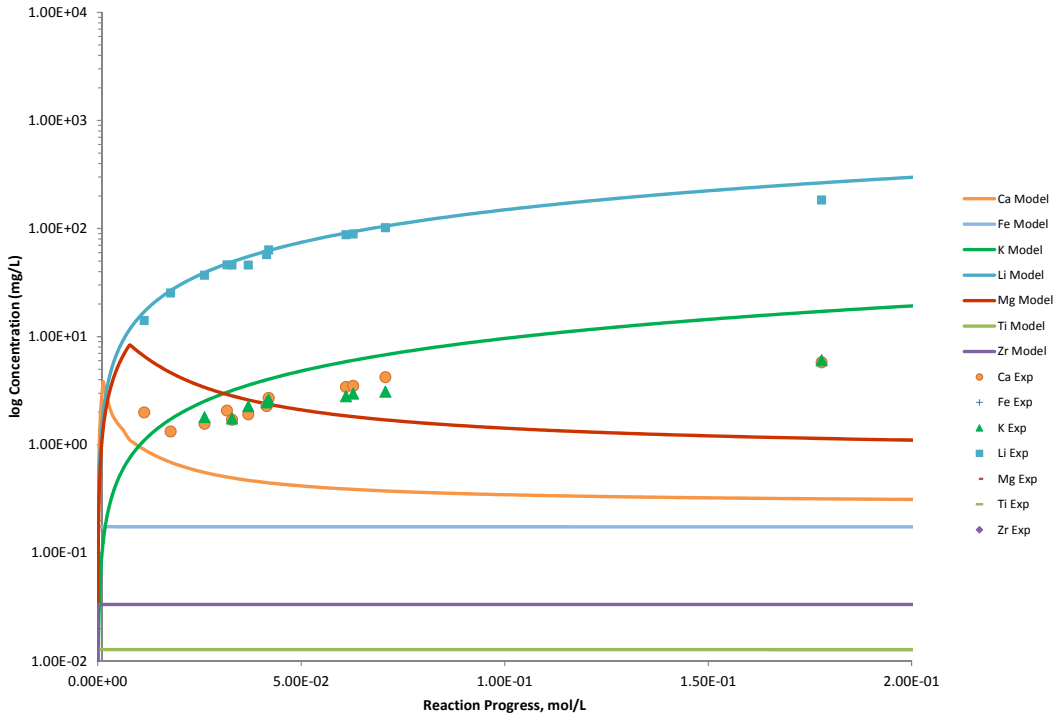


**Figure B.321**. Measured Solution Concentrations (mg/L) and Model Results for Ca, Fe, K, Li, Mg, Ti, and Zr, as a Function of Reaction Progress (mol-glass/kg) Determined for Glass Sample LAWB94

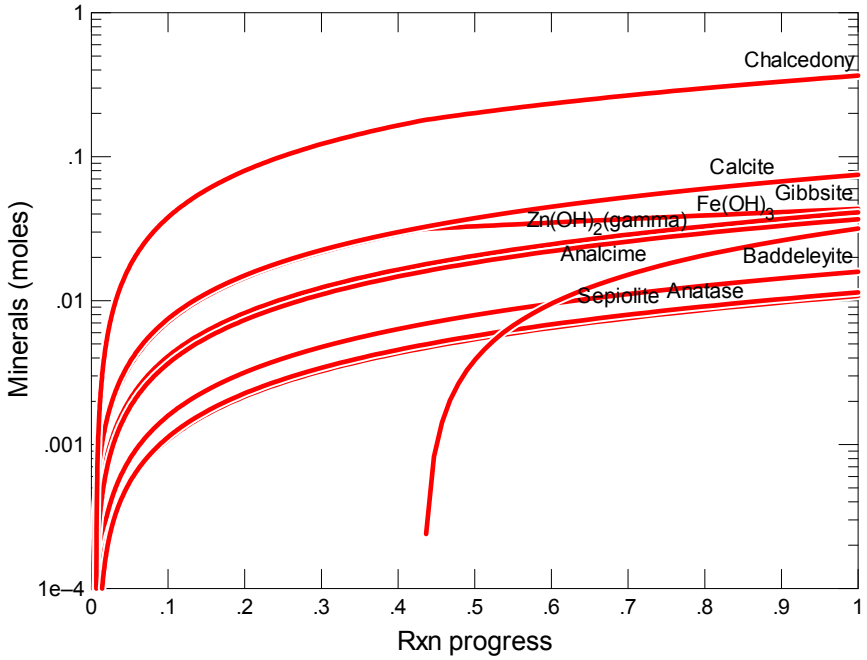


**Figure B.322**. Secondary Phases Calculated to Form as a Function of Reaction Progress (mol-glass/kg) Determined for Glass Sample LAWB95

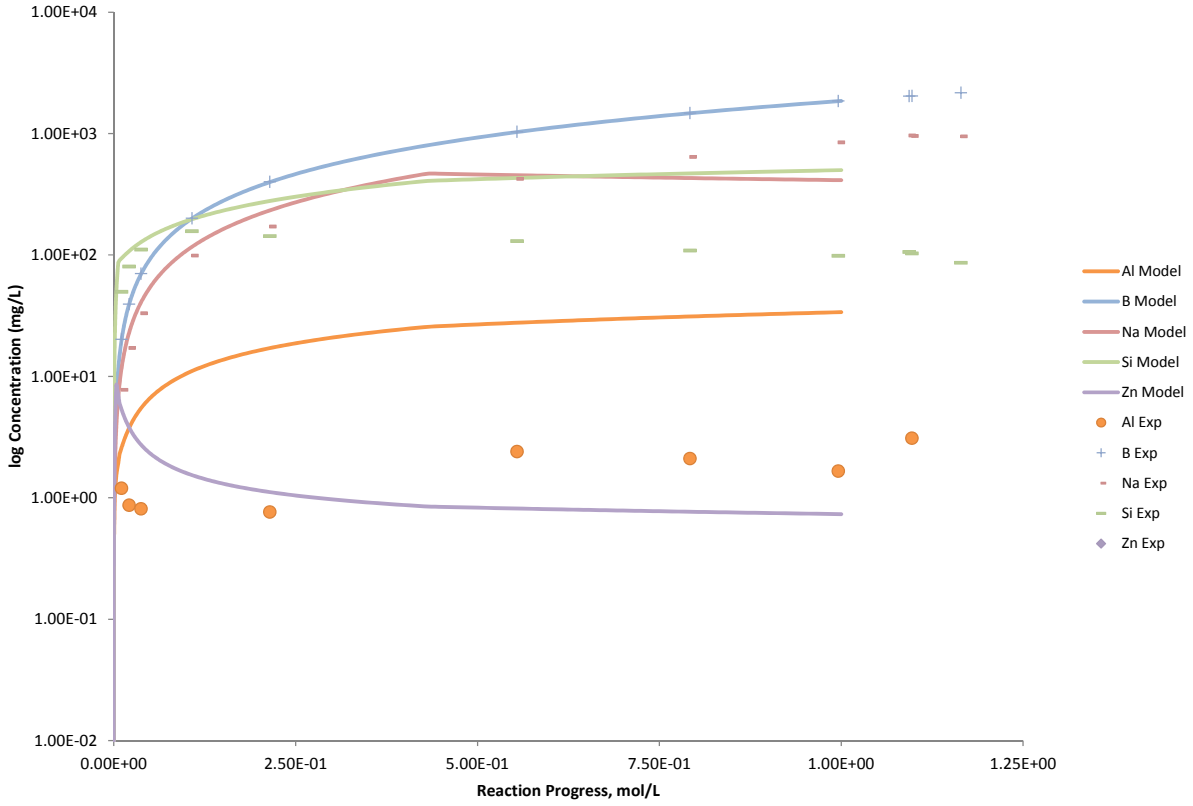


**Figure B.323**. Measured Solution Concentrations (mg/L) and Model Results for Al, B, Na, Si, and Zn, as a Function of Reaction Progress (mol-glass/kg) Determined for Glass Sample LAWB95

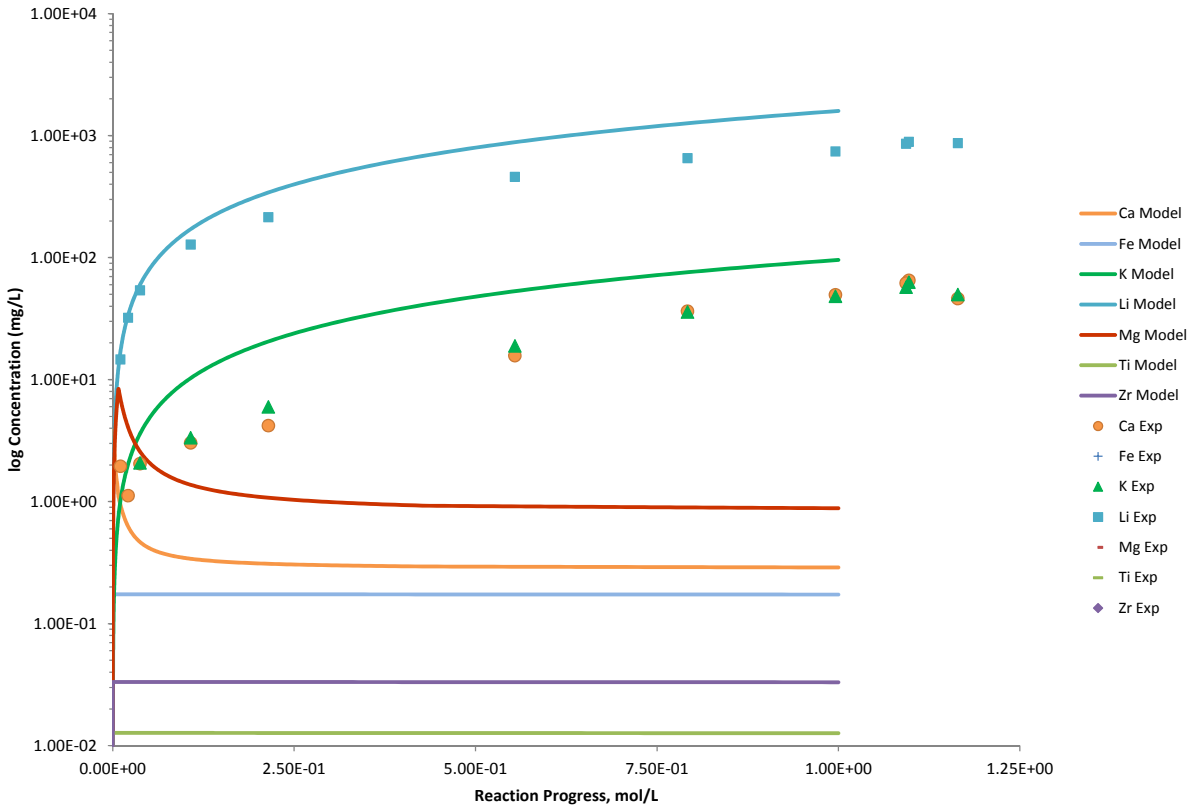


**Figure B.324**. Measured Solution Concentrations (mg/L) and Model Results for Ca, Fe, K, Li, Mg, Ti, and Zr, as a Function of Reaction Progress (mol-glass/kg) Determined for Glass Sample LAWB95

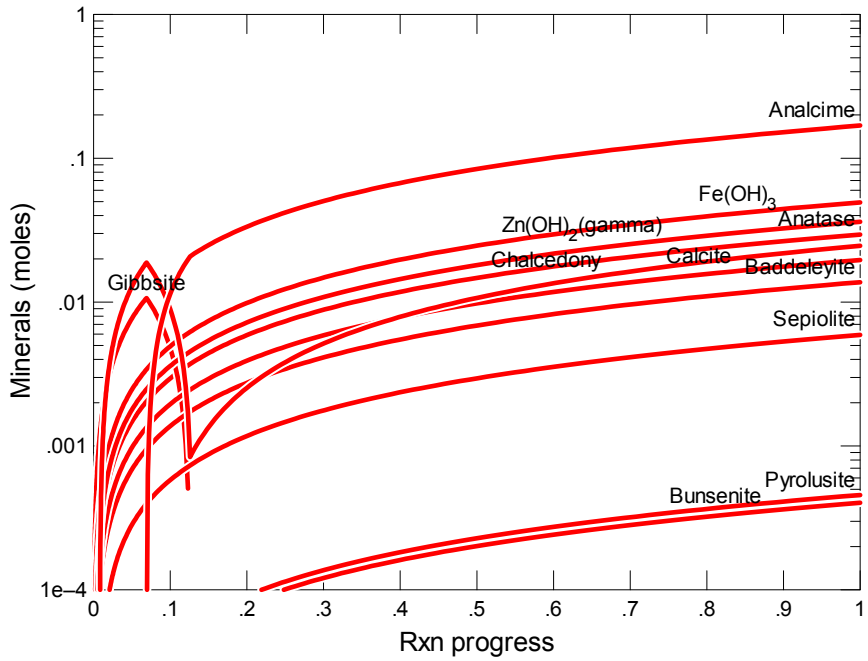


**Figure B.325**. Secondary Phases Calculated to Form as a Function of Reaction Progress (mol-glass/kg) Determined for Glass Sample LAWC12

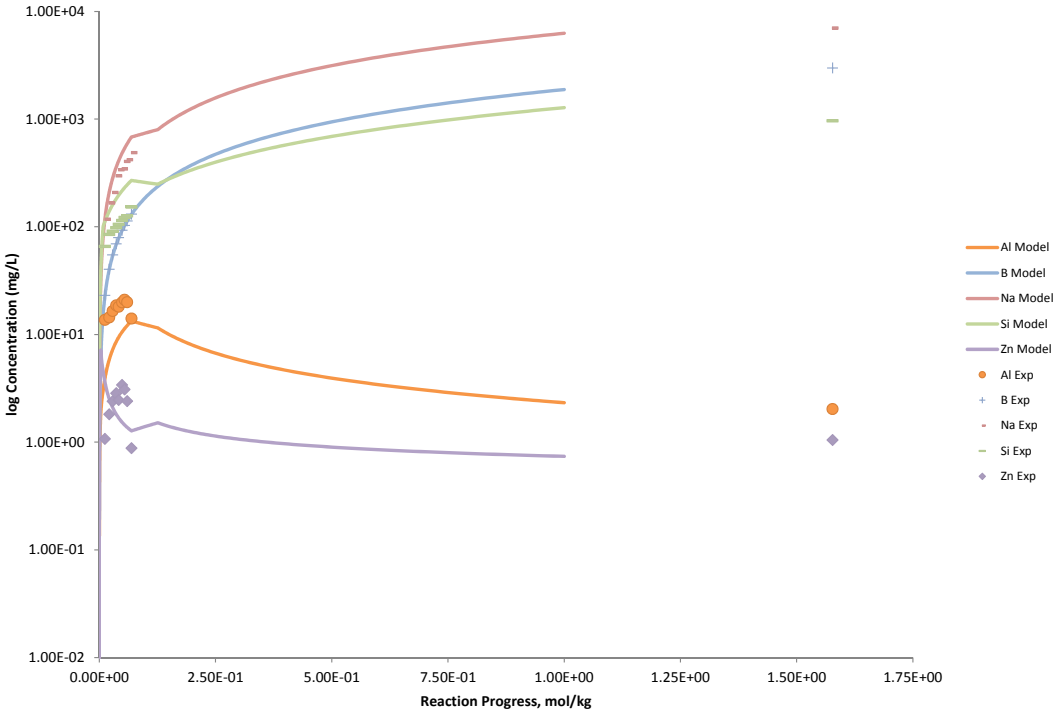


**Figure B.326**. Measured Solution Concentrations (mg/L) and Model Results for Al, B, Na, Si, and Zn, as a Function of Reaction Progress (mol-glass/kg) Determined for Glass Sample LAWC12

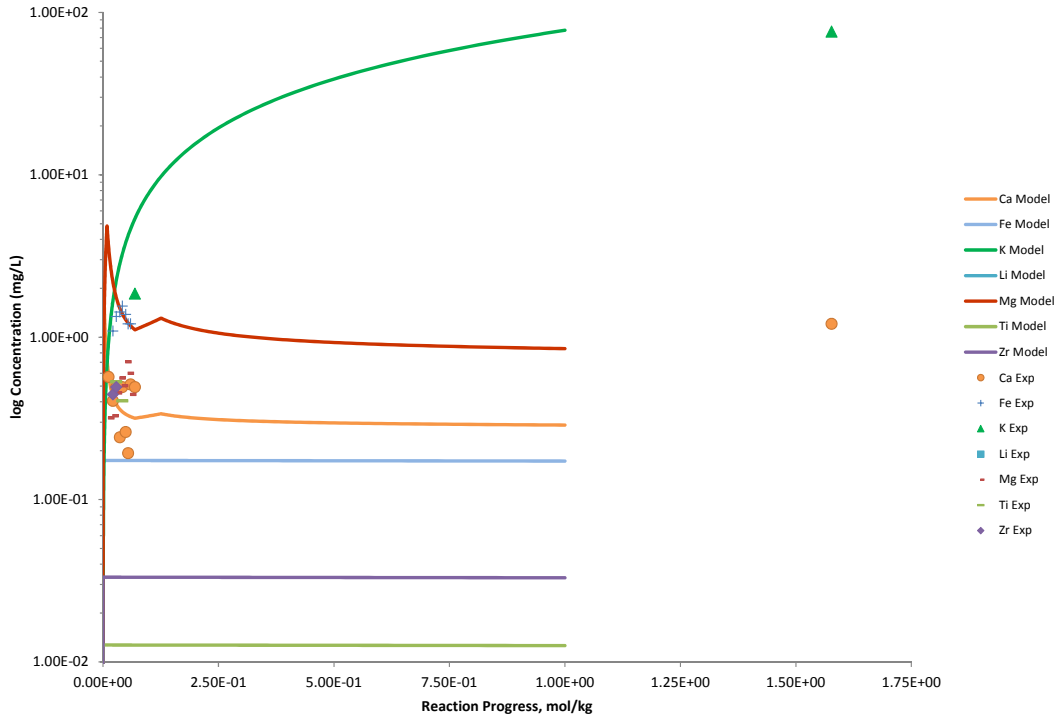


**Figure B.327**. Measured Solution Concentrations (mg/L) and Model Results for Ca, Fe, K, Li, Mg, Ti, and Zr, as a Function of Reaction Progress (mol-glass/kg) Determined for Glass Sample LAWC12

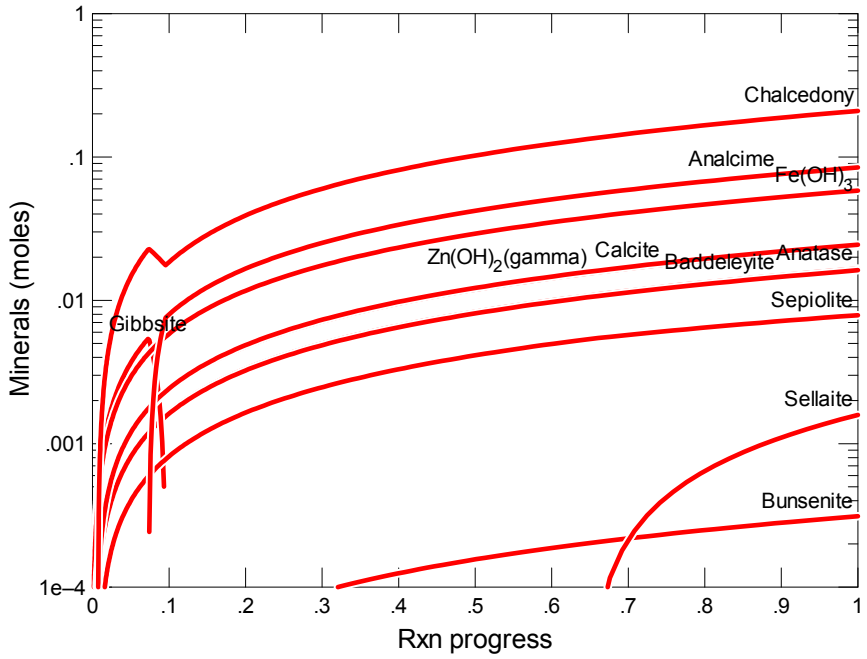


**Figure B.328**. Secondary Phases Calculated to Form as a Function of Reaction Progress (mol-glass/kg) Determined for Glass Sample LAWC15

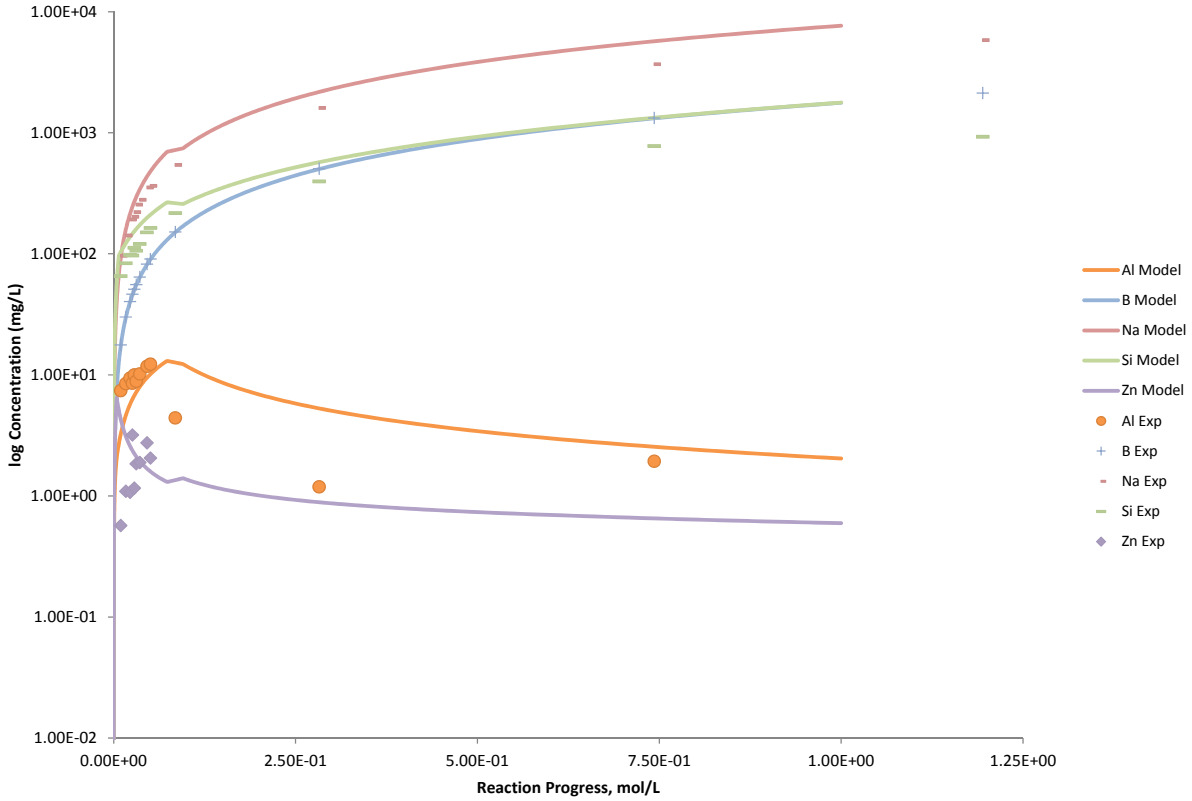


**Figure B.329**. Measured Solution Concentrations (mg/L) and Model Results for Al, B, Na, Si, and Zn, as a Function of Reaction Progress (mol-glass/kg) Determined for Glass Sample LAWC15

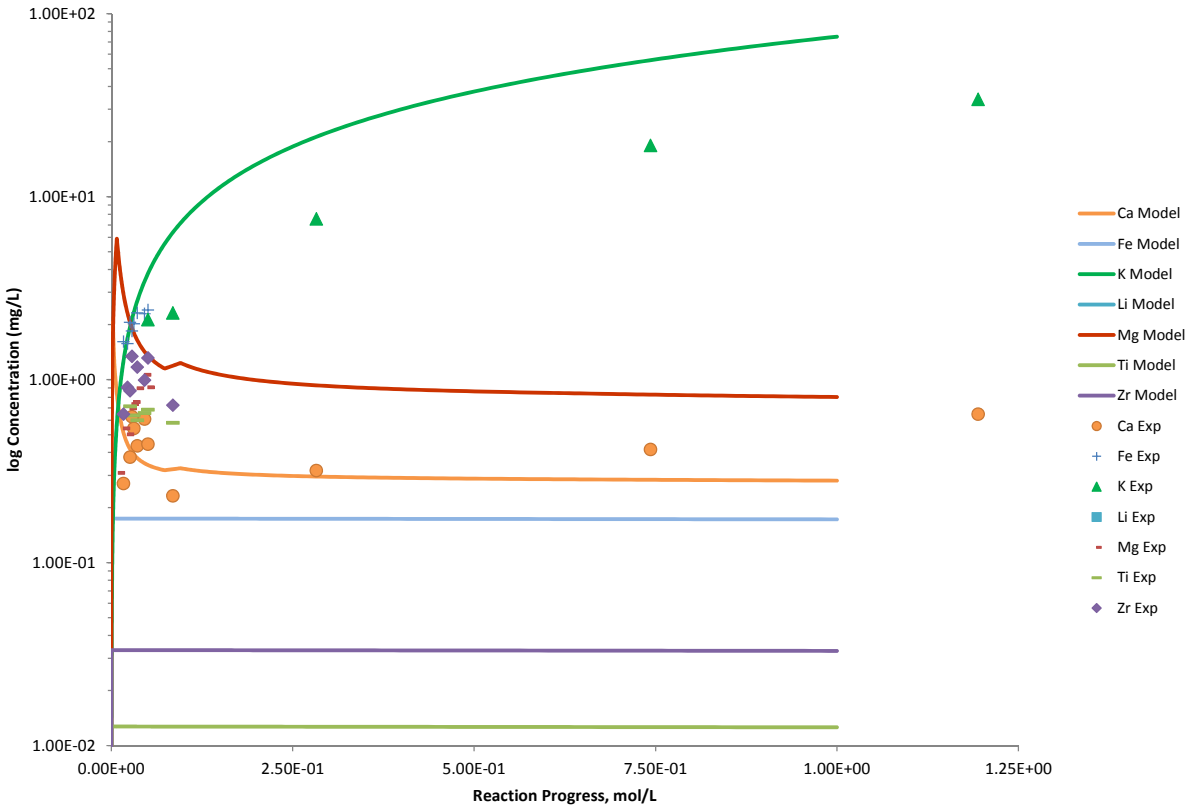


**Figure B.330**. Measured Solution Concentrations (mg/L) and Model Results for Ca, Fe, K, Li, Mg, Ti, and Zr, as a Function of Reaction Progress (mol-glass/kg) Determined for Glass Sample LAWC15

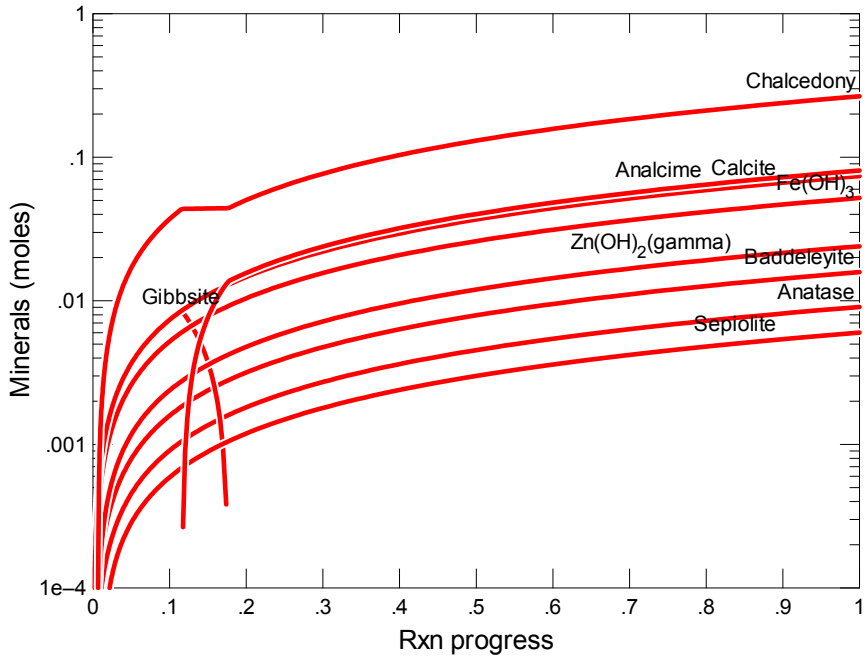


**Figure B.331**. Secondary Phases Calculated to Form as a Function of Reaction Progress (mol-glass/kg) Determined for Glass Sample LAWC21rev2

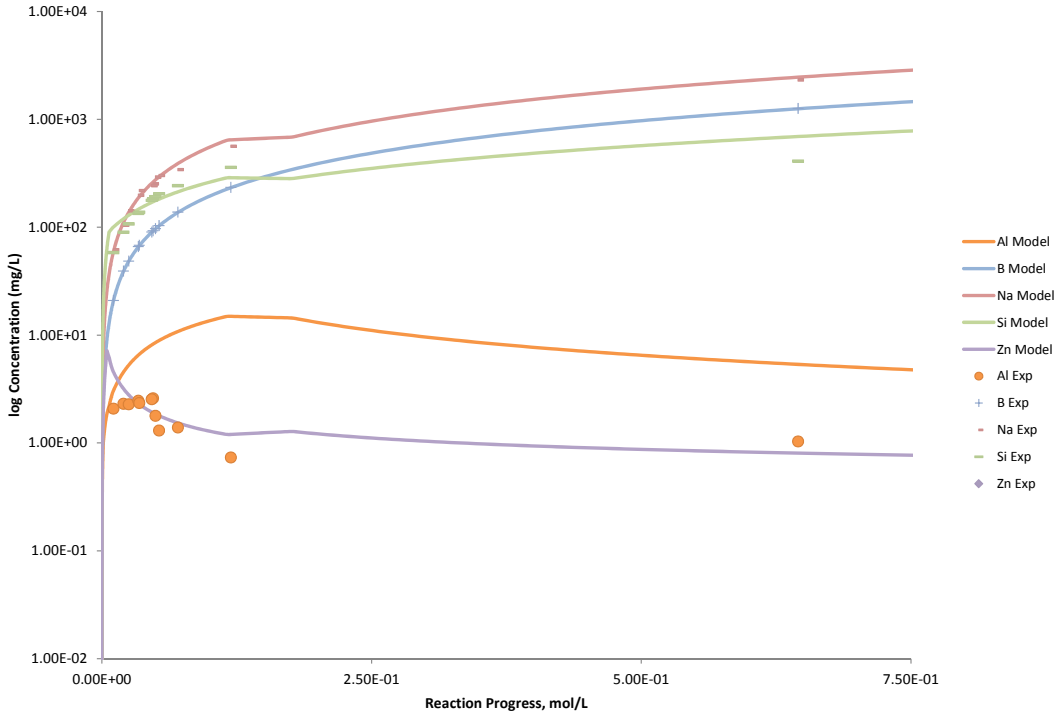


**Figure B.332**. Measured Solution Concentrations (mg/L) and Model Results for Al, B, Na, Si, and Zn, as a Function of Reaction Progress (mol-glass/kg) Determined for Glass Sample LAWC21rev2

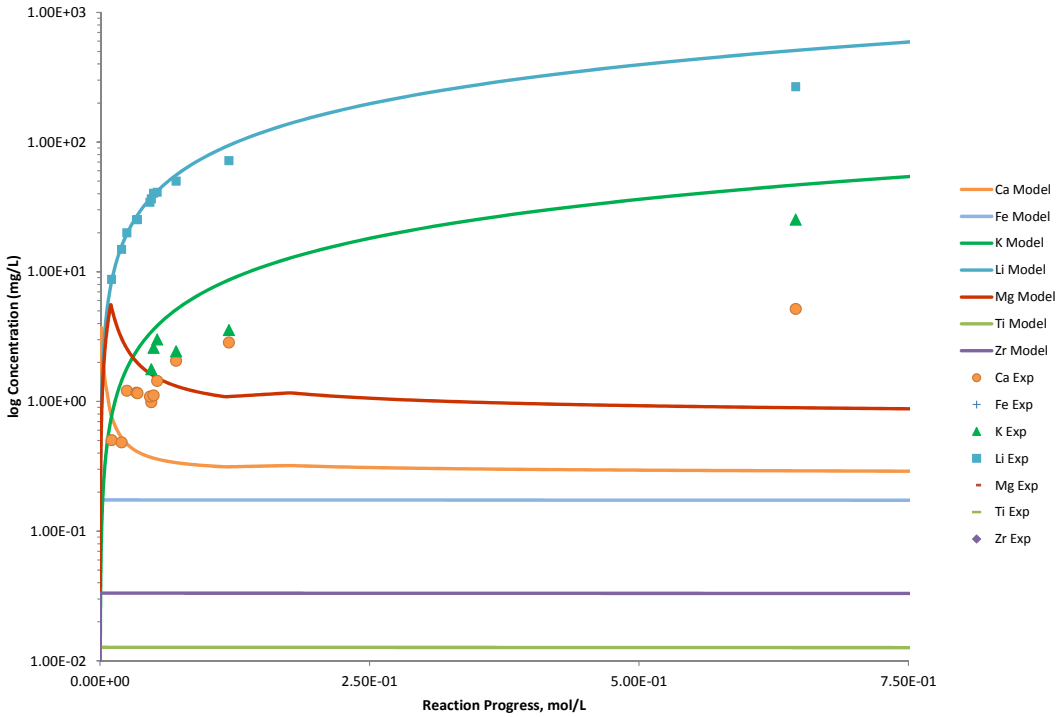


**Figure B.333**. Measured Solution Concentrations (mg/L) and Model Results for Ca, Fe, K, Li, Mg, Ti, and Zr, as a Function of Reaction Progress (mol-glass/kg) Determined for Glass Sample LAWC21rev2

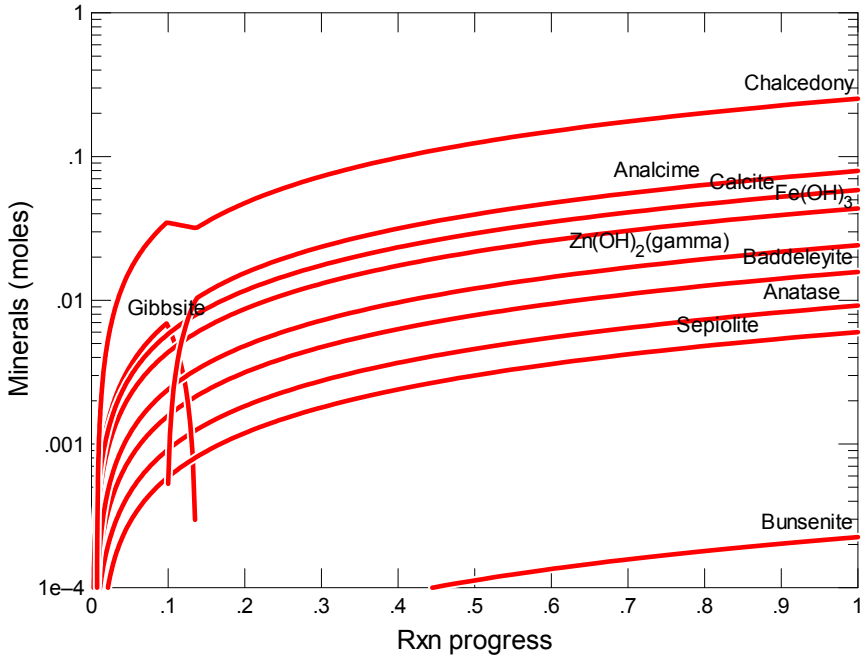


**Figure B.334**. Secondary Phases Calculated to Form as a Function of Reaction Progress (mol-glass/kg) Determined for Glass Sample LAWC22

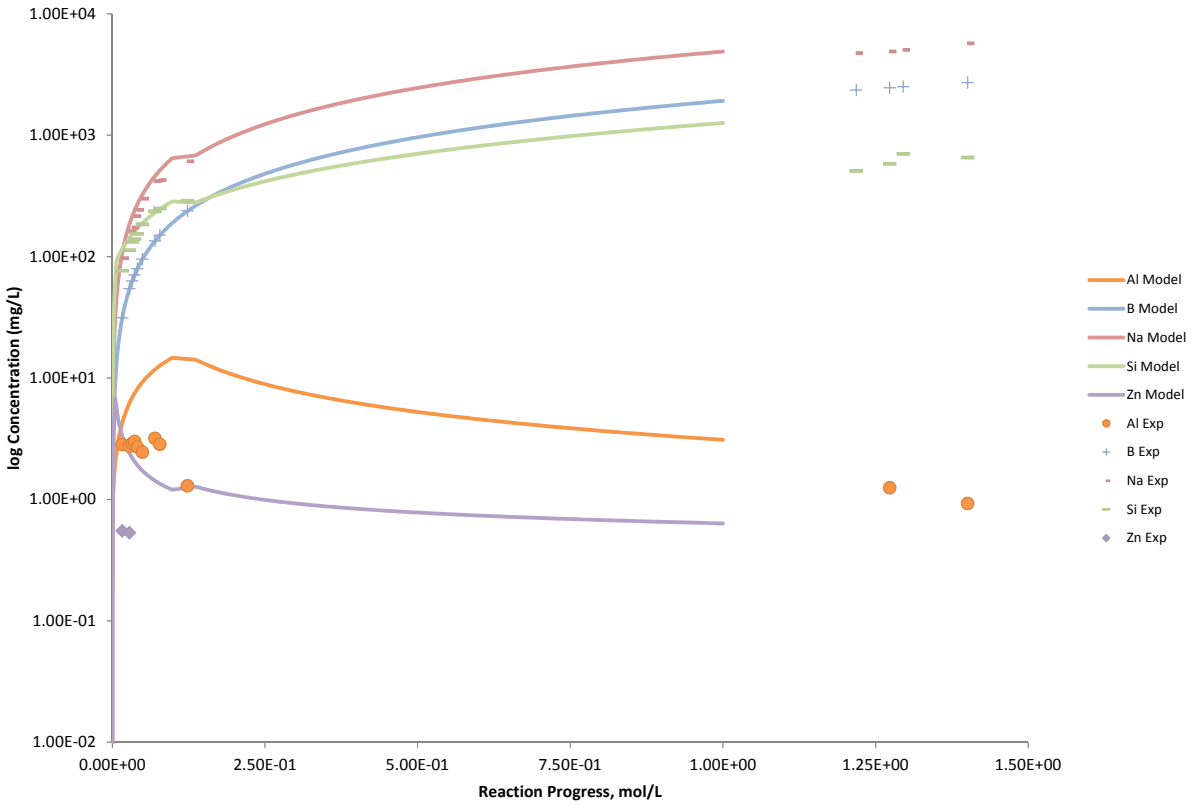


**Figure B.335**. Measured Solution Concentrations (mg/L) and Model Results for Al, B, Na, Si, and Zn, as a Function of Reaction Progress (mol-glass/kg) Determined for Glass Sample LAWC22

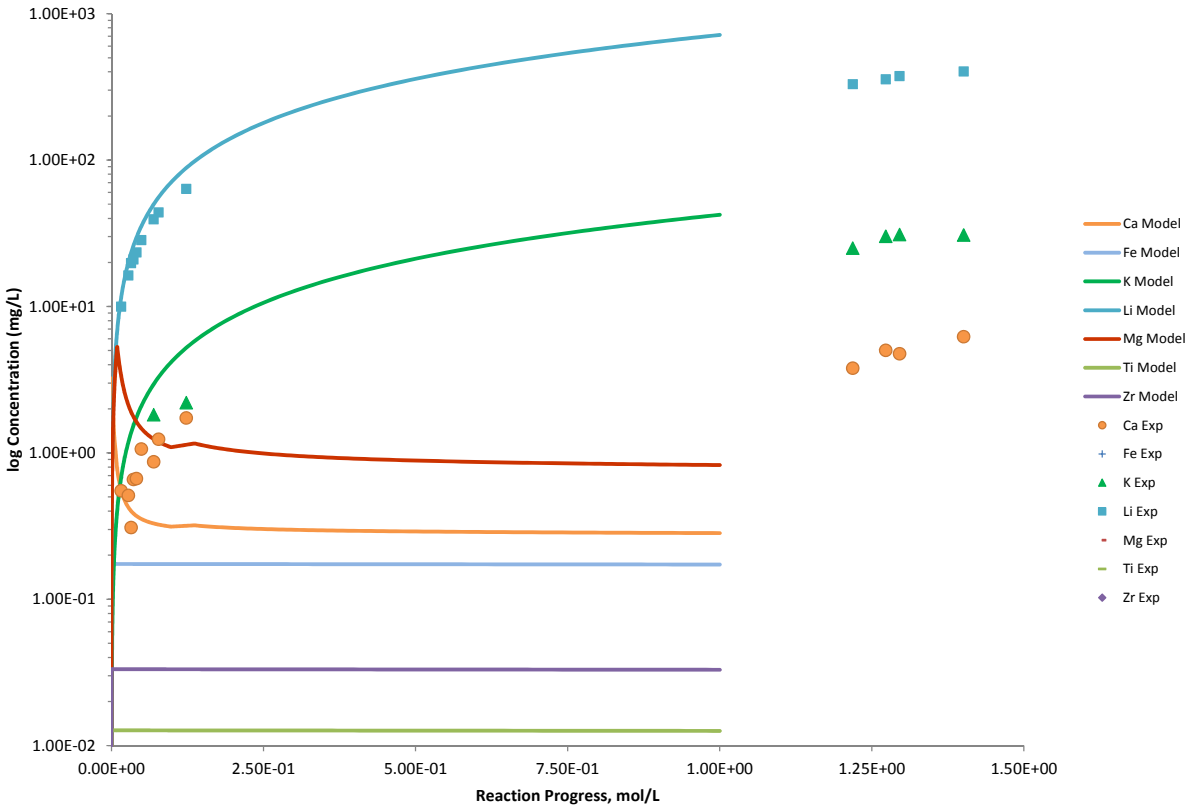


**Figure B.336**. Measured Solution Concentrations (mg/L) and Model Results for Ca, Fe, K, Li, Mg, Ti, and Zr, as a Function of Reaction Progress (mol-glass/kg) Determined for Glass Sample LAWC22

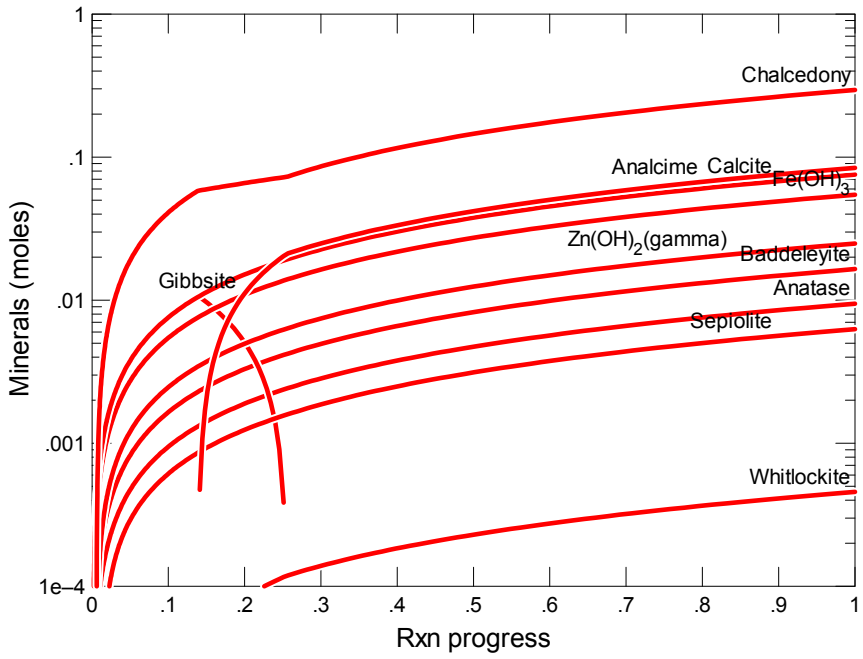


**Figure B.337**. Secondary Phases Calculated to Form as a Function of Reaction Progress (mol-glass/kg) Determined for Glass Sample LAWC23

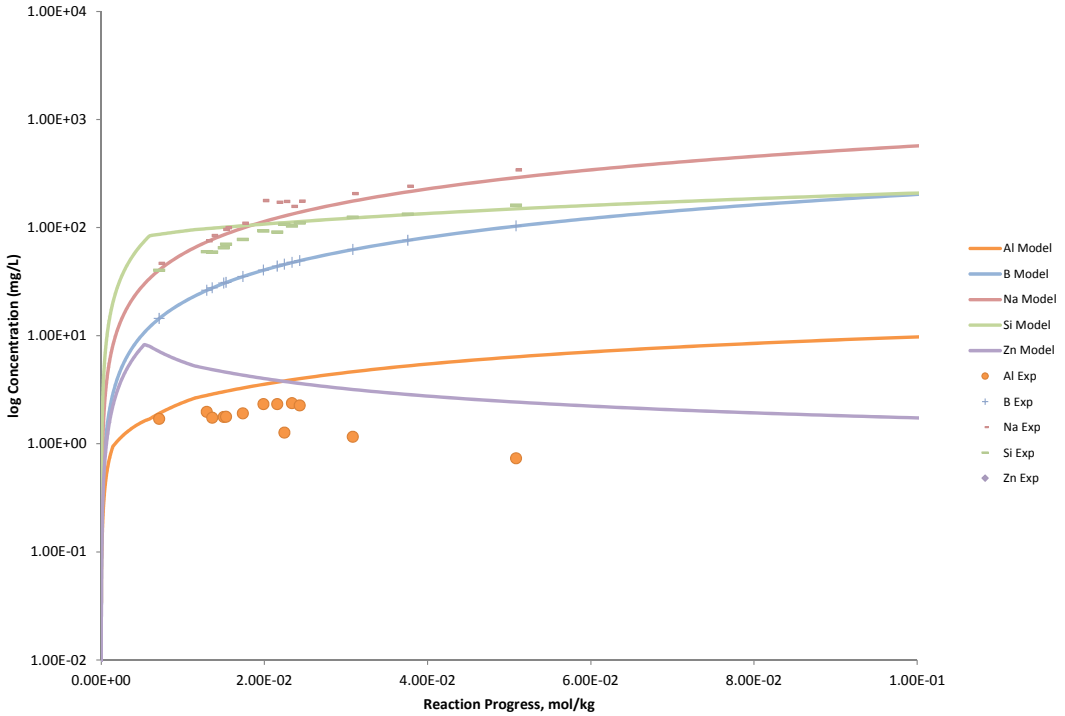


**Figure B.338**. Measured Solution Concentrations (mg/L) and Model Results for Al, B, Na, Si, and Zn, as a Function of Reaction Progress (mol-glass/kg) Determined for Glass Sample LAWC23

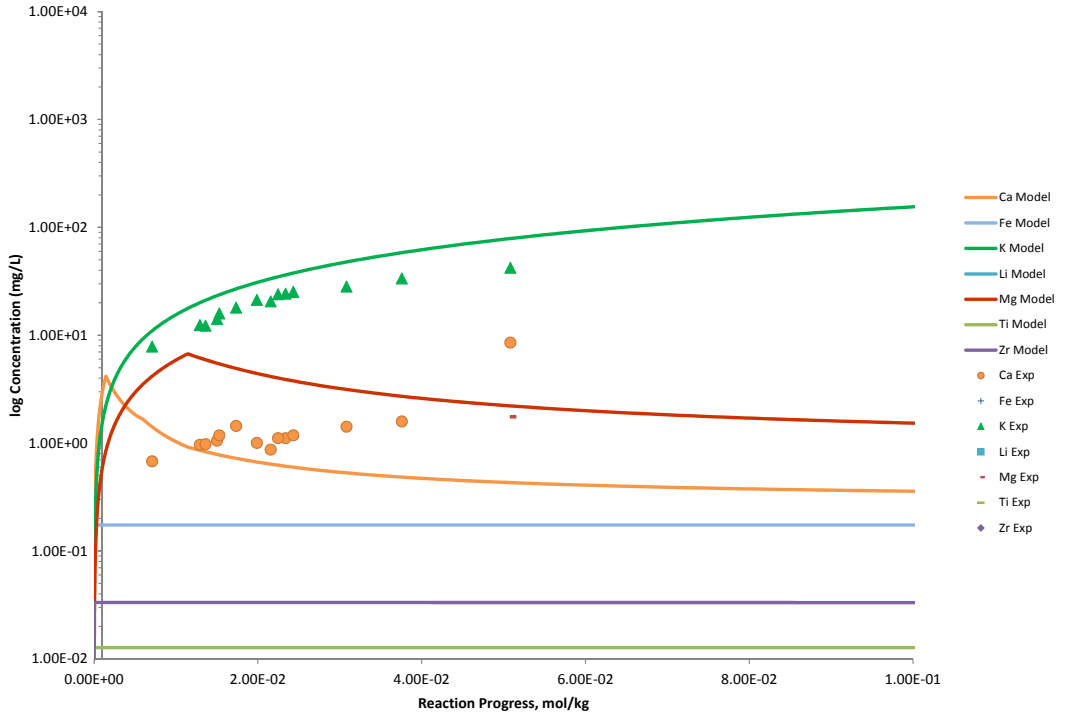


**Figure B.339**. Measured Solution Concentrations (mg/L) and Model Results for Ca, Fe, K, Li, Mg, Ti, and Zr, as a Function of Reaction Progress (mol-glass/kg) Determined for Glass Sample LAWC23

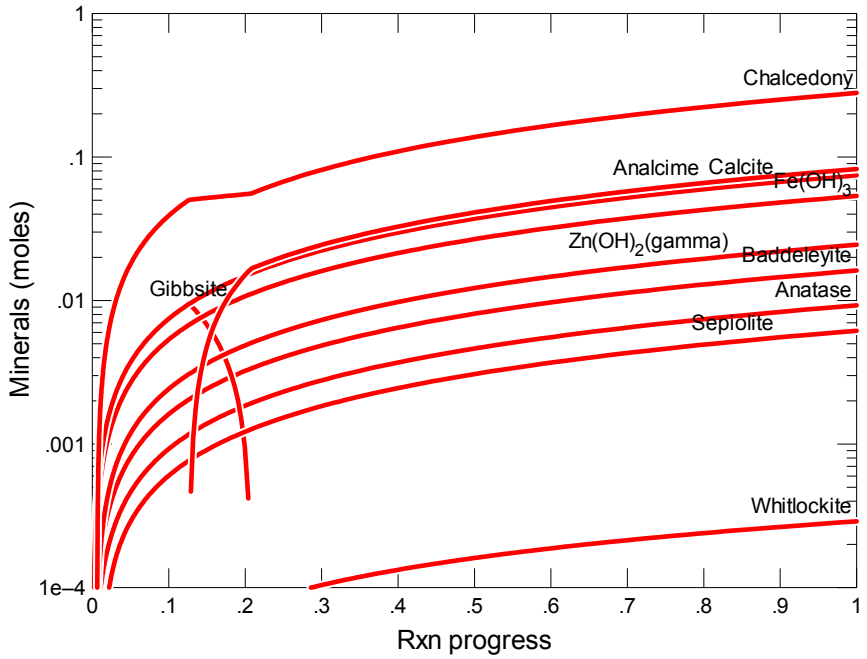


**Figure B.340**. Secondary Phases Calculated to Form as a Function of Reaction Progress (mol-glass/kg) Determined for Glass Sample LAWC24

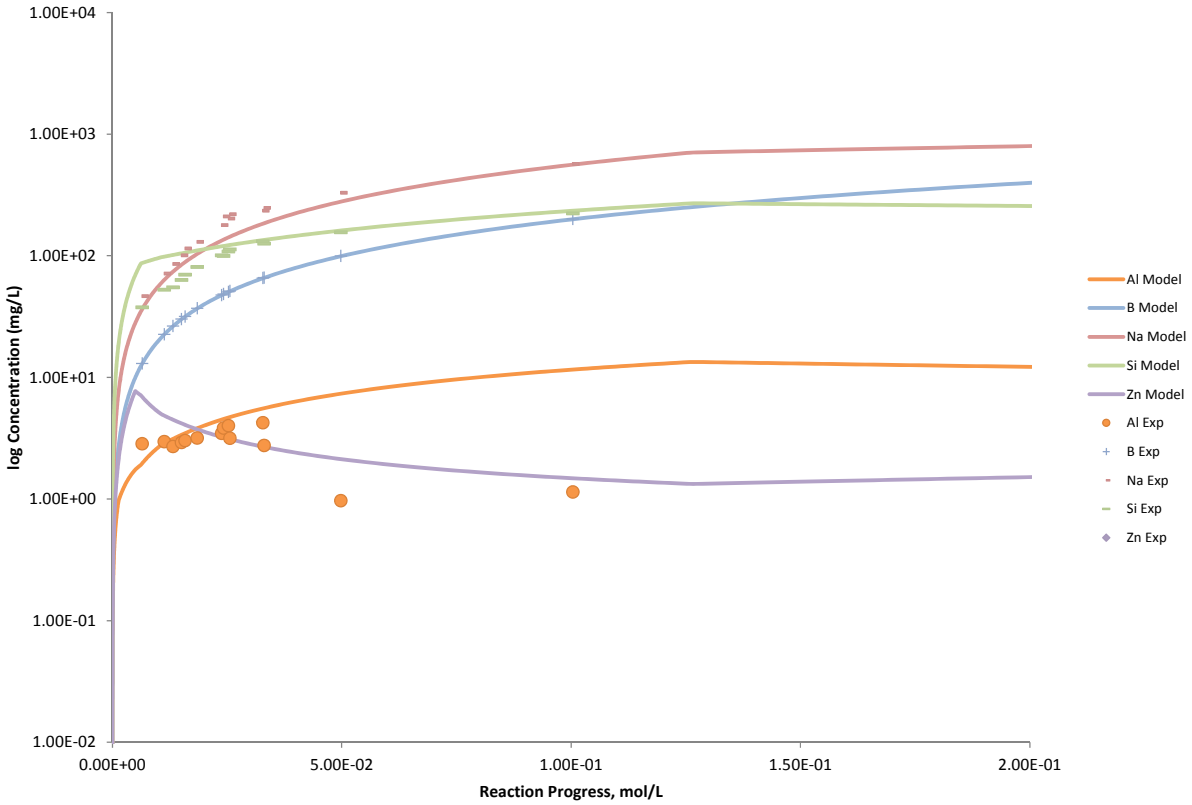


**Figure B.341**. Measured Solution Concentrations (mg/L) and Model Results for Al, B, Na, Si, and Zn, as a Function of Reaction Progress (mol-glass/kg) Determined for Glass Sample LAWC24

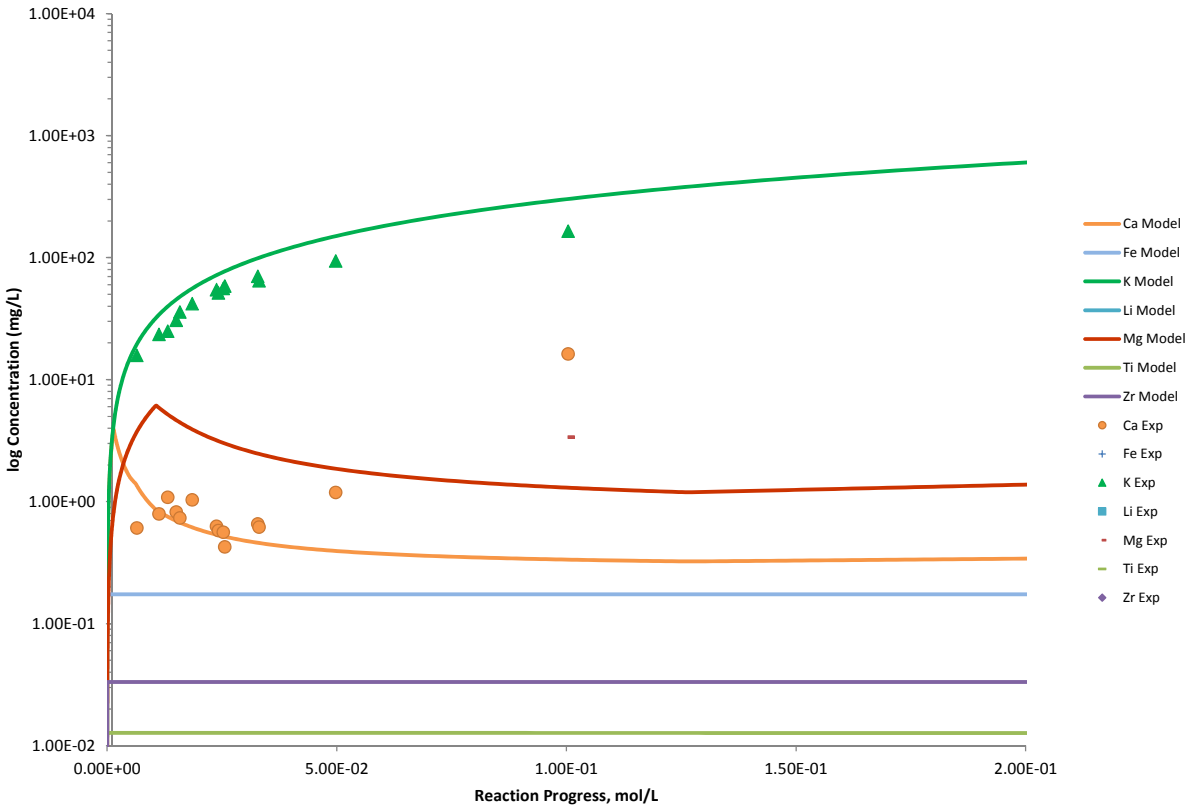


**Figure B.342**. Measured Solution Concentrations (mg/L) and Model Results for Ca, Fe, K, Li, Mg, Ti, and Zr, as a Function of Reaction Progress (mol-glass/kg) Determined for Glass Sample LAWC24

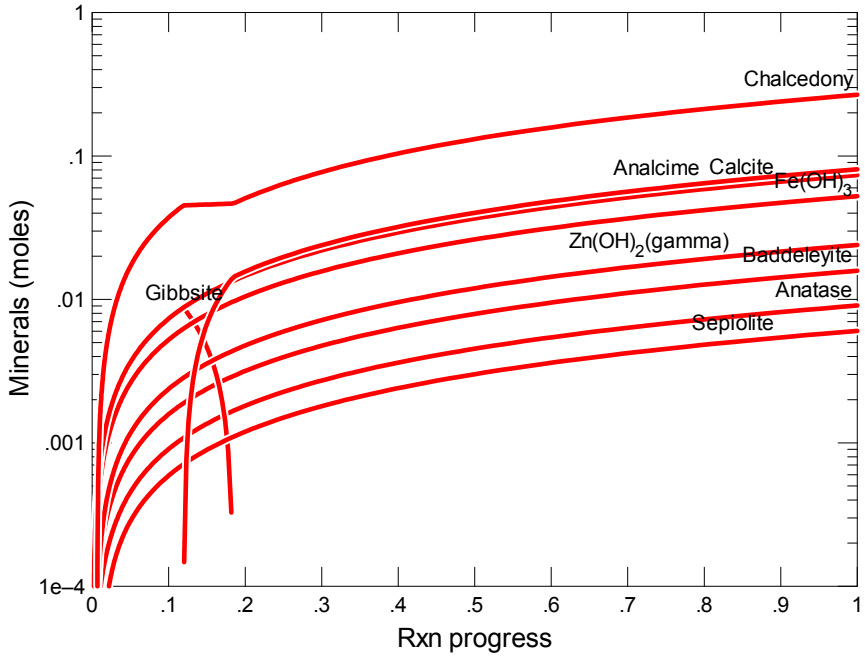


**Figure B.343**. Secondary Phases Calculated to Form as a Function of Reaction Progress (mol-glass/kg) Determined for Glass Sample LAWC25

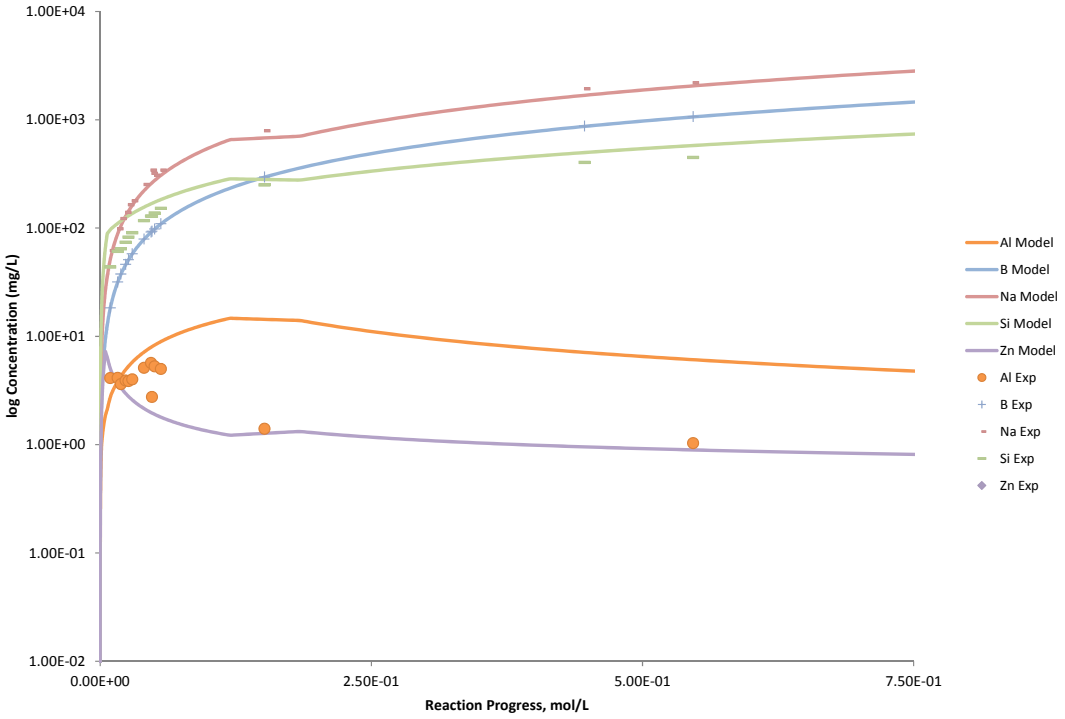


**Figure B.344**. Measured Solution Concentrations (mg/L) and Model Results for Al, B, Na, Si, and Zn, as a Function of Reaction Progress (mol-glass/kg) Determined for Glass Sample LAWC25

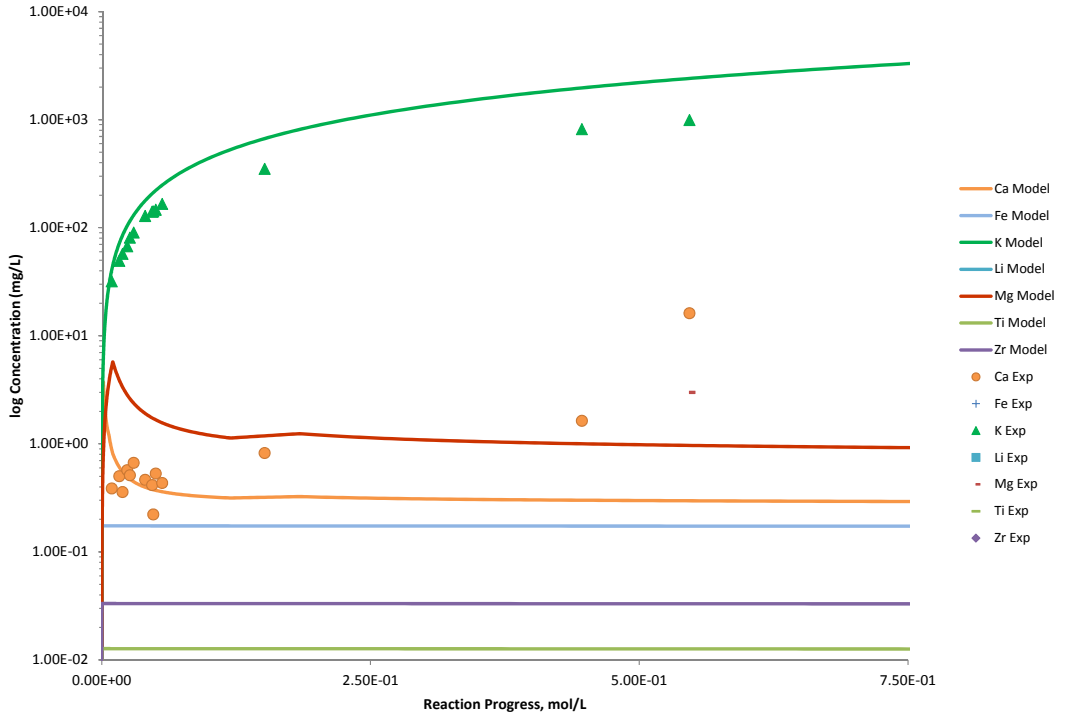


**Figure B.345**. Measured Solution Concentrations (mg/L) and Model Results for Ca, Fe, K, Li, Mg, Ti, and Zr, as a Function of Reaction Progress (mol-glass/kg) Determined for Glass Sample LAWC25

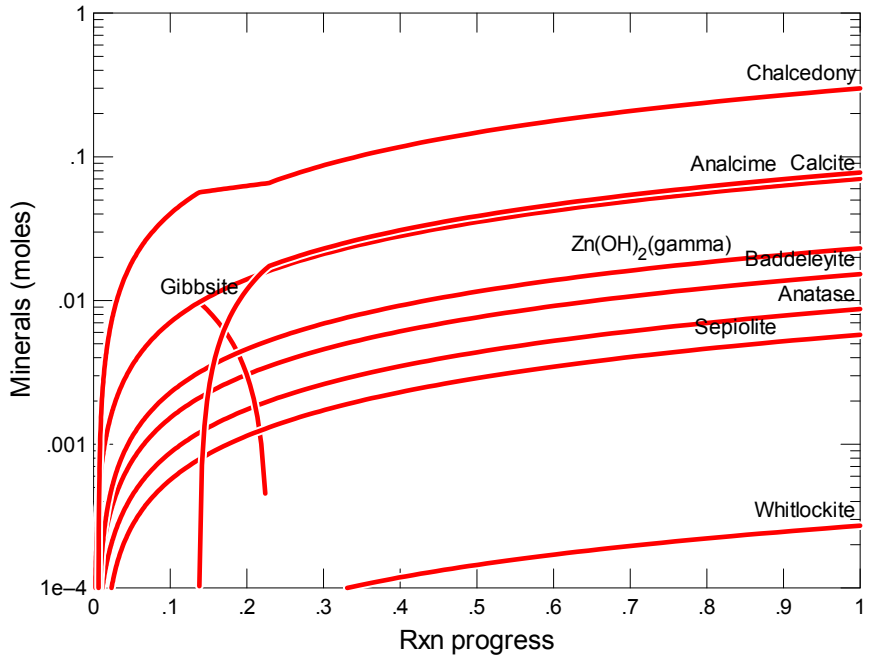


**Figure B.346**. Secondary Phases Calculated to Form as a Function of Reaction Progress (mol-glass/kg) Determined for Glass Sample LAWC26

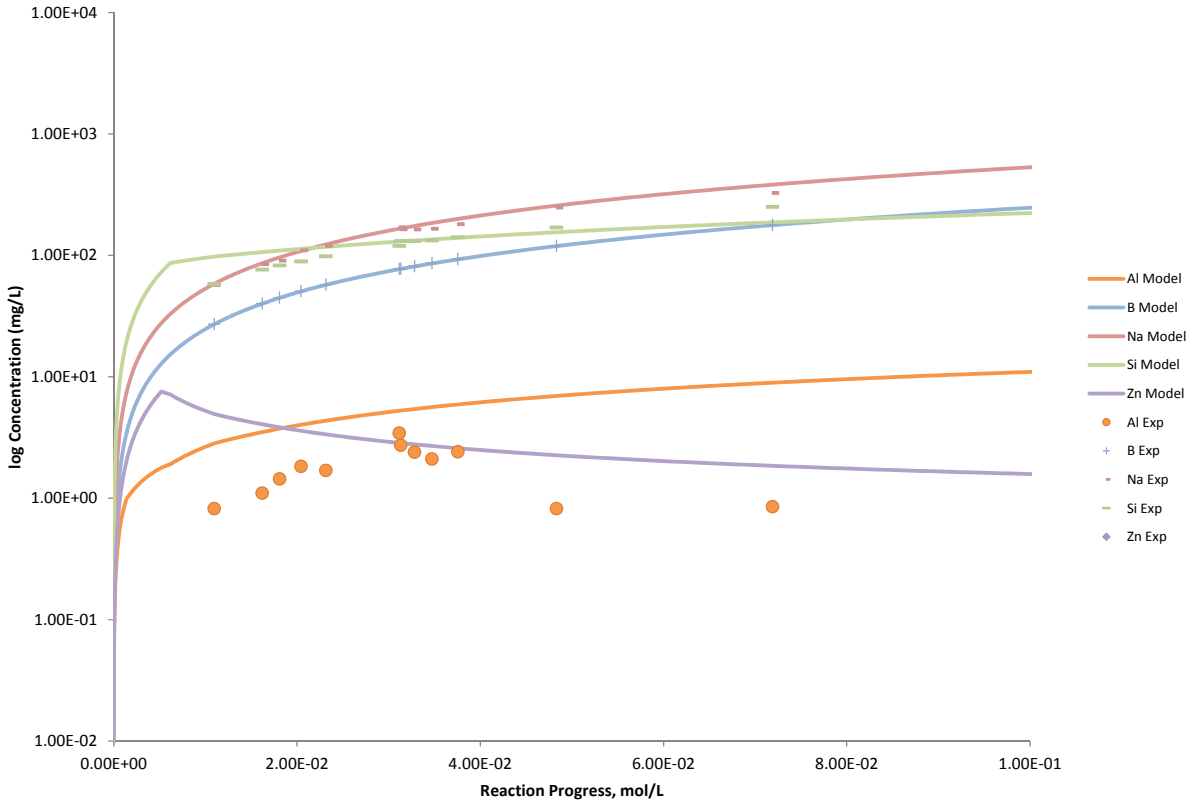


**Figure B.347**. Measured Solution Concentrations (mg/L) and Model Results for Al, B, Na, Si, and Zn, as a Function of Reaction Progress (mol-glass/kg) Determined for Glass Sample LAWC26

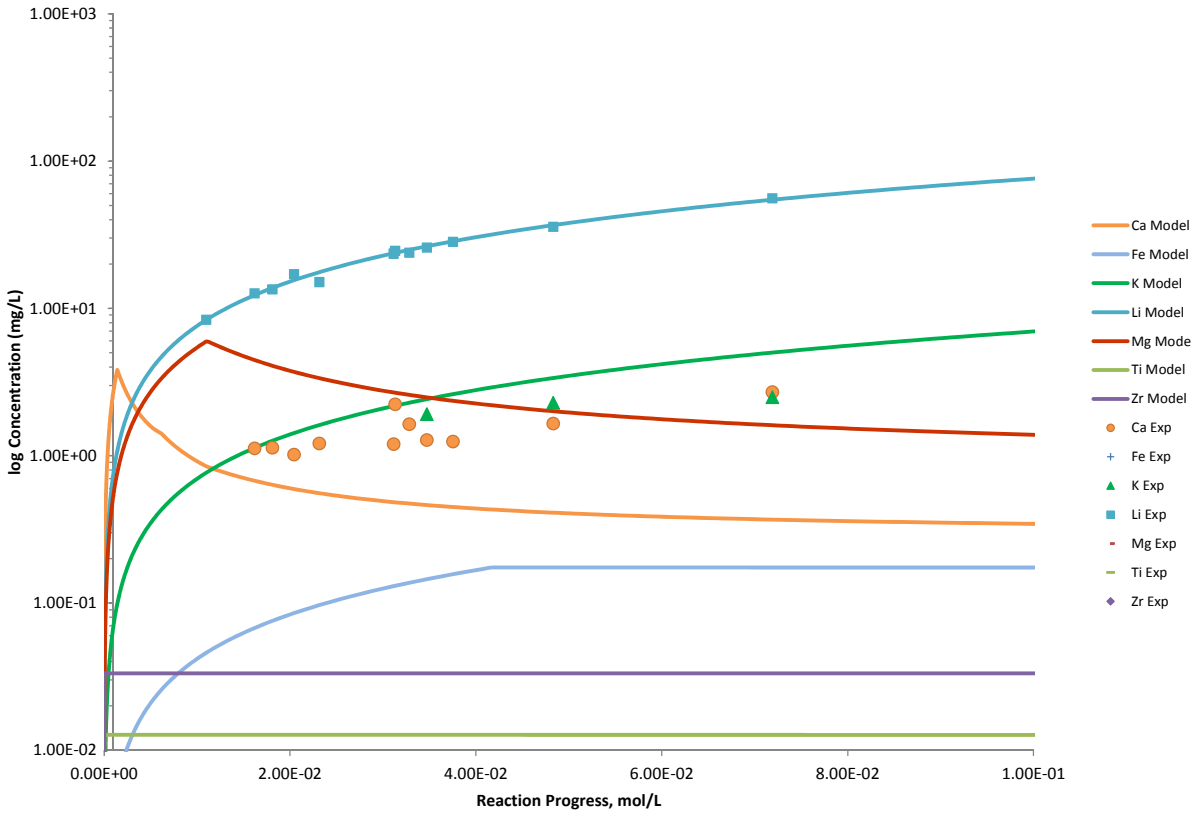


**Figure B.348**. Measured Solution Concentrations (mg/L) and Model Results for Ca, Fe, K, Li, Mg, Ti, and Zr, as a Function of Reaction Progress (mol-glass/kg) Determined for Glass Sample LAWC26

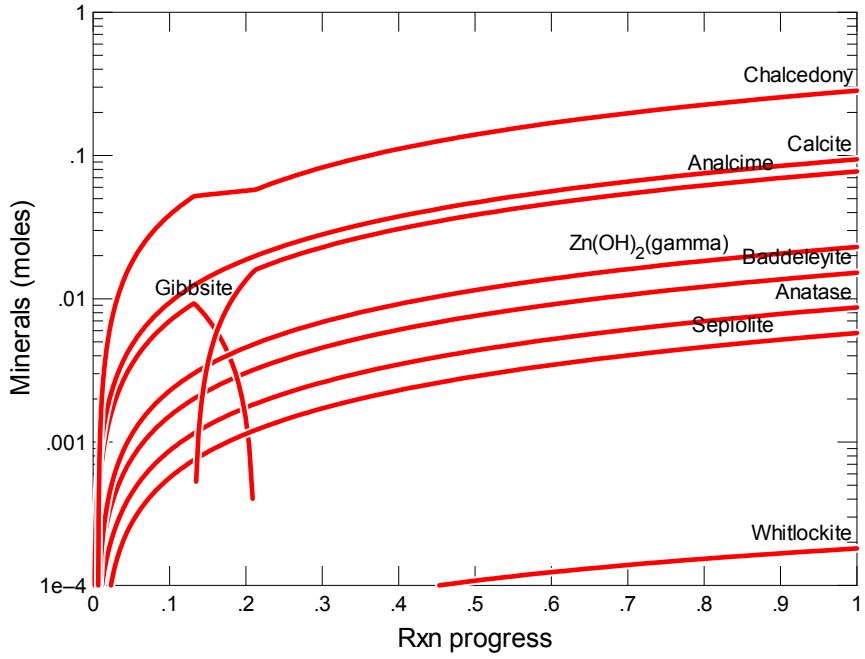


**Figure B.349**. Secondary Phases Calculated to Form as a Function of Reaction Progress (mol-glass/kg) Determined for Glass Sample LAWC27

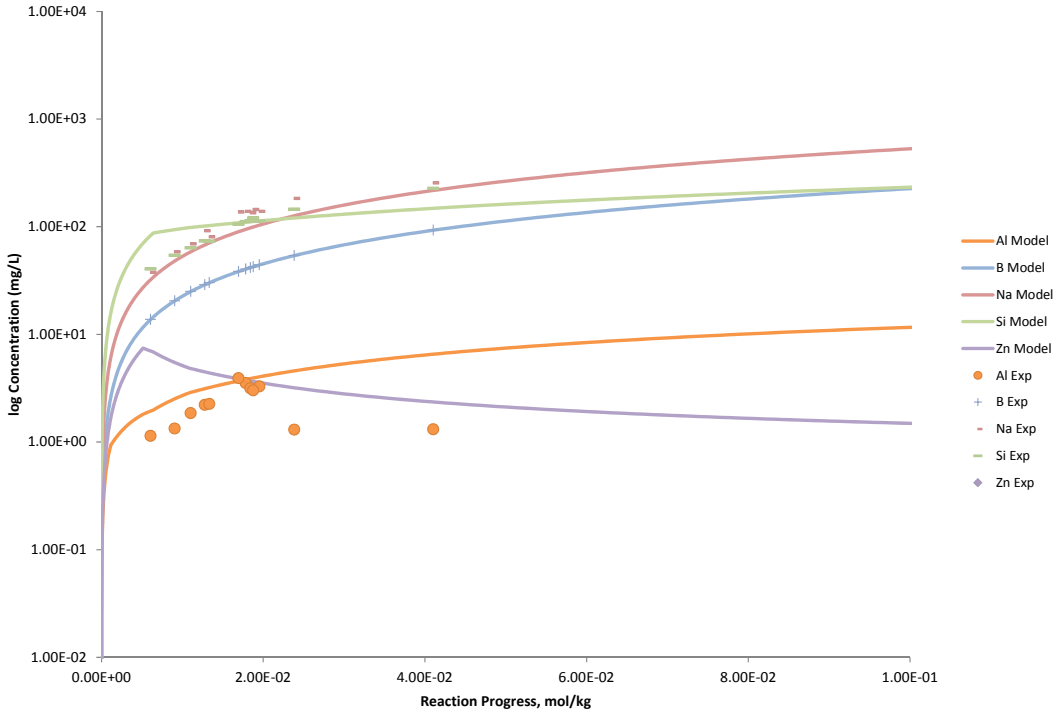


**Figure B.350**. Measured Solution Concentrations (mg/L) and Model Results for Al, B, Na, Si, and Zn, as a Function of Reaction Progress (mol-glass/kg) Determined for Glass Sample LAWC27

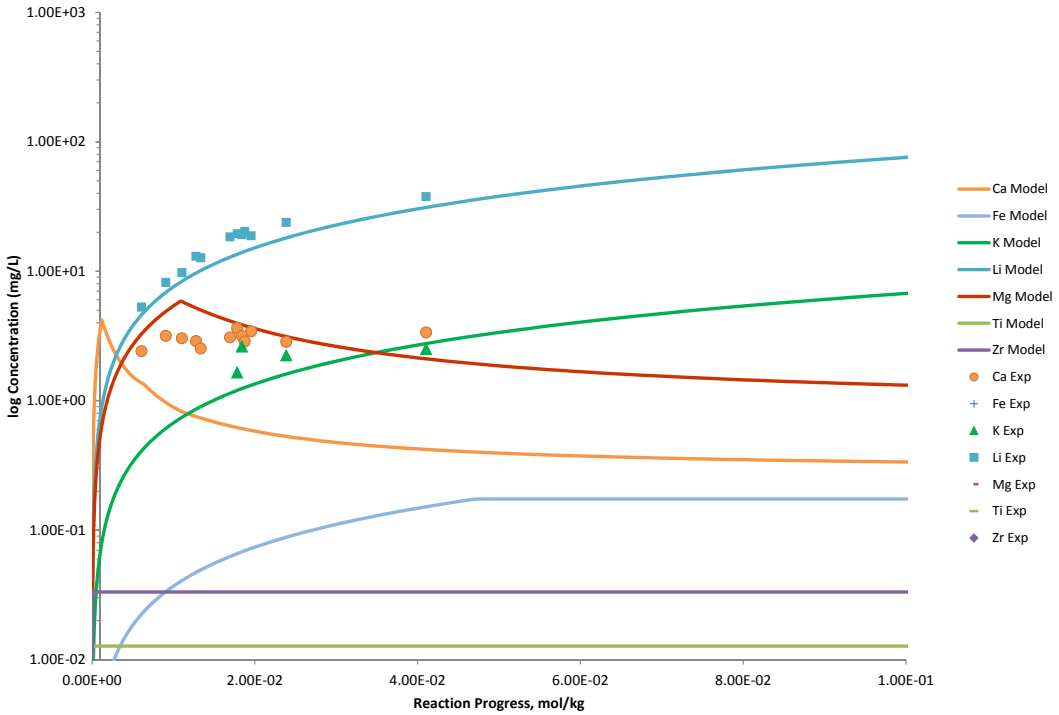


**Figure B.351**. Measured Solution Concentrations (mg/L) and Model Results for Ca, Fe, K, Li, Mg, Ti, and Zr, as a Function of Reaction Progress (mol-glass/kg) Determined for Glass Sample LAWC27

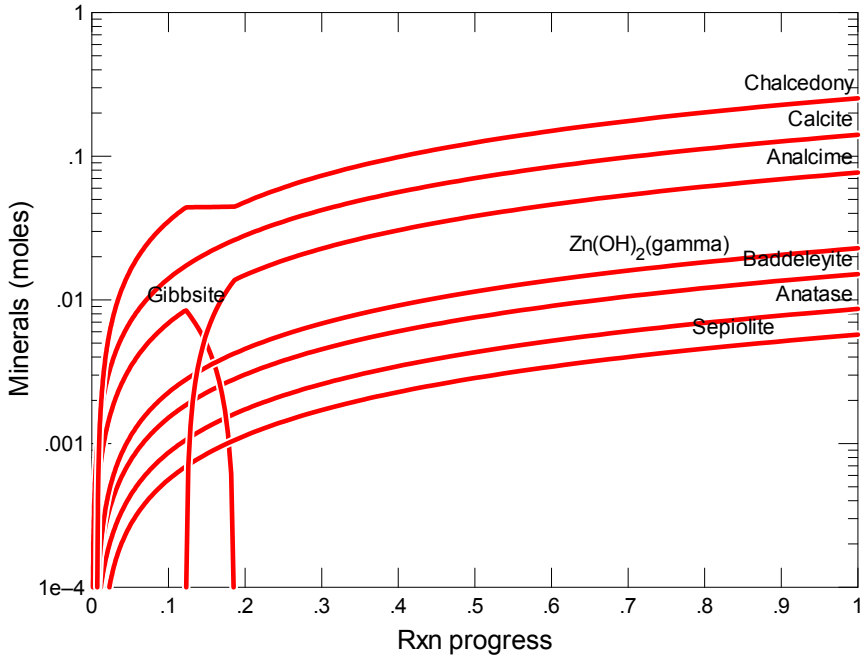


**Figure B.352**. Secondary Phases Calculated to Form as a Function of Reaction Progress (mol-glass/kg) Determined for Glass Sample LAWC28

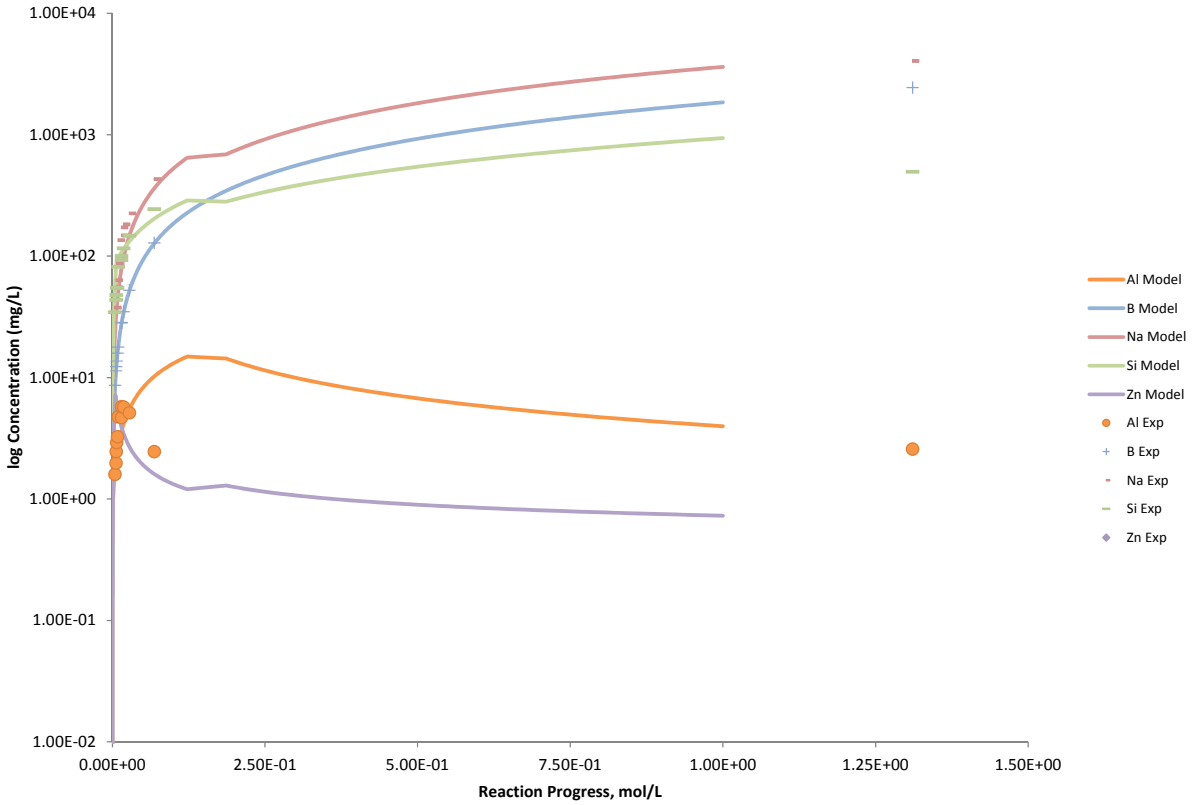


**Figure B.353**. Measured Solution Concentrations (mg/L) and Model Results for Al, B, Na, Si, and Zn, as a Function of Reaction Progress (mol-glass/kg) Determined for Glass Sample LAWC28

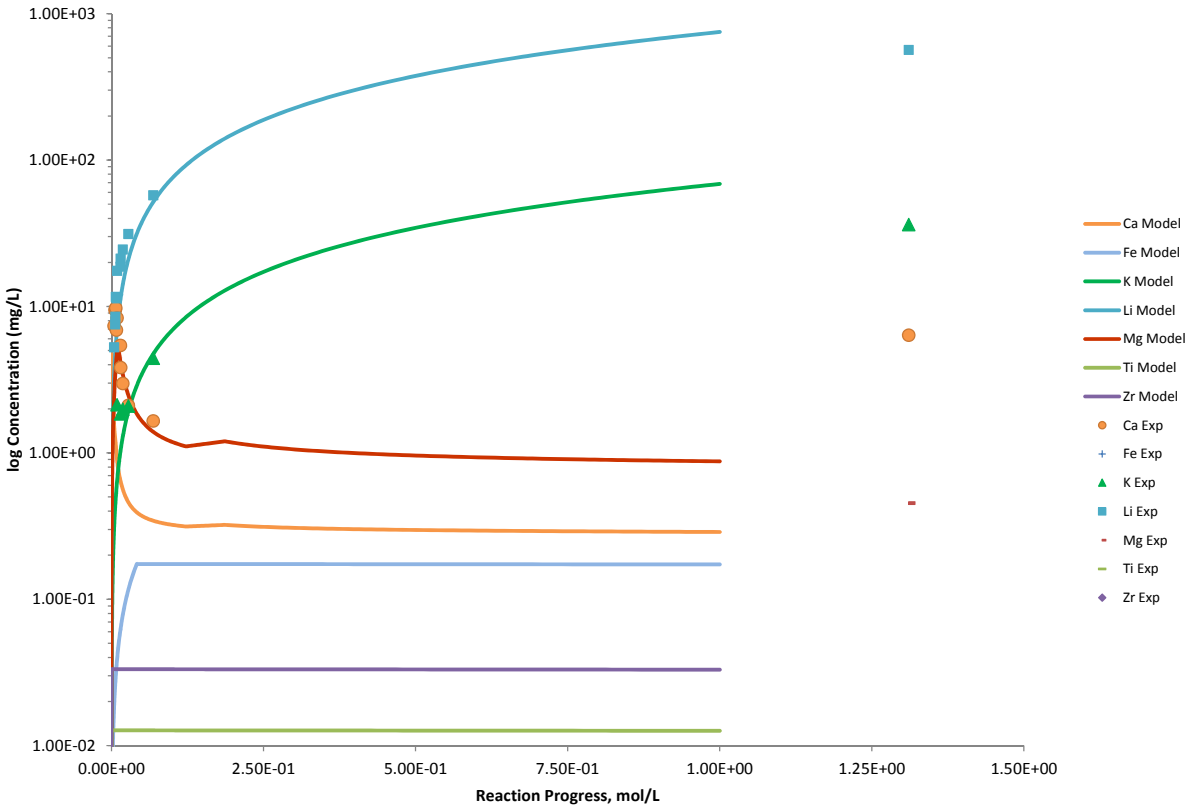


**Figure B.354**. Measured Solution Concentrations (mg/L) and Model Results for Ca, Fe, K, Li, Mg, Ti, and Zr, as a Function of Reaction Progress (mol-glass/kg) Determined for Glass Sample LAWC28

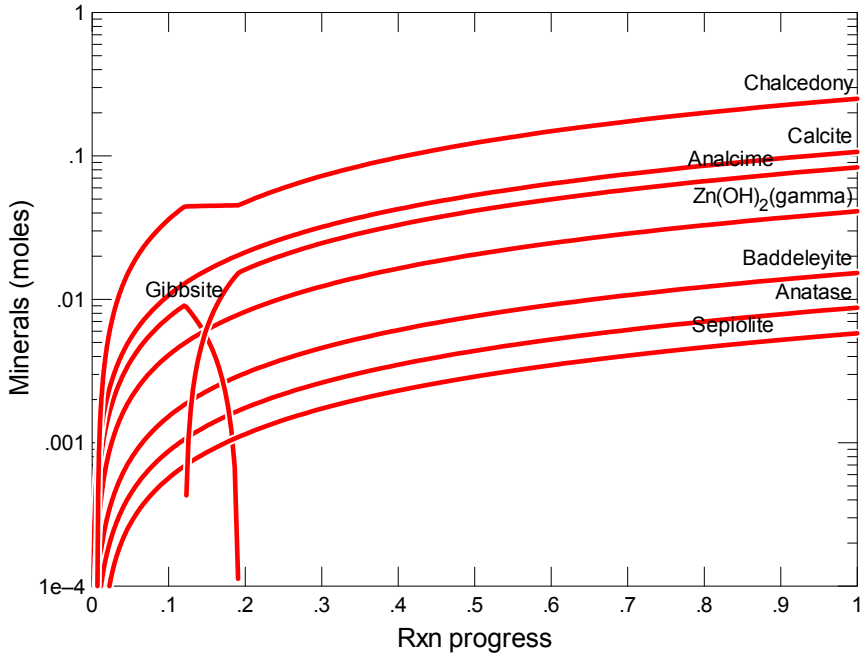


**Figure B.355**. Secondary Phases Calculated to Form as a Function of Reaction Progress (mol-glass/kg) Determined for Glass Sample LAWC29

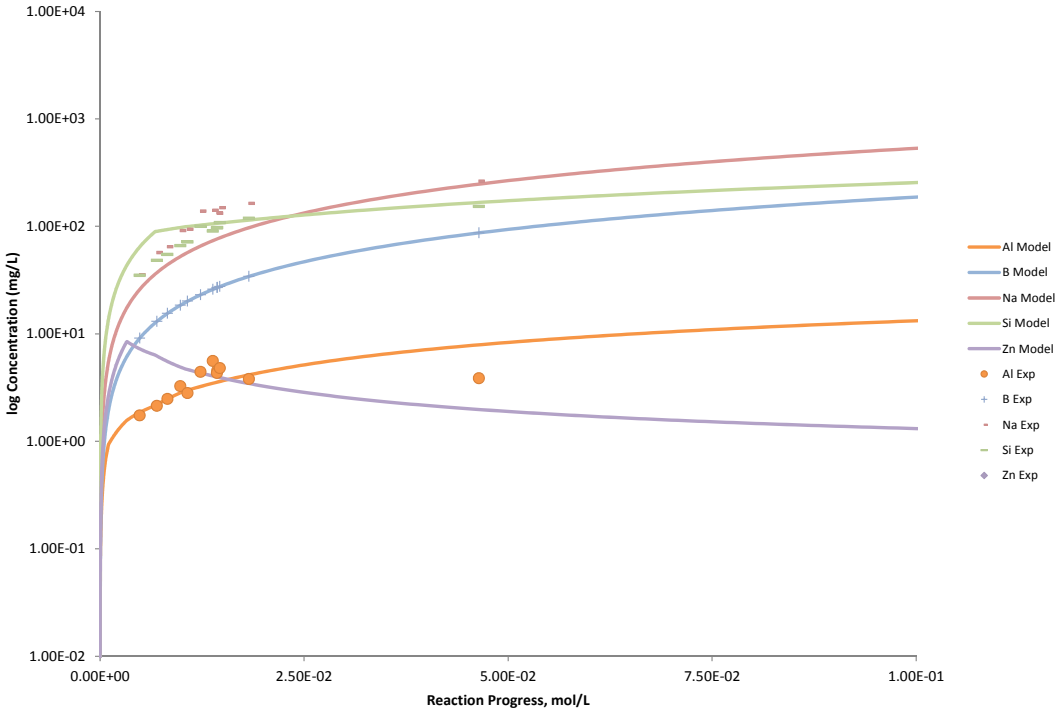


**Figure B.356**. Measured Solution Concentrations (mg/L) and Model Results for Al, B, Na, Si, and Zn, as a Function of Reaction Progress (mol-glass/kg) Determined for Glass Sample LAWC29

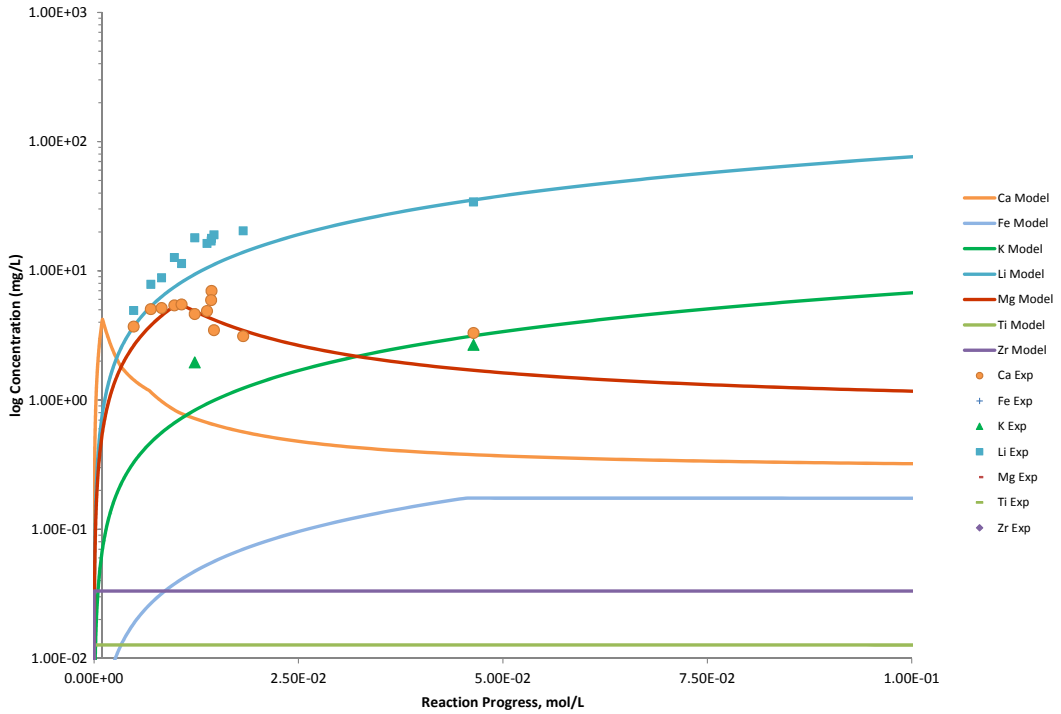


**Figure B.357**. Measured Solution Concentrations (mg/L) and Model Results for Ca, Fe, K, Li, Mg, Ti, and Zr, as a Function of Reaction Progress (mol-glass/kg) Determined for Glass Sample LAWC29

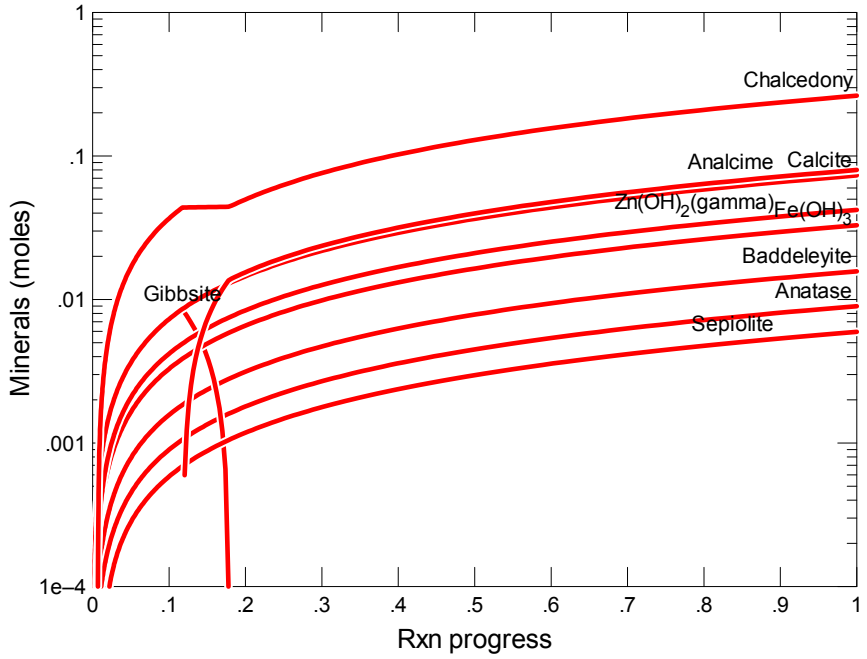


**Figure B.358**. Secondary Phases Calculated to Form as a Function of Reaction Progress (mol-glass/kg) Determined for Glass Sample LAWC30

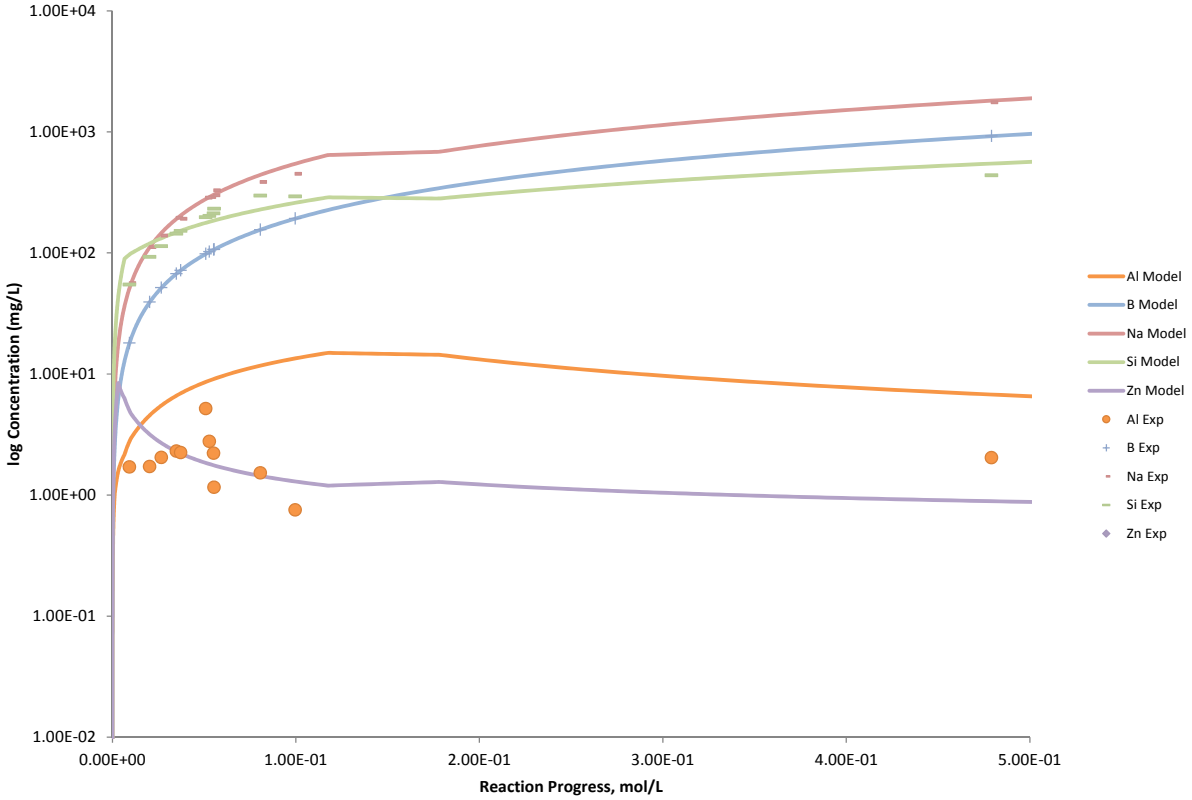


**Figure B.359**. Measured Solution Concentrations (mg/L) and Model Results for Al, B, Na, Si, and Zn, as a Function of Reaction Progress (mol-glass/kg) Determined for Glass Sample LAWC30

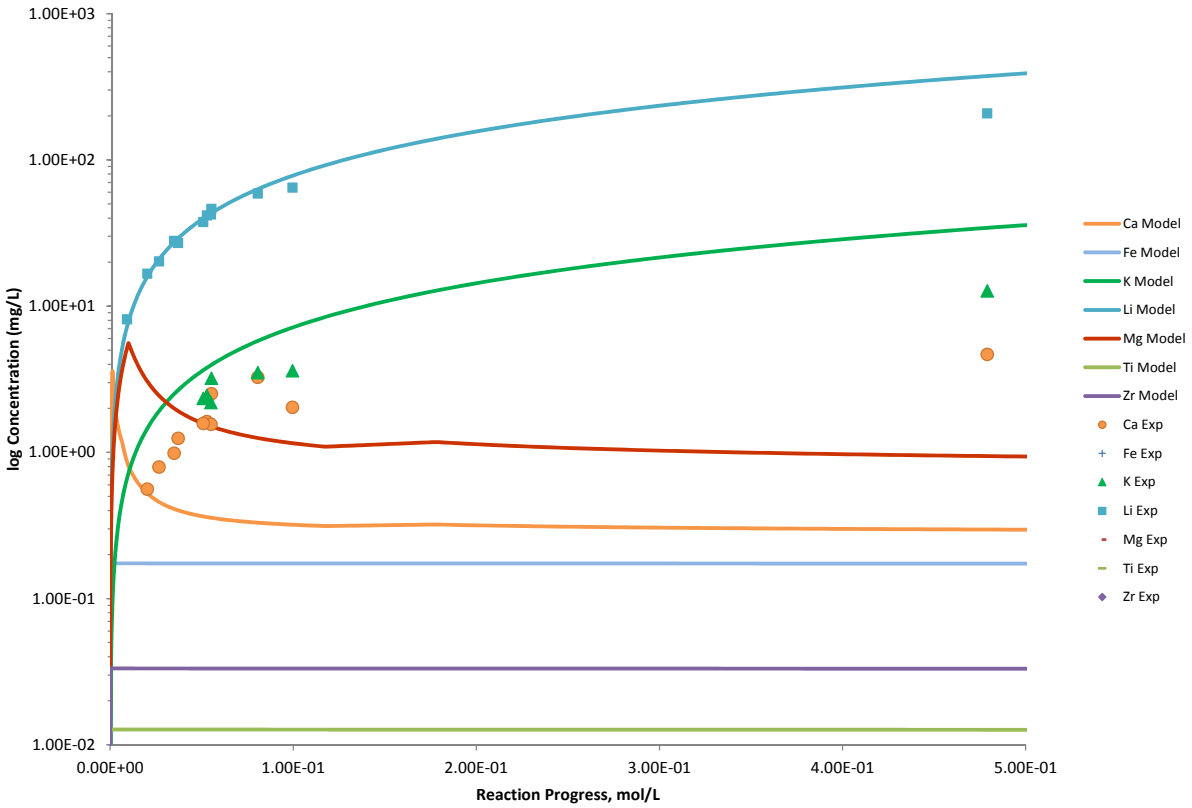


**Figure B.360**. Measured Solution Concentrations (mg/L) and Model Results for Ca, Fe, K, Li, Mg, Ti, and Zr, as a Function of Reaction Progress (mol-glass/kg) Determined for Glass Sample LAWC30

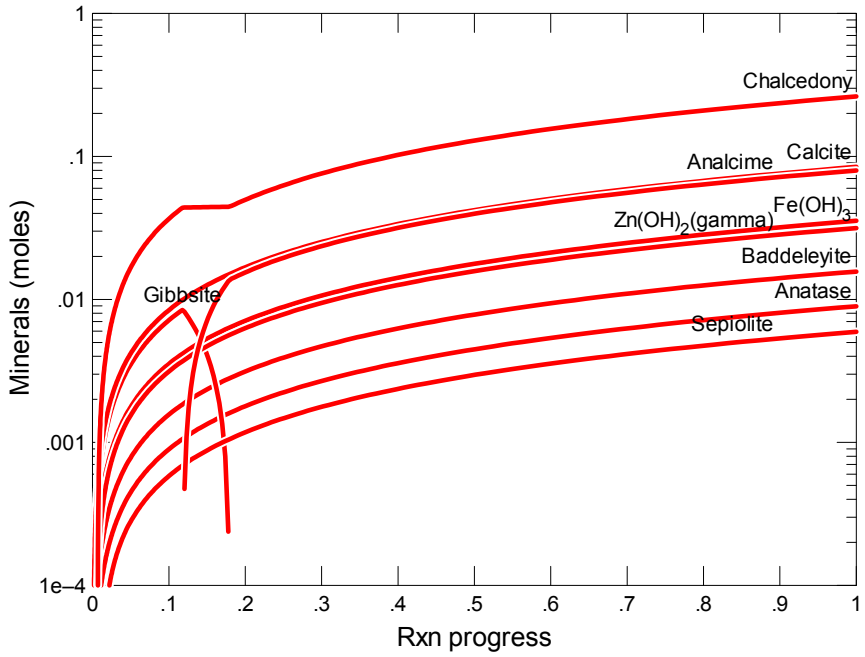


**Figure B.361**. Secondary Phases Calculated to Form as a Function of Reaction Progress (mol-glass/kg) Determined for Glass Sample LAWC31

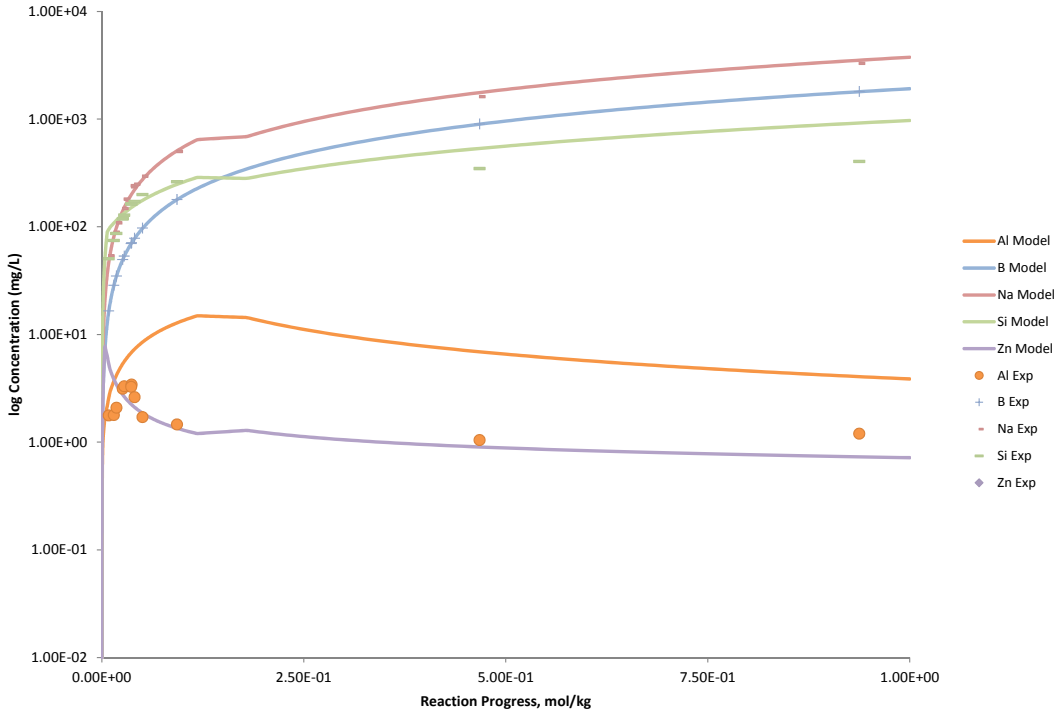


**Figure B.362**. Measured Solution Concentrations (mg/L) and Model Results for Al, B, Na, Si, and Zn, as a Function of Reaction Progress (mol-glass/kg) Determined for Glass Sample LAWC31

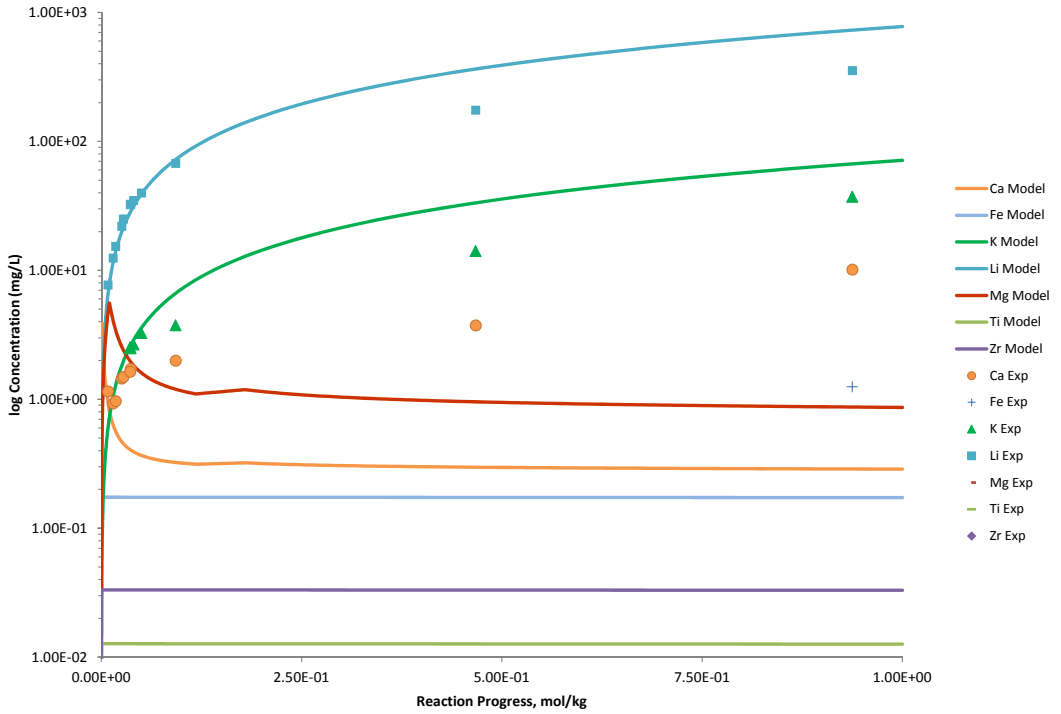


**Figure B.363**. Measured Solution Concentrations (mg/L) and Model Results for Ca, Fe, K, Li, Mg, Ti, and Zr, as a Function of Reaction Progress (mol-glass/kg) Determined for Glass Sample LAWC31

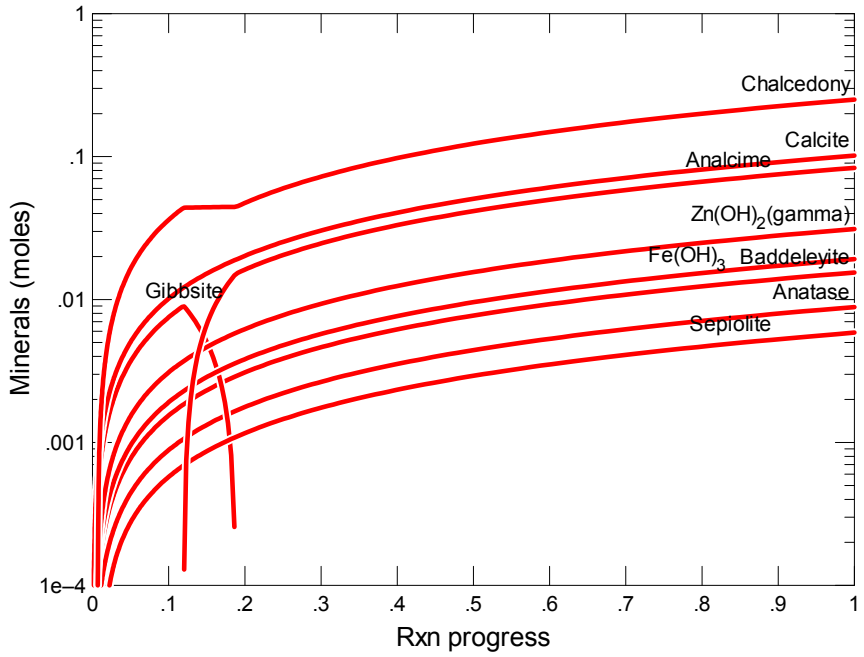


**Figure B.364**. Secondary Phases Calculated to Form as a Function of Reaction Progress (mol-glass/kg) Determined for Glass Sample LAWC32

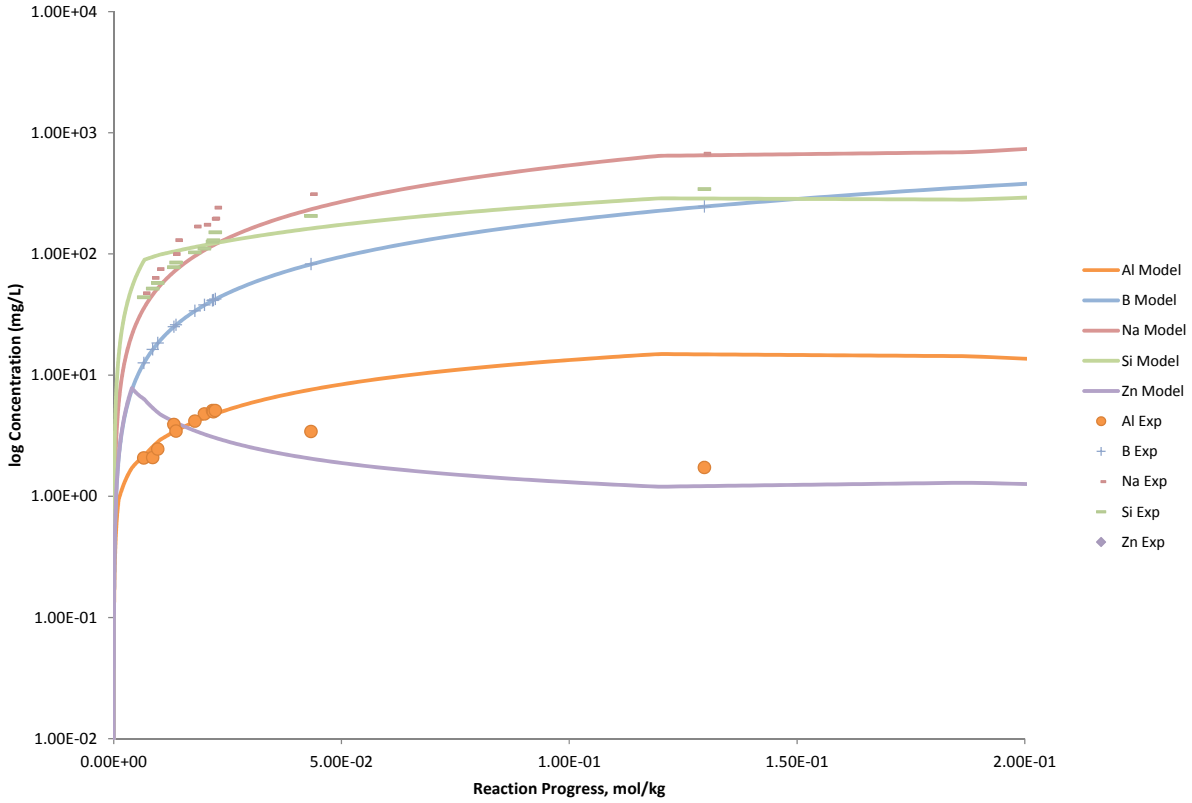


**Figure B.365**. Measured Solution Concentrations (mg/L) and Model Results for Al, B, Na, Si, and Zn, as a Function of Reaction Progress (mol-glass/kg) Determined for Glass Sample LAWC32

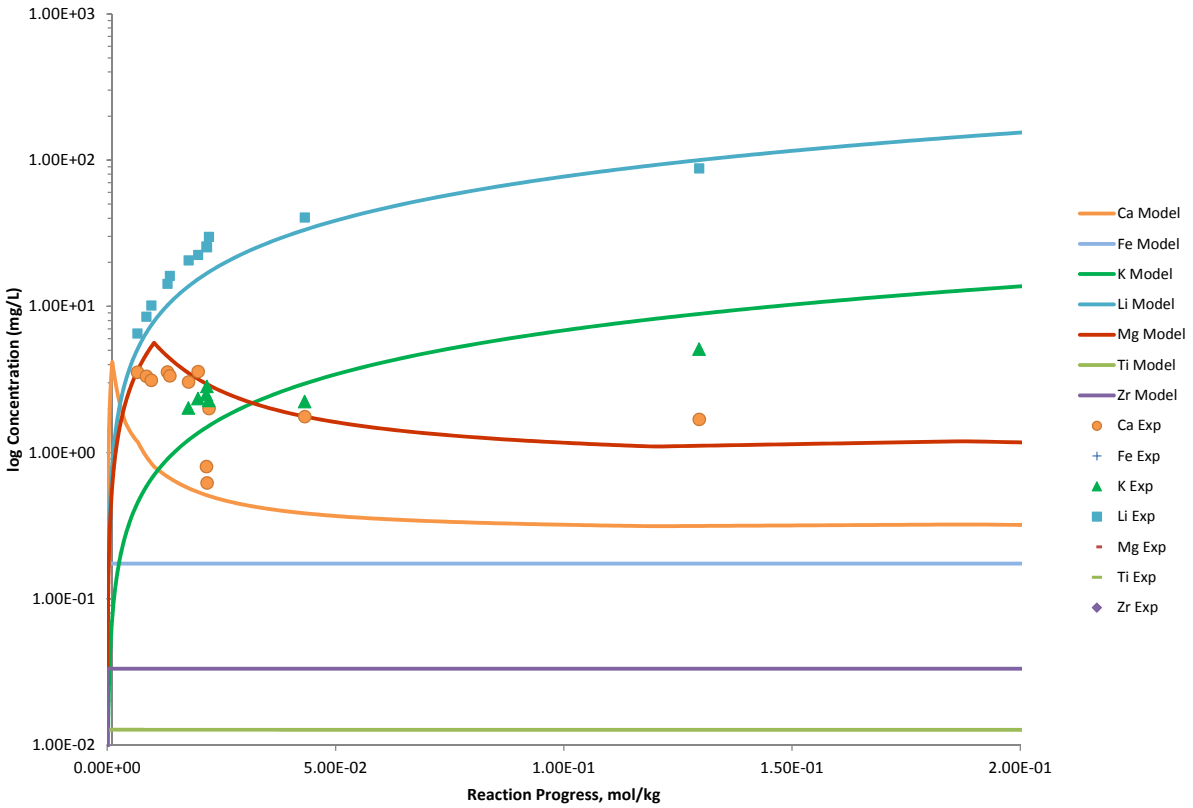


**Figure B.366**. Measured Solution Concentrations (mg/L) and Model Results for Ca, Fe, K, Li, Mg, Ti, and Zr, as a Function of Reaction Progress (mol-glass/kg) Determined for Glass Sample LAWC32

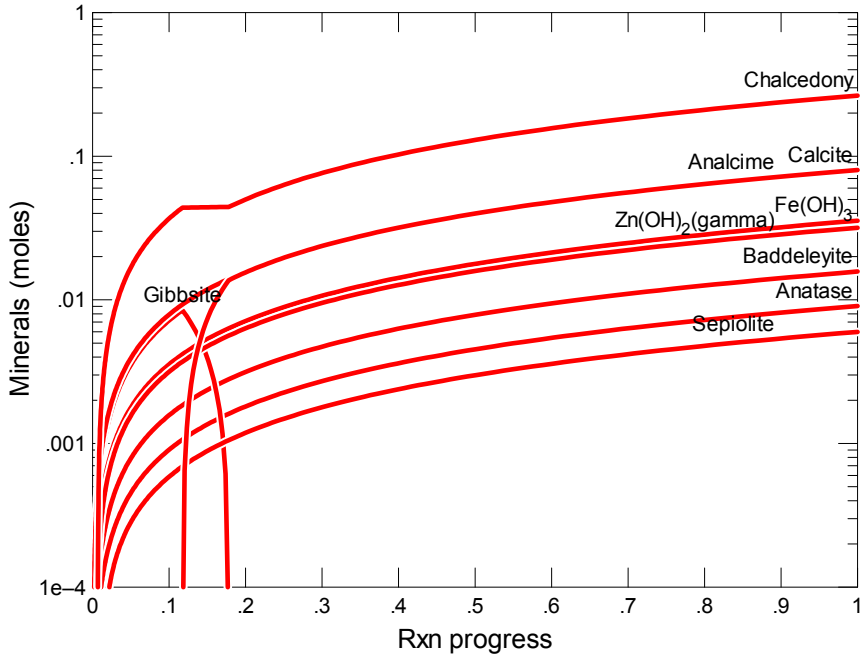


**Figure B.367**. Secondary Phases Calculated to Form as a Function of Reaction Progress (mol-glass/kg) Determined for Glass Sample LAWC33

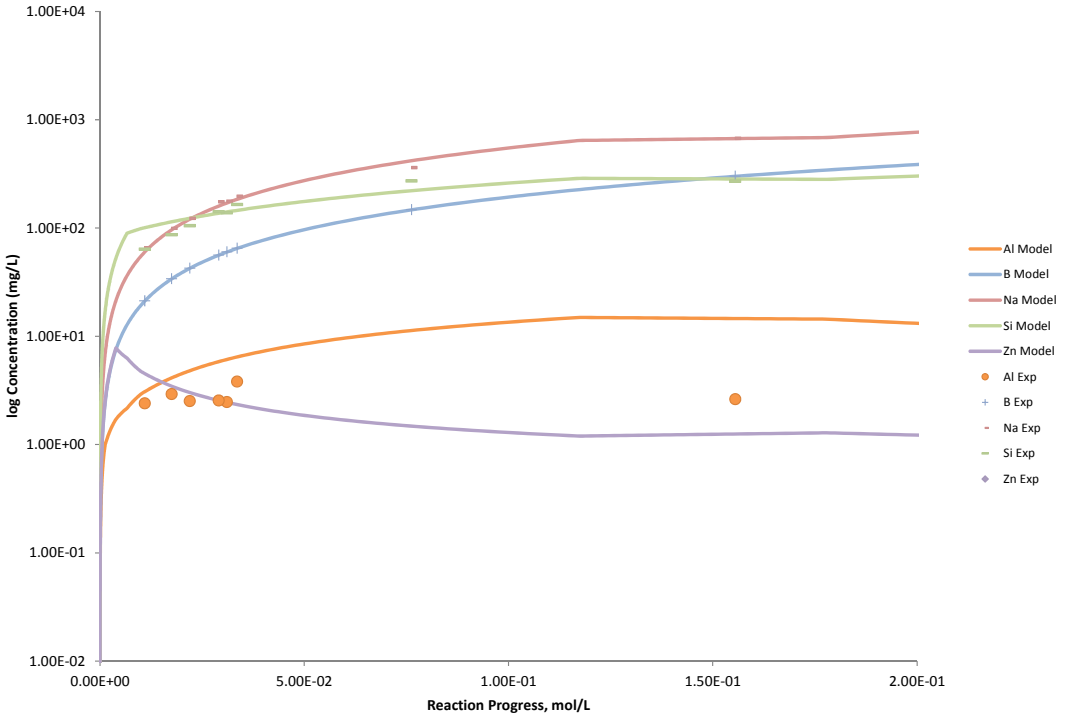


**Figure B.368**. Measured Solution Concentrations (mg/L) and Model Results for Al, B, Na, Si, and Zn, as a Function of Reaction Progress (mol-glass/kg) Determined for Glass Sample LAWC33

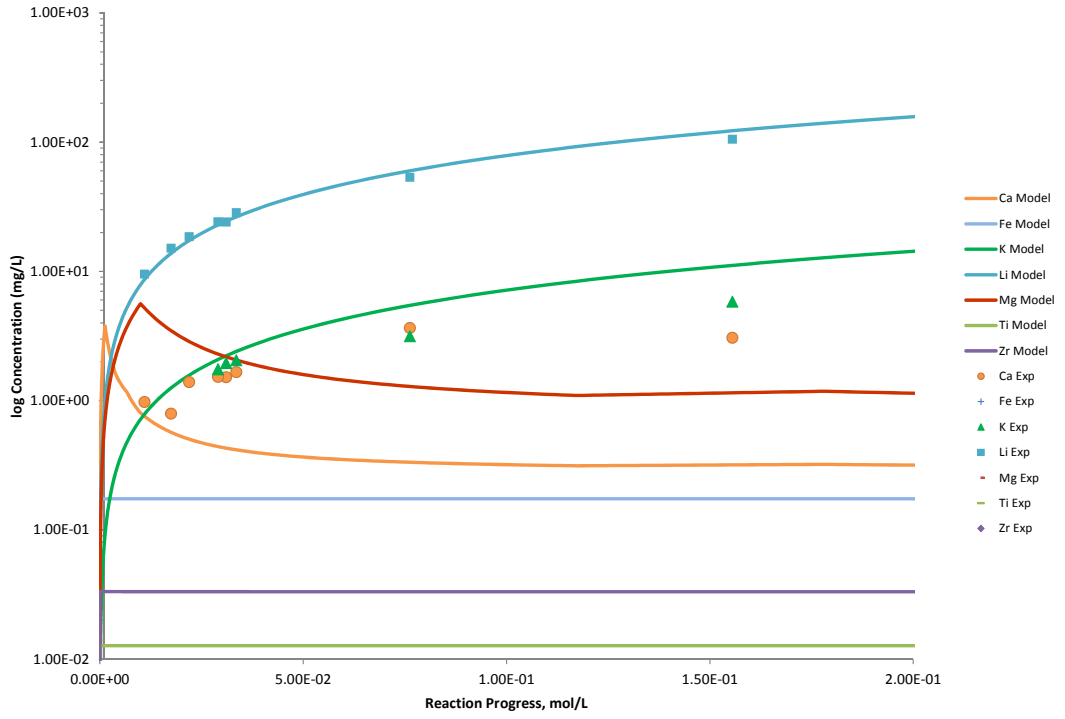


**Figure B.369**. Measured Solution Concentrations (mg/L) and Model Results for Ca, Fe, K, Li, Mg, Ti, and Zr, as a Function of Reaction Progress (mol-glass/kg) Determined for Glass Sample LAWC33

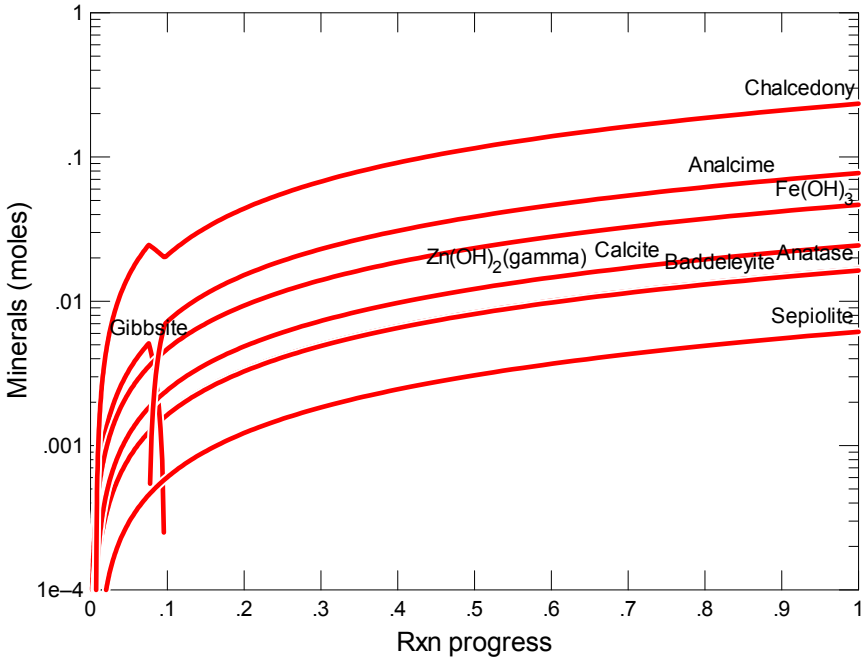


**Figure B.370**. Secondary Phases Calculated to Form as a Function of Reaction Progress (mol-glass/kg) Determined for Glass Sample PNLA126CC

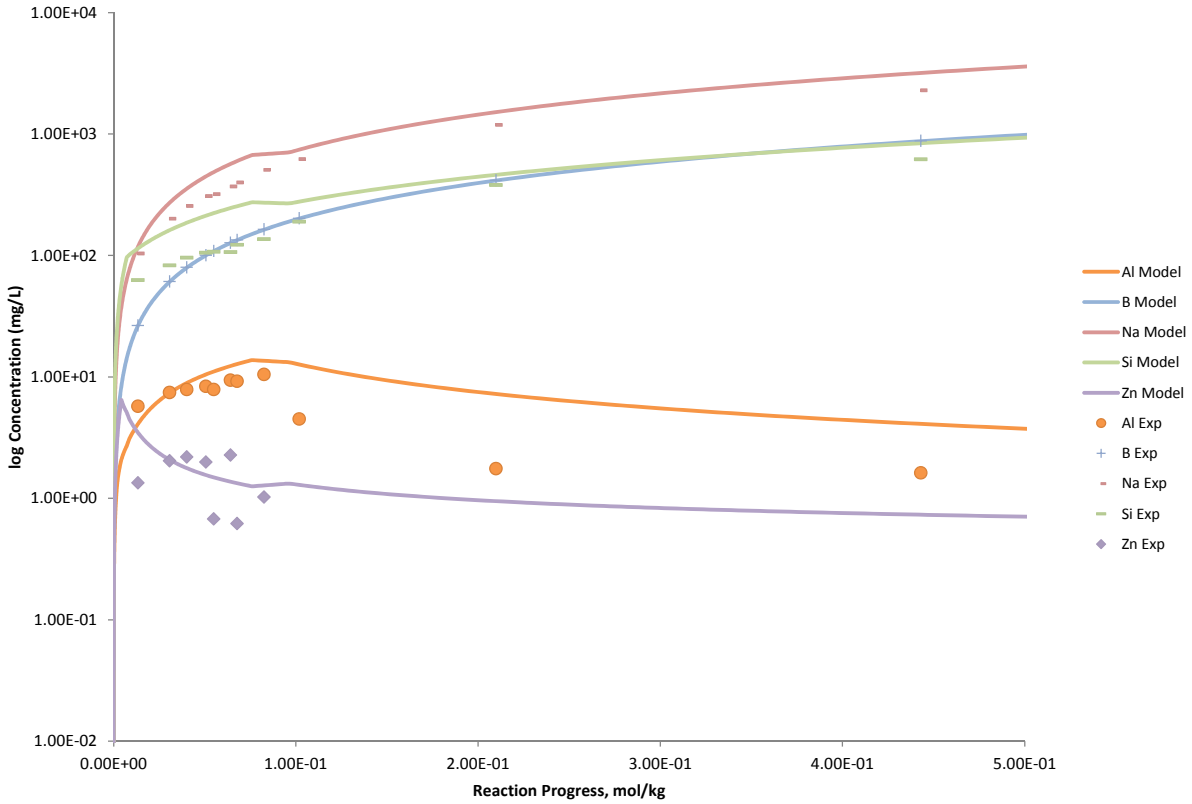


**Figure B.371**. Measured Solution Concentrations (mg/L) and Model Results for Al, B, Na, Si, and Zn, as a Function of Reaction Progress (mol-glass/kg) Determined for Glass Sample PNLA126CC

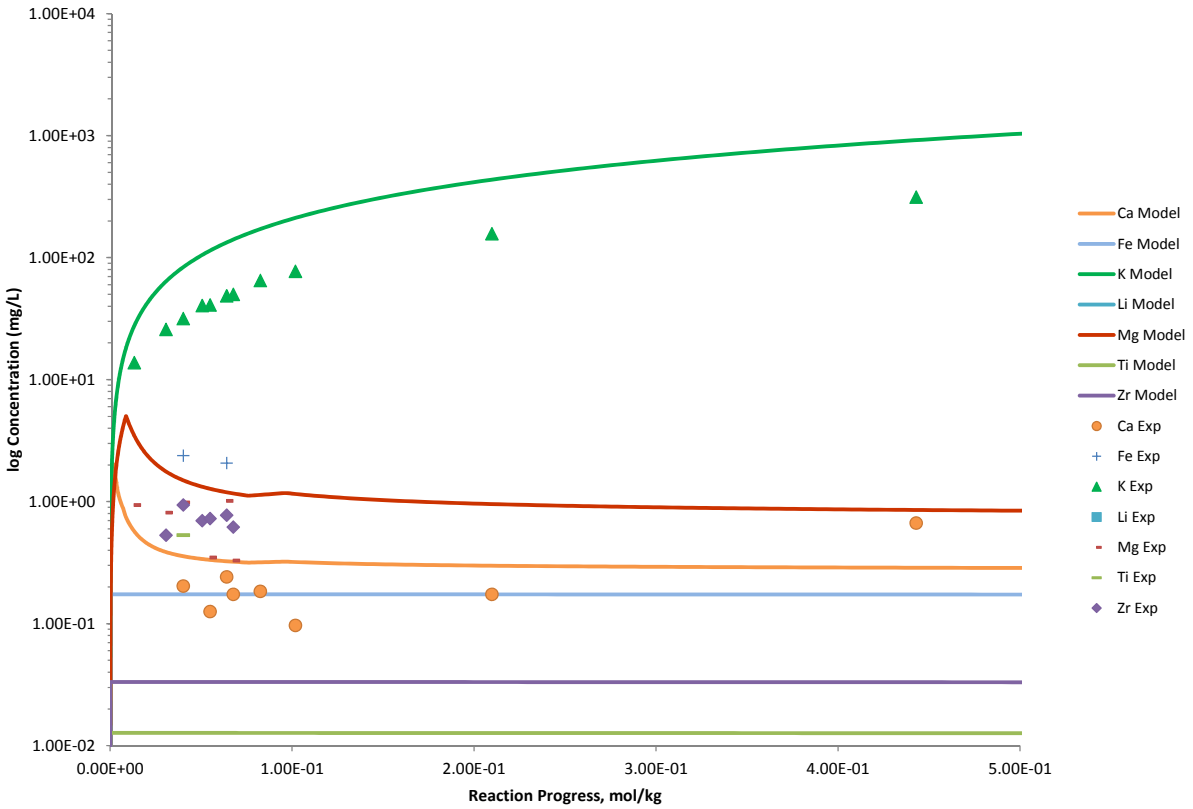


**Figure B.372**. Measured Solution Concentrations (mg/L) and Model Results for Ca, Fe, K, Li, Mg, Ti, and Zr, as a Function of Reaction Progress (mol-glass/kg) Determined for Glass Sample PNLA126CC

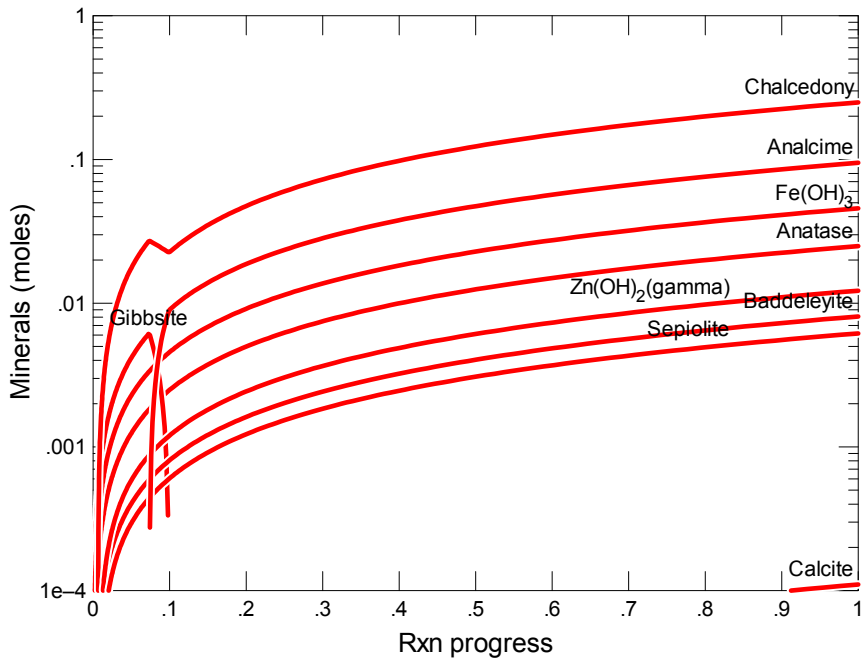


**Figure B.373**. Secondary Phases Calculated to Form as a Function of Reaction Progress (mol-glass/kg) Determined for Glass Sample TFA-BASE

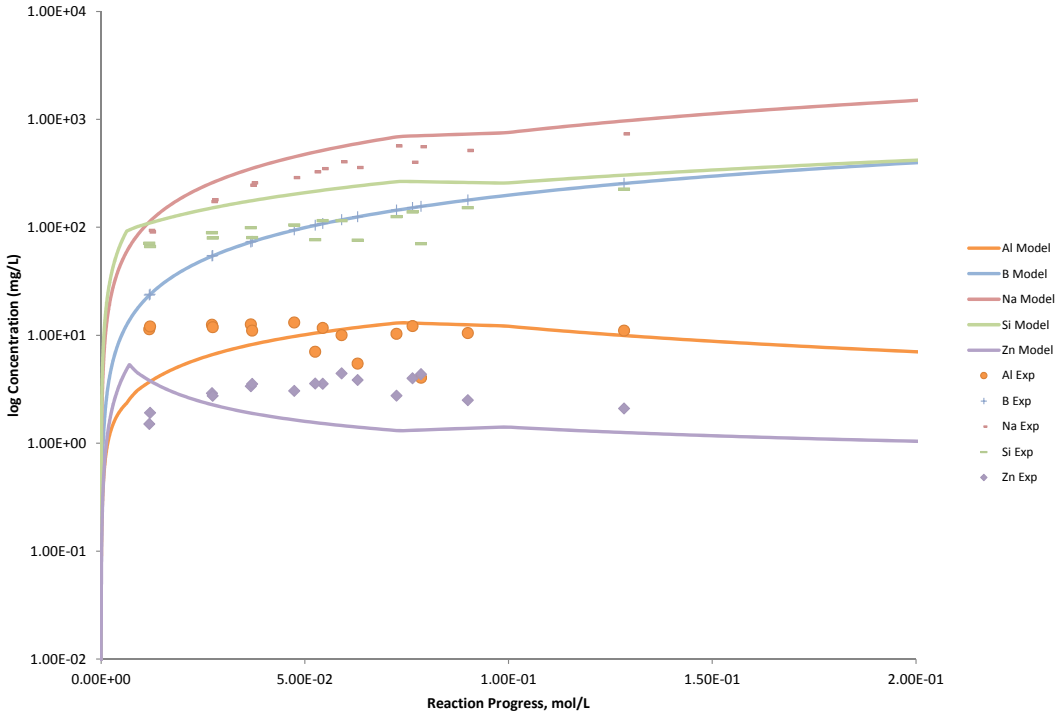


**Figure B.374**. Measured Solution Concentrations (mg/L) and Model Results for Al, B, Na, Si, and Zn, as a Function of Reaction Progress (mol-glass/kg) Determined for Glass Sample TFA-BASE

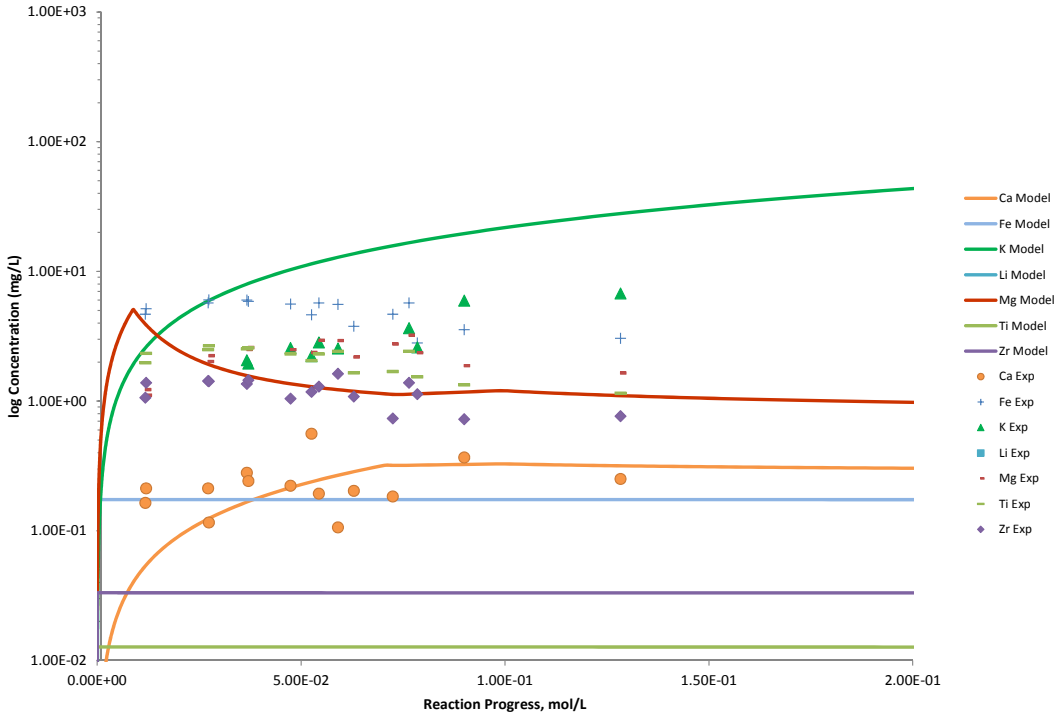


**Figure B.375**. Measured Solution Concentrations (mg/L) and Model Results for Ca, Fe, K, Li, Mg, Ti, and Zr, as a Function of Reaction Progress (mol-glass/kg) Determined for Glass Sample TFA-BASE

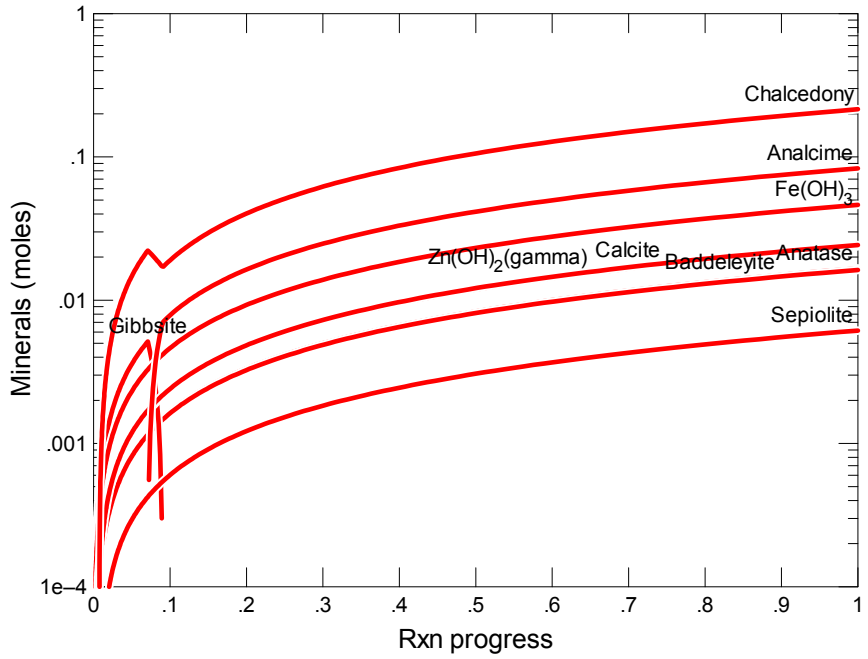


**Figure B.376**. Secondary Phases Calculated to Form as a Function of Reaction Progress (mol-glass/kg) Determined for Glass Sample WVF-G-21B

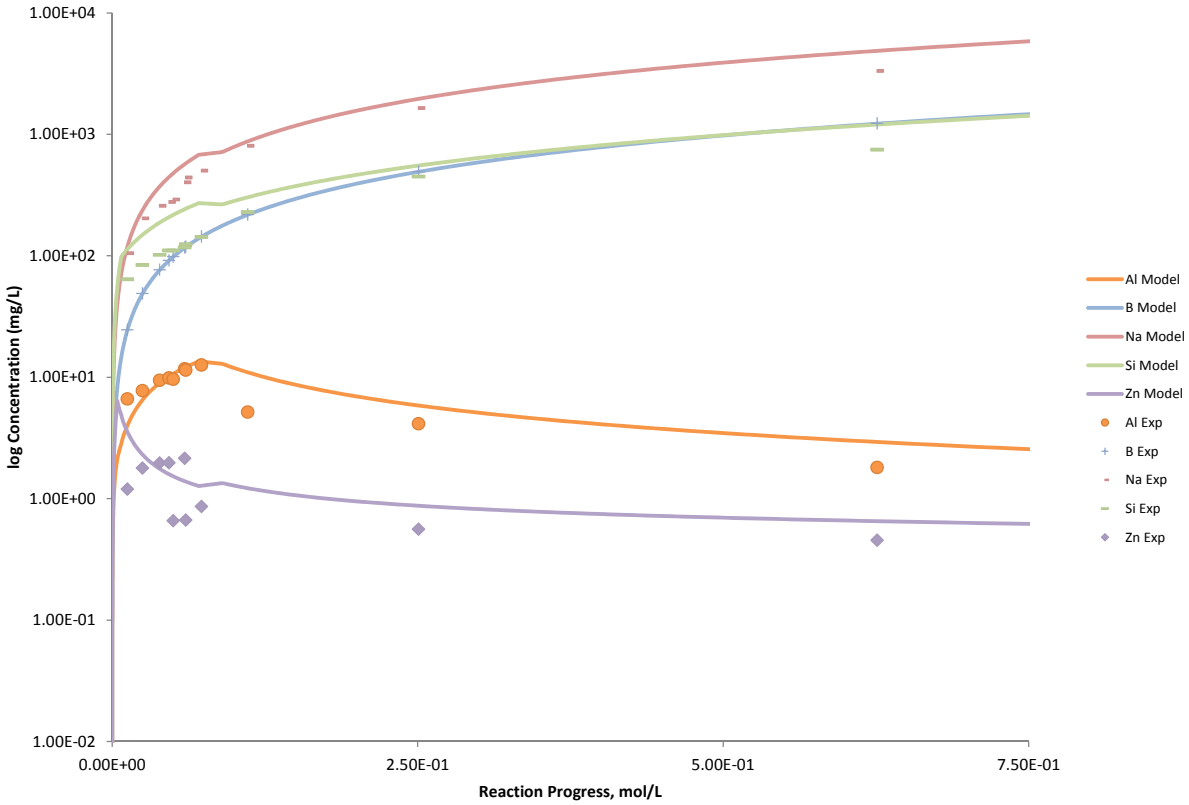


**Figure B.377**. Measured Solution Concentrations (mg/L) and Model Results for Al, B, Na, Si, and Zn, as a Function of Reaction Progress (mol-glass/kg) Determined for Glass Sample WVF-G-21B

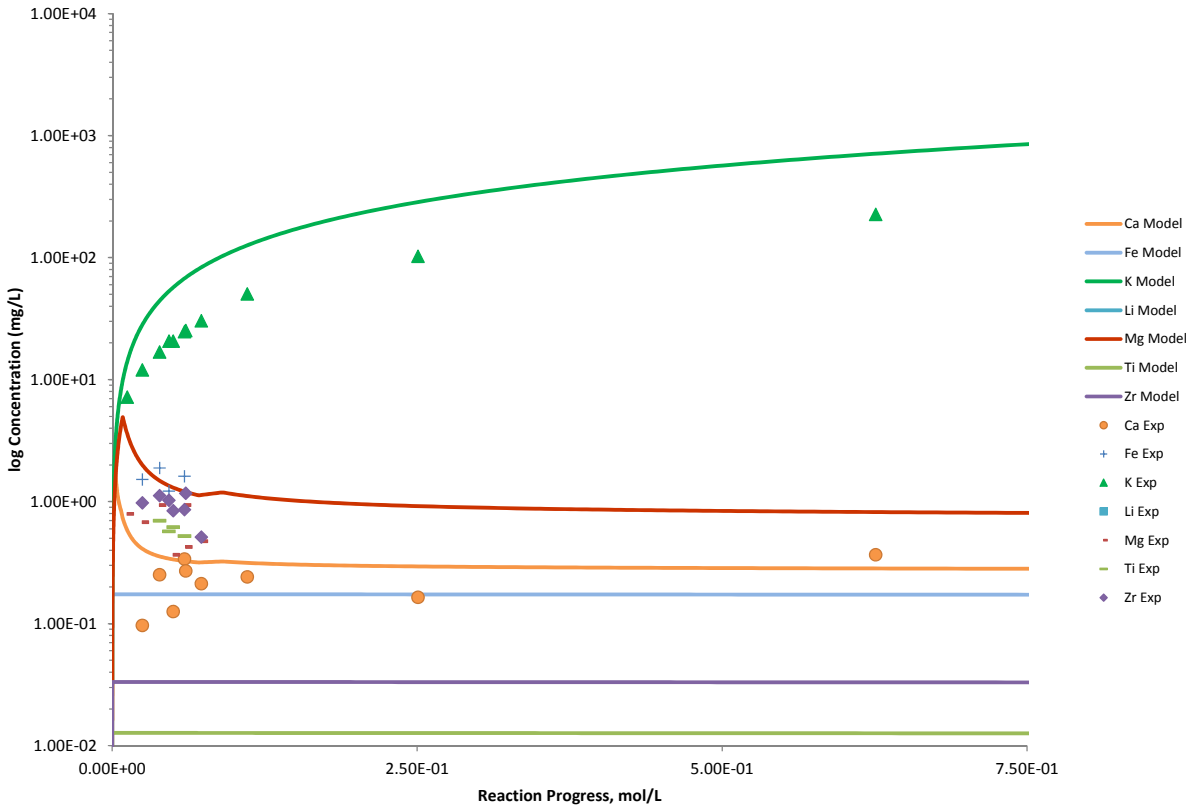


**Figure B.378**. Measured Solution Concentrations (mg/L) and Model Results for Ca, Fe, K, Li, Mg, Ti, and Zr, as a Function of Reaction Progress (mol-glass/kg) Determined for Glass Sample WVF-G-21B

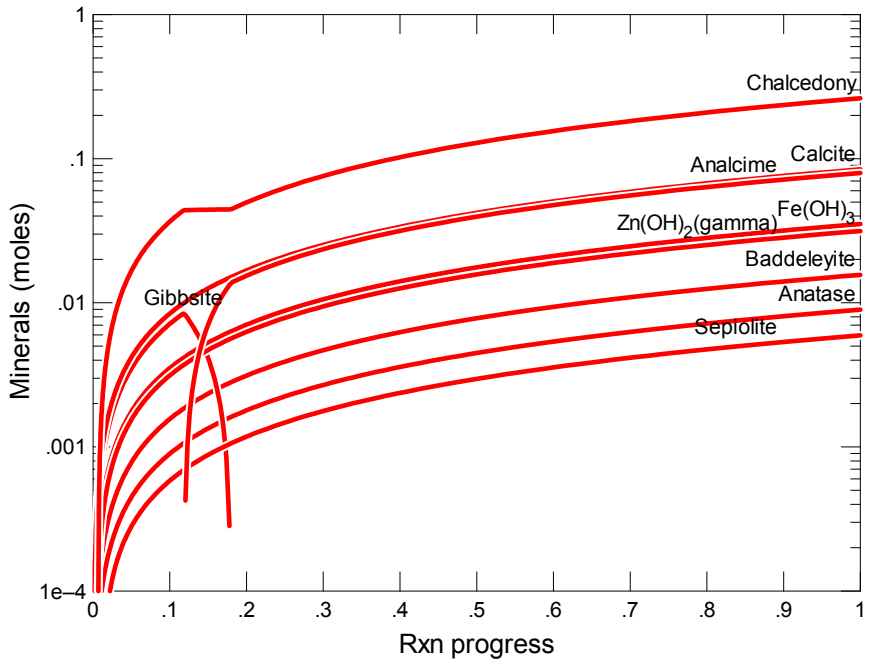


**Figure B.379**. Secondary Phases Calculated to Form as a Function of Reaction Progress (mol-glass/kg) Determined for Glass Sample WVH-G-57B

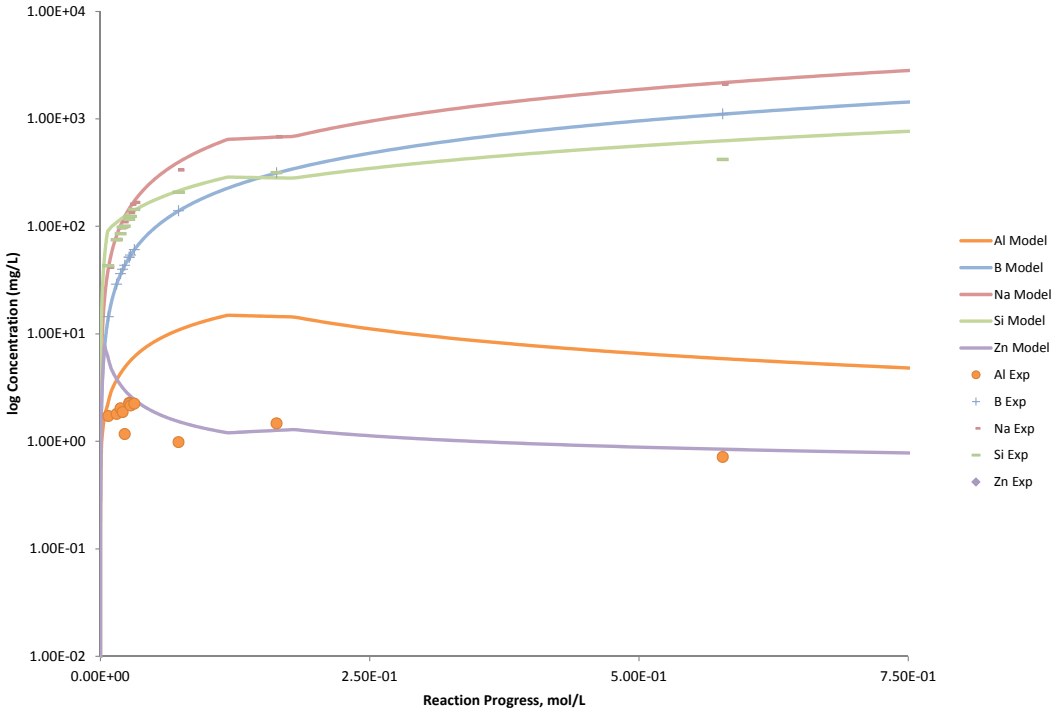


**Figure B.380**. Measured Solution Concentrations (mg/L) and Model Results for Al, B, Na, Si, and Zn, as a Function of Reaction Progress (mol-glass/kg) Determined for Glass Sample WVH-G-57B

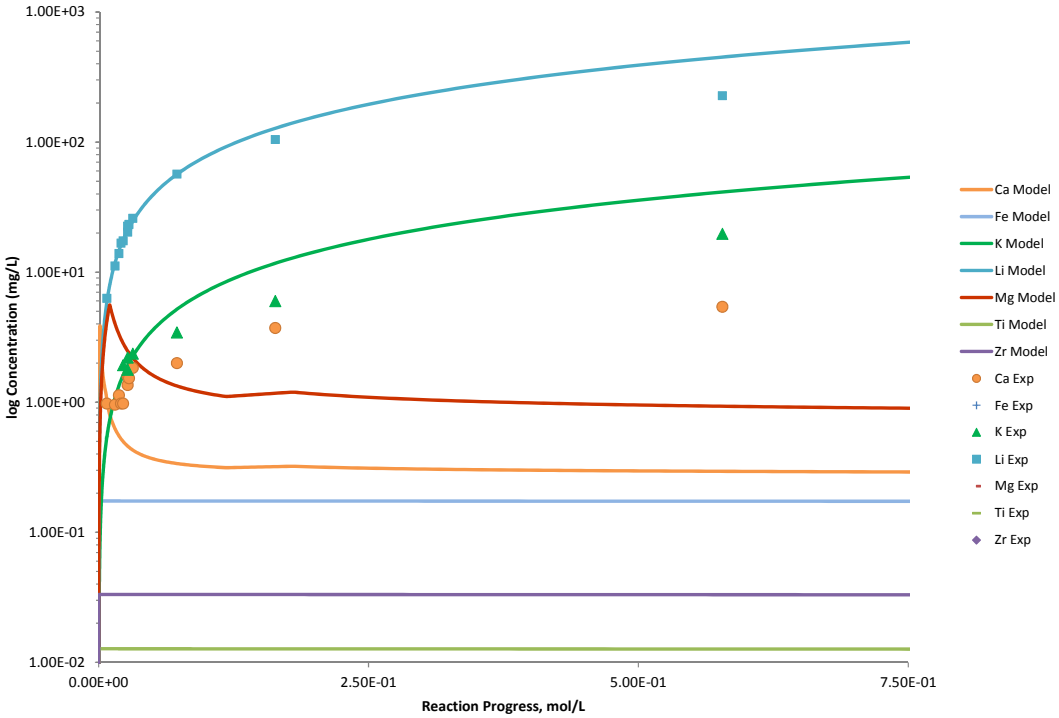


**Figure B.381**. Measured Solution Concentrations (mg/L) and Model Results for Ca, Fe, K, Li, Mg, Ti, and Zr, as a Function of Reaction Progress (mol-glass/kg) Determined for Glass Sample WVH-G-57B

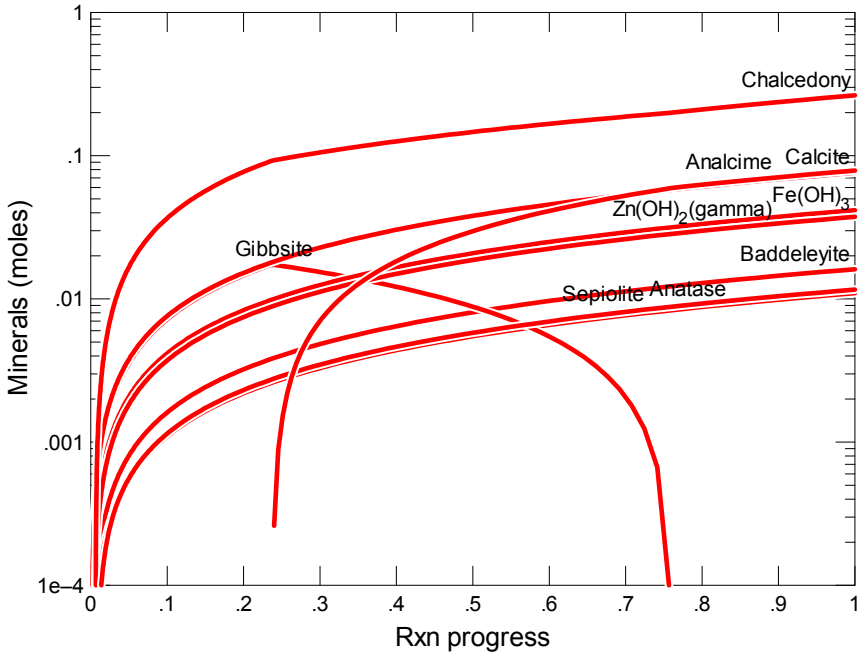


**Figure B.382**. Secondary Phases Calculated to Form as a Function of Reaction Progress (mol-glass/kg) Determined for Glass Sample WVJ-G-109D

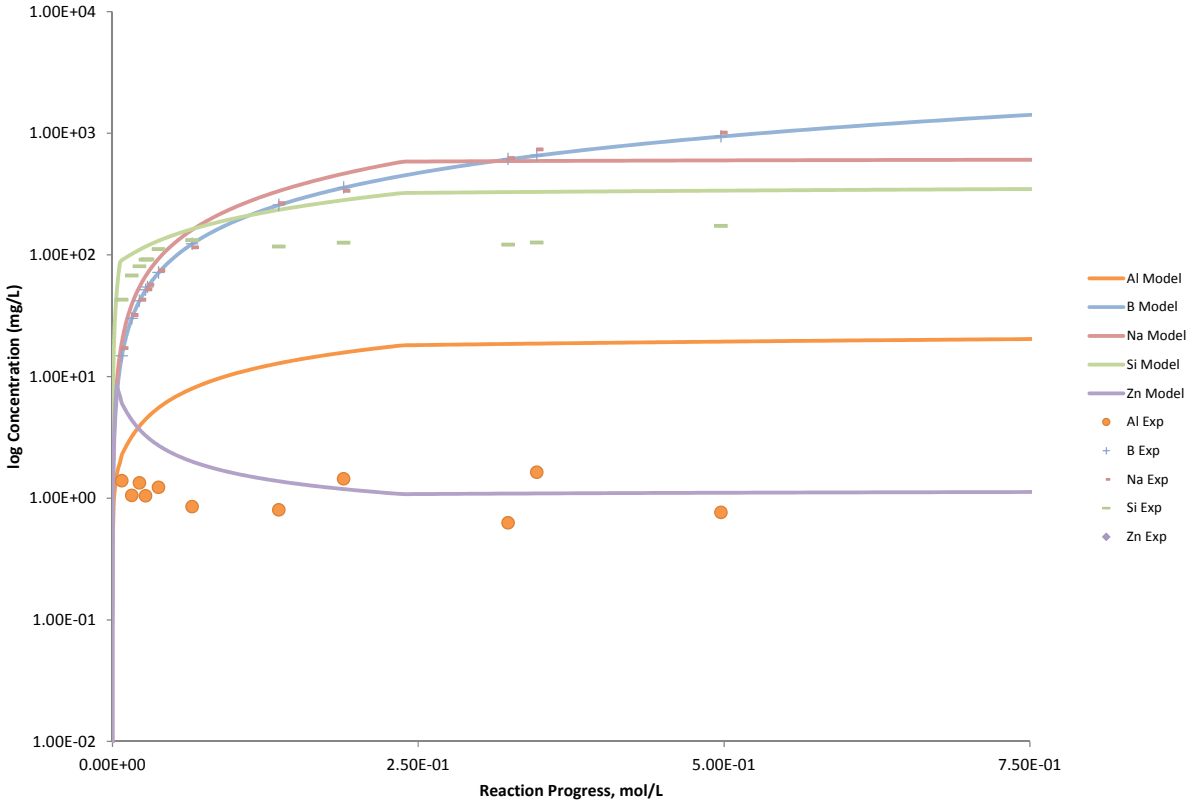


**Figure B.383**. Measured Solution Concentrations (mg/L) and Model Results for Al, B, Na, Si, and Zn, as a Function of Reaction Progress (mol-glass/kg) Determined for Glass Sample WVJ-G-109D

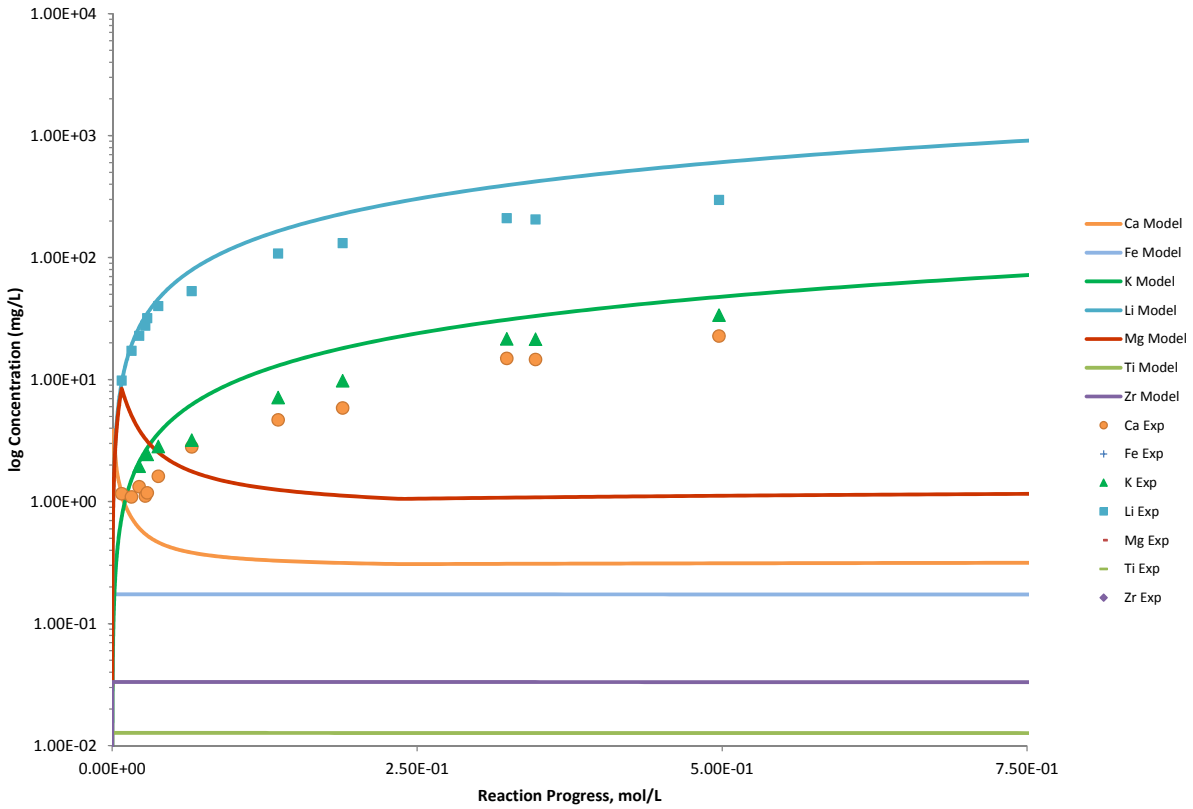


**Figure B.384**. Measured Solution Concentrations (mg/L) and Model Results for Ca, Fe, K, Li, Mg, Ti, and Zr, as a Function of Reaction Progress (mol-glass/kg) Determined for Glass Sample WVJ-G-109D

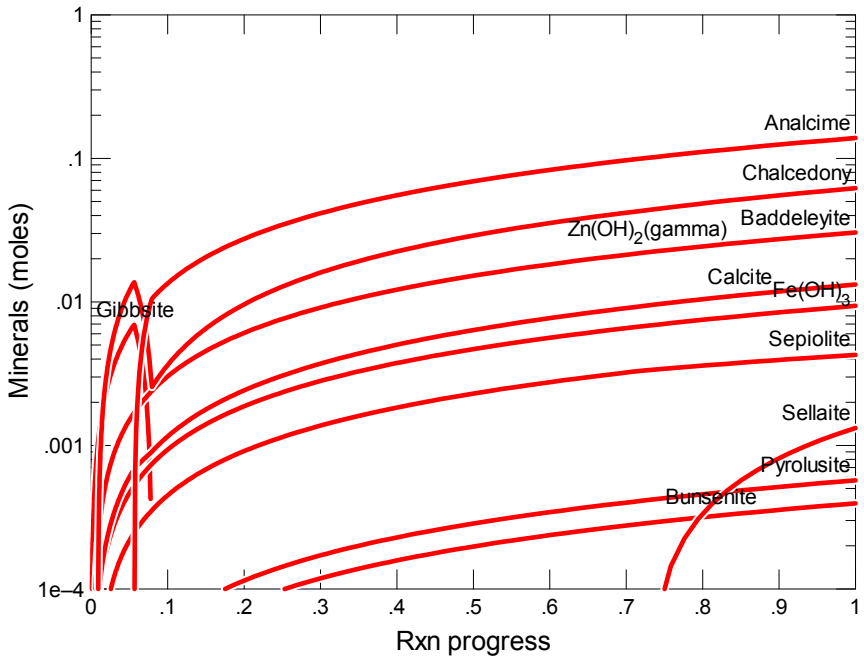


**Figure B.385**. Secondary Phases Calculated to Form as a Function of Reaction Progress (mol-glass/kg) Determined for Glass Sample IDF1B2CCC

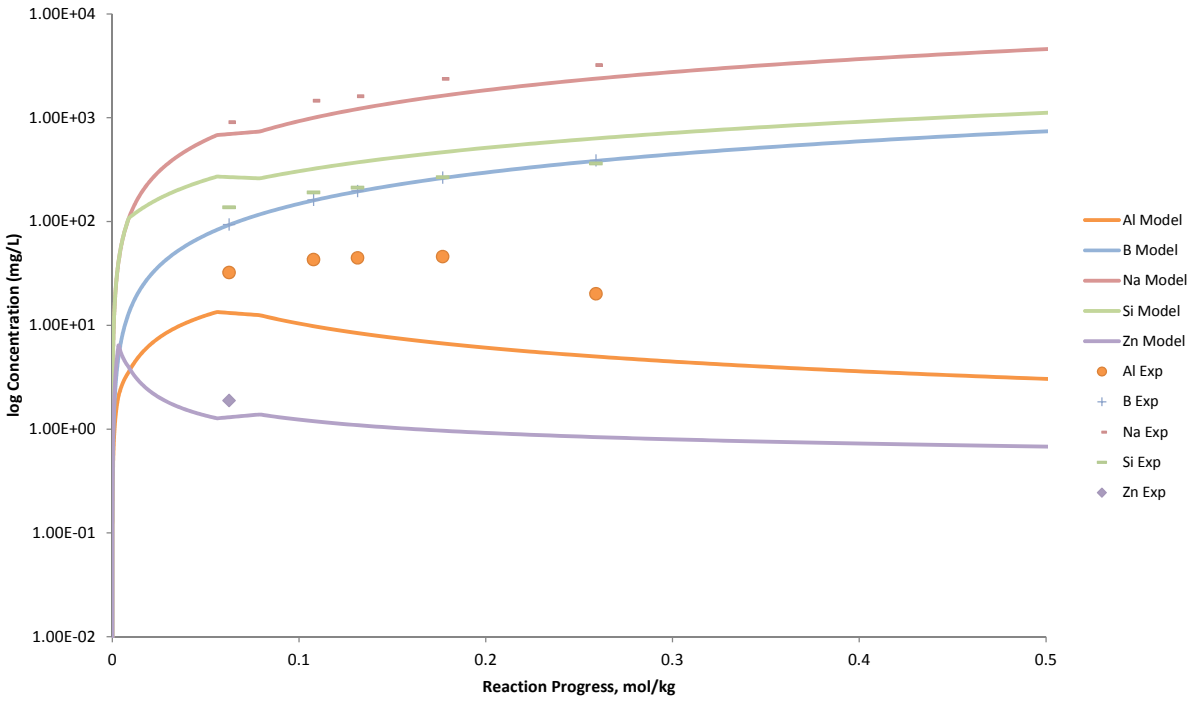


**Figure B.386**. Measured Solution Concentrations (mg/L) and Model Results for Al, B, Na, Si, and Zn, as a Function of Reaction Progress (mol-glass/kg) Determined for Glass Sample IDF1B2CCC

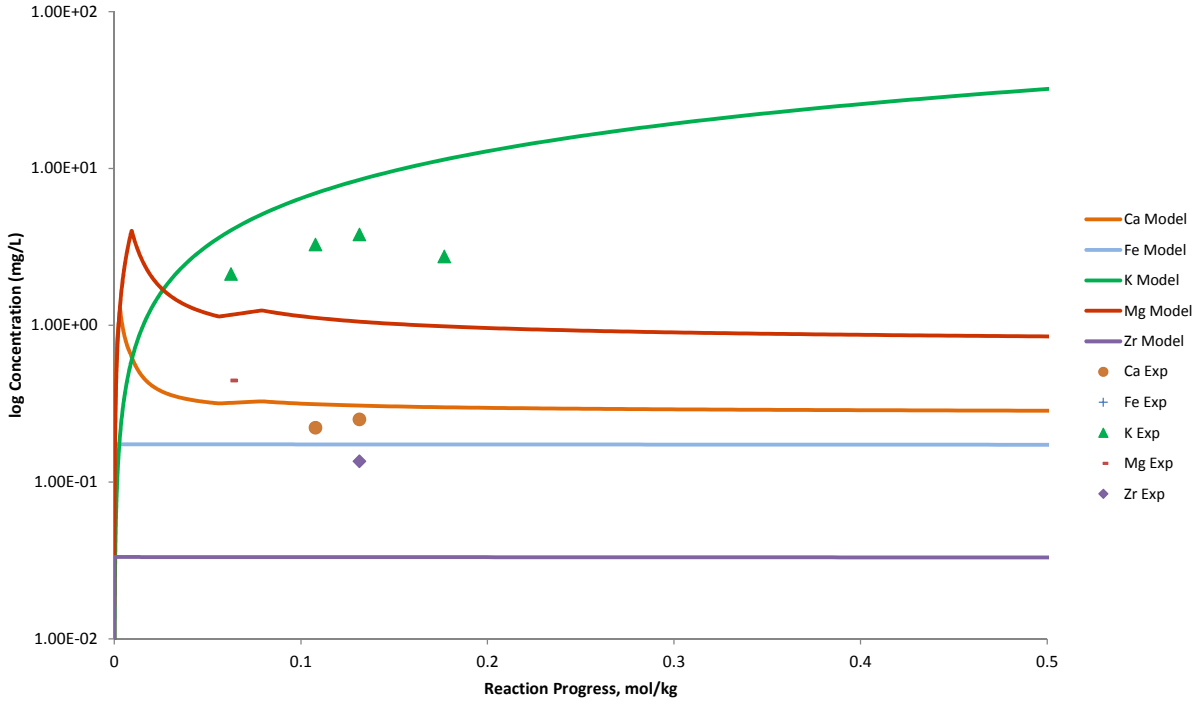


**Figure B.387**. Measured Solution Concentrations (mg/L) and Model Results for Ca, Fe, K, Li, Mg, and Zr, as a Function of Reaction Progress (mol-glass/kg) Determined for Glass Sample IDF1B2CCC

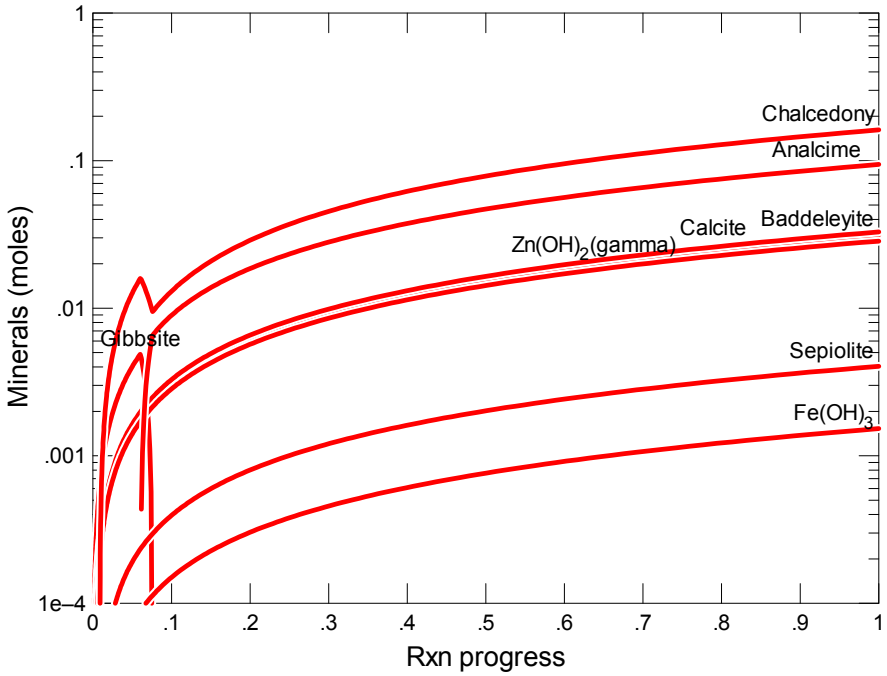


**Figure B.388**. Secondary Phases Calculated to Form as a Function of Reaction Progress (mol-glass/kg) Determined for Glass Sample IDF2G9CCC

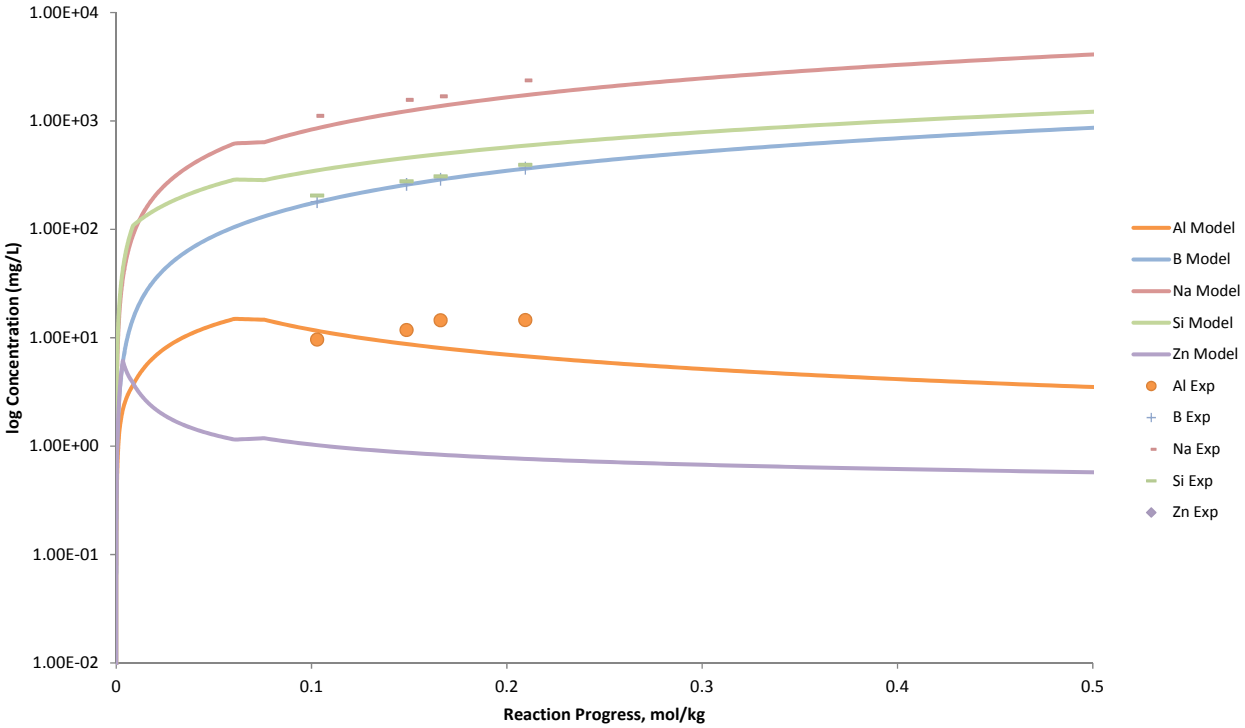


**Figure B.389**. Measured Solution Concentrations (mg/L) and Model Results for Al, B, Na, and Si, as a Function of Reaction Progress (mol-glass/kg) Determined for Glass Sample IDF2G9CCC

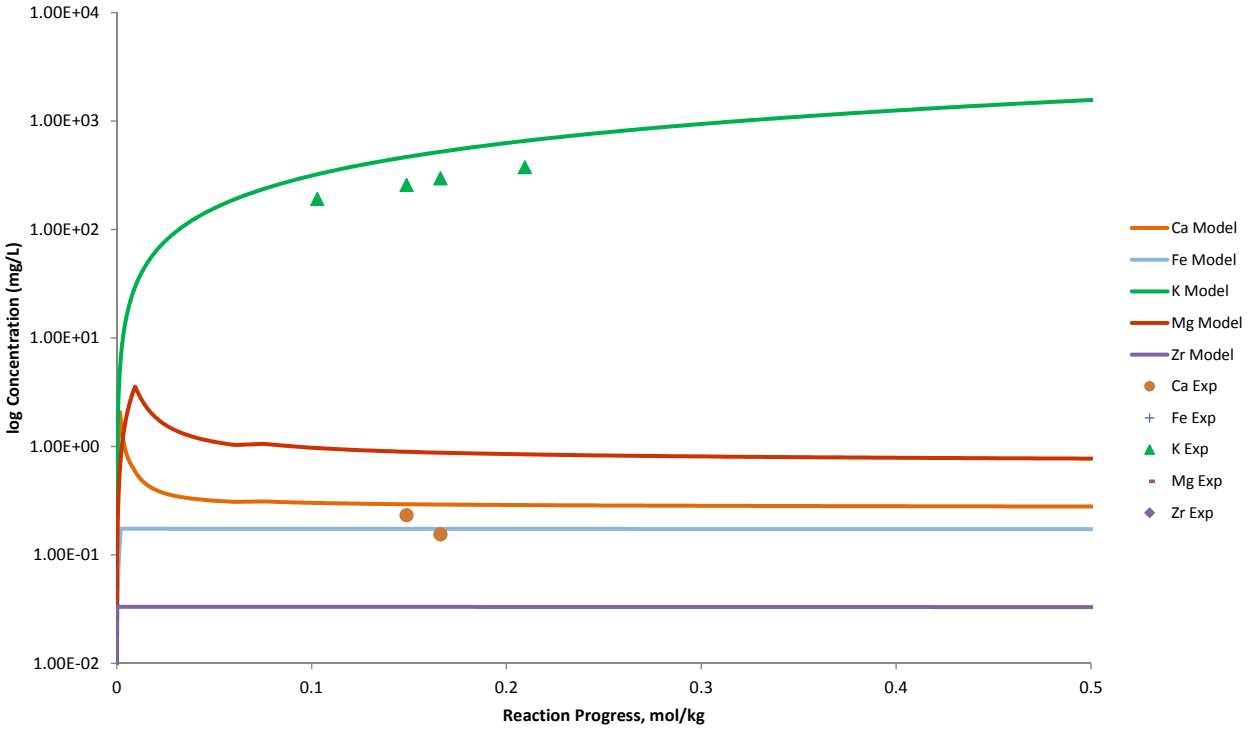


**Figure B.390**. Measured Solution Concentrations (mg/L) and Model Results for Ca and K as a Function of Reaction Progress (mol-glass/kg) Determined for Glass Sample IDF2G9CCC

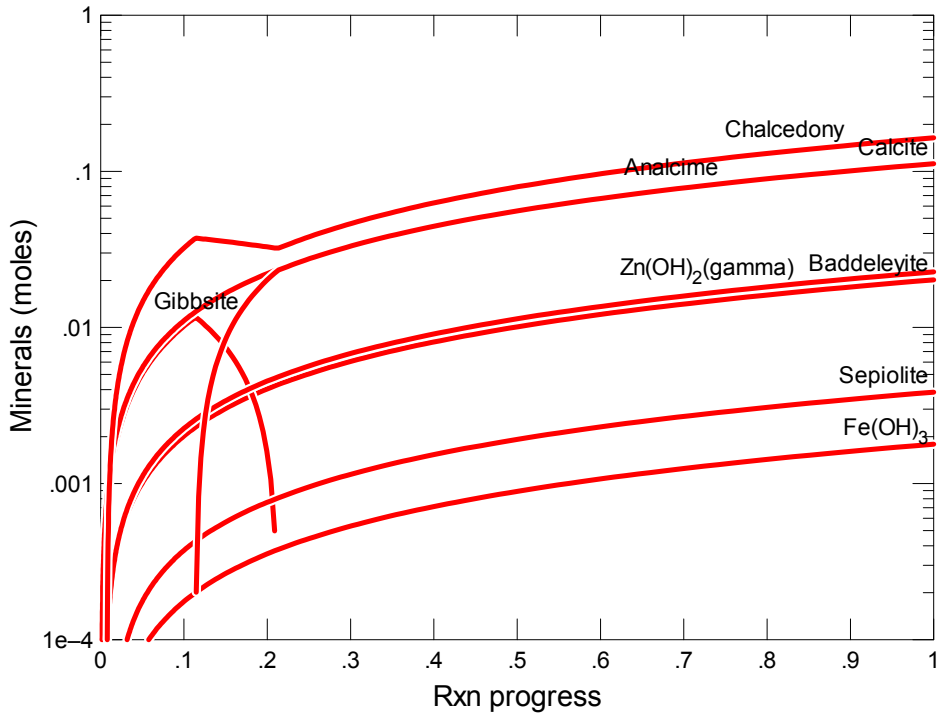


**Figure B.391**. Secondary Phases Calculated to Form as a Function of Reaction Progress (mol-glass/kg) Determined for Glass Sample IDF3F7CCC

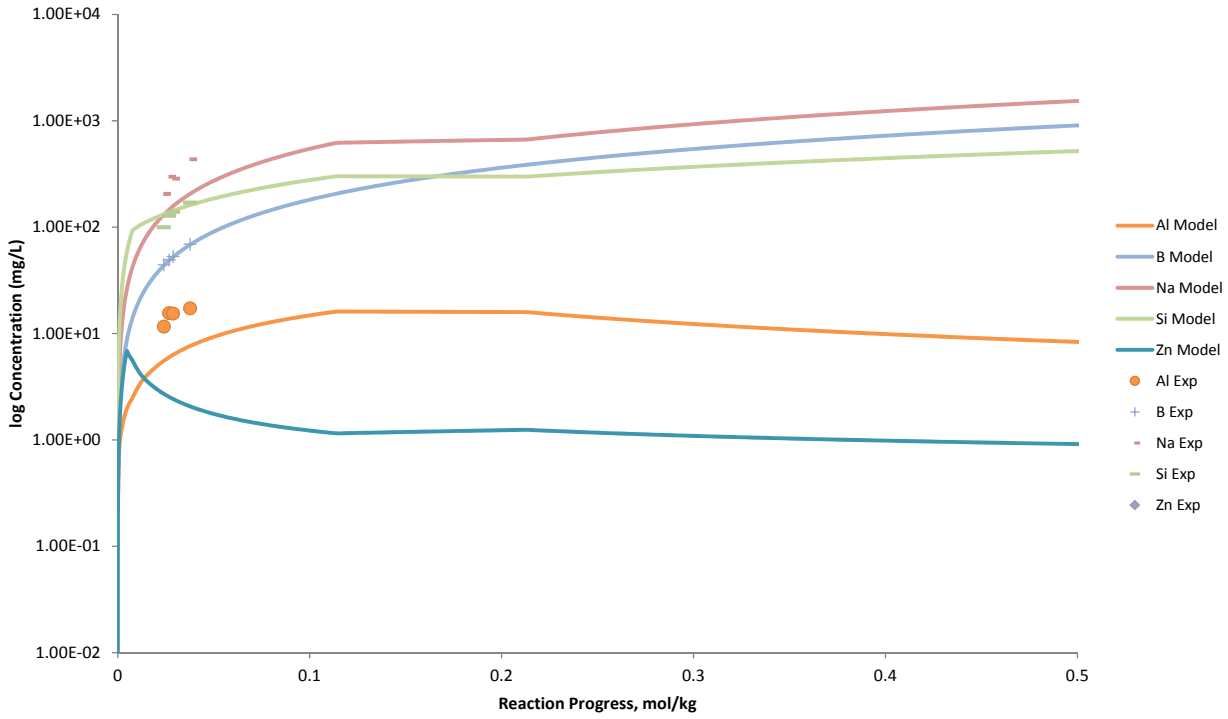


**Figure B.392**. Measured Solution Concentrations (mg/L) and Model Results for Al, B, Na, Si, and Zn, as a Function of Reaction Progress (mol-glass/kg) Determined for Glass Sample IDF3F7CCC

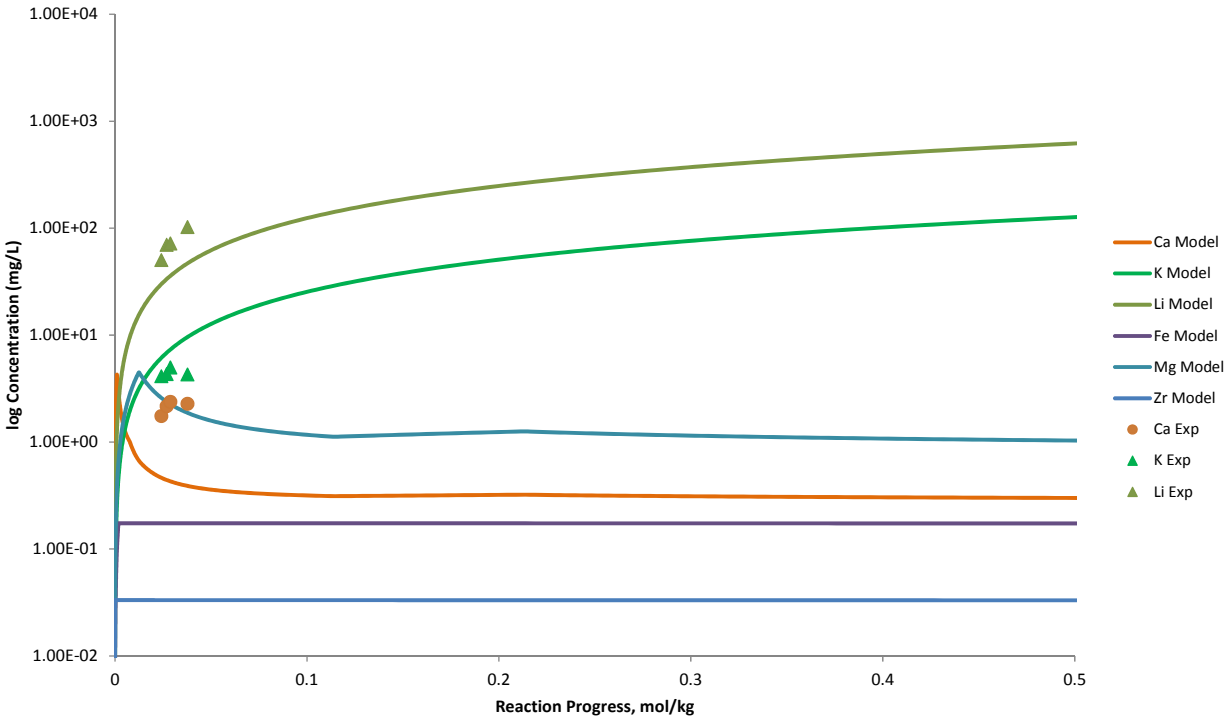


**Figure B.393**. Measured Solution Concentrations (mg/L) and Model Results for Ca, Fe, K, Li, Mg, and Zr, as a Function of Reaction Progress (mol-glass/kg) Determined for Glass Sample IDF3F7CCC

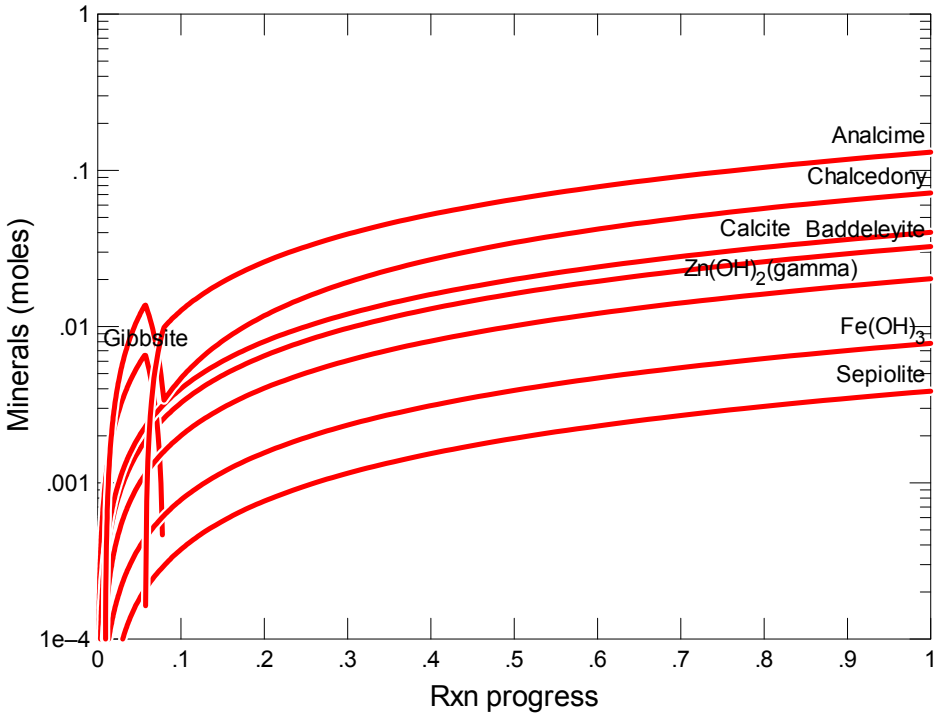


**Figure B.394**. Secondary Phases Calculated to Form as a Function of Reaction Progress (mol-glass/kg) Determined for Glass Sample IDF4A15CCC

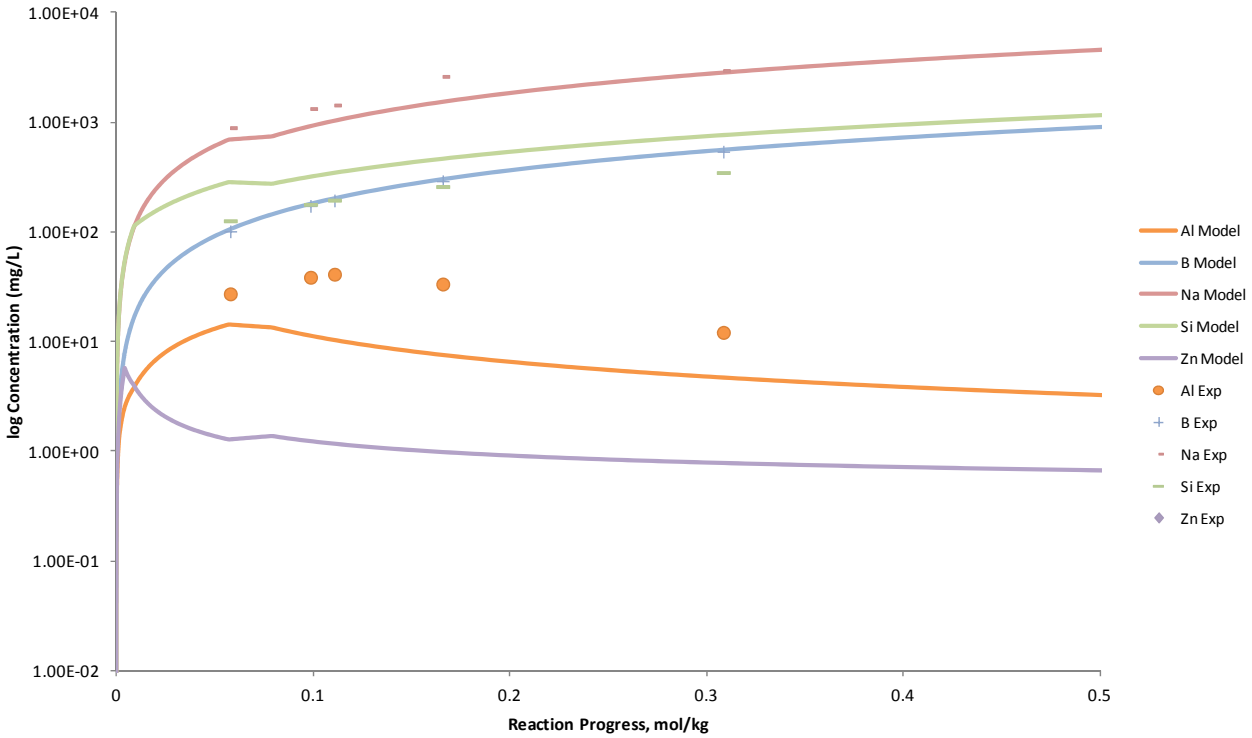


**Figure B.395**. Measured Solution Concentrations (mg/L) and Model Results for Al, B, Na, Si, and Zn, as a Function of Reaction Progress (mol-glass/kg) Determined for Glass Sample IDF4A15CCC

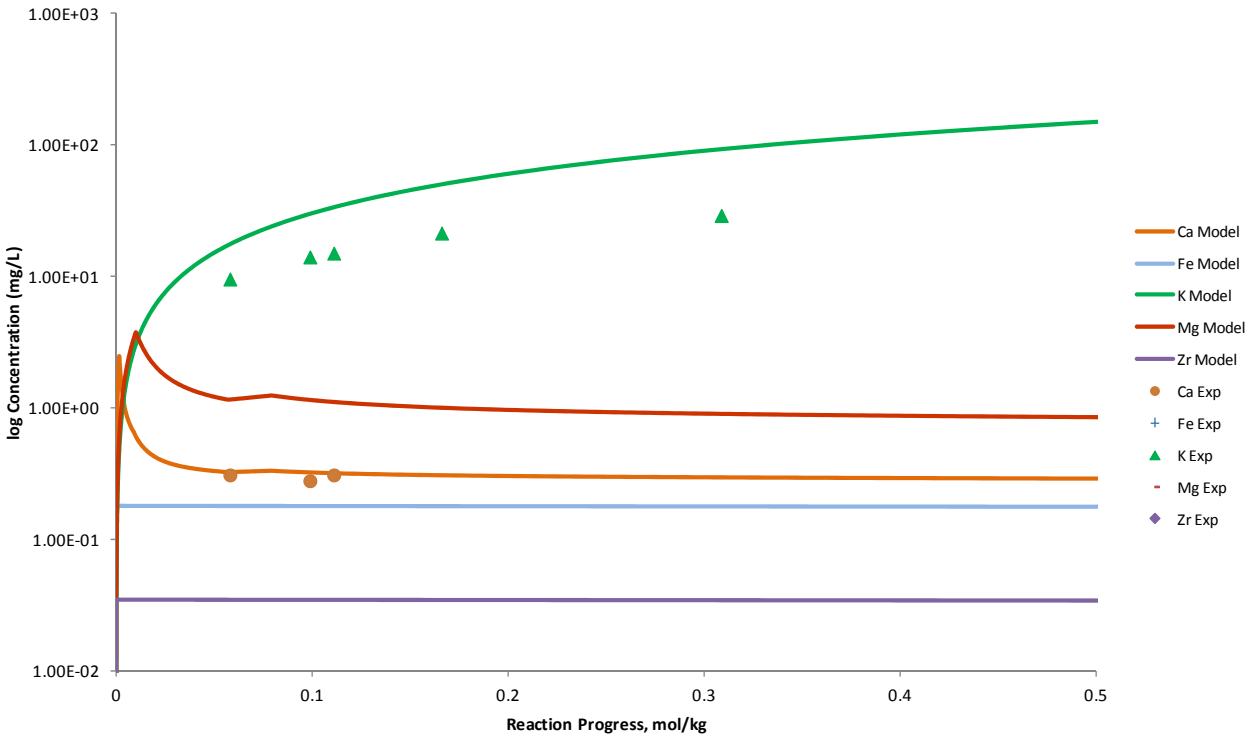


**Figure B.396**. Measured Solution Concentrations (mg/L) and Model Results for Ca, Fe, K, Mg, and Zr, as a Function of Reaction Progress (mol-glass/kg) Determined for Glass Sample IDF4A15CCC

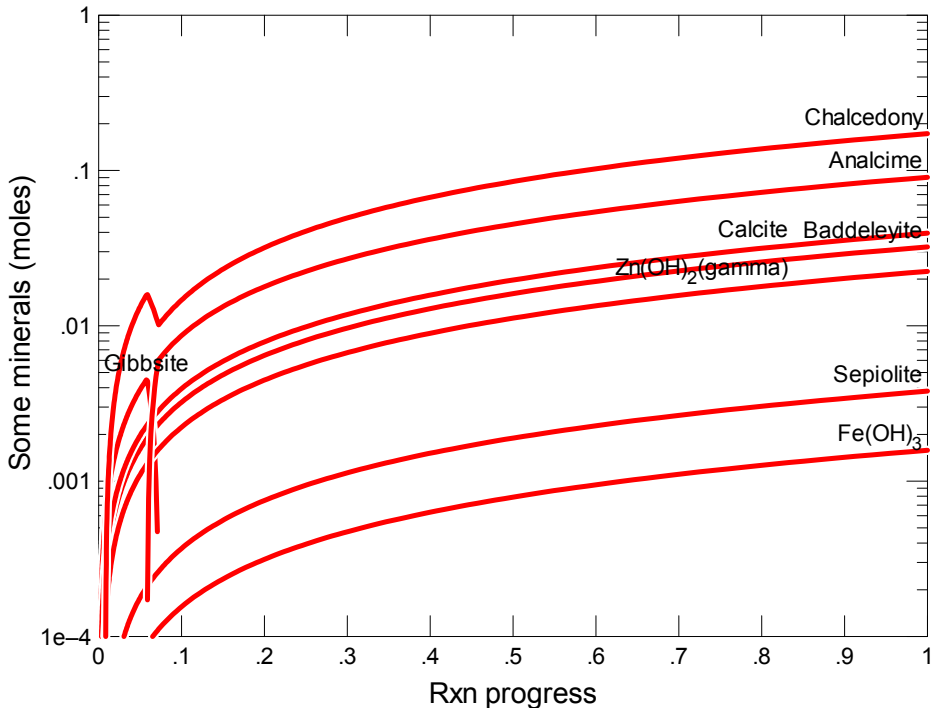


**Figure B.397**. Secondary Phases Calculated to Form as a Function of Reaction Progress (mol-glass/kg) Determined for Glass Sample IDF5A20CCC

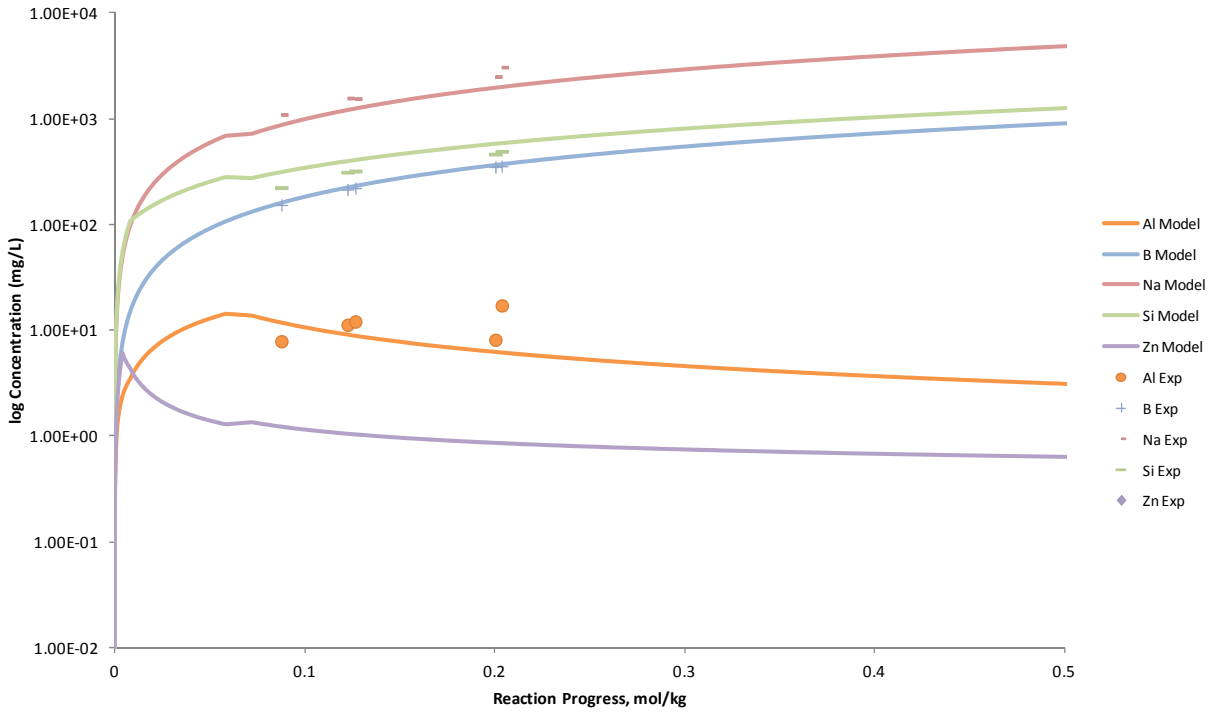


**Figure B.398**. Measured Solution Concentrations (mg/L) and Model Results for Al, B, Na, Si, and Zn, as a Function of Reaction Progress (mol-glass/kg) Determined for Glass Sample IDF5A20CCC

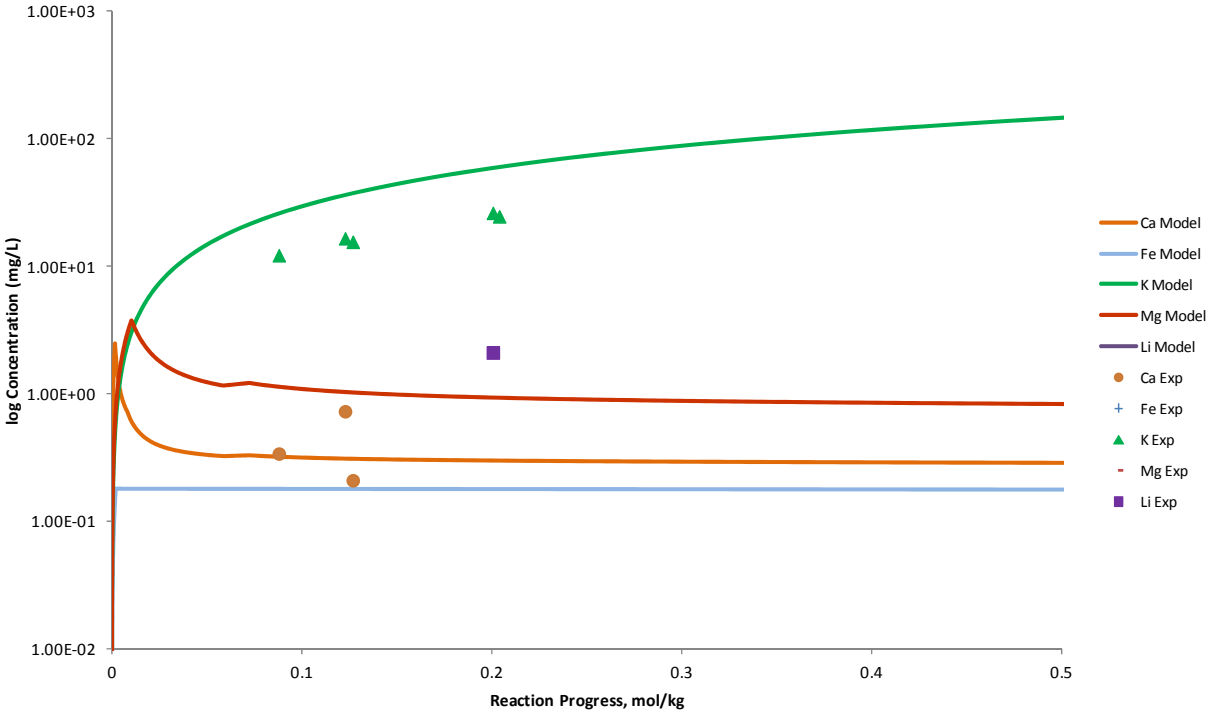


**Figure B.399**. Measured Solution Concentrations (mg/L) and Model Results for Ca, Fe, K, Li, Mg, and Zr, as a Function of Reaction Progress (mol-glass/kg) Determined for Glass Sample IDF5A20CCC

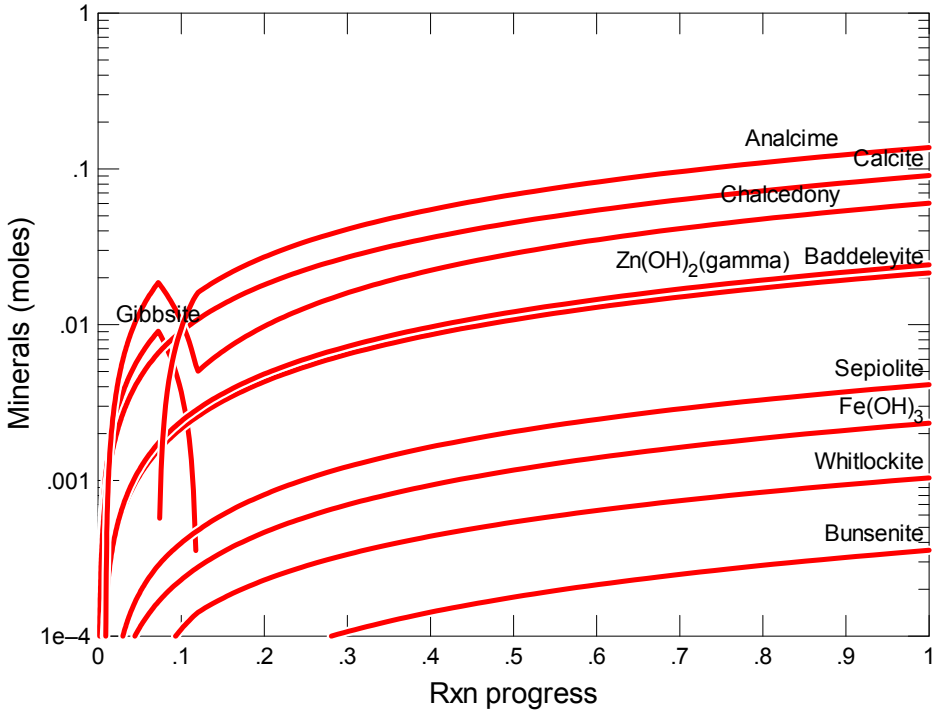


**Figure B.400**. Secondary Phases Calculated to Form as a Function of Reaction Progress (mol-glass/kg) Determined for Glass Sample IDF6D6CCC

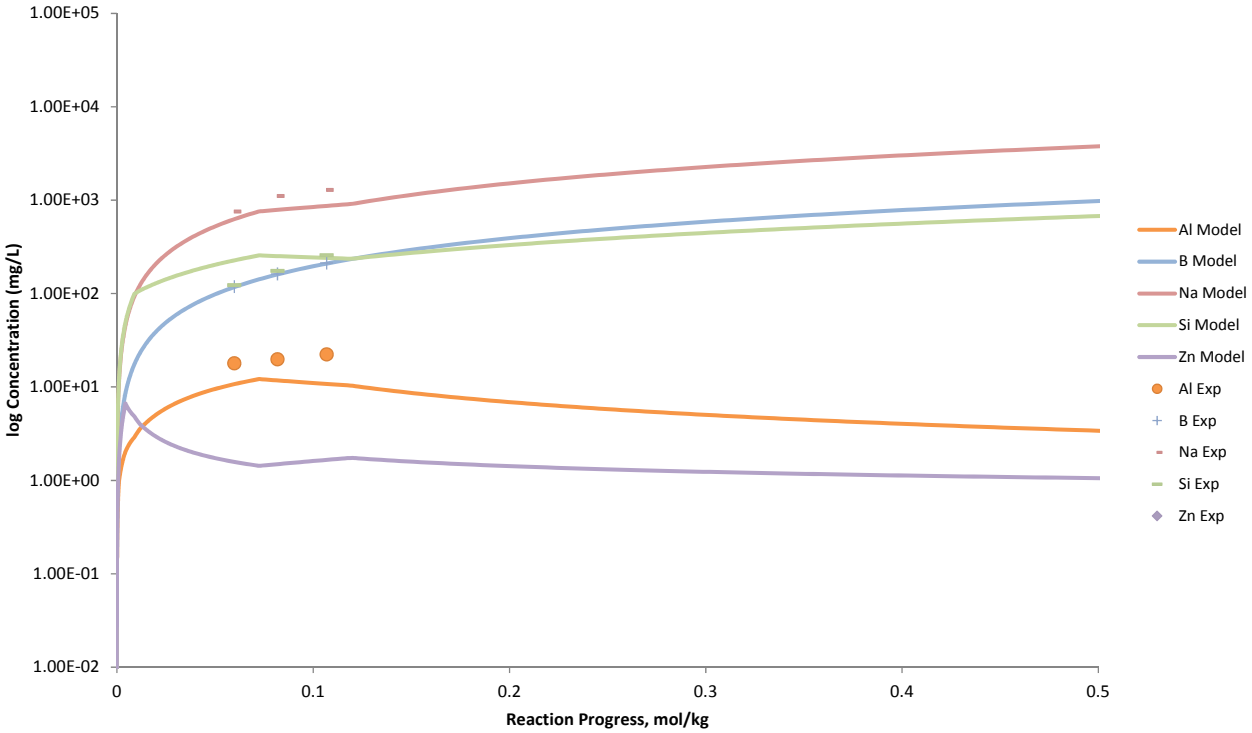


**Figure B.401**. Measured Solution Concentrations (mg/L) and Model Results for Al, B, Na, Si, and Zn, as a Function of Reaction Progress (mol-glass/kg) Determined for Glass Sample IDF6D6CCC

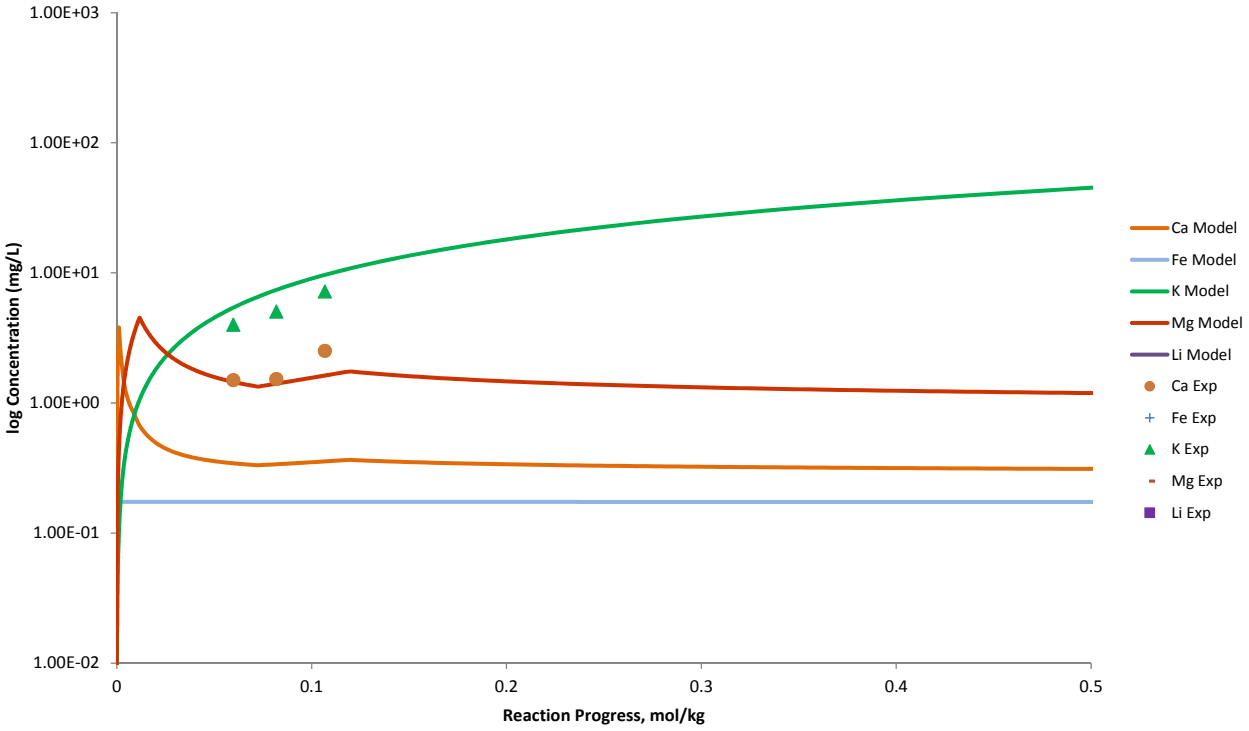


**Figure B.402**. Measured Solution Concentrations (mg/L) and Model Results for Ca, Fe, K, Li, Mg, and Zr, as a Function of Reaction Progress (mol-glass/kg) Determined for Glass Sample IDF6D6CCC

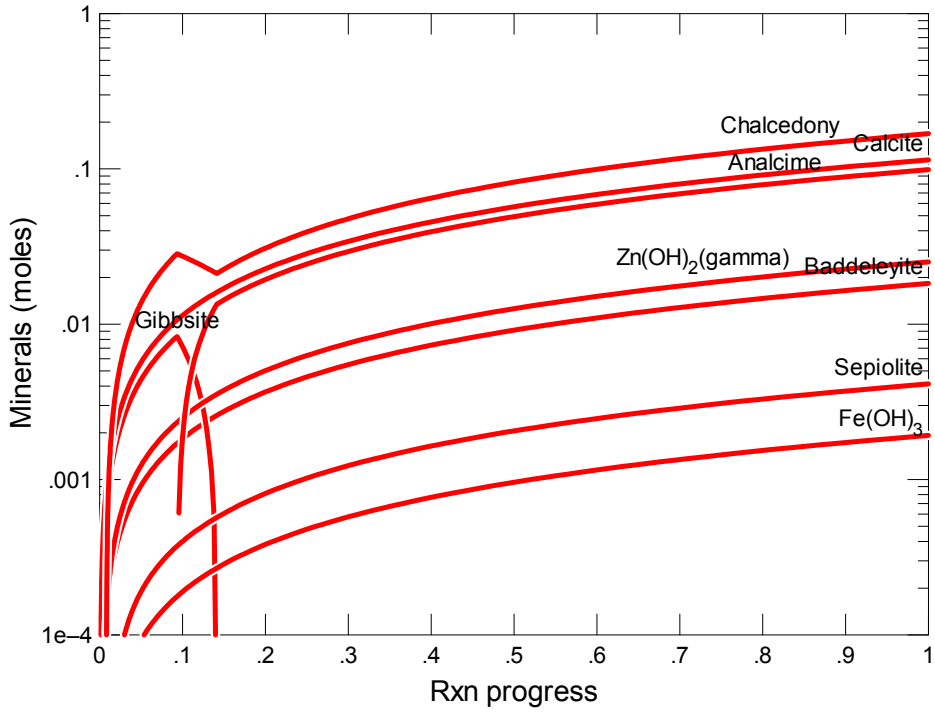


**Figure B.403**. Secondary Phases Calculated to Form as a Function of Reaction Progress (mol-glass/kg) Determined for Glass Sample IDF7E12CCC

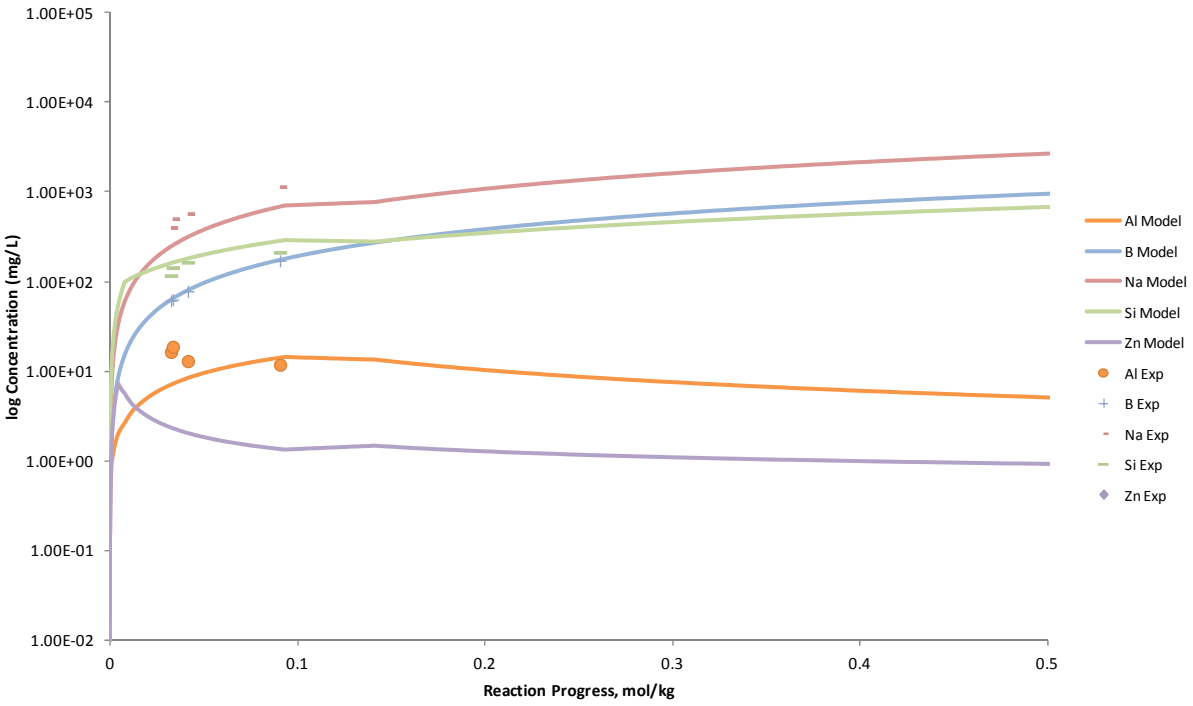


**Figure B.404**. Measured Solution Concentrations (mg/L) and Model Results for Al, B, Na, Si, and Zn, as a Function of Reaction Progress (mol-glass/kg) Determined for Glass Sample IDF7E12CCC

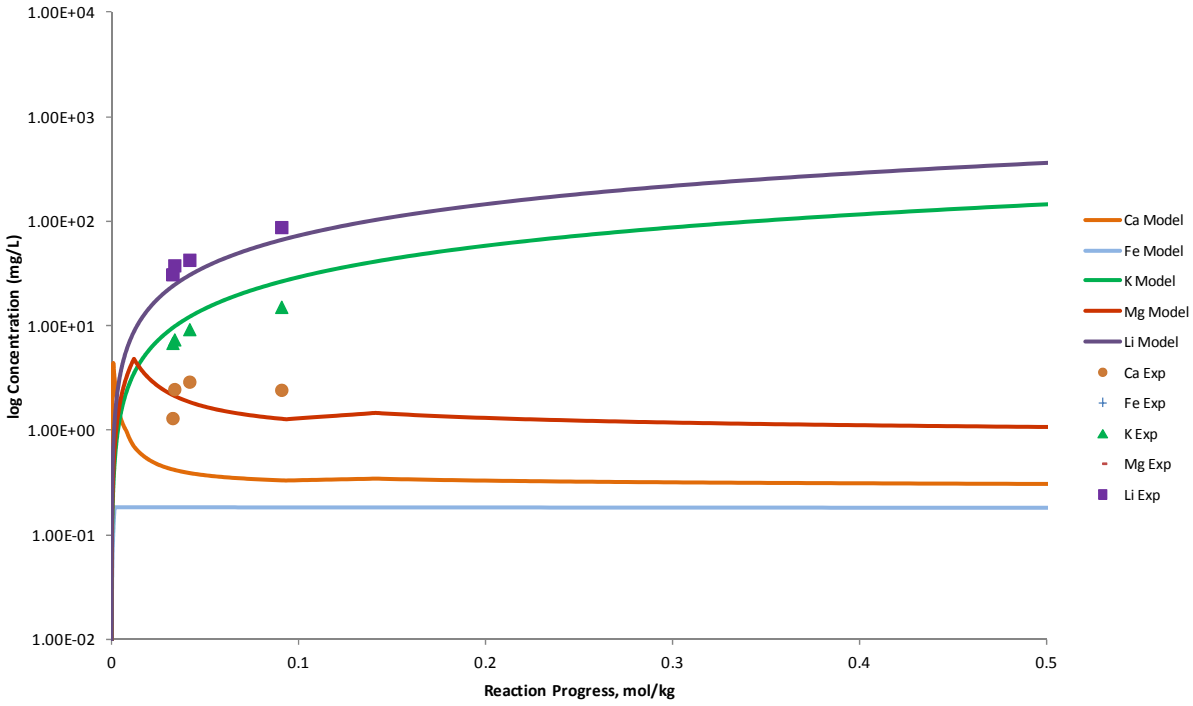


**Figure B.405**. Measured Solution Concentrations (mg/L) and Model Results for Ca, Fe, K, Li, Mg, and Zr, as a Function of Reaction Progress (mol-glass/kg) Determined for Glass Sample IDF7E12CCC

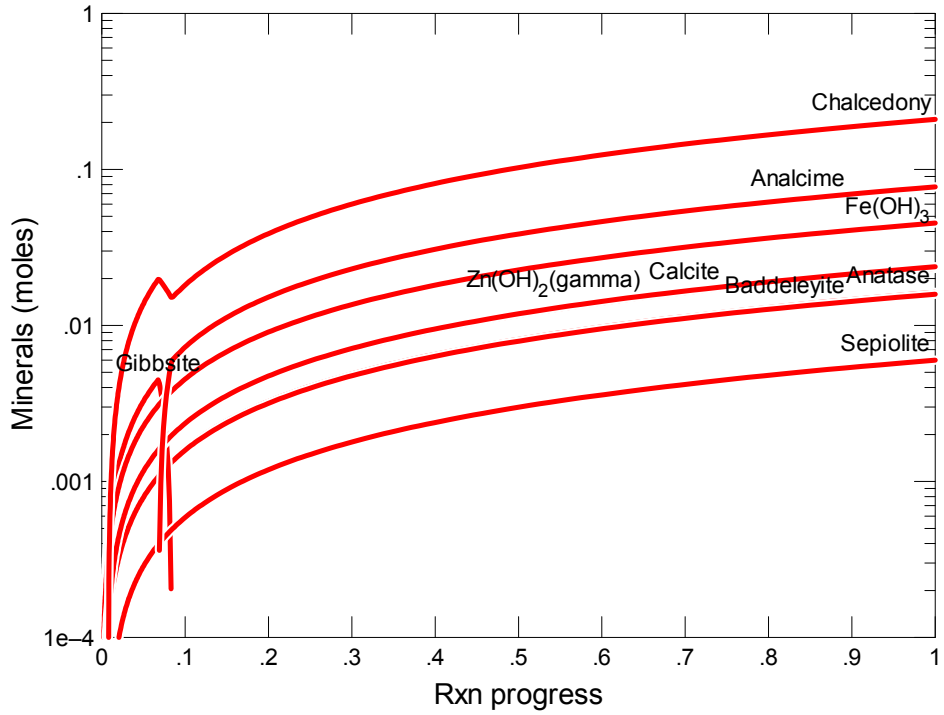


**Figure B.406**. Secondary Phases Calculated to Form as a Function of Reaction Progress (mol-glass/kg) Determined for Glass Sample IDF8A125CCC

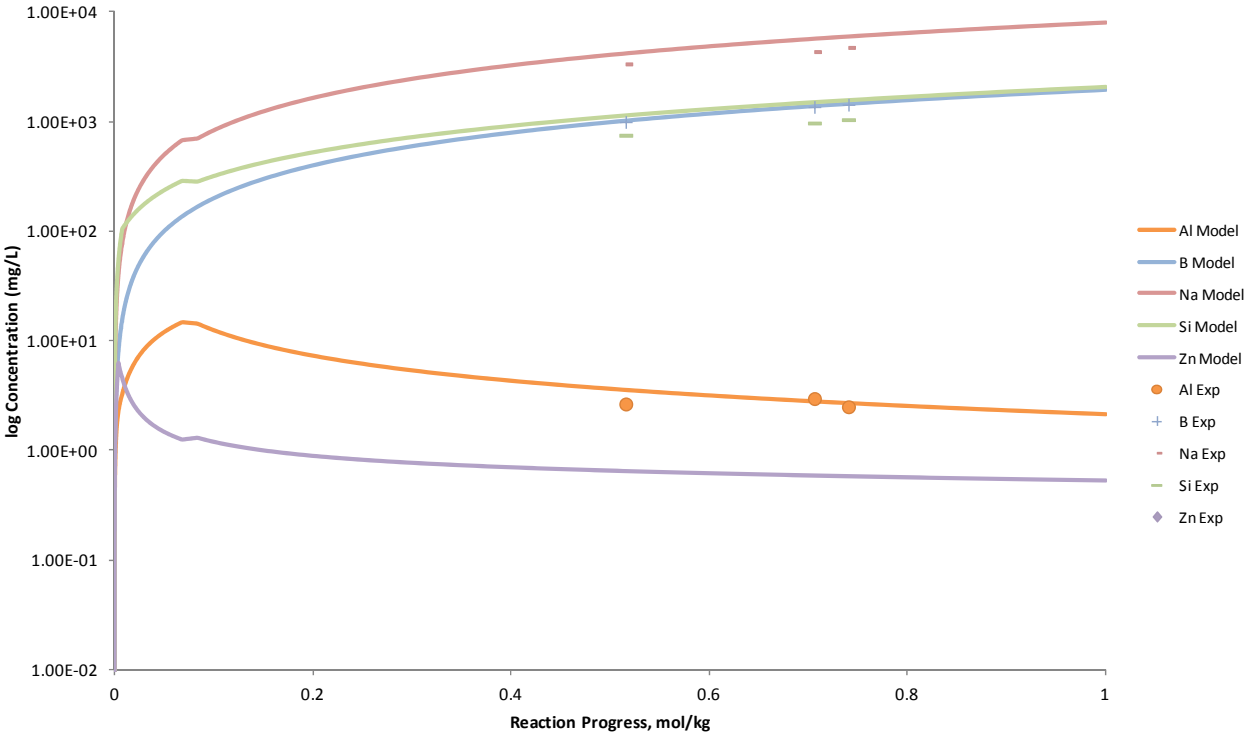


**Figure B.407**. Measured Solution Concentrations (mg/L) and Model Results for Al, B, Na, Si, and Zn, as a Function of Reaction Progress (mol-glass/kg) Determined for Glass Sample IDF8A125CCC

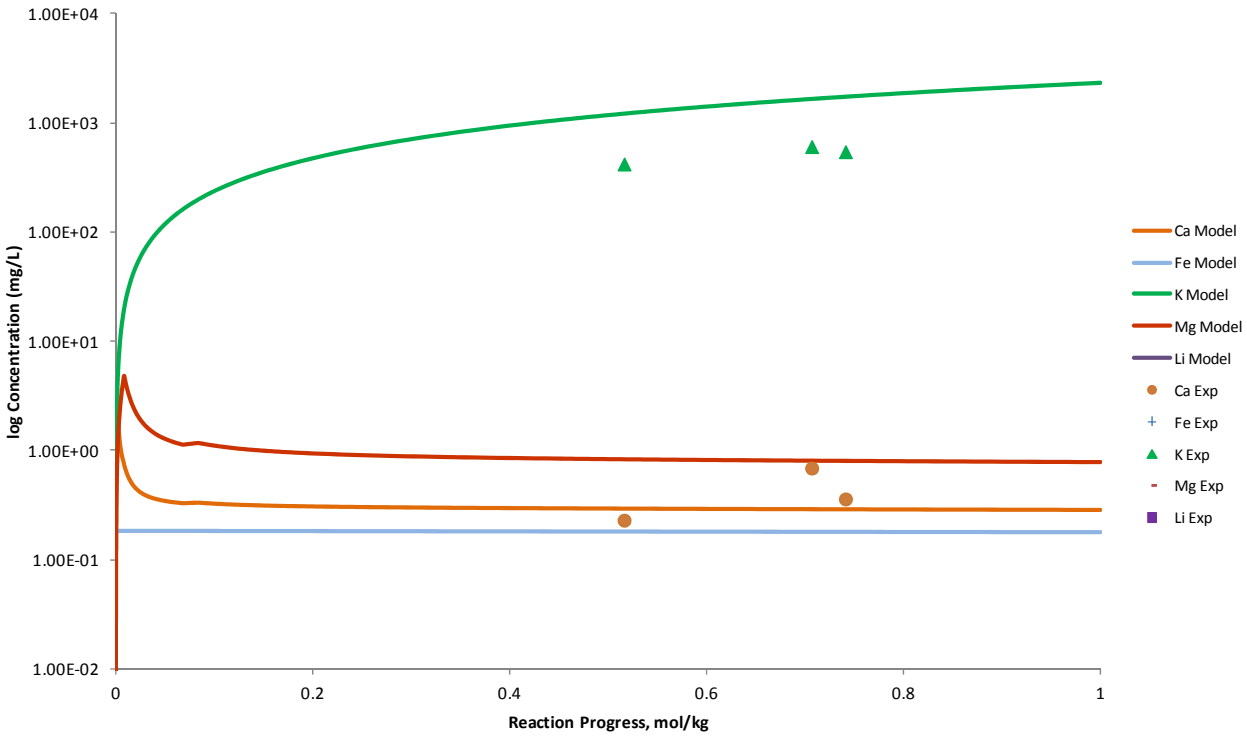


**Figure B.408**. Measured Solution Concentrations (mg/L) and Model Results for Ca, Fe, K, Li, Mg, and Zr, as a Function of Reaction Progress (mol-glass/kg) Determined for Glass Sample IDF8A125CCC

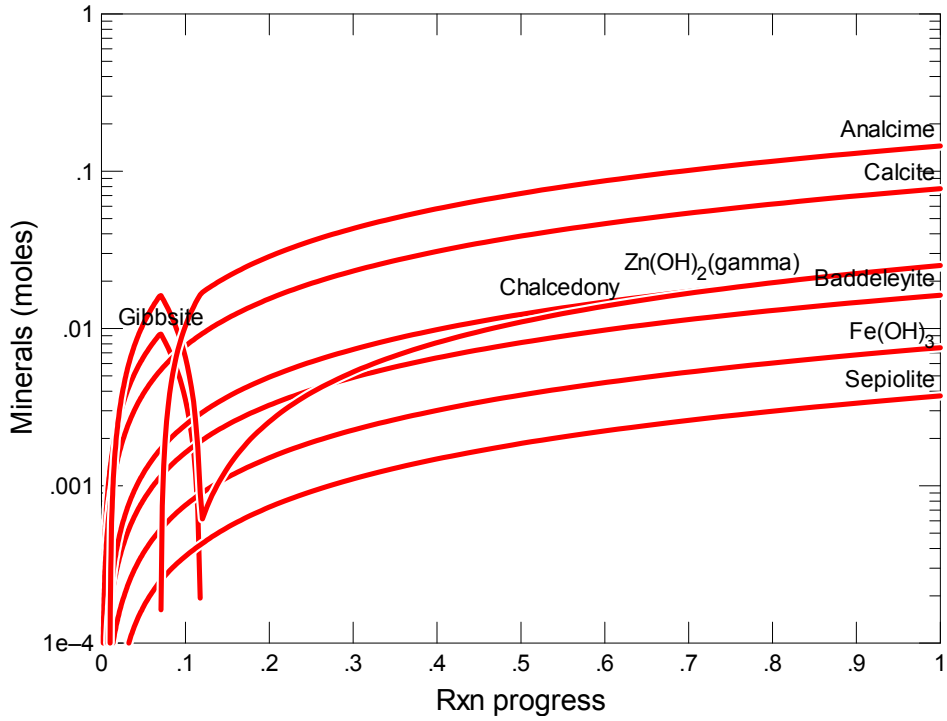


**Figure B.409**. Secondary Phases Calculated to Form as a Function of Reaction Progress (mol-glass/kg) Determined for Glass Sample IDF9A187CCC

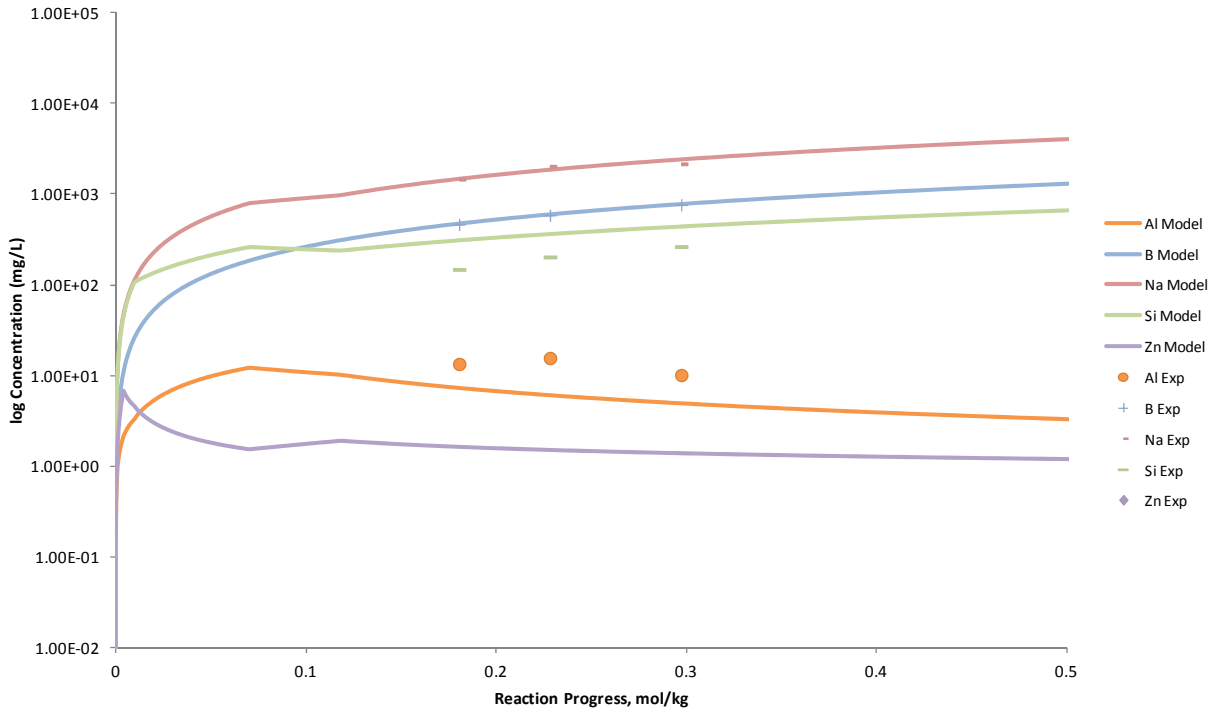


**Figure B.410**. Measured Solution Concentrations (mg/L) and Model Results for Al, B, Na, Si, and Zn, as a Function of Reaction Progress (mol-glass/kg) Determined for Glass Sample IDF9A187CCC

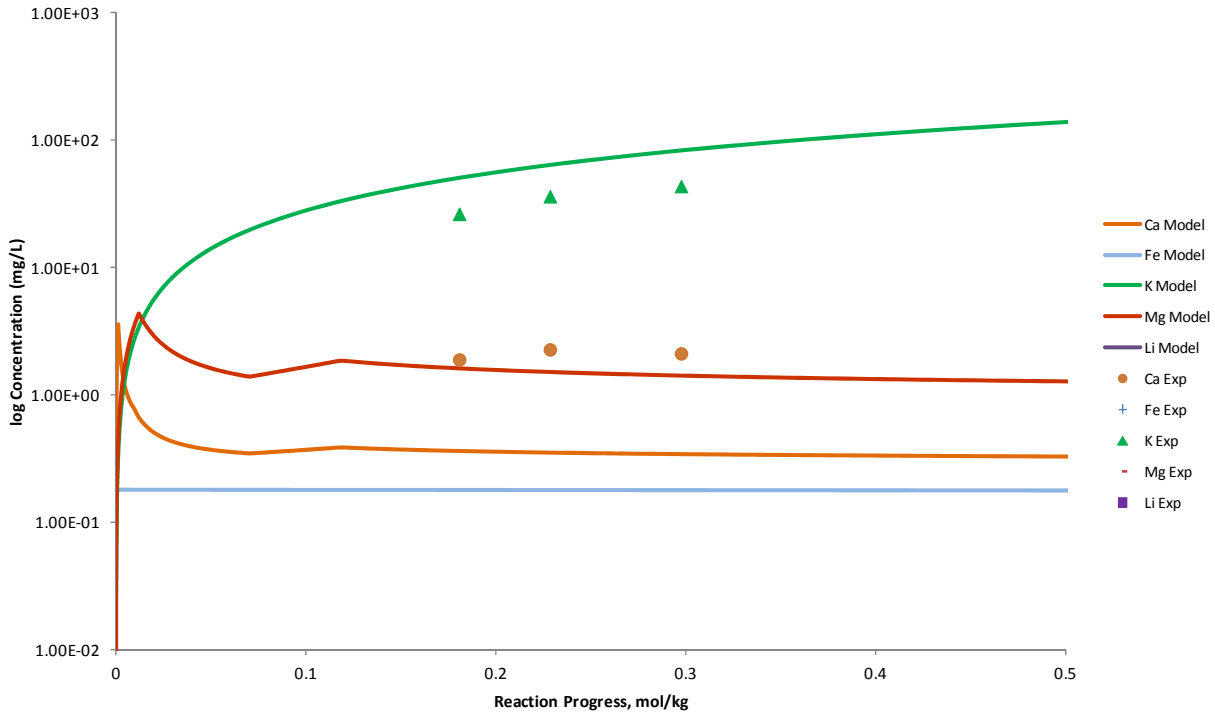


**Figure B.411**. Measured Solution Concentrations (mg/L) and Model Results for Ca, Fe, K, Li, Mg, and Zr, as a Function of Reaction Progress (mol-glass/kg) Determined for Glass Sample IDF9A187CCC

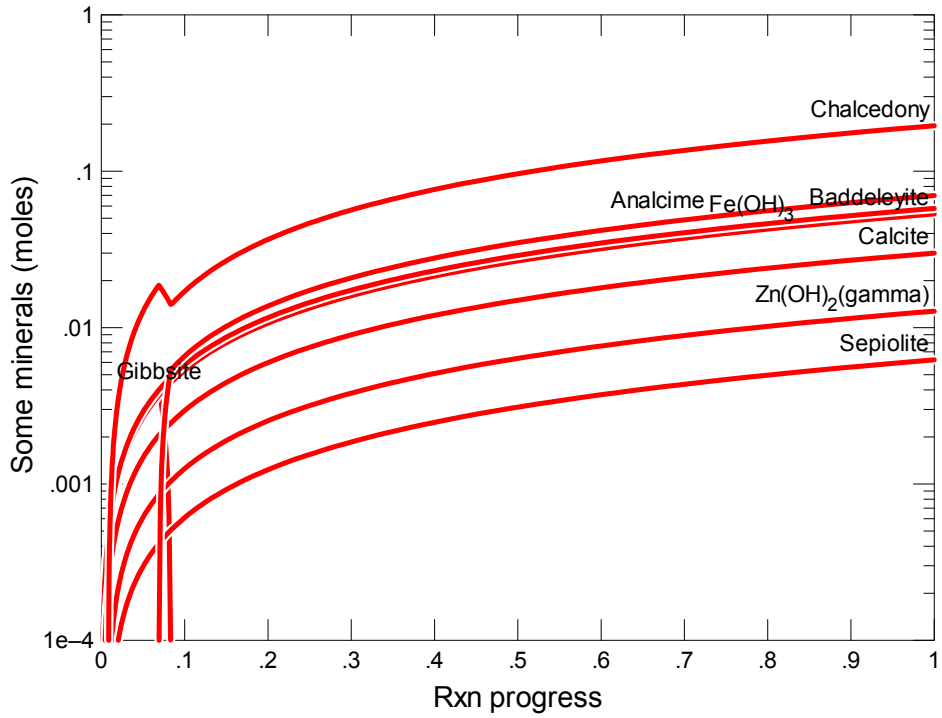


**Figure B.412**. Secondary Phases Calculated to Form as a Function of Reaction Progress (mol-glass/kg) Determined for Glass Sample IDF10Zr6CCC

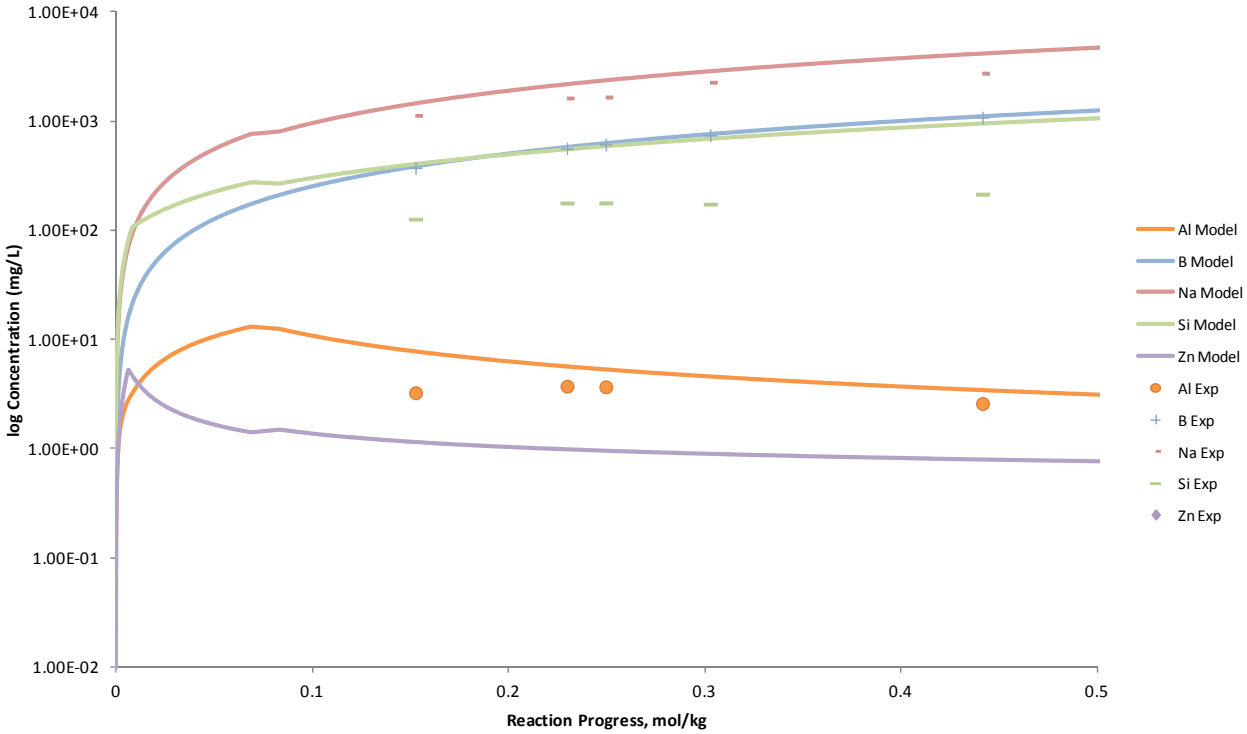


**Figure B.413**. Measured Solution Concentrations (mg/L) and Model Results for Al, B, Na, Si, and Zn, as a Function of Reaction Progress (mol-glass/kg) Determined for Glass Sample IDF10Zr6CCC

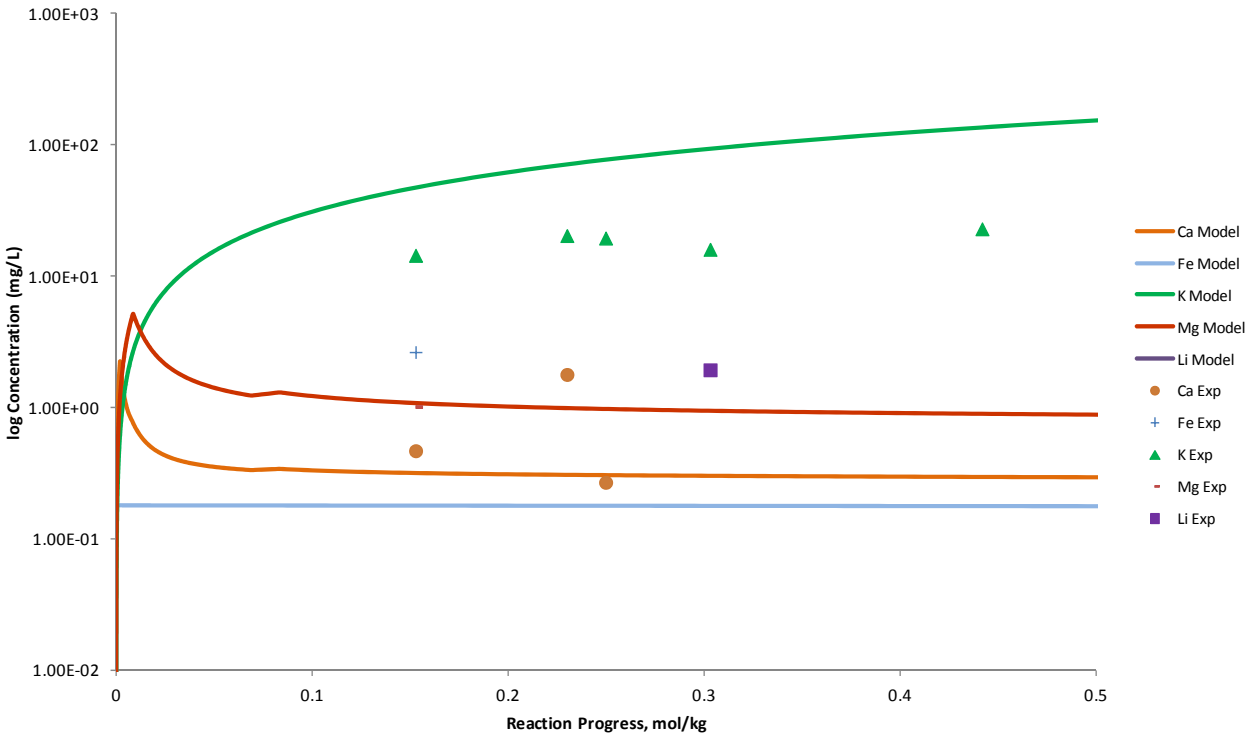


**Figure B.414**. Measured Solution Concentrations (mg/L) and Model Results for Ca, Fe, K, Li, Mg, and Zr, as a Function of Reaction Progress (mol-glass/kg) Determined for Glass Sample IDF10Zr6CCC

# Distribution

**No. of Copies**

**OFFSITE**

EM Pierce
Building 1505, MS 6038
Oak Ridge National Laboratory
P.O. Box 2008
Oak Ridge, TN 37831-6038

3 **Washington River Protection Solutions, LLC**

| | |
|---|---|
| WG Ramsey | B1-55 |
| DJ Swanberg | B1-55 |
| LE Thompson | E6-20 |

**No. of Copies**

**ONSITE**

8 **Pacific Northwest National Laboratory**

| | |
|---|---|
| DH Bacon | K9-33 |
| SD Burton | K8-98 |
| KJ Cantrell | K6-81 |
| VL Freedman | K9-36 |
| SN Kerisit | K8-96 |
| RJ Serne | K6-81 |
| MM Valenta | P7-54 |
| JH Westsik, Jr. | K7-15 |

Pacific Northwest
NATIONAL LABORATORY

U.S. DEPARTMENT OF
ENERGY

*Proudly Operated by* Battelle *Since 1965*

902 Battelle Boulevard
P.O. Box 999
Richland, WA 99352
1-888-375-PNNL (7665)
www.pnnl.gov